
HYDRODYNAMICS – ADVANCED TOPICS

Edited by **Harry Edmar Schulz,**
André Luiz Andrade Simões
and **Raquel Jahara Lobosco**

INTECHWEB.ORG

Hydrodynamics – Advanced Topics

Edited by Harry Edmar Schulz, André Luiz Andrade Simões and Raquel Jahara Lobosco

Published by InTech

Janeza Trdine 9, 51000 Rijeka, Croatia

Copyright © 2011 InTech

All chapters are Open Access distributed under the Creative Commons Attribution 3.0 license, which allows users to download, copy and build upon published articles even for commercial purposes, as long as the author and publisher are properly credited, which ensures maximum dissemination and a wider impact of our publications. After this work has been published by InTech, authors have the right to republish it, in whole or part, in any publication of which they are the author, and to make other personal use of the work. Any republication, referencing or personal use of the work must explicitly identify the original source.

As for readers, this license allows users to download, copy and build upon published chapters even for commercial purposes, as long as the author and publisher are properly credited, which ensures maximum dissemination and a wider impact of our publications.

Notice

Statements and opinions expressed in the chapters are these of the individual contributors and not necessarily those of the editors or publisher. No responsibility is accepted for the accuracy of information contained in the published chapters. The publisher assumes no responsibility for any damage or injury to persons or property arising out of the use of any materials, instructions, methods or ideas contained in the book.

Publishing Process Manager Bojana Zelenika

Technical Editor Teodora Smiljanic

Cover Designer InTech Design Team

Image Copyright André Luiz Andrade Simões, 2011.

First published December, 2011

Printed in Croatia

A free online edition of this book is available at www.intechopen.com

Additional hard copies can be obtained from orders@intechweb.org

Hydrodynamics – Advanced Topics,

Edited by Harry Edmar Schulz, André Luiz Andrade Simões and Raquel Jahara Lobosco

p. cm.

ISBN 978-953-307-596-9

INTECH OPEN ACCESS
PUBLISHER

INTECH open

free online editions of InTech
Books and Journals can be found at
www.intechopen.com

Contents

Preface IX

Part 1 Mathematical Models in Fluid Mechanics 1

- Chapter 1 **One Dimensional Turbulent Transfer Using Random Square Waves – Scalar/Velocity and Velocity/Velocity Interactions 3**
H. E. Schulz, G. B. Lopes Júnior,
A. L. A. Simões and R. J. Lobosco
- Chapter 2 **Generalized Variational Principle for Dissipative Hydrodynamics: Shear Viscosity from Angular Momentum Relaxation in the Hydrodynamical Description of Continuum Mechanics 35**
German A. Maximov
- Chapter 3 **Nonautonomous Solitons: Applications from Nonlinear Optics to BEC and Hydrodynamics 51**
T. L. Belyaeva and V. N. Serkin
- Chapter 4 **Planar Stokes Flows with Free Boundary 77**
Sergey Chivilikhin and Alexey Amosov
- ### **Part 2 Biological Applications and Biohydrodynamics 93**
- Chapter 5 **Laser-Induced Hydrodynamics in Water and Biotissues Nearby Optical Fiber Tip 95**
V. I. Yusupov, V. M. Chudnovskii and V. N. Bagratashvili
- Chapter 6 **Endocrine Delivery System of NK4, an HGF-Antagonist and Anti-Angiogenic Regulator, for Inhibitions of Tumor Growth, Invasion and Metastasis 119**
Shinya Mizuno and Toshikazu Nakamura

	Part 3 Detailed Experimental Analyses of Fluids and Flows	143
Chapter 7	Microrheology of Complex Fluids	145
	Laura J. Bonales, Armando Maestro, Ramón G. Rubio and Francisco Ortega	
Chapter 8	Hydrodynamics Influence on Particles Formation Using SAS Process	169
	A. Montes, A. Tenorio, M. D. Gordillo, C. Pereyra and E. J. Martinez de la Ossa	
Chapter 9	Rotational Dynamics of Nonpolar and Dipolar Molecules in Polar and Binary Solvent Mixtures	185
	Sanjeev R. Inamdar	
Chapter 10	Flow Instabilities in Mechanically Agitated Stirred Vessels	227
	Chiara Galletti and Elisabetta Brunazzi	
Chapter 11	Hydrodynamic Properties of Aggregates with Complex Structure	251
	Lech Gmachowski	
	Part 4 Radiation-, Electro-, Magnetohydrodynamics and Magnetorheology	267
Chapter 12	Electro-Hydrodynamics of Micro-Discharges in Gases at Atmospheric Pressure	269
	O. Eichwald, M. Yousfi, O. Ducasse, N. Merbahi, J.P. Sarrette, M. Meziane and M. Benhenni	
Chapter 13	An IMEX Method for the Euler Equations that Posses Strong Non-Linear Heat Conduction and Stiff Source Terms (Radiation Hydrodynamics)	293
	Samet Y. Kadioglu and Dana A. Knoll	
Chapter 14	Hydrodynamics on Charged Superparamagnetic Microparticles in Water Suspension: Effects of Low-Confinement Conditions and Electrostatics Interactions	319
	P. Domínguez-García and M.A. Rubio	
Chapter 15	Magnetohydrodynamics of Metallic Foil Electrical Explosion and Magnetically Driven Quasi-Isentropic Compression	347
	Guiji Wang, Jianheng Zhao, Binqiang Luo and Jihao Jiang	

Part 5 Special Topics on Simulations and Experimental Data 379

- Chapter 16 **Hydrodynamics of a Droplet in Space 381**
Hitoshi Miura
- Chapter 17 **Flow Evolution Mechanisms of Lid-Driven Cavities 411**
José Rafael Toro and Sergio Pedraza R.
- Chapter 18 **Elasto-Hydrodynamics of
Quasicrystals and Its Applications 429**
Tian You Fan and Zhi Yi Tang

Preface

“Water is the beginning of everything” (Tales of Mile to)

“Air is the beginning of everything” (Anaxagoras of Mile to)

Introduction

Why is it important to study Hydrodynamics? The answer may be strictly technical, but it may also involve some kind of human feeling about our environment and our (eventual) limitations to deal with its fluidic constituents.

As teachers, when talking to our students about the importance of quantifying fluids, we (authors) go to the blackboard and draw, in blue color, a small circumference in the center of the board, and add the obvious name 'Earth'. Some words are then said, in the sense that Hydrodynamics is important, because we are beings strictly adapted to live immersed in a fluidic environment (air), and because we are beings composed basically by simple fluidic solutions (water solutions), encapsulated in fine carbon membranes. Then, with a red chalk, we draw two crosses: one inside and the other outside the circumference, explaining: “our environment is very limited. We can only survive in the space covered by the blue line. No one of us can survive in the inner part of this sphere, or in the outer space. Despite all films, games, and books about contacts with aliens, and endless journeys across the universe, our present knowledge only allows to suggest that it is most probable that the human being will extinct while in this fine fluid membrane, than to create sustainable artificial environments in the cosmos”.

Sometimes, to add some drama, we project the known image of the earth on a wall (the image of the blue sphere), and then we blow a soap bubble explaining that the image gives the false impression that the entire sphere is our home. But our “home” is better represented by the liquid film of the soap bubble (only the film) and then we touch the bubble, exploding it, showing its fragility.

In the sequence, we explain that a first reason to understand fluids would be, then, to guarantee the maintenance of the fluidic environment (the film) so that we could also guarantee our survival as much as possible. Further, as we move ourselves and produce our things immersed in fluid, it is interesting to optimize such operations in order to facilitate our survival. Still further, because our organisms interchange heat

and mass in cellular and corporal scales between different fluids, the understanding of these transports permits us to understand the spreading of diseases, the delivering of medicines to cells, and the use of physical properties of fluids in internal treatments. Thus, understanding these transports allows us to improve our quality of life. Finally, the observation of the inner part of the sphere, the outer space and its constituents, shows that many “highly energetic” phenomena behave like the fluids around us. It gives us the hope that the knowledge of fluids can help, in the future, to quantify, reproduce, control and use energy sources similar to those of the stars, allowing us to “move through the cosmos”, to create sustainable artificial environments and to leave this “limited film” when necessary. Of course, this “speech” may be viewed as a sort of escapism, related to a fiction of the future. In fact, the day-by-day activities show that we are spending our time with “more important” things, like fighting among us for the dividends of the next fashion wave (or the next technical wave), the hierarchy among nations, or the hierarchy of the cultures of the different nations. So, fighters, warriors, or generals still seem to be the agents that write our history. But global survival, or, in other words, the guarantee of any future history, will need other agents, devoted to other activities. The hope lies on the generation of knowledge, in which the knowledge about fluids is vital.

Context of the present book “Hydrodynamics - Advanced Topics”

A quick search in virtual book stores may result in more than one hundred titles involving the word “Hydrodynamics”. Considering the superposition existing with Fluid Mechanics, the number of titles grows much more. Considering all these titles, why try to organize another book on Hydrodynamics? One answer could be that the researchers always try new points of view to understand and treat the problems related to Hydrodynamics. Even a much known phenomenon may be re-explained from a point of view that introduces different tools (conceptual, numerical or practical) into the discussion of fluids. And eventually, a detail shows to be useful, or even very relevant. So, it is necessary to give the opportunity for the different authors to expose their points of view.

Among the historically relevant books on Hydrodynamics, some should be mentioned here. For example, the volumes “Hydrodynamics” and “Hydraulics”, by Daniel Bernoulli (1738) and his father, Johann Bernoulli (1743) present many interesting sketches and the analyses that converged to the so called “Bernoulli equation”, later deduced more properly by Leonhard Euler. Although there are unpleasant questions about the authorship of the main ideas, as pointed out by Rouse (1967) and Calero (2008), both books are placed in a “prominent position” in history, because of their significant contributions. The volume written by Sir Horace Lamb (1879), now named “Hydrodynamics”, considers the basic equations, the vortex motion, and tidal waves, among other interesting topics. Considering the classical equations and procedures followed to study fluid motion, the books “Fundamentals of Hydro and Aerodynamics” and “Applied Hydro and Aerodynamics” by Prandtl and Tietjens (1934) present the theory and its practical applications in a comprehensive way,

influencing the experimental procedures for several decades. For over fifty years, the classical volume of Landau and Lifschitz (1959) remains an extremely valuable work for researchers in fluid mechanics.

In addition to the usual themes, like the basic equations and turbulence, this book also covers themes like the relativistic fluid dynamics and the dynamics of superfluids. Each of the major topics considered in the studies of fluid mechanics can be widely discussed, generating specific texts and books. An example is the theory of boundary layers, in which the book of Schlichting (1951) has been considered an indispensable reference, because it condenses most of the basic concepts on this subject. Further, still considering specific topics, Stoker (1957) and Lighthill (1978) wrote about waves in fluids, while Chandrasekhar (1961) and Drazin and Reid (1981) considered hydrodynamic and hydromagnetic stability. It is also necessary to mention the books of Batchelor (1953), Hinze (1958), and Monin and Yaglom (1965), which are notable examples of texts on turbulence and statistical fluid mechanics, showing basic concepts and comparative studies between theory and experimental data. A more recent example may be the volume written by Kundu e Cohen (2008), which furnishes a chapter on "biofluid mechanics". The list of the "relevant books" is obviously not complete, and grows continuously, because new ideas are continuously added to the existing knowledge.

The present book is one of the results of a project that generated three volumes, in which recent studies on Hydrodynamics are described. The remaining two titles are "Hydrodynamics - Natural Water Bodies", and "Hydrodynamics - Optimizing Methods and Tools". Along the chapters of the present volume, the authors show the application of concepts of Hydrodynamics in different fields, using different points of view and methods. The editors thank all authors for their efforts in presenting their chapters and conclusions, and hope that this effort will be welcomed by the professionals working with Hydrodynamics.

The book "Hydrodynamics - Advanced Topics" is organized in the following manner:

Part 1: Mathematical Models in Fluid Mechanics

Part 2: Biological Applications and Biohydrodynamics

Part 3: Detailed Experimental Analyses of Fluids and Flows

Part 4: Radiation-, Electro-, Magneto-hydrodynamics and Magnetorheology

Part 5: Special Topics on Simulations and Experimental Data

Hydrodynamics is a very rich area of study, involving some of the most intriguing theoretical problems, considering our present level of knowledge. General nonlinear solutions, closed statistical equations, explanation of sudden changes, for example, are wanted in different areas of research, being also a matter of study in Hydromechanics. Further, any solution in this field depends on many factors, or many "boundary conditions". The changing of the boundary conditions is one of the ways through which the human being affects its fluidic environment. Changes in a specific site can impose catastrophic consequences in a whole region. For example, the permanent leakage of petroleum in one point in the ocean may affect the life along the entire

region covered by the marine currents that transport this oil. Gases or liquids, the changes in the quality of the fluids in which we live, certainly affect our quality of life.

The knowledge about fluids, their movements, and their ability to transport physical properties and compounds is thus recognized as important for life. As a consequence, thinking about new solutions for general or specific problems in Hydromechanics may help to attain a sustainable relationship with our environment. Re-contextualizing the classical discussion about the truth, in which it was suggested that the “thinking” is the guarantee of our “existence” (St. Augustine, 386a, b, 400), we can say that we agree that thinking guarantees the human existence, and that there are too many warriors, and too few thinkers. Following this re-contextualized sense, it was also said that the man is a bridge between the “animal” and “something beyond the man” (Nietzsche, 1883). This is an interesting metaphor, because bridges are built crossing fluids (even abysms are filled with fluids). Considering all possible interpretations of this phrase, let us study and understand the fluids, and let us help to build the bridge.

Dr. Harry Edmar Schulz

Nucleus of Thermal Engineering and Fluids,
Department of Hydraulics and Sanitary Engineering,
School of engineering at Sao Carlos,
University of Sao Paulo,
Brazil

Dr. Andre Luiz Andrade Simoes

Laboratory of Turbulence and Rheology,
Department of Hydraulics and Sanitary Engineering,
School of engineering at Sao Carlos,
University of Sao Paulo,
Brazil

Dr. Raquel Jahara Lobosco

Laboratory of Turbulence and Rheology,
Department of Hydraulics and Sanitary Engineering,
School of engineering at Sao Carlos,
University of Sao Paulo,
Brazil

References

- Batchelor, G.K. (1953), The theory of homogeneous turbulence. First published in the Cambridge Monographs on Mechanics and Applied Mathematics series 1953. Reissued in the Cambridge Science Classics series 1982 (ISBN: 0 521 04117 1).
- Bernoulli, D. (1738), Hydrodynamics. Dover Publications, Inc., Mineola, New York, 1968 (first publication) and reissued in 2005, ISBN-10: 0486441857.

- Hydrodynamica, by Daniel Bernoulli, as published by Johann Reinhold Dulsecker at Strassburg in 1738.
- Bernoulli, J. (1743), *Hydraulics*. Dover Publications, Inc., Mineola, New York, 1968 (first publication) and reissued in 2005, ISBN-10: 0486441857. *Hydraulica*, by Johann Bernoulli, as published by Marc-Michel Bousquet et Cie. at Lausanne and Geneva in 1743.
- Calero, J.S. (2008), *The genesis of fluid mechanics (1640-1780)*. Springer, ISBN 978-1-4020-6413-5. Original title: *La génesis de la Mecánica de los Fluidos (1640-1780)*, UNED, Madrid, 1996.
- Chandrasekhar, S. (1961), *Hydrodynamic and Hydromagnetic Stability*. Clarendon Press edition, 1961. Dover edition, first published in 1981 (ISBN: 0-486-64071-X).
- Drazin, P.G. & Reid, W.H. (1981), *Hydrodynamic stability*. Cambridge University Press (second edition 2004). (ISBN: 0 521 52541 1).
- Hinze, J.O. (1959), *Turbulence*. McGraw-Hill, Inc. second edition, 1975 (ISBN:0-07-029037-7).
- Kundu, P.K. & Cohen, I.M. (2008), *Fluid Mechanics*. 4th ed. With contributions by P.S. Ayyaswamy and H.H. Hu. Elsevier/Academic Press (ISBN 978-0-12-373735-9).
- Lamb, H. (1879), *Hydrodynamics* (Regarded as the sixth edition of a *Treatise on the Mathematical Theory of the Motion of Fluids*, published in 1879). Dover Publications, New York., sixth edition, 1993 (ISBN-10: 0486602567).
- Landau, L.D.; Lifschitz, E.M. (1959), *Fluid Mechanics*. Course of theoretical Physics, Volume 6. Second edition 1987 (Reprint with corrections 2006). Elsevier (ISBN-10: 0750627670).
- Lighthill, J. (1978), *Waves in Fluids*. Cambridge University Press, Reissued in the Cambridge Mathematical Library series 2001, Third printing 2005 (ISBN-10: 0521010454).
- Monin, A.S. & Yaglom, A.M. (1965), *Statistical fluid mechanics: mechanics of turbulence*. Originally published in 1965 by Nauka Press, Moscow, under the title *Statisticheskaya Gidromekhanika-Mekhanika Turbulentnosti*. Dover edition, first published in 2007. Volume 1 and Volume 2.
- St. Augustine (386a), *Contra Academicos*, in Abbagnano, N. (2007), *Dictionary of Philosophy, "Cogito"*, Martins Fontes, Brasil (Text in Portuguese).
- St. Augustine (386b), *Soliloquia*, in Abbagnano, N. (2007), *Dictionary of Philosophy, "Cogito"*, Martins Fontes, Brasil (Text in Portuguese).
- St. Augustine (400-416), *De Trinitate*, in Abbagnano, N. (2007), *Dictionary of Philosophy, "Cogito"*, Martins Fontes, Brasil (Text in Portuguese).
- Nietzsche, F. (1883), *Also sprach Zarathustra*, Publicações Europa-América, Portugal (Text in Portuguese, Ed. 1978).
- Rouse, H. (1967). Preface to the english translation of the books *Hydrodynamics and Hydraulics*, already mentioned in this list. Dover Publications, Inc.
- Prandtl, L. & Tietjens, O.G. (1934) *Fundamentals of Hydro & Aeromechanics*, Dover Publications, Inc. Ed. 1957.

Prandtl, L. & Tietjens, O.G. (1934) Applied Hydro & Aeromechanics, Dover Publications, Inc. Ed. 1957.

Schlichting, H. (1951), Grenzschicht-Theorie. Karlsruhe: Verlag und Druck.

Stoker, J.J. (1957). Water waves: the mathematical theory with applications. Interscience Publishers, New York (ISBN-10: 0471570346).

Part 1

Mathematical Models in Fluid Mechanics

One Dimensional Turbulent Transfer Using Random Square Waves – Scalar/Velocity and Velocity/Velocity Interactions

H. E. Schulz^{1,2}, G. B. Lopes Júnior², A. L. A. Simões² and R. J. Lobosco²

¹*Nucleus of Thermal Engineering and Fluids*

²*Department of Hydraulics and Sanitary Engineering School of Engineering of São Carlos, University of São Paulo Brazil*

1. Introduction

The mathematical treatment of phenomena that oscillate randomly in space and time, generating the so called “statistical governing equations”, is still a difficult task for scientists and engineers. Turbulence in fluids is an example of such phenomena, which has great influence on the transport of physical proprieties by the fluids, but which statistical quantification is still strongly based on *ad hoc* models. In turbulent flows, parameters like velocity, temperature and mass concentration oscillate continuously in turbulent fluids, but their detailed behavior, considering all the possible time and space scales, has been considered difficult to be reproduced mathematically since the very beginning of the studies on turbulence. So, statistical equations were proposed and refined by several authors, aiming to describe the evolution of the “mean values” of the different parameters (see a description, for example, in Monin & Yaglom, 1979, 1981).

The governing equations of fluid motion are nonlinear. This characteristic imposes that the classical statistical description of turbulence, in which the oscillating parameters are separated into mean functions and fluctuations, produces new unknown parameters when applied on the original equations. The generation of new variables is known as the “closure problem of statistical turbulence” and, in fact, appears in any phenomena of physical nature that oscillates randomly and whose representation is expressed by nonlinear conservation equations. The closure problem is described in many texts, like Hinze (1959), Monin & Yaglom (1979, 1981), and Pope (2000), and a general form to overcome this difficulty is matter of many studies.

As reported by Schulz et al. (2011a), considering scalar transport in turbulent fluids, an early attempt to theoretically predict RMS profiles of the concentration fluctuations using “ideal random signals” was proposed by Schulz (1985) and Schulz & Schulz (1991). The authors used random square waves to represent concentration oscillations during mass transfer across the air-water interface, and showed that the RMS profile of the concentration fluctuations may be expressed as a function of the mean concentration profile. In other words, the mean concentration profile helps to know the RMS profile. In these studies, the authors did not consider the effect of diffusion, but argued that their

equation furnished an upper limit for the normalized RMS value, which is not reached when diffusion is taken into account.

The random square waves were also used by Schulz et al. (1991) to quantify the so called “intensity of segregation” in the superficial boundary layer formed during mass transport, for which the explanations of segregation scales found in Brodkey (1967) were used. The time constant of the intensity of segregation, as defined in the classical studies of Corrsin (1957, 1964), was used to correlate the mass transfer coefficient across the water surface with more usual parameters, like the Schmidt number and the energy dissipation rate. Random square waves were also applied by Janzen (2006), who used the techniques of Particle Image Velocimetry (PIV) and Laser Induced Fluorescence (LIF) to study the mass transfer at the air-water interface, and compared his measurements with the predictions of Schulz & Schulz (1991) employing *ad hoc* concentration profiles. Further, Schulz & Janzen (2009) confirmed the upper limit for the normalized RMS of the concentration fluctuations by taking into account the effect of diffusion, also evaluating the thickness of diffusive layers and the role of diffusive and turbulent transports in boundary layers. A more detailed theoretical relationship for the RMS of the concentration fluctuation showed that several different statistical profiles of turbulent mass transfer may be interrelated.

Intending to present the methodology in a more organized manner, Schulz et al. (2011a) showed a way to “model” the records of velocity and mass concentration (that is, to represent them in an *a priori* simplified form) for a problem of mass transport at gas-liquid interfaces. The fluctuations of these variables were expressed through the so called “partition, reduction, and superposition functions”, which were defined to simplify the oscillating records. As a consequence, a finite number of basic parameters was used to express all the statistical quantities of the equations of the problem in question. The extension of this approximation to different Transport Phenomena equations is demonstrated in the present study, in which the mentioned statistical functions are derived for general scalar transport (called here “scalar-velocity interactions”). A first application for velocity fields is also shown (called here “velocity-velocity interactions”). A useful consequence of this methodology is that it allows to “close” the turbulence equations, because the number of equations is bounded by the number of basic parameters used. In this chapter we show 1) the *a priori* modeling (simplified representation) of the records of turbulent variables, presenting the basic definitions used in the random square wave approximation (following Schulz et al., 2011a); 2) the generation of the usual statistical quantities considering the random square wave approximation (scalar-velocity interactions); 3) the application of the methodology to a one-dimensional scalar transport problem, generating a closed set of equations easy to be solved with simple numerical resources; and 4) the extension of the study of Schulz & Johannes (2009) to velocity fields (velocity-velocity interactions).

Because the method considers primarily the oscillatory records itself (*a priori* analysis), and not phenomenological aspects related to physical peculiarities (*a posteriori* analysis, like the definition of a turbulent viscosity and the use of turbulent kinetic energy and its dissipation rate), it is applicable to any phenomenon with oscillatory characteristics.

2. Scalar-velocity interactions

2.1 Governing equations for transport of scalars: Unclosed statistical set

The turbulent transfer equations for a scalar F are usually expressed as

$$\frac{\partial \bar{F}}{\partial t} + \bar{V}_i \frac{\partial \bar{F}}{\partial x_i} = \frac{\partial}{\partial x_i} \left(D_F \frac{\partial \bar{F}}{\partial x_i} - \overline{v_i f} \right) + \bar{g}, \quad i = 1, 2, 3. \quad (1)$$

where \bar{F} and f are the mean scalar function and the scalar fluctuation, respectively. \bar{V}_i ($i = 1, 2, 3$) are mean velocities and v_i are velocity fluctuations, t is the time, x_i are the Cartesian coordinates, \bar{g} represents the scalar sources and sinks and D_F is the diffusivity coefficient of F . For one-dimensional transfer, without mean movements and generation/consumption of F , equation (1) with $x_3=z$ and $v_3=\omega$ is simplified to

$$\frac{\partial \bar{F}}{\partial t} = \frac{\partial}{\partial z} \left(D_F \frac{\partial \bar{F}}{\partial z} - \overline{\omega f} \right) \quad (2)$$

As can be seen, a second variable, given by the mean product $\overline{\omega f}$, is added to the equation of \bar{F} , so that a second equation involving $\overline{\omega f}$ and \bar{F} is needed to obtain solutions for both variables. Additional statistical equations may be generated averaging the product between equation (1) and the instantaneous fluctuations elevated to some power (f^θ). As any new equation adds new unknown statistical products to the problem, the resulting system is never closed, so that no complete solution is obtained following strictly statistical procedures (closure problem). Studies on turbulence consider a low number of statistical equations (involving only the first statistical moments), together with additional equations based on *ad hoc* models that close the systems. This procedure seems to be the most natural choice, because having already obtained equation (2), it remains to model the new parcel $\overline{\omega f}$ *a posteriori* (that is, introducing hypotheses and definitions to solve it). An example is the combined use of the Boussinesq hypothesis (in which the turbulent viscosity/diffusivity is defined) with the Komogoroff reasoning about the relevance of the turbulent kinetic energy and its dissipation rate. The $\kappa - \varepsilon$ model for statistical turbulence is then obtained, for which two new statistical equations are generated, one of them for k and the other for ε . Of course, new unknown parameters appear, but also additional *ad hoc* considerations are made, relating them to already defined variables.

In the present chapter, as done by Schulz et al. (2011a), we do not limit the number of statistical equations based on *a posteriori* definitions for $\overline{\omega f}$. Convenient *a priori* definitions are used on the oscillatory records, obtaining transformed equations for equation (1) and additional equations. The central moments of the scalar fluctuations, $\overline{f^\theta} = \overline{[F - \bar{F}]^\theta}$, $\theta = 1, 2, 3, \dots$ are considered here. For example, the one-dimensional equations for $\theta=2, 3$ and 4, are given by

$$\frac{1}{2} \frac{\partial \overline{f^2}}{\partial t} + \overline{f \omega} \frac{\partial \bar{F}}{\partial z} + \frac{1}{2} \frac{\partial \overline{f^2 \omega}}{\partial z} = D_F \left(\overline{f \frac{\partial^2 f}{\partial z^2}} \right) \quad (3a)$$

$$\frac{1}{3} \frac{\partial \overline{f^3}}{\partial t} + \overline{f^2} \frac{\partial \bar{F}}{\partial t} + \overline{f^2 \omega} \frac{\partial \bar{F}}{\partial z} + \frac{1}{3} \frac{\partial \overline{\omega f^3}}{\partial z} = D_F \left(\overline{f^2 \frac{\partial^2 \bar{F}}{\partial z^2}} + \overline{f^2 \frac{\partial^2 f}{\partial z^2}} \right) \quad (3b)$$

$$\frac{1}{4} \frac{\partial \overline{f^4}}{\partial t} + \overline{f^3} \frac{\partial \overline{F}}{\partial t} + \overline{f^3 \omega} \frac{\partial \overline{F}}{\partial z} + \frac{1}{4} \frac{\partial \overline{\omega f^4}}{\partial z} = D_F \left(\overline{f^3} \frac{\partial^2 \overline{F}}{\partial z^2} + \overline{f^3} \frac{\partial^2 f}{\partial z^2} \right) \quad (3c)$$

In this example, equation (3a) involves \overline{F} and $\overline{f\omega}$ of equation (2), but adds three new unknowns. The first four equations (2) and (3 a, b, c) already involve eleven different statistical quantities: \overline{F} , $\overline{f^2}$, $\overline{f^3}$, $\overline{f^4}$, $\overline{f\omega}$, $\overline{f^2\omega}$, $\overline{f^3\omega}$, $\overline{f^4\omega}$, $\overline{f \frac{\partial^2 f}{\partial z^2}}$, $\overline{f^2 \frac{\partial^2 f}{\partial z^2}}$, and $\overline{f^3 \frac{\partial^2 f}{\partial z^2}}$, and the “closure” is not possible. The general equation for central moments, for any θ , is given by [20]

$$\frac{1}{\theta} \frac{\partial \overline{f^\theta}}{\partial t} + \overline{f^{\theta-1}} \frac{\partial \overline{F}}{\partial t} + \overline{f^{\theta-1} \omega} \frac{\partial \overline{F}}{\partial z} + \frac{1}{\theta} \frac{\partial \overline{\omega f^\theta}}{\partial z} = D_F \left(\overline{f^{\theta-1}} \frac{\partial^2 \overline{F}}{\partial z^2} + \overline{f^{\theta-1}} \frac{\partial^2 f}{\partial z^2} \right) \quad (3d)$$

(using $\theta=1$ reproduces equation (2)).

As mentioned, the method models the records of the oscillatory variables, using random square waves. The number of equations is limited by the number of the basic parameters defined “a priori”.

2.2 “Modeling” the records of the oscillatory variables

As mentioned in the introduction, the term “modeling” is used here as “representing in a simplified way”. Following Schulz et al. (2011a), consider the function $F(z, t)$ shown in Figure 1. It represents a region of a turbulent fluid in which the scalar quantity F oscillates between two functions F_p (p =previous) and F_n (n =next) in the interval $z_1 < z < z_2$. Turbulence is assumed stationary.

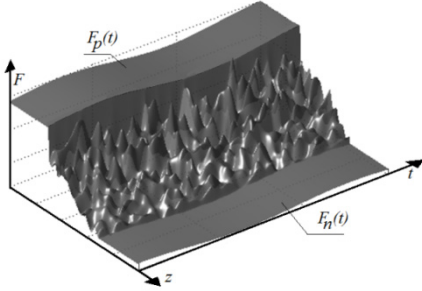


Fig. 1a. A two-dimensional random scalar field F oscillating between the boundary functions $F_p(t)$ and $F_n(t)$.

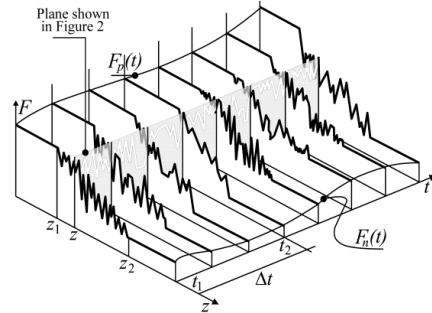


Fig. 1b. Sketch of the region shown in figure (1a). Turbulence is stationary. Adapted from Schulz et al. (2011a)

The time average of $F(z, t)$ for $z_1 < z < z_2$, indicated by $\overline{F}(z, t)$ is defined as usual

$$\overline{F}(z, t) = \frac{1}{\Delta t} \int_{t_1}^{t_2} F(z, t) dt \quad \text{for} \quad z_1 < z < z_2 \quad (4)$$

$\Delta t = t_2 - t_1$ is the time interval for the average operation. Equation (4) generates a mean value $\bar{F}(z)$ for $z_1 < z < z_2$ and $t_1 < t < t_2$. Any statistical quantity present in equations 3, like, for example, the central moments $\overline{f^\theta} = \overline{[F - \bar{F}]^\theta}$, is defined according to equation (4). To simplify notation, both coordinates (z, t) are dropped off in the rest of the text. The method described in the next sections allows to obtain the relevant statistical quantities of the governing equations, like the mean function \bar{F} , using simplified records of F .

2.3 Bimodal square wave: Mean values using a time-partition function for the scalar field - n

The basic assumptions made to “model” the original oscillatory records may be followed considering Figure 2. In this sense, figure 2a is a sketch of the original record of the scalar variable F at a position $z_1 < z < z_2$, as shown in the gray vertical plane of Figure 1. The objective of this analysis is to obtain an equation for the mean function $\bar{F}(z)$ for $t_1 < t < t_2$, which is also shown in figure 2a. The values of the scalar variable during the turbulent transfer are affected by both the advective turbulent movements and diffusion. Discarding diffusion, the value of F would ideally alternate between the limits F_p and F_n (the bimodal square wave), as shown in Figure 2b (the fluid particles would transport only the two mentioned F values). This condition was assumed as a first simplification, but maintaining the correct mean, in which $\bar{F}(z)$ is unchanged. It is known that diffusion induces fluxes governed by F differences between two regions of the fluid (like the Fourier law for heat transfer and the Fick law for mass transfer). These fluxes may significantly lower the amplitude of the oscillations in small patches of fluid, and are taken into account using $F_p - P$ and $F_n + N$ for the two new limiting F values, as shown in Figure 2c. The parcels P and N depend on z .

In other words, the amplitude of the square oscillations is “adjusted” (modeled), in order to approximate it to the mean amplitude of the original record. As can be seen, the aim of the method is not only to evaluate \bar{F} adequately, but also the lower order statistical quantities that depend on the fluctuations, which are relevant to close the statistical equations. The parcels P and N were introduced based on diffusion effects, but any cause that inhibits oscillations justifies these corrective parcels.

The first statistical parameter is represented by n , and is defined as the fraction of the time for which the system is at each of the two F values (equations 5 and 6), being thus named as “partition function”. This function n depends on z and is mathematically defined as

$$n = \frac{t \text{ at } (F_p - P)}{\Delta t \text{ of the observation}} \quad (5)$$

This definition also implies that

$$1 - n = \frac{t \text{ at } (F_n + N)}{\Delta t \text{ of the observation}} \quad (6)$$

\bar{F} remains the same in figures 2a, b and c. The constancy between figures 2b and c is obtained using mass conservation, implying that P and N are related through equation (7):

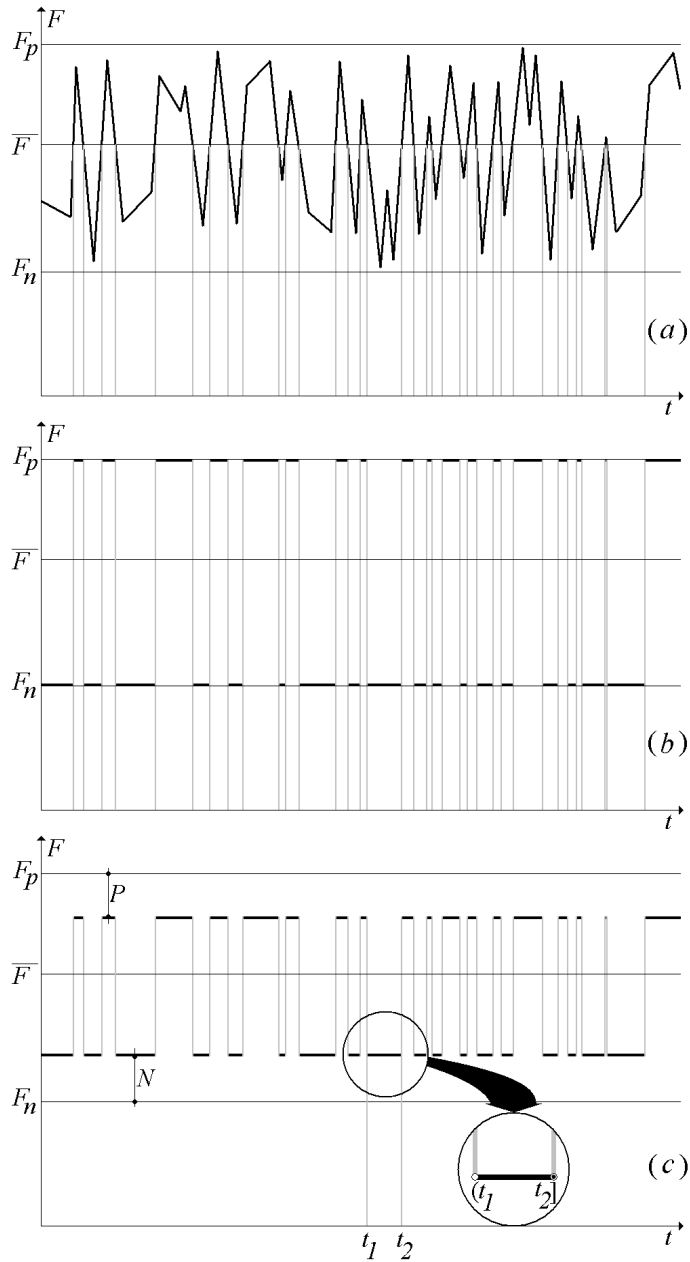


Fig. 2. a) Sketch of the F record of the gray plane of figure 1, at z , b) Simplified record alternating F between F_p and F_n , c) Simplified record with amplitude damping. Upper and lower points do not superpose at the discontinuities (the F segments are open at the left and closed at the right, as shown in the detail).

$$N = \frac{Pn}{(1-n)} \quad (7)$$

The mean value of F is obtained from a weighted average operation between $F_p - P$ and $F_n + N$, using equations (5) through (7). It follows that

$$\bar{F} = nF_p + (1-n)F_n \quad (8)$$

Isolating n , equation (8) leads to

$$n = \frac{\bar{F} - F_n}{F_p - F_n} \quad (9)$$

Thus, the partition function n previously defined by equation (5) coincides with the normalized form of \bar{F} given by equation (9). Note that n is used as weighting factor for any statistical parameter that depends on F . For example, the mean value \bar{Q} of a function $Q(F)$ is calculated similarly to equation (8), furnishing

$$\bar{Q} = n Q(F_p - P) + (1-n) Q(F_n + N) \quad (9a)$$

As a consequence, equations (9) and (9a) show that any new mean function \bar{Q} is related to the mean function \bar{F} . Or, in other words: because n is used to calculate the different mean profiles, all profiles are interrelated.

From the above discussion it may be inferred that any new variable added to the problem will have its own partition function. In the present section of scalar-velocity interactions, two partition functions are described: n for F (scalar) and m for V (velocity).

2.4 Bimodal square wave: Adjusting amplitudes using a reduction coefficient function for scalars - α_f

The sketch of figure 2c shows that the parcel P is always smaller or equal to $F_p - \bar{F}$. As already mentioned, this parcel shows that the amplitude of the fluctuations is reduced. Thus, a reduction coefficient α_f is defined here as

$$P = \alpha_f [F_p - \bar{F}] \quad 0 \leq \alpha_f \leq 1 \quad (10)$$

where α_f is a function of z and quantifies the reduction of the amplitude due to interactions between parcels of liquid with different F values (described here as a measure of diffusion effects, but which can be a measure of any cause that inhibits fluctuations). Using the effect of diffusion to interpret the new function, values of α_f close to 1 or 0 indicate strong or weak influence of diffusion, respectively. Considering this interpretation, Schulz & Janzen (2009) reported experimental profiles for α_f in the mass concentration boundary layer during air-water interfacial mass-transfer, which showed values close to 1 in both the vicinity of the surface and in the bulk liquid, and closer to 0 in an intermediate region (giving therefore a minimum value in this region).

From equations (7), (8) and (10), N and P are now expressed as

$$\left. \begin{aligned} N &= \alpha_f n (F_p - F_n) \\ P &= \alpha_f (1-n) (F_p - F_n) \end{aligned} \right\} 0 \leq \alpha_f \leq 1 \quad (11)$$

As for the partition functions, any new variable implies in a new reduction coefficient. In the present section of scalar-velocity interactions, only the reduction coefficient for F is used (that is, α_f). In the section for velocity-velocity interactions, a reduction coefficient α_v for V (velocity) is used.

2.5 Bimodal square wave: Quantifying superposition using the superposition coefficient function - β

Let us now consider the two main variables of turbulent scalar transport, the scalar F and the velocity V , oscillating simultaneously in the interval $z_1 < z < z_2$ of Figure 1. As usual, they are represented as $F = \bar{F} + f$ and $V = \bar{V} + \omega$, where \bar{F} and \bar{V} are the mean values, and f and ω are the fluctuations. The correlation coefficient function $\rho(z)$ for the fluctuations f and ω is given by

$$\rho(z) = \frac{1}{\Delta t} \int_{t_1}^{t_2} \rho(z, t) dt = \frac{1}{\Delta t} \int_{t_1}^{t_2} \frac{\omega f}{\sqrt{\omega^2} \sqrt{f^2}} dt = \frac{\overline{\omega f}}{\sqrt{\overline{\omega^2}} \sqrt{\overline{f^2}}} \quad (12)$$

If the fluctuations are generated by the same cause, it is expected that the records of ω and f are at least partially superposed. As done for F , it is assumed that the oscillations ω can be positive or negative and so a partition function m (a function of z) may be defined. If we consider a perfect superposition between f and ω , it would imply in $n=m$, though this is not usually the case. Aiming to consider all the cases, a superposition coefficient β is defined so that $\beta=1.0$ reflects the direct superposition ($m=n$), and $\beta=0.0$ implies the inverse superposition of the positive and the negative fluctuations ($m=1-n$) of both fields.

The definition of β is better understood considering the scheme presented in figure 3. In this figure all positive fluctuations of the scalar variable were put together, so that the nondimensional time intervals were added, furnishing the value n . As a consequence, the nondimensional fraction of time of the juxtaposed negative fluctuations appears as $1-n$. The velocity fluctuations also appear juxtaposed, showing that $\beta=1$ superposes f and n with the same sign ($++$ and $--$), while $\beta=0$ superposes f and n with opposite signs ($+-$ and $-+$). The positive and negative scalar fluctuations are represented by f_1 and f_2 , respectively. The downwards and upwards velocity fluctuations are represented by ω_d and ω_u , respectively.

Thus, m , which defines the fraction of the time for which the system is at ω_d , is expressed as

$$m = 1 - (\beta + n - 2\beta n) \quad (13)$$

β is a function of z . Also here any new variable implies in new superposition functions. In the present section of scalar-velocity interactions only one superposition coefficient function is used (linking scalar and velocity fluctuations).

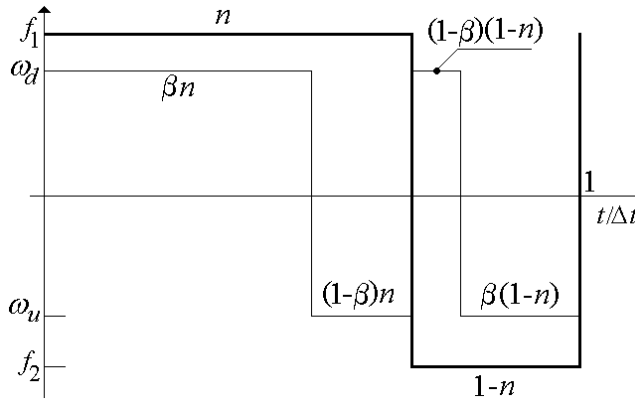


Fig. 3. Juxtaposed fluctuations of f and ω , showing a compact form of the time fractions n and $(1-n)$, and the use of the superposition function β . The horizontal axis represents the time as shown in equations (5) and (6).

2.6 The fluctuations around the mean for bimodal square waves

An advantage of using random square waves as shown in Figure 2 is that they generate only two fluctuation amplitudes for each variable, which are then used to calculate the wished statistical quantities. Of course, the functions defined in sections 2.3 through 2.5 (partition, reduction and superposition functions) are also used, and they must “adjust” the statistical quantities to adequate values. From equations (8), (10), and (11), the two instantaneous scalar fluctuations are then given by equations (14) and (15)

$$f_1 = (F_p - P - \bar{F}) = (1-n)(F_p - F_n)(1-\alpha_f) \quad (\text{positive}) \quad (14)$$

$$f_2 = (F_n + N - \bar{F}) = -n(F_p - F_n)(1-\alpha_f) \quad (\text{negative}) \quad (15)$$

2.7 Velocity fluctuations and the RMS velocity

In figure 1 the scalar variable is represented oscillating between two homogeneous values. But nothing was said about the velocity field that interacts with the scalar field. It may also be bounded by homogeneous velocity values, but may as well have zero mean velocities in the entire physical domain, without any evident reference velocity. This is the case, for example, of the problem of interfacial mass transfer across gas-liquid interfaces, the application shown by Schulz et al. (2011a). In such situations, it is more useful to use the rms velocity $\sqrt{\omega^2}$ as reference, as commonly adopted in turbulence. For the one-dimensional case, with null mean motion, all equations must be derived using only the vertical velocity fluctuations ω . It is necessary, thus, to obtain equations for $\sqrt{\omega^2}$ and for the velocity fluctuations (like equations 14 and 15 for f) considering the random square waves approximation. An auxiliary velocity scale U is firstly defined, shown in figure 4, considering “downwards” (ω_d) and “upwards” (ω_u) fluctuations, which amplitudes are functions of z .

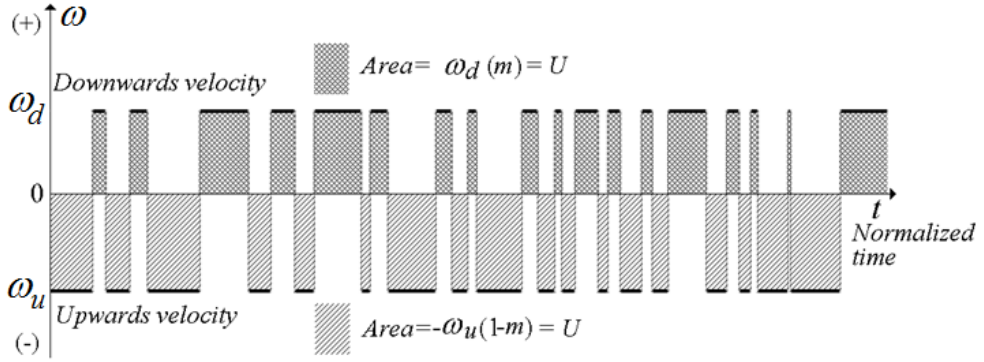


Fig. 4. The definition of the partition function m and the velocity scale U . Upwards (-) and downwards (+) velocities are shown. The dark and light gray areas are equal, so that the mean velocity is zero.

Using m for the partition function of the velocity, the scale U shown in figure 4 is defined as the integration of the upper or the lower parts of the graph in Figure 4, as

$$U = \omega_d m \quad \text{and} \quad U = -\omega_u (1-m) \quad (16)$$

Equation (17) describes the zero mean velocity (remembering that ω_u is negative)

$$\omega_d m + \omega_u (1-m) = 0 \quad \text{or} \quad U - U = 0 \quad (17)$$

U is a function of z . Let us now consider the RMS velocity $\sqrt{\overline{\omega^2}}$, which is calculated as

$$\overline{\omega^2} = m\omega_d^2 + (1-m)(-\omega_u)^2 \quad \text{and} \quad \sqrt{\overline{\omega^2}} = \sqrt{m\omega_d^2 + (1-m)(-\omega_u)^2} \quad (18)$$

U and $\sqrt{\overline{\omega^2}}$ may be easily related. From equations (13), (16), and (18) it follows that

$$U = \sqrt{\overline{\omega^2}} \sqrt{[1 - (\beta + n - 2\beta n)](\beta + n - 2\beta n)} \quad (19)$$

Finally, the velocity fluctuations may be related to $\sqrt{\overline{\omega^2}}$, n and β using equations (16) and (19)

$$\omega_d = \sqrt{\overline{\omega^2}} \sqrt{\frac{\beta + n - 2\beta n}{1 - (\beta + n - 2\beta n)}} \quad \text{and} \quad \omega_u = -\sqrt{\overline{\omega^2}} \sqrt{\frac{1 - (\beta + n - 2\beta n)}{\beta + n - 2\beta n}} \quad (20)$$

$\sqrt{\overline{\omega^2}}$ is a function of z and is used as basic parameter for situations in which no evident reference velocities are present. For the example of interfacial mass transfer, $\sqrt{\overline{\omega^2}}$ is zero at the water surface ($z=0$) and constant ($\neq 0$) in the bulk liquid ($z \rightarrow \infty$).

The basic functions $n, \alpha_f, \beta, \sqrt{\omega^2}$, defined in items 2.3 through 2.7, are used in the sequence to calculate the statistical quantities of the one-dimensional equations for scalar-velocity interactions. Further, incorporating them into equations (2) and (3), a closed set of equations for these functions is generated. In other words, the one dimensional turbulent transport problem reduces to the calculation of these functions, defined *a priori* to their inclusion in the equations. Some of their general characteristics are described in table 1.

The RMS velocity may be normalized to be also bounded by the (absolute) values of 0.0 and 1.0. Because the position of the maximum value depends on the situation under study, needing more detailed explanations, the table is presented with the RMS velocity in dimensional form and having an undetermined maximum value.

Function	n	α_f	β	$\sqrt{\omega^2}$
Dimension	Nondimensional	Nondimensional	Nondimensional	Velocity
Physical ground	Partition	Reduction	Superposition	Ref. velocity
Maximum value	1	1	1	Undetermined
Minimum value	0	0	0	0

Table 1. Characteristics of the functions defined for one dimensional scalar transport.

A further conclusion is that, because four functions need to be calculated, it implies that only four equations must be transformed to the random square waves representation in this one-dimensional situation. As a consequence, only lower order statistical quantities present in these equations need to be transformed, which is a positive consequence of this approximation, because the simplifications (and associated deviations) will not be propagated to the much higher order terms (they will not be present in the set of equations).

2.8 The central moments of scalar quantities using random square waves

It was shown that equations (3) involve central moments like $\overline{f^2}, \overline{f^3}, \overline{f^4}$, which, as mentioned, must be converted to the square waves representation. The general form of the central moments is defined as

$$\overline{f^\theta} = \overline{[F - \bar{F}]^\theta} \quad \theta = 1, 2, 3, \dots \quad (21)$$

For any statistical phenomenon, the first order central moment ($\theta=1$) is always zero. Using equations (14) and (15), Schulz & Janzen (2009) showed that the second order central moment ($\overline{f^2}$ for $\theta=2$) is given by

$$\overline{f^2} = f_1^2 n + f_2^2 (1-n) = n(1-n)(1-\alpha_f)^2 (F_p - F_n)^2 \quad (22)$$

or, normalizing the RMS value (f'_2)

$$f'_2 = \frac{\sqrt{f^2}}{(F_p - F_n)} = \sqrt{n(1-n)}(1 - \alpha_f) \quad \alpha_f = 1 - \frac{\sqrt{f^2}}{(F_p - F_n)\sqrt{n(1-n)}} \quad (23)$$

This form is useful to obtain the reduction function α_f from experimental data, using the normalized mean profile and the RMS profile, as shown by Schulz & Janzen (2009). Equation (23) shows that diffusion, or other causes that inhibit the fluctuations and imply in $\alpha_f \neq 0$, imposes a peak of f'_2 lower than 0.5.

The general central moments ($\theta=1, 2, 3\dots$) for the scalar fluctuation f are given by

$$\overline{f^\theta} = f_1^\theta n + f_2^\theta (1-n) = n(1-n) \left[(1-n)^{\theta-1} + (-1)^\theta (n)^{\theta-1} \right] (F_p - F_n)^\theta (1 - \alpha_f)^\theta \quad (24)$$

or, normalizing the θ^{th} root (f_θ)

$$f'_\theta = \frac{\sqrt[\theta]{\overline{f^\theta}}}{(F_p - F_n)} = \sqrt[n(1-n)]{\left[(1-n)^{\theta-1} + (-1)^\theta (n)^{\theta-1} \right]} (1 - \alpha_f) \quad (25)$$

The functional form of the statistical quantities shown here must be obtained solving the transformed turbulent transport equations (that is, the equations involving these quantities). Equations (21) through (25) show that, given n and α_f , it is possible to calculate all the central moments ($\overline{f^\theta}$ statistical profiles) needed in the one-dimensional equations for scalar transfer.

2.9 The covariances and correlation coefficient functions using random square waves

2.9.1 The turbulent flux of the scalar \dot{F}

The turbulent scalar flux, denoted by \dot{F} , is defined as the mean product between scalar fluctuations (f) and velocity fluctuations (ω)

$$\dot{F} = \overline{\omega f} \quad (26)$$

Thus $\overline{\omega f}$ in equation (2) is the turbulent flux of F along z . The statistical correlation between ω and f is given by the correlation coefficient function, r , defined as

$$r = \frac{\overline{\omega f}}{\sqrt{\overline{\omega^2}} \sqrt{\overline{f^2}}} \quad (27)$$

r is a function of z , and $0 \leq |r| \leq 1$. As it is clear from equations (26) and (27), r is also the normalized turbulent flux of F and reaches a peak amplitude less than or equal to 1.0, a range convenient for the present method, coinciding with the defined functions n , α_f , β , also bounded by 0.0 and 1.0 (as shown in table 1). The present method allows to express r as dependent on n , the normalized mean profile of F .

2.9.2 The correlation coefficient functions $\overline{f^\theta \omega}$

Equations (3) involve turbulent fluxes like $\overline{f\omega}$, $\overline{f^2\omega}$, $\overline{f^3\omega}$, $\overline{f^4\omega}$, which are unknown variables that must be expressed as functions of n , α_f , β and $\sqrt{\omega^2}$. For products between any power of f and ω , the superposition coefficient β must be used to account for an “imperfect” superposition between the scalar and the velocity fluctuations. Therefore the flux $\overline{f\omega}$ is calculated as shown in equation (28), with β being equally applied for the positive and negative fluctuations, as shown in figure 3

$$\overline{f\omega} = \omega_d [f_1 n \beta + f_2 (1-n)(1-\beta)] + \omega_u [f_1 n (1-\beta) + f_2 (1-n)\beta] \quad (28)$$

Equations (13) through (20) and (28) lead to

$$\overline{f\omega} = \sqrt{\omega^2} (F_p - F_n) (1 - \alpha_f) (1 - n) n (2\beta - 1) \left\{ \sqrt{\frac{\beta + n - 2\beta n}{1 - (\beta + n - 2\beta n)}} + \sqrt{\frac{1 - (\beta + n - 2\beta n)}{\beta + n - 2\beta n}} \right\} \quad (29)$$

Rearranging, the turbulent scalar flux is expressed as

$$\overline{f\omega} = \frac{n(1-n)(1-\alpha_f)\sqrt{\omega^2}(F_p - F_n)}{\sqrt{n(1-n) + \frac{\beta(1-\beta)}{(2\beta-1)^2}}} \quad (30)$$

Equations (23), (27) and (30) lead to the correlation coefficient function

$$r|_{\omega, f} = \frac{\overline{f\omega}}{\sqrt{\omega^2}\sqrt{f^2}} = \frac{n(1-n)}{\sqrt{n(1-n) + \frac{\beta(1-\beta)}{(2\beta-1)^2}}} \quad \text{with} \quad 0 \leq |r|_{\omega, f}| \leq 1 \quad (31)$$

Schulz et al. (2010) used this equation together with data measured by Janzen (2006). The “ideal” turbulent mass flux at gas-liquid interfaces was presented (perfect superposition of f and ω , obtained for $\beta = 1.0$). In this case, $r|_{\omega, f} = 1$, and $\overline{f\omega} = \sqrt{\omega^2}\sqrt{f^2}$. The measured peak of $\sqrt{\omega^2}$, represented by W , was used to normalize $\overline{f\omega}$, as shown in Figure 5.

Considering r as defined by equation (27), it is now a function of n and β only. Generalizing for f^θ , we have

$$\overline{f^\theta \omega} = \omega_d [f_1^\theta n \beta + f_2^\theta (1-n)(1-\beta)] + \omega_u [f_1^\theta n (1-\beta) + f_2^\theta (1-n)\beta] \quad (32)$$

The correlation coefficient function is now given by

$$r|_{\omega, f^\theta} = \frac{\overline{f^\theta \omega}}{\sqrt{f^{2\theta}}\sqrt{\omega^2}} = \frac{n(1-n)}{\sqrt{n(1-n) + \frac{\beta(1-\beta)}{(2\beta-1)^2}}} \left\{ \frac{[(1-n)^\theta - (-n)^\theta]}{\sqrt{[(1-n)^{2\theta-1} + (-1)^{2\theta} (n)^{2\theta-1}]}} \right\} \quad (33)$$

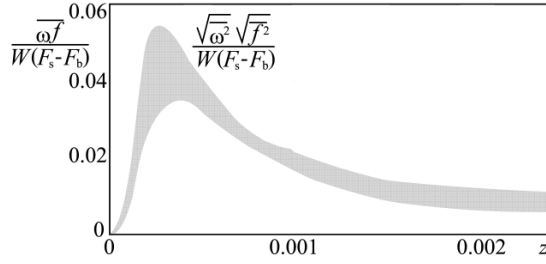


Fig. 5. Normalized “ideal” turbulent fluxes for $\beta=1$ using measured data. W is the measured peak of $\sqrt{\overline{\omega^2}}$. z is the vertical distance from the interface. Adapted from Schulz et al. (2011a).

Equation (32) is used to calculate covariances like $\overline{f^2\omega}$, $\overline{f^3\omega}$, $\overline{f^4\omega}$, present in equations (3). For example, for $\theta=2, 3$ and 4 the normalized fluxes are given, respectively, by:

$$r_{|\omega, f^2} = \frac{\overline{\omega f^2}}{\sqrt{f^4} \sqrt{\overline{\omega^2}}} = \sqrt{\frac{n(1-n)}{n(1-n) + \frac{\beta(1-\beta)}{(2\beta-1)^2}}} \left\{ \frac{(1-2n)}{\sqrt{[(1-n)^3 + (n)^3]}} \right\} \quad (34a)$$

$$r_{|\omega, f^3} = \frac{\overline{\omega f^3}}{\sqrt{f^6} \sqrt{\overline{\omega^2}}} = \sqrt{\frac{n(1-n)}{n(1-n) + \frac{\beta(1-\beta)}{(2\beta-1)^2}}} \left\{ \frac{[(1-n)^3 + n^3]}{\sqrt{[(1-n)^5 + (n)^5]}} \right\} \quad (34b)$$

$$r_{|\omega, f^4} = \frac{\overline{\omega f^4}}{\sqrt{f^8} \sqrt{\overline{\omega^2}}} = \sqrt{\frac{n(1-n)}{n(1-n) + \frac{\beta(1-\beta)}{(2\beta-1)^2}}} \left\{ \frac{[(1-n)^4 - n^4]}{\sqrt{[(1-n)^7 + (n)^7]}} \right\} \quad (34c)$$

As an ideal case, for $\beta=1$ (perfect superposition) equation 33 furnishes

$$r_{|\omega, f^\theta} = \frac{\overline{\omega f^\theta}}{\sqrt{f^{2\theta}} \sqrt{\overline{\omega^2}}} = \left\{ \frac{[(1-n)^\theta - (-n)^\theta]}{\sqrt{[(1-n)^{2\theta-1} + (-1)^{2\theta}(n)^{2\theta-1}]} \right\} \quad (35)$$

and the normalized covariances $\overline{f^2\omega}$, $\overline{f^3\omega}$, $\overline{f^4\omega}$, for $\theta=2, 3$ and 4 , are then given, respectively, by:

$$r_{|\omega, f^2} = \left\{ \frac{(1-2n)}{\sqrt{[(1-n)^3 + (n)^3]}} \right\} \quad (36a)$$

$$r|_{\omega, f^3} = \left\{ \frac{[(1-n)^3 + n^3]}{\sqrt{[(1-n)^5 + (n)^5]}} \right\} \quad (36b)$$

$$r|_{\omega, f^4} = \left\{ \frac{[(1-n)^4 - n^4]}{\sqrt{[(1-n)^7 + (n)^7]}} \right\} \quad (36c)$$

Equations (34a) and (36a) can be used to analyze the general behavior of the flux $\overline{f^2\omega}$. These equations involve the factor $(1-2n)$, which shows that this flux changes its direction at $n=0.5$. For $0 < n < 0.5$ the flux $\overline{f^2\omega}$ is positive, while for $0.5 < n < 1.0$, it is negative. In the mentioned example of gas-liquid mass transfer, the positive sign indicates a flux entering into the bulk liquid, while the negative sign indicates a flux leaving the bulk liquid. This behavior of $\overline{f^2\omega}$ was described by Magnaudet & Calmet (2006) based on results obtained from numerical simulations. A similar change of direction is observed for the flux $\overline{f^4\omega}$, easily analyzed through the polynomial $(1-n)^4 - n^4$.

The equations of items 2.9.1 and 2.9.2 confirm that the normalized turbulent fluxes are expressed as functions of n and β only, while the covariances may be expressed as functions of n , β , α_f and $\sqrt{\omega^2}$.

2.10 Transforming the derivatives of the statistical equations

2.10.1 Simple derivatives

The governing differential equations (2) and (3) involve the derivatives of several mean quantities. The different physical situations may involve different physical principles and boundary conditions, so that "particular" solutions may be found. For the example of interfacial mass transfer reported in the cited literature (e.g. Wilhelm & Gulliver, 1991; Jähne & Monahan, 1995; Donelan, et al., 2002; Janzen et al., 2010, 2011), F_p is taken as the constant saturation concentration of gas at the gas-liquid interface, and F_n is the homogeneous bulk liquid gas concentration. In this chapter this mass transfer problem is considered as example, because it involves an interesting definition of the time derivative of F_n .

The p^{th} -order space derivative $\frac{\partial^p \overline{F}}{\partial z^p}$ is obtained directly from equation (8), and is given by

$$\frac{\partial^p \overline{F}}{\partial z^p} = (F_p - F_n) \frac{\partial^p n}{\partial z^p} \quad (37)$$

The time derivative of the mean concentration, $\frac{\partial \overline{F}}{\partial t}$, is also obtained from equation (8) and eventual previous knowledge about the time evolution of F_p and F_n . For interfacial mass transfer the time evolution of the mass concentration in the bulk liquid follows equation (38) (Wilhelm & Gulliver, 1991; Jähne & Monahan, 1995; Donelan, et al., 2002; Janzen et al., 2010, 2011)

$$\frac{dF_n}{dt} = K_f (F_p - F_n) \quad (38)$$

This equation applies to the boundary value F_n or, in other words, it expresses the time variation of the boundary condition F_n shown in figure 1. K_f is the transfer coefficient of F (mass transfer coefficient in the example). To obtain the time derivative of \bar{F} , equations (8) and (38) are used, thus involving the partition function n . In this example, n depends on the agitation conditions of the liquid phase, which are maintained constant along the time (stationary turbulence). As a consequence, n is also constant in time. The time derivative of \bar{F} in equation (8) is then given by

$$\frac{\partial \bar{F}}{\partial t} = \frac{\partial [nF_p + (1-n)F_n]}{\partial t} = (1-n) \frac{\partial F_n}{\partial t} \quad (39)$$

From equations (38) and (39), it follows that

$$\frac{\partial \bar{F}}{\partial t} = K_f (1-n) (F_p - F_n) \quad (40)$$

Equation (40) is valid for boundary conditions given by equation (38) (usual in interfacial mass and heat transfers). As already stressed, different physical situations may conduce to different equations.

The time derivatives of the central moments $\overline{f^\theta}$ are obtained from equation (24), furnishing:

$$\frac{\partial \overline{f^\theta}}{\partial t} = -\theta n (1-n) \left[(1-n)^{\theta-1} + (-1)^\theta (n)^{\theta-1} \right] (F_p - F_n)^{\theta-1} (1-\alpha_f)^\theta \frac{\partial F_n}{\partial t}$$

or

(41)

$$\frac{\partial \overline{f^\theta}}{\partial t} = -\theta K n (1-n) \left[(1-n)^{\theta-1} + (-1)^\theta (n)^{\theta-1} \right] (F_p - F_n)^\theta (1-\alpha_f)^\theta$$

As no velocity fluctuation is involved, only the partition function n is needed to obtain the mean values of the derivatives of $\overline{f^\theta}$, that is, no superposition coefficient is needed. The obtained equations depend only on n and α_f , the basic functions related to F .

2.10.2 Mean products between powers of the scalar fluctuations and their derivatives

Finally, the last “kind” of statistical quantities existing in equations (3) involve mean products of fluctuations and their second order derivatives, like $f \frac{\partial^2 f}{\partial z^2}$, $f^2 \frac{\partial^2 f}{\partial z^2}$, and $f^3 \frac{\partial^2 f}{\partial z^2}$. The

general form of such mean products is given in the sequence. From equations (14) and (15), it follows that

$$f_1^\theta \frac{\partial^2 f_1}{\partial z^2} = \left[(1-n) (F_p - F_n) (1-\alpha_f) \right]^\theta \frac{\partial^2 \left[(1-n) (1-\alpha_f) \right]}{\partial z^2} (F_p - F_n) \quad (42)$$

$$f_2^\theta \frac{\partial^2 f_2}{\partial z^2} = \left[-n(F_p - F_n)(1 - \alpha_f) \right]^\theta \frac{\partial^2 \left[-n(1 - \alpha_f) \right]}{\partial z^2} (F_p - F_n) \quad (43)$$

Using the partition function n , we obtain the mean product

$$\overline{f^\theta \frac{\partial^2 f}{\partial z^2}} = \left\{ (1-n)^{\theta-1} \frac{\partial^2 \left[(1-n)(1-\alpha_f) \right]}{\partial z^2} + (-n)^{\theta-1} \frac{\partial^2 \left[-n(1-\alpha_f) \right]}{\partial z^2} \right\} n(1-n)(1-\alpha_f)^\theta (F_p - F_n)^{\theta+1} \quad (44)$$

Equation (44) shows that mean products between powers of f and its derivatives are expressed as functions of n and α_f only.

2.11 The heat/mass transport example

In this section, the simplified example presented by Schulz et al. (2011a) is considered in more detail. The simplified condition was obtained by using a constant α_f , in the range from 0.0 to 1.0. The obtained differential equations are nonlinear, but it was possible to reduce the set of equations to only one equation, solvable using mathematical tables like Microsoft Excel® or similar.

2.11.1 Obtaining the transformed equations for the one-dimensional transport of F

Equation (2) may be transformed to its random square waves correspondent using equations (2), (8), (30), (37), and (40), leading to

$$K_f(1-n) = D_f \frac{d^2 n}{dz^2} - \frac{d}{dz} \left\{ \frac{n(1-n)(1-\alpha_f)\sqrt{\omega^2}}{\sqrt{n(1-n) + \frac{\beta(1-\beta)}{(2\beta-1)^2}}} \right\} \quad (45)$$

In the same way, equation (3d) is transformed to its random square waves correspondent using equations (3d), (8), (24), (32), (37), (41), and (44), leading to

$$\begin{aligned} & -K_f n(1-n) \left[(1-n)^{\theta-1} + (-1)^\theta (n)^{\theta-1} \right] (1-\alpha_f)^\theta + \\ & + K_f n(1-n)^2 \left[(1-n)^{\theta-2} + (-1)^{\theta-1} (n)^{\theta-2} \right] (1-\alpha_f)^{\theta-1} + \\ & + \frac{\left[n(1-n) \right]^{3-\theta}}{\sqrt{n(1-n) + \frac{\beta(1-\beta)}{(2\beta-1)^2}}} \left[(1-n)^{\theta-1} - (-n)^{\theta-1} \right] \left[n(1-n) \right]^{(\theta-1)/2} \sqrt{\omega^2} (1-\alpha_f)^{\theta-1} \frac{\partial n}{\partial z} + \\ & + \frac{1}{\theta} \frac{\partial}{\partial z} \left\{ \frac{\left[n(1-n) \right]^{2-\theta}}{\sqrt{n(1-n) + \frac{\beta(1-\beta)}{(2\beta-1)^2}}} \left[(1-n)^\theta - (-n)^\theta \right] \left[n(1-n)(1-\alpha_f)^2 \right]^{\theta/2} \sqrt{\omega^2} \right\} = \end{aligned}$$

$$\begin{aligned}
&= D_f n(1-n) \left[(1-n)^{\theta-2} + (-1)^{\theta-1} (n)^{\theta-2} \right] (1-\alpha_f)^{\theta-1} \frac{\partial^2 n}{\partial z^2} + \\
&+ D_f \left\{ (1-n)^{\theta-2} \frac{\partial^2 [(1-n)(1-\alpha_f)]}{\partial z^2} + (-n)^{\theta-2} \frac{\partial^2 [-n(1-\alpha_f)]}{\partial z^2} \right\} n(1-n)(1-\alpha_f)^{\theta-1} \quad (46)
\end{aligned}$$

2.11.2 Simplified case of interfacial heat/mass transfer

Although involving few equations for the present case, the set of the coupled nonlinear equations (45) and (46) may have no simple solution. As mentioned, the original one-dimensional problem needs four equations. But as the simplified solution of interfacial transfer using a mean constant $\alpha_f = \overline{\alpha_f}$ is considered here, only three equations would be needed. Further, recognizing in equations (45) and (46) that β and $\sqrt{\omega^2}$ appear always together in the form

$$IJ = \frac{n(1-n)(1-\alpha_f)\sqrt{\omega^2}}{\sqrt{n(1-n) + \frac{\beta(1-\beta)}{(2\beta-1)^2}}} \quad (47)$$

It is possible to reduce the problem to a set of only two coupled equations, for n and the function IJ . Thus, only equations (45) and (46) for $\theta=2$ are necessary to close the problem when using $\alpha_f = \overline{\alpha_f}$. Defining $A = (1 - \overline{\alpha_f})$ the set of the two equations is given by

$$K_f(1-n) = D_f \frac{d^2 n}{dz^2} - \frac{d(IJ)}{dz} \quad (48a)$$

$$-K_f n(1-n)A^2 + (IJ) \frac{dn}{dz} + \frac{A}{2} \frac{d}{dz} [(IJ)(1-2n)] = -2D_f n(1-n)A^2 \frac{d^2 n}{dz^2} \quad (48b)$$

Equations (48) may be presented in nondimensional form, using $z^*=z/E$, with $E=z_2-z_1$, and $S=1/\kappa=D_f/K_f E^2$

$$IJ^* = \frac{n(1-n)(1-\alpha_f) \left(\sqrt{\omega^2} / KE \right)}{\sqrt{n(1-n) + \frac{\beta(1-\beta)}{(2\beta-1)^2}}} \quad (49)$$

$$(1-n) = S \frac{d^2 n}{dz^{*2}} - \frac{d(IJ^*)}{dz^*} \quad (50a)$$

$$-n(1-n)A^2 + (IJ^*) \frac{dn}{dz^*} + \frac{A}{2} \frac{d}{dz^*} [(IJ^*)(1-2n)] = -2Sn(1-n)A^2 \frac{d^2 n}{dz^{*2}} \quad (50b)$$

Equation (50a) is used to obtain dII/dz^* , which leads, when substituted into equation (50b), to the following governing equation for n (see appendix 1)

$$\begin{aligned}
 & A \left[2An(1-n) + \frac{(1-2n)}{2} \right] \frac{d^3n}{dz^{*3}} \frac{dn}{dz^*} + \\
 & + A \left\{ - \left[2An(1-n) + \frac{(1-2n)}{2} \right] \frac{d^2n}{dz^{*2}} + \kappa(1-n) \left[\frac{2n(A-1)+1}{2} \right] + \frac{\{1+2A[A(1-2n)-1]\}}{A} \left(\frac{dn}{dz^*} \right)^2 \right\} \frac{d^2n}{dz^{*2}} + \quad (51) \\
 & + \kappa \left\{ (A-1)(1-n) - A \left[A(1-2n) - \left(\frac{3}{2} - 2n \right) \right] \right\} \left(\frac{dn}{dz^*} \right)^2 = 0
 \end{aligned}$$

Thus, the one-dimensional problem is reduced to solve equation (51) alone. It admits non-trivial analytical solution for the extreme case $A=0$ (or $\overline{\alpha_f} = 1$), in the form

$$\frac{d^2n}{dz^{*2}} = \kappa(1-n) \quad \text{or} \quad n = 1 - \frac{\sin(\sqrt{\kappa}z^*)}{\sin(\sqrt{\kappa})} \quad (52)$$

But this effect of diffusion for all $0 < z^* < 1$ is considered overestimated. Equation (51) was presented by Schulz et al. (2011a), but with different coefficients in the last parcel of the first member (the parcel involving $3/2-2n$ in equation (51) involved $1-n$ in the mentioned study). Appendix 1 shows the steps followed to obtain this equation. Numerical solutions were obtained using Runge-Kutta schemes of third, fourth and fifth orders. Schulz et al. (2011a) presented a first evaluation of the n profile using a fourth order Runge-Kutta method and comparing the predictions with the measured data of Janzen (2006). An improved solution was proposed by Schulz et al. (2011b) using a third order Runge-Kutta method, in which a good superposition between predictions and measurements was obtained. In the present chapter, results of the third, fourth and fifth orders approximations are shown. The system of equations derived from (51) and solved with Runge-Kutta methods is given by:

$$\left\{ \begin{aligned}
 & \frac{dn}{dz^*} = j, \quad \frac{dj}{dz^*} = w, \quad \frac{dw}{dz^*} = \frac{f_1 + f_2}{f_3} \quad \text{where} \\
 & f_1 = -A \left\{ - \left[2An(1-n) + \frac{(1-2n)}{2} \right] w + \kappa(1-n) \left[\frac{2n(A-1)+1}{2} \right] + \frac{\{1+2A[A(1-2n)-1]\}}{A} j^2 \right\} w, \\
 & f_2 = -\kappa \left\{ (A-1)(1-n) - A \left[A(1-2n) - \left(\frac{3}{2} - 2n \right) \right] \right\} j^2, \\
 & \text{and} \\
 & f_3 = A \left[2An(1-n) + \frac{(1-2n)}{2} \right] j.
 \end{aligned} \right. \quad (53)$$

Equations (53) were solved as an initial value problem, that is, with the boundary conditions expressed at $z^*=0$. In this case, $n(0)=1$ and $j(0)=-3$ (considering the experimental data of Janzen, 2006). The value of $w(0)$ was calculated iteratively, obeying the boundary condition $0 < n(1) < 0.01$. The Runge-Kutta method is explicit, but iterative procedures were used to

evaluate the parameters at $z^*=0$ applying the quasi-Newton method and the Solver device of the Excel® table. Appendix 2 explains the procedures followed in the table. The curves of figure 6a were obtained for $0.001 \leq \kappa \leq 0.005$, a range based on the κ experimental values of Janzen (2006), for which $\sim 0.003 < \kappa < \sim 0.004$. The values $A=0.5$ and $n''(0)=3.056$ were used to calculate n in this figure. As can be seen, even using a constant A , the calculated curve $n(z^*)$ closely follows the form of the measured curve. Because it is known that α_f is a function of z^* , more complete solutions must consider this dependence. The curve of Schulz et al. (2011a) in figure 6a was obtained following different procedures as those described here. The curves obtained in the present study show better agreement than the former one.

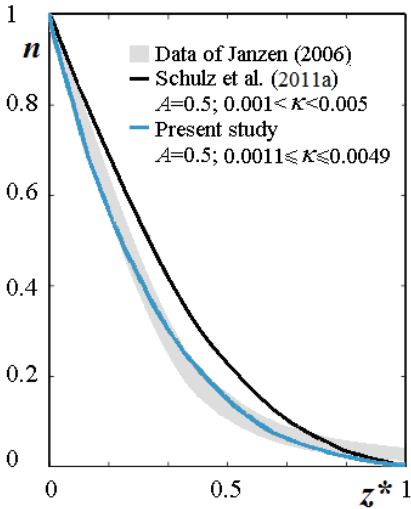


Fig. 6a. Predictions of n for $n''(0) = 3.056$. Fourth order Runge-Kutta.

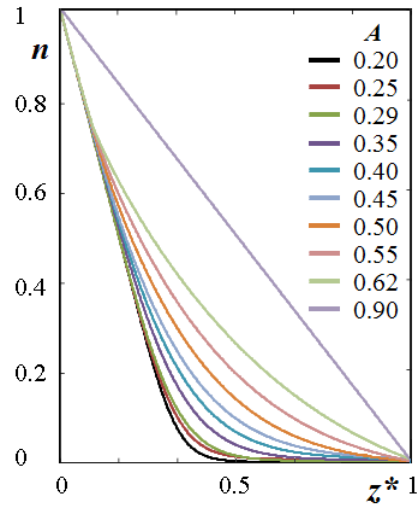


Fig. 6b. Predictions of n for $\kappa = 0.0025$, and $0.0449 \leq n''(0) \leq 3.055$. Fifth order Runge-Kutta

Fig. 6b. was obtained with following conditions for the pairs $[A, n''(0)]$: $[0.2, 0.00596]$, $[0.25, -0.0145]$, $[0.29, -0.04495]$, $[0.35, 1.508]$, $[0.4, 1.8996]$, $[0.45, 1.849]$, $[0.5, 2.509]$, $[0.55, 3.0547]$, $[0.62, 2.9915]$, $[0.90, 0.00125]$. Further, $n'(0) = -3$ for A between 0.20 and 0.62, and $n'(0) = -1$ for $A=0.90$.

Figure 7a shows results for $\kappa \sim 0.4$, that is, having a value around 100 times higher than those of the experimental range of Janzen (2006), showing that the method allows to study phenomena subjected to different turbulence levels. $\kappa = (K_f E^2/D_f)$ is dependent on the turbulence level, through the parameters E and K_f , and different values of these variables allow to test the effect of different turbulence conditions on n . Figure 7b presents results similar to those of figure 6a, but using a third order Runge-Kutta method, showing that simpler schemes can be used to obtain adequate results.

As the definitions of item 3 are independent of the nature of the governing differential equations, it is expected that the present procedures are useful for different phenomena governed by statistical differential equations. In the next section, the first steps for an application in velocity-velocity interactions are presented.

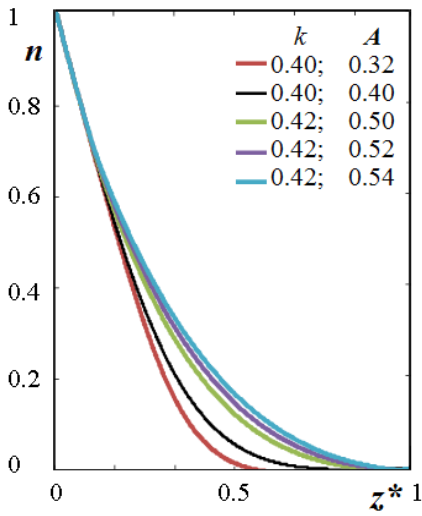


Fig. 7a. Predictions of n for $n''(0) = 3.056$, and $\kappa \sim 0.40$. Fourth order Runge-Kutta.

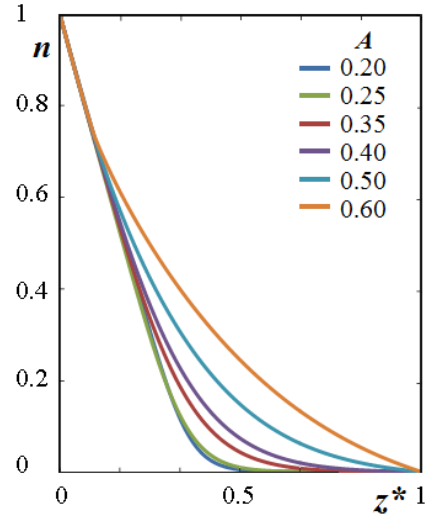


Fig. 7b. Predictions of n for $\kappa=0.003$ and $2.99812 \leq n''(0) \leq 3.2111$. Third order Runge-Kutta

3. Velocity-velocity interactions

The aim of this section is to present some first correlations for a simple velocity field. In this case, the flow between two parallel plates is considered. We follow a procedure similar to that presented by Schulz & Janzen (2009), in which the measured functional form of the reduction function is shown. As a basis for the analogy, some governing equations are first presented. The Navier-Stokes equations describe the movement of fluids and, when used to quantify turbulent movements, they are usually rewritten as the Reynolds equations:

$$\frac{\partial \bar{V}_j}{\partial t} + \bar{V}_i \frac{\partial \bar{V}_j}{\partial x_i} = \frac{\partial}{\partial x_i} \left(\nu \frac{\partial \bar{V}_j}{\partial x_i} - \overline{v_i v_j} \right) - \frac{1}{\rho} \frac{\partial \bar{p}}{\partial x_j} + B_i, \quad i, j = 1, 2, 3. \quad (54)$$

\bar{p} is the mean pressure, ν is the kinematic viscosity of the fluid and B_i is the body force per unit mass (acceleration of the gravity). For stationary one-dimensional horizontal flows between two parallel plates, equation (1), with $x_1=x$, $x_3=z$, $v_1=u$ and $v_3=\omega$, is simplified to:

$$\frac{1}{\rho} \frac{\partial \bar{p}}{\partial x} = \frac{\partial}{\partial z} \left(\nu \frac{\partial \bar{U}}{\partial z} - \overline{\omega u} \right) \quad (55)$$

This equation is similar to equation (2) for one dimensional scalar fields. As for the scalar case, the mean product $\overline{\omega u}$ appears as a new variable, in addition to the mean velocity \bar{U} . In this chapter, no additional governing equation is presented, because the main objective is to expose the analogy. The observed similarity between the equations suggests also to use the partition, reduction and superposition functions for this velocity field.

Both the upper and the lower parts of the flow sketched in figure 8 may be considered. We consider here the lower part, so that it is possible to define a zero velocity (U_n) at the lower surface of the flow, and a “virtual” maximum velocity (U_p) in the center of the flow. This virtual value is constant and is at least higher or equal to the largest fluctuations (see figure 8), allowing to follow the analogy with the previous scalar case.

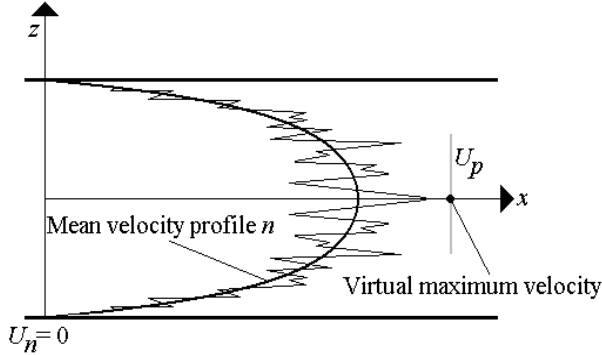


Fig. 8. The flow between two parallel planes, showing the reference velocities U_n and U_p . The partition function n_v , for the longitudinal component of the velocity, is defined as:

$$n_v = \frac{t \text{ at } (U_p - P)}{\Delta t \text{ of the observation}} \quad (56)$$

It follows that:

$$1 - n_v = \frac{t \text{ at } (U_n + N)}{\Delta t \text{ of the observation}} \quad (57)$$

Equation (7) must be used to reduce the velocity amplitudes around the same mean velocity. It implies that the same mass is subjected to the velocity corrections P and N . As for the scalar functions, the partition function n_v is then also represented by the normalized mean velocity profile:

$$n_v = \frac{\bar{U} - U_n}{U_p - U_n} \quad (58)$$

To quantify the reduction of the amplitudes of the longitudinal velocity fluctuations, a reduction coefficient function α_u is now defined, leading, similarly to the scalar fluctuations, to:

$$\left. \begin{aligned} N &= \alpha_u n_v (U_p - U_n) \\ P &= \alpha_u (1 - n_v) (U_p - U_n) \end{aligned} \right\} \quad 0 \leq \alpha_u \leq 1 \quad (59)$$

It follows, for the x components, that:

$$u_1 = (1 - n_v) (U_p - U_n) (1 - \alpha_u) \quad (\text{positive}) \quad (60)$$

$$u_2 = -n_v (U_p - U_n) (1 - \alpha_u) \quad (\text{negative}) \quad (61)$$

The second order central moment for the x component of the velocity fluctuations is given by:

$$\overline{u^2} = u_1^2 n_v + u_2^2 (1 - n_v) = n_v (1 - n_v) (1 - \alpha_u)^2 (U_p - U_n)^2 \quad (62)$$

Or, normalizing the RMS value (u'_2):

$$u'_2 = \frac{\sqrt{\overline{u^2}}}{(U_p - U_n)} = \sqrt{n_v (1 - n_v)} (1 - \alpha_u) \quad (63)$$

Equation 63 shows that the relative turbulence intensity profile is obtained from the mean velocity profile n_v and the reduction coefficient profile α_u . As done by Schulz & Janzen (2009), the profile of α_u can be obtained from experimental data, using equation (63).

$$1 - \alpha_u = \frac{\sqrt{\overline{u^2}}}{(U_p - U_n) \sqrt{n_v (1 - n_v)}} \quad (64)$$

As can be seen, the functional form of α_u is obtainable from usual measured data, with exception of the proportionality constant given by $1/U_p$, which must be adjusted or conveniently evaluated. Figure 9 shows data adapted from Wei & Willmarth (1989), cited by Pope (2000), and the function $\sqrt{n_v (1 - n_v)}$ is calculated from the linear and log-law profiles close to the wall, also measured by Wei & Wilmarth (1989).

To obtain a first evaluation of the virtual constant velocity U_p , the following procedure was adopted. The value of the maximum normalized mean velocity is $U/u^* \sim 24.2$ (measured), where U is the mean velocity and u^* is the shear velocity. The value of the normalized RMS u velocity, close to the peak of U , is $u'/u^* \sim 1.14$. Considering a Gaussian distribution, 99.7% of the measured values are within the range from $U/u^* - 3 u'/u^*$ to $U/u^* + 3 u'/u^*$. A first value of U_p is then given by $U + 3u'$, furnishing $U_p/u^* \sim 24.2 + 3 * 1.14 \sim 27.6$. Physically it implies that patches of fluid with U_p are “transported” and reduce their velocity while approaching the wall. With this approximation, the partition function is given by:

$$n_v = \frac{u^+}{27.6} = \frac{0.41 \ln y^+ + 5.2}{27.6} \quad (65)$$

The value 0.41 is the von Karman constant and the value 5.2 is adjusted from the experimental data. The notation u^+ and y^+ corresponds to the nondimensional velocity and distance, respectively, used for wall flows. In this case, $u^+ = U/u^*$ and $y^+ = zu^*/\nu$, where ν is the kinematic viscosity of the fluid. Equation (65) is the well-known logarithmic law for the velocity close to surfaces. It is generally applied for $y^+ > 11$. For $0 < y^+ < 11$, the linear form $u^+ = y^+$ is valid so that equation (65) is then replaced by a linear equation between n_v and y^+ . From equation (63) it follows that:

$$\frac{\sqrt{\overline{u^2}}}{u^*} = \frac{U_p}{u^*} \sqrt{n_v (1 - n_v)} (1 - \alpha_u) = 27.6 \sqrt{n_v (1 - n_v)} (1 - \alpha_u) \quad (66)$$

Figure 9 shows the measured u'_2 values together with the curve given by $27.6 \sqrt{n_v(1-n_v)}$. As can be seen, the curve $27.6 \sqrt{n_v(1-n_v)}$ leads to a peak close to the wall. In this case, the function is normalized using the friction velocity, so that the peak is not limited by the value of 0.5 (which is the case if the function is normalized using U_p-U_n). It is interesting that the forms of $\sqrt{u'^2}/u^*$ and $27.6 \sqrt{n_v(1-n_v)}$ are similar, which coincides with the conclusions of Janzen (2006) for mass transfer, using *ad hoc* profiles for the mean mass concentration close to interfaces.

Figure 10 shows the cloud of points for $1-\alpha_u$ obtained from the data of Wei & Willmarth (1989), following the procedures of Janzen (2006) and Schulz & Janzen (2009) for mass transfer. As for the case of mass transfer, α_u presents a minimum peak in the region of the boundary layer (maximum peak for $1-\alpha_u$).

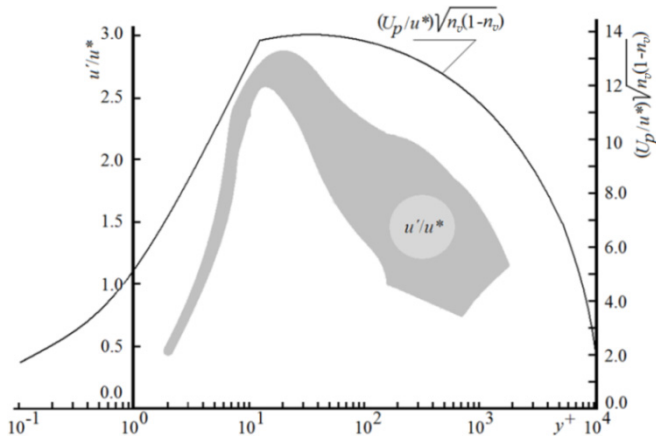


Fig. 9. Comparison between measured values of u'/u^* and $(U_p/u^*)\sqrt{n_v(1-n_v)}$. The gray cloud envelopes the data from Wei & Willmarth (1989).

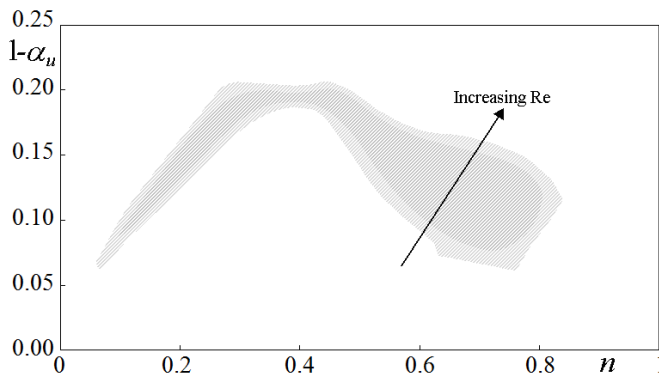


Fig. 10. $1-\alpha_u$ plotted against n , following the procedures of Schulz & Janzen (2009). The gray cloud envelopes the points calculated using the data of Wei & Willmarth (1989).

As a last observation, the conclusion of section 2.7, valid for the scalar-velocity interactions, are now also valid for the transversal component of the velocity. The mean transversal velocity is null along all the flow, leading to the use of the RMS velocity for this component.

4. Challenges

After having presented the one-dimensional results for turbulent scalar transfer using the approximation of random square waves, some brief comments are made here, about some characteristics of this approximation, and about open questions, which may be considered in future studies.

As a general comment, it may be interesting to remember that the mean functions of the statistical variables are continuous, and that, in the present approximation they are defined using discrete values of the relevant variables. As described along the paper, the defined functions (n , α , β , RMS) “adjust” these two points of view (this is perhaps more clearly explained when defining the function α). This concomitant dual form of treating the random transport did not lead to major problems in the present application. Eventual applications in 2-D, 3-D problems or in phenomena that deal with discrete variables may need more refined definitions.

In the present study, the example of mass transfer was calculated by using constant reduction coefficients (α), presenting a more detailed and improved version of the study of Schulz et al. (2011a). However, it is known that this coefficient varies along z , which may introduce difficulties to obtain a solution for n . This more complete result is still not available.

It was assumed, as usual in turbulence problems, that the lower statistical parameters (e.g. moments) are appropriate (sufficient) to describe the transport phenomena. So, the finite set of equations presented here was built using the lower order statistical parameters. However, although only a finite set of equations is needed, this set may also use higher order statistics. In fact, the number of possible sets is still “infinite”, because the unlimited number of statistical parameters and related equations still exists. A challenge for future studies may be to verify if the lower order terms are really sufficient to obtain the expected predictions, and if the influence of the higher order terms alter the obtained predictions. It is still not possible to infer any behavior (for example, similar results or anomalous behavior) for solutions obtained using higher order terms, because no studies were directed to answer such questions.

In the present example, only the records of the scalar variable F and the velocity V were “modeled” through square waves. It may eventually be useful for some problems also to “model” the derivatives of the records (in time or space). The use of such “secondary records”, obtained from the original signal, was still not considered in this methodology.

The problem considered in this chapter was one-dimensional. The number of basic functions for two and three dimensional problems grows substantially. How to generate and solve the best set of equations for the 2-D and 3-D situations is still unknown.

Considering the above comments, it is clear that more studies are welcomed, intending to verify the potentialities of this methodology.

5. Conclusions

It was shown that the methodology of random square waves allows to obtain a closed set of equations for one-dimensional turbulent transfer problems. The methodology adopts *a priori* models for the records of the oscillatory variables, defining convenient functions that allow to “adjust” the records and to obtain predictions of the mean profiles. This is an alternative procedure in relation to the *a posteriori* “closures” generally based on *ad hoc* models, like the

use of turbulent diffusivities/viscosities, together with physical/phenomenological reasoning about relevant parameters to be considered in these diffusivities/viscosities. The basic functions are: the partition functions, the reduction coefficients and the superposition coefficients. The obtained transformed equations for the one-dimensional turbulent transport allow to obtain predictions of these functions.

In addition, the RMS of the velocity was also used as a basic function. The equations are nonlinear. An improved analysis of the one-dimensional scalar transfer through air-water interfaces was presented, leading to mean curves that superpose well with measured mean concentration curves for gas transfer. In this analysis, different constant values were used for α , κ and the second derivative at the interface, allowing to obtain well behaved and realistic mean profiles. Using the constant α values, the system of equations for one-dimensional scalar turbulent transport could be reduced to only one equation for n ; in this case, a third order differential equation. In the sequence, a first application of the methodology to velocity fields was made, following the same procedures already presented in the literature for mass concentration fields. The form of the reduction coefficient function for the velocity fluctuations was calculated from measured data found in the literature, and plotted as a function of n , generating a cloud of points. As for the case of mass transfer, α_u presents a minimum peak in the region of the boundary layer (maximum peak for $1-\alpha_u$). Because this methodology considers *a priori* definitions, applied to the records of the random parameters, it may be used for different phenomena in which random behaviors are observed.

6. Acknowledgements

The first author thanks: 1) Profs. Rivadavia Wollstein and Beate Frank (Universidade Regional de Blumenau), and Prof. Nicanor Poffo, (Conjunto Educacional Pedro II, Blumenau), for relevant advises and 2) "Associação dos Amigos da FURB", for financial support.

7. Appendix I: Obtaining equation (51)

The starting point is the set of equations (45), (46), and the definition (47).

The "*" was dropped from z^* and IJ^* in order to simplify the representation of the equations. The main equation (45) (or 50a) then is written as

$$(1-n) = S \frac{d^2 n}{dz^2} - \frac{d(IJ)}{dz} \quad (\text{AI-1})$$

Equation (46), for $\theta=2$, is presented as:

$$\begin{aligned} & -K_f n(1-n)(1-\alpha_f)^2 + \frac{\sqrt{\frac{[n(1-n)]}{n(1-n) + \frac{\beta(1-\beta)}{(2\beta-1)^2}}}}{[n(1-n)]^{1/2} \sqrt{\omega^2}} (1-\alpha_f) \frac{\partial n}{\partial z} + \\ & + \frac{1}{2} \frac{\partial}{\partial z} \left\{ \frac{1}{\sqrt{n(1-n) + \frac{\beta(1-\beta)}{(2\beta-1)^2}}} [(1-2n)] [n(1-n)(1-\alpha_f)^2] \sqrt{\omega^2} \right\} = \\ & = D_f \left\{ \frac{\partial^2 [(1-n)(1-\alpha_c)]}{\partial z^2} + \frac{\partial^2 [-n(1-\alpha_c)]}{\partial z^2} \right\} n(1-n)(1-\alpha_f) \end{aligned} \quad (\text{AI-2})$$

Using the definitions $IJ = \frac{n(1-n)(1-\alpha_f)\sqrt{\omega^2}}{Ke}$ and $S = \frac{D}{Ke^2}$:

$$IJ = \frac{n(1-n)(1-\alpha_f)\sqrt{\omega^2}}{\sqrt{n(1-n) + \frac{\beta(1-\beta)}{(2\beta-1)^2}}}$$

$$\begin{aligned} & -n(1-n)(1-\alpha_c)^2 + IJ \frac{\partial n}{\partial z} + \frac{1}{2} \frac{\partial}{\partial z} \{(1-2n)(1-\alpha_c)IJ\} = \\ & = S \left\{ \frac{\partial^2 [(1-n)(1-\alpha_c)]}{\partial z^2} + \frac{\partial^2 [-n(1-\alpha_c)]}{\partial z^2} \right\} n(1-n)(1-\alpha_c) \end{aligned} \quad (AI-3)$$

For α_f constant and defining $A=(1-\alpha_f)$:

$$-n(1-n)A^2 + IJ \frac{dn}{dz} - IJ A \frac{dn}{dz} + \frac{(1-2n)}{2} A \frac{dIJ}{dz} = -2S \left\{ \frac{d^2n}{dz^2} \right\} n(1-n)A^2 \quad (AI-4)$$

Using equations (AI1) and (AI4)

$$\begin{aligned} & -n(1-n)A^2 - \frac{(1-n)(1-2n)}{2} A + IJ(1-A) \frac{dn}{dz} = \\ & = -2S \left\{ \frac{d^2n}{dz^2} \right\} n(1-n)A^2 - S \frac{(1-2n)}{2} A \left\{ \frac{d^2n}{dz^2} \right\} \end{aligned} \quad (AI-5)$$

Solving equation (AI5) for IJ :

$$IJ = \frac{-2S \left\{ \frac{d^2n}{dz^2} \right\} n(1-n)A^2 - S \frac{(1-2n)}{2} A \left\{ \frac{d^2n}{dz^2} \right\} + n(1-n)A^2 + \frac{(1-n)(1-2n)}{2} A}{(1-A) \frac{dn}{dz}} \quad (AI-6)$$

Rearranging equation (AI6):

$$\frac{(1-A)}{A} IJ = \frac{-S \left\{ 2An(1-n) + \frac{(1-2n)}{2} \right\} \left\{ \frac{d^2n}{dz^2} \right\} + (1-n) \left[\frac{2n(A-1)+1}{2} \right]}{\frac{dn}{dz}} \quad (AI-7)$$

Differentiating equation (AI7) and using equation (AI1):

$$\begin{aligned} & \frac{(1-A)}{A} \left[S \frac{d^2n}{dz^2} - (1-n) \right] = \\ & = \frac{-S \left\{ 2A \left[\frac{dn}{dz} - 2n \frac{dn}{dz} \right] - \frac{dn}{dz} \right\} \left\{ \frac{d^2n}{dz^2} \right\} - S \left\{ 2An(1-n) + \frac{(1-2n)}{2} \right\} \left\{ \frac{d^3n}{dz^3} \right\} +}{\frac{dn}{dz}} \end{aligned}$$

$$\begin{aligned}
& + \frac{\left(\frac{dn}{dz}\right)\left[\frac{2n(A-1)+1}{2}\right] + (1-n)\left[\frac{(A-1)dn}{dz}\right]}{\frac{dn}{dz}} \\
& - S \left\{ 2An(1-n) + \frac{(1-2n)}{2} \right\} \left\{ \frac{d^2n}{dz^2} \right\} + (1-n) \left[\frac{2n(A-1)+1}{2} \right] \left\{ \frac{d^2n}{dz^2} \right\} \\
& \frac{\quad}{\left(\frac{dn}{dz}\right)^2}
\end{aligned} \tag{AI-8}$$

Multiplying by $\left(\frac{dn}{dz}\right)^2$ and simplifying $\frac{dn}{dz}$:

$$\begin{aligned}
& \frac{(1-A)}{A} \left[S \frac{d^2n}{dz^2} - (1-n) \right] \left(\frac{dn}{dz}\right)^2 = \\
& - \left(\frac{dn}{dz}\right)^2 S \left\{ 2A[1-2n] - 1 \right\} \left\{ \frac{d^2n}{dz^2} \right\} - \\
& - \left(\frac{dn}{dz}\right) S \left\{ 2An(1-n) + \frac{(1-2n)}{2} \right\} \left\{ \frac{d^3n}{dz^3} \right\} + \\
& + \left(\frac{dn}{dz}\right)^2 \left\{ - \left[\frac{2n(A-1)+1}{2} \right] + (1-n)(A-1) \right\} - \\
& - \left\{ -S \left\{ 2An(1-n) + \frac{(1-2n)}{2} \right\} \left\{ \frac{d^2n}{dz^2} \right\} + (1-n) \left[\frac{2n(A-1)+1}{2} \right] \right\} \left\{ \frac{d^2n}{dz^2} \right\}
\end{aligned} \tag{AI-9}$$

Rearranging (after multiplying the equation by A and using $S=1/\kappa$):

$$\begin{aligned}
& A \left[2An(1-n) + \frac{(1-2n)}{2} \right] \frac{d^3n}{dz^3} \frac{dn}{dz} + \\
& + A \left\{ - \left[2An(1-n) + \frac{(1-2n)}{2} \right] \frac{d^2n}{dz^2} + \kappa(1-n) \left[\frac{2n(A-1)+1}{2} \right] + \right. \\
& \left. + \frac{\left\{ 1 + 2A \left[A(1-2n) - 1 \right] \right\} \left(\frac{dn}{dz}\right)^2}{A} \right\} \left\{ \frac{d^2n}{dz^2} \right\} + \\
& + \kappa \left\{ (A-1)(1-n) - A \left[A(1-2n) - \left(\frac{3}{2} - 2n\right) \right] \right\} \left(\frac{dn}{dz}\right)^2 \\
& = 0
\end{aligned} \tag{AI-10}$$

Equation (AI10) is the equation (51) presented in the text.

8. Appendix II: Solving equation (51) using mathematical tables

Equation (51) (or equation (AI-10)) of this chapter is a third order nonlinear ordinary differential equation, for which adequate numerical methods must be applied. Some methods were considered to solve it.

A first attempt was made using the second order Finite Differences Method and the solver device from the Microsoft Excel® table, intending to solve the problem with simple and practical tools, but the results were not satisfactory. It does not imply that the Finite Differences Method does not apply, but only that we wanted more direct ways to check the applicability of equation (51).

The second attempt was made using Runge-Kutta methods, also furnished in mathematical tables like Excel®, maintaining the objective of solving the one-dimensional problem with simple tools. In this case, the results were adequate, superposing well the experimental data.

The Runge-Kutta methods were developed for ordinary differential equations (ODEs) or systems of ODEs. Equation (AI-10) is a nonlinear differential equation, so that it was necessary to first rewrite it as a system of ODEs, as follows

$$\frac{dn}{dz} = j \tag{AII-1}$$

$$\frac{d^2n}{dz^2} = w \tag{AII-2}$$

$$\frac{dw}{dz} = (f_1 + f_2) / f_3 \tag{AII-3}$$

in which

$$f_1 = -A \left\{ \begin{array}{l} - \left[2An(1-n) + \frac{(1-2n)}{2} \right] w + \kappa(1-n) \left[\frac{2n(A-1)+1}{2} \right] + \\ + \frac{\{1+2A[A(1-2n)-1]\}}{A} j^2 \end{array} \right\} w \tag{AII-4}$$

$$f_2 = -\kappa \left\{ (A-1)(1-n) - A \left[A(1-2n) - \left(\frac{3}{2} - 2n \right) \right] \right\} j^2 \tag{AII-5}$$

$$f_3 = A \left[2An(1-n) + \frac{(1-2n)}{2} \right] j \tag{AII-6}$$

Figure 6 shows that 3th, 4th and 5th orders Runge-Kutta methods were applied to obtain numerical results for the profile of *n*. This Appendix shows a summary of the use of the 5th order method. Of course, similar procedures were followed for the lower orders. As usual in this chapter, equations (AII-1) up to (AII-3) use the nondimensional variable *z* without the star "*" (that is, it corresponds to *z**). Considering "y" the dependent variable in a given ODE, the of 5th order method, presented by Butcher (1964) appud Chapra and Canale (2006), is written as follows

$$y_{k+1} = y_k + \frac{\Delta x}{90} (7\psi_1 + 32\psi_3 + 12\psi_4 + 32\psi_5 + 7\psi_6) \tag{AII-7}$$

in which

$$\left\{ \begin{array}{l} \psi_1 = f(x_k, y_k) \\ \psi_2 = f\left(x_k + \frac{1}{4}\Delta x, y_k + \frac{1}{4}\psi_1\Delta x\right) \\ \psi_3 = f\left(x_k + \frac{1}{4}\Delta x, y_k + \frac{1}{8}\psi_1\Delta x + \frac{1}{8}\psi_2\Delta x\right) \\ \psi_4 = f\left(x_k + \frac{1}{2}\Delta x, y_k - \frac{1}{2}\psi_2\Delta x + \psi_3\Delta x\right) \\ \psi_5 = f\left(x_k + \frac{3}{4}\Delta x, y_k + \frac{3}{16}\psi_1\Delta x + \frac{9}{16}\psi_4\Delta x\right) \\ \psi_6 = f\left(x_k + \Delta x, y_k - \frac{3}{7}\psi_1\Delta x + \frac{2}{7}\psi_2\Delta x + \frac{12}{7}\psi_3\Delta x - \frac{12}{7}\psi_4\Delta x + \frac{8}{7}\psi_5\Delta x\right) \end{array} \right. \quad (\text{AII-8})$$

In the system of equations (AII-8), generated from equations (AII-4) through (AII-6), $x = z$ and $y = n$, following the representation used in this chapter.

The system of equations (AII-1) through (AII-6) was solved using a spreadsheet for Microsoft Excel®, available at www.stoa.usp.br/hidraulica/files/. Two initial values were fixed and one was calculated. Note that in the present study it was intended to verify if the method furnishes a viable profile, so that boundary or initial values obtained from the experimental data were assumed as adequate. The first was $n(0)=1$. The second was $n'(0)=-3$, corresponding to the experiments of Janzen (2006). The third information did not constitute an initial value, and was $n(1)=0$ or $0 < n(1) < 0.01$ (threshold value corresponding to the definition of the boundary layer). As the Runge-Kutta methods need initial values, this information was used to obtain $n''(0)$, the remaining initial value needed to perform the calculations. With the aid of the Newton (or quasi-Newton) method, it was possible to obtain values for $n''(0)$ that satisfied the third condition imposed at $z = 1$.

The derivative of n at $z=0$ is generally unknown in such mass transfer problems. In this case, solutions must be found considering, for example, $n(0)=1$, $0 < n(1) < 0.01$ and $n'(1)=0$ (three reasonable boundary conditions), for which another scheme must be developed to calculate the first and second derivatives at the origin. As mentioned, the aim of this study was to verify the applicability of the method. The details of solutions for different purposes must be considered by the researchers interested in that solution.

The construction of the spreadsheet is described in the following steps:

- i. determine the initial values: $n(0) = 1$, $n'(0) = -3$ (or other appropriate value) $n''(0) =$ initial guess;
- ii. Compute $\psi_{1,1}$ and $\psi_{1,2}$, the function values f_1, f_2 e f_3 with the initial values, and then $\psi_{1,3}$. In the variable $\psi_{i,j}$, $i = 1,2,\dots,6$ and $j = 1,2,3$, the first index corresponds to the six stages of the method and the second to the order of the ODE that generated the original system to be solved;
- iii. With the values calculated in (ii), calculate now $n_{k+(1/4)} \psi_{1,1} \Delta z$, $n_{j+(1/4)} \psi_{1,1} \Delta z$ and $w_{k+(1/4)} \psi_{1,1} \Delta z$. The following steps are similar until $j = 6$;
- iv. Equation AII-7 (a system) is then used to advance in space z .

The spreadsheet available at www.stoa.usp.br/hidraulica/files/ presents some suggestions that simplify some items of the above described steps (some manual work is simplified). The estimate of $n''(0)$, for example, is obtained following simplified procedures.

9. References

- Brodkey, R.S. (1967) The phenomena of Fluid Motions, *Addison-Wesley Publishing Company*, Reading, Massachusetts.
- Butcher, J.C. (1964). On Runge-Kutta methods of high order. *J.Austral. Math. Soc.*4, p.179-194.
- Chapra, S.C.; Canale, R.P. (2006). Numerical methods for engineers. McGraw-Hill, 5th ed., 926 p.
- Corrsin, S. (1957) Simple theory of an idealized turbulent mixer, *AIChE J.*, 3(3), pp. 329-330.
- Corrsin, S. (1964) The isotropic turbulent mixer: part II - arbitrary Schmidt number, *AIChE J.*, 10(6), pp. 870-877.
- Donelan, M.A., Drennan, W.M., Saltzman, E.S. & Wanninkhof, R. (2002) Gas Transfer at Water Surfaces, Geophysical Monograph Series, American Geophysical Union, Washington, U.S.A., 383 p.
- Hinze, J.O. (1959), Turbulence, Mc. Graw-Hill Book Company, USA, 586 p.
- Jähne, B. & Monahan, E.C. (1995) Air-Water Gas Transfer, Selected papers from the Third International Symposium on Air-Water Gas Transfer, Heidelberg, Germany, AEON Verlag & Studio, 918 p.
- Janzen, J.G. (2006) Fluxo de massa na interface ar-água em tanques de grades oscilantes e detalhes de escoamentos turbulentos isotrópicos (Gas transfer near the air-water interface in an oscillating-grid tanks and properties of isotropic turbulent flows – text in Portuguese). Doctoral thesis, University of Sao Paulo, São Carlos, Brazil.
- Janzen, J.G., Herlina, H., Jirka, G.H., Schulz, H.E. & Gulliver, J.S. (2010), Estimation of Mass Transfer Velocity based on Measured Turbulence Parameters, *AIChE Journal*, V.56, N.8, pp. 2005-2017.
- Janzen J.G, Schulz H.E. & Jirka GH. (2006) Air-water gas transfer details (portuguese). *Revista Brasileira de Recursos Hídricos*; 11, pp. 153-161.
- Janzen, J.G., Schulz, H.E. & Jirka, G.H. (2011) Turbulent Gas Flux Measurements near the Air-Water Interface in an Oscillating-Grid Tank. In Komori, S; McGillis, W. & Kurose, R. *Gas Transfer at Water Surfaces 2010*, Kyoto University Press, Kyoto, pp. 65-77.
- Monin, A.S. & Yaglom, A.M. (1979), *Statistical Fluid Mechanics: Mechanics of Turbulence*, Volume 1, the MIT Press, 4th ed., 769p.
- Monin, A.S. & Yaglom, A.M. (1981), *Statistical Fluid Mechanics: Mechanics of Turbulence*, Volume 2, the MIT Press, 2th ed., 873p.
- Pope, S.B. (2000), *Turbulent Flows*, Cambridge University Press, 1st ed., UK, 771p.
- Schulz, H.E. (1985) Investigação do mecanismo de reoxigenação da água em escoamento e sua correlação com o nível de turbulência junto à superfície - 1. (Investigation of the roxygenation mechanism in flowing waters and its relation to the turbulence level at the surface-1 – text in Portuguese) MSc dissertation, University of São Paulo, Brazil São Carlos. 299p.
- Schulz, H.E.; Bicudo, J.R., Barbosa, A.R. & Giorgetti, M.F. (1991) Turbulent Water Aeration: Analytical Approach and Experimental Data, In Wilhelms, S.C. and Gulliver, J.S., eds. *Air Water Mass Transfer*, ASCE, New York, pp.142-155.
- Schulz, H.E. & Janzen, J.G. (2009) Concentration fields near air-water interfaces during interfacial mass transport: oxygen transport and random square wave analysis. *Braz. J. Chem. Eng.* vol.26, n.3, pp. 527-536.
- Schulz, H.E., Lopes Junior, G.B. & Simões, A.L.A. (2011b) Gas-liquid mass transfer in turbulent boundary layers using random square waves, 3rd workshop on fluids

- and PDE, June 27 to July 1, Institute of Mathematics, Statistics and Scientific Computation, Campinas, Brazil.
- Schulz H.E. & Schulz S.A.G. (1991) Modelling below-surface characteristics in water reaeration. *Water pollution, modelling, measuring and prediction*. Computational Mechanics Publications and Elsevier Applied Science, pp. 441-454.
- Schulz, H.E., Simões, A.L.A. & Janzen, J.G. (2011a), *Statistical Approximations in Gas-Liquid Mass Transfer*, In Komori, S; McGillis, W. & Kurose, R. *Gas Transfer at Water Surfaces 2010*, Kyoto University Press, Kyoto, pp. 208-221.
- Wilhelms, S.C. & Gulliver, J.S. (1991) *Air-Water Mass Transfer, Selected Papers from the Second International Symposium on Gas Transfer at Water Surfaces*, Minneapolis, U.S.A., ASCE, 802 p.

Generalized Variational Principle for Dissipative Hydrodynamics: Shear Viscosity from Angular Momentum Relaxation in the Hydrodynamical Description of Continuum Mechanics

German A. Maximov
*N. N. Andreyev Acoustical Institute
Russia*

1. Introduction

A system of hydrodynamic equations for a viscous, heat conducting fluid is usually derived on the basis of the mass, the momentum and the energy conservation laws (Landau & Lifshitz, 1986). Certain assumptions about the form of the viscous stress tensor and the energy density flow vector are made to derive such a system of equations for the dissipative viscous, heat conductive fluid. The system of equations based on the mass, the momentum and the energy conservation laws describes adequately a large set of hydrodynamical phenomena. However, there are some aspects which suggest that this system is only an approximation.

For example, if we consider propagation of small perturbations described by this system, then it is possible to separate formally the longitudinal, shear and heat or entropy waves. The coupling of the longitudinal and heat waves results in their splitting into independent acoustic-thermal and thermo-acoustic modes. For these modes the limits of phase velocities tends to infinity at high frequencies so that the system is in formal contradiction with the requirements for a finite propagation velocity of any perturbation which the medium can undergo. Thus it is possible to suggest that such a hydrodynamic equation system is a mere low frequency approximation. Introducing the effects of viscosity relaxation (Landau & Lifshitz, 1972), guarantees a limit for the propagation velocity of the shear mode, and the introduction of the heat relaxation term (Deresiewicz, 1957; Nettleton, 1960; Lykov, 1967) in turn ensures finite propagation velocities of the acoustic-thermal and thermo-acoustic modes. However, the introduction of such relaxation processes requires serious effort with motivation.

Classical mechanics provides us with the Lagrange's variational principle which allows us to derive rigorously the equations of motion for a mechanical system knowing the forms of kinetic and potential energies. The difference between these energies determines the form of the Lagrange function. This approach translates directly into continuum mechanics by introduction of the Lagrangian density for non-dissipative media. In this approach the dissipation forces can be accounted for by the introduction of the dissipation function derivatives into the corresponding equations of motion in accordance with Onsager's

principle of symmetry of kinetic coefficients (Landau & Lifshitz, 1964). There is an established opinion that for a dissipative system it is impossible to formulate the variational principle analogously to the least action principle of Hamilton (Landau & Lifshitz, 1964). At the same time there are successful approaches (Onsager, 1931a, 1931b; Glensdorf & Prigogine, 1971; Biot, 1970; Gyarmati, 1970; Berdichevsky, 2009) in which the variational principles for heat conduction theory and for irreversible thermodynamics are applied to account explicitly for the dissipation processes. In spite of many attempts to formulate a variational principle for dissipative hydrodynamics or continuum mechanics (see for example (Onsager, 1931a, 1931b; Glensdorf & Prigogine, 1971; Biot, 1970; Gyarmati, 1970; Berdichevsky, 2009) and references inside) a consistent and predictive formulation is still absent. Therefore, there are good reasons to attempt to formulate the generalized Hamilton's variational principle for dissipative systems, which argues against its established opposition (Landau & Lifshitz, 1964). Thus the objective of the chapter is a new formulation of the generalized variational principle (GVP) for dissipative hydrodynamics (continuum mechanics) as a direct combination of Hamilton's and Osager's variational principles. The first part of the chapter is devoted to formulation of the GVP by itself with application to the well-known Navier-Stokes hydrodynamical system for heat conductive fluid. The second part of the chapter is devoted to the consistent introduction of viscous terms into the equation of fluid motion on the basis of the GVP. Two different approaches are considered. The first one dealt with internal degree of freedom described in terms of some internal parameter in the framework of Mandelshtam - Leontovich approach (Mandelshtam & Leontovich, 1937). In the second approach the rotational degree of freedom as independent variable appears additionally to the mean mass displacement field. For the dissipationless case this approach leads to the well-known Cosserat continuum (Kunin, 1975; Novatsky, 1975; Erofeev, 1998). When dissipation prevails over angular inertia this approach describes local relaxation of angular momentum and corresponds to the sense of internal parameter. Finally, it is shown that the nature of viscosity phenomenon can be interpreted as relaxation of angular momentum of material points on the kinetic level.

2. Generalized variational principle for dissipative hydrodynamics

2.1 Hamilton's variational principle

The non-dissipative case of Hamilton's variational principle can be formulated for a continuous medium in the form of the extreme condition for the action functional $\delta S = 0$:

$$S = \int_{t_1}^{t_2} dt \int_V d\vec{r} L , \quad (1)$$

which is an integral over the time interval (t_1, t_2) and the initial volume V of a given mass of a continuum medium in terms of Lagrangian's coordinates. From the principles of particle mechanics the Lagrangian density L is represented as the difference between the kinetic K and potential U energies:

$$L(\dot{\vec{u}}, \nabla \vec{u}) = K(\dot{\vec{u}}) - U(\nabla \vec{u}) . \quad (2)$$

Expression (2) implies that the Lagrangian can be considered as a function of the velocities of the displacements $\dot{\vec{u}} = \frac{\partial \vec{u}}{\partial t}$ and deformations $\nabla \vec{u} = \text{div}(\vec{u})$.

The motion equations derived from variational principles (1), (2) have the following form

$$\frac{d}{dt} \frac{\partial L}{\partial \dot{\bar{u}}} + \nabla \frac{\partial L}{\partial \nabla \bar{u}} = 0. \quad (3)$$

In the simplest case, when the kinetic and potential energies are determined by the quadratic forms

$$2K(\dot{\bar{u}}^2) = \rho_0 \dot{\bar{u}}^2, \quad 2U = \lambda \varepsilon_{ll}^2 + 2\mu \varepsilon_{ik}^2, \quad \varepsilon_{ik} = \frac{1}{2} \left(\frac{\partial u_i}{\partial x_k} + \frac{\partial u_k}{\partial x_i} \right) \quad (4)$$

the well-known equation of motion for an elastic medium (Landau & Lifshitz, 1972) can be derived:

$$\rho_0 \frac{d}{dt} \dot{\bar{u}} - \mu \Delta \bar{u} - (\lambda + \mu) \nabla (\nabla \bar{u}) = 0, \quad (5)$$

where ρ_0 is the density of the medium, and λ and μ are the Lamé's constants.

2.2 Onsager's variational principle

If we consider quasi-equilibrium systems, then the Onsager's variational principle for least energy dissipation can be formulated (Onsager, 1931a, 1931b). This principle is based on the symmetry of the kinetic coefficients and can be formulated as the extreme condition for the functional constructed as the difference between the rate of increase of entropy, \dot{s} , and the dissipation function, D . Here the entropy s is considered as a function of some thermodynamic relaxation process α , and the dissipation function D as a function of the rate of change of α , i.e.

$$\delta_{\dot{\alpha}} [\dot{s}(\alpha) - D(\dot{\alpha})] = 0 \quad (6)$$

The kinetic equation can then be derived from variational principle (6) to describe the relaxation of a thermodynamic system to its equilibrium state, i.e.:

$$\frac{d}{dt} s(\alpha) = 2D(\dot{\alpha}). \quad (7)$$

The above equation satisfies strictly the symmetry principle for the kinetic coefficients (Landau & Lifshitz, 1986).

2.3 Variational principle for mechanical systems with dissipation

As was mentioned above, the generalization of the equation of motion (3) in the presence of dissipation is obtained by introducing the derivative of the dissipation function with respect to the velocities into the right hand side of the equation (3). Therefore, in accordance with Onsager's symmetry principle for the kinetic coefficients (Landau & Lifshitz, 1964) we have

$$\frac{d}{dt} \frac{\partial L}{\partial \dot{\bar{u}}} + \nabla \frac{\partial L}{\partial \nabla \bar{u}} = - \frac{\partial D}{\partial \dot{\bar{u}}}. \quad (8)$$

Now it is possible to show, that the equation of motion can be derived in the form of equation (8) if Hamilton's variational principle is adapted with the following form of the Lagrangian function:

$$L(\dot{\bar{u}}, \nabla \bar{u}) = K(\dot{\bar{u}}) - U(\nabla \bar{u}) - \int_0^t D(\dot{\bar{u}}) dt', \quad (9)$$

where the time integral of the dissipation function is introduced into equation (2). The initial time in integral (9) denoted for simplicity equal to 0 corresponds to the time t_1 in functional (1).

It needs, however, to pay attention that at variation of dissipative term in such approach an additional item appears, which has to be neglected by hands. Indeed, variation of the last term in (9) leads us to result

$$\delta \int_0^t D(\dot{\bar{u}}) dt' = \int_0^t \frac{\partial D(\dot{\bar{u}})}{\partial \dot{\bar{u}}} \delta \dot{\bar{u}} dt' = \int_0^t \frac{d}{dt'} \left(\frac{\partial D(\dot{\bar{u}})}{\partial \dot{\bar{u}}} \delta \bar{u} \right) dt' - \int_0^t \frac{d}{dt'} \left(\frac{\partial D(\dot{\bar{u}})}{\partial \dot{\bar{u}}} \right) \delta \bar{u} dt' \quad (10a)$$

If to neglect by the last item in this expression

$$\delta \int_0^t D(\dot{\bar{u}}(t')) dt' = \frac{\partial D(\dot{\bar{u}})}{\partial \dot{\bar{u}}} \delta \bar{u}(t) - \int_0^t \frac{d}{dt'} \left(\frac{\partial D(\dot{\bar{u}})}{\partial \dot{\bar{u}}} \right) \delta \bar{u} dt' \approx \frac{\partial D(\dot{\bar{u}})}{\partial \dot{\bar{u}}} \delta \bar{u}(t), \quad (10b)$$

then the result gives us the same term $\frac{\partial D(\dot{\bar{u}})}{\partial \dot{\bar{u}}}$, which we need artificially introduce in the motion equation (8) for account of dissipation. From the one hand this approach can be considered as some rule at variation of integral term, because it leads us to the required form of the motion equation (8). From the other hand the following supporting basement can be proposed. Variation of action containing all terms in Lagrangian (9) with account of initial and boundary conditions can be written in the form

$$\int_{t_1}^{t_2} dt \int dV \left\{ \left(-\frac{d}{dt} \frac{\partial K(\dot{\bar{u}})}{\partial \dot{\bar{u}}} + \nabla \frac{\partial U(\nabla \bar{u})}{\partial \nabla \bar{u}} - \frac{\partial D(\dot{\bar{u}})}{\partial \dot{\bar{u}}} \right) \delta \bar{u} + \int_0^t \frac{d}{dt'} \left(\frac{\partial D(\dot{\bar{u}})}{\partial \dot{\bar{u}}} \right) \delta \bar{u} dt' \right\} = \quad (11a)$$

It is seen from (11a) that the required form of the motion equation with dissipation arises due to zero value of coefficient at arbitrary variation of the displacement field $\delta \bar{u}$. The last additional item, containing variation $\delta \bar{u}$ under integral, prevent to the strict conclusion in the given case. Nevertheless, if to rewrite the first term in (11a) in the same integral form as the last term

$$= \int_{t_1}^{t_2} dt \int dV \int_0^t dt' \left\{ \delta(t-t') \left(-\frac{d}{dt'} \frac{\partial K(\dot{\bar{u}})}{\partial \dot{\bar{u}}} + \nabla \frac{\partial U(\nabla \bar{u})}{\partial \nabla \bar{u}} - \frac{\partial D(\dot{\bar{u}})}{\partial \dot{\bar{u}}} \right) + \frac{d}{dt'} \left(\frac{\partial D(\dot{\bar{u}})}{\partial \dot{\bar{u}}} \right) \right\} \delta \bar{u} \quad (11b)$$

then due to the same reason of arbitrary variation $\delta \bar{u}$ the multiplier in brackets at this variation has to be equal to zero. It is possible to see now, that, if the function $\frac{d}{dt'} \left(\frac{\partial D(\dot{\bar{u}})}{\partial \dot{\bar{u}}} \right)$ is

not singular in the point $t' = t$, then its contribution can be neglected in this point in comparison with singular contribution from delta-function. The presented arguments can be considered as a basis for variation rule of integral term in Lagrangian.

In particular, if the dissipation function is considered as a quadratic form of the deformation velocities, i.e.:

$$2D(\nabla\dot{\bar{u}}) = \eta' \left(\frac{\partial\dot{u}_i}{\partial x_k} + \frac{\partial\dot{u}_k}{\partial x_i} \right)^2 + \zeta' \left(\frac{\partial\dot{u}_l}{\partial x_l} \right)^2, \quad (12)$$

then the derived equation of motion with account of (4) corresponds to the linearized Navier-Stokes equation:

$$\rho_0 \frac{d}{dt} \dot{\bar{u}} - (\lambda + \mu) \Delta \bar{u} - \lambda \nabla (\nabla \bar{u}) = \eta \Delta \dot{\bar{u}} + \left(\zeta + \frac{\eta}{3} \right) \nabla (\nabla \dot{\bar{u}}), \quad (13)$$

where the shear and volume viscosities, η and ζ respectively are given by $\eta'/2$ and $\zeta' + \frac{4}{3}\eta'$ respectively, from the constants in (12).

2.4 Independent variables

When GVP is formulated in the form (9) we need to determine variables in which terms the Lagrange's function has to be expressed. To answer on this question let's return to the hydrodynamics equations and look at variables for their description.

In absence of dissipation, as it easy to see, these variables are velocity, density, pressure and entropy \bar{v}, ρ, P, s . For the dissipationless case the entropy holds to be constant for given material point, hence a pressure can be considered, for example, as a function of solely density $P(\rho, s = const)$. The density of the given mass of continuum is expressed in terms of its volume. Hence variation of density can be expressed in terms of variation of volume or through divergence of the displacement field $\rho = \rho(\text{div}\bar{u})$. In particular, linearization of the continuity equation leads to relation

$$\rho = \rho_0(1 - \text{div}\bar{u}) \quad (14)$$

Velocity by definition is a time derivative from displacement $\bar{v} = \dot{\bar{u}}$. Thus, the displacement field \bar{u} can be considered as the principal hydrodynamical variable for the dissipationless case.

In the presence of dissipation, the hydrodynamic equations also involve the temperature T , implying in the following set of variables: \bar{v}, ρ, P, s, T . If pressure and entropy depend on density and temperature $P(\rho, T)$, $s(\rho, T)$ in accordance to the state equation, then the fields of displacements and temperatures: \bar{u}, T can be considered as the principal hydrodynamical variables.

Further, we will adopt the idea of Biot (Biot, 1970), and introduce some vector field \bar{u}_T (some vector potential), called the heat displacement, as independent variable instead temperature, so that the relative deviation of temperature T from its equilibrium state T_0 is determined by the divergence of the field \bar{u}_T . Namely in analogy with (14)

$$T = T_0(1 - \theta \text{div}\bar{u}_T) \quad (15a)$$

where θ is some dimensionless constant which is specially introduced in definition (15a) for simplification of the expression for the dissipation function. Thus, the divergence of the heat displacement field \bar{u}_T determines temperature deviation from its equilibrium level

$$\frac{T - T_0}{T_0} = -\theta \nabla \bar{u}_T. \quad (15b)$$

2.5 Generalized variational principle (GVP) for dissipative hydrodynamics

The above example (12), (13) of the derivation of the equation of motion for dissipative systems on the basis of Hamilton's variational principle with the Lagrange's function (9) suggests the possibility of formulating a generalized variational principle for dissipative hydrodynamical systems. This formulation can be obtained by a simple combination of Hamilton's variational principle (eqs. (1) and (2)) and Onsager's variational principle (eq. (6)), if the latter is integrated over time and multiplied by a temperature term (Maximov, 2008, 2010, originally formulated by Maximov, 2006). The Lagrangian density in this case can be written in the following form:

$$L = K - E + T \left[s - \int_0^t D dt' \right] = K - F - T \int_0^t D dt', \quad (16)$$

where E and F are the internal energy (potential for the dissipationless case) and the free energy respectively. For the non-dissipative case, the Lagrangian depends on the time and spatial derivatives of the mean mass displacement field \bar{u} , which is a basic independent variable in this formulation. For the dissipative case, the temperature should be considered as an additional independent variable for a complete description. Hence, a free energy and dissipation function should also depend on the temperature variations. But temperature by itself is not a convenient variable here. Instead it is more convenient to consider the heat displacements \bar{u}_T , introduced in previous section, of which the divergence will give us temperature.

In this case the generalized Lagrangian can be written in the following form:

$$L(\dot{\bar{u}}, \nabla \bar{u}, \nabla \bar{u}_T) = K(\dot{\bar{u}}) - F(\nabla \bar{u}, \nabla \bar{u}_T) - T_0 \int_0^t D(\dot{\bar{u}}, \dot{\bar{u}}_T) dt'. \quad (17)$$

It is important to note here that the opportunity to formulate the variational principle for a dissipative system arises due to the energy conservation for two interacting fields: the mean mass displacement \bar{u} and the heat displacement \bar{u}_T . The dissipation function only plays a role in the transformation rate between these fields.

In this way the motion equations derived by variation of action with the Lagrangian (17), can be expressed in the following forms

$$\begin{aligned} \frac{d}{dt} \frac{\partial K}{\partial \dot{\bar{u}}} - \nabla \frac{\partial F}{\partial \nabla \bar{u}} &= -T_0 \frac{\partial D}{\partial \dot{\bar{u}}}, \\ T_0 \frac{\partial D}{\partial \dot{\bar{u}}_T} - \nabla \frac{\partial F}{\partial \nabla \bar{u}_T} &= 0. \end{aligned} \quad (18)$$

Taking into account that the kinetic energy is given by quadratic form (4), the free energy is given by its usual expression for thermo-elasticity in quadratic form (Landau & Lifshitz, 1972):

$$2F(\nabla\bar{u}, T) = 2\mu\varepsilon_{ik}^2 + \lambda\varepsilon_{ll}^2 + \tilde{\kappa}\left(\frac{T-T_0}{\theta T_0}\right)^2 + 2\tilde{\alpha}\varepsilon_{ll}\left(\frac{T-T_0}{\theta T_0}\right), \quad (19a)$$

or with substitution of expression (13) instead of the temperature terms:

$$2F(\nabla\bar{u}, \nabla\bar{u}_T) = 2\mu\varepsilon_{ik}^2 + \lambda\varepsilon_{ll}^2 + \tilde{\kappa}(\nabla\bar{u}_T)^2 + 2\tilde{\alpha}\varepsilon_{ll}(\nabla\bar{u}_T), \quad (19b)$$

The dissipation function is the square of the difference between the mean mass and the heat displacements

$$2D(\dot{\bar{u}}, \dot{\bar{u}}_T) = \beta(\dot{\bar{u}} - \dot{\bar{u}}_T)^2. \quad (20)$$

The meanings of the coefficients $\tilde{\kappa}$, $\tilde{\alpha}$ and β in quadratic forms (19), (20) will be defined in the next section by comparison with the classical Navier-Stokes hydrodynamical system of equations.

In this case the motion equations for the mean displacement field and for the temperature field derived on the basis of the generalized variational principle are just equivalent (at $\mu = 0$) to the linearized traditional system of hydrodynamics equations:

$$\rho_0 \frac{d}{dt} \dot{\bar{u}} - \mu \Delta \bar{u} - (\lambda + \mu + \tilde{\alpha}) \nabla(\nabla \bar{u}) = (\tilde{\alpha} + \tilde{\kappa}) / (\theta T_0) \nabla T \quad (21)$$

$$\beta(\dot{T} - T_0 \theta \nabla \dot{\bar{u}}) - \tilde{\kappa} \Delta T = \tilde{\alpha} T_0 \theta \Delta \nabla \bar{u}. \quad (22)$$

2.6 Comparison with the system of hydrodynamics equations

Coefficients of the quadratic forms in equations (19) and (20) can be determined by comparison between the system of equation (21) and (22) and the linearized system of hydrodynamics equations (Landau & Lifshitz, 1986) considering the variables \bar{u}, T :

$$\rho = \rho_0(1 - \nabla \bar{u}), \quad (23)$$

$$\rho_0 \frac{d^2 \bar{u}}{dt^2} - \rho_0 c_0^2 \Delta \bar{u} = -\rho_0 \alpha \nabla T + \eta \Delta \dot{\bar{u}} + \left(\zeta + \frac{\eta}{3} \right) \nabla(\nabla \dot{\bar{u}}), \quad (24)$$

$$\rho_0 C_V \frac{dT}{dt} + \rho_0 T_0 \alpha \nabla \dot{\bar{u}} - \kappa \Delta T = 0. \quad (25)$$

where c_0 is the isothermal sound velocity, C_V - the heat capacity at constant volume, κ the heat conductivity coefficient, and α the thermal expansion coefficient. In the absence of viscosity $\eta = 0$ and $\zeta = 0$, which was not taken into account in the dissipation function (20), the structure of equations (21), (22) nearly coincides with the second (24) and the third (25) equations in the system of hydrodynamics equations (Landau & Lifshitz, 1986). The only

difference is the additional term in the right part of equation (22) in comparison with (25). We note here briefly that the reason for the introduction of this term is related to a generalized form of the Fourier law for heat energy flow. Besides the term of the temperature gradient in the Fourier law, an additional density or pressure gradient term should appear in spite of the contradicting argument presented in (Landau & Lifshitz, 1986). The independent support of this result can be found in refs. (Martynov, 2001; Zhdanov & Roldugin 1998).

The coefficients of equations (21), (22) and (24), (25) for the fluid case ($rot(\bar{u})=0$) can be found by comparison. One needs to take into account the different dimensions of equation (22) and (25), and, hence, the presence of common dimension multiplier in the comparison of coefficients for these equations.

The parameters of the quadratic forms are expressed explicitly in terms of the physical parameters by the following expressions

$$\beta = \frac{\rho_0 c_0^2}{\chi} (\gamma^2 - 1), \quad \theta = -\frac{\gamma - 1}{\alpha T_0}, \quad \tilde{\alpha} = \rho_0 c_0^2 (\gamma - 1), \quad \lambda + 2\mu = \rho_0 c_0^2 \gamma, \quad \tilde{\kappa} = \rho_0 c_0^2 (\gamma^2 - 1), \quad (26)$$

where γ is the specific temperature ratio, $\gamma = C_p / C_v$, and $\chi = \kappa / \rho_0 C_v$ is the temperature conductivity coefficient. It is remarkable that the coefficient in the dissipation function β is inversely proportional to the temperature conductivity coefficient.

3. Viscous terms in dissipative hydrodynamics

3.1 Account of viscosity relaxation for a fluid

To take into account fluid viscosity in the equation of motion in the framework of the generalized variational principle it is possible to introduce additional internal parameters to describe the quasi-equilibrium state of the medium, analogous to the Mandelshtam – Leontovich approach (Mandelshtam & Leontovich, 1937). As will be shown, in order to describe both the shear and the volume viscosities simultaneously, this internal parameter needs to possess the properties of a tensor. To simplify the description we consider the case when the temperature variation variable T is not essential so that the heat displacement \bar{u}_T terms can be omitted. In this case the additional terms associated with the tensor internal parameter ξ_{ik} , will appear in the expression for the free energy of an elastic medium (19), and it can be written as:

$$2F(\nabla \bar{u}, \xi_{ij}) = 2\mu \varepsilon_{ik}^2 + \lambda \varepsilon_{ll}^2 + a_1 \xi_{ll}^2 + a_2 \xi_{ik}^2 + 2b_1 \xi_{kk} \varepsilon_{ll} + 2b_2 \xi_{ik} \varepsilon_{ki}, \quad (19c)$$

where a_i and b_i are some coefficients of a positively determined quadratic form. The kinetic energy is then given by the ordinal expression (4) and the dissipative function in the absence of the temperature term can be written as the following quadratic form:

$$2D(\dot{\xi}_{ij}) = \gamma_1 \dot{\xi}_{ll}^2 + \gamma_2 \dot{\xi}_{ik}^2 \quad (27)$$

with some coefficients γ_1, γ_2 .

The system of motion equations, derived on the basis of the generalized variational principle for this case can be rewritten as

$$\rho_0 \frac{d}{dt} \dot{\bar{u}} - \mu \Delta \bar{u} - (\lambda + \mu) \nabla (\nabla \bar{u}) - b_1 \nabla \xi_{ll} - b_2 \frac{\partial \xi_{ik}}{\partial x_k} = 0, \quad (28)$$

$$\gamma_1 \delta_{ik} \frac{d \xi_{ll}}{dt} + \gamma_2 \frac{d \xi_{ik}}{dt} + a_1 \delta_{ik} \xi_{ll} + a_2 \xi_{ik} + b_1 \delta_{ik} \nabla \bar{u} + b_2 \varepsilon_{ik} = 0. \quad (29)$$

Here in the first equation (28) we use for shortness the tensor notation for vector obtained as divergence of internal parameter tensor. Equation (28) is the motion equation for an elastic medium. Equation (29) is the kinetic equation for the internal parameter tensor ξ_{ik} . Convolving the kinetic equation by indexes it is possible to obtain the separate kinetic equation for the spherical part of the internal parameter tensor ξ_{ll} :

$$\tilde{\gamma} \frac{d \xi_{ll}}{dt} + \tilde{a} \xi_{ll} + \tilde{b} \varepsilon_{ll} = 0, \quad (30)$$

where the coefficients with tilde have the following meaning:

$$\tilde{\gamma} = 3\gamma_1 + \gamma_2, \quad \tilde{a} = 3a_1 + a_2, \quad \tilde{b} = 3b_1 + b_2 \quad (31)$$

Kinetic equation (29) is an inhomogeneous ordinary differential equation of the first order. Its solution can be written as:

$$\xi_{ll} = -\frac{\tilde{b}}{\tilde{\gamma}} \int_{-\infty}^t e^{-\frac{\tilde{a}}{\tilde{\gamma}}(t-t')} \varepsilon_{ll}(t') dt' \quad (32)$$

For the other components of the internal tensor parameter ξ_{ik} we can also obtain a kinetic equation of similar form to equation (29), but with added inhomogeneous terms, i.e.

$$\gamma_2 \frac{d \xi_{ik}}{dt} + a_2 \xi_{ik} + b_2 \varepsilon_{ik} + \tilde{a}_1 \delta_{ik} \xi_{ll} + \tilde{b}_1 \delta_{ik} \varepsilon_{ll} = 0 \quad (33)$$

where the following notations are introduced

$$\begin{aligned} \tilde{a}_1 &= \left(a_1 - \tilde{a} \frac{\gamma_1}{\tilde{\gamma}} \right), \\ \tilde{b}_1 &= \left(b_1 - \tilde{b} \frac{\gamma_1}{\tilde{\gamma}} \right) \end{aligned} \quad (34)$$

Again, the solution of equation (33) has a form analogous to expression (32) with additional contributions from the terms with multipliers \tilde{a}_1 and \tilde{b}_1 . Specifically,

$$\xi_{ik} = -\frac{b_2}{\gamma_2} \int_{-\infty}^t dt' e^{-\frac{a_2}{\gamma_2}(t-t')} \left(\varepsilon_{ik} - \delta_{ik} \varepsilon_{ll} \left(1 - \frac{\tilde{b}}{b_2} \frac{(a_1 \gamma_2 - a_2 \gamma_1)}{(\tilde{a} \gamma_2 - a_2 \tilde{\gamma})} \right) \right) - \delta_{ik} \frac{\tilde{b}}{\tilde{\gamma}} \frac{(a_1 \tilde{\gamma} - \tilde{a} \gamma_1)}{(\tilde{a} \gamma_2 - a_2 \tilde{\gamma})} \int_{-\infty}^t dt' e^{-\frac{\tilde{a}}{\tilde{\gamma}}(t-t')} \varepsilon_{ll} \quad (35)$$

Taking the divergence of tensor (35), we obtain the following vector

$$\begin{aligned} \frac{\partial \xi_{ik}^e}{\partial x_k} = & -\frac{b_2}{\gamma_2} \int_{-\infty}^t dt' e^{-\frac{a_2}{\gamma_2}(t-t')} \left(\frac{1}{2} (\Delta \bar{u} + \nabla(\nabla \bar{u})) - \nabla(\nabla \bar{u}) \left(1 - \frac{\tilde{b}}{b_2} \frac{(a_1 \gamma_2 - a_2 \gamma_1)}{(\tilde{a} \gamma_2 - a_2 \tilde{\gamma})} \right) \right) - \\ & - \frac{\tilde{b}}{\tilde{\gamma}} \frac{(a_1 \tilde{\gamma} - \tilde{a} \gamma_1)}{(\tilde{a} \gamma_2 - a_2 \tilde{\gamma})} \int_{-\infty}^t dt' e^{-\frac{\tilde{a}}{\tilde{\gamma}}(t-t')} \nabla(\nabla \bar{u}) \end{aligned} \quad (36)$$

If we substitute (36) and (32) in the motion equation (28), we can write:

$$\begin{aligned} \rho_0 \frac{d}{dt} \dot{\bar{u}} - \mu \Delta \bar{u} - (\lambda + \mu) \nabla(\nabla \bar{u}) = & -\frac{\tilde{b}}{\tilde{\gamma}} \left(b_1 - b_2 \frac{(a_1 \tilde{\gamma} - \tilde{a} \gamma_1)}{(\tilde{a} \gamma_2 - a_2 \tilde{\gamma})} \right) \int_{-\infty}^t dt' e^{-\frac{\tilde{a}}{\tilde{\gamma}}(t-t')} \nabla(\nabla \bar{u}) - \\ & - \frac{b_2^2}{\gamma_2} \int_{-\infty}^t dt' e^{-\frac{a_2}{\gamma_2}(t-t')} \left(\frac{1}{2} (\Delta \bar{u} + \nabla(\nabla \bar{u})) - \nabla(\nabla \bar{u}) \left(1 - \frac{\tilde{b}}{b_2} \frac{(a_1 \gamma_2 - a_2 \gamma_1)}{(\tilde{a} \gamma_2 - a_2 \tilde{\gamma})} \right) \right) \end{aligned} \quad (37)$$

In the low frequency limit, at times greater than the relaxation times $\tilde{\gamma}/\tilde{a}$ and γ_2/a_2 , it is possible to derive an equation analogous to the Navier - Stokes motion equation with shear and volume viscosities:

$$\rho_0 \frac{d}{dt} \dot{\bar{u}} - \tilde{\mu} \Delta \bar{u} - (\tilde{\lambda} + \tilde{\mu}) \nabla(\nabla \bar{u}) = \tilde{\eta} \Delta \dot{\bar{u}} + \left(\tilde{\zeta} + \frac{\tilde{\eta}}{3} \right) \nabla(\nabla \dot{\bar{u}}) \quad (38)$$

where the effective elastic moduli $\tilde{\lambda}$ and $\tilde{\mu}$ and coefficients of shear and volume viscosities are expressed as

$$\begin{aligned} \tilde{\mu} = \mu - \frac{b_2^2}{2a_2}, \quad \tilde{\lambda} = \lambda + \frac{b_2^2}{2a_2} - \frac{\tilde{b}}{\tilde{a}} \left(b_1 - b_2 \frac{(a_1 \tilde{\gamma} - \tilde{a} \gamma_1)}{(\tilde{a} \gamma_2 - a_2 \tilde{\gamma})} \right), \quad \tilde{\eta} = \frac{1}{2} \gamma_2 \frac{b_2^2}{a_2^2}, \\ \tilde{\zeta} + \frac{\tilde{\eta}}{3} = \tilde{\gamma} \frac{\tilde{b}}{\tilde{a}^2} \left(b_1 - b_2 \frac{(a_1 \tilde{\gamma} - \tilde{a} \gamma_1)}{(\tilde{a} \gamma_2 - a_2 \tilde{\gamma})} \right) - \gamma_2 \frac{b_2}{a_2^2} \left(\frac{b_2}{2} - \tilde{b} \frac{(a_1 \gamma_2 - a_2 \gamma_1)}{(\tilde{a} \gamma_2 - a_2 \tilde{\gamma})} \right) \end{aligned} \quad (39)$$

It is important to note that the structure of the effective shear modulus $\tilde{\mu}$ in (39) is determined by a difference, which can be equal to zero, in which case equation (38) becomes completely equivalent to the Navier - Stokes equation for a viscous fluid. Thus the condition

$$\mu = \frac{b_2^2}{2a_2} \quad (40)$$

should be satisfied to consider a solid with shear relaxation like a viscous fluid. If $\tilde{\mu} > 0$, then we have the case of elastic medium with a shear viscosity (the Voigt's model) or with relaxation in the more general case (37). Thus, in the framework of the uniform approach it is possible to describe viscous fluids and solids with visco-elastic properties.

As a final remark of this section it is possible to say several words about physical sense of the introduced internal parameter. Since in the low frequency limit the majority of gases and

fluids, including the simplest of them, is described by the Navier-Stokes equation, then the only available value, which could relax in all cases, and hence could be considered as common scalar internal parameter, is the mean distance between molecules in gas or liquid. In the condensed and especially in the solid media the mutual space placement of atoms becomes to be essential, hence a space variation of their mutual positions, holding rotational invariance of a body as whole, has to be described by symmetrical tensor of the second order. Hence the corresponding internal parameter could be the same tensor. Thus, the discrete structure of medium on the kinetic level predetermines existence, at least, of mentioned internal parameters, responsible for relaxation.

3.2 Shear viscosity as a consequence of the angular momentum relaxation for the hydrodynamical description of continuum mechanics

As shown in the previous section, it is possible to derive the system of hydrodynamical equations on the GVP basis for viscous, compressible fluid in the form of Navier-Stokes equations. However for the account of terms responsible for viscosity it is required to introduce some tensor internal parameter ξ_{ik} in agreement with Mandelshtam-Leontovich approach (Mandelshtam & Leontovich, 1937). Relaxation of this internal parameter provides appearance of viscous terms in the Navier-Stokes equation. It is worth mentioning that the developed approach allowed to generalize the Navier-Stokes equation with constant viscosity coefficient to more general case accounting for viscosity relaxation in analogy to the Maxwell's model (Landau & Lifshitz, 1972). However the physical interpretation of the tensor internal parameter, which should be enough universal due to general character of the Navier-Stokes equation, requires more clear understanding. On the intuition level it is clear that corresponding internal parameter should be related with neighbor order in atoms and molecules placement and their relaxation. In the present section such physical interpretation is represented.

As was mentioned in Introduction the system of hydrodynamical equations in the form of Navier-Stokes is usually derived on the basis of conservation laws of mass M , momentum \vec{P} and energy E . The correctness of equations of the traditional hydrodynamics is confirmed by the large number of experiments where it is adequate. However the conservation law of angular momentum \vec{M} is absent among the mentioned balance laws laying in the basis of traditional hydrodynamics. In this connection it is interesting to understand the role of conservation law of angular momentum \vec{M} in hydrodynamical description. It is worth mentioning that equation for angular momentum appeared in hydrodynamics early (Sorokin, 1943; Shliomis, 1966) and arises and develops in the momentum elasticity theory. The Cosserat continuum is an example of such description (Kunin, 1975; Novatsky, 1975; Erofeev, 1998). However some internal microstructure of medium is required for application of such approach.

In the hydrodynamical description as a partial case of continuum mechanics the definition of material point is introduced as sufficiently large ensemble of structural elements of medium (atoms and molecules) that on one hand one has to describe properties of this ensemble in statistical way and on the other one has to consider the size of material point as small in comparison with specific scales of the problem. A material point itself as closed ensemble of particles possesses the following integrals of motion: mass, momentum, energy and angular momentum.

The basic independent variables, in terms of which the hydrodynamical description should be constructed, are the values which can be determined for separate material point in

accordance with its integrals of motion: mean mass displacement vector \bar{u} (velocity of this displacement $\bar{v} = \partial \bar{u} / \partial t$ is determined by integrals of motion $\bar{v} = \bar{P} / M$), rotation angle $\bar{\varphi}$ (angular velocity of rotation $\bar{\Omega} = \dot{\bar{\varphi}}$ is determined by integrals of motion $\bar{\Omega} = \bar{M} / I$, where I - inertia moment) and heat displacement \bar{u}_T , determining variation of temperature and related with integral of energy E .

In accordance with the set of independent field variables we can represent the kinetic K and the free F energies as corresponding quadratic forms

$$2K = \rho \dot{\bar{u}}^2 + I \dot{\bar{\varphi}}^2 \quad (41)$$

$$2F = (\lambda + 2\mu)(\nabla \bar{u})^2 + \mu[\nabla \bar{u}]^2 + 2\delta \bar{\varphi}[\nabla \bar{u}] + \sigma(\bar{\varphi})^2 + \varepsilon(\nabla \bar{\varphi})^2 + \zeta[\nabla \bar{\varphi}]^2 \quad (42)$$

Taking into account that the dissipation dealt only with field of micro rotations, and omitting for shortness dissipation of mean displacement field, described by heat conductivity, we can write the dissipation function in the following form

$$2D = \gamma \dot{\bar{\varphi}}^2 \quad (43)$$

Equations of motion derived from GVP without temperature terms have the forms:

$$\frac{d}{dt} \frac{\partial K}{\partial \dot{\bar{u}}} - \nabla \frac{\partial F}{\partial \nabla \bar{u}} - \left[\nabla \frac{\partial F}{\partial [\nabla \bar{u}]} \right] = - \frac{\partial D}{\partial \dot{\bar{u}}} \quad (44a)$$

$$\frac{d}{dt} \frac{\partial K}{\partial \dot{\bar{\varphi}}} + \frac{\partial K}{\partial \bar{\varphi}} - \nabla \frac{\partial F}{\partial \nabla \bar{\varphi}} - \left[\nabla \frac{\partial F}{\partial [\nabla \bar{\varphi}]} \right] = - \frac{\partial D}{\partial \dot{\bar{\varphi}}} \quad (45a)$$

Without dissipation $\beta = 0$ the motion equations obtained with use of quadratic forms (41)-(43) correspond to the ones for Cosserat continuum (Kunin, 1975; Novatsky, 1975; Erofeev, 1998). Indeed for this case the equations (44) have forms:

$$\rho \frac{d}{dt} \dot{\bar{u}} - (\lambda + 2\mu) \nabla(\nabla \bar{u}) + \mu[\nabla[\nabla \bar{u}]] - \delta[\nabla \bar{\varphi}] = 0 \quad (44b)$$

$$I \frac{d}{dt} \dot{\bar{\varphi}} - \varepsilon \nabla(\nabla \bar{\varphi}) + \zeta[\nabla[\nabla \bar{\varphi}]] + \sigma \bar{\varphi} + \delta[\nabla \bar{u}] = 0 \quad (45b)$$

The explicit form of these equations confirms that they are indeed the Cosserat continuum. If one sets formally $\delta = 0$, then equations (44b) and (45b) are split and the equation (44b) reduces to ordinal equation of the elasticity theory and the equation (45b) represents the wave equation for angular momentum.

When dissipation exists the system of equations (44)-(45) contains additional terms responsible for this dissipation

$$\rho \ddot{\bar{u}} - (\lambda + 2\mu) \nabla(\nabla \bar{u}) + \mu[\nabla[\nabla \bar{u}]] - \delta[\nabla \bar{\varphi}] = 0 \quad (44c)$$

$$I \ddot{\bar{\varphi}} - \varepsilon \nabla(\nabla \bar{\varphi}) + \zeta[\nabla[\nabla \bar{\varphi}]] + \sigma \bar{\varphi} + \delta[\nabla \bar{u}] = -\gamma \dot{\bar{\varphi}} \quad (45c)$$

For the case $\varepsilon = 0$, $\zeta = 0$ and $I = 0$ the second equation (45c) reduces to the pure relaxation form:

$$\dot{\bar{\varphi}} = -\frac{\sigma}{\gamma}\bar{\varphi} - \frac{\delta}{\gamma}[\nabla\bar{u}] \quad (46)$$

Its solution can be represented in the form:

$$\bar{\varphi} = -\frac{\delta}{\gamma} \int_{-\infty}^t dt' e^{-\frac{\sigma}{\gamma}(t-t')} [\nabla\bar{u}] \quad (47a)$$

Substitution (47a) in (44c) leads to the following result

$$\rho\ddot{\bar{u}} - (\lambda + 2\mu)\nabla(\nabla\bar{u}) + \mu[\nabla[\nabla\bar{u}]] = -\frac{\delta^2}{\gamma} \int_{-\infty}^t dt' e^{-\frac{\sigma}{\gamma}(t-t')} [\nabla[\nabla\bar{u}]] \quad (48a)$$

For the case of large times $t\sigma/\gamma \gg 1$ the upper limit of integration gives the principal contribution and equation reduces to the form

$$\rho\ddot{\bar{u}} - (\lambda + 2\mu)\nabla(\nabla\bar{u}) + \left(\mu - \frac{\delta^2}{\sigma}\right)[\nabla[\nabla\bar{u}]] = \gamma \frac{\delta^2}{\sigma^2} [\nabla\dot{\bar{u}}] \quad (48b)$$

By the reason that the medium at large times should behave like a fluid then the following condition has to be satisfied

$$\mu - \frac{\delta^2}{\sigma} = 0 \quad (49)$$

Taking into account condition (49) let's make more accurate estimation of the integral, computing it by parts

$$\rho\ddot{\bar{u}} - (\lambda + 2\mu)\nabla(\nabla\bar{u}) = -\frac{\delta^2}{\sigma} \int_{-\infty}^t dt' e^{-\frac{\sigma}{\gamma}(t-t')} [\nabla[\nabla\dot{\bar{u}}]] \quad (48c)$$

The corresponding estimation for the large time limit $t \gg \gamma/\sigma$ reduces to the equation

$$\rho\ddot{\bar{u}} - (\lambda + 2\mu)\nabla(\nabla\bar{u}) = \gamma \frac{\mu^2}{\delta^2} [\nabla[\nabla\dot{\bar{u}}]] \quad (48d)$$

which coincides with the structure of Navier-Stokes equation in the presence of shear viscosity.

Let's consider the case with non zero moment of inertia $I \neq 0$. For this case the second equation (45c) is also local in space and it can be resolved for the function $\bar{\varphi}$ in Fourier representation ($t \rightarrow \omega$)

$$\bar{\varphi} = \frac{-\delta}{-I\omega^2 + i\omega\gamma + \sigma} [\nabla\bar{u}] \quad (50)$$

The zeros of the denominator

$$i\omega_{1,2} = \frac{1}{2I} \left(-\gamma \pm \sqrt{\gamma^2 - 4\sigma I} \right) \quad (51)$$

determine two modes of angular momentum relaxation. Under condition $I < \gamma^2/(4\sigma)$ both zeros are real and have the following asymptotics for small momentum of inertia $I \rightarrow 0$:

$$i\omega_1 \approx -\frac{\sigma}{\gamma} \quad i\omega_2 \approx -\frac{\gamma}{I} \quad (52)$$

The first zero does not depend on momentum of inertia I and the second root goes to infinity when $I \rightarrow 0$. Under condition $I = \gamma^2/(4\sigma)$ the zeros coincide and have the value $i\omega_1 \approx -2\frac{\sigma}{\gamma}$, and under the condition $I > \gamma^2/(4\sigma)$ the zeros are complex conjugated with negative real part, which decreases with increase of I . The last case corresponds to the resonant relaxation of angular momentum.

In the time representation the solution of the equation (50) can be written in the form

$$\bar{\varphi} = - \int_{-\infty}^t dt' e^{-\frac{\gamma}{2I}(t-t')} [\nabla \bar{u}] \left\{ \frac{2\delta}{\sqrt{\dots}} \operatorname{sh} \left(\frac{\sqrt{\dots}}{2I} (t-t') \right) \right\} \quad (47b)$$

here the notation $\sqrt{\dots} = \sqrt{\gamma^2 - 4\sigma I}$ is used. For the case of resonant relaxation $I > \gamma^2/(4\sigma)$ the corresponding expression has the form

$$\bar{\varphi} = - \int_{-\infty}^t dt' e^{-\frac{\gamma}{2I}(t-t')} [\nabla \bar{u}] \left\{ \frac{2\delta}{\sqrt{\dots}} \sin \left(\frac{\sqrt{\dots}}{2I} (t-t') \right) \right\} \quad (47c)$$

Substitution of the explicit expressions (47b) or (47c) in the equation (44c) gives the generalisation of the Navier – Stokes equation for a solid medium with local relaxation of angular momentum. As was mentioned above under special condition (49) and in the limiting case (52) this equation reduces exactly to the form of Navier – Stokes equation.

Thus, it is shown that relaxation of angular momentum of material points consisting a continuum can be considered as physical reason for appearance of terms with shear viscosity in Navier-Stokes equation. Without dissipation additional degree of freedom dealt with angular momentum leads to the well known Cosserat continuum.

4. Conclusion

The first part of the chapter presents an original formulation of the generalized variational principle (GVP) for dissipative hydrodynamics (continuum mechanics) as a direct combination of Hamilton's and Onsager's variational principles. The GVP for dissipative continuum mechanics is formulated as Hamilton's variational principle in terms of two independent field variables i.e. the mean mass and the heat displacement fields. It is important to mention that existence of two independent fields gives us opportunity to consider a closed mechanical system and hence to formulate variational principle. Dissipation plays only a role of energy transfer between the mean mass and the heat displacement fields. A system of equations for these fields is derived from the extreme condition for action with a Lagrangian density in the form of the difference between the kinetic and the free energies minus the time integral of the dissipation function. All mentioned potential functions are considered as a general positively determined quadratic

forms of time or space derivatives of the mean mass and the heat displacement fields. The generalized system of hydrodynamical equations is then evaluated on the basis of the GVP. At low frequencies this system corresponds to the traditional Navier – Stokes equation system. It allowed us to determine all coefficients of quadratic forms by direct comparison with the Navier – Stokes equation system.

The second part of the chapter is devoted to consistent introduction of viscous terms into the equation of fluid motion on the basis of the GVP. A tensor internal parameter is used for description of relaxation processes in vicinity of quasi-equilibrium state by analogy with the Mandelshtam – Leontovich approach. The derived equation of motion describes the viscosity relaxation phenomenon and generalizes the well known Navier – Stokes equation. At low frequencies the equation of fluid motion reduces exactly to the form of Navier – Stokes equation. Nevertheless there is still a question about physical interpretation of the used internal parameter. The answer on this question is presented in the last section of the chapter.

It is shown that the internal parameter responsible for shear viscosity can be interpreted as a consequence of relaxation of angular momentum of material points constituting a mechanical continuum. Due to angular momentum balance law the rotational degree of freedom as independent variable appears additionally to the mean mass displacement field. For the dissipationless case this approach leads to the well-known Cosserat continuum. When dissipation prevails over momentum of inertia this approach describes local relaxation of angular momentum and corresponds to the sense of the internal parameter. It is important that such principal parameter of Cosserat continuum as the inertia moment of intrinsic microstructure can completely vanish from the description for dissipative continuum. The independent equation of motion for angular momentum in this case reduces to local relaxation and after its substitution into the momentum balance equation leads to the viscous terms in Navier – Stokes equation. Thus, it is shown that the nature of viscosity phenomenon can be interpreted as relaxation of angular momentum of material points on the kinetic level.

5. Acknowledgment

The work was supported by ISTC grant 3691 and by RFBR grant №09-02-00927-a.

6. References

- Berdichevsky V.L. (2009). *Variational principles of continuum mechanics*, Springer-Verlag, ISBN 978-3-540-88466-8, Berlin.
- Biot M. (1970). *Variational principles in heat transfer*. Oxford, University Press.
- Deresiewicz H. (1957). Plane wave in a thermoplastic solids. *The Journal of the Acoustical Society of America*, Vol.29, pp.204-209, ISSN 0001-4966.
- Erofeev V.I. (1998). *Wave processes in solids with microstructure*, Moscow State University, Moscow.
- Glensdorf P., Prigogine I., (1971). *Thermodynamic Theory of Structure, Stability, and Fluctuations*, Wiley, New York.
- Gyarmati I. (1970). *Non-equilibrium thermodynamics. Field theory and variational principles*. Berlin, Springer-Verlag.
- Kunin I.A. (1975). *Theory of elastic media with micro structure*, Nauka, Moscow.
- Landau L.D., Lifshitz E.M. (1986). *Theoretical physics. Vol.6. Hydrodynamics*, Nauka, Moscow.

- Landau L.D., Lifshitz E.M. (1972). *Theoretical physics. Vol.7. Theory of elasticity*, Nauka, Moscow.
- Landau L.D., Lifshitz E.M. (1964). *Theoretical physics. Vol.5. Statistical physics*. Nauka, Moscow.
- Lykov A.V. (1967). *Theory of heat conduction*, Moscow, Vysshaya Shkola.
- Mandelsham L.I., Leontovich M.A. (1937). To the sound absorption theory in liquids, *The Journal of Experimental and Theoretical Physics*, Vol.7, No.3, pp. 438-444, ISSN 0044-4510 (in Russian).
- Martynov G.A. (2001). Hydrodynamic theory of sound wave propagation. *Theoretical and Mathematical Physics*, Vol.129, pp.1428-1438, ISSN 0564-6162.
- Maximov G.A. (2006). On the variational principle for dissipative hydrodynamics. *Preprint 006-2006, Moscow Engineering Physics Institute*, Moscow. (in Russian)
- Maximov G.A. (2008). Generalized variational principle for dissipative hydrodynamics and its application to the Biot's equations for multicomponent, multiphase media with temperature gradient, In: *New Research in Acoustics*, B.N. Weis, (Ed.), 21-61, Nova Science Publishers Inc., ISBN 978-1-60456-403-7.
- Maximov G.A. (2010). Generalized variational principle for dissipative hydrodynamics and its application to the Biot's theory for the description of a fluid shear relaxation, *Acta Acustica united with Acustica*, Vol.96, pp. 199-207, ISSN 1610-1928.
- Nettleton R.E. (1960). Relaxation theory of thermal conduction in liquids. *Physics of Fluids*, Vol.3, pp.216-223, ISSN 1070-6631
- Novatsky V. (1975). *Theory of elasticity*, Mir, Moscow.
- Onsager L. (1931a). Reciprocal relations in irreversible process I. *Physical Review*, Vol.37, pp.405-426.
- Onsager L. (1931b). Reciprocal relations in irreversible process II. *Physical Review*, Vol. 38, p.2265-2279.
- Shliomis M.I. (1966). Hydrodynamics of a fluid with intrinsic rotation, *The Journal of Experimental and Theoretical Physics*, Vol.51, No.7, pp.258-265, ISSN 0044-4510 (in Russian).
- Sorokin V.S. (1943). On internal friction of liquids and gases possessed hidden angular momentum, *The Journal of Experimental and Theoretical Physics*, Vol.13, No.7-8, pp. 306-312, ISSN 0044-4510 (in Russian).
- Zhdanov V.M., Roldugin V.I. (1998). Non-equilibrium thermodynamics and kinetic theory of rarefied gases. *Physics-Uspekhi*, Vol.41, No.4, pp. 349-381, ISSN 0042-1294.

Nonautonomous Solitons: Applications from Nonlinear Optics to BEC and Hydrodynamics

T. L. Belyaeva¹ and V. N. Serkin²

¹*Universidad Autónoma del Estado de México*

²*Benemerita Universidad Autónoma de Puebla
Mexico*

1. Introduction

Nonlinear science is believed by many outstanding scientists to be the most deeply important frontier for understanding Nature (Christiansen et al., 2000; Krumhansl, 1991). The interpenetration of main ideas and methods being used in different fields of science and technology has become today one of the decisive factors in the progress of science as a whole. Among the most spectacular examples of such an interchange of ideas and theoretical methods for analysis of various physical phenomena is the problem of solitary wave formation in nonautonomous and inhomogeneous dispersive and nonlinear systems. These models are used in a variety of fields of modern nonlinear science from hydrodynamics and plasma physics to nonlinear optics and matter waves in Bose-Einstein condensates. The purpose of this Chapter is to show the progress that is being made in the field of the exactly integrable nonautonomous and inhomogeneous nonlinear evolution equations possessing the exact soliton solutions. These kinds of solitons in nonlinear nonautonomous systems are well known today as nonautonomous solitons. Most of the problems considered in the present Chapter are motivated by their practical significance, especially the hydrodynamics applications and studies of possible scenarios of generations and controlling of monster (rogue) waves by the action of different nonautonomous and inhomogeneous external conditions.

Zabusky and Kruskal (Zabusky & Kruskal, 1965) introduced for the first time the soliton concept to characterize nonlinear solitary waves that do not disperse and preserve their identity during propagation and after a collision. The Greek ending "on" is generally used to describe elementary particles and this word was introduced to emphasize the most remarkable feature of these solitary waves. This means that the energy can propagate in the localized form and that the solitary waves emerge from the interaction completely preserved in form and speed with only a phase shift. Because of these defining features, the classical soliton is being considered as the ideal natural data bit. It should be emphasized that today, the optical soliton in fibers presents a beautiful example in which an abstract mathematical concept has produced a large impact on the real world of high technologies (Agrawal, 2001; Akhmediev, 1997; 2008; Dianov et al., 1989; Hasegawa, 1995; 2003; Taylor, 1992).

Solitons arise in any physical system possessing both nonlinearity and dispersion, diffraction or diffusion (in time or/and space). The classical soliton concept was developed for nonlinear and dispersive systems that have been autonomous; namely, time has only played the role of

the independent variable and has not appeared explicitly in the nonlinear evolution equation. A not uncommon situation is one in which a system is subjected to some form of external time-dependent force. Such situations could include repeated stress testing of a soliton in nonuniform media with time-dependent density gradients.

Historically, the study of soliton propagation through density gradients began with the pioneering work of Tappert and Zabusky (Tappert & Zabusky, 1971). As early as in 1976 Chen and Liu (Chen, 1976; 1978) substantially extended the concept of classical solitons to the accelerated motion of a soliton in a linearly inhomogeneous plasma. It was discovered that for the nonlinear Schrödinger equation model (NLSE) with a linear external potential, the inverse scattering transform (IST) method can be generalized by allowing the time-varying eigenvalue (TVE), and as a consequence of this, the solitons with time-varying velocities (but with time invariant amplitudes) have been predicted (Chen, 1976; 1978). At the same time Calogero and Degasperis (Calogero, 1976; 1982) introduced a general class of soliton solutions for the nonautonomous Korteweg-de Vries (KdV) models with varying nonlinearity and dispersion. It was shown that the basic property of solitons, to interact elastically, was also preserved, but the novel phenomenon was demonstrated, namely the fact that each soliton generally moves with variable speed as a particle acted by an external force rather than as a free particle (Calogero, 1976; 1982). In particular, to appreciate the significance of this analogy, Calogero and Degasperis introduced the terms boomerons and trappons instead of classical KdV solitons (Calogero, 1976; 1982). Some analytical approaches for the soliton solutions of the NLSE in the nonuniform medium were developed by Gupta and Ray (Gupta, 1981), Herrera (Herrera, 1984), and Balakrishnan (Balakrishnan, 1985). More recently, different aspects of soliton dynamics described by the nonautonomous NLSE models were investigated in (Serkin & Hasegawa, 2000a;b; 2002; Serkin et al., 2004; 2007; 2001a;b). In these works, the “ideal” soliton-like interaction scenarios among solitons have been studied within the generalized nonautonomous NLSE models with varying dispersion, nonlinearity and dissipation or gain. One important step was performed recently by Serkin, Hasegawa and Belyaeva in the Lax pair construction for the nonautonomous nonlinear Schrödinger equation models (Serkin et al., 2007). Exact soliton solutions for the nonautonomous NLSE models with linear and harmonic oscillator potentials substantially extend the concept of classical solitons and generalize it to the plethora of nonautonomous solitons that interact elastically and generally move with varying amplitudes, speeds and spectra adapted both to the external potentials and to the dispersion and nonlinearity variations. In particular, solitons in nonautonomous physical systems exist only under certain conditions and varying in time nonlinearity and dispersion cannot be chosen independently; they satisfy the exact integrability conditions. The law of soliton adaptation to an external potential has come as a surprise and this law is being today the object of much concentrated attention in the field. The interested reader can find many important results and citations, for example, in the papers published recently by Zhao et al. (He et al., 2009; Luo et al., 2009; Zhao et al., 2009; 2008), Shin (Shin, 2008) and (Kharif et al., 2009; Porsezian et al., 2007; Yan, 2010).

How can we determine whether a given nonlinear evolution equation is integrable or not? The ingenious method to answer this question was discovered by Gardner, Green, Kruskal and Miura (GGKM) (Gardner et al., 1967). Following this work, Lax (Lax, 1968) formulated a general principle for associating of nonlinear evolution equations with linear operators, so that the eigenvalues of the linear operator are integrals of the nonlinear equation. Lax developed the method of inverse scattering transform (IST) based on an abstract formulation of evolution equations and certain properties of operators in a Hilbert space, some of which

are well known in the context of quantum mechanics. Ablowitz, Kaup, Newell, Segur (AKNS) (Ablowitz et al., 1973) have found that many physically meaningful nonlinear models can be solved by the IST method.

In the traditional scheme of the IST method, the spectral parameter Λ of the auxiliary linear problem is assumed to be a time independent constant $\Lambda'_t = 0$, and this fact plays a fundamental role in the development of analytical theory (Zakharov, 1980). The nonlinear evolution equations that arise in the approach of variable spectral parameter, $\Lambda'_t \neq 0$, contain, as a rule, some coefficients explicitly dependent on time. The IST method with variable spectral parameter makes it possible to construct not only the well-known models for nonlinear autonomous physical systems, but also discover many novel integrable and physically significant nonlinear nonautonomous equations.

In this work, we clarify our algorithm based on the Lax pair generalization and reveal generic properties of nonautonomous solitons. We consider the generalized nonautonomous NLSE and KdV models with varying dispersion and nonlinearity from the point of view of their exact integrability. It should be stressed that to test the validity of our predictions, the experimental arrangement should be inspected to be as close as possible to the optimal map of parameters, at which the problem proves to be exactly integrable (Serkin & Hasegawa, 2000a;b; 2002). Notice, that when Serkin and Hasegawa formulated their concept of solitons in nonautonomous systems (Serkin & Hasegawa, 2000a;b; 2002), known today as nonautonomous solitons and SH-theorems (Serkin & Hasegawa, 2000a;b; 2002) published for the first time in (Serkin & Hasegawa, 2000a;b; 2002), they emphasized that "the methodology developed provides for a systematic way to find an infinite number of the novel stable bright and dark "soliton islands" in a "sea of solitary waves" with varying dispersion, nonlinearity, and gain or absorption" (Belyaeva et al., 2011; Serkin et al., 2010a;b). The concept of nonautonomous solitons, the generalized Lax pair and generalized AKNS methods described in details in this Chapter can be applied to different physical systems, from hydrodynamics and plasma physics to nonlinear optics and matter-waves and offer many opportunities for further scientific studies. As an illustrative example, we show that important mathematical analogies between different physical systems open the possibility to study optical rogue waves and ocean rogue waves in parallel and, due to the evident complexity of experiments with rogue waves in open oceans, this method offers remarkable possibilities in studies nonlinear hydrodynamic problems by performing experiments in the nonlinear optical systems with nonautonomous solitons and optical rogue waves.

2. Lax operator method and exact integrability of nonautonomous nonlinear and dispersive models with external potentials

The classification of dynamic systems into autonomous and nonautonomous is commonly used in science to characterize different physical situations in which, respectively, external time-dependent driving force is being present or absent. The mathematical treatment of nonautonomous system of equations is much more complicated than of traditional autonomous ones. As a typical illustration we may mention both a simple pendulum whose length changes with time and parametrically driven nonlinear Duffing oscillator (Nayfeh & Balachandran, 2004).

In the framework of the IST method, the nonlinear integrable equation arises as the compatibility condition of the system of the linear matrix differential equations

$$\psi_x = \widehat{F}\psi(x, t), \quad \psi_t = \widehat{G}\psi(x, t). \quad (1)$$

Here $\psi(x, t) = \{\psi_1, \psi_2\}^T$ is a 2-component complex function, $\widehat{\mathcal{F}}$ and $\widehat{\mathcal{G}}$ are complex-valued (2×2) matrices. Let us consider the general case of the IST method with a time-dependent spectral parameter $\Lambda(T)$ and the matrices $\widehat{\mathcal{F}}$ and $\widehat{\mathcal{G}}$

$$\widehat{\mathcal{F}}(\Lambda; S, T) = \widehat{\mathcal{F}} \left\{ \Lambda(T), q[S(x, t), T]; \frac{\partial q}{\partial S} \left(\frac{\partial S}{\partial x} \right); \frac{\partial^2 q}{\partial S^2} \left(\frac{\partial S}{\partial x} \right)^2; \dots; \frac{\partial^n q}{\partial S^n} \left(\frac{\partial S}{\partial x} \right)^n \right\}$$

$$\widehat{\mathcal{G}}(\Lambda; S, T) = \widehat{\mathcal{G}} \left\{ \Lambda(T), q[S(x, t), T]; \frac{\partial q}{\partial S} \left(\frac{\partial S}{\partial x} \right); \frac{\partial^2 q}{\partial S^2} \left(\frac{\partial S}{\partial x} \right)^2; \dots; \frac{\partial^n q}{\partial S^n} \left(\frac{\partial S}{\partial x} \right)^n \right\},$$

dependent on the generalized coordinates $S = S(x, t)$ and $T(t) = t$, where the function $q[S(x, t), T]$ and its derivatives denote the scattering potentials $Q(S, T)$ and $R(S, T)$ and their derivatives, correspondingly. The condition for the compatibility of the pair of linear differential equations (1) takes a form

$$\frac{\partial \widehat{\mathcal{F}}}{\partial T} + \frac{\partial \widehat{\mathcal{F}}}{\partial S} S_t - \frac{\partial \widehat{\mathcal{G}}}{\partial S} S_x + [\widehat{\mathcal{F}}, \widehat{\mathcal{G}}] = 0, \quad (2)$$

where

$$\widehat{\mathcal{F}} = -i\Lambda(T)\widehat{\sigma}_3 + \widehat{U}\widehat{\phi}, \quad (3)$$

$$\widehat{\mathcal{G}} = \begin{pmatrix} A & B \\ C & -A \end{pmatrix}, \quad (4)$$

$\widehat{\sigma}_3$ is the Pauli spin matrix and matrices \widehat{U} and $\widehat{\phi}$ are given by

$$\widehat{U} = \sqrt{\sigma} F^\gamma(T) \begin{pmatrix} 0 & Q(S, T) \\ R(S, T) & 0 \end{pmatrix}, \quad (5)$$

$$\widehat{\phi} = \begin{pmatrix} \exp[-i\varphi/2] & 0 \\ 0 & \exp[i\varphi/2] \end{pmatrix}. \quad (6)$$

Here $F(T)$ and $\varphi(S, T)$ are real unknown functions, γ is an arbitrary constant, and $\sigma = \pm 1$. The desired elements of $\widehat{\mathcal{G}}$ matrix (known in the modern literature as the AKNS elements) can be constructed in the form $\widehat{\mathcal{G}} = \sum_{k=0}^{k=3} G_k \Lambda^k$, with time varying spectral parameter given by

$$\Lambda_T = \lambda_0(T) + \lambda_1(T) \Lambda(T), \quad (7)$$

where time-dependent functions $\lambda_0(T)$ and $\lambda_1(T)$ are the expansion coefficients of Λ_T in powers of the spectral parameter $\Lambda(T)$.

Solving the system (2-6), we find both the matrix elements A, B, C

$$A = -i\lambda_0 S/S_x + a_0 - \frac{1}{4}a_3 \sigma F^{2\gamma} (QR\varphi_S S_x + iQR_S S_x - iRQ_S S_x) + \frac{1}{2}a_2 \sigma F^{2\gamma} QR + \Lambda \left(-i\lambda_1 S/S_x + \frac{1}{2}a_3 \sigma F^{2\gamma} QR + a_1 \right) + a_2 \Lambda^2 + a_3 \Lambda^3, \quad (8)$$

$$B = \sqrt{\sigma} F^\gamma \exp[i\varphi S/2] \left\{ -\frac{i}{4}a_3 S_x^2 \left(Q_{SS} + \frac{i}{2}Q\varphi_{SS} - \frac{1}{4}Q\varphi_S^2 + iQ_S\varphi_S \right) - \frac{i}{4}a_2 Q\varphi_S S_x - \frac{1}{2}a_2 Q_S S_x + iQ \left(-i\lambda_1 S/S_x + \frac{1}{2}a_3 \sigma F^{2\gamma} QR + a_1 \right) + \Lambda \left(-\frac{i}{4}a_3 Q\varphi_S S_x - \frac{1}{2}a_3 Q_S S_x + ia_2 Q \right) + ia_3 \Lambda^2 Q \right\},$$

$$\begin{aligned}
C = & \sqrt{\sigma} F^\gamma \exp[-i\varphi S/2] \left\{ -\frac{i}{4} a_3 S_x^2 \left(R_{SS} - \frac{i}{2} R \varphi_{SS} - \frac{1}{4} R \varphi_S^2 - i R_S \varphi_S \right) \right. \\
& - \frac{i}{4} a_2 R \varphi_S S_x + \frac{1}{2} a_2 R_S S_x + i R \left(-i \lambda_1 S/S_x + \frac{1}{2} a_3 \sigma F^{2\gamma} Q R + a_1 \right) \\
& \left. + \Lambda \left(-\frac{i}{4} a_3 R \varphi_S S_x + \frac{1}{2} a_3 R_S S_x + i a_2 R \right) + i a_3 \Lambda^2 R \right\},
\end{aligned}$$

and two general equations

$$\begin{aligned}
iQ_T = & \frac{1}{4} a_3 Q_{SSS} S_x^3 + \frac{3i}{8} a_3 Q_{SS} \varphi_S S_x^3 - \frac{3i}{4} a_3 \sigma F^{2\gamma} Q^2 R \varphi_S S_x \\
& - \frac{3}{2} a_3 \sigma F^{2\gamma} Q R Q_S S_x - \frac{i}{2} a_2 Q_{SS} S_x^2 + i a_2 \sigma F^{2\gamma} Q^2 R
\end{aligned} \quad (9)$$

$$\begin{aligned}
+iQ_S \left(-S_t + \lambda_1 S + i a_1 S_x - \frac{i}{2} a_2 \varphi_S S_x^2 + \frac{3}{8} a_3 \varphi_{SS} S_x^3 + \frac{3i}{16} a_3 \varphi_S^2 S_x^3 \right) \\
+ Q \left(i \lambda_1 - i \gamma \frac{F_T}{F} + \frac{1}{2} a_2 \varphi_{SS} S_x^2 - \frac{3}{16} a_3 \varphi_S \varphi_{SS} S_x^3 \right) \\
+ Q \left[2 \lambda_0 S/S_x + 2 i a_0 + \frac{1}{2} (\varphi_T + \varphi_S S_t) - \frac{1}{2} \lambda_1 S \varphi_S - \frac{i}{2} a_1 \varphi_S S_x \right] \\
+ Q \left(\frac{i}{8} a_2 \varphi_S^2 S_x^2 - \frac{i}{32} a_3 \varphi_S^3 S_x^3 + \frac{i}{8} a_3 \varphi_{SSS} S_x^3 \right)
\end{aligned}$$

$$\begin{aligned}
iR_T = & \frac{1}{4} a_3 R_{SSS} S_x^3 - \frac{3i}{8} a_3 R_{SS} \varphi_S S_x^3 + \frac{3i}{4} a_3 \sigma F^{2\gamma} R^2 Q \varphi_S S_x \\
& - \frac{3}{2} a_3 \sigma F^{2\gamma} R^2 Q_S S_x + \frac{i}{2} a_2 R_{SS} S_x^2 - i a_2 \sigma F^{2\gamma} R^2 Q
\end{aligned} \quad (10)$$

$$\begin{aligned}
+iR_S \left(-S_t + \lambda_1 S + i a_1 S_x - \frac{i}{2} a_2 \varphi_S S_x^2 - \frac{3}{8} a_3 \varphi_{SS} S_x^3 + \frac{3i}{16} a_3 \varphi_S^2 S_x^3 \right) \\
+ R \left(i \lambda_1 - i \gamma \frac{F_T}{F} + \frac{1}{2} a_2 \varphi_{SS} S_x^2 - \frac{3}{16} a_3 \varphi_S \varphi_{SS} S_x^3 \right) \\
+ R \left[-2 \lambda_0 S/S_x - 2 i a_0 - \frac{1}{2} (\varphi_T + \varphi_S S_t) + \frac{1}{2} \lambda_1 S \varphi_S + \frac{i}{2} a_1 \varphi_S S_x \right] \\
+ R \left(-\frac{i}{8} a_2 \varphi_S^2 S_x^2 + \frac{i}{32} a_3 \varphi_S^3 S_x^3 - \frac{i}{8} a_3 \varphi_{SSS} S_x^3 \right),
\end{aligned}$$

where the arbitrary time-dependent functions $a_0(T)$, $a_1(T)$, $a_2(T)$, $a_3(T)$ have been introduced within corresponding integrations.

By using the following reduction procedure $R = -Q^*$, it is easy to find that two equations (9) and (10) take the same form if the following conditions

$$\begin{aligned}
a_0 = -a_0^*, \quad a_1 = -a_1^*, \quad a_2 = -a_2^*, \quad a_3 = -a_3^*, \\
\lambda_0 = \lambda_0^*, \quad \lambda_1 = \lambda_1^*, \quad F = F^*
\end{aligned} \quad (11)$$

are fulfilled.

3. Generalized nonlinear Schrödinger equation and solitary waves in nonautonomous nonlinear and dispersive systems: nonautonomous solitons

Let us study a special case of the reduction procedure for Eqs. (9,10) when $a_3 = 0$

$$A = -i\lambda_0 S/S_x + a_0(T) - \frac{1}{2}a_2(T)\sigma F^{2\gamma} |Q|^2 - i\lambda_1 S/S_x \Lambda + a_1(T)\Lambda + a_2(T)\Lambda^2,$$

$$B = \sqrt{\sigma} F^\gamma \exp(i\varphi/2) \left\{ -\frac{i}{4}a_2(T)Q\varphi_S S_x - \frac{1}{2}a_2(T)Q_S S_x \right\} + i\{Q[-i\lambda_1 S/S_x + a_1(T) + \Lambda a_2(T)]\},$$

$$C = \sqrt{\sigma} F^\gamma \exp(-i\varphi/2) \left\{ \frac{i}{4}a_2(T)Q^* \varphi_S S_x - \frac{1}{2}a_2(T)Q_S^* S_x \right\} - i\{Q^*[-i\lambda_1 x + a_1(T) + \Lambda a_2(T)]\}.$$

In accordance with conditions (11), the imaginary functions $a_0(T)$, $a_1(T)$, $a_2(T)$ can be defined in the following way: $a_0(T) = i\gamma_0(T)$, $a_1(T) = iV(T)$, $a_2(T) = -iD_2(T)$, $R_2(T) = F^{2\gamma}D_2(T)$, where $D_2(T)$, $V(T)$, $\gamma_0(T)$ are arbitrary real functions. The coefficients $D_2(T)$ and $R_2(T)$ are represented by positively defined functions (for $\sigma = -1$, γ is assumed as a semi-entire number).

Then, Eqs. (9,10) can be transformed into

$$iQ_T = -\frac{1}{2}D_2 Q_{SS} S_x^2 - \sigma R_2 |Q|^2 Q - i\tilde{V}Q_S + i\Gamma Q + UQ, \quad (12)$$

where

$$\tilde{V}(S, T) = \frac{1}{2}D_2 S_x^2 \varphi_S + VS_x + S_t - \lambda_1 S,$$

$$U(S, T) = \frac{1}{8}D_2 S_x^2 \varphi_S^2 - 2\gamma_0 + \frac{1}{2}(\varphi_T + \varphi_S S_t + VS_x \varphi_S) + 2\lambda_0 S/S_x - \frac{1}{2}\lambda_1 \varphi_S S, \quad (13)$$

$$\Gamma = \left(-\gamma \frac{F_T}{F} - \frac{1}{4}D_2 S_x^2 \varphi_{SS} + \lambda_1 \right) = \left(\frac{1}{2} \frac{W(R_2, D_2)}{R_2 D_2} - \frac{1}{4}D_2 S_x^2 \varphi_{SS} + \lambda_1 \right). \quad (14)$$

Eq.(12) can be written down in the independent variables (x, t)

$$iQ_t + \frac{1}{2}D_2(t)Q_{xx} + \sigma R_2(t)|Q|^2 Q - U(x, t)Q + i\tilde{V}'Q_x = i\Gamma(t)Q. \quad (15)$$

Let us transform Eq.(15) into the more convenient form

$$iQ_t + \frac{1}{2}D_2 Q_{xx} + \sigma R_2 |Q|^2 Q - UQ = i\Gamma Q \quad (16)$$

using the following condition

$$\tilde{V}' = \frac{1}{2}D_2 S_x \varphi_S + V - \lambda_1 S/S_x = 0. \quad (17)$$

If we apply the commonly accepted in the IST method (Ablowitz et al., 1973) reduction: $V = -ia_1 = 0$, we find a parameter λ_1 from (17)

$$\lambda_1 = \frac{1}{2}D_2 S_x^2 \varphi_S / S, \quad (18)$$

and the corresponding potential $U(S, T)$ from Eq.(13):

$$U(S, T) = -2\gamma_0 + 2\lambda_0 S/S_x + \frac{1}{2}(\varphi_T + \varphi_S S_t) - \frac{1}{8}D_2 S_x^2 \varphi_S^2. \quad (19)$$

According to Eq.(14), the gain or absorption coefficient now is represented by

$$\Gamma = \frac{1}{2} \frac{W(R_2, D_2)}{R_2 D_2} - \frac{1}{4} D_2 S_x^2 \varphi_{SS} + \frac{1}{2} D_2 S_x^2 \varphi_S / S. \quad (20)$$

Let us consider some special choices of variables to specify the solutions of (16). First of all, we assume that variables are factorized in the phase profile $\varphi(S, T)$ as $\varphi = C(T)S^\alpha$. The first term in the real potential (19) represents some additional time-dependent phase $e^{2\gamma_0(t)t}$ of the solution $Q(x, t)$ for the equation (16) and, without loss of the generality, we use $\gamma_0 = 0$. The second term in (19) depends linearly on S . The NLSE with the linear spatial potential and constant λ_0 , describing the case of Alfen waves propagation in plasmas, has been studied previously in Ref. (Chen, 1976). We will study the more general case of chirped solitons in the Section 4 of this Chapter. Now, taking into account three last terms in (19), we obtain

$$U(S, T) = 2\lambda_0 S/S_x + \frac{1}{2} C_T S^\alpha + 1/2\alpha C S^{\alpha-1} S_t - \frac{1}{8} D_2 C^2 S_x^2 \alpha^2 S^{2\alpha-2}. \quad (21)$$

The gain or absorption coefficient (20) becomes

$$\Gamma(T) = \frac{1}{2} \frac{W(R_2, D_2)}{R_2 D_2} + \frac{\alpha}{4} (3 - \alpha) D_2 S_x^2 C S^{\alpha-2} \quad (22)$$

and Eq.(18) takes a form

$$\lambda_1 = \frac{1}{2} D_2 S_x^2 C \alpha S^{\alpha-2}. \quad (23)$$

If we assume that the functions $\Gamma(T)$ and $\lambda_1(T)$ depend only on T and do not depend on S , we conclude that $\alpha = 0$ or $\alpha = 2$.

The study of the soliton solutions of the nonautonomous NLSE with varying coefficients without time and space phase modulation (chirp) and corresponding to the case of $\alpha = 0$ has been carried out in Ref. (Serkin & Belyaeva, 2001a;b). Let us find here the solutions of Eq.(16) with chirp in the case of $\alpha = 2$, $\varphi(S, T) = C(T)S^2$. In this case, Eq. (18) becomes $\lambda_1 = D_2 S_x^2 C$. Now, the real spatial-temporal potential (21) takes the form

$$U[S(x, t), T] = 2\lambda_0 S/S_x + \frac{1}{2} (C_T - D_2 S_x^2 C^2) S^2 + C S S_t$$

Consider the simplest option to choose the variable $S(x, t)$ when the variables (x, t) are factorized: $S(x, t) = P(t)x$. In this case, all main characteristic functions: the phase modulation

$$\varphi(x, t) = \Theta(t)x^2, \quad (24)$$

the real potential

$$U(x, t) = 2\lambda_0 x + \frac{1}{2} (\Theta_t - D_2 \Theta^2) x^2 \equiv 2\lambda_0(t)x + \frac{1}{2} \Omega^2(t)x^2, \quad (25)$$

the gain (or absorption) coefficient

$$\Gamma(t) = \frac{1}{2} \left(\frac{W(R_2, D_2)}{R_2 D_2} + D_2 P^2 C \right) = \frac{1}{2} \left(\frac{W(R_2, D_2)}{R_2 D_2} + D_2 \Theta \right) \quad (26)$$

and the spectral parameter λ_1

$$\lambda_1(t) = D_2 P^2 C = D_2(t) \Theta(t) \quad (27)$$

are found to be dependent on the self-induced soliton phase shift $\Theta(t)$. Notice that the definition $\Omega^2(t) \equiv \Theta_t - D_2 \Theta^2$ has been introduced in Eq.(25).

Now we can rewrite the generalized NLSE (16) with time-dependent nonlinearity, dispersion and gain or absorption in the form of the nonautonomous NLSE with linear and parabolic potentials

$$iQ_t + \frac{1}{2} D_2(t) Q_{xx} + \sigma R_2(t) |Q|^2 Q - 2\lambda_0(t)x - \frac{1}{2} \Omega^2(t)x^2 Q = i\Gamma Q. \quad (28)$$

4. Hidden features of the soliton adaptation law to external potentials: the generalized Serkin-Hasegawa theorems

It is now generally accepted that solitary waves in nonautonomous nonlinear and dispersive systems can propagate in the form of so-called nonautonomous solitons or solitonlike similaritons (see (Atre et al., 2006; Avelar et al., 2009; Belić et al., 2008; Chen et al., 2007; Hao, 2008; He et al., 2009; Hernandez et al., 2005; Hernandez-Tenorio et al., 2007; Liu et al., 2008; Porsezian et al., 2009; 2007; Serkin et al., 2007; Shin, 2008; Tenorio et al., 2005; Wang et al., 2008; Wu, Li & Zhang, 2008; Wu, Zhang, Li, Finot & Porsezian, 2008; Zhang et al., 2008; Zhao et al., 2009; 2008) and references therein). Nonautonomous solitons interact elastically and generally move with varying amplitudes, speeds and spectra adapted both to the external potentials and to the dispersion and nonlinearity variations. The existence of specific laws of soliton adaptation to external gain and loss potentials was predicted by Serkin and Hasegawa in 2000 (Serkin & Hasegawa, 2000a;b; 2002). The physical mechanism resulting in the soliton stabilization in nonautonomous and dispersive systems was revealed in this paper. From the physical point of view, the adaptation means that solitons remain self similar and do not emit dispersive waves both during their interactions with external potentials and with each other. The soliton adaptation laws are known today as the Serkin-Hasegawa theorems (SH theorems). Serkin and Hasegawa obtained their SH-theorems by using the symmetry reduction methods when the initial nonautonomous NLSE can be transformed by the canonical autonomous NLSE under specific conditions found in (Serkin & Hasegawa, 2000a;b). Later, SH-theorems have been confirmed by different methods, in particular, by the Painleve analysis and similarity transformations (Serkin & Hasegawa, 2000a;b; 2002; Serkin et al., 2004; 2007; 2001a;b).

Substituting the phase profile $\Theta(t)$ given by Eq. (26) into Eq. (25), it is straightforward to verify that the frequency of the harmonic potential $\Omega(t)$ is related with dispersion $D_2(t)$, nonlinearity $R_2(t)$ and gain or absorption coefficient $\Gamma(t)$ by the following conditions

$$\begin{aligned} \Omega^2(t) D_2(t) &= D_2(t) \frac{d}{dt} \left(\frac{\Gamma(t)}{D_2(t)} \right) - \Gamma^2(t) \\ &\quad - \frac{d}{dt} \left(\frac{W(R_2, D_2)}{R_2 D_2} \right) + \left(2\Gamma(t) + \frac{d}{dt} \ln R_2(t) \right) \frac{W(R_2, D_2)}{R_2 D_2} \\ &= D_2(t) \frac{d}{dt} \left(\frac{\Gamma(t)}{D_2(t)} \right) - \Gamma^2(t) + \left(2\Gamma(t) + \frac{d}{dt} \ln R_2(t) \right) \frac{d}{dt} \ln \frac{D_2(t)}{R_2(t)} - \frac{d^2}{dt^2} \ln \frac{D_2(t)}{R_2(t)}, \end{aligned} \quad (29)$$

where $W(R_2, D) = R_2 D'_{2t} - D_2 R'_{2t}$ is the Wronskian.

After the substitutions

$$Q(x, t) = q(x, t) \exp \left[\int_0^t \Gamma(\tau) d\tau \right], \quad R(t) = R_2(t) \exp \left[2 \int_0^t \Gamma(\tau) d\tau \right], \quad D(t) = D_2(t),$$

Eq. (28) is transformed to the generalized NLSE without gain or loss term

$$i \frac{\partial q}{\partial t} + \frac{1}{2} D(t) \frac{\partial^2 q}{\partial x^2} + \left[\sigma R(t) |q|^2 - 2\lambda_0(t)x - \frac{1}{2} \Omega^2(t)x^2 \right] q = 0. \quad (30)$$

Finally, the Lax equation (2) with matrices (3-6) provides the nonautonomous model (30) under condition that dispersion $D(t)$, nonlinearity $R(t)$, and the harmonic potential satisfy to the following exact integrability conditions

$$\begin{aligned} \Omega^2(t)D(t) &= \frac{W(R, D)}{RD} \frac{d}{dt} \ln R(t) - \frac{d}{dt} \left(\frac{W(R, D)}{RD} \right) \\ &= \frac{d}{dt} \ln D(t) \frac{d}{dt} \ln R(t) - \frac{d^2}{dt^2} \ln D(t) - R(t) \frac{d^2}{dt^2} \frac{1}{R(t)}. \end{aligned} \quad (31)$$

The self-induced soliton phase shift is given by

$$\Theta(t) = - \frac{W[(R(t), D(t))]}{D^2(t)R(t)} \quad (32)$$

and the time-dependent spectral parameter is represented by

$$\Lambda(t) = \kappa(t) + i\eta(t) = \frac{D_0 R(t)}{R_0 D(t)} \left[\Lambda(0) + \frac{R_0}{D_0} \int_0^t \frac{\lambda_0(\tau) D(\tau)}{R(\tau)} d\tau \right], \quad (33)$$

where the main parameters: time invariant eigenvalue $\Lambda(0) = \kappa_0 + i\eta_0$; $D_0 = D(0)$; $R_0 = R(0)$ are defined by the initial conditions.

We call Eq. (31) as the law of the soliton adaptation to the external potentials. The basic property of classical solitons to interact elastically holds true, but the novel feature of the nonautonomous solitons arises. Namely, both amplitudes and speeds of the solitons, and consequently, their spectra, during the propagation and after the interaction are no longer the same as those prior to the interaction. All nonautonomous solitons generally move with varying amplitudes $\eta(t)$ and speeds $\kappa(t)$ adapted both to the external potentials and to the dispersion $D(t)$ and nonlinearity $R(t)$ changes.

Having obtained the eigenvalue equations for scattering potential, we can write down the general solutions for bright ($\sigma = +1$) and dark ($\sigma = -1$) nonautonomous solitons applying the auto-Bäcklund transformation (Chen, 1974) and the recurrent relation

$$q_n(x, t) = -q_{n-1}(x, t) - \frac{4\eta_n \tilde{\Gamma}_{n-1}(x, t)}{1 + |\tilde{\Gamma}_{n-1}(x, t)|^2} \times \sqrt{\frac{D(t)}{R(t)}} \exp[-i\Theta x^2/2], \quad (34)$$

which connects the $(n-1)$ and n -soliton solutions by means of the so-called pseudo-potential $\tilde{\Gamma}_{n-1}(x, t) = \psi_1(x, t)/\psi_2(x, t)$ for the $(n-1)$ -soliton scattering functions $\psi(x, t) = (\psi_1 \psi_2)^T$.

Bright $q_1^+(x, t)$ and dark $q_1^-(x, t)$ soliton solutions are represented by the following analytic expressions:

$$q_1^+(x, t | \sigma = +1) = 2\eta_1(t) \sqrt{\frac{D(t)}{R(t)}} \operatorname{sech} [\zeta_1(x, t)] \times \exp \left\{ -i \left(\frac{\Theta(t)}{2} x^2 + \chi_1(x, t) \right) \right\}; \quad (35)$$

$$q_1^-(x, t | \sigma = -1) = 2\eta_1(t) \sqrt{\frac{D(t)}{R(t)}} \left[\sqrt{(1-a^2)} + ia \tanh \zeta(x, t) \right] \times \exp \left\{ -i \left(\frac{\Theta(t)}{2} x^2 + \phi(x, t) \right) \right\}, \quad (36)$$

$$\zeta(x, t) = 2a\eta_1(t)x + 4a \int_0^t D(\tau) \eta_1(\tau) \kappa_1(\tau) d\tau, \quad (37)$$

$$\begin{aligned} \phi(x, t) = & 2 \left[\kappa_1(t) - \eta_1(t) \sqrt{(1-a^2)} \right] x \\ & + 2 \int_0^t D(\tau) \left[\kappa_1^2 + \eta_1^2 (3-a^2) - 2\kappa_1 \eta_1 \sqrt{(1-a^2)} \right] d\tau. \end{aligned} \quad (38)$$

Dark soliton (36) has an additional parameter, $0 \leq a \leq 1$, which designates the depth of modulation (the blackness of gray soliton) and its velocity against the background. When $a = 1$, dark soliton becomes black. For optical applications, Eq.(36) can be easily transformed into the Hasegawa and Tappert form for the nonautonomous dark solitons (Hasegawa, 1995) under the condition $\kappa_0 = \eta_0 \sqrt{(1-a^2)}$ that corresponds to the special choice of the retarded frame associated with the group velocity of the soliton

$$\begin{aligned} q_1^-(x, t | \sigma = -1) = & 2\eta_1(t) \sqrt{\frac{D(t)}{R(t)}} \left[\sqrt{(1-a^2)} + ia \tanh \tilde{\zeta}(x, t) \right] \\ & \times \exp \left\{ -i \left(\frac{\Theta(t)}{2} x^2 + \tilde{\phi}(x, t) \right) \right\}, \\ \tilde{\zeta}(x, t) = & 2a\eta_1(t)x + 4a \int_0^t D(\tau) \eta_1(\tau) \left[\eta_1(\tau) \sqrt{(1-a^2)} + K(\tau) \right] d\tau, \\ \tilde{\phi}(x, t) = & 2K(t)x + 2 \int_0^t D(\tau) \left[K^2(\tau) + 2\eta_1^2(\tau) \right] d\tau, \\ K(t) = & \frac{R(t)}{D(t)} \int_0^t \lambda_0(\tau) \frac{D(\tau)}{R(\tau)} d\tau. \end{aligned}$$

Notice that the solutions considered here hold only when the nonlinearity, dispersion and confining harmonic potential are related by Eq. (31), and both $D(t) \neq 0$ and $R(t) \neq 0$ for all times by definition.

Two-soliton $q_2(x, t)$ solution for $\sigma = +1$ follows from Eq. (34)

$$q_2(x, t) = 4\sqrt{\frac{D(t)}{R(t)}} \frac{N(x, t)}{D(x, t)} \exp\left[-\frac{i}{2}\Theta(t)x^2\right], \quad (39)$$

where the numerator $N(x, t)$ is given by

$$\begin{aligned} N &= \cosh \xi_2 \exp(-i\chi_1) \\ &\times [(\kappa_2 - \kappa_1)^2 + 2i\eta_2(\kappa_2 - \kappa_1) \tanh \xi_2 + \eta_1^2 - \eta_2^2] + \eta_2 \cosh \xi_1 \exp(-i\chi_2) \\ &\times [(\kappa_2 - \kappa_1)^2 - 2i\eta_1(\kappa_2 - \kappa_1) \tanh \xi_1 - \eta_1^2 + \eta_2^2], \end{aligned} \quad (40)$$

and the denominator $D(x, t)$ is represented by

$$\begin{aligned} D &= \cosh(\xi_1 + \xi_2) [(\kappa_2 - \kappa_1)^2 + (\eta_2 - \eta_1)^2] \\ &+ \cosh(\xi_1 - \xi_2) [(\kappa_2 - \kappa_1)^2 + (\eta_2 + \eta_1)^2] - 4\eta_1\eta_2 \cos(\chi_2 - \chi_1). \end{aligned} \quad (41)$$

Arguments and phases in Eqs.(39-41)

$$\xi_i(x, t) = 2\eta_i(t)x + 4 \int_0^t D(\tau)\eta_i(\tau)\kappa_i(\tau)d\tau, \quad (42)$$

$$\chi_i(x, t) = 2\kappa_i(t)x + 2 \int_0^t D(\tau) [\kappa_i^2(\tau) - \eta_i^2(\tau)] d\tau \quad (43)$$

are related with the amplitudes

$$\eta_i(t) = \frac{D_0 R(t)}{R_0 D(t)} \eta_{0i}, \quad (44)$$

and velocities

$$\kappa_i(t) = \frac{D_0 R(t)}{R_0 D(t)} \left[\kappa_{0i} + \frac{R_0}{D_0} \int_0^t \frac{\lambda_0(\tau) D(\tau)}{R(\tau)} d\tau \right] \quad (45)$$

of the nonautonomous solitons, where κ_{0i} and η_{0i} correspond to the initial velocity and amplitude of the i -th soliton ($i = 1, 2$).

Eqs. (39-45) describe the dynamics of two bounded solitons at all times and all locations. Obviously, these soliton solutions reduce to classical soliton solutions in the limit of autonomous nonlinear and dispersive systems given by conditions: $R(t) = D(t) = 1$, and $\lambda_0(t) = \Omega(t) \equiv 0$ for canonical NLSE without external potentials.

5. Chirped optical solitons with moving spectra in nonautonomous systems: colored nonautonomous solitons

Both the nonlinear Schrödinger equations (28, 30) and the Lax pair equations (3–6) are written down here in the most general form. The transition to the problems of optical solitons is accomplished by the substitution $x \rightarrow T$ (or $x \rightarrow X$); $t \rightarrow Z$ and $q^+(x, t) \rightarrow \tilde{u}^+(Z, T$ (or X)) for bright solitons, and $[q^-(x, t)]^* \rightarrow \tilde{u}^-(Z, T$ (or X)) for dark solitons, where the asterisk denotes the complex conjugate, Z is the normalized distance, and T is the retarded time for temporal solitons, while X is the transverse coordinate for spatial solitons.

The important special case of Eq.(30) arises under the condition $\Omega^2(Z) = 0$. Let us rewrite Eq. (30) by using the reduction $\Omega = 0$, which denotes that the confining harmonic potential is vanishing

$$i \frac{\partial u}{\partial Z} + \frac{\sigma}{2} D(Z) \frac{\partial^2 u}{\partial T^2} + R(Z) |u|^2 u - 2\sigma \lambda_0(Z) T u = 0. \quad (46)$$

This implies that the self-induced soliton phase shift $\Theta(Z)$, dispersion $D(Z)$, and nonlinearity $R(Z)$ are related by the following law of soliton adaptation to external linear potential

$$D(Z)/D_0 = R(Z)/R_0 \exp \left\{ -\frac{\Theta_0 D_0}{R_0} \int_0^Z R(\tau) d\tau \right\}. \quad (47)$$

Nonautonomous exactly integrable NLSE model given by Eqs. (46,47) can be considered as the generalization of the well-studied Chen and Liu model (Chen, 1976) with linear potential $\lambda_0(Z) \equiv \alpha_0 = \text{const}$ and $D(Z) = D_0 = R(Z) = R_0 = 1$, $\sigma = +1$, $\Theta_0 = 0$. It is interesting to note that the accelerated solitons predicted by Chen and Liu in plasma have been discovered in nonlinear fiber optics only decade later (Agrawal, 2001; Dianov et al., 1989; Taylor, 1992). Notice that nonautonomous solitons with nontrivial self-induced phase shifts and varying amplitudes, speeds and spectra for Eq. (46) are given in quadratures by Eqs. (35-45) under condition $\Omega^2(Z) = 0$.

Let us show that the so-called Raman colored optical solitons can be approximated by this equation. Self-induced Raman effect (also called as soliton self-frequency shift) is being described by an additional term in the NLSE: $-\sigma_R U \partial |U|^2 / \partial T$, where σ_R originates from the frequency dependent Raman gain (Agrawal, 2001; Dianov et al., 1989; Taylor, 1992). Assuming that soliton amplitude does not vary significantly during self-scattering $|U|^2 = \eta^2 \text{sech}^2(\eta T)$, we obtain that

$$\sigma_R \frac{\partial |U|^2}{\partial T} \approx -2\sigma_R \eta^4 T = 2\alpha_0 T$$

and $dv/dZ = \sigma_R \eta^4 / 2$, where $v = \kappa / 2$. The result of soliton perturbation theory (Agrawal, 2001; Dianov et al., 1989; Taylor, 1992) gives $dv/dZ = 8\sigma_R \eta^4 / 15$. This fact explains the remarkable stability of colored Raman solitons that is guaranteed by the property of the exact integrability of the Chen and Liu model (Chen, 1976). More general model Eq. (46) and its exact soliton solutions open the possibility of designing an effective soliton compressor, for example, by drawing a fiber with $R(Z) = 1$ and $D(Z) = \exp(-c_0 Z)$, where $c_0 = \Theta_0 D_0$. It seems very attractive to use the results of nonautonomous solitons concept in ultrashort photonic applications and soliton lasers design.

Another interesting feature of the novel solitons, which we called colored nonautonomous solitons, is associated with the nontrivial dynamics of their spectra. Frequency spectrum of the chirped nonautonomous optical soliton moves in the frequency domain. In particular,

if dispersion and nonlinearity evolve in unison $D(t) = R(t)$ or $D = R = 1$, the solitons propagate with identical spectra, but with totally different time-space behavior.

Consider in more details the case when the nonlinearity $R = R_0$ stays constant but the dispersion varies exponentially along the propagation distance

$$\begin{aligned} D(Z) &= D_0 \exp(-c_0 Z), \\ \Theta(Z) &= \Theta_0 \exp(c_0 Z). \end{aligned}$$

Let us write the one and two soliton solutions in this case with the lineal potential that, for simplicity, does not depend on time: $\lambda_0(Z) = \alpha_0 = \text{const}$

$$U_1(Z, T) = 2\eta_{01} \sqrt{D_0 \exp(c_0 Z)} \operatorname{sech}[\xi_1(Z, T)] \times \exp\left[-\frac{i}{2}\Theta_0 \exp(c_0 Z) T^2 - i\chi_1(Z, T)\right], \quad (48)$$

$$U_2(Z, T) = 4\sqrt{D_0 \exp(-c_0 Z)} \frac{N(Z, T)}{D(Z, T)} \exp\left[-\frac{i}{2}\Theta_0 \exp(c_0 Z) T^2\right], \quad (49)$$

where the nominator $N(Z, T)$ and denominator $D(Z, T)$ are given by Eqs. (40,41) and

$$\begin{aligned} \xi_i(Z, T) &= 2\eta_{0i} T \exp(c_0 Z) + 4D_0 \eta_{0i} \\ &\times \left\{ \frac{\kappa_{0i}}{c_0} [\exp(c_0 Z) - 1] + \frac{\alpha_0}{c_0} \left[\frac{\exp(c_0 Z) - 1}{c_0} - Z \right] \right\}, \end{aligned} \quad (50)$$

$$\begin{aligned} \chi_i(Z, T) &= 2\kappa_{0i} T \exp(c_0 Z) + 2D_0 \left(\kappa_{0i}^2 - \eta_{0i}^2 \right) \frac{\exp(2c_0 Z) - 1}{2c_0} \\ &+ 2T \frac{\alpha_0}{c_0} [\exp(c_0 Z) - 1] + 4D_0 \kappa_{0i} \frac{\alpha_0}{c_0} \left[\frac{\exp(c_0 Z) - 1}{c_0} - Z \right] \\ &+ 2D_0 \left(\frac{\alpha_0}{c_0} \right)^2 \left[\frac{\exp(c_0 Z) - \exp(-c_0 Z)}{c_0} - 2Z \right]. \end{aligned} \quad (51)$$

The initial velocity and amplitude of the i -th soliton ($i = 1, 2$) are denoted by κ_{0i} and η_{0i} . We display in Fig.1(a,b) the main features of nonautonomous colored solitons to show not only their acceleration and reflection from the lineal potential, but also their compression and amplitude amplification. Dark soliton propagation and dynamics are presented in Fig.1(c,d). The limit case of the Eqs.(48-51) appears when $c_0 \rightarrow \infty$ (that means $D(Z) = D_0 = \text{constant}$) and corresponds to the Chen and Liu model (Chen, 1976). The solitons with argument and phase

$$\begin{aligned} \xi(Z, T) &= 2\eta_0 \left(T + 2\kappa_0 Z + \alpha_0 Z^2 - T_0 \right), \\ \chi(Z, T) &= 2\kappa_0 T + 2\alpha_0 T Z + 2 \left(\kappa_0^2 - \eta_0^2 \right) Z + 2\kappa_0 \alpha_0 Z^2 + \frac{2}{3} \alpha_0^2 Z^3 \end{aligned}$$

represents the particle-like solutions which may be accelerated and reflected from the lineal potential.

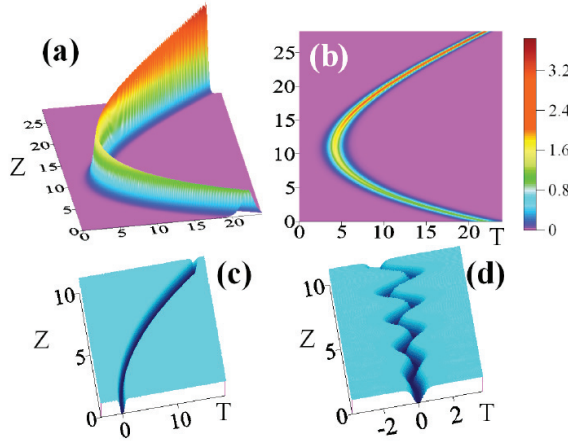


Fig. 1. Evolution of nonautonomous bright (a,b) optical soliton calculated within the framework of the generalized model given by Eqs. (46-51) after choosing the soliton management parameters $c_0=0.05$, $\alpha_0 = -0.2$, $\eta_{10} = 0.5$, $\kappa_{10} = 1.5$. (a) the temporal behavior; (b) the corresponding contour map. (c,d) Dark nonautonomous soliton dynamics within the framework of the model Eqs. (46,47) after choosing the soliton management parameters: (c) $R=-D=1.0$ and $\alpha_0 = -1.0$ and (d) $R=-D=\cos(\omega Z)$, where $\omega = 3.0$.

6. Bound states of colored nonautonomous optical solitons: nonautonomous "agitated" breathers.

Let us now give the explicit formula of the soliton solutions (48,49) for the case where all eigenvalues are pure imaginary, or the initial velocities of the solitons are equal to zero. In the case $N = 1$ and $\lambda_0(Z) = 0$, we obtain

$$U_1(Z, T) = 2\eta_{01} \sqrt{D_0 \exp(c_0 Z)} \operatorname{sech} [2\eta_{01} T \exp(c_0 Z)] \times \exp \left[-\frac{i}{2} \Theta_0 \exp(c_0 Z) T^2 + i2D_0 \eta_{01}^2 \frac{\exp(2c_0 Z) - 1}{2c_0} \right]. \quad (52)$$

This result shows that the laws of soliton adaptation to the external potentials (31) allow to stabilize the soliton even without a trapping potential. In addition, Eq.(52) indicates the possibility for the optimal compression of solitons, which is shown in Fig.2. We stress that direct computer experiment confirms the exponential in time soliton compression scenario in full accordance with analytical expression Eq.(52).

The bound two-soliton solution for the case of the pure imaginary eigenvalues is represented by

$$U_2(Z, T) = 4\sqrt{D_0 \exp(-c_0 Z)} \frac{N(Z, T)}{D(Z, T)} \exp \left[-\frac{i}{2} \Theta_0 \exp(c_0 Z) T^2 \right], \quad (53)$$

where

$$N = \left(\eta_{01}^2 - \eta_{02}^2 \right) \exp(c_0 Z) [\eta_{01} \cosh \xi_2 \exp(-i\chi_1) - \eta_{02} \cosh \xi_1 \exp(-i\chi_2)], \quad (54)$$

$$D = \cosh(\xi_1 + \xi_2) (\eta_{01} - \eta_{02})^2 + \cosh(\xi_1 - \xi_2) (\eta_{01} + \eta_{02})^2 - 4\eta_{01}\eta_{02} \cos(\chi_2 - \chi_1), \quad (55)$$

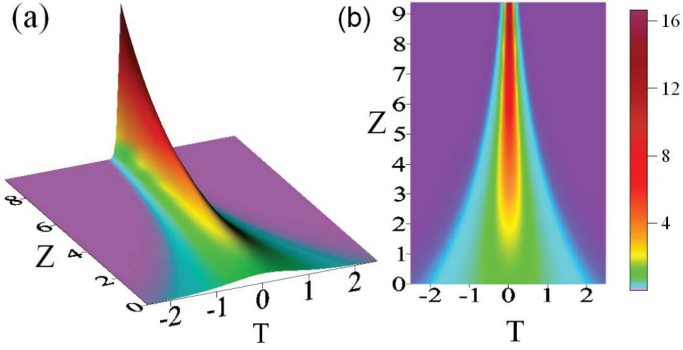


Fig. 2. Self-compression of nonautonomous soliton calculated within the framework of the model Eq. (46) after choosing the soliton management parameters $c_0 = 0.05$; $\alpha = 0$ and $\eta_0 = 0.5$. (a) the temporal behavior; (b) the corresponding contour map.

and

$$\xi_i(Z, T) = 2\eta_{0i}T \exp(c_0Z), \quad (56)$$

$$\chi_i(Z, T) = -2D_0\eta_{0i}^2 \frac{\exp(2c_0Z) - 1}{2c_0} + \chi_{i0}. \quad (57)$$

For the particular case of $\eta_{10} = 1/2$, $\eta_{20} = 3/2$ Eqs.(53-57) are transformed to

$$\begin{aligned} U_2(Z, T) = & 4\sqrt{D_0 \exp(-c_0Z)} \exp\left[-\frac{i}{2}\Theta_0 \exp(c_0Z) T^2\right] \\ & \times \exp\left[\frac{i}{4c_0}D_0 [\exp(2c_0Z) - 1] + \chi_{10}\right] \\ & \times \frac{\cosh 3X - 3 \cosh X \exp\{i2D_0 [\exp(2c_0Z) - 1] / c_0 + i\Delta\varphi\}}{\cosh 4X + 4 \cosh 2X - 3 \cos\{2D_0 [\exp(2c_0Z) - 1] / c_0 + \Delta\varphi\}}, \end{aligned} \quad (58)$$

where $X = T \exp(c_0Z)$, $\Delta\varphi = \chi_{20} - \chi_{10}$.

In the $D(Z) = D_0 = 1$, $c_0 = 0$ limit, this solution is reduced to the well-known breather solution, which was found by Satsuma and Yajima (Satsuma & Yajima, 1974) and was called as the Satsuma-Yajima breather:

$$U_2(Z, T) = 4 \frac{\cosh 3T + 3 \cosh T \exp(4iZ)}{\cosh 4T + 4 \cosh 2T + 3 \cos 4Z} \exp\left(\frac{iZ}{2}\right).$$

At $Z = 0$ it takes the simple form $U(Z, T) = 2\text{sech}(T)$. An interesting property of this solution is that its form oscillates with the so-called soliton period $T_{sol} = \pi/2$.

In more general case of the varying dispersion, $D(Z) = D_0 \exp(-c_0Z)$, shown in Fig.3 ($c_0 = 0.25$, $\eta_{10} = 0.25$, $\eta_{20} = 0.75$), the soliton period, according to Eq.(58), depends on time.

The Satsuma and Yajima breather solution can be obtained from the general solution if and only if the soliton phases are chosen properly, precisely when $\Delta\varphi = \pi$. The intensity profiles of the wave build up a complex landscape of peaks and valleys and reach their peaks at the points of the maximum. Decreasing group velocity dispersion (or increasing nonlinearity) stimulates the Satsuma-Yajima breather to accelerate its period of "breathing" and to increase its peak amplitudes of "breathing", that is why we call this effect as "agitated breather" in nonautonomous system.

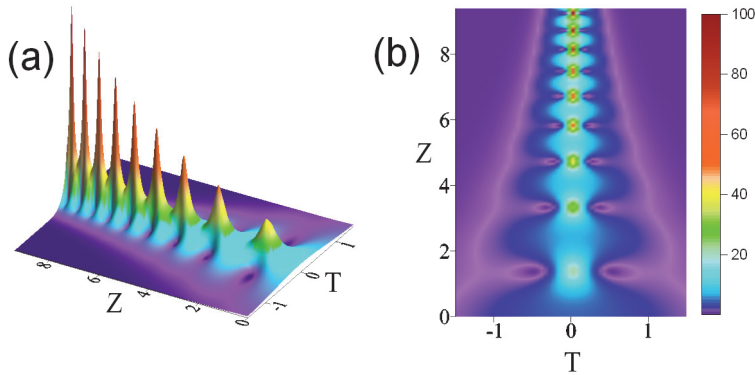


Fig. 3. Nonautonomous "agitated" breather (58) calculated within the framework of the model (46) after choosing the soliton management parameters $c_0 = 0.25$, $\eta_{10} = 0.5$, $\eta_{20} = 1.5$. (a) the temporal behavior; (b) the corresponding contour map.

7. Rogue waves, "quantized" modulation instability, and dynamics of nonautonomous Peregrine solitons under "hyperbolic hurricane wind"

Recently, a method of producing optical rogue waves, which are a physical counterpart to the rogue (monster) waves in oceans, have been developed (Solli et al., 2007). Optical rogue waves have been formed in the so-called soliton supercontinuum generation, a nonlinear optical process in which broadband "colored" solitons are generated from a narrowband optical background due to induced modulation instability and soliton fission effects (Dudley, 2009; Dudley et al., 2006; 2008).

Ordinary, the study of rogue waves has been focused on hydrodynamic applications and experiments (Clamond et al., 2006; Kharif & Pelinovsky, 2003). Nonlinear phenomena in optical fibers also support rogue waves that are considered as soliton supercontinuum noise. It should be noticed that because optical rogue waves are closely related to oceanic rogue waves, the study of their properties opens novel possibilities to predict the dynamics of oceanic rogue waves. By using the mathematical equivalence between the propagation of nonlinear waves on water and the evolution of intense light pulses in optical fibers, an international research team (Kibler et al., 2010) recently reported the first observation of the so-called Peregrine soliton (Peregrine, 1983). Similar to giant nonlinear water waves, the Peregrine soliton solutions of the NLSE experience extremely rapid growth followed by just as rapid decay (Peregrine, 1983). Now, the Peregrine soliton is considered as a prototype of the famous ocean monster (rogue) waves responsible for many maritime catastrophes.

In this Section, the main attention will be focused on the possibilities of generation and amplification of nonautonomous Peregrine solitons. This study is an especially important for understanding how high intensity rogue waves may form in the very noisy and imperfect environment of the open ocean.

First of all, let us summarize the main features of the phenomenon known as the induced modulation instability. In 1984, Akira Hasegawa discovered that modulation instability of continuous (cw) wave optical signal in a glass fiber combined with an externally applied amplitude modulation can be utilized to produce a train of optical solitons (Hasegawa,

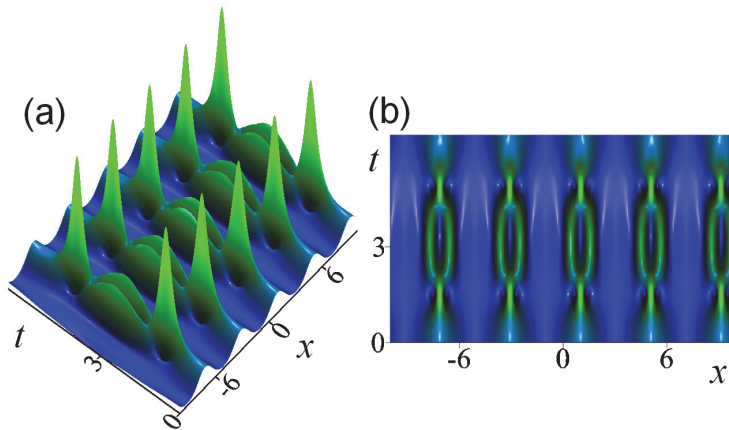


Fig. 4. Illustrative example of the temporal-spatial dynamics of the induced modulation instability and the Fermi-Pasta-Ulam recurrence effect calculated in the framework of the canonical NLSE model : (a) the intensity distribution; (b) the corresponding contour map.

1984). In the sense that the external modulation induces the modulation instability, Hasegawa called the total process as the induced modulation instability. To demonstrate the induced modulation instability (IMI), following Hasegawa, we solved the NLSE numerically with different depths and wavelength of modulation of cw wave. The main features of the induced modulation instability are presented in Fig.4. In Figure 4, following Hasegawa (Hasegawa, 1984), we present the total scenario of IMI and the restoration of the initial signal due to the Fermi-Pasta-Ulama recurrence effect. In our computer experiments, we have found novel and interesting feature of the IMI. Varying the depth of modulation and the level of continuous wave, we have discovered the effect which we called a "quantized" IMI. Figure 5 shows typical results of the computation. As can be clearly seen, the high-intensity IMI peaks are formed and split periodically into two, three, four, and more high-intensity peaks. In Fig.5 we present this splitting ("quantization") effect of the initially sinus like modulated cw signal into two and five high-intensity and "long-lived" components.

The Peregrine soliton can be considered as the utmost stage of the induced modulation instability, and its computer simulation is presented in Fig.6. When we compare the high-energy peaks of the IMI generated upon a distorted background (see Figs.4, 5) with exact form of the Peregrine soliton shown in Fig.7(a) we can understand, how such extreme wave structures may appear as they emerge suddenly on an irregular surface such as the open ocean.

There are two basic questions to be answered. What happens if arbitrary modulated cw wave is subjected to some form of external force? Such situations could include effects of wind, propagation of waves in nonuniform media with time dependent density gradients and slowly varying depth, nonlinearity and dispersion. For example, in Fig.7(b), we show the possibility of amplification of the Peregrine soliton when effects of wind are simulated by additional gain term in the canonical NLSE. The general questions naturally arise: To what extent the Peregrine soliton can be amplified under effects of wind, density gradients and

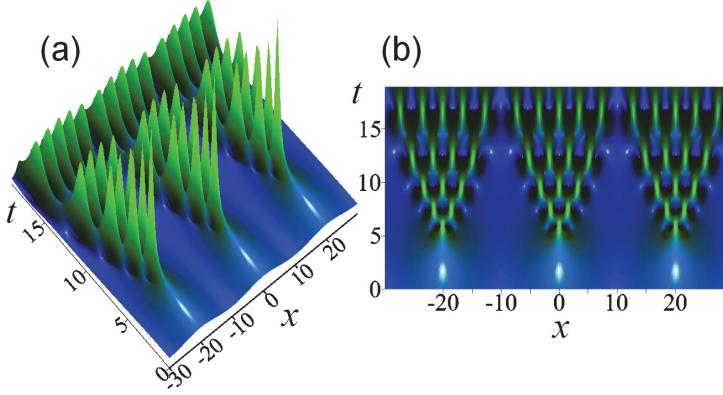


Fig. 5. Illustrative example of the "quantized" induced modulation instability: (a) the temporal-spatial behavior; (b) the corresponding contour map.

slowly varying depth, nonlinearity and dispersion? To answer these questions, let us consider the dynamics of the Peregrine soliton in the framework of the nonautonomous NLSE model. In the previous chapters, the auto-Bäcklund transformation has been used to find soliton solutions of the nonautonomous NLSE model. Now, we consider another remarkable method to study nonautonomous solitons. The following transformation

$$q(x, t) = A(t)u(X, T) \exp [i\phi(X, T)] \quad (59)$$

has been used by Serkin and Hasegawa in (Serkin & Hasegawa, 2000a;b; 2002) to reduce the nonautonomous NLSE with varying dispersion, nonlinearity and gain or loss to the "ideal" NLSE

$$i \frac{\partial u}{\partial T} + \frac{\sigma}{2} \frac{\partial^2 u}{\partial X^2} + |u|^2 u = 0,$$

where the following notations may be introduced

$$A(t) = \sqrt{P(t)}; \quad X = P(t)x; \quad T(t) = \int_0^t D(\tau)P^2(\tau)d\tau; \quad (60)$$

$$\phi(X, T) = \frac{1}{2} \frac{W(R, D)}{R^3} X^2 - \varphi(X, T), \quad (61)$$

where $\varphi(X, T)$ is the phase of the canonical soliton.

It is easy to see that by using Eq.(59-61), the one-soliton solution may be written in the following form

$$q_1^+(x, t | \sigma = +1) = 2\tilde{\eta}_0 A(t) \operatorname{sech} [2\tilde{\eta}_0 X + 4\tilde{\eta}_0 \tilde{\kappa}_0 T(t)]$$

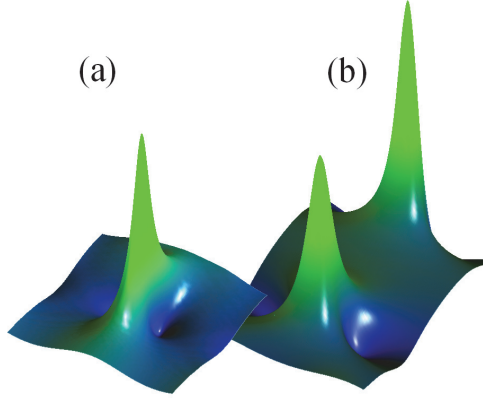


Fig. 6. Illustrative examples of the Peregrine soliton dynamics: (a) - classical Peregrine soliton calculated in the framework of the canonical NLSE model; (b) its behavior under linear amplification associated with continuous wind.

$$\times \exp \left\{ i \left[\frac{1}{2} \frac{W(R, D)}{R^3} X^2 - 2\tilde{\kappa}_0 X - 2(\tilde{\kappa}_0^2 - \tilde{\eta}_0^2) T(t) \right] \right\},$$

$$\tilde{\eta}_0 = \frac{D_0}{R_0} \eta_0; \quad \tilde{\kappa}_0 = \frac{D_0}{R_0} \kappa_0; \quad P(t) = R(t)/D(t). \quad (62)$$

The transformation (59) can be applied to obtain all solutions of the nonautonomous NLSE (30) and, in particular, the nonautonomous rational solutions known as the Peregrine solitons. Thus, the Peregrine soliton (Peregrine, 1983) can be discovered for the nonautonomous NLSE model as well

$$q_P(x, t) = A(t)r(X, T) \exp [i\phi(T)] \quad (63)$$

where

$$r(X, T) = 1 - \frac{4(1 + 2iT)}{1 + 4T^2 + 4X^2}, \quad (64)$$

$$\phi(X, T) = \frac{1}{2} \frac{W(R, D)}{R^3} X^2 + T(t) \quad (65)$$

Figure 7 shows spatiotemporal behavior of the nonautonomous Peregrine soliton. The nonautonomous Peregrine soliton (63-65) shown in Fig.7(b) has been calculated in the framework of the nonautonomous NLSE model (28) after choosing the parameters $\lambda_0 = \Omega = 0$, $D_2 = R_2 = 1$ and the gain coefficient $\Gamma(t) = \Gamma_0/(1 - \Gamma_0 t)$. Somewhat surprisingly, however, this figure indicates a sharp compression and strong amplification of the nonautonomous Peregrine soliton under the action of hyperbolic gain which, in particular, in the open ocean can be associated with "hyperbolic hurricane wind".

It should be stressed that since the nonautonomous NLSE model is applied in many other physical systems such as plasmas and Bose-Einstein condensates (BEC), the results obtained in this Section can stimulate new research directions in many novel fields (see, for example, (Bludov et al., 2009; Yan, 2010)).

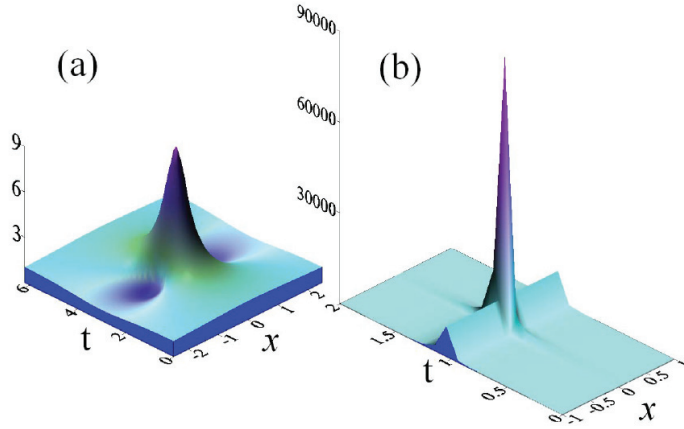


Fig. 7. (a) Autonomous and (b) nonautonomous Peregrine solitons calculated within the framework of the model (63-65) after choosing the soliton management parameters $\Gamma_0 = 0.33$.

8. Nonautonomous KdV solitons

Notice, that the nonlinear evolution equations that arise in the approach of variable spectral parameter contain, as a rule, an explicit dependence on the coordinates. Our general approach makes it possible to construct not only the well-known equations, but also a number of new integrable equations (NLSE, KdV, modified KdV, Hirota and Satsuma and so on) by extending the Zakharov–Shabat (ZS) and AKNS formalism. In particular, Eqs.(9,10) under the conditions (11) with $a_2=0$, $a_3=-4iD_3$ and $R=1$ become

$$\begin{aligned}
 Q_T = & -D_3 Q_{SSS} S_x^3 - 6iD_3 Q_{SS} \varphi_S S_x^3 + 3iD_3 \sigma F^{2\gamma} Q^2 \varphi_S S_x + 6D_3 \sigma F^{2\gamma} Q Q_S S_x \quad (66) \\
 & + Q_S \left(-S_t + \lambda_1 S - V_1 S_x - 6iD_3 \varphi_{SS} S_x^3 + \frac{3}{4} D_3 \varphi_S^2 S_x^3 \right) \\
 & - iQ \left[2\lambda_0 S / S_x - 2\gamma + \frac{1}{2} (\varphi_T + \varphi_S S_t) - \frac{1}{2} \lambda_1 S \varphi_S + \frac{1}{2} V \varphi_S S_x \right] \\
 & + Q \left(\lambda_1 - \gamma \frac{F_T}{F} + \frac{3}{4} D_3 \varphi_S \varphi_{SS} S_x^3 \right) - iQ \left(-\frac{1}{8} D_3 \varphi_S^3 S_x^3 + \frac{1}{2} D_3 \varphi_{SSS} S_x^3 \right),
 \end{aligned}$$

Eq.(66) can be rewritten in the independent variables (x, t)

$$\begin{aligned}
 Q_t = & -D_3 Q_{xxx} - 6iD_3 Q_{xx} \varphi_x + 3iD_3 \sigma F^{2\gamma} Q^2 \varphi_x + 6D_3 \sigma F^{2\gamma} Q Q_x \quad (67) \\
 & + Q_x \left(\lambda_1 S / S_x - V_1 - 6iD_3 \varphi_{xx} + \frac{3}{4} D_3 \varphi_x^2 \right) \\
 & - iQ \left[2\lambda_0 S / S_x - 2\gamma + \frac{1}{2} (\varphi_T + \varphi_S S_t) - \frac{1}{2} \lambda_1 S \varphi_x / S_x + \frac{1}{2} V \varphi_x \right] \\
 & + Q \left(\lambda_1 - \gamma \frac{F_t}{F} + \frac{3}{4} D_3 \varphi_x \varphi_{xx} \right) - iQ \left(-\frac{1}{8} D_3 \varphi_x^3 + \frac{1}{2} D_3 \varphi_{xxx} \right).
 \end{aligned}$$

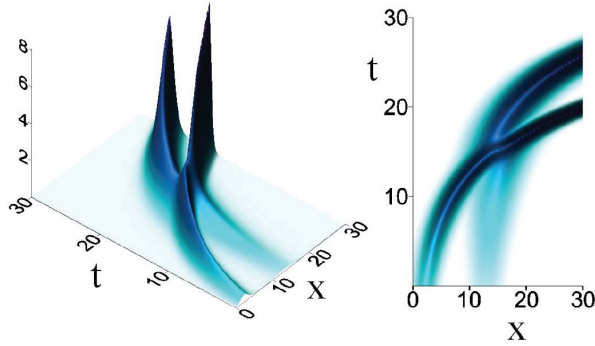


Fig. 8. Nonautonomous KdV solitons calculated within the framework of the model (71) after choosing the soliton management parameters $\alpha = 0.15$, $\eta_{10} = 0.40$, $\eta_{20} = 0.75$. On the left hand side the temporal behavior is presented, while the corresponding contour map is presented on the right hand side.

Let us consider the simplest option to choose the real solution $Q(x, t)$, which leads to the only possibility of $\varphi = \lambda_1 = 0$. In this case, Eq.(67) is reduced to the KdV with variable coefficients

$$Q_t - 6\sigma R_3(t)QQ_x + D_3(t)Q_{xxx} + \frac{1}{2} \frac{W(D_3, R_3)}{D_3 R_3} = 0, \quad (68)$$

where the notation $R_3(t) = F^{2\gamma} D_3(t)$ has been introduced. It is easy to verify that Eq.(68) can be mapped into the standard KdV under the transformations

$$Q(x, t) = \frac{D_3(T)}{R_3(T)} q(x, T),$$

where $T = \int_0^t D_3(\tau) d\tau$ so that $q(x, T)$ is given by the canonical KdV:

$$q_t - 6\sigma q q_x + q_{xxx} = 0.$$

Applying the auto-Backlund transformation, we can write down the two-soliton solution of the nonautonomous KdV

$$Q_2(x, t) = -2\sigma(\beta_1 - \beta_2) \frac{D_3(T)}{R_3(T)} \frac{\mathfrak{N}_1}{\mathfrak{D}_1}, \quad (69)$$

where

$$\mathfrak{N}_1 = \beta_1 (\sinh \xi_2)^2 + \beta_2 (\cosh \xi_1)^2, \quad (70)$$

$$\mathfrak{D}_1 = \left[\sqrt{2\beta_1} \sinh \xi_1 \sinh \xi_2 - \sqrt{2\beta_2} \cosh \xi_1 \cosh \xi_2 \right]^2, \\ \xi_i = \sqrt{\beta_i/2} (x - 2\beta_i T), \quad \beta_i = 2\eta_{0i}^2, \quad i = 1, 2;$$

and $\eta_{02} > \eta_{01}$ are initial amplitudes of the solitons.

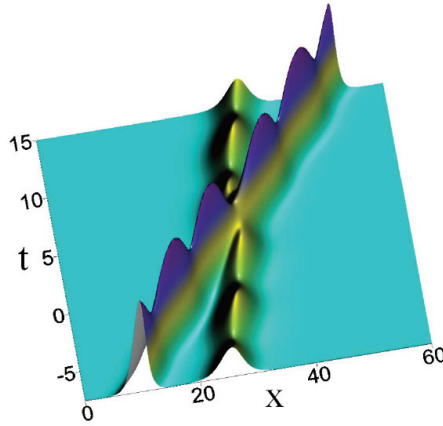


Fig. 9. Nonautonomous KdV solitons calculated within the framework of the model (72) after choosing the soliton management parameters $\alpha = 2.0$, $\beta = -0.25$, $\eta_{10} = 0.40$, $\eta_{20} = 0.75$.

As two illustrative examples, in Fig.8, we present the behavior of nonautonomous KdV soliton in the framework of the model

$$Q_t - 6\sigma QQ_x + \exp(\alpha t)Q_{xxx} - \frac{1}{2}\alpha Q = 0 \quad (71)$$

with lineal gain (or loss) accompanying by exponential variation of the dispersion coefficient; and in Fig.9 we show the dynamics of the KdV soliton in the nonautonomous system described by the model

$$Q_t - 6\sigma QQ_x + [1 + \beta \cos(\alpha t)] / (1 + \beta) Q_{xxx} + \frac{\alpha \beta \sin(\alpha t)}{2[1 + \beta \cos(\alpha t)](1 + \beta)} Q = 0 \quad (72)$$

where $D_3(t) = [1 + \beta \cos(\alpha t)] / (1 + \beta)$, $R_3(t) = 1$.

It is important to compare our exactly integrable nonautonomous KdV model with the model proposed by Johnson to describe the KdV soliton dynamics under the influence of the depth variation (Johnson, 1997) and given by

$$u_X - 6\sigma \mathcal{D}(X)^{-3/2} u u_\xi + \mathcal{D}(X)^{1/2} u_{\xi\xi\xi} + \frac{1}{2} \frac{\mathcal{D}_X}{\mathcal{D}} u = 0. \quad (73)$$

We stress that after choosing the parameters $R_3(t) = \mathcal{D}(t)^{-3/2}$ and $D_3(t) = \mathcal{D}(t)^{1/2}$, the potential in Eq.(68) becomes $\frac{W(D_3, R_3)}{D_3 R_3} = -2\mathcal{D}' / \mathcal{D}$, which is very nearly similar to the potential in Eq.(73) calculated by Johnson (Johnson, 1997).

9. Conclusions

The solution technique based on the generalized Lax pair operator method opens the possibility to study in details the nonlinear dynamics of solitons in nonautonomous nonlinear and dispersive physical systems. We have focused on the situation in which the generalized nonautonomous NLSE model was found to be exactly integrable from the point of view of

the inverse scattering transform method. We have derived the laws of a soliton adaptation to the external potential. It is precisely this soliton adaptation mechanism which was of prime physical interest in our Chapter. We clarified some examples in order to gain a better understanding into this physical mechanism which can be considered as the interplay between nontrivial time-dependent parabolic soliton phase and external time-dependent potential. We stress that this nontrivial time-space dependent phase profile of nonautonomous soliton depends on the Wronskian of nonlinearity $R(t)$ and dispersion $D(t)$ and this profile does not exist for canonical NLSE soliton when $R(t) = D(t) = 1$.

Several novel analytical solutions for water waves have been presented. In particular, we have found novel solutions for the generalized Peregrine solitons in inhomogeneous and nonautonomous systems, "quantized" modulation instability, and the exactly integrable model for the Peregrine solitons under "hyperbolic hurricane wind". It was shown that important mathematical analogies between optical rogue waves and the Peregrine solitons in water open the possibility to study optical rogue waves and water rogue waves in parallel and, due to the evident complexity of experiments with rogue waves in oceans, this method offers remarkable possibilities in studies nonlinear hydrodynamics problems by performing experiments in the nonlinear optical systems.

We would like to conclude by saying that the concept of adaptation is of primary importance in nature and nonautonomous solitons that interact elastically and generally move with varying amplitudes, speeds, and spectra adapted both to the external potentials and to the dispersion and nonlinearity changes can be fundamental objects of nonlinear science.

This investigation is a natural follow up of the works performed in collaboration with Professor Akira Hasegawa and the authors would like to thank him for this collaboration. We thank BUAP and CONACyT, Mexico for support.

10. References

- Ablowitz, M. J., Kaup, D. J., Newell, A. C. & Segur, H. (1973). Nonlinear-evolution equations of physical significance, *Phys. Rev. Lett.* 31(2): 125–127.
- Agrawal, G. P. (2001). *Nonlinear Fiber Optics, 3rd ed.*, Academic Press, San Diego.
- Akhmediev, N. N. & Ankiewicz, A. (1997). *Solitons. Nonlinear pulses and beams*, Charman and Hall, London.
- Akhmediev, N. N. & Ankiewicz, A. (2008). *Dissipative Solitons: From Optics to Biology and Medicine*, Springer-Verlag Berlin.
- Atre, R., Panigrahi, P. K. & Agarwal, G. S. (2006). Class of solitary wave solutions of the one-dimensional gross-pitaevskii equation, *Phys. Rev. E* 73(5): 056611.
- Avelar, A. T., Bazeia, D. & Cardoso, W. B. (2009). Solitons with cubic and quintic nonlinearities modulated in space and time, *Phys. Rev. E* 79(2): 025602.
- Balakrishnan, R. (1985). Soliton propagation in nonuniform media, *Phys. Rev. A* 32(2): 1144–1149.
- Belić, M., Petrović, N., Zhong, W.-P., Xie, R.-H. & Chen, G. (2008). Analytical light bullet solutions to the generalized (3 + 1)-dimensional nonlinear schrödinger equation, *Phys. Rev. Lett.* 101(12): 123904.
- Belyaeva, T., Serkin, V., Agüero, M., Hernandez-Tenorio, C. & Kovachev, L. (2011). Hidden features of the soliton adaptation law to external potentials, *Laser Physics* 21: 258–263.
- Bludov, Y. V., Konotop, V. V. & Akhmediev, N. (2009). Matter rogue waves, *Phys. Rev. A* 80(3): 033610.

- Calogero, F. & Degasperis, A. (1976). Coupled nonlinear evolution equations solvable via the inverse spectral transform, and solitons that come back: the boomeron, *Lettere Al Nuovo Cimento* 16: 425–433.
- Calogero, F. & Degasperis, A. (1982). *Spectral transform and solitons: tools to solve and investigate nonlinear evolution equations*, Elsevier Science Ltd.
- Chen, H.-H. (1974). General derivation of bäcklund transformations from inverse scattering problems, *Phys. Rev. Lett.* 33(15): 925–928.
- Chen, H. H. & Liu, C. S. (1976). Solitons in nonuniform media, *Phys. Rev. Lett.* 37(11): 693–697.
- Chen, H. H. & Liu, C. S. (1978). Nonlinear wave and soliton propagation in media with arbitrary inhomogeneities, *Phys. Fluids* 21: 377–380.
- Chen, S., Yang, Y. H., Yi, L., Lu, P. & Guo, D. S. (2007). Phase fluctuations of linearly chirped solitons in a noisy optical fiber channel with varying dispersion, nonlinearity, and gain, *Phys. Rev. E* 75(3): 036617.
- Christiansen, P. L., Sorensen, M. P. & Scott, A. C. (2000). *Nonlinear science at the dawn of the 21st century*, Lecture Notes in Physics, Springer, Berlin.
- Clamond, D., Francius, M., Grue, J. & Kharif, C. (2006). Long time interaction of envelope solitons and freak wave formations, *Eur. J. Mech. B/Fluids* 25(5): 536–553.
- Dianov, E. M., Mamyshev, P. V., Prokhorov, A. M. & Serkin, V. N. (1989). *Nonlinear Effects in Optical Fibers*, Harwood Academic Publ., New York.
- Dudley, J. M. & Taylor, J. R. (2009). Ten years of nonlinear optics in photonic crystal fibre, *Nature Photonics* 3: 85–90.
- Dudley, J. M., Genty, G. & Coen, S. (2006). Supercontinuum generation in photonic crystal fiber, *Rev. Mod. Phys.* 78(4): 1135–1184.
- Dudley, J. M., Genty, G. & Eggleton, B. J. (2008). Harnessing and control of optical rogue waves insupercontinuum generation, *Opt. Express* 16(6): 3644–3651.
- Gardner, C. S., Greene, J. M., Kruskal, M. D. & Miura, R. M. (1967). Method for solving the korteweg-devries equation, *Phys. Rev. Lett.* 19(19): 1095–1097.
- Gupta, M. R. & Ray, J. (1981). Extension of inverse scattering method to nonlinear evolution equation in nonuniform medium, *J. Math. Phys.* 22(10): 2180–2183.
- Hao, R. & Zhou, G. (2008). Exact multi-soliton solutions in nonlinear optical systems, *Optics Communications* 281(17): 4474–4478.
- Hasegawa, A. (1984). Generation of a train of soliton pulses by induced modulational instability in optical fibers, *Opt. Lett.* 9(7): 288–290.
- Hasegawa, A. & Kodama, Y. (1995). *Solitons in Optical Communications*, Oxford University Press.
- Hasegawa, A. & Matsumoto, M. (2003). *Optical Solitons in Fibers, 3rd Edition*, Springer-Verlag, Berlin.
- He, X.-G., Zhao, D., Li, L. & Luo, H. G. (2009). Engineering integrable nonautonomous nonlinear schrödinger equations, *Phys. Rev. E* 79(5): 056610.
- Hernandez, T. C., Villargan, V. E., Serkin, V. N., Aguero, G. M., Belyaeva, T. L., Pena, M. R. & Morales, L. L. (2005). Dynamics of solitons in the model of nonlinear schrödinger equation with an external harmonic potential: 1. bright solitons, *Quantum Electronics* 35(9): 778.
- Hernandez-Tenorio, C., Belyaeva, T. L. & Serkin, V. N. (2007). Parametric resonance for solitons in the nonlinear schrödinger equation model with time-dependent harmonic oscillator potential, *Physica B: Condensed Matter* 398(2): 460–463.

- Herrera, J. J. E. (1984). Envelope solitons in inhomogeneous media, *J. Phys. A: Math. Gen.* 17(1): 95–98.
- Johnson, R. S. (1997). *A modern introduction to the mathematical theory of water waves*, Cambridge University Press, New York.
- Kharif, C. & Pelinovsky, E. (2003). Physical mechanisms of the rogue wave phenomenon, *Eur. J. Mech. B. Fluid* 22(6): 603–634.
- Kharif, C., Pelinovsky, E. & Slunyaev, A. (2009). *Rogue Waves in the Ocean*, Springer-Verlag, Berlin.
- Kibler, B., Fatome, J., Finot, C., Millot, G., Dias, F., Genty, G., Akhmediev, N. & Dudley, J. M. (2010). The peregrine soliton in nonlinear fibre optics, *Nature Physics* 6(10): 790–795.
- Krumhansl, J. A. (1991). Unity in the science of physics, *Physics Today* 44(3): 33–38.
- Lax, P. D. (1968). Integrals of nonlinear equations of evolution and solitary waves, *Commun. on Pure and Applied Mathematics* 21: 467–490.
- Liu, W.-J., Tian, B. & Zhang, H.-Q. (2008). Types of solutions of the variable-coefficient nonlinear schrödinger equation with symbolic computation, *Phys. Rev. E* 78(6): 066613.
- Luo, H., Zhao, D. & He, X. (2009). Exactly controllable transmission of nonautonomous optical solitons, *Phys. Rev. A* 79(6): 063802.
- Nayfeh, A. H. & Balachandran, B. (2004). *Applied Nonlinear Dynamics*, Wiley-VCH Verlag GmbH & Co. KGaA, Weinheim.
- Peregrine, D. H. (1983). Water waves, nonlinear schrödinger equations and their solutions, *Austral. Math. Soc. Ser. B* 25: 16–43.
- Porsezian, K., Ganapathy, R., Hasegawa, A. & Serkin, V. (2009). Nonautonomous soliton dispersion management, *Quantum Electronics, IEEE Journal of* 45(12): 1577–1583.
- Porsezian, K., Hasegawa, A., Serkin, V., Belyaeva, T. & Ganapathy, R. (2007). Dispersion and nonlinear management for femtosecond optical solitons, *Phys. Lett. A* 361(6): 504–508.
- Satsuma, J. & Yajima, N. (1974). Initial value problems of one-dimensional self-modulation of nonlinear waves in dispersive media, *Prog. Theor. Phys. Supplement* 55: 284–306.
- Serkin, V. N. & Belyaeva, T. L. (2001a). High-energy optical schrödinger solitons, *JETP Letters* 74: 573–577.
- Serkin, V. N. & Belyaeva, T. L. (2001b). The lax representation in the problem of soliton management, *Quantum Electronics* 31(11): 1007.
- Serkin, V. N. & Hasegawa, A. (2000a). Novel soliton solutions of the nonlinear schrödinger equation model, *Phys. Rev. Lett.* 85(21): 4502–4505.
- Serkin, V. N. & Hasegawa, A. (2000b). Soliton management in the nonlinear schrödinger equation model with varying dispersion, nonlinearity, and gain, *JETP Letters* 72: 89–92.
- Serkin, V. N. & Hasegawa, A. (2002). Exactly integrable nonlinear schrödinger equation models with varying dispersion, nonlinearity and gain: application for soliton dispersion, *Selected Topics in Quantum Electronics, IEEE Journal of* 8(3): 418–431.
- Serkin, V. N., Hasegawa, A. & Belyaeva, T. L. (2004). Comment on "exact self-similar solutions of the generalized nonlinear schrödinger equation with distributed coefficients", *Phys. Rev. Lett.* 92(19): 199401.
- Serkin, V. N., Hasegawa, A. & Belyaeva, T. L. (2007). Nonautonomous solitons in external potentials, *Phys. Rev. Lett.* 98(7): 074102.
- Serkin, V. N., Hasegawa, A. & Belyaeva, T. L. (2010a). Nonautonomous matter-wave solitons near the feshbach resonance, *Phys. Rev. A* 81(2): 023610.

- Serkin, V. N., Hasegawa, A. & Belyaeva, T. L. (2010b). Solitary waves in nonautonomous nonlinear and dispersive systems: nonautonomous solitons, *Journal of Modern Optics* 57(14-15): 1456–1472.
- Serkin, V. N., Matsumoto, M. & Belyaeva, T. L. (2001a). Bright and dark solitary nonlinear bloch waves in dispersion managed fiber systems and soliton lasers, *Optics Communications* 196(1-6): 159–171.
- Serkin, V. N., Matsumoto, M. & Belyaeva, T. L. (2001b). Nonlinear bloch waves, *JETP Letters* 73: 59–62.
- Shin, H. J. (2008). Darboux invariants of integrable equations with variable spectral parameters, *Journal of Physics A: Mathematical and Theoretical* 41(28): 285201.
- Solli, D. R., Ropers, C., Koonath, P. & Jalali, B. (2007). Optical rogue waves, *Nature* 450: 1054–1057.
- Tappert, F. D. & Zabusky, N. J. (1971). Gradient-induced fission of solitons, *Phys. Rev. Lett.* 27(26): 1774–1776.
- Taylor, J. R. (1992). *Optical solitons - theory and experiment*, Cambridge Univ. Press, Cambridge.
- Tenorio, C. H., Villagran-Vargas, E., Serkin, V. N., Agüero-Granados, M., Belyaeva, T. L., Pena-Moreno, R. & Morales-Lara, L. (2005). Dynamics of solitons in the model of nonlinear schrödinger equation with an external harmonic potential: 2. dark solitons, *Quantum Electronics* 35(10): 929.
- Wang, J., Li, L. & Jia, S. (2008). Nonlinear tunneling of optical similaritons in nonlinear waveguides, *J. Opt. Soc. Am. B* 25(8): 1254–1260.
- Wu, L., Li, L. & Zhang, J. F. (2008). Controllable generation and propagation of asymptotic parabolic optical waves in graded-index waveguide amplifiers, *Phys. Rev. A* 78(1): 013838.
- Wu, L., Zhang, J.-F., Li, L., Finot, C. & Porsezian, K. (2008). Similariton interactions in nonlinear graded-index waveguide amplifiers, *Phys. Rev. A* 78(5): 053807.
- Yan, Z. (2010). Nonautonomous "rogons" in the inhomogeneous nonlinear schrödinger equation with variable coefficients, *Physics Letters A* 374(4): 672–679.
- Zabusky, N. J. & Kruskal, M. D. (1965). Interaction of "solitons" in a collisionless plasma and the recurrence of initial states, *Phys. Rev. Lett.* 15(6): 240–243.
- Zakharov, V. E. (1980). The inverse scattering method, in R. Bullough & P. J. Caudrey (eds), *Solitons*, Springer-Verlag, Berlin, pp. 243–285.
- Zhang, J.-F., Wu, L. & Li, L. (2008). Self-similar parabolic pulses in optical fiber amplifiers with gain dispersion and gain saturation, *Phys. Rev. A* 78(5): 055801.
- Zhao, D., He, X.-G. & Luo, H.-G. (2009). Transformation from the nonautonomous to standard nls equations, *Eur. Phys. J. D* 53: 213–216.
- Zhao, D., Luo, H. G. & Chai, H. Y. (2008). Integrability of the gross-pitaevskii equation with feshbach resonance management, *Physics Letters A* 372(35): 5644–5650.

Planar Stokes Flows with Free Boundary

Sergey Chivilikhin¹ and Alexey Amosov²

¹*National Research University of Information
Technologies, Mechanics and Optics,*

²*Corning Scientific Center, Corning Incorporated
Russia*

1. Introduction

The quasi-stationary Stokes approximation (Frenkel, 1945; Happel & Brenner, 1965) is used to describe viscous flows with small Reynolds numbers. Two-dimensional Stokes flow with free boundary attracted the attention of many researches. In particular, an analogy is drawn (Ionescu, 1965) between the equations of the theory of elasticity (Muskeleshvili, 1966) and the equations of hydrodynamics in the Stokes approximation. This idea allowed (Antanovskii, 1988) to study the relaxation of a simply connected cylinder under the effect of capillary forces. Hopper (1984) proposed to describe the dynamics of the free boundary through a family of conformal mappings. This approach was later used in (Jeong & Moffatt, 1992; Tanveer & Vasconcelos, 1994) for analysis of free-surface cusps and bubble breakup.

We have developed a method of flow calculation, which is based on the expansion of pressure in a complete system of harmonic functions. The structure of this system depends on the topology of the region. Using the pressure distribution, we calculate the velocity on the boundary and investigate the motion of the boundary. In case of capillary forces the pressure is the projection of a generalized function with the carrier on the boundary on the subspace of harmonic functions (Chivilikhin, 1992).

We show that in the 2D case there exists a non-trivial variation of pressure and velocity which keeps the Reynolds stress tensor unchanged. The correspondent variations of pressure give us the basis for pressure presentation in form of a series. Using this fact and the variation formulation of the Stokes problem we obtain a system of equations for the coefficients of this series. The variations of velocity give us the basis for the vortical part of velocity presentation in the form of a serial expansion with the same coefficients as for the pressure series.

We obtain the potential part of velocity on the boundary directly from the boundary conditions - known external stress applied to the boundary. After calculating velocity on the boundary with given shape we calculate the boundary deformation during a small time step.

Based on this theory we have developed a method for calculation of the planar Stokes flows driven by arbitrary surface forces and potential volume forces. We can apply this method for investigating boundary deformation due to capillary forces, external pressure, centrifugal forces, etc.

Taking into account the capillary forces and external pressure, the strict limitations for motion of the free boundary are obtained. In particular, the lifetime of the configurations with given number of bubbles was predicted.

2. General equations

2.1 The quasi-stationary Stokes approximation

The equations of viscous fluid motion in the quasi-stationary Stokes approximation due to arbitrary surface force f_α and the continuity equation in the region $G \subset R^2$ with boundary Γ have the form

$$\frac{\partial p_{\alpha\beta}}{\partial x_\beta} = 0, \quad (1)$$

$$\frac{\partial v_\beta}{\partial x_\beta} = 0, \quad (2)$$

where $p_{\alpha\beta} = -p\delta_{\alpha\beta} + \mu \left(\frac{\partial v_\alpha}{\partial x_\beta} + \frac{\partial v_\beta}{\partial x_\alpha} \right)$ is the Newtonian stress tensor; v_α are the components of the velocity; p is the pressure; μ is the coefficient of the dynamical viscosity, which is assumed to be constant. The indices α, β take the values 1, 2. Summation over repeated indices is expected. The boundary conditions have the form

$$p_{\alpha\beta} n_\beta = f_\alpha, \quad \mathbf{x} \in \Gamma \quad (3)$$

where n_α and f_α are the components of the vector of outer normal to the boundary and the surface force. Let Γ_0 be the outer boundary of the region; Γ_k ($k=1, 2, \dots, m$) - the inner boundaries (boundaries of bubbles); $\Gamma = \bigcup_{k=0}^m \Gamma_k$ - see Fig.1.

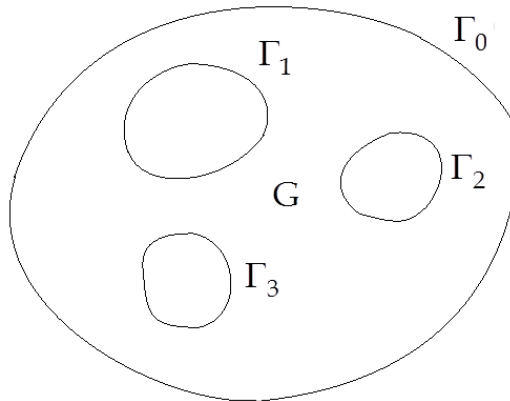


Fig. 1. Region G with multiply connected boundary Γ

The free boundary evolution is determined from the condition of equality of the normal velocity V_n of the boundary and the normal component of the velocity of the fluid at the boundary:

$$V_n = v_\beta n_\beta, \quad \mathbf{x} \in \Gamma \quad (4)$$

In case of a volume force F_α acting on G , the equation of motion takes the form

$$\frac{\partial p_{\alpha\beta}}{\partial x_\beta} = -F_\alpha \quad (5)$$

If the volume force is potential $F_\alpha = -\frac{\partial U}{\partial x_\alpha}$ one can renormalize the pressure $p \rightarrow p + U$ and present (3), (5) in the form

$$\frac{\partial p_{\alpha\beta}}{\partial x_\beta} = 0 \quad (6)$$

$$p_{\alpha\beta} n_\beta = f'_\alpha, \quad \mathbf{x} \in \Gamma \quad (7)$$

where $f'_\alpha = f_\alpha + U n_\alpha$ is the renormalized surface force.

2.2 The transformational invariance of the Stokes equations

Let's point out a specificity of the quasi-stationary Stokes approximation (1), (2). This system is invariant under the transformation

$$v_\alpha \rightarrow \tilde{v}_\alpha + V_\alpha + e_{\alpha\beta} x_\beta \omega \quad (8)$$

where V_α and ω are constants, $e_{\alpha\beta}$ is the unit antisymmetric tensor. Therefore, for this approximation the total linear momentum and the total angular momentum are indefinite. These values should be determined from the initial conditions.

2.3 The conditions of the quasi-stationary Stokes approximation applicability

The Navier-Stokes equations

$$\rho \left(\frac{\partial v_\alpha}{\partial t} + v_\beta \frac{\partial v_\alpha}{\partial x_\beta} \right) = \frac{\partial p_{\alpha\beta}}{\partial x_\beta} + F_\alpha, \quad (9)$$

where ρ is the density of liquid, lead to the quasi-stationary Stokes equations (5) if the convective and non-stationary terms in (9) can be neglected. The neglect of the convective term leads to the requirement of a small Reynolds number $\text{Re} = VL/\nu$, where V is the characteristic velocity, L is the spatial scale of the region G , and ν is the kinematic viscosity. The non-stationary term in the equation (9) can be omitted if during the velocity field relaxation time $T = L^2/\nu$ the shape of the boundary changes insignificantly, namely $VT \ll L$ which again leads to the condition $\text{Re} \ll 1$. The change of the volume force F_α and the surface force f_α during the time T should also be small:

$$\frac{\delta F_\alpha}{\delta t} T \ll F_\alpha, \quad \frac{\delta f_\alpha}{\delta t} T \ll f_\alpha, \quad (10)$$

For the forces determined by the region shape (like capillary force or centrifugal force) the conditions (10) lead to $\text{Re} \ll 1$ again.

The neglect of the non-stationary term is a singular perturbation of the motion equation in respect of the time variable. It leads to the formation of a time boundary layer of duration T , during which the initial velocity field relaxes to a quasi-steady state. The condition of a small deformation of the region during this time interval $V^0 T \ll L^0$ is ensured by the requirement of a small Reynolds number Re^0 constructed from the characteristic initial velocity V^0 and the initial region scale L^0 .

Let's integrate the motion equation (5) over the region G and use the boundary condition (3). As a result we obtain the condition

$$\Phi_\alpha = \int F_\alpha dG + \int f_\alpha d\Gamma = 0. \quad (11)$$

The equations of viscous fluid motion in the quasi-stationary Stokes approximation (5) have the form of local equilibrium conditions. Correspondingly, the total force Φ_α which acts on the system should be zero. The same way, using (5) and (3) one can obtain the condition

$$M = \int e_{\alpha\beta} x_\alpha F_\beta dG + \int e_{\alpha\beta} x_\alpha f_\beta d\Gamma = 0. \quad (12)$$

where $e_{\alpha\beta}$ is the unit antisymmetric tensor. Therefore, the total moment of force M acting on the system should be zero.

2.4 The Stokes equations in the special noninertial system of reference

Conditions (11) and (12) are the classical conditions of solubility of system (2), (5) with boundary conditions (3). Let's show that these conditions are too restrictive. For example, for a small drop of high viscous liquid falling in the gravitation field the total force is not zero, but equal to the weight of the drop. Therefore, we cannot use the quasi-stationary Stokes approximation to describe the evolution of the drop's shape due to capillary forces. But in a noninertial system of reference which falls together with the drop with the same acceleration, the total force is equal to zero.

In a general case, the total force Φ_α and total moment of force M acting on the system are not equal to zero. The Newton's second law for translational motion has the form

$$\rho S \frac{d\langle v_\alpha \rangle}{dt} = \Phi_\alpha, \quad (13)$$

where S is the area of the region, $\langle v_\alpha \rangle = \frac{1}{S} \int v_\alpha dG$ is the average velocity of the system, and Φ_α is the total force. Let's choose the center-of-mass reference system K' instead of the initial laboratory system K . The velocity and coordinate transformations have the form

$$v'_\alpha = v_\alpha - \langle v_\alpha \rangle, \quad x'_\alpha = x_\alpha - \langle x_\alpha \rangle, \quad (14)$$

where $\langle x_\alpha \rangle = \frac{1}{S} \int x_\alpha dG$ is the coordinate of the center of mass in the initial system K , $\langle v_\alpha \rangle = \frac{d\langle x_\alpha \rangle}{dt}$. In the new system the surface force is the same as in the initial system $f'_\alpha = f_\alpha$, but the volume force transforms to $F'_\alpha = F_\alpha - \Phi_\alpha$ and total force is equal to zero: $\Phi'_\alpha = 0$. So, we eliminated the total force Φ_α using a noninertial center-of-mass reference system K' .

The total moment of force in the new system stays unchanged: $M' = M$. To eliminate the total moment of force M we switch from the system K' to the rotating reference system K'' :

$$v''_\alpha \rightarrow v'_\alpha - e_{\alpha\beta} x'_\beta \Omega, \quad (15)$$

where Ω is the angular velocity of the rigid-body rotation

$$I \frac{d\Omega}{dt} = M, \quad (16)$$

where $I = \rho \int x'_\alpha x'_\alpha dG$ is the moment of inertia of our system. In the new system the surface force is the same as in the initial system $f''_\alpha = f'_\alpha$, but the volume force transforms to:

$$F''_\alpha \rightarrow F'_\alpha + \rho \left(e_{\alpha\beta} x'_\beta \dot{\Omega} + 2e_{\alpha\beta} v'_\beta \Omega + \Omega^2 x'_\alpha \right), \quad (17)$$

and the total moment of force is equal zero: $M'' = 0$. In case of a small Reynolds number, the Coriolis force $2\rho e_{\alpha\beta} v'_\beta \Omega$ is small compared with the viscous force.

So in case of the total force Φ_α and total moment of force M not equal to zero we can eliminate them using the noninertial reference system with the rigid-body motion due to the force and moment of force.

3. Pressure calculation

Let χ_α and ψ be smooth fields in the region G related by

$$\frac{\partial \chi_\alpha}{\partial x_\beta} + \frac{\partial \chi_\beta}{\partial x_\alpha} = 2\psi \delta_{\alpha\beta}. \quad (18)$$

Multiplying the equation of motion (1) by χ_α , integrating over G , and using (2), (3), (18), we obtain

$$\int p\psi dG = -\frac{1}{2} \int f_\alpha \chi_\alpha dG \quad (19)$$

In the special case when $\psi = 1$ the expression (18) gives us $\chi_\alpha = x_\alpha$ and, according with (19),

$$\int p dG = -\frac{1}{2} \int f_\alpha x_\alpha dG \quad (20)$$

see (Landau & Lifshitz, 1986). In a general case, according with (18), ψ is an arbitrary harmonic function and $\chi = \chi_1 + i\chi_2$ is the analytical function associated with ψ as

$$d\chi = (\psi + i\omega)dz \quad (21)$$

where ω is a harmonic function conjugate to ψ .

The expressions (18) and (19) are basic in our theory. There is also an alternative way to derive them. The equations of motion (1), continuity (2) and the boundary conditions (3) can be obtained from the variation principle (Berdichevsky, 2009).

$$\delta \left[\frac{1}{4\mu} \int (p_{\alpha\beta} p_{\alpha\beta} - 2p^2) dG - \int f_\alpha v_\alpha d\Gamma \right] = 0 \quad (22)$$

or

$$\frac{1}{2\mu} \int (p_{\alpha\beta} \delta p_{\alpha\beta} - 2p \delta p) dG - \int f_\alpha \delta v_\alpha d\Gamma = 0 \quad (23)$$

Since (23) is valid for arbitrary variations of pressure δp and velocity δv_α we choose them such that $p_{\alpha\beta}$ is left unchanged:

$$\delta p_{\alpha\beta} = -\delta p \cdot \delta_{\alpha\beta} + \mu \left(\frac{\partial \delta v_\alpha}{\partial x_\beta} + \frac{\partial \delta v_\beta}{\partial x_\alpha} \right) = 0. \quad (24)$$

In this case (23) gives us

$$\frac{1}{\mu} \int p \delta p dG + \int f_\alpha \delta v_\alpha d\Gamma = 0. \quad (25)$$

We introduce the one-parameter family of variations $\delta v_\alpha = \frac{\chi_\alpha}{2\mu} \delta \varepsilon$, $\delta p = \psi \delta \varepsilon$. Then (24) and (25) take the form (18) and (19).

Suppose $x \in R^N$. Then it follows from (18) that

$$(N-2) \frac{\partial^2 \psi}{\partial x_\alpha \partial x_\beta} = 0. \quad (26)$$

Therefore, in the three-dimensional case ψ is a linear function. Only in the two-dimensional case ψ can be an arbitrary harmonic function. Formulating in terms of (3.5), only in the two-dimensional space there exists a non-trivial system of pressure and velocity variations providing zero stress tensor variation.

The complete set of analytical functions ζ_k in the region G with the multiply connected boundary Γ consists of functions of the form $z_k + (z - z_m^o)^{-k}$, where z_m^o are fixed points, each situated in one bubble. The complete set of harmonic functions ψ_k can be obtained in the form of $\text{Re}\zeta_k$ and $\text{Im}\zeta_k$.

According with (1), (2) the pressure p is a harmonic function. We present it in the form

$$p = \sum_k p_k \psi_k. \quad (27)$$

Using the expression (19) we obtain the algebraic system for coefficients p_k :

$$\sum_k \left(\int \psi_k \psi_n dG \right) p_k = -\frac{1}{2} \int f_\alpha \chi_{\alpha n} d\Gamma, \quad n = 0, 1, \dots \quad (28)$$

4. Velocity calculation

The stress tensor, expressed in terms of the Airy function φ ,

$$p_{\alpha\beta} = \frac{\partial^2 \varphi}{\partial x_\alpha \partial x_\beta} - \frac{\partial^2 \varphi}{\partial x_\gamma \partial x_\gamma} \delta_{\alpha\beta}, \quad (29)$$

satisfies the equation of motion (1) identically. The boundary conditions (3) take the form

$$e_{\alpha\beta} \tau_\gamma \frac{\partial^2 \varphi}{\partial x_\beta \partial x_\gamma} = -f_\alpha, \quad x \in \Gamma, \quad (30)$$

where τ_γ are the components of the unit tangential vector to the boundary, its direction being matched to the direction of circulation. Integrating (30) along the component boundary Γ_k from a fixed point to an arbitrary one we obtain

$$\frac{\partial \varphi}{\partial x_\alpha} = e_{\alpha\beta} \int f_\alpha d\Gamma_k, \quad x \in \Gamma_k. \quad (31)$$

Using (1), (29) and the explicit form of the stress tensor, we get

$$d \left(\frac{\partial \varphi}{\partial x_\alpha} \right) = 2\mu d v_\alpha + d\Phi_\alpha, \quad x \in G, \quad (32)$$

where

$$d(\Phi_1 + i\Phi_2) = (p + i\Omega), \quad \Omega = \mu \left(\frac{\partial v_1}{\partial x_2} - \frac{\partial v_2}{\partial x_1} \right), \quad (33)$$

Ω is a harmonic function conjugate to p ,

$$\frac{\partial \Phi_\alpha}{\partial x_\beta} + \frac{\partial \Phi_\beta}{\partial x_\alpha} = 2p \delta_{\alpha\beta}. \quad (34)$$

Therefore

$$\Phi_\alpha = \sum_n p_n \chi_{\alpha n}, \quad (35)$$

where p_k are the coefficients of the pressure expansion (27). These coefficients are the solution of the system (28). According with (32) the velocity in the region G can be presented in the form

$$v_\alpha = \frac{1}{2\mu} \left(\frac{\partial \varphi}{\partial x_\alpha} - \Phi_\alpha \right), \quad x \in G. \quad (36)$$

The first term in the right-hand part of (36) is the potential part of velocity; the second term is the vortex part.

The gradient of the Airy function on the boundary was calculated in (31). Then we can calculate the velocity on the boundary as

$$v_\alpha = \frac{1}{2\mu} \left(e_{\alpha\beta} \int f_\alpha d\Gamma_k - \Phi_\alpha \right), \quad x \in \Gamma_k. \quad (37)$$

The expression (37) gives us the explicit presentation of the velocity on the boundary.

5. Limitations for the motion of the boundary

5.1 The rate of change of region perimeter

The strong limitation for the motion of the boundary is based on a general expression regarding the rate of change of perimeter L . To obtain this expression we use the fact (Dubrovina et al, 1984) that

$$\frac{d|\Gamma|}{dt} = \int v_\alpha n_\alpha H d\Gamma, \quad (38)$$

where $H = \frac{\partial n_\beta}{\partial x_\beta}$ is the mean curvature of the boundary. In the 2D case $|\Gamma|$ is the perimeter of the region, and in the 3D case $|\Gamma|$ is the area of the boundary. We introduce the operator of differentiation along the boundary $D_{\alpha\beta} = n_\alpha \frac{\partial}{\partial x_\beta} - n_\beta \frac{\partial}{\partial x_\alpha}$. Then we can write (38) in the form

$$\frac{dL}{dt} = \int v_\alpha D_{\alpha\beta} n_\beta d\Gamma. \quad (39)$$

Using the identity

$$\int D_{\alpha\beta} A d\Gamma = 0, \quad (40)$$

where A is an arbitrary field which is continuous on the boundary, and also the equation of continuity (2) and the boundary conditions (3) we can write (39) in the final form

$$\frac{d|\Gamma|}{dt} = - \int \frac{p + f_\alpha n_\alpha}{2\mu} d\Gamma. \quad (41)$$

This expression is valid for any flow of incompressible Newtonian liquid (without Stokes approximation), generally speaking, with variable viscosity. We will use it for a 2D flow ($|\Gamma| = L$ is the perimeter of region), in case of constant viscosity:

$$\frac{dL}{dt} = -\frac{1}{2\mu} \int (p + f_\alpha n_\alpha) d\Gamma. \quad (42)$$

5.2 The dynamics of bubbles due to capillarity and air pressure

Let's take into account the capillary forces on the boundary, the external pressure p_0 and the pressure inside of the bubbles $p_k = p_b$, $k = 1, 2, \dots, m$, equal in every bubble. Then the boundary force has the form

$$f_\alpha = -\sigma n_\alpha \frac{\partial n_\beta}{\partial x_\beta} - p_k n_\alpha, \quad x \in \Gamma_k, \quad (43)$$

where σ is the coefficient of surface tension. Using (42), (43) we get

$$\frac{dL}{dt} = -\frac{1}{2\mu} \left[\int p d\Gamma - (p_0 L_0 + p_b L_b) + 2\pi\sigma(m-1) \right], \quad (44)$$

where L_0 and L_b are the perimeter of external boundary and the total perimeter of the bubbles correspondingly.

Using (20) we obtain

$$\int p dG = p_0 S + (p_0 - p_b) S_b + \frac{\sigma}{2} L, \quad (45)$$

where S and S_b are the area of region and the total area of the bubbles.

For $\psi = p$, $\chi_\alpha = \Phi_\alpha$, the expressions (19), (34), (37) give us

$$\begin{aligned} \int p^2 dG &= \frac{\sigma}{2} (p_0 L_0 + p_b L_b + \int p d\gamma) + p_0^2 S + (p_0^2 - p_b^2) S_b - \\ &- \mu (p_0 - p_b) \frac{dS_b}{dt}. \end{aligned} \quad (46)$$

Using (44) - (46) and the inequality $\int p^2 dG \geq \frac{1}{S} \left(\int p dG \right)^2$ we obtain the differential inequality

$$\begin{aligned} \mu \left[\sigma \frac{dL}{dt} + (p_0 - p_b) \frac{dS_b}{dt} \right] &\leq \\ &\leq -(p_0 - p_b) \left[\sigma L_b + (p_0 - p_b) S_b \right] - \\ &- \frac{1}{S} \left[(p_0 - p_b) S_b + \frac{\sigma}{2} L \right]^2 - \pi\sigma^2(m-1). \end{aligned} \quad (47)$$

This expression gives us the possibility to obtain the strict limitations for the motion of the free boundary in some special cases.

5.3 The influence of capillary forces only

In this case the inequality (47) may be simplified:

$$\frac{dL}{dt} \leq -\frac{\sigma}{2\mu} \left[\frac{L^2}{2S} + 2\pi(m-1) \right]. \quad (48)$$

where m is the number of bubbles. Let $L_\infty = 2\sqrt{\pi S}$ be the asymptotic value of the perimeter and let $\tau = \frac{\sigma t}{2\mu} \sqrt{\frac{\pi}{S}}$ be the dimensionless time. Then, according with (48), $L(\tau) \leq L_{up}(\tau)$,

$$\begin{aligned} L_{up} &= \frac{L_0 + L_\infty th(\tau)}{L_\infty + L_0 th(\tau)}, & m = 0, \\ L_{up} &= \frac{L_0 L_\infty}{L_\infty + L_0 \tau} (L_\infty + L_0 \tau), & m = 1, \\ L_{up} &= \frac{\sqrt{m-1} (L_0 - L_\infty \sqrt{m-1} tg(\sqrt{m-1} \tau))}{\sqrt{m-1} + \lambda_0 tg(\sqrt{m-1} \tau)}, & m \geq 2. \end{aligned} \quad (49)$$

where $L_{up}(\tau)$ is the upper limitation for time dependence of the perimeter - see Fig.2. The perimeter of system L lies in the interval $L_\infty \leq L \leq L_{up}(\tau)$.

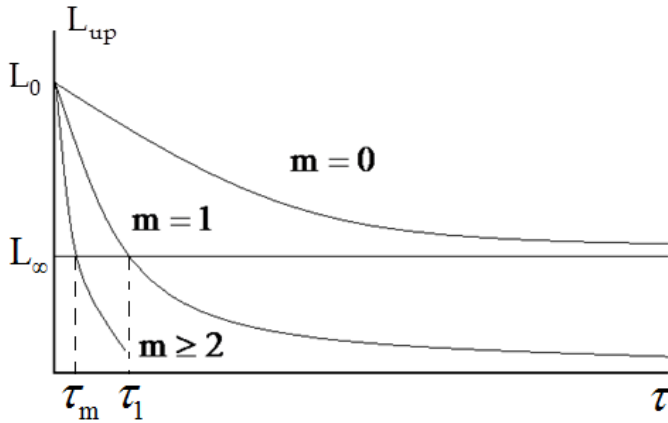


Fig. 2. The upper limitation for the time dependence of the perimeter for various number of bubbles m .

Therefore, if we have no bubbles in the region, the characteristic dimensionless time of relaxation of the boundary to the circle $\tau_0 \leq 1$. In case of one bubble ($m = 1$), $L_{up}(\tau) \geq L_\infty$ at the time $\tau \leq \tau_1 = 1 - L_\infty/L_0$. The system with this topology can exist in this time period only. The bubble must collapse or break into two bubbles in time $\tau_* \leq \tau_1$. In case of $m > 2$ bubbles, such configuration will exist during the time

$$\tau \leq \tau_m = \frac{1}{\sqrt{m-1}} \operatorname{arctg} \left(\frac{\sqrt{m-1}(L_0 - L_\infty)}{L_0 + (m-1)L_\infty} \right). \quad (50)$$

5.4 Bubbles in an infinite region

The outer boundary of the region is a circle with a large radius R . The bubbles are localized around the center of the circle. Using the expressions $\pi R^2 - S_b = S$, $L = 2\pi R + L_b$, we can see that the inequality (47) in the limit $R \rightarrow \infty$ takes the form

$$\mu \frac{dW}{dt} \leq -(p_0 - p_b)W - \pi\sigma^2 m, \quad (51)$$

where $W = \sigma L_b + (p_0 - p_b)S_b$. Therefore, at $p_0 - p_b > 0$

$$W + \frac{\pi\sigma^2 m}{p_0 - p_b} \leq \left(W(0) + \frac{\pi\sigma^2 m}{p_0 - p_b} \right) \exp\left(-\frac{p_0 - p_b}{\mu} t \right). \quad (52)$$

Because $W \geq 0$, this configuration exists without change of the number of bubbles during the time

$$t \leq \frac{\mu}{p_0 - p_b} \ln \left[1 + \frac{p_0 - p_b}{\pi\sigma^2 m} (\sigma L_b(0) + (p_0 - p_b)S_b(0)) \right]. \quad (53)$$

6. Motion of the boundary due to capillary forces

6.1 Calculation of pressure and velocity

In case of capillary forces action

$$f_\alpha = -\sigma n_\alpha \frac{\partial n_\beta}{\partial x_\beta}, \quad x \in \Gamma \quad (54)$$

and expression (19) takes the form

$$\int p \psi dG = \frac{\sigma}{2} \int \psi d\Gamma, \quad (55)$$

or

$$\langle p\psi \rangle_G = \langle p \rangle_G \langle \psi \rangle_\Gamma, \quad (56)$$

where

$$\langle f \rangle_G = \frac{1}{S} \int f dG, \quad \langle f \rangle_\Gamma = \frac{1}{L} \int f d\Gamma, \quad \langle P \rangle_G = \frac{\sigma}{2S}. \quad (57)$$

The expression (56) is valid for any harmonic function ψ . Let's apply $\psi = p$. Then we obtain

$$\langle p^2 \rangle_G = \langle p \rangle_G \langle p \rangle_\Gamma, \quad (58)$$

It can be seen from (58) that

$$\langle p \rangle_{\Gamma} \geq \langle p \rangle_{\Gamma}. \quad (59)$$

Introducing the generalized function (simple layer)

$$\delta_s(\mathbf{x}) = \int \delta(\mathbf{x} - \mathbf{y}) dl_y, \quad (60)$$

we see that p is the projection of δ_s onto the subspace of harmonic functions.

Introducing in G a complete system of orthonormal harmonic functions $\{\mathcal{E}_k\}_{k=0}^{\infty}$ which obey the orthogonality condition $\langle \mathcal{E}_k \mathcal{E}_n \rangle_G = \delta_{kn}$, we obtain from (56) the following expression for the pressure

$$p = \langle p \rangle_G \sum_{k=0}^{\infty} \mathcal{E}_k \langle \mathcal{E}_k \rangle_{\Gamma}. \quad (61)$$

In case of capillary forces the expression (37) takes the form

$$v_{\alpha} = \frac{1}{2\mu} (\sigma n_{\alpha} - \Phi_{\alpha}), \quad x \in \Gamma. \quad (62)$$

6.2 Relaxation of a small perturbation of a circular cylinder

Consider a small perturbation of the circular cylinder boundary, given by $r = R + h(\varphi, t)$, $|h| \ll R$. Then we have from (62)

$$\frac{\partial h}{\partial t} = -\frac{\sigma}{2\mu R} \sum_{k=-\infty}^{\infty} |k| \exp(ik\varphi) h_k, \quad (63)$$

$$h_k(t) \equiv \int_0^{2\pi} \exp(-ik\varphi) h(\varphi, t) \frac{d\varphi}{2\pi} = h_k(0) \exp\left(-\frac{\sigma|k|t}{2\mu}\right), \quad (64)$$

in agreement with (Levich, 1962). According with (64), a small boundary perturbation of characteristic with $a \ll R$ and amplitude $H \ll a$ has a characteristic decay time $\tau \sim \frac{\mu a}{\sigma}$.

6.3 The capillary relaxation of an ellipse

Let's test our theory on an example of a large amplitude perturbation. We calculate the capillary relaxation of boundary with initial shape $\frac{x_1^2}{a^2} + \frac{x_2^2}{b^2} = 1$ in two ways - using the numerical calculation based on (6.4) and the finite-element software ANSYS POLYFLOW (see Fig. 3 and Fig.4). These methods of calculation give us the same results with discrepancy about 1%.

6.4 The collapse of a cavity

Let's now consider a large amplitude perturbation in the shape of a cavity (Fig. 5). By symmetry, the pressure must be an even function with respect to x_2 , i.e. $p(x_1, -x_2) = p(x_1, x_2)$.

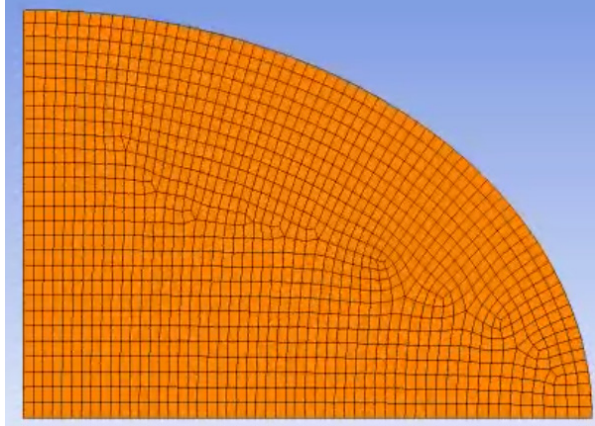


Fig. 3. Computational domain used in finite-element calculation of ellipse relaxation.

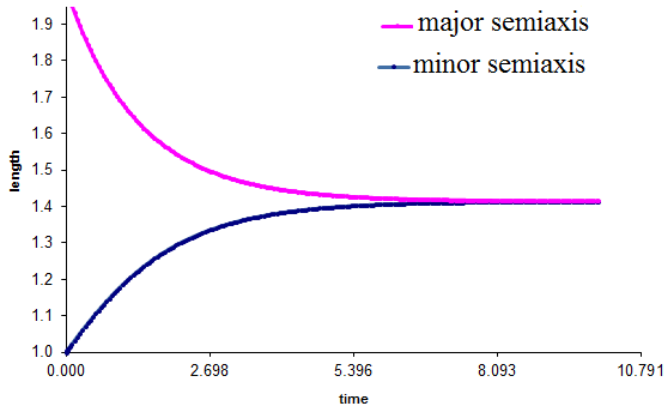


Fig. 4. Relaxation from ellipse to a circle in finite-element calculation.

We introduce a space of two-variable harmonic functions which are even with respect to the second argument, and choose in it the complete system of functions in the form $\psi_n = r^n \cos(n\varphi)$ (r and φ are the polar coordinates in the x_1, x_2 plane). Since the width δ is small $\langle \psi_m \psi_n \rangle_g = R^{2n} \frac{\delta_{mn}}{2(n+1)}$. Then the complete system of orthogonal harmonic functions in this space is

$$\Xi_n = \sqrt{2(n+1)} \left(\frac{r}{R} \right)^n \cos(n\varphi). \tag{65}$$

Inserting (65) in (61) and summing the series yields

$$p = \sigma \left[\frac{1}{R} - \frac{H}{\pi R^2} - \frac{2}{\pi} \operatorname{Re} \left(\frac{1}{R-z} - \frac{R-H}{R^2 - (R-H)R} \right) \right], \tag{66}$$

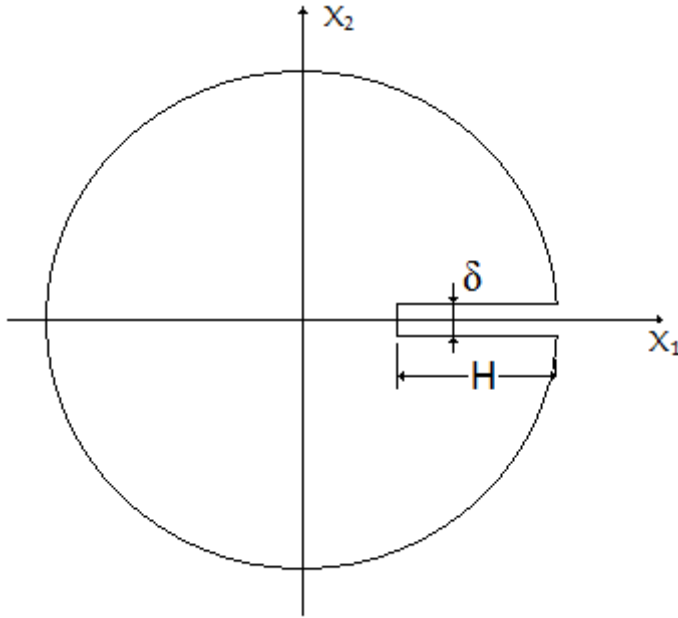


Fig. 5. Cavity perturbation.

whence, using (35), we have

$$\Phi = \sigma \left[\left(1 - \frac{H}{\pi R} \right) \frac{z}{R} + \frac{2}{\pi} \ln \left(\frac{R^2 - (R-H)z}{(R-H)R} \right) \right]. \quad (67)$$

In spite of the logarithm, (67) is a single-valued analytical function in G , because the boundary perturbation constitutes a branch cut. If we insert (67) in (62), we find that the normal velocity of the cut edges $V = \frac{\sigma}{2\mu}$ (in the zero approximation with respect to the small

parameter $\frac{\delta}{H}$). The edges close up after a time $\tau = \frac{\mu\delta}{\sigma}$. Although capillary forces generally tend to flatten the boundary perturbation, in this case they produce the opposite effect. Acting to reduce the length of the cut, the capillary forces generate a flow of scale H in the region. The velocities along x_1 and x_2 have the scales \dot{H} and $\dot{\delta}$, respectively. If we equate the work of surface-tension force with the rate of energy dissipation by viscous forces, we find that $\sigma\dot{H} \approx -\mu \left(\frac{\dot{H}}{H} \right)^2 H^2$ or $\dot{H} \approx \dot{\delta} \approx -\frac{\sigma}{\mu}$; this conforms to the rigorous result we obtained before.

7. Conclusion

We presented a method to calculate two-dimensional Stokes flow with free boundary, based on the expansion of pressure in a complete system of harmonic functions. The theory forms the basis for strict analytical results and numerical approximations. Using this approach we analyse the collapse of bubbles and relaxation of boundary perturbation. The results obtained by this method are correlating well with numerical calculations performed using commercial FEM software.

8. Acknowledgment

The authors would like to express their sincere gratitude to Prof. V. Pukhnachov and Prof. C. Pozrikidis for their attention to this research.

9. References

- Antanovskii, L.K. (1988). Interface boundary dynamics under the action of capillary forces. Quasisteady-state plane-parallel motion., *J. Appl. Mech. and Techn. Phys.* Vol. 29, No 3, pp. 396-399.
- Berdichevsky, V. (2009). *Variational principles of continuum mechanics*, Vol. 1, Springer-Verlag, Berlin-Heidelberg
- Chivilikhin, S.A. (1992). Plane capillary flow of a viscous fluid with multiply connected boundary in the Stokes approximation, *Fluid Dynamics*, Vol. 27, No. 1, pp. 88 - 92.
- Frenkel, J. (1945). Viscous flow of crystalline bodies under the action of surface tension, *Journal of Physics*, Vol. 9, No. 5, pp. 385-391
- Dubrovin, B.A., Fomenko, A.T. & Novikov, S.P. (1984). *Modern Geometry. Methods and Applications*. Part 1. Springer-Verlag
- Happel, S.J. & Brenner, H. (1965). *Low Reynolds Number Hydrodynamics*, Prentice-Hall, Englewood Cliffs
- Hopper, R.W. (1984). Coalescence of two equal cylinders: exact results for creeping viscous plane flow driven by capillarity, *J. Am. Ceram. Soc.*, Vol. 67, No. 12, pp. 262 - 264.
- Ionescu, D.G. (1965). Theory of analytic functions and hydrodynamics, in: *Applications of the Theory of Functions in the Mechanics of Continuous Media*, Vol. 2, Mechanics of Liquids and Gases [in Russian], Nauka, Moscow.
- Jeong, J.-T. & Moffatt, H.K. (1992). Free-surface cusps associated with flow at low Reynolds number, *J. Fluid Mech.*, Vol. 241, pp. 1-22.
- Landau, L.D. & Lifshitz E.M. (1986). *Theory of Elasticity*. Course of Theoretical Physics. Vol.7. Butterworth-Heinemann.
- Levich, V.G. (1962). *Physicochemical hydrodynamics*, Prentice-Hall, Englewood Cliffs, New Jersey
- Muskeleshvili, N.I. (1966). *Some Fundamental Problems of the Mathematical Theory of Elasticity* [in Russian], Nauka, Moscow
- Pozrikidis, C. (1997). Numerical studies of singularity formation at free surfaces and fluid interfaces in two-dimensional Stokes flow, *J. Fluid Mech.* 331, pp. 145-167.
- Richardson, S. (2000). Plane Stokes flow with time-dependent free boundaries in which the fluid occupies a doubly-connected region, *Eur. J. Appl. Math.*, 11, pp. 249-269.

Tanveer, S. & Vasconcelos, G.L. (1994). Bubble Breakup in two-dimensional Stokes flow, *Phys. Rev. Lett.*, Vol. 73, No. 21, pp. 2845-2848.

Part 2

Biological Applications and Biohydrodynamics

Laser-Induced Hydrodynamics in Water and Biotissues Nearby Optical Fiber Tip

V. I. Yusupov¹, V. M. Chudnovskii¹ and V. N. Bagratashvili²

¹*V.I. Il'ichev Pacific Oceanological Institute, Far Eastern
Branch of Russian Academy of Sciences*

²*Institute of Laser and Information Technologies,
Russian Academy of Sciences
Russia*

1. Introduction

This paper is aimed at revealing the mechanisms of therapeutic effects stimulated by a medium power (1–10 W) fiber laser induced hydrodynamics in water-saturated bio-tissues. Modern laser medical technologies widely employ delivery of laser light to irradiated tissues via optical fibers. Optical fiber easily penetrates through needle and endoscopic channels, and laser light can be delivered through a fiber for puncture and endoscopic operations. Several laser medical technologies (puncture multichannel laser decompression of disc, laser intervention upon osteochondrosis, surgical treatment of chronic osteomyelitis, endovenous laser ablation, etc.) are based on effective hydrodynamic processes in water-saturated bio-tissues. These hydrodynamic processes trigger cellular response and regenerative effects through the specific mechanisms of mechano-biology. In this work, we consider different kinds of effects stimulated by a medium power laser-induced hydrodynamics in the vicinity of a fiber tip surface, in particular, generation of vapor-gas bubbles, fiber tip degradation, and generation of intense acoustic waves. Presence of strongly absorbed agents (in a form of Ag nanoparticles, in particular) in laser irradiated water nearby optical fiber tip results in appearance of pronounced filamentary structures of these agents.

2. Therapeutic motivation

One of the modern tendencies in a low-invasive medical therapy is a medium power (1–10 W) laser treatment of connective tissues. The examples of such technologies are: laser engineering of cartilages (Bagratashvili et al., 2006); puncture multichannel laser decompression of disc (Sandler et al., 2002; Sandler et al., 2004); laser intervention upon osteochondrosis (Chudnovskii & Yusupov, 2008); laser treatment of chronic osteomyelitis (Privalov et al., 2001); endovenous laser ablation (Van den Bos et al., 2009); fractional photothermolysis (Rokhsar & Ciocon, 2009).

Treatment of osteochondrosis, for example, is based on laser-induced (0.97 μm in wavelength and 2–10 W in power) formation of multiple channels inside an intervertebral disc using silica fiber with a carbon coated fiber tip surface, in order to enhance laser light absorption nearby the fiber tip. Osteochondrosis is caused by such partial destruction of

intervertebral disc, followed by release of nucleus pulposus from disc in the form of hernia, which exerts pressure upon nervous roots thus giving pain. Fig 1a shows the scheme of formation of multiple laser channels inside intervertebral disc in the course of laser treatment of osteochondrosis (Sandler et al., 2002; Sandler et al., 2004; Chudnovskii & Yusupov, 2008). Transport laser delivery fiber passes inside the disc under treatment through a thin needle inserted to the disc (laser puncture procedure). Optical fiber is inserted through a thin needle via a posterolateral percutaneous approach under a local anesthesia. Important, that saline water is permanently introduced into the disc through the needle. Channel is formed by the heated fiber moving forward inside the disc. The fiber forms the channel and is shifted 1 -2 cm per 5 - 10 s inside the disc. Fig. 1b shows the example of such channels in nucleus pulposus of spinal disc formed by a fiber laser in the course of laboratory experiment (Sandler et al., 2004).

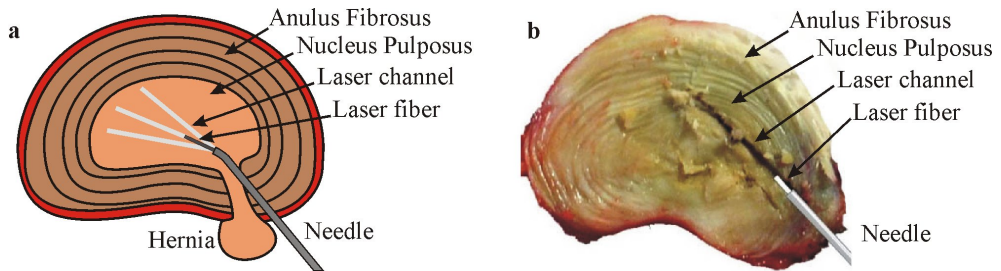


Fig. 1. a - Scheme of laser irradiation of spinal disc. b - Laser channel formed in spinal disc through optical fiber in presence of physiological solution (Sandler et al., 2004).

Surprisingly, that such action on herniated disc causes significant effect in some period of time on tissues located out of laser irradiated zone. As one can see, for example, on tomography picture (Fig. 2b), some cavities appear in the hernia, and its density decreases significantly compared with the density of hernia before laser treatment (Fig. 2a).

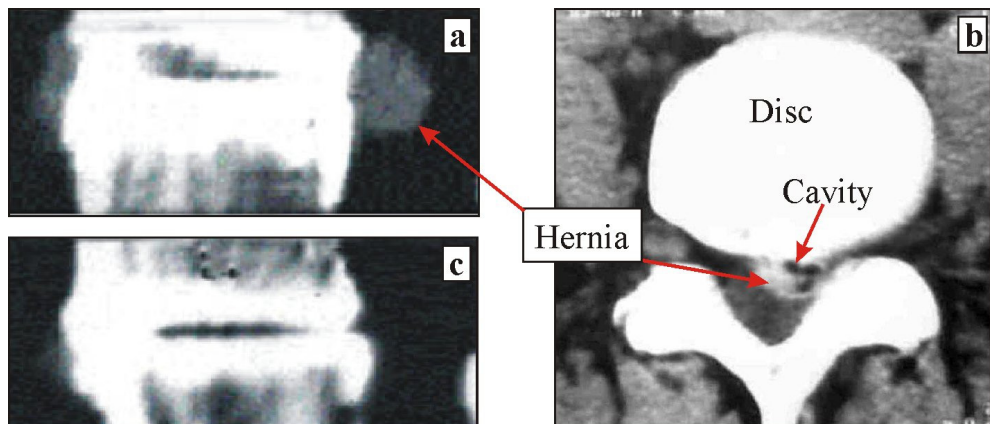


Fig. 2. Computer tomography pictures of herniated disc area. a- before healing: big sequester of hernia (side view); b - cavity inside hernia, stimulated by laser-induced channel formation in disc; c -three month after laser healing : no hernia.

As a result, the hernia transforms into a soft sponge, the pressure of hernia on nervous roots decreases, and relevant pain releases. The hernia itself disappears after some period of time, and regenerative processes take place which result (in a few month) in recovery of the disc structure and their main functions (Sandler et al., 2002, 2004; Chudnovskii et al., 2008, 2010a, 2010b).

Another important example of a medium power laser therapy is a laser treatment of chronic osteomyelitis. Fig. 3a demonstrates the X-ray image of femoral bone of the 14 year old patient heavily affected by osteomyelitis (Privalov et al., 2001). Significant destruction and rarefication of bone structure takes place. Typically, such bone tissue degradation requires amputation of organ. However, application of medium power laser treatment approach in this case gave, as a result, a complete regeneration of affected femoral bone (Fig. 3b), and no amputation was required. Again, therapy was based on a medium power laser-induced formation of channels (similar to that presented at Fig.1) in a bone medullary tissue, which stimulate successively the regeneration processes in the bone tissue.

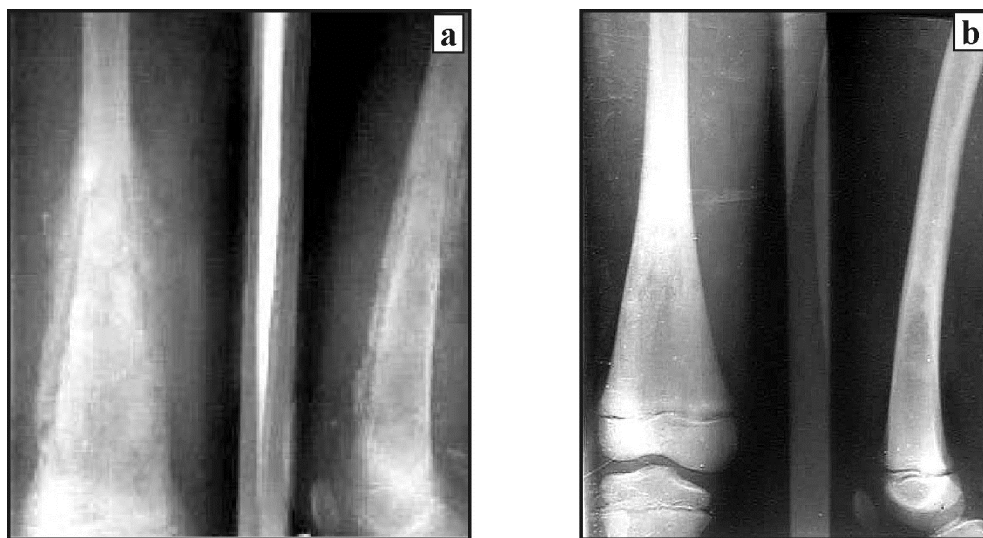


Fig. 3. X-ray images of right hip of the 14 y.o. patient with chronic osteomyelitis (Privalov et al., 2001). a - destruction and rarefication of bone structure before treatment. b - complete regeneration of bone structure 11 month after laser treatment.

Strong regenerative potential of medium power laser treatment for different kinds of tissues is already well recognized (Sandler et al., 2002, 2004; Chudnovskii & Yusupov, 2008, Chudnovskii et al., 2010a, 2010b), however the dominant primary physical mechanisms of such regeneration are still the subject of controversy. It is commonly accepted that the effects of medium power laser irradiation result from laser heating of tissues. However in most of cases, the pronounced therapeutic effect cannot be rationalized by laser-induced thermal tissue degradation only. For example, appearance of cavities in the hernia and significant decrease of its density observed immediately after laser manipulation (Fig. 2b), takes place without its heating, since hernia is located quite far from the area of laser-induced channel formation, and, thus, heating of hernia is negligible.

We believe that *effective hydrodynamic processes* play dominant role for the effect of a medium power laser-induced regeneration and healing of connective tissues diseases (intervertebral hernia, osteomyelitis and some other diseases) using laser puncture procedures (Chudnovskii & Yusupov, 2008; Chudnovskii et al., 2010a, 2010b). Main features of these processes will be considered below.

3. Laser-induced generation of micro-bubbles in water

The key process for the mechanism of medium power laser-induced regeneration and healing of musculoskeletal system diseases is the generation of micro-bubbles in inter-tissue water (Yusupov et al., 2010).

3.1 Laser-induced generation of micro-bubbles in a free water

Formation of micro-bubbles in a free water was studied with the aid of the optical methods using a water filled plastic cell (the horizontal dimensions are 150×100 mm and the height is 15 mm) and glass capillaries with an inner diameter of 1 mm. In the most of experiments, the working fiber tip is preliminary blackened by a short (~ 1 s) contact of the fiber tip with a wooden plate at a laser power of about 3 W. The fiber tip surface thus covers by a thin carbon layer owing to the wood burning. Such a procedure is well reproduced, so that from 10 to 20% of the laser power is absorbed in the thin carbon layer. Computer controlled fiber lasers (LS-0.97 and LS-1.55 of IRE-Polus, Russia) with the wavelengths of 0.97 μm and 1.55 μm , 1–10 W in power were interfaced with a 400 μm core diameter silica fiber. Low intensity (up to 1 mW) green pilot beam from the built in diode laser was used to highlight the laser irradiated zone in the cell. The fiber is horizontally fixed in the cell, which is placed on the worktable of a MICROS MC300 microscope equipped with a Vision digital color camera interfaced with PC. The water cell was also placed on the table with illumination, and the processes in the vicinity of the heated fiber tip were visualized using a Photron Fastcam SA-3 camera at rates of 2000 or 10000 frames per second. To control the laser induced spectrum, an Ocean Optics USB4000 fiber spectrum analyzer was used, which is interfaced with PC and has an optical resolution of about 1.5 nm and 200–1100 nm wavelength range. For better visualization of hydrodynamic flows the collargol (albumin coated Ag nanoparticles) have been added to water in the cell (Yusupov et al., 2011b).

Hydrodynamic flows taking place nearby the fiber tip when laser power is on, can be clearly seen in a scattering mode using illumination with green light of pilot laser beam through the same transport fiber (Fig. 4). Such flows result in intrusion of collargol from neighboring area into the area in front of the fiber tip. One can also see here the initial process of new intrusion formation (outlined with a dashed line). The rate of rise-up front of a given intrusion (which is about 150 μm in average thickness) is found to be described by exponential law (Yusupov et al., 2011b)

$$V = 0.6 \cdot \exp(-1.5 \cdot r), \quad (1)$$

where r is the distance from fiber tip: at 1 mm from fiber tip $V = 150 \mu\text{m/s}$, while at 2 mm from fiber tip V falls down to $30 \mu\text{m/s}$.

The bubbles don't occur up to laser power of 10 W with non-blackened fiber tip and for 0.97 μm laser radiation, while for 1.56 μm laser radiation (which is much stronger absorbed by water) the bubbles are generated at about 1 W of laser power. Blackening of fiber tip results in generation of bubbles for both 0.97 μm and 1.56 μm laser wavelengths.

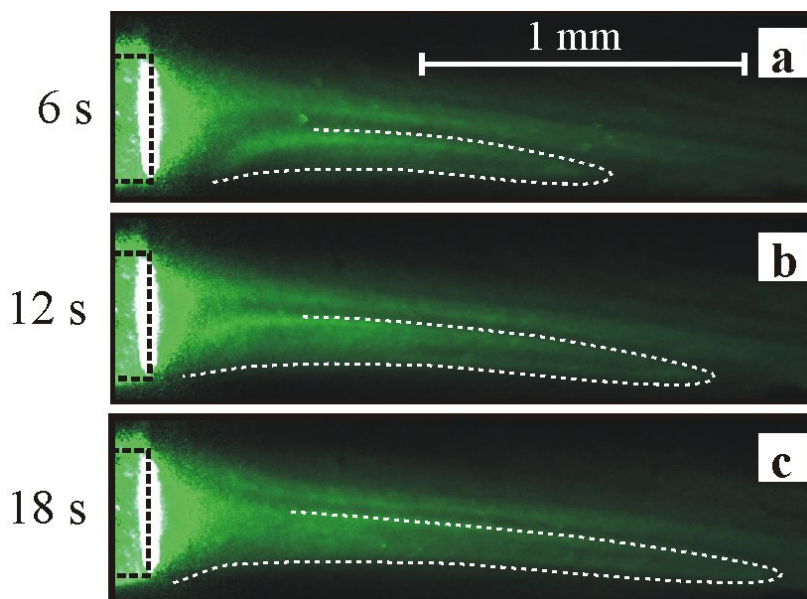


Fig. 4. Microscope pictures (in scattering mode) of intrusions of Ag nanoparticles in water (outlined with dashed line) stimulated by laser induced hydrodynamics nearby optical fiber tip at 1.0 W of 0.97 μm laser power in 6 s (a), 12 s (b), and 18 s (c) of laser irradiation. Fiber tip is shown by dashed line (Yusupov et al., 2011b).

Energy of incident laser light is partly (10–20%) absorbed by the carbon layer on the blackened fiber, so that the fiber is heated. When laser radiation with a power of greater than 3 W is transmitted by the fiber tip in air, the spectrum of the optical radiation from the fiber tip contains the fundamental line (0.97 μm or 1.56 μm) and the broadband visible and near-IR radiation caused by the heating of the tip surface to relatively high temperatures. When a blackened tip is placed into water, the tip surface is effectively cooled and the absence of the broadband radiation means the substantially lower temperatures of the tip surface. However, a medium power laser radiation (1–5 W) is sufficient for surface heating and generation of vapor-gas bubbles. When water is heated, the dissolved gases are liberated in the vicinity of the tip surface and gas bubbles emerge. Water is evaporated inside the bubbles, so that the bubbles are filled with vapor and, consequently, increase in size. At the lower boundary of the above power interval, the bubbles increase in size residing on the tip surface (Fig. 5a). When a critical size is reached, the bubbles are detached and move to the surface.

Water molecules which approach the heated tip surface acquire additional kinetic energy and momentum. The component of the total momentum of vapor molecules that is directed perpendicularly to the tip surface of the fiber towards water appears insufficient for the detachment of the bubble. Figure 5a shows that the bubbles sizes can be close to the diameter of the silica fiber core (400 μm). In the experiments, the bubbles normally emerge at same spots on a tip surface, which correspond to a high temperature areas. Evidently, the presence of such spots is related to the nonuniformity of the carbon layer: the absorbed energy (and, hence, the temperature) is greater for thicker regions. The stabilization (i.e., the

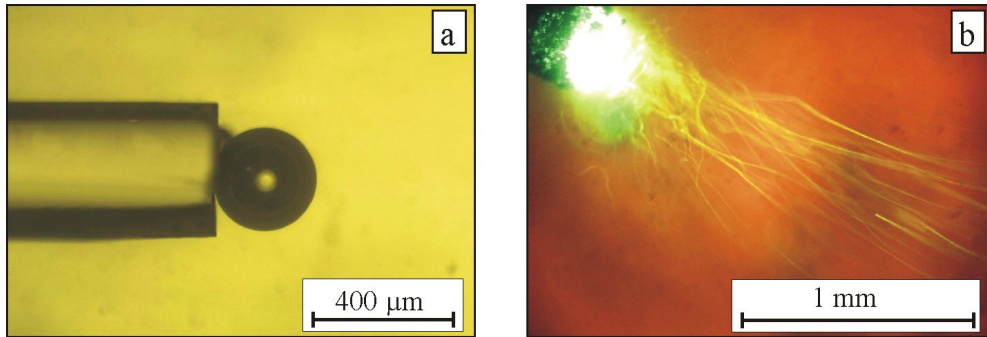


Fig. 5. Laser-induced generation of microbubbles in the vicinity of the blackened end surface of the optical fiber in water for the laser radiation with a wavelength of $0.97 \mu\text{m}$ and a power of (a) 1 and (b) 5 W. The photograph is taken from above at an exposure time of 250 ms.

attachment of the vapor-gas bubbles to the high temperature spots) can be caused by two reasons. First, the temperature at the hot spot additionally increases owing to the formation of the bubble and the consequent decrease in the local heat sink to water. The second reason is related to the Marangoni effect (Berry et al., 2000): the temperature gradient gives rise to the gradient of surface tension, so that convective flows emerge on the surface of the bubble and cause the force that presses the bubble to the hot spot. The experiments on the growth of the bubbles in the vicinity of the tip surface show that the rate of growth gradually decreases and, finally, the growth is terminated. At a laser power of 1 W, the duration of a relatively fast growth is about 200 ms. Bubble size increases at this stage from zero to 25% of the maximum size. Then, over a few seconds, the growth is well described with the formula (Yusupov et al, 2010):

$$D \propto t^{4/5}, \quad (2)$$

where D is the diameter of bubble and t is time. When laser light is terminated (Fig. 5a), the size of bubble gradually decreases (the bubble remains attached to the tip surface of the fiber) and, finally, the bubble vanishes. Note that a decrease in the size is also non-monotonic. At the first stage with a duration of less than 1 s, the diameter decreases by 8–10%. Then, the slowing takes place. Such a non-monotonic behavior must be related to the fact that the size of bubble decreases at the first stage predominantly, due to a decrease in the temperature of the vapor-gas mixture inside the bubble to the temperature of water in the cell, whereas the second stage is isothermal. The lifetime of such bubbles ranges from 3 to 8 h, and the rate of a decrease in the diameter with time always monotonically increases. At the second stage, the dependence of the diameter on time is well approximated with the formula (Yusupov et al., 2010):

$$D = D_0 \cdot (1 - t / \tau_0)^a, \quad (3)$$

where D_0 is the initial diameter, τ_0 is the lifetime, and $a = 0.1\text{--}0.5$ is the empirical parameter. Note a similar decrease in the diameter with time at $a = 0.5$ in (Taylor & Hnatovsky, 2004). A qualitatively different scenario corresponds to higher laser powers. The explosive boiling of water is observed in the vicinity of the hot end: the vapor-gas bubbles are ejected from the

fiber to water (Fig. 5b) and, then, the velocity decreases due to viscosity. At a finite exposure time the tracks of bubbles moving in water was observed. Notice that the track length corresponds to the mean velocity of the bubble over the exposure time. Bright spots in the vicinity of the tip surface (Fig. 5) are related to stray light: the Vision video camera is sensitive to the near-IR laser radiation.

The side measurements (Fig. 6a) show that the bubbles come to the surface at a certain distance from the fiber. Knowing the vertical velocity of the bubbles (about 5 mm/s in accordance with visual observations) and the trajectories, we can estimate the horizontal velocity (Fig. 6b). The analysis of the trajectories yields an exponential decrease in the horizontal velocity with increasing distance from the fiber: for the slowest and fastest bubbles, we obtain the dependences (Yusupov et al, 2010)

$$V = 67 \cdot \exp(-0,82 \cdot r) \quad (4)$$

and

$$V = 101 \cdot \exp(-0,74 \cdot r), \quad (5)$$

respectively, where V is the horizontal velocity in mm/s and r is the distance from the fiber tip surface in millimeters. The relationships show that the velocity of bubbles at the moment of the detachment from the fiber tip ($r = 0$) ranges from 67 to 101 mm/s.

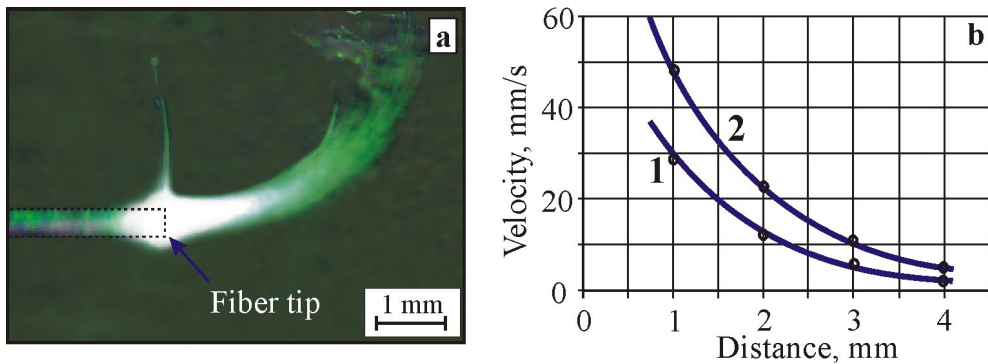
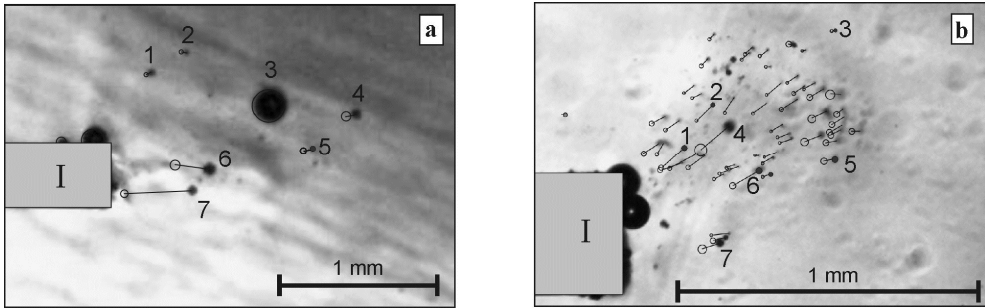


Fig. 6. a - Side view of the tracks of microbubbles in the vicinity of the blackened optical fiber tip surface in water; b - Plots of the horizontal velocity vs. distance from the end surface for slowest (1) and fastest (2) bubbles at a laser wavelength of $0.97 \mu\text{m}$ and a power of 5 W (Yusupov et al., 2010).

We have directly observed motion of bubbles even in the immediate vicinity of the surface tip (at the maximum velocities) in the experiments on the generation of microbubbles performed with the aid of the Photron Fastcam SA3. Fig. 7 shows the bubbles as dark circles with different sizes. Previous (at time step Δt) positions and sizes are shown as open circles, and the trajectories are shown as rectilinear segments. Table 1 presents the calculated sizes and velocities of the bubbles shown in Fig. 7. It is seen that the bubble with a diameter of $47 \mu\text{m}$ (bubble 7 in Fig. 7a and Table 1), which is initially located at a distance of about $100 \mu\text{m}$ from the fiber tip, moves at a mean velocity of 97 mm/s over the observation interval (4.4 ms).



Closed circles 1-7 show positions of bubbles, open circles show previous positions, and rectilinear segments show bubbles trajectories.

The images are taken from above at rates of (a) 10000 and (b) 2000 frames per second.

Laser powers of (a) 3 and (b) 6 W, time intervals $\Delta t =$ (a) 4.4 and (b) 2.0 ms, and a laser wavelength of $0.97 \mu\text{m}$.

The pulse duration is 50 ms and the interval between pulses is 500 ms.

Fig. 7. Displacements of microbubbles (that are generated in the vicinity of the schematically shown blackened tip surface of quartz fiber **I**) over short time intervals Δt in the presence of laser radiation (Yusupov et al., 2010). **a** - CW laser radiation. **b** - Pulsed laser radiation.

Such result is in good agreement with the above estimations of the initial velocities in the vicinity of the fiber tip. The velocities of the bubbles rises rapidly with increasing distance from the fiber: the velocities are not higher than 50 and 20 mm/s at distances of 0.5 mm and 2 mm, respectively (Table 1). When bubbles are generated in a viscous liquid over a relatively long time interval the steady-state flow results in increase of the bubbles velocities. To determine the relative contribution of such a flow, we have measured the motion of microbubbles under the pulsed laser irradiation (Fig. 7b). It is seen that the bubbles predominantly move at relatively large angles relative to the fiber axis. That is caused by the features of the tip surface and hydrodynamic effects. Note that the asymmetry also corresponds to the motion of microbubbles under the continuous wave laser irradiation.

Number of the bubble (Fig. 7)	Parameters of radiation			
	CW radiation, 3 W (Fig. 7a)		pulsed radiation, 6W (Fig. 7b)	
	Diameter, μm	Velocity, mm/s	Diameter, μm	Velocity, mm/s
1	26	9	17	38
2	26	9	10	37
3	200	3	10	5
4	58	16	41	60
5	42	12	21	20
6	63	48	21	52
7	47	97	27	32

Table 1. Parameters of the bubbles shown at Fig. 7

Figure 7b and Table 1 show that a short laser pulse with power of 6 W causes generation of many bubbles, whose diameters range from 10 to 41 μm . The velocities of bubbles are 60 and 20 mm/s in the vicinity of the fiber and at a distance of 300 and 800 μm , respectively. In spite of a twofold increase in the laser power, the maximum velocities of the bubbles in the vicinity of the fiber under the pulsed irradiation are significantly less than the velocities corresponding to the continuous wave irradiation. At a relatively large distance from the fiber end, the velocities corresponding to the pulsed irradiation are also less than the velocities corresponding to the continuous wave irradiation: the velocity of bubble 4 in Fig. 7a is almost equal to the velocity of bubble 5 in Fig. 7b, whose distance from the fiber tip is almost two times shorter. Such result indicates to the presence of water flows in the case of the continuous wave laser irradiation and shows that the flow velocity is comparable with the mean velocity of bubbles.

Such liquid flows are more clearly observed in the microscopic measurements of the laser-induced hydrodynamic effects in the vicinity of the fiber tip surface of the fiber that is placed in a glass capillary filled with water.

3.2 Laser-induced generation of micro-bubbles in a glass capillary

Liquid flows are more clearly observed in the microscopic measurements of the laser-induced hydrodynamic effects in the vicinity of the fiber tip surface of the laser fiber that is placed in the glass capillary filled with water (model of the laser channel).

As it follows from Fig. 8, the attached vapor-gas bubbles at a laser power of 1–2 W emerge at the tip surface and the convective motion is observed in the liquid. A qualitatively different scenario corresponds to a power of 3 W: the microscopic bubbles ejected from the fiber tip move along arc shaped trajectories and entrain liquid flows (Fig. 8a). The intensity of the resulting vortices rapidly increases with increasing radiation power (Fig. 8b). In accordance with the estimations based on the frame-to-frame analysis of the video records, the period of the typical circulating liquid flows at laser powers of 3–5 W ranges from 0.2 to 1 s. Note that the above effects can be observed in the experiments with the blackened fiber tip at both laser wavelengths (0.97 μm and 1.55 μm). In the absence of the preliminary blackening, the effects are observed only for a radiation wavelength of 1.55 μm . Such a difference is caused by the fact that the radiation with a wavelength of 1.55 μm (unlike the short wavelength

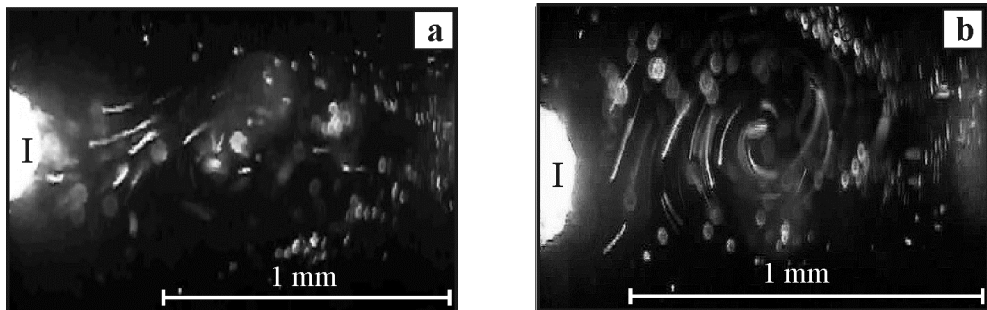


Fig. 8. Water flows that actively circulate inside the glass capillary (with a diameter of 1 mm) in the vicinity of the blackened tip surface I heated by the laser radiation with a wavelength of 0.97 μm and a power of 3 W (a) and 5 W (b)

radiation) is capable of heating a thin water layer in the vicinity of the tip surface to the boiling point, since the absorbance at a wavelength of $1.56\ \mu\text{m}$ is higher than the that at a wavelength of $0.97\ \mu\text{m}$ by a factor of about 20 (Hale & Querry, 1973).

It is possible to visualize the hydrodynamic flows occurring in capillary and caused by laser-induced bubbles generation by microscope visual observing the meniscus. To accomplish this, the silica optical fiber with a $400\ \mu\text{m}$ diameter was introduced into a thin water-filled capillary with a $500\ \mu\text{m}$ internal diameter. The volume of liquid in a capillary was about $20\ \text{mm}^3$, and meniscus was located at a $25\ \text{mm}$ distance from the fiber tip surface.

Fig. 9 demonstrates the observed variations of a meniscus shape in a glass capillary at a power of laser radiation of $1\ \text{W}$ and at laser wavelength of $1.56\ \mu\text{m}$. Switching of laser radiation on has resulted in growing the distance between optical fiber tip surface, which is caused by the fact that vapor-gas bubbles are formed in a liquid in the course of laser irradiation nearby a fiber tip. Simultaneously with a gradual rise of average volume of liquid in a capillary, quite a strong variations of meniscus shape takes place in this case, which are caused by hydrodynamic processes observing in a capillary water cell. At a certain period of laser irradiation time even water flows occur (Fig. 9b and 9c) caused, presumably, by the appearance and fast motion of quite large vapor-gas bubbles in a water capillary cell. Decrease of laser power causes increase of water streams, and in some cases the eruption of some portion of liquid from a capillary takes place.

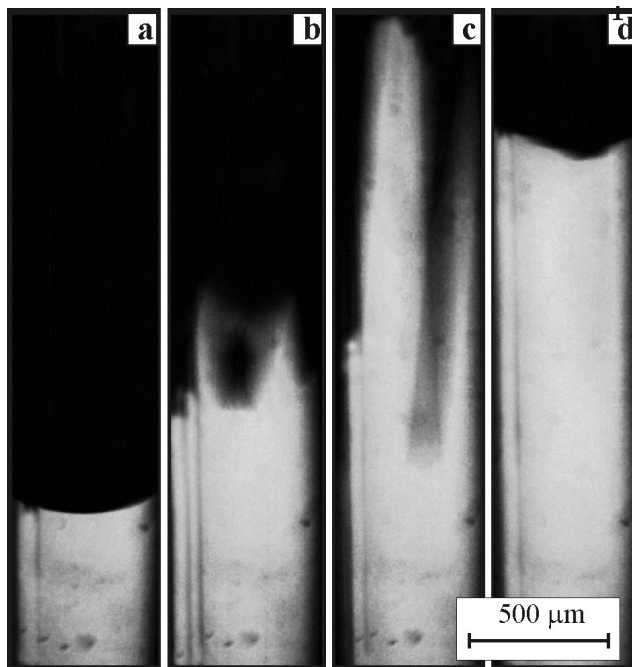
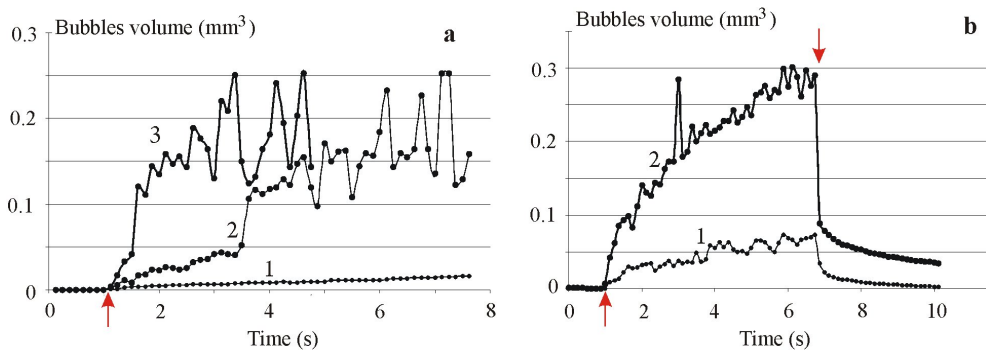


Fig. 9. Variation of a meniscus shape in a capillary caused by laser induce hydrodynamics and bubbles formation. Laser wavelength is $1.56\ \mu\text{m}$, laser power - $1\ \text{W}$, internal diameter of capillary - $500\ \mu\text{m}$.

Knowing the level of the meniscus in a capillary it is possible to determine easily the total volume of vapor-gas bubbles. Fig.10 shows change in the volume of generated bubbles at different laser powers and different laser wavelengths. Our experiments show that the total volume of bubbles rises gradually with time by a logarithmic law after the laser radiation switching on. The total volume at 1 W of laser power rises with time monotonically for both wavelengths, while at higher laser power quite strong fluctuations take place, with the growing in time amplitude. As this takes place, at laser power of 3 W the strong eruption of liquid from the capillary was observed after 4.7 s of laser irradiation (curve 3 at Fig. 10a). At that moment the curve 3 interrupts, since the meniscus went out of visualization zone because of the abrupt decrease of meniscus level.

The total volume of generated bubbles increases with laser power. Comparison of curves 1 and 2 at Fig.10b shows that twofold increase of laser power (from 1 to 2 W) causes about the fourfold rise of the generated bubbles volume. After the laser radiation switching off, the total volume of bubbles first rapidly decreases (vapor condensation inside bubbles), and next decreases more slowly. It should be noted that quite a strong low-frequency oscillations are observed, caused by variation of total bubbles volume in a capillary.



In the case of $0.97\mu\text{m}$ wavelength the fiber tip surface was covered by a thin carbon layer. Arrows show the moments of laser on and laser off. Digits at curves shows laser power in Watts.

Fig. 10. Change of the total bubbles volume at different powers of lasers with $0.97\mu\text{m}$ (a) and $1.56\mu\text{m}$ (b) wavelengths of radiation.

Thus, the hydrodynamic processes related to the explosive boiling in the vicinity of the hot tip surface are observed in the liquid even at medium laser powers. Note that the intracapillary liquid exhibits effective mechanical oscillations with a frequency of 1– 5 Hz and appears saturated with microbubbles. We expect the development of such laser-induced hydrodynamic processes in water-saturated biotissues at medium laser powers.

On the one hand, such processes provide the saturation of cavities and fractures in a spinal disc or bone with the water solution containing vapor-gas bubbles. On the other hand, they give rise to high-power acoustic oscillations and vibrations in the organ containing the connective tissue. Apparently, the filling of hernia with vapor-gas bubbles provides the reproducible decrease in the density of herniation immediately after the laser treatment (Sandler et al., 2004; Chudnovskii & Yusupov, 2008).

It is known from (Bagratashvili et al., 2006) that the mechanical action on cartilages in the hertz frequency range actively stimulates the synthesis of collagen and proteoglycans even at relatively small amplitudes. The above estimations show that the pressure on biotissue provided by the vapor-gas bubbles can reach tens of kilopascals. In accordance with (Buschmann et al., 1995; Millward-Sadler & Salter, 2004), such pressures in the hertz frequency range can lead to regenerative processes in cartilage owing to the activation of the interaction of the extracellular matrix with the mechanoreceptors of chondrocytes (integrins).

3.3 Laser-induced generation of bubbles microjets

Note an interesting phenomenon in the experiments on the generation of bubbles in the vicinity of the blackened tip surface of the fiber in the water cell: bubble microjets can be generated at a laser power of less than 3 W (Fig. 11) (Yusupov et al., 2010). The lengths of the microjets (Fig. 11a), which always start in the immediate vicinity of the fiber tip, reach several millimeters, the transverse sizes normally range from 10 to 50 μm , and the sizes of the bubbles that form the jets range from several to ten microns. The lifetime of the microjets ranges from a few fractions of a second to tens of seconds. A microjet that emerges at a certain spot on the tip surface remains attached to this spot and exhibits bending relative to the mean position. Bubble microjets didn't use to be continuous from start to end, the discontinuities used to appear on them, which used to restore quite often. The observations show (Yusupov et al., 2010) that the discontinuities are always related to the hydrodynamic perturbations and are caused by relatively large bubbles that move in the vicinity of the microjet. The appearance of quite a large bubble attached to the fiber tip caused the bubble microjet bending around large bubble (Fig. 11b). Thus, we conclude that two conditions must be satisfied for the generation of the bubble microjets. First, a hot spot must be formed on the tip surface. Second, the neighborhood of such a spot must be free of the centers that provide the generation and detachment of large bubbles. Note that the possibility of bubble microjets in the vicinity of a point heat source is demonstrated in (Taylor & Hnatovsky, 2004).

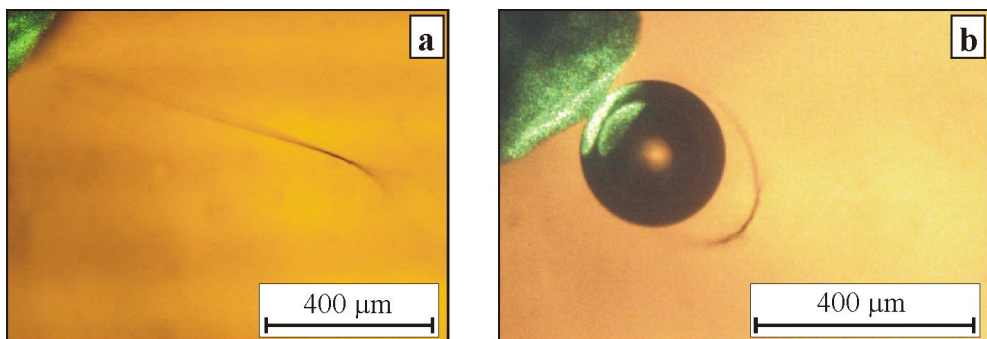


Fig. 11. Bubble microjets in the vicinity of the tip surface of optical fiber.

A part of the blackened fiber tip is shown at the right upper corner.

4. Degradation of optical fiber tip

Laser-induced hydrodynamic effects in water and bio-tissues can lead to the significant degradation of the fiber tip (Yusupov et al., 2011a). The most significant degradation of the

fiber tip surface occurs in the regime of channel formation when the fiber is shifted inside the wooden bar that mimics the biotissue. In this case, we observe substantial modifications and distortion of tip surface. The comparison of the sequential photographs (Fig. 12) shows a significant increase in the volume of the fiber fragment (swelling) in the vicinity of fiber tip.

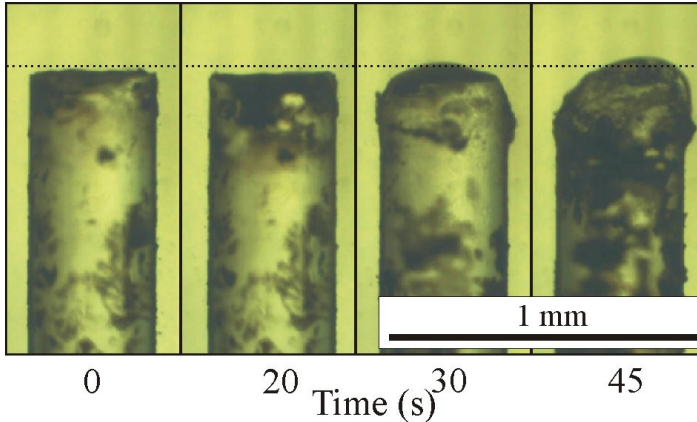


Fig. 12. Modifications of the profile of the blackened fiber tip surface (side view) for regime of channel formation (the channel is formed by the fiber that moves inside the wooden bar with water and the radiation power is 5 W). The left-hand panel shows the original fiber just after its blackening (Yusupov et al., 2011a).

SEM images (Fig. 13) show that the laser action in the regime of the channel formation in the presence of water causes substantial modifications of the working surface: the sharp edge is rounded and surface irregularities (craters) emerge on the tip surface. The image shows that a thin shell (film) with circular holes is formed at the tip surface of the optical fiber. Multiple cracks pass through some of the holes. In addition, we observe elongated crystal-like structures on the surface (Fig. 13b). Looking through the largest hole in the film on the tip surface (at the center of the lower part of the fragment at Fig. 13a), whose dimension in any direction is greater than 10 μm , we observe the inner micron-scale porous structure.

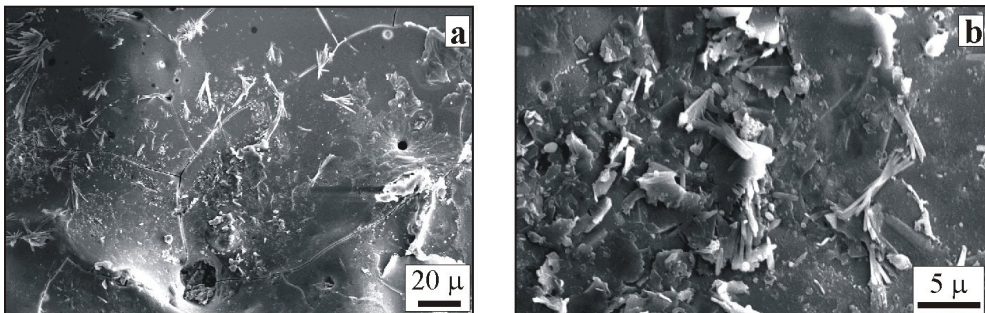


Fig. 13. The microstructure of the fiber tip surface after laser action. **a** - SEM image of a fragment of the fiber end surface; **b** - magnified SEM image of a fragment of the end surface with the crystal-like structures on the surface (Yusupov et al., 2011a).

Typical micron-scale circular holes on the film surface (Fig. 13a) can be caused by cavitation collapse of single bubbles. It is well known that cavitation collapse of bubbles in liquid in the vicinity of the solid surface gives rise to the high-speed cumulative microjets which can destroy the solid surface (Suslick, 1994). Apparently, this effect leads to multiple cracks on the film and the formation of the porous structure (Fig. 13a), since the cumulative microjets can punch holes, cause cracks in the film, and destroy the structure of silica fiber tip. Collapse of cavitation bubble apart from high pressure generation (up to 10^6 MPa) can cause overheating of gas up to temperatures as high as 10^4 K. Such high values of water pressure and temperature can result in formation of supercritical water (critical pressure of water is $P_c=218$ atm, critical temperature - $T_c=374^\circ\text{C}$), which can dissolve silica fiber (Bagratashvili et al., 2009).

Fig. 14 shows Raman spectra of some areas of laser irradiated fiber tip surface (curves 3-5) compared with that of graphite (1) and diamond (2). Raman bands at 1590 cm^{-1} and 1350 cm^{-1} to diamond and graphite nano-phases correspondingly (Yusupov et al., 2011a).

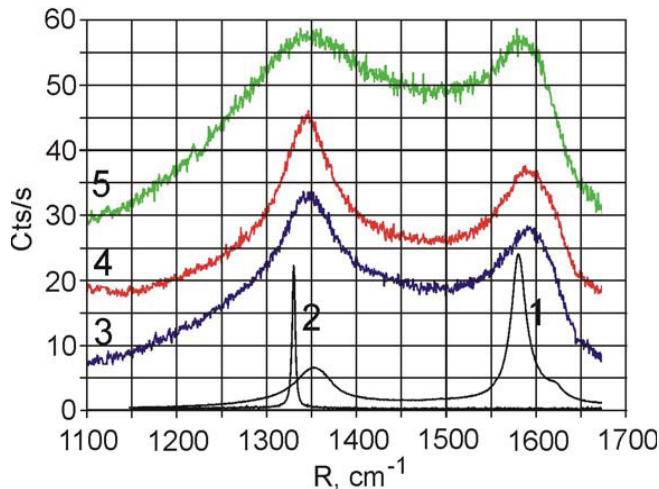
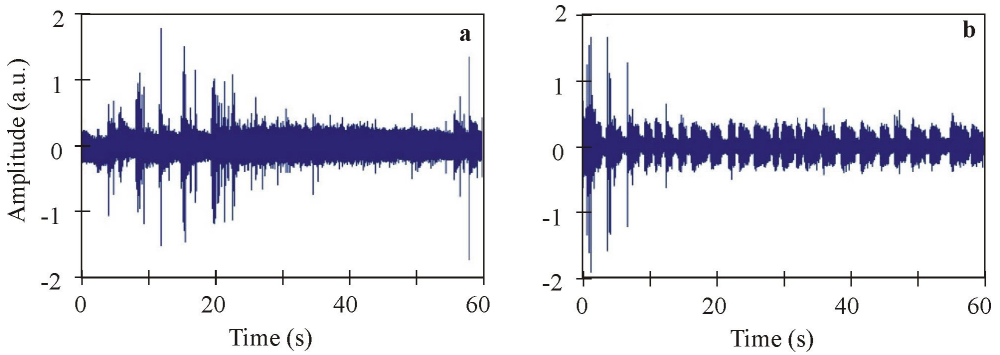


Fig. 14. Raman spectra from different areas of laser fiber tip surface (curves 3, 4 and 5) compared with that of graphite (1) and diamond (2) (Yusupov et al., 2011a).

Formation of diamond nanophase at a fiber tip surface in this case is rationalized by extremely high pressures and temperatures caused by cavitation processes stimulated by laser irradiation (Yusupov et al., 2011a).

5. Laser-induced acoustic effects

Laser-induced hydrodynamics processes in water-saturated bio-tissues causes generation of intense acoustic waves. We have studied the peculiarities of generation of such acoustic waves in water and water-saturated biotissue (intervertebral disc, bone, et al.) in the vicinity of blackened optical fiber tip using acoustic hydrophone (Brul and Kier 8100, Denmark). The hydrophone with 0 - 200 KHz band was placed in water or biotissue at 1cm distance from optical fiber tip. Fig. 15 demonstrates typical example of acoustic response to laser irradiation for two different cases: in the bath of free water (Fig. 15a) and in the case of water

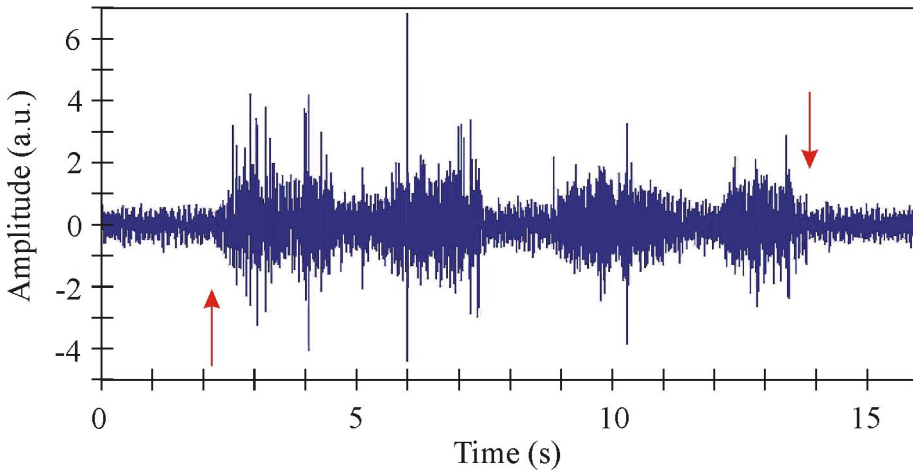


The fiber tip surface is blackened before laser irradiation with $0.97\ \mu\text{m}$ wavelength.

Fig. 15. Fragments of acoustic response to 3 W laser irradiation of water for two different cases: in a bath of free water (a) and in a water-filled capillary (b).

filled capillary (Fig. 15b). In the case of the bath with free water, the short random laser-induced acoustic spikes take place. At the same time, the acoustic response to laser irradiation in the case of water-filled capillary (which imitates situation in real water-filled biotissue channel) is different (Fig. 15b). Acoustic signal is amplitude-modulated by its feature, and low-frequency modulation period is about 2 s.

Fig. 16 demonstrates acoustic response to laser irradiation of nucleus pulposus *in vivo* when optical fiber was moved forward (regime of channels formation in the course of laser healing of degenerated disc). The acoustic signal is non-stationary by its nature. The short-pulse intense acoustic spikes take place and the signal itself is amplitude modulated (similarly to that in water-filled capillary) with a modulation period of about 3 s.



Arrows show the moments of laser on and laser off.

Fig. 16. Acoustic response to 3 W laser irradiation with $0.97\ \mu\text{m}$ wavelength of nucleus pulposus *in vivo*, when optical fiber was moved forward in the intervertebral disc.

The more detailed studies show that for both *in vivo* and *in vitro* cases laser-induced generation of short-pulse intense quasi-periodic acoustic signals. The fragment of spectrogram of acoustic response given at Fig. 17 clearly demonstrates temporal change of spectral components for acoustic signal generated from laser irradiated nucleus pulposus *in vitro* when optical fiber was moved forward in the intervertebral disc (similar to shown at Fig. 1).

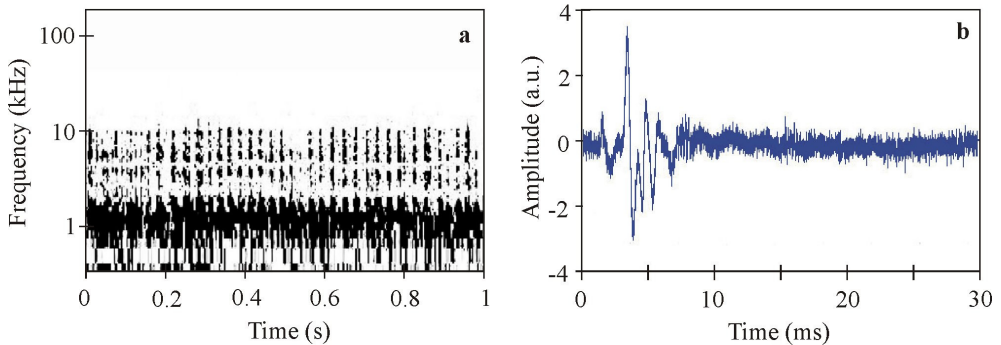


Fig. 17. The fragment of spectrogram (a) and temporal structure of single pulse (b) of acoustic response generated from laser irradiated nucleus pulposus *in vitro*.

As one can see, the acoustic response in this case has the form of short, intense and broadband (from 0 to 10 kHz) pulses of about 10 ms in duration combined into the series of pulses generated with frequency of 40 Hz. Fig. 17b shows that the amplitude of single pulse is an order of amplitude higher than the background acoustic noise. The most of acoustic power is concentrated in such pulses. The broad spectrum of acoustic pulses and their low duration indicate to shock-type of generated acoustic waves. The acoustic noise has broad spectral maxima in the following spectral intervals: 600 – 700 Hz, 1 - 2 kHz and nearby 10 kHz. Appearance of these bands are caused by the dynamics of vapor-gas mixture and are associated with acoustic resonances of the system. Notice that laser-induced formation of channels in degenerated spinal discs *in vitro* has been accompanied by 4 Hz in frequency strong visual vibrations of needle with laser fiber.

Generation of such a strong acoustic vibrations is caused in our opinion by contact of overheated (up to >1000 °C (Yusupov et al., 2011a)) fiber tip with water and water-saturated tissue of spinal disc. Such contact can result in explosive boiling of water solution nearby the fiber tip and, also, in burning of collagen in cartilage tissues. Intense hydrodynamic processes can take place nearby optical fiber tip, which are caused by fast heating of water and tissue, by generation and collapse of vapor-gas bubbles (Chudnovskii et al., 2010a, 2010b; Leighton, 1994). As a result, the free space of disc or bone is filled by liquid saturated by vapor-gas bubbles. Resonance vibrations are excited, since both disc and bone are quite good acoustic resonators. These vibrations give rise to low-frequency modulation of acoustic noise (Fig. 16) and to quasi-periodic generation of short intense pulses (Fig. 17) (Chudnovskii et al., 2010a). The acousto- mechanic shock-type processes in resonance conditions results in mixing and transport of gas-saturated degenerated tissue in the space of defect (Chudnovskii et al., 2010b). These processes destroy hernia and decrease its density (Fig. 2b), thus lowering the pressure to nervous roots. Another important impact of such processes is the regeneration of disc tissues through the effects of mechanobiology (Buschmann et al., 1995; Bagratashvili et al., 2006).

6. Formation of filaments

In this division we will show that existence of strongly absorbed agents (in a form of Ag nanoparticles, in particular) in laser irradiated water nearby optical fiber tip can result in appearance of filamentary structures of these agents (Yusupov et al., 2011b). Medium power (0.3 – 8.0 W) 0.97 μm in wavelength laser irradiation of water with added Ag nanoparticles (in the form of Ag-albumin complexes) through 400 μm optical fiber stimulates self-organization of filaments of Ag nanoparticles for a few minutes. These filaments represent themselves long (up to 14 cm) liquid gradient fibers with unexpectedly thin (10 – 80 μm) core diameter. They are stable in the course of laser irradiation, being destroyed after laser radiation off. Such effect of filaments of Ag nanoparticles self-organization is rationalized by the peculiarities of laser-induced hydrodynamic processes developed in water in presence of laser light and by formation of liquid fibers.

Fiber laser radiation (LS-0,97 IRE-Polus, Russia) 0-10 W in output and 0.97 μm in wavelength was delivered into water-filled plastic cell through 400 μm transport silica optical fiber, which was placed horizontally in the cell. Low intensity (up to 1 mW) green pilot beam from the built in diode laser was used to highlight the 0.97 μm laser irradiated zone in the cell. The cell was placed at the sample compartment of optical microscope (MC300, MICROS, Austria) equipped with color digital video-camera (Vision). Spectroscopic studies were performed with fiber-optic spectrum analyzer (USB4000, Ocean Optics) and UV/vis absorption spectrometer (Cary 50, Varian). To measure the refraction index of collargol we have applied the fiber-optic reflectometer FOR-11 (LaserChem, Russia), which provides 10^{-4} precision of refraction index measurements at 1256 nm wavelength. Cleavage of transport optical fiber has been always produced just before each experiment. Ten minutes later (to provide reasonable attenuation of hydrodynamic motions in the cell) the drop (0.01-1 ml in volume) of brown colored collargol (complex of 25 nm in size Ag nanoparticles with albumin) has been smoothly introduced into the water cell 0.5-10 mm aside from the optical fiber tip.

Our in situ optical microscopic studies of laser-induced filament formation were accomplished in two different modes: 1) in transmission mode, using illumination with white light from microscope lamp; 2) in scattering mode, using illumination with green light of pilot laser beam through the same transport fiber.

Experiments show that 0.97 μm fiber laser irradiation of water in the cell with introduced collargol drop causes (in some period of time from seconds to minutes) formation of thin and long quite homogenous filaments, growing along the axis of 0.97 μm laser beam in water. These filaments are brown colored (that gives the evidence of enhanced Ag nanoparticles concentration in filament) and can be seen even with unaided eye.

Fig. 18 demonstrates the microscope image (in transmission mode) of one of such filaments. This filament is located along the axis of output laser beam and is about 17 mm in length. The measured profile of optical density of this filament is triangular in its shape with about the same widths along filament (determined at half-maximum) of $\sim 200 \mu\text{m}$.



Fig. 18. Micro-image (in transmission mode) of filament of Ag nanoparticles fabricated in water nearby optical fiber tip at 2.5 W of laser power (Yusupov et al, 2011b).

Fig. 19a demonstrates the micro-image of another laser fabricated filament in scattering mode. Intensity of light scattered from this filament decreases gradually with the distance from fiber tip. Attenuation of green light in this case is caused by absorption and scattering of green light in the course of its propagation through the filament. To reveal the peculiarities of filament (given at Fig. 19a) we have performed the following processing of its microscope image: all vertical profiles of image were normalized to local maximum (Fig. 19c); the microscope image was represented in shades of gray (Fig. 19b); As it follows from figures 19b and 19c the length of given filament is about 6 mm, its average width is about 40 μm , and scattering intensity decreases rapidly with the distance from filament axis. Notice that vertical profiles of all fabricated filaments (in both transmission and scattering modes) are almost triangular with a sharp top. It was also established that the end of filament has always a needle-like shape and, also, the width of filament obtained in transmission mode measurements exceeds 3-5 times that obtained in scattering mode.

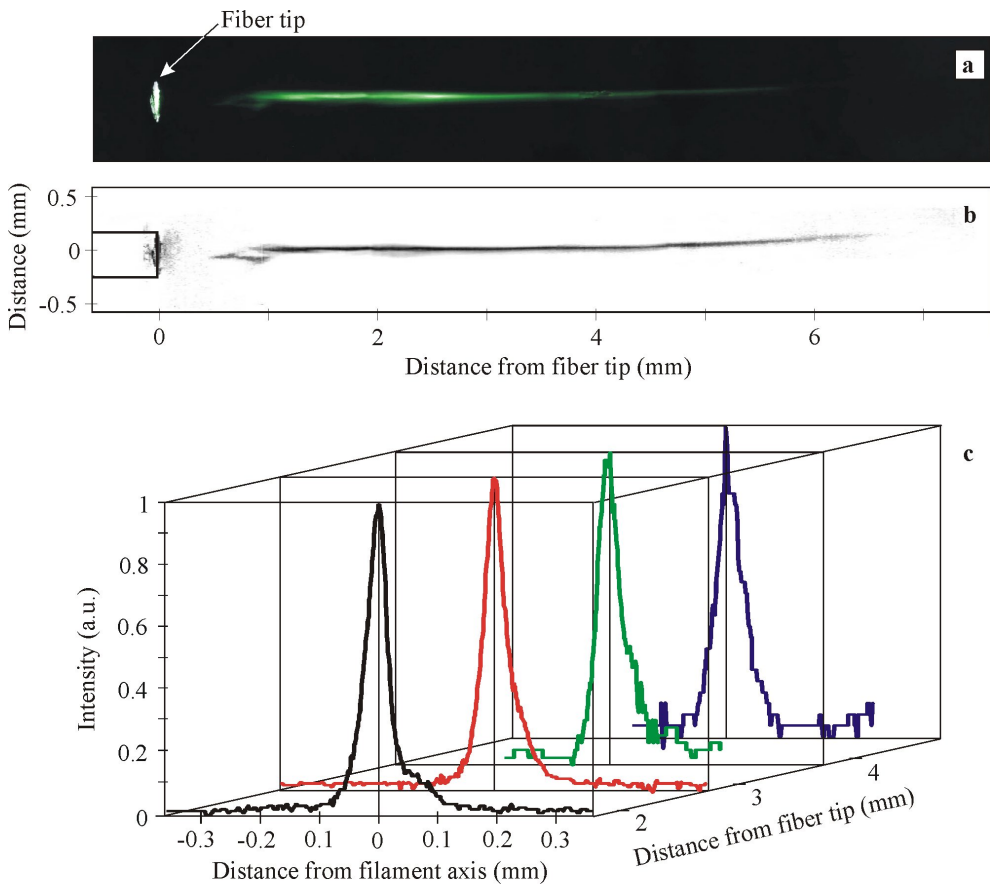


Fig. 19. a - Microscopic picture of filament (in scattering mode) of Ag nanoparticles fabricated in water nearby optical fiber tip at 0.4 W of laser power. b - Image of this filament represented in shades of gray after processing of (see text) of Fig. 19a. c - Normalized vertical profiles of image given at Fig. 19b. (Yusupov et al, 2011b).

It is of importance that filaments of Ag nanoparticles have been formed in our experiments only in the case of existence of initial collargol concentration gradient in laser irradiated water (when collargol drop was introduced initially into water aside from fiber tip). When collargol drop was premixed in water cell before laser irradiation, formation of filaments has never been observed (at any collargol concentrations in the cell and at any laser powers and dozes).

The initial stage of filament self-organization process can be clearly seen in scattering mode (Fig. 4). Some visible hydrodynamic flows take place nearby the fiber tip when laser power is on. Such flows result in intrusion of collargol from neighboring area into the area in front of the fiber tip. The slanting filament structure is clearly seen at Fig. 4. One can also see here the initial process of new intrusion formation (outlined with dashed line). The rate of rise-up front of a given intrusion (which is about 150 μm in average thickness) is found to be described by exponential law (1): at 1 mm from laser fiber tip $V = 1.5 \cdot 10^{-2}$ cm/s, while at 2 mm from laser fiber tip V falls down to $3 \cdot 10^{-3}$ cm/s.

We revealed that filaments of Ag nanoparticles self-organized in the course of 0.97 μm laser irradiation can exist in the cell (in the presence of laser beam and with no external mechanical distortions of liquid in the cell) for quite a long period of time. We have supported such filaments for tens of minutes. Notice that both rectilinear and curved filaments were self-organized in our experiments.

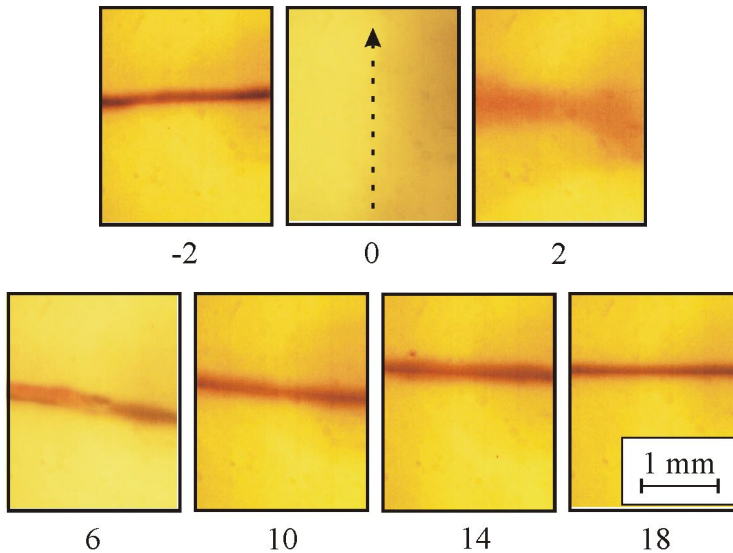
After 0.97 μm laser radiation being off, the filaments of Ag nanoparticles have been completely destroyed for 10 – 30 s period of time. Notice that time Δt of diffusion blooming of filament by value, estimated by formula

$$\frac{-2}{x} = D\Delta t = \frac{kT}{3\pi\mu d}\Delta t, \quad (6)$$

where D – is diffusion coefficient of nanoparticle; $k = 1.38 \cdot 10^{-23}$ J/K – Boltzmann constant; $T(K)$ – absolute temperature; $\mu = 1,002 \cdot 10^{-3}$ (N · s/m²) – dynamic viscosity of water; $d = 25$ nm (Ag nanoparticle diameter) gives $\Delta t = 25$ s for $x = 100$ μm .

External mechanical distortions of filament of Ag nanoparticles results in its destruction. However after mechanical distortion being off, the filament can be renewed completely in presence of 0.97 μm laser radiation. Fig. 20 shows the dynamic of such filament renovation after the distortion of self-organized filament (produced by its rapid crossing within a metal needle). As one can see from Fig. 20, complete renewal took place for quite a short period of time (~ 20 s).

Our experiments have shown that there is some range of 0.97 μm laser powers for which the effect of laser-induced filament self-organization takes place and is, also, stable and reproducible. At laser powers higher than 8 W we have never observed filament formation. At 0.2-0.5 W laser power filaments have been formed but have been unstable. The most stable and long-living filaments were observed in 0.5-3 W laser power range. At laser power less than 0.2 W we have never observed such filament formation. The instability of filaments and even their absence at high laser powers is caused by intense laser-induced hydrodynamic processes nearby the fiber tip. Our experiments show that the fiber tip surface is gradually covered by a deposit, which absorbs laser radiation quite well. The wide absorption band of deposit observed at fiber tip can be caused by island film of Ag nanoparticles, and, possibly, by elementary carbon absorption (deposited at fiber tip due to albumin thermo-decomposition). As a result of such deposits, the fiber tip becomes an



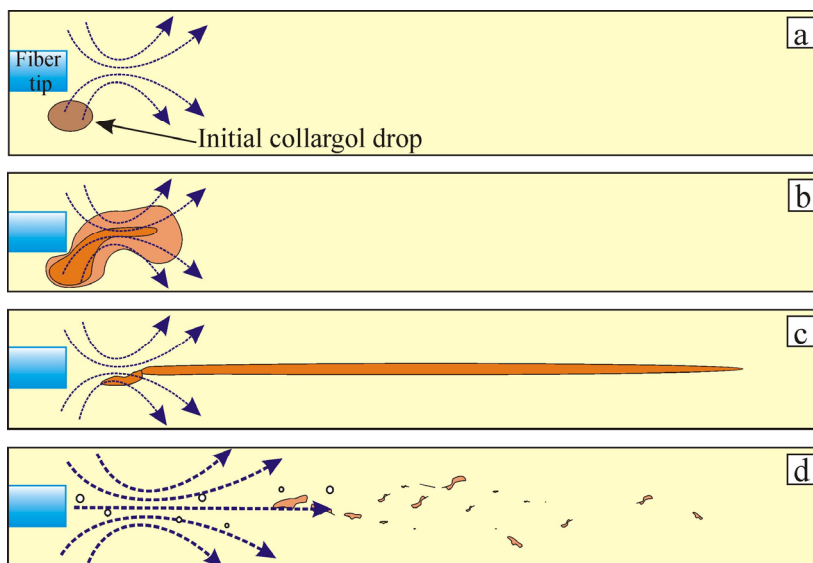
Digits show the period of time from the beginning of filament destruction (Yusupov et al., 2011b).

Fig. 20. Renewal of destroyed filament of Ag nanoparticles in water nearby the tip of optical fiber.

intense heat source. That causes explosive water boiling, intense formation of micro-bubbles, moving rapidly away from fiber tip to liquid (see for example Fig. 1,b) and destroying filament.

We rationalize the observed effect of laser-induced self-organization of filaments from Ag nanoparticles by following mechanisms. Initially (Fig. 21a), laser light absorption by water (the absorption coefficient in water at $0.97 \mu\text{m}$ is about 0.5 cm^{-1}) causes its heating with the $2\text{-}10^\circ\text{C/s}$ rate. Besides, the intense transfer of impulse to water takes place in this case. As a result, the closed axis-symmetric liquid flows are developed being directed from fiber tip. These flows promote Ag nanoparticles intrusion into the laser beam nearby the fiber tip (Fig. 21b). Such intrusions are clearly seen in scattered green laser light (Fig. 4).

Another factor dominates at the second stage of filament self-organization. The refractive index for collargol n_c is higher than that for clean water n_w . The value of $n_c - n_w = 0.0044$ at wavelength $\lambda = 1256 \text{ nm}$ was directly measured in our experiments using fiber-optic densitometer. Due to the effect of total internal reflection laser light is concentrated inside intrusion which work in fact as a liquid optical fiber. Channeling of laser light inside intrusion with Ag nanoparticles results in deeper propagation of laser light into water. Light pressure promotes faster movement of intrusion front giving rise to filament (Fig. 21c). As it was shown in (Brasselet et al., 2008), for example, laser light pressure is also able to force through the boundary between two unmixed liquids and to form thin channel of one liquid inside another one, thus forming liquid optical fiber with gradient core. Thus, the image of filament in transmission mode shows optical density of Ag nanoparticles. At the same time the image of filament in scattering mode clearly demonstrate channeling effect in fabricated filament which in fact is a liquid gradient fiber. Such liquid gradient fiber provides also effective channeling of 970nm laser beam, thus promoting filament elongation and spatial stability.



- Formation of water flow nearby the fiber tip.
- Formation of Ag nanoparticles intrusions.
- Fabrication of filaments from Ag nanoparticles.
- Intense formation of micro-bubbles, hampering filament formation at high laser power.

Fig. 21. To the explanation of the effect of laser-induced formation of filaments of Ag nanoparticles (Yusupov et al., 2011b).

Laser induced formation of 10-50 μm in thickness and up to few millimeters micro-bubble streams (Fig. 11) can also promote the filaments fabrication observed in our experiments. It is clear, however, that too intense chaotic formation of micro-bubble streams observed at high laser power can hamper filament fabrication (Fig. 21d).

We believe that such filaments of nanoparticles can be developed not only in water media but, also, in other fluids, with other laser wavelength and particles types. The indispensable conditions in this case are the availability of sufficient level of laser light absorption in irradiated medium nearby fiber tip and possibility of liquid fiber formation.

7. Conclusion

Hydrodynamic effects induced by a medium power (1-5 W) laser radiation in the vicinity of the heated fiber tip surface in water and in water-saturated tissues are considered. A threshold character of the dynamics of liquid is demonstrated. At a relatively low laser power (about 1 W), the slow formation of vapor-gas bubbles with sizes of hundreds of microns are observed at the optical fiber tip surface. The bubbles can be attached to the tip surface in the course of laser radiation. At higher laser power increases, effective hydrodynamic processes related to the explosive boiling in the vicinity of the overheated fiber tip surface take place. The resulting bubbles with sizes ranging from a few microns to several tens of microns provide the motion of liquid. The estimated velocities of bubbles in

the vicinity of the fiber tip surface can be as high as 100 mm/s. Generation of bubbles in the capillary leads to the circulating water flows with periods ranging from 0.2 to 1 s. Such circulation intensity increases with the laser power. For the laser radiation with a wavelength of 0.97 μm , we observe such effects only for the blackened fiber tip surface, which serves as a local heat source. At a laser power of less than 3 W, stable bubble microjets, which consist of the bubbles (ranging from several to ten microns) can be generated in the vicinity of the blackened tip surface.

Laser-induced hydrodynamic effects in water and bio-tissues can cause the significant degradation of the fiber tip. Cavitation collapse of bubbles in liquid in the vicinity of fiber tip surface gives rise to the high-speed cumulative microjets which can destroy the solid surface. This effect leads to multiple cracks on the film and the formation of the porous structure, formation of supercritical water and even generation of diamonds nano-crystal.

Laser-induced hydrodynamics processes in water and water-saturated bio-tissues are accompanied by generation of intense acoustic waves in resonance conditions, even of shock-type waves. The acousto-mechanic processes results in mixing and transport of gas-saturated degenerated tissue in the space of defect.

We found that medium power (0.3- 8 W) 0.97 μm in wavelength laser irradiation of water with added Ag nanoparticles (in the form of Ag-albumin complexes) through 400 μm optical fiber stimulates self-organization of unexpectedly thin (10-80 μm) and lengthy (up to 14 cm) filaments of Ag nanoparticles in the form of liquid gradient fibers. These filaments in water are stable in the course of laser irradiation being destroyed after laser radiation off. Such effect of filaments of Ag nanoparticles self-organization is rationalized by the peculiarities of laser-induced hydrodynamic processes developed in water in presence of laser light.

8. Acknowledgment

This work is supported by Russian Foundation for Basic Research (grant № 09-02-00714).

9. References

- Bagratashvili V.N., Sobol E.N., Shekhter A.B. (Eds). (2006). *Laser Engineering of Cartilage*. Fizmatlit, ISBN 5-9221-0729-1, Moscow
- Bagratashvili V.N., Kononov A.N., Novitskiy A.A., Poliakov M., and Tsypina S.I. (2009). Reflectometric studies of the etching of a silica fiber with a germanium silicate core in sub- and supercritical water. *Russian Journal of Physical Chemistry B, Focus on Physics*, Vol. 3, No. 8, pp. 1154-1164, ISSN 1990-7931
- Berry D.W., Heckenberg N.R., and Rubinsztein Dunlop H. (2000). Effects associated with bubble formation in optical trapping. *Journal of Modern Optics*, Vol. 47, No. 9, pp. 1575 – 1585, ISSN 0950-0340
- Brasselet E., Wunenburger R., and Delville J.-P. (2008). Liquid optical fibers with multistable core actuated by light radiation pressure. *Physical Review Letters*, Vol. 101, pp. 1-5, ISSN 1079-7114
- Buschmann M.D., Gluzband Y.A., Grodzinsky A.J., and Hunziker E.B. (1995). Mechanical Compression Modulates Matrix Biosynthesis in Chondrocyte Agarose Culture. *Journal of Cell Science*, Vol. 108, pp. 1497-1508, ISSN 0021-9533

- Chudnovskii V.M. and Yusupov V.I. (2008). Method of Laser Intervention Effects in Osteochondrosis, Patent RF No. 2321373
- Chudnovskii V., Bulanov V., and Yusupov V. (2010a). Laser Induction of Acoustic Hydrodynamical Effects in Medicine. *Photonics*, Vol. 1, pp. 30-36, ISSN 1993-7296
- Chudnovskii V.M., Bulanov V.A., Yusupov V.I., Korskov V.I., and Timoshenko V.S. (2010b). Experimental justification of laser puncture treatment of spine osteochondrosis. *Laser Medicine*, Vol. 14, No. 1, pp. 30-35, ISSN 2071-8004
- Hale G.M. and Querry M.R. (1973). Optical constants of water in the 200-nm to 200- μ m wavelength region. *Applied Optics*, Vol. 12, pp. 555-563, ISSN 0003-6935
- Leighton T. G. (Ed.). (1994). *The Acoustic Bubble*, Academic Press Limited, ISBN 0124419208 9780124419209, London
- Millward-Sadler S.J. and Salter D.M. (2004). Integrin-dependent signal cascades in chondrocyte mechanotransduction. *Annals of Biomedical Engineering*, Vol. 32, No. 3, pp. 435-446, ISSN 0090-6964
- Privalov V.A., Krochek I.V., and Lappa A.V. (2001). Diode laser osteoperforation and its application to osteomyelitis treatment. *Proceedings of the SPIE*, Vol. 4433, pp. 180-185, ISSN 0277-786X
- Rokhsar C.K. and Ciocon D.H. (2009). Fractional Photothermolysis for the Treatment of Postinflammatory Hyperpigmentation after Carbon Dioxide Laser Resurfacing. *Dermatologic Surgery*, Vol. 35, No. 3, (March 2009), pp. 535-537, ISSN 1524-4725
- Sandler B.I., Sulyandziga L.N., Chudnovskii V.M., Yusupov V.I., and Galin Y.M. (2002). *Bulletin physiology and pathology of respiration*, Vol. 11, pp. 46-49, ISSN 1998-5029
- Sandler B.I., Sulyandziga L.N., Chudnovskii V.M., Yusupov V.I., Kosareva O.V., and Timoshenko V.C. (2004). *Prospects for Treatment of Compression Forms of Discogenic Lumbosacral Radiculitis by Means of Puncture Nonendoscopic Laser Operations* (Skoromec A.A.), Dalnauka, ISBN 5-8044-0443-1, Vladivostok
- Suslick K.S. (1994). The chemistry of ultrasound. *The Yearbook of Science & the Future*, pp 138-155, Encyclopaedia Britannica, ISBN 0852294026, Chicago
- Taylor R.S. and Hnatovsky C. (2004). Growth and decay dynamics of a stable microbubble produced at the end of a near-field scanning optical microscopy fiber probe. *Journal of Applied Physics*, Vol. 95, No. 12, (June 2004), pp. 8444-8449, ISSN 0021-8979
- Van den Bos R., Arends L., Kockaert M., Neumann M., Nijsten T. (2009). Endovenous therapies of lower extremity varicosities: a meta-analysis. *Journal of Vascular Surgery*, Vol. 49, No. 1, pp. 230-239, ISSN 0741-5214
- Yusupov V.I., Chudnovskii V.M., and Bagratashvili V.N. (2010). Laser-induced hydrodynamics in water-saturated biotissues. 1. Generation of bubbles in liquid. *Laser Physics*, Vol. 20, No. 7, pp.1641-1646, ISSN 1054 660X
- Yusupov V.I., Chudnovskii V.M., and Bagratashvili V.N. (2011a). Laser-induced hydrodynamics in water-saturated biotissues. 2. Effect on Delivery Fiber. *Laser Physics*, Vol. 21, No. 7, pp. 1230-1234, ISSN 1054 660X

Yusupov V.I., Chudnovskii V.M., Kortunov I.V., Bagratashvili V.N. (2011b). Laser-induced self-organization of filaments from Ag nanoparticles. *Laser Physics Letters*, Vol. 8, No. 3, (March 2011), pp. 214–218, ISSN 1612-2011

Endocrine Delivery System of NK4, an HGF-Antagonist and Anti-Angiogenic Regulator, for Inhibitions of Tumor Growth, Invasion and Metastasis

Shinya Mizuno¹ and Toshikazu Nakamura²

¹*Division of Virology, Department of Microbiology and Immunology, Osaka University Graduate School of Medicine, Osaka*

²*Kringle Pharma Joint Research Division for Regenerative Drug Discovery, Center for Advanced Science and Innovation, Osaka University, Osaka Japan*

1. Introduction

Estimates of the worldwide incidence and mortality from 27 cancers in 2008 have been prepared for 182 countries by the International Agency for Research on Cancer (Ferlay *et al.*, 2010). Overall, an estimated 12.7 million new cancer cases and 7.6 million cancer deaths occur in 2008, with 56% of new cancer cases and 63% of the cancer deaths occurring in the less developed regions of the world. The most commonly diagnosed cancers worldwide are lung (1.61 million, 12.7% of the total), breast (1.38 million, 10.9%) and colorectal cancers (1.23 million, 9.7%). Cancer is neither rare anywhere in the world, nor mainly confined to high-resource countries. Many cancer subjects die from cancer as a result of organ failure due to “metastasis” (Geiger & Peeper, 2009), thus indicating that medical control of tumor metastasis leads to a marked improvement in cancer prognosis.

The acquisition of the metastatic phenotype is not simply the result of oncogene mutations, but instead is achieved through an interstitial stepwise selection process (Mueller & Fusenig, 2004). The dissociation and migration of cancer cells, together with a breakdown of basement membranes between the parenchyme and stroma, are a prerequisite for tumor invasion. The next sequential events involved in cancer metastasis include the following: (i) penetration of cancer cells to adjacent vessels (*i.e.*, intravasation); (ii) suppressed anoikis (*i.e.*, suspension-induced apoptosis) of cancer cells in blood flow; and (iii) an extravascular migration and re-growth of metastatic cells in the secondary organ. For an establishment of anti-metastasis therapy, it is important to elucidate the basic mechanism(s) whereby tumor metastasis is achieved through a molecular event(s).

Hepatocyte growth factor (HGF) was discovered and cloned as a potent mitogen of rat hepatocytes in a primary culture system (Nakamura *et al.*, 1984, 1989; Nakamura, 1991). Beyond its name, HGF is now recognized as an essential organotrophic regulator in almost all tissues (Nakamura, 1991; Rubin *et al.*, 1993; Zarnegar & Michalopoulos, 1995; Birchmeier & Gherardi, 1998; Nakamura & Mizuno, 2010). Actually, HGF induces mitogenic, motogenic

and morphogenic activities in various types of cells via its receptor, MET (Bottaro *et al.*, 1991; Higuchi *et al.*, 1992). HGF is required for organogenesis in an embryonic stage and for tissue repair in adulthood during various diseases (Nakamura, 1991; Birchmeier & Gherardi, 1998; Nakamura & Mizuno, 2010). Several lines of *in vitro* studies indicate that HGF stimulates scattering and migration of cancer cells (Matsumoto *et al.*, 1994, 1996a; Nakamura *et al.*, 1997). In malignant tumors, HGF is expressed by stromal cells, such as fibroblasts, while MET is over-expressed by cancer cells, thus suggesting in the mid-1990s that a paracrine signal from HGF-producing stroma cells to carcinomas may cause malignant behaviors, such as invasion and metastasis (Matsumoto *et al.*, 1996b).

NK4 is an intra-molecular fragment of HGF, which is generated by a chemical cleavage of mature form HGF (Date *et al.*, 1997; Nakamura *et al.*, 2010). NK4 includes an N-terminal hairpin domain and 4-kringle domains (K1-K4) of HGF α -chain, which binds to MET. Thus, NK4 antagonizes HGF activities as a competitive inhibitor. Using NK4 as an HGF-antagonist in rodents with malignant tumors, we have accumulated evidence showing that endogenous HGF-MET cascade is a key conductor for tumor metastasis, while inhibition of MET signals leads to the arrests of tumor growth. Unexpectedly, NK4 prohibits tumor angiogenesis through a MET-independent mechanism. This review focuses on the roles of HGF in cancer biology and pathology. We also emphasize the effectiveness of NK4 in experimental cancer models where NK4 is supplemented via a “hydrodynamics-based” gene therapy.

2. Effects of HGF on intra-tumor cells during cancer progression

In the mid-1980s, MET was identified as a mutated oncogene from carcinogen-induced osteosarcoma cells (MNNG-HOS) that transform NIH3T3 fibroblasts (Cooper *et al.*, 1984). MET-encoding protein has a tyrosine kinase activity (Dean *et al.*, 1985), suggesting that MET may be an orphan receptor of growth factors. In the early 1990s, MET-coding product was demonstrated to be a high-affinity receptor for HGF (Bottaro *et al.*, 1991; Higuchi *et al.*, 1992). Scatter factor (SF) stimulates tumor cell movement, as its name indicates, and is shown molecularly identical to HGF (Konishi *et al.*, 1991; Weidner *et al.*, 1991). HGF has several activities required for tumor cell invasion and metastasis, as described below. In this section, we summarize the direct effects of HGF on intra-tumor cells, including carcinoma, and on vascular and lymphatic cells prior to discussion of the contribution of HGF-MET cascades during tumor malignancy.

2.1 Scattering and migration of tumor cells

Initial events for the metastatic spread of tumors involve loss of cell-cell contact within the primary tumor mass. The integrity and morphology of epithelial tumor cell colonies are maintained by cell-cell contact mediated by cadherins and its associated intracellular catenin molecules. Cancer cells must lose their tight cell-to-cell contact by down-regulation of cadherin-cadherin complex during invasion into adjacent tissues. HGF induces scattering (*i.e.*, dispersion of cluster cells into single cells) via an endocytosis of E-cadherin from cell surface to cytoplasm (Watabe *et al.*, 1993; Miura *et al.*, 2001). During cell migration, HGF activates the Ras-Rab5 pathway for endocytosis of cadherins (Kimura *et al.*, 2006), which triggers nuclear localization of β -catenin, a transcription factor of genes responsible for cell motility (Hiscox & Jiang, 1999). Stimulation of an Rho small G protein cascade and activation of cdc42, rac and PAK by HGF leads to the disassembly of stress fiber or focal adhesions, while lamellipodia

formation and cell spreading are enhanced by HGF (Royal *et al.*, 2000). These changes confer a down-stream mechanism of MET-mediated cancer invasion.

2.2 Breakdown of basement membranes

During cancer invasion, tumor cells must move across a basement membrane between epithelium and lamina propria (*i.e.*, sub-epithelium). HGF stimulates motility in a biphasic process: cells spread rapidly and form focal adhesions, and then they disassemble these condensations, followed by increased cell locomotion. In the early phase (*i.e.*, within a few minutes post-stimulation), HGF induces phosphorylation of focal adhesion kinase (FAK) together with a tight bridge between the extra-cellular matrix (ECM) and integrins of cancer cells (Matsumoto *et al.*, 1994; Parr *et al.*, 2001). In the later phase, HGF-stimulated cancer cells invade into matrix-based gels *in vitro*, or across basement membrane ECM *in vivo* (Nakamura *et al.*, 1997). In this process, HGF up-regulates several types of matrix metalloproteinase (MMP), such as MMP-1, -2, and -9, through activation of Ets, a transcriptional factor of MMPs (Li *et al.*, 1998; Nagakawa *et al.*, 2000; Jiang *et al.*, 2001). Considering that MMP-inhibitors diminish HGF-mediated migration, the induction of MMP through HGF-Ets cascade is essential for tumor invasion into adjacent normal tissues.

2.3 Endothelial attachment and extravasation of cancer cells

Needless to say, tumor angiogenesis as well as lymphatic vessel formation are important for delivery of cancer cells from the primary tumor to secondary organs. HGF enhances angiogenesis via induction of the proliferation and morphogenesis of endothelial cells (EC) (Bussolino *et al.*, 1992; Nakamura *et al.*, 1996). Actually, HGF supplementation leads to the enhancement of tumor angiogenesis *in vivo* (Lattera *et al.*, 1997). Recent studies delineated the capacity of HGF to induce lymphatic morphogenesis (Kajiya *et al.*, 2005; Saito *et al.*, 2006). Thus, HGF is considered to facilitate cancer metastasis via neo-induction of vascular or lymphatic vessel beds. HGF has a direct effect on EC for enhancing tight adhesion of tumor cells on endothelium via FAK phosphorylation (Kubota *et al.*, 2009a). Furthermore, HGF decreases endothelial occludin, a cell-cell adhesion molecule (Jiang *et al.*, 1999a). Under such a loss of EC-EC integrity, HGF decreases the trans-endothelial resistance of tumor vessels and enhances cancer invasion across an EC barrier (*i.e.*, intravasation in primary tumors and extravasation in metastatic organs) (Fig. 1).

2.4 Prevention of cancer cell anoikis

Anoikis, also known as suspension-induced apoptosis, is a term used to describe programmed cell death (apoptosis) of epithelial cells induced by loss of matrix attachment. In addition to gaining functions of invasion and angiogenesis, cell resistance to anoikis also appears to play an important role in tumor progression and metastasis as tumor cells lose matrix attachment during metastasis. However, it is unknown how cancer cells escape from anoikis-like death during metastasis. It was demonstrated, in a non-adherent culture models, that HGF is a key molecule inhibiting suspension-induced anoikis, and this effect is mediated via a crosstalk that is, in turn, mediated by phosphatidylinositol 3-kinase (PI-3K) and extracellular signal-regulated kinase (ERK)-1/2 (Zeng *et al.*, 2002; Kanayama *et al.*, 2008). A recent report described that tetraspanin CD151-knockdown abolishes preventive effect of HGF on tumor anoikis (Franco *et al.*, 2010). Thus, it is likely that cell surface tetraspanins are important for signaling complexes between MET and integrin- β 4, a known amplifier of HGF-mediated cell survival.

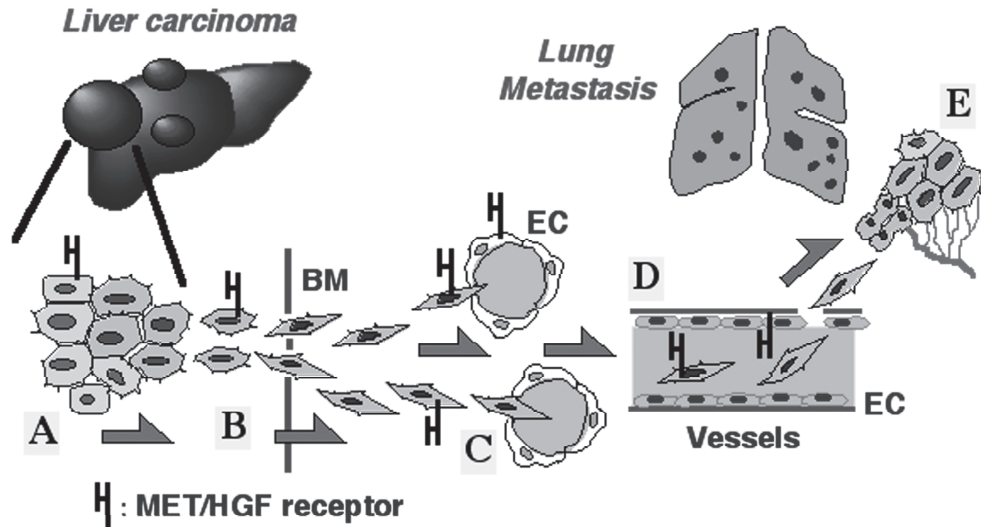


Fig. 1. Various effect of HGF on cancer cells and endothelial cells (EC) during tumor progression. For example, sequential events during the lung metastasis of hepatic carcinoma are summarized as follows: (A) dissociation and scattering of hepatocellular cancer cells through an HGF-induced endocytosis of cadherins; (B) tumor migration into stromal areas across the basement membrane (BM) is mediated via MMP-dependent matrix degradation and Rho-dependent cell movement; (C) invasion of tumor cells into neighboring vessels (*i.e.*, intravasation) where the tight junction between ECs is lost by HGF-MET signaling; (D) inhibition of tumor cell anoikis by MET-AKT cascades during blood flow, and out-flux of tumor cells across vessel walls (*i.e.*, extravasation); and (E) in the lung, HGF supports growth of metastatic nodules via providing vascular beds as an angiogenic factor.

Overall, HGF is shown to take direct action on carcinoma cells: (i) cell spreading via an endocytosis of cadherins; (ii) enhancement of invasion across basement membranes via Rho-dependent and MMP-dependent pathways; and (iii) anti-anoikis activity during blood circulation. Toward tumor vessels, HGF elicits vascular and lymphatic EC proliferation and branching angiogenesis, while intravasation and extravasation are achieved through HGF-induced reduction of EC-EC integrity. These HGF-MET-mediated biological functions seem advantageous for invasion and metastasis of malignant tumors, including carcinoma and sarcoma (Fig. 1).

[Note] Long-term administration of recombinant HGF does not elicit tumor formation in healthy animals, and this result supports a rationale of HGF supplement therapy for treating chronic organ diseases, such as liver cirrhosis, at least in cancer-free patients.

3. Regulation of HGF production by cancer cells

Several lines of histological evidence indicate that HGF is produced in stroma cells, such as fibroblasts, vascular EC and smooth muscle cells in tumor tissues. In contrast, MET is over-expressed mainly by tumor cells, particular near invasive areas, implying a possible paracrine signal from HGF-producing stroma cells to MET-expressing carcinoma cells

(Matsumoto *et al.*, 1996b). Herein, we will discuss the molecular basis whereby stromal HGF production is up-regulated by tumor cells during cancer invasion and metastasis.

3.1 Stroma as a microenvironment to determine behaviors of tumors

The important roles of stroma during tumor progression are demonstrated through several independent studies. Carcinoma-associated fibroblasts, but not normal fibroblasts, stimulate tumor progression of initiated non-tumorigenic epithelial cells both in an *in vivo* tissue recombination and in an *in vitro* co-culture system (Olumi *et al.*, 1999). Transforming growth factor (TGF)- β signaling is critical for down-regulating HGF production (Matsumoto *et al.*, 1992). Of note, an inactivation of TGF- β type II receptor gene in stromal fibroblasts leads to the onset of epithelial growth and invasion (Bhowmick *et al.*, 2004). In this process, activation of paracrine HGF is a key mechanism for stimulation of epithelial proliferation (Bhowmick *et al.*, 2004). Thus, the suppression of HGF production by TGF- β seems to be important for an escape from cancer metastasis (Matsumoto & Nakamura, 2006).

3.2 Regulation of HGF production in stroma by tumor cells

As repeated, a major source of HGF in tumors is stromal cells (including fibroblasts, endothelium, macrophages and neutrophils) (Wislez *et al.*, 2003; Matsumoto & Nakamura, 2006; Grugan *et al.*, 2010). Thus, how stromal HGF is up-regulated during tumor progression should be discussed. There is now ample evidence that numerous types of carcinoma cells secrete soluble factors that induce HGF production in stromal cells (*i.e.*, HGF-inducers). For example, conditioned medium obtained from breast cancer cells enhances HGF production in fibroblasts, along with a raise in prostaglandin-E2 (Matsumoto-Taniura *et al.*, 1999). Of note, suppression of prostaglandin-E2 production by indomethacin leads to down-regulation of stromal HGF production and suppression of tumor migration *in vitro* (Matsumoto-Taniura *et al.*, 1999), indicating that cancer-derived prostaglandins are important for up-regulating HGF in stromal cells (Matsumoto-Taniura *et al.*, 1999; Pai *et al.*, 2003). Other carcinoma-derived HGF-inducers are interleukin-1 β (IL-1 β), basic fibroblast growth factor (b-FGF), platelet-derived growth factor (PDGF), and TGF- α (Hasina *et al.*, 1999; Matsumoto & Nakamura, 2003). These results indicate a crosstalk between carcinoma and stroma, mediated via a paracrine loop of HGF-inducers produced by carcinoma and HGF secreted from stroma cells, such as fibroblasts (Matsumoto *et al.*, 1996a).

3.3 Inflammation-mediated HGF up-regulation mechanism

In addition to stromal fibroblasts, tumor-associated macrophages (TAM) are known to highly produce HGF during non-small lung cancer invasion (Wang *et al.*, 2011). It is reported that TAM isolated from 98 primary lung cancer tissues show the higher production of HGF, along with the concomitant increases in urokinase-type plasmin activator (uPA), cyclooxygenase-2 (Cox2) and MMP-9 (Wang *et al.*, 2011). Anti-MMP-9 antibody largely diminishes TAM-induced invasion, while Cox2 and uPA are critical for HGF production and activation, respectively, suggesting that Cox2-uPA-HGF-MMP cascades in TAM participate in non-small lung cancer invasion. Likewise, HGF production is enhanced by neutrophils infiltrating bronchiolo-alveolar subtype pulmonary adenocarcinoma (Wislez *et al.*, 2003).

Clinical studies demonstrate that serum levels of HGF are elevated in patients with recurrent malignant tumors (Wu *et al.*, 1998; Osada *et al.*, 2008), thus suggesting an

endocrine mechanism of the HGF delivery system. In this regard, it is known that peripheral blood monocytes produce HGF, contributing to the increase in blood HGF levels via an endocrine mechanism (Beppu *et al.*, 2001). Overall, production of HGF by inflammatory cells is involved in carcinoma invasion and metastasis (*i.e.*, local system), while peripheral blood monocytes seem to prevent tumor cell anoikis during metastasis, possibly by a release of HGF into blood (*i.e.*, systemic system).

4. Structure and activity of NK4 as HGF antagonist

HGF is a stromal-derived paracrine factor that has stimulated cancer invasion at least *in vitro* (Matsumoto *et al.*, 1994; Matsumoto *et al.*, 1996a; Nakamura *et al.*, 1997). Clinical studies suggest that the degree of serum HGF and Met expressions in cancer tissues appears to correlate with a given prognosis (Yoshinaga *et al.*, 1993; Osada *et al.*, 2008). Thus, it is hypothesized that *in vivo* inhibition of HGF-MET signaling may be a reasonable strategy to prohibit cancer metastasis. To test this hypothesis, we prepared NK4 as an intra-molecular fragment of HGF via a chemical digestive process (Date *et al.*, 1997; Matsumoto *et al.*, 1998). As expected, NK4 bounded to MET and inhibited HGF-MET coupling as a competitive inhibitor. An additional “unexpected” value was that NK4 inhibited tumor angiogenesis via a MET-independent pathway. This section focuses on the biological value of NK4 as an HGF-antagonist and as an angiogenesis inhibitor.

4.1 Structure and anti-invasive function of NK4

NK4 was initially purified as a fragment from elastase-digested samples of recombinant human HGF (Date *et al.*, 1997). The N-terminal amino acid sequence of NK4 and of the remnant fragment, assumed to be composed of an HGF β -chain, revealed that NK4 is cleaved between the 478th valine and the 479th asparagine. The N-terminal amino acid sequence of NK4 revealed that the N-terminal structure of NK4 is the same as undigested HGF (*i.e.*, 32nd pyroglutamate), indicating that NK4 is composed of the N-terminal 447 amino acids of the α -chain of HGF and contains the N-terminal hairpin domain and four kringle domains (thus designated NK4) (Fig. 2A). The binding domains that are responsible for high-affinity binding to MET are the N-terminal hairpin and the first kringle domains in NK4 (and HGF). MET tyrosine phosphorylation occurs in A549 lung carcinoma within 10 minutes after HGF addition, while NK4 inhibits the HGF-mediated MET activation (Fig. 2B). Actually, NK4 functions as an HGF-antagonist: HGF induces invasion and migration of the gallbladder and bile duct carcinoma cells in ECM-based gels, while NK4 inhibits HGF-induced invasion in a dose-dependent manner (Fig. 2C) (Date *et al.*, 1998). These anti-invasive effects of NK4 are seen in distinct types of cancer cells (Hiscox *et al.*, 2000; Maehara *et al.*, 2001; Parr *et al.*, 2001), strengthening the common role of NK4 during cancer migration.

4.2 Perlecan-dependent anti-angiogenic mechanism by NK4

Vascular EC highly express MET, while HGF stimulates mitogenic and morphogenic activities in EC (Nakamura *et al.*, 1996), thus suggesting that NK4 could inhibit HGF-induced angiogenesis. Actually, NK4 potently inhibited the HGF-mediated proliferation of EC *in vitro* (Jiang *et al.*, 1999b). Strikingly, NK4 also inhibited microvascular EC proliferation and migration, induced by other angiogenic factors, such as b-FGF and vascular endothelial

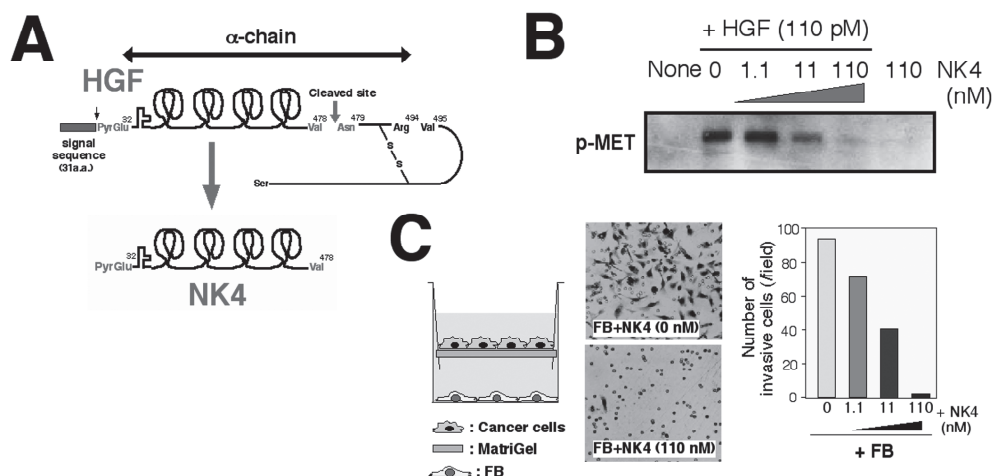


Fig. 2. Preparation of NK4 as an HGF-antagonist and its inhibitory effects on tumor invasion *in vitro*. (A) Preparation and structure of NK4. NK4 is generated via a cleavage of HGF between 478th Val and 479th Asn. (B) Inhibition of HGF-mediated MET tyrosine phosphorylation by NK4 in lung carcinoma cells. (C) Biological activity of NK4. Cancer cell invasion (upper chamber) is induced across a Matrigel layer when fibroblasts (FB) are placed on a lower chamber. In this co-culture system, NK4 inhibits FB-induced tumor cell invasion in a dose-dependent manner.

growth factor (VEGF) (Fig. 3A) (Kuba *et al.*, 2000). When a pellet containing b-FGF was implanted under the rabbit cornea, angiogenesis was rapidly induced. In this model, NK4 inhibited b-FGF-induced angiogenesis (Fig. 3B). *In vitro* models of EC proliferation, HGF and VEGF phosphorylate MET and KDR/VEGF receptor, respectively, whereas NK4 inhibits HGF-induced MET tyrosine phosphorylation, but not VEGF-induced KDR phosphorylation (Kuba *et al.*, 2000). Nevertheless, NK4 inhibited the VEGF-mediated EC proliferation without modification of VEGF-mediated ERK1/2 (p44/42 mitogen-activated protein kinase) activation. These results suggest the presence of another mechanism whereby NK4 inhibits VEGF- and b-FGF-mediated angiogenesis.

The fibronectin-integrin signal is essential for the spreading and proliferation of EC. Based on this background, we demonstrated that NK4-mediated growth arrest of EC is due to a loss of the fibronectin-integrin signal. Affinity purification with NK4-immobilized beads revealed that NK4 binds to perlecan (Sakai *et al.*, 2009). Consistent with this result, NK4 was co-localized with perlecan in EC. Perlecan is a multi-domain heparan sulfate proteoglycan that interacts with basement membrane components such as fibronectin. Of interest, knockdown of perlecan expression by siRNA diminished the fibronectin assembly and EC spreading, indicating an essential role of fibronectin-perlecan interaction during EC movement. A recent report described that NK4-perlecan interaction suppressed the normal assembly of fibronectin by perlecan (Sakai *et al.*, 2009). As a result, FAK activation became faint in EC after NK4 treatment. Under such a loss of fibronectin-integrin signaling by NK4, EC growth and motility were suppressed, even in the presence of b-FGF or VEGF. This is the reason why NK4 arrests b-FGF- or VEGF-mediated angiogenesis (Fig. 3C).

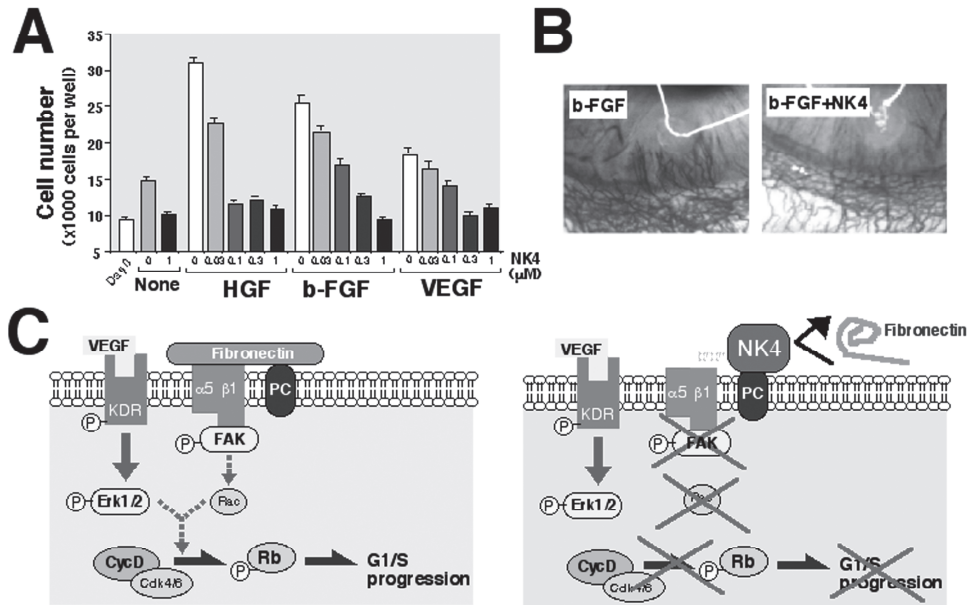


Fig. 3. Anti-angiogenic effects of NK4 via a perlecan-dependent mechanism. (A) NK4 suppresses HGF-, b-FGF-, and VEGF-induced proliferation of EC *in vitro* (Kuba *et al.*, 2000). (B) Inhibition of b-FGF-induced corneal neovascularization by NK4 treatment in rabbits. (C) Involvement of perlecan (PC) in NK4-mediated growth arrest of EC. Left: Cell surface PC is required for the binding of fibronectin and $\alpha 5 \beta 1$ -integrin, leading to FAK phosphorylation and crosstalk of VEGF-VEGF receptor (KDR) signaling. Right: NK4 binds to PC, and then the binding of integrin to fibronectin is impaired. As a result, VEGF fails to elicit G1/S progression of EC in the presence of NK4 (Sakai *et al.*, 2009).

We have accumulated *in vitro* evidence showing that HGF-MET system may elicit cancer invasion via a paracrine loop of stroma-carcinoma interaction. This phenomenon is also demonstrated *in vivo*: anti-HGF antibody potently suppressed the tumor invasion in a mouse model of pancreas cancer (Tomioia *et al.*, 2001). On the other hand, several investigators proposed, in the late-1990's, a new concept that tumor angiogenesis inhibition leads to the arrest of cancer growth and metastasis (Yancopoulos *et al.*, 1998). Inhibition of tumor angiogenesis leads to local hypoxia, and then apoptotic death of cancer cells is associated with the arrests of tumor growth and metastasis (*i.e.*, cytostatic therapy). In this regard, NK4 also elicits an anti-angiogenic effect via perlecan-dependent mechanism. Thus, bi-functional properties of NK4 as an HGF antagonist and angiogenesis inhibitor raise a possibility that NK4 may prove therapeutic for cancer patients, as follows.

5. Anti-cancer therapy using NK4 in animal models

Carcinoma and sarcoma show malignant phenotypes prompted by a stroma-derived HGF-MET signal at least *in vitro*. If NK4 could block MET signaling as an HGF-antagonist *in vivo*, supplemental therapy with NK4 would be a pathogenesis-based strategy to counteract

tumor invasion and metastasis. This hypothesis is widely demonstrated through extensive studies using tumor-bearing animals, as described below.

5.1 First evidence of NK4 for inhibition of carcinoma progression *in vivo*

HGF, or co-cultured fibroblasts, are known to induce invasion of gallbladder carcinoma cells (GB-b1) across Matri-gel basement membrane components (Li *et al.*, 1998). NK4 competitively inhibits the binding of HGF to MET on GB-d1 cells. As a result, NK4 diminishes HGF-induced, or fibroblast-induced, motogenic activities (Date *et al.*, 1998), thus suggesting that stroma-derived HGF is a key conductor for provoking tumor invasion. Such an important role of HGF was also demonstrated *in vivo*. Subcutaneous inoculations of human gallbladder carcinoma GB-d1 cells in nude mice allow for primary tumor growth and invasion to adjacent muscular tissues. Using this conceptual model, we provided the first evidence of NK4 as an anti-tumor drug (Date *et al.*, 1998). Recombinant NK4 has inhibited the growth and muscular invasion in a mouse model of gallbladder carcinoma. Consistent with tumor growth arrest, apoptotic change becomes evident during NK4 injections. Since HGF has an anti-apoptotic effect on cancer cells (Zeng *et al.*, 2002), reverse of HGF-induced protection by NK4 may be one of the mechanisms whereby carcinoma growth can be suppressed during NK4 supplemental therapy.

5.2 Inhibition of tumor angiogenesis by NK4 treatment

In a culture of EC, NK4 produces anti-angiogenetic effects via a MET-independent pathway (Kuba *et al.*, 2000; Nakabayashi *et al.*, 2003). These effects are also observed in animal models of malignant tumors: administration of recombinant NK4 suppressed primary tumor growth, metastasis of Lewis lung carcinoma, and Jyg-MC(A) mammary carcinoma implanted into mice (Kuba *et al.*, 2000), although neither HGF nor NK4 affected proliferation and survival of these tumor cells *in vitro*. NK4 treatment resulted in a remarkable decrease in microvessel density and an increase in apoptotic tumor cells in primary tumors, suggesting that the inhibition of tumor growth by NK4 may be achieved by the suppression of tumor angiogenesis (Kuba *et al.*, 2000). The anti-angiogenic effects of NK4 are widely demonstrated in various types of cancers [see our review articles (Matsumoto & Nakamura, 2005; Matsumoto *et al.*, 2008a,b)]. Because the inhibition of angiogenesis by NK4 leads to tumor hypoxia, hypoxia-primed apoptosis may contribute to a reduction in tumor size during NK4 supplemental therapy.

5.3 Delayed NK4 therapy for attenuation of end-stage pancreas carcinoma

Anti-tumor effect of NK4 is also observed in a mouse model of advanced pancreas carcinoma (Tomioka *et al.*, 2001). When NK4 treatment was initiated on day 10, a time when cancer cells were already invading surrounding tissues, NK4 potently inhibited the tumor growth, peritoneal dissemination, and ascites accumulation at 4 weeks after the inoculation. Such an anti-tumor effects of NK4 correlated with decreased vessel density in pancreatic tumors. In an end-stage of pancreas cancer, NK4 inhibited the malignant phenotypes, such as peritoneal dissemination, invasion of cancer cells into the peritoneal walls and ascites accumulation (Tomioka *et al.*, 2001). As a result, NK4 prolonged the survival time of mice at an end-stage of cancer (Fig. 4). Because effective systemic therapy for pancreatic cancer is currently not available, and diagnosing pancreatic cancer in its early stages is difficult, the highly invasive and metastatic behaviors of pancreatic cancer lead to difficulty in attaining a

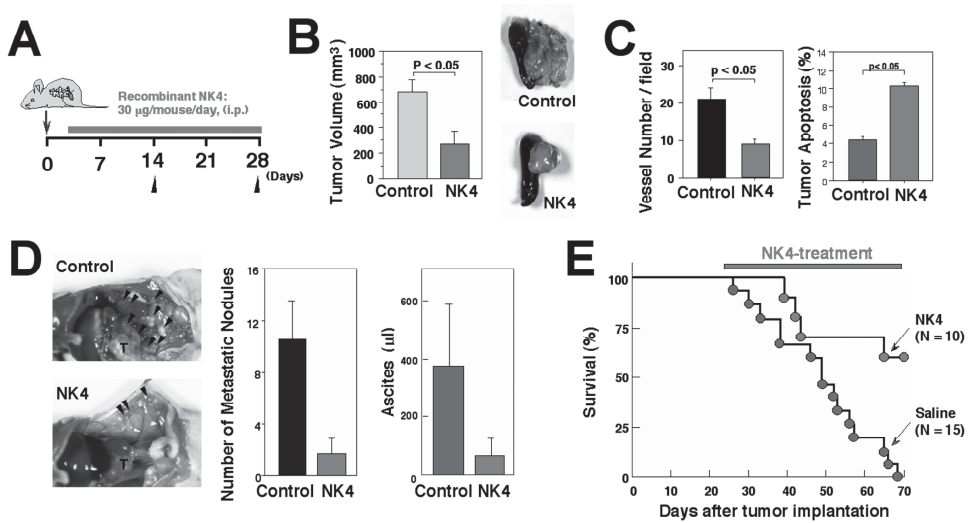


Fig. 4. Anti-tumor effects of NK4 on advanced pancreas cancer in mice. (A) Schedules for NK4 treatment of mice with pancreatic cancer. NK4 was injected into mice between 3 and 28 days after the inoculation of human pancreatic cancer cells (SUIT-2). (B) Inhibition of primary tumor growth by NK4. Photographs show appearance of the primary pancreatic cancer. (C) Histological analysis of the effect of NK4-treatment on tumor angiogenesis (left) and apoptosis (right). NK4-treatment reduced the number of vessel numbers, while apoptotic death of cancers was enhanced by NK4. (D) Inhibitory effects of NK4 on peritoneal metastasis. Left: Typical macroscopic findings. Middle: Changes in the number of metastatic nodules. Right: Changes in the ascite volumes. (E) Prolonged survival of tumor-bearing mice treated with NK4.

long-term survival and a recurrence-free status. Targeting tumor angiogenesis and blockade of HGF-mediated invasion of cancer cells may prove to be potential therapy for patients with pancreatic cancer.

5.4 Therapy combining NK4 with other treatments

Anti-cancer chemotherapy is widely used for the suppression of malignant tumors with or without surgical treatment. Therapy regimens that combine anti-cancer chemo drugs and NK4 enhance their anti-tumor effect (Matsumoto *et al.*, 2011). Irradiation therapy often enhances cancer metastasis, especially in cases of pancreatic carcinoma, and this is associated with the irradiation-induced up-regulation of HGF in fibroblasts (Qian *et al.*, 2003; Ohuchida *et al.*, 2004). Thus, NK4 may overcome these irradiation-associated side effects.

Epidermal growth factor receptor (EGFR) kinase inhibitors, such as Gefitinib, are used to treat non-small cell lung cancers that have activating mutations in the EGFR gene, but most of these tumors become resistant to EGFR-kinase inhibitors due to enhancement of HGF-MET signals (Engelman *et al.*, 2007; Yano *et al.*, 2008; Okamoto *et al.*, 2010). Thus, NK4 treatment may reverse HGF-induced resistance to Gefitinib.

Recently, it was demonstrated that NK4-mediated tumor regression depends on the infiltration of cytotoxic T lymphocytes (Kubota *et al.*, 2009b). Importantly, depletion of CD8+ cells markedly abrogated the anti-tumor activity of NK4 in a mouse model of colon cancer. NK4 enhances immune responses in dendritic cells *in vitro*. Thus, NK4 may also have utility for anti-tumor immunotherapy.

There is now ample evidence that NK4 is useful for the inhibition of growth, invasion and metastasis in various types of tumors, such as gastric carcinoma (Hirao *et al.*, 2002), pancreas cancer (Tomioka *et al.*, 2001), prostate cancer (Davies *et al.*, 2003), multiple myeloma (Du *et al.*, 2007) and melanoma (Kishi *et al.*, 2009) (**Table-1**). These results support our hypothesis that HGF is a key determinant of tumor malignancy (Matsumoto *et al.*, 1996b).

Tumor diseases (Cell lines and treatment)	NK4 therapy	Outcome	Literature
A. Digestive system:			
Gastric carcinoma (TMK1 cells, ip, Mouse)	Adeno-NK4, ip	Inhibitions of growth and metastasis, Anti-angiogenesis, Reduced ascites	Ueda K <i>et al.</i> , Eur J Cancer 40: 2135-2142 (2004)
Hepatic carcinoma (HUH7 cells, portal vein, Mouse)	Adeno-NK4, iv	Inhibitions of growth, Anti-angiogenesis, Prolonged survival	Son G <i>et al.</i> , J Hepatol 45: 688-695 (2006)
Gallbladder cancer (GB-d1 cells, sc, Mouse)	NK4, sc	Inhibitions of growth and invasion	Date K <i>et al.</i> , Oncogene 17: 3045-354 (1998)
Pancreatic carcinoma (SUIT-2 cells, intra-pancreas, Mouse)	r-NK4, ip	Inhibitions of growth, invasion and metastasis, Anti-angiogenesis, Reduced ascites, Prolonged survival	Tomioka Det <i>al.</i> , Cancer Res 61: 7518-7524 (2001)
Colon carcinoma (MC-38 cells, intra-spleen, Mouse)	NK4 cDNA, bolus iv (hydrodynamics)	Inhibitions of growth, invasion and metastasis, Anti-angiogenesis, Prolonged survival	Wen J <i>et al.</i> , Cancer Gen Ther 11: 419-430 (2004)
B. Respiratory system:			
Lung carcinoma (Lewis carcinoma, sc, Mouse)	r-NK4, sc	Inhibitions of growth and metastasis, Anti-angiogenesis, Enhanced apoptosis	Kuba K <i>et al.</i> , Cancer Res 60: 6737-6743 (2000)
Lung carcinoma (A549 cells, sc, Mouse)	Adeno-NK4, intra-tumor or ip	Inhibition of growth, Anti-angiogenesis	Maemondo M <i>et al.</i> , Mol Ther 5: 177-185 (2002)
Mesothelioma (EHMES-10 cells, sc, Mouse)	Adeno-NK4, intra-tumor	Inhibition of growth, Enhanced apoptosis, Anti-angiogenesis	Suzuki Y <i>et al.</i> , Int J Cancer 127: 1948-1957 (2010)

C. Reproductive system:			
Prostate carcinoma (PC-3 cells, sc, Mouse)	r-NK4, sc (osmotic pump)	Inhibition of growth, Anti-angiogenesis	Davies G <i>et al.</i> , Int J Cancer 106: 348-354 (2003)
Ovarian carcinoma (HRA cells, ip, Mouse)	NK4 gene, Stable transfection	Inhibition of metastasis, Prolonged survival	Saga Y <i>et al.</i> , Gene Ther 8: 1450-1455 (2001)
D. Hematopoietic system:			
Lymphoma (E.G7-OVA cells, sc, Mouse)	Adeno-NK4, intra-tumor (with DC)	Inhibition of growth, Anti-angiogenesis, Induction of CTL	Kikuchi T <i>et al.</i> , Blood 100: 3950-3959 (2003)
Multiple myeloma (KMS11/34 cells, sc, Mouse)	Adeno-NK4, im	Inhibition of growth, Anti-angiogenesis, Enhanced apoptosis	Du W <i>et al.</i> , Blood 109: 3042-3049 (2007)
E. Other organ or tissues:			
Melanoma (B16F10 cells, sc, Mouse)	Adeno-NK4, iv	Inhibitions of growth and metastasis, Anti-angiogenesis	Kishi Y <i>et al.</i> , Cancer Sci 100: 1351-1358 (2009)
Glioblastoma (U-87 MG cells, Intra-brain, Mouse)	r-NK4, intra-tumor	Inhibition of growth, Anti-angiogenesis, Enhanced apoptosis	Brockmann MA <i>et al.</i> , Clin Cancer Res 9: 4578-4585 (2003)
Breast carcinoma (MDAMB231 cells, sc, Mouse)	r-NK4, sc	Inhibition of growth, Anti-angiogenesis	Martin TA <i>et al.</i> , Carcinogenesis 24: 1317-1323 (2003)

Adeno-NK4, adenoviral vector carrying NK4 cDNA; r-NK4, recombinant NK4 protein; sc, subcutaneous; iv, intravenous; ip, intraperitoneal; im, intramuscular; DC, dendritic cells; and CTL, cytotoxic T lymphocytes.

Table 1. Representative studies to show therapeutic effects of NK4 on distinct types of tumors in animal models

6. Hydrodynamics-based NK4 gene therapy for colon cancer inhibition

Hydrodynamic delivery has emerged as the simplest and effective method for intracellular delivery of subjective genes in rodents; this process requires no special equipment. The system employs a physical force generated by the rapid injection of a large volume of solution into a blood vessel to enhance the permeability of endothelium and the plasma membrane of the parenchyma cells, such as hepatocytes, to facilitate a delivery of the substance into cells (Bonamassa *et al.*, 2011). Using this technique in mice, we established an endocrine delivery system for NK4 that leads to an inhibition of the malignant behavior of cancers, as follows.

6.1 NK4 supplementation system via hydrodynamic gene delivery in mice

Numerous clinical studies have indicated the apparent increases in serum HGF levels in patients during the progression of cancers (Wu *et al.*, 1998; Osada *et al.*, 2008). It is likely that HGF in blood protects cancer cell suspension from anoikis-like cell death (Zeng *et al.*, 2002). Thus, we predict that over-production of NK4 in blood would overcome the HGF-mediated metastatic events seen in blood flow (and possibly in local sites). Hydrodynamic-based gene delivery is known to achieve an efficient expression of exogenous genes predominantly in the liver but much lesser in the kidney and spleen (Suda *et al.*, 2007). Based on this background, we established a method for the induction and maintenance of higher levels of NK4 in blood through repeated injections of NK4 cDNA-containing plasmid.

For hydrodynamic-based gene delivery, 5 microgram of plasmid DNA (pCAGGS-NK4), or pCAGGS-empty (as a control), in saline was injected within 5 seconds into tail veins of mice at 2.4 ml per 30g body weight (Wen *et al.*, 2004; 2007). As a result, exogenous NK4 was detected, and plasma NK4 reached a mean value of 49.5 ng/ml 24 hours post-bolus injection and decreased to 15.4 ng/ml on day 3. Following the second and third injections, the plasma NK4 level again reached approximately 70 and 130 ng/ml on days 8 and 15, respectively. Thus, plasma NK4 levels increased following additional administration of the expression plasmid, and were maintained at levels of > 8 ng/ml during 3 weeks post-treatment (Fig. 5).

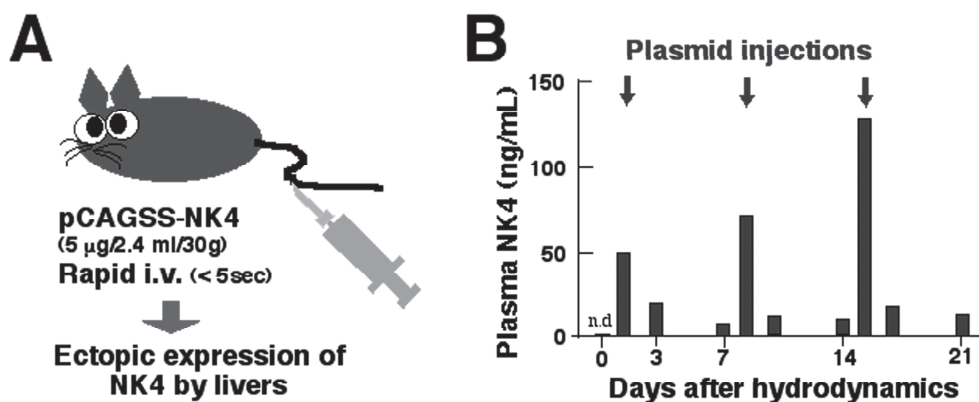


Fig. 5. Hydrodynamics-mediated NK4 delivery system in mice. (A) An experimental protocol of NK4 gene administration. Five microgram of pCAGGS-NK4 was administered intravenously into mice on day 0, 7 and 14. (B) Changes in plasma NK4 levels following repetitive administration of expression plasmid for NK4. Arrows mean the time of plasmid administration. See reference (Wen *et al.*, 2007) for further information.

6.2 Inhibition of colon cancer metastasis by NK4 gene delivery

Colon cancer is one of the most common cancers in the world, with a high propensity to metastasize: 30-40% of patients have metastatic disease at the initial diagnosis. The liver is the most frequent site of metastasis, and hepatic failure is a lethal event during colon cancer. Thus, direct inhibition of the dissociation, spreading and invasion of cancer cells is expected to become efficient treatment. With regard to this, HGF stimulates the invasion of MC-38 mouse colon cancer cells across MatriGel (Parr *et al.*, 2000), which is composed of laminin and other matrices and mimics the basement membrane *in vivo*. In this model, NK4 has

inhibited the HGF-mediated migration of MC-38 cells in a culture model of colon cancer invasion. This anti-invasive effect of NK4, obtained by *in vitro* studies, is demonstrated *in vivo* in the following two studies.

An hepatic metastatic model was prepared by the injection of mouse MC-38 cells into the spleen. During the progression of colon cancer in hepatic tissues, HGF was over-produced by hepatic sinusoidal cells, while MET tyrosine phosphorylation became evident, particularly around the front lines of invasive zones. Supplementation of NK4 in blood and livers via a single injection of NK4-cDNA containing plasmid (pCAGGS-NK4) resulted in the loss of MET tyrosine phosphorylation (Fig. 6). Under such a MET-inactivated condition by NK4 treatment, hepatic invasion by colon carcinoma was strongly inhibited (Wen *et al.*, 2004).

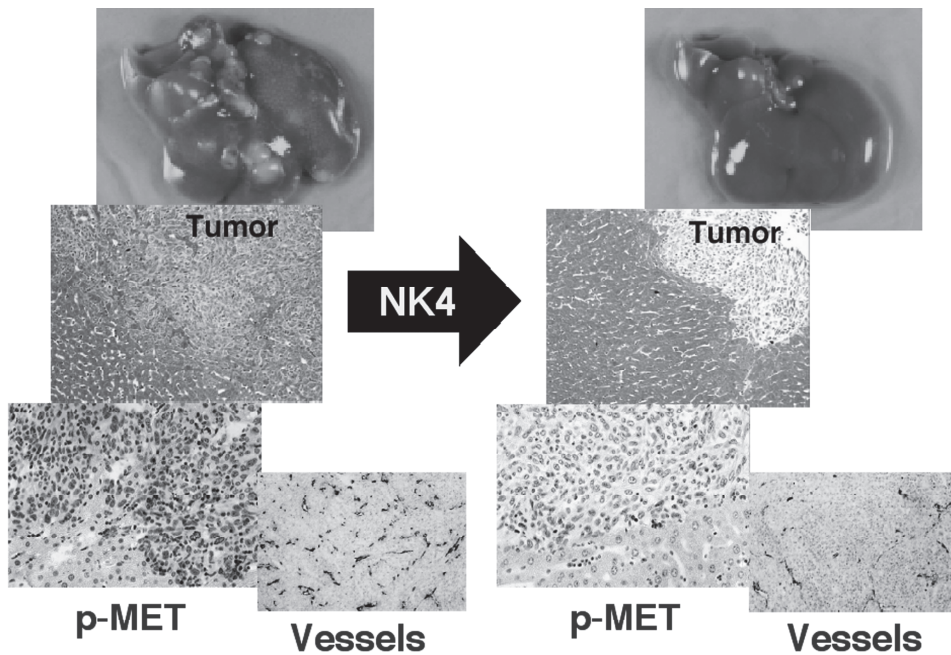


Fig. 6. Successful outcome of hydrodynamics-based NK4 gene therapy in a mouse model of colon cancer. The hepatic invasion model is prepared by intra-splenic inoculation of MC-38 colon carcinoma in mice. In the control group, invasion of carcinoma cells into neighboring hepatic areas becomes evident, along with an induction of MET tyrosine phosphorylation (p-MET) and an increase in vessel numbers. In contrast, NK4 suppresses tumor invasion by inhibiting MET tyrosine phosphorylation and reducing angiogenesis. As a result, NK4 gene therapy prolongs the survival of these mice (Wen *et al.*, 2004).

Repeated administrations of NK4-containing plasmid DNA also inhibited the malignant behaviors of colon carcinoma (Wen *et al.*, 2007). Actually, NK4 repetitive gene therapy potently inhibited the muscular invasion of MC-38 carcinoma cells. Furthermore, angiogenesis in the colon cancer was markedly suppressed by NK4 repetitive therapy, along with an increase in tumor apoptosis. Overall, the number of hepatic metastatic nodules was

dramatically decreased by the repeated injections of NK4-cDNA containing plasmid. This study provides an anti-tumor model where NK4 is supplemented via a hydrodynamic-based gene therapy (Wen *et al.*, 2007).

Recently, hydrodynamic gene delivery using a rapid injection of a relatively large volume of DNA solution has facilitated experimental gene therapy studies, particularly in rodents (Suda *et al.*, 2007). This method is superior to the existing delivery systems because of its simplicity, efficiency, and versatility. Hydrodynamic gene delivery is also useful for supplementation of HGF, an intrinsic repair factor, for the inhibition of, or recovery from, intractable organ diseases, such as acute renal failure (Dai *et al.*, 2002) or pulmonary airway hyper-responsiveness during asthma (Okunishi *et al.*, 2005). In these experiments, plasma HGF levels were sustained within a pharmacological range (3-30 ng/ml). Wide success in applying hydrodynamic principles to delivery of NK4- or HGF-related DNA, RNA, proteins, and synthetic compounds, into the cells in various tissues of small animals, has inspired the recent attempts at establishing a hydrodynamic procedure for clinical use.

7. Summary and perspective

NK4-related studies provided a proof-of-concept that MET signaling from stroma-derived HGF plays a pivotal role in eliciting tumor invasion and metastasis (Matsumoto & Nakamura, 2005; Nakamura *et al.*, 2010). Human genetic studies also strengthened the important role of MET activation for tumor malignancy. There is now ample evidence to demonstrate the role of MET mutations in tumor malignancy (Lengyel *et al.*, 2007; Matsumoto *et al.*, 2008a,b; Pao *et al.*, 2011). Of interest, mutation of the von-Hippel-Lindau (VHL) gene leads to renal clear cell carcinoma through constitutive MET tyrosine phosphorylation (Nakaigawa *et al.*, 2006), hence suggesting a critical role of wild-type VHL in inhibiting MET over-activation as a negative regulator.

During the progression of malignant tumors, soluble MET is producible by carcinoma cells through an ectodomain shedding cascade (Wader *et al.*, 2011). Soluble MET inhibits the HGF-MET complex and signaling transduction. Thus, MET shedding system is considered as a self-defense response that minimizes tumor metastasis. Likewise, an NK4-like fragment of the HGF α -chain can be secreted from human breast carcinoma, which inhibits MET tyrosine phosphorylation (Wright *et al.*, 2009). Thus, "endogenous" soluble MET and NK4-like variant appear to reduce HGF-MET signaling and delay tumor progression, but this response is insufficient, allowing for tumor metastasis. Thus, supplemental therapy with NK4 is a reasonable strategy to completely block tumor metastasis.

The hope is that angiogenesis inhibition might control tumor metastasis (Yancopoulos *et al.*, 1998). However, long-term use of angiogenesis inhibitors, such as VEGF inhibitor, results in hypoxia-resistance (Fischer *et al.*, 2007), possibly due to hypoxia-induced MET up-regulation by cancer (Bottaro & Liotta, 2003). NK4 is an angiogenesis inhibitor with the ability to inhibit MET activation, and discovery of this fragment opened up a new avenue for the development of freeze-and-dormancy therapy (Fig. 7). Thus, NK4 is now defined as "Malignostatin". In addition to NK4, several anti-metastatic drugs have been proposed, with a major focus on small molecules that inhibit the tyrosine kinase activity of MET; ribozyme; small-interfering RNA; anti-HGF antibodies; soluble MET; and HGF-variant decoys (Jiang *et al.*, 2005; Benvenuti & Comoglio, 2007; Eder *et al.*, 2009; Underiner *et al.*, 2010; Cecchi *et al.*, 2010). HGF-MET targeting research will shed more light on cancer biology, pathology and new technologies to overcome host death due to cancer metastasis.

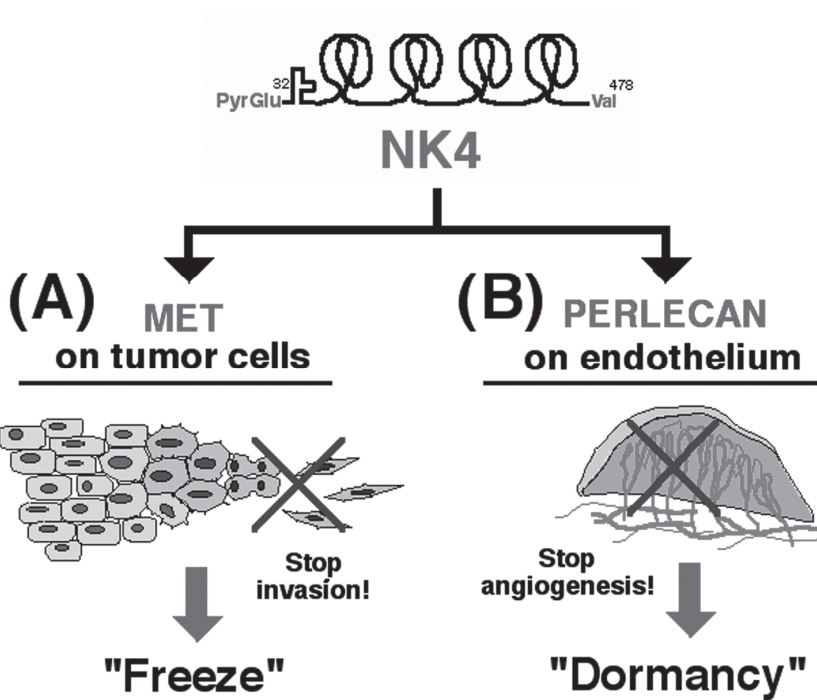


Fig. 7. Freeze-and-dormancy therapy of malignant tumors by NK4/malignostatin. NK4 blocks tumor invasion and metastasis through an inhibition of HGF-MET signals as an HGF-antagonist. Furthermore, NK4 inhibits tumor angiogenesis via a perlecan-dependent mechanism. Such a dual function of NK4 contributes to “freeze” and “dormancy” anti-cancer therapy.

8. Acknowledgement

The publication of this manuscript was supported by grants from the Ministry of Education, Science, Technology, Sports and Culture of Japan (the 21st Century global COE program to TN). We would like to thank all co-workers for the continuous studies on the roles of HGF and NK4 during cancer progression. We are also grateful to James L. McDonald (Scientific Editorial Services; Harrison, AR) for language assistance.

9. References

- Benvenuti, S. & Comoglio, P. M. (2007). The MET receptor tyrosine kinase in invasion and metastasis. *Journal of Cellular Physiology*, Vol.213, No.2, (November 2009), pp. 316-325, ISSN 0021-9541
- Beppu, K.; Uchiyama, A.; Morisaki, T.; Matsumoto, K.; Nakamura, T.; Tanaka, M. & Katano, M. (2001). Hepatocyte growth factor production by peripheral blood mononuclear

- cells of recurrent cancer patients. *Anticancer Research*, Vol.21, No.3C, (May-June 2001), pp. 2195-2200, ISSN 0250-7005.
- Bhowmick, N. A.; Chytil, A.; Plieth, D.; Gorska, A. E.; Dumont, N.; Shappell, S.; Washington, M. K.; Neilson, E. G. & Moses, H. L. (2004). TGF-beta signaling in fibroblasts modulates the oncogenic potential of adjacent epithelia. *Science*, Vol.303, No.5659, (February 2004), pp. 848-851, ISSN 0036-8075
- Birchmeier, C. & Gherardi, E. (1998). Developmental roles of HGF/SF and its receptor, the c-Met tyrosine kinase. *Trends in Cell Biology*, Vol.8, No.10, (October 1998), pp. 404-410, ISSN: 0962-8924.
- Bonamassa, B.; Hai, L. & Liu, D. (2011) Hydrodynamic gene delivery and its applications in pharmacological research. *Pharmaceutical Research*, Vol.28, No.4, (April 2011), pp. 694-701, ISSN 0724-8741
- Bottaro, D. P.; Rubin, J. S.; Falletto, D. L.; Chan, A. M.; Kmiecik, T. E.; Vande Woude, G. F. & Aaronson, S. A. (1991). Identification of the hepatocyte growth factor receptor as the c-met proto-oncogene product. *Science*, Vol.251, No.4995, (February 1991) pp. 802-804, ISSN 0036-8075
- Bottaro, D. P. & Liotta, L. (2003). Cancer: Out of air is not out of action. *Nature*, Vol.423, No.6940, (June 2003), 593-595, ISSN 0028-0836
- Bussolino, F.; Di Renzo, M. F.; Ziche, M.; Bocchietto, E.; Olivero, M.; Naldini, L.; Gaudino, G.; Tamagnone, L.; Coffey, A. & Comoglio, P. M. (1992). Hepatocyte growth factor is a potent angiogenic factor which stimulates endothelial cell motility and growth. *The Journal of Cell Biology*, Vol.119, No.3, (November 1992), pp. 629-641, ISSN 0021-9525
- Cecchi, F.; Rabe, D. C. & Bottaro, D. P. (2010). Targeting the HGF/Met signalling pathway in cancer. *European Journal of Cancer*, Vol.46, No.7, (May 2010), pp. 1260-1270, ISSN 0959-8049
- Cooper, C. S.; Park, M.; Blair, D. G.; Tainsky, M. A.; Huebner, K.; Croce, C. M. & Vande Woude, G. F. (1984). Molecular cloning of a new transforming gene from a chemically transformed human cell line. *Nature*, Vol.311, No.5981, (September 1984), pp. 29-33, ISSN 0028-0836
- Dai, C.; Yang, J. & Liu, Y. (2002). Single injection of naked plasmid encoding hepatocyte growth factor prevents cell death and ameliorates acute renal failure in mice. *Journal of the American Society of Nephrology*, Vol.13, No.2, (February 2002) pp. 411-422, ISSN 1046-6673
- Date, K.; Matsumoto, K.; Shimura, H.; Tanaka, M. & Nakamura, T. (1997). HGF/NK4 is a specific antagonist for pleiotrophic actions of hepatocyte growth factor. *FEBS Letter*, Vol.420, No.1, (December 1997), pp. 1-6, ISSN 0014-5793
- Date, K.; Matsumoto, K.; Kuba, K.; Shimura, H.; Tanaka, M. & Nakamura, T. (1998). Inhibition of tumor growth and invasion by a four-kringle antagonist (HGF/NK4) for hepatocyte growth factor. *Oncogene*, Vol.17, No.23, (December 1998), pp. 3045-3054, ISSN 0950-9232
- Davies, G.; Mason, M. D.; Martin, T. A.; Parr, C.; Watkins, G.; Lane, J.; Matsumoto, K.; Nakamura, T. & Jiang, W. G. (2003). The HGF/SF antagonist NK4 reverses fibroblast- and HGF-induced prostate tumor growth and angiogenesis in vivo. *International Journal of Cancer*, Vol.106, No.3, (September 2003), pp. 348-354, ISSN 0020-7136
- Dean, M.; Park, M.; Le Beau, M. M.; Robins, T. S.; Diaz, M. O.; Rowley, J. D.; Blair, D. G. & Vande Woude, G. F. (1985). The human met oncogene is related to the tyrosine

- kinase oncogenes. *Nature*. Vol.318, No.6044, (November-December 1985), pp. 385-388, ISSN 0028-0836
- Du, W.; Hattori, Y.; Yamada, T.; Matsumoto, K.; Nakamura, T.; Sagawa, M.; Otsuki, T.; Niikura, T.; Nukiwa, T. & Ikeda, Y. (2007). NK4, an antagonist of hepatocyte growth factor (HGF), inhibits growth of multiple myeloma cells: molecular targeting of angiogenic growth factor. *Blood*, Vol.109, No.7, (April 2007), pp. 3042-3049, ISSN 0006-4971
- Eder, J. P.; Vande Woude, G. F.; Boerner, S. A. & LoRusso, P. M. (2009). Novel therapeutic inhibitors of the c-Met signaling pathway in cancer. *Clinical Cancer Research*, Vol.15, No.7, (April 2009), pp. 2207-2214, ISSN 1078-0432
- Engelman, J. A.; Zejnullahu, K.; Mitsudomi, T.; Song, Y.; Hyland, C.; Park, J. O.; Lindeman, N.; Gale, C. M.; Zhao, X.; Christensen, J.; Kosaka, T.; Holmes, A. J.; Rogers, A. M.; Cappuzzo, F.; Mok, T.; Lee, C.; Johnson, B. E.; Cantley, L. C. & Jänne, P. A. (2007). MET amplification leads to gefitinib resistance in lung cancer by activating ERBB3 signaling. *Science*, Vol.316, No.5827, (May 2007), pp. 1039-1043, ISSN 0036-8075
- Ferlay, J.; Shin, H. R.; Bray, F.; Forman, D.; Mathers, C. & Parkin, D. M. (2010). Estimates of worldwide burden of cancer in 2008: GLOBOCAN 2008. *International Journal of Cancer*, Vol.127, No.12, (December 2010), pp. 2893-2917, ISSN 0020-7136
- Fischer, C.; Jonckx, B.; Mazzone, M.; Zacchigna, S.; Loges, S.; Pattarini, L.; Chorianopoulos, E.; Liesenborghs, L.; Koch, M.; De Mol, M.; Autiero, M.; Wyns, S.; Plaisance, S.; Moons, L.; van Rooijen, N.; Giacca, M.; Stassen, J. M.; Dewerchin, M.; Collen, D. & Carmeliet, P. (2007). Anti-PlGF inhibits growth of VEGF(R)-inhibitor-resistant tumors without affecting healthy vessels. *Cell*, Vol.131, No.3, (November 2007), pp. 463-475, ISSN 0092-8674
- Franco, M.; Muratori, C.; Corso, S.; Tenaglia, E.; Bertotti, A.; Capparuccia, L.; Trusolino, L.; Comoglio, P. M. & Tamagnone, L. (2010). The tetraspanin CD151 is required for Met-dependent signaling and tumor cell growth. *Journal of Biological Chemistry*, Vol.285, No.50, (December 2010), pp. 38756-38764, ISSN 0021-9258
- Geiger, T. R. & Peeper, D. S. (2009). Metastasis mechanisms. *Biochimica et Biophysica Acta*, Vol.1796, No.2, (August 2009), pp. 293-308, ISSN 0006-3002
- Grugan, K. D.; Miller, C. G.; Yao, Y.; Michaylira, C. Z.; Ohashi, S.; Klein-Szanto, A. J.; Diehl, J. A.; Herlyn, M.; Han, M.; Nakagawa, H. & Rustgi, A. K. (2010). Fibroblast-secreted hepatocyte growth factor plays a functional role in esophageal squamous cell carcinoma invasion. *Proceeding of National Academy of Sciences*, Vol.107, No.24, (June 2010), pp. 11026-11031, ISSN 0027-8424
- Hasina, R.; Matsumoto, K.; Matsumoto-Taniura, N.; Kato, I.; Sakuda, M. & Nakamura, T. (1999). Autocrine and paracrine motility factors and their involvement in invasiveness in a human oral carcinoma cell line. *British Journal of Cancer*, Vol.80, No.11, (August 1999), pp. 1708-1717, ISSN 0007-0920
- Higuchi, O.; Mizuno, K.; Vande Woude, G. F. & Nakamura, T. (1992). Expression of c-met proto-oncogene in COS cells induces the signal transducing high-affinity receptor for hepatocyte growth factor. *FEBS Letter*, Vol.301, No.3, (April 1999), pp. 282-286, ISSN 0014-5793
- Hiscox, S. & Jiang, W. G. (1999). Hepatocyte growth factor/scatter factor disrupts epithelial tumour cell-cell adhesion: involvement of beta-catenin. *Anticancer Research*, Vol.19, No.1A, (January February, 1999), pp. 509-517, ISSN 0250-7005.
- Hiscox, S.; Parr, C.; Nakamura, T.; Matsumoto, K.; Mansel, R. E. & Jiang, W. G. (2000). Inhibition of HGF/SF-induced breast cancer cell motility and invasion by the

- HGF/SF variant, NK4. *Breast Cancer Research and Treatment*, Vol.59, No.3, (February 2000), pp. 245-254, ISSN 0167-6806
- Hirao, S.; Yamada, Y.; Koyama, F.; Fujimoto, H.; Takahama, Y.; Ueno, M.; Kamada, K.; Mizuno, T.; Maemondo, M.; Nukiwa, T.; Matsumoto, K.; Nakamura, T. & Nakajima, Y. (2002). Tumor suppression effect using NK4, a molecule acting as an antagonist of HGF, on human gastric carcinomas. *Cancer Gene Therapy*, Vol.9, No.8, (August 2002), pp. 700-707, ISSN 0929-1903
- Jiang, W. G.; Martin, T. A.; Matsumoto, K.; Nakamura, T. & Mansel, R. E. (1999a). Hepatocyte growth factor/scatter factor decreases the expression of occludin and transendothelial resistance (TER) and increases paracellular permeability in human vascular endothelial cells. *Journal of Cellular Physiology*, Vol.181, No.2, (November 1999), pp. 319-329, ISSN 0021-9541
- Jiang, W. G.; Hiscox, S. E.; Parr, C.; Martin, T. A.; Matsumoto, K.; Nakamura, T. & Mansel, R. E. (1999b) Antagonistic effect of NK4, a novel hepatocyte growth factor variant, on in vitro angiogenesis of human vascular endothelial cells. *Clinical Cancer Research*, Vol.5, No.11, (November 1999), pp. 3695-3703, ISSN 1078-0432
- Jiang, Y.; Xu, W.; Lu, J.; He, F. & Yang, X. (2001). Invasiveness of hepatocellular carcinoma cell lines: contribution of hepatocyte growth factor, c-met, and transcription factor Ets-1. *Biochemical and Biophysical Research Communications*, Vol.286, No.5, (September, 2001), pp. 1123-1130, ISSN 0006-291X
- Jiang, W. G.; Martin, T. A.; Parr, C.; Davies, G.; Matsumoto, K. & Nakamura, T. (2005). Hepatocyte growth factor, its receptor, and their potential value in cancer therapies. *Critical Reviews in Oncology/Hematology*, Vol.53, No.1, (January 2005), pp. 35-69, ISSN 1040-8428
- Kajiya, K.; Hirakawa, S.; Ma, B.; Drinnenberg, I. & Detmar, M. (2005). Hepatocyte growth factor promotes lymphatic vessel formation and function. *EMBO Journal*, Vol.24, No.16, (August 2005), pp. 2885-2895, ISSN 0261-4189
- Kanayama, S.; Yamada, Y.; Kawaguchi, R.; Tsuji, Y.; Haruta, S. & Kobayashi, H. (2008). Hepatocyte growth factor induces anoikis resistance by up-regulation of cyclooxygenase-2 expression in uterine endometrial cancer cells. *Oncology Reports*, Vol.19, No.1, (January 2008), pp. 117-122, ISSN 1021-335X
- Kimura, T.; Sakisaka, T.; Baba, T.; Yamada, T. & Takai Y. (2006). Involvement of the Ras-Ras-activated Rab5 guanine nucleotide exchange factor RIN2-Rab5 pathway in the hepatocyte growth factor-induced endocytosis of E-cadherin. *Journal of Biological Chemistry*, Vol.281, No.15, (April 2006), pp. 10598-10609, ISSN 0021-9258
- Kishi, Y.; Kuba, K.; Nakamura, T.; Wen, J.; Suzuki, Y.; Mizuno, S.; Nukiwa, T.; Matsumoto, K. & Nakamura, T. (2009). Systemic NK4 gene therapy inhibits tumor growth and metastasis of melanoma and lung carcinoma in syngeneic mouse tumor models. *Cancer Science*, Vol.100, No.7, (July 2009) pp. 1351-1358, ISSN 1347-9032
- Kuba, K.; Matsumoto, K.; Date, K.; Shimura, H.; Tanaka, M. & Nakamura, T. (2000) HGF/NK4, a four-kringle antagonist of hepatocyte growth factor, is an angiogenesis inhibitor that suppresses tumor growth and metastasis in mice. *Cancer Research*, Vol.60, No.23, (December 2000), pp. 6737-6743, ISSN 0008-5472
- Kubota, T.; Taiyoh, H.; Matsumura, A.; Murayama, Y.; Ichikawa, D.; Okamoto, K.; Fujiwara, H.; Ikoma, H.; Nakanishi, M.; Kikuchi, S.; Sakakura, C.; Ochiai, T.; Kokuba, Y.; Taniguchi, H.; Sonoyama, T.; Matsumoto, K.; Nakamura, T. & Otsuji. E. (2009a). NK4, an HGF antagonist, prevents hematogenous pulmonary metastasis by

- inhibiting adhesion of CT26 cells to endothelial cells. *Clinical and Experimental Metastasis*, Vol.26, No.5, (May 2009), pp. 447-456, ISSN 0262-0898
- Kubota, T.; Taiyoh, H.; Matsumura, A.; Murayama, Y.; Ichikawa, D.; Okamoto, K.; Fujiwara, H.; Ikoma, H.; Nakanishi, M.; Kikuchi, S.; Ochiai, T.; Sakakura, C.; Kokuba, Y.; Sonoyama, T.; Suzuki, Y.; Matsumoto, K.; Nakamura, T. & Otsuji, E. (2009b). Gene transfer of NK4, an angiogenesis inhibitor, induces CT26 tumor regression via tumor-specific T lymphocyte activation. *International Journal of Cancer*, Vol.125, No.12, (December 2009), pp. 2879-2886, ISSN 0020-7136
- Konishi, T.; Takehara, T.; Tsuji, T.; Ohsato, K.; Matsumoto, K. & Nakamura, T. (1991). Scatter factor from human embryonic lung fibroblasts is probably identical to hepatocyte growth factor. *Biochemical and Biophysical Research Communications*, Vol.180, No.2, (October, 1991), pp. 765-773, ISSN 0006-291X
- Laterra, J.; Nam, M.; Rosen, E.; Rao, J. S.; Lamszus, K.; Goldberg, I. D. & Johnston, P. (1997). Scatter factor/hepatocyte growth factor gene transfer enhances glioma growth and angiogenesis in vivo. *Laboratory Investigation*, Vol.76, No.4, (April 1997), pp. 565-577, ISSN 0023-6837
- Lengyel, E.; Sawada, K. & Salgia, R. (2007). Tyrosine kinase mutations in human cancer. *Current Molecular Medicine*, Vol.7, No.1, (February 2007), pp. 77-84, ISSN 1566-5240
- Li, H.; Shimura, H.; Aoki, Y.; Date, K.; Matsumoto, K.; Nakamura, T. & Tanaka, M. (1998). Hepatocyte growth factor stimulates the invasion of gallbladder carcinoma cell lines in vitro. *Clinical and Experimental Metastasis*, Vol.16, No.1, (January 1998), pp. 74-82, ISSN 0262-0898
- Maehara, N.; Matsumoto, K.; Kuba, K.; Mizumoto, K.; Tanaka, M. & Nakamura, T. (2001). NK4, a four-kringle antagonist of HGF, inhibits spreading and invasion of human pancreatic cancer cells. *British Journal of Cancer*, Vol.84, No.6, (March 2001), pp. 864-873, ISSN 0007-0920
- Matsumoto, K.; Tajima, H.; Okazaki, H. & Nakamura, T. (1992). Negative regulation of hepatocyte growth factor gene expression in human lung fibroblasts and leukemic cells by transforming growth factor-beta1 and glucocorticoids. *Journal of Biological Chemistry*, Vol.267, No.35, (December 1992), pp. 24917-24920, ISSN 0021-9258
- Matsumoto, K.; Matsumoto, K.; Nakamura, T. & Kramer, R. H. (1994). Hepatocyte growth factor/scatter factor induces tyrosine phosphorylation of focal adhesion kinase (p125FAK) and promotes migration and invasion by oral squamous cell carcinoma cells. *Journal of Biological Chemistry*, Vol.269, No.50, (December 1994), pp. 31807-31813, ISSN 0021-9258
- Matsumoto, K.; Date, K.; Shimura, H. & Nakamura, T. (1996a). Acquisition of invasive phenotype in gallbladder cancer cells via mutual interaction of stromal fibroblasts and cancer cells as mediated by hepatocyte growth factor. *Japanese Journal of Cancer Research*, Vol.87, No.7, (July 1996), pp. 702-710, ISSN 0910-5050
- Matsumoto, K.; Date, K.; Ohmichi, H. & Nakamura, T. (1996b). Hepatocyte growth factor in lung morphogenesis and tumor invasion: role as a mediator in epithelium-mesenchyme and tumor-stroma interactions. *Cancer Chemotherapy and Pharmacology*, Vol.38 (Supplement), pp. S42-S47, ISSN 0344-5704
- Matsumoto, K.; Kataoka, H.; Date, K. & Nakamura, T. (1998). Cooperative interaction between alpha- and beta-chains of hepatocyte growth factor on c-Met receptor confers ligand-induced receptor tyrosine phosphorylation and multiple biological responses. *Journal of Biological Chemistry*, Vol.273, No.36, (September 1998), pp. 22913-22920, ISSN 0021-9258

- Matsumoto-Taniura, N.; Matsumoto, K. & Nakamura, T. (1999). Prostaglandin production in mouse mammary tumour cells confers invasive growth potential by inducing hepatocyte growth factor in stromal fibroblasts. *British Journal of Cancer*, Vol.81, No.2, (September 1999), pp. 194-202, ISSN 0007-0920
- Matsumoto, K. & Nakamura, T. (2003). NK4 (HGF-antagonist/angiogenesis inhibitor) in cancer biology and therapeutics. *Cancer Science*, Vol.94, No.4, (April 2003), pp. 321-327, ISSN 1347-9032
- Matsumoto, K. & Nakamura, T. (2005). Mechanisms and significance of bifunctional NK4 in cancer treatment. *Biochemical and Biophysical Research Communications*, Vol.333, No.2, (July 2005), pp. 316-327, ISSN 0006-291X
- Matsumoto, K. & Nakamura, T. (2006). Hepatocyte growth factor and the Met system as a mediator of tumor-stromal interactions. *International Journal of Cancer*, Vol.119, No.3, (August, 2006), pp. 477-483, ISSN 0020-7136
- Matsumoto, K. & Nakamura, T. (2008a). NK4 gene therapy targeting HGF-Met and angiogenesis. *Frontiers in Bioscience*, Vol.13, No.1, (January 2008), pp. 1943-1951, ISSN 1093-9946
- Matsumoto, K.; Nakamura, T.; Sakai, K. & Nakamura, T. (2008b). Hepatocyte growth factor and Met in tumor biology and therapeutic approach with NK4. *Proteomics*, Vol.8, No.16, (August 2008), pp. 3360-3370, ISSN 1615-9861
- Matsumoto, G.; Omi, Y.; Lee, U.; Kubota, E. & Tabata, Y. (2011). NK4 gene therapy combined with cisplatin inhibits tumour growth and metastasis of squamous cell carcinoma. *Anticancer Research*, Vol.31, No.1, (January 2011), pp. 105-111, ISSN 0250-7005
- Miura, H.; Nishimura, K.; Tsujimura, A.; Matsumiya, K.; Matsumoto, K.; Nakamura, T. & Okuyama, A. (2001). Effects of hepatocyte growth factor on E-cadherin-mediated cell-cell adhesion in DU145 prostate cancer cells. *Urology*, Vol.58, No.6, (December 2001), pp. 1064-1069, ISSN 0090-4295
- Mueller, M. M. & Fusenig, N. E. (2004). Friends or foes - bipolar effects of the tumour stroma in cancer. *Nature Reviews Cancer*, Vol.4, No.11, (November 2004), pp. 839-849, ISSN 1474-175X
- Nakabayashi, M.; Morishita, R.; Nakagami, H.; Kuba, K.; Matsumoto, K.; Nakamura, T.; Tano, Y. & Kaneda, Y. (2003). HGF/NK4 inhibited VEGF-induced angiogenesis in in vitro cultured endothelial cells and in vivo rabbit model. *Diabetologia*, Vol.46, No.1, (January 2003), pp. 115-123, ISSN 0012-186X
- Nagakawa, O.; Murakami, K.; Yamaura, T.; Fujiuchi, Y.; Murata, J.; Fuse, H. & Saiki, I. (2000). Expression of membrane-type 1 matrix metalloproteinase (MT1-MMP) on prostate cancer cell lines. *Cancer Letter*, Vol.155, No.2, (July 2000), pp. 173-179, ISSN 0304-3835
- Nakaigawa, N.; Yao, M.; Baba, M.; Kato, S.; Kishida, T.; Hattori, K.; Nagashima, Y. & Kubota, Y. (2006). Inactivation of von Hippel-Lindau gene induces constitutive phosphorylation of MET protein in clear cell renal carcinoma. *Cancer Research*, Vol.66, No.7, (April 2006), pp. 3699-3705, ISSN 0008-5472
- Nakamura, T.; Nawa, K. & Ichihara, A. (1984). Partial purification and characterization of hepatocyte growth factor from serum of hepatectomized rats. *Biochemical and Biophysical Research Communications*, Vol.122, No.3, (August 1984), pp. 1450-1459, ISSN 0006-291X

- Nakamura, T.; Nishizawa, T.; Hagiya, M.; Seki, T.; Shimonishi, M.; Sugimura, A.; Tashiro, K. & Shimizu, S. (1989). Molecular cloning and expression of human hepatocyte growth factor. *Nature*, Vol.342, No.6248, (November 1989), pp. 440-443, ISSN 0028-0836
- Nakamura, T. (1991). Structure and function of hepatocyte growth factor. *Progress in Growth Factor Research*, Vol.3, No.1. pp. 67-85, ISSN: 0955-2235
- Nakamura, T.; Matsumoto, K.; Kiritoshi, A.; Tano, Y. & Nakamura, T. (1997) Induction of hepatocyte growth factor in fibroblasts by tumor-derived factors affects invasive growth of tumor cells: in vitro analysis of tumor-stromal interactions. *Cancer Research*, Vol.57, No.15, (August 1997), pp. 3305-3313, ISSN 0008-5472
- Nakamura, T. & Mizuno, S. (2010). The discovery of hepatocyte growth factor (HGF) and its significance for cell biology, life sciences and clinical medicine. *Proceedings of the Japan Academy Series B*, Vol.86, No.6, (June 2010), pp. 588-610 (2010), ISSN 0386-2208
- Nakamura, T.; Sakai, K.; Nakamura, T. & Matsumoto, K. (2010). Anti-cancer approach with NK4: Bivalent action and mechanisms. *Anti-Cancer Agents in Medicinal Chemistry*, Vol.10, No.1, (January 2010), pp. 36-46, ISSN 1871-5206
- Nakamura, Y.; Morishita, R.; Higaki, J.; Kida, I.; Aoki, M.; Moriguchi, A.; Yamada, K.; Hayashi, S.; Yo, Y.; Nakano, H.; Matsumoto, K.; Nakamura, T. & Ogihara, T. (1996). Hepatocyte growth factor is a novel member of the endothelium-specific growth factors: additive stimulatory effect of hepatocyte growth factor with basic fibroblast growth factor but not with vascular endothelial growth factor. *Journal of Hypertension*, Vol.14, No.9, (September 1996), pp. 1067-1072, ISSN 0263-6352
- Ohuchida, K.; Mizumoto, K.; Murakami, M.; Qian, L. W.; Sato, N.; Nagai, E.; Matsumoto, K.; Nakamura, T. & Tanaka, M. (2004) Radiation to stromal fibroblasts increases invasiveness of pancreatic cancer cells through tumor-stromal interactions. *Cancer Research*, Vol.64, No.9, (May 2004), pp. 3215-3222, ISSN 0008-5472
- Okamoto, W.; Okamoto, I.; Tanaka, K.; Hatashita, E.; Yamada, Y.; Kuwata, K.; Yamaguchi, H.; Arao, T.; Nishio, K.; Fukuoka, M.; Jänne, P. A. & Nakagawa, K. (2010). TAK-701, a humanized monoclonal antibody to hepatocyte growth factor, reverses gefitinib resistance induced by tumor-derived HGF in non-small cell lung cancer with an EGFR mutation. *Molecular Cancer Therapeutics*, 2010 Oct; Vol.9, No.10, (October 2010), pp. 2785-92, ISSN 1535-7163
- Okunishi, K.; Dohi, M.; Nakagome, K.; Tanaka, R.; Mizuno, S.; Matsumoto, K.; Miyazaki, J.; Nakamura, T. & Yamamoto, K. (2005) A novel role of hepatocyte growth factor as an immune regulator through suppressing dendritic cell function. *The Journal of Immunology*, Vol.175, No.7, (October 2005), pp. 4745-4753, ISSN 0022-1767
- Olumi, A. F.; Grossfeld, G. D.; Hayward, S. W.; Carroll, P. R.; Tlsty, T.D. & Cunha, G. R. (1999). Carcinoma associated fibroblasts direct tumor progression of initiated human prostatic epithelium. *Cancer Research*, Vol.59, No.19, (October 1999), pp. 5002-5011, ISSN 0008-5472
- Osada, S.; Kanematsu, M.; Imai, H. & Goshima, S. (2008). Clinical significance of serum HGF and c-Met expression in tumor tissue for evaluation of properties and treatment of hepatocellular carcinoma. *Hepatology*, Vol.55, No.82-83, (March-April 2008), pp. 544-549, ISSN 0172-6390
- Pai, R.; Nakamura, T.; Moon, W. S. & Tarnawski, A. S. (2003). Prostaglandins promote colon cancer cell invasion; signaling by cross-talk between two distinct growth factor receptors. *FASEB Journal*, Vol.17, No.12, (September 2003), pp. 1640-1647, ISSN 0892-6638

- Parr, C.; Hiscox, S.; Nakamura, T.; Matsumoto, K. & Jiang, W. G. (2000). NK4, a new HGF/SF variant, is an antagonist to the influence of HGF/SF on the motility and invasion of colon cancer cells. *International Journal of Cancer*, Vol.85, No.4, (February 2000), pp. 563-570, ISSN 0020-7136
- Parr, C.; Davies, G.; Nakamura, T.; Matsumoto, K.; Mason, M. D. & Jiang, W. G. (2001). The HGF/SF-induced phosphorylation of paxillin, matrix adhesion, and invasion of prostate cancer cells were suppressed by NK4, an HGF/SF variant. *Biochemical and Biophysical Research Communications*, Vol.285, No.5, (August 2010), pp. 1330-1337, ISSN 0006-291X
- Pao, W. & Girard, N. (2011). New driver mutations in non-small-cell lung cancer. *The Lancet Oncology*, Vol.12, No.2, (February 2011), pp. 175-180, ISSN 1470-2045
- Qian, L. W.; Mizumoto, K.; Inadome, N.; Nagai, E.; Sato, N.; Matsumoto, K.; Nakamura, T. & Tanaka, M. (2003). Radiation stimulates HGF receptor/c-Met expression that leads to amplifying cellular response to HGF stimulation via upregulated receptor tyrosine phosphorylation and MAP kinase activity in pancreatic cancer cells. *International Journal of Cancer*, Vol.104, No.5, (May 2003), pp. 542-549, ISSN 0020-7136
- Royal, I.; Lamarche-Vane, N.; Lamorte, L.; Kaibuchi, K. & Park, M. (2000). Activation of cdc42, rac, PAK, and rho-kinase in response to hepatocyte growth factor differentially regulates epithelial cell colony spreading and dissociation. *Molecular Biology of the Cell*, Vol.11, No.5, (May 2000), pp. 1709-1725, ISSN 1059-1524
- Rubin, J. S.; Bottaro, D. P. & Aaronson, S. A. (1993). Hepatocyte growth factor/scatter factor and its receptor, the c-met proto-oncogene product. *Biochimica et Biophysica Acta*, Vol.1155, No.3, (December 1993), pp. 357-371, ISSN 0006-3002
- Saito, Y.; Nakagami, H.; Morishita, R.; Takami, Y.; Kikuchi, Y.; Hayashi, H.; Nishikawa, T.; Tamai, K.; Azuma, N.; Sasajima, T. & Kaneda, Y. (2006). Transfection of human hepatocyte growth factor gene ameliorates secondary lymphedema via promotion of lymphangiogenesis. *Circulation*, Vol.114, No.11, (September 2006), pp. 1177-1184, ISSN 0009-7322
- Sakai, K.; Nakamura, T.; Matsumoto, K. & Nakamura, T. (2009). Angioinhibitory action of NK4 involves impaired extracellular assembly of fibronectin mediated by perlecan-NK4 association. *Journal of Biological Chemistry*, Vol.284, No.33, (August 2009), pp. 22491-22499, ISSN 0021-9258
- Suda, T. & Liu, D. (2007). Hydrodynamic gene delivery: its principles and applications. *Molecular Therapy*, Vol.15, No.12, (December 2007), pp. 2063-2069, ISSN 1525-0016
- Tomioka, D.; Maehara, N.; Kuba, K.; Mizumoto, K.; Tanaka, M.; Matsumoto, K. & Nakamura, T. (2001). Inhibition of growth, invasion, and metastasis of human pancreatic carcinoma cells by NK4 in an orthotopic mouse model. *Cancer Research*, Vol.61, No.20, (October 2001), pp. 7518-7524, ISSN 0008-5472
- Underiner, T. L.; Herbertz, T. & Miknyoczki, S. J. (2010) Discovery of small molecule c-Met inhibitors: Evolution and profiles of clinical candidates. *Anti-Cancer Agents in Medicinal Chemistry*, Vol.10, No.1, (January 2010), pp. 7-27, ISSN 1871-5206
- Wader, K.; Fagerli, U.; Holt, R.; Børset, M.; Sundan, A. & Waage, A. (2011). Soluble c-Met in serum of multiple myeloma patients: correlation with clinical parameters. *European Journal of Haematology*, in press, ISSN 0902-4441
- Wang, R.; Zhang, J.; Chen, S.; Lu, M.; Luo, X.; Yao, S.; Liu, S.; Qin, Y. & Chen, H. (2011) Tumor-associated macrophages provide a suitable microenvironment for non-small lung cancer invasion and progression. *Lung Cancer*, in press, ISSN 0169-5002

- Watabe, M.; Matsumoto, K.; Nakamura, T. & Takeichi, M. (1993). Effect of hepatocyte growth factor on cadherin-mediated cell-cell adhesion. *Cell Structure and Function*, Vol.18, No.2, (April 1993), pp. 117-1124, ISSN1347-3700
- Wislez, M.; Rabbe, N.; Marchal, J.; Milleron, B.; Crestani, B.; Mayaud, C.; Antoine, M.; Soler, P. & Cadranel, J. (2003). Hepatocyte growth factor production by neutrophils infiltrating bronchioloalveolar subtype pulmonary adenocarcinoma: role in tumor progression and death. *Cancer Research*, Vol.63, No.6, (March 2003), pp. 1405-1412, ISSN 0008-5472
- Wu, C. W.; Chi, C. W.; Su, T. L.; Liu, T. Y.; Lui, W. Y. & P'eng, F. K. (1998). Serum hepatocyte growth factor level associate with gastric cancer progression. *Anticancer Research*, Vol.18, No.5B, (September-October 1998), pp. 3657-3659, ISSN 0250-7005
- Weidner, K. M.; Arakaki, N.; Hartmann, G.; Vandekerckhove, J.; Weingart, S.; Rieder, H.; et al. (1991). Evidence for the identity of human scatter factor and human hepatocyte growth factor. *Proceeding of National Academy Sciences*, Vol.88, No.16, (August 1991), pp. 7001-7005, ISSN 0027-8424
- Wen, J.; Matsumoto, K.; Taniura, N.; Tomioka, D. & Nakamura, T. (2004). Hepatic gene expression of NK4, an HGF-antagonist/angiogenesis inhibitor, suppresses liver metastasis and invasive growth of colon cancer in mice. *Cancer Gene Therapy*, Vol.11, No.6, (June 2004), pp. 419-430, ISSN 0929-1903
- Wen, J.; Matsumoto, K.; Taniura, N.; Tomioka, D. & Nakamura, T. (2007). Inhibition of colon cancer growth and metastasis by NK4 gene repetitive delivery in mice. *Biochemical and Biophysical Research Communications*, Vol.358, No.1, (June 2007), pp. 117-123, ISSN 0006-291X
- Wright, T. G.; Singh, V. K.; Li, J. J.; Foley, J. H.; Miller, F.; Jia, Z. & Elliott, B. E. (2009). Increased production and secretion of HGF alpha-chain and an antagonistic HGF fragment in a human breast cancer progression model. *International Journal of Cancer*, Vol.125, No.5, (September 2009), pp. 1004-1015, ISSN 0020-7136
- Yancopoulos, G. D.; Klagsbrun, M. & Folkman, J. (1998). Vasculogenesis, angiogenesis, and growth factors: ephrins enter the fray at the border. *Cell*, Vol.93, No.5, (May 1998), pp. 661-664, ISSN: 0092-8674
- Yano, S.; Wang, W.; Li, Q.; Matsumoto, K.; Sakurama, H.; Nakamura, T.; Ogino, H.; Kakiuchi, S.; Hanibuchi, M.; Nishioka, Y.; Uehara, H.; Mitsudomi, T.; Yatabe, Y.; Nakamura, T. & Sone, S. (2008). Hepatocyte growth factor induces gefitinib resistance of lung adenocarcinoma with epidermal growth factor receptor-activating mutations. *Cancer Research*, Vol.68, No.22, (November 2008), pp. 9479-9487, ISSN 0008-5472
- Yoshinaga, Y.; Matsuno, Y.; Fujita, S.; Nakamura, T.; Kikuchi, M.; Shimosato, Y. & Hirohashi, S. (1993). Immunohistochemical detection of hepatocyte growth factor/scatter factor in human cancerous and inflammatory lesions of various organs. *Japanese Journal of Cancer Research*, Vol.84, No.11, (November 1993), pp. 1150-1158, ISSN 0910-5050
- Zarnegar, R. & Michalopoulos, G. K. (1995). The many faces of hepatocyte growth factor: from hepatopoiesis to hematopoiesis. *The Journal of Cell Biology*, Vol.129, No.5, (June 1995), pp. 1177-1180, ISSN 0021-9525
- Zeng, Q.; Chen, S.; You, Z.; Yang, F.; Carey, T. E.; Saims, D. & Wang, C. Y. (2002). Hepatocyte growth factor inhibits anoikis in head and neck squamous cell carcinoma cells by activation of ERK and Akt signaling independent of NFkappa B. *Journal of Biological Chemistry*, Vol.277, No.28, (July 2002), pp. 25203-25208, ISSN 0021-9258

Part 3

Detailed Experimental Analyses of Fluids and Flows

Microrheology of Complex Fluids

Laura J. Bonales, Armando Maestro, Ramón G. Rubio and Francisco Ortega
*Departamento de Química Física I, Facultad de Química,
Universidad Complutense, Madrid
Spain*

1. Introduction

Many of the diverse material properties of soft materials (polymer solutions, gels, filamentous proteins in cells, etc.) stem from their complex structures and dynamics with multiple characteristic length and time scales. A wide variety of technologies, from paints to foods, from oil recovery to processing of plastics, all heavily rely on the understanding of how complex fluids flow (Larson, 1999).

Rheological measurements on complex materials reveal viscoelastic responses which depend on the time scale at which the sample is probed. In order to characterize the rheological response one usually measures the shear or the Young modulus as a function of frequency by applying a small oscillatory strain of frequency ω . Typically, commercial rheometers probe frequencies up to tens of Hz, the upper range being limited by the onset of inertial effects, when the oscillatory strain wave decays appreciably before propagating throughout the entire sample. If the strain amplitude is small, the structure is not significantly deformed and the material remains in equilibrium; in this case the affine deformation of the material controls the measured stress, and the time-dependent stress is linearly proportional to the strain (Riande et al., 2000).

Even though standard rheological measurements have been very useful in characterizing soft materials and complex fluids (e.g. colloidal suspensions, polymer solutions and gels, emulsions, and surfactant solutions), they are not always well suited for all systems because milliliter samples are needed thus precluding the study of rare or precious materials, including many biological samples that are difficult to obtain in large quantities. Moreover, conventional rheometers provide an average measurement of the bulk response, and do not allow for local measurements in inhomogeneous systems. To address these issues, a new methodology, microrheology, has emerged that allows to probe the material response on micrometer length scales with microliter sample volumes. Microrheology does not correspond to a specific experimental technique, but rather a number of approaches that attempt to overcome some limitations of traditional bulk rheology (Squires & Mason, 2010; Wilson & Poon, 2011). Advantages over macrorheology include a significantly higher range of frequencies available without time-temperature superposition (Riande et al., 2000), the capability of measuring material inhomogeneities that are inaccessible to macrorheological methods, and rapid thermal and chemical homogenization that allow the transient rheology of evolving systems to be studied (Ou-Yang & Wei, 2010). Microrheology methods typically use embedded micron-sized probes to locally deform the sample, thus allowing one to use this type of rheology on very small volumes, of the order of a microliter. Macro-

and microrheology probe different aspects of the material: the former makes measurements over extremely long (macroscopic) length scales using a viscometric flow field, whereas the latter effectively measures material properties on the scale of the probe itself (Squires & Mason, 2010; Breedveld & Pine, 2003). As the probe increases in size, one might expect that micro- and macrorheology would converge, however, as it has been suggested, it is possible that macro- and microrheology techniques do not probe exactly the same physical properties because - even in the continuum (large probe) limit - one experiment uses a viscometric flow whereas the other does not (Kahir & Brady, 2005; Lee et al., 2010; Schmidt et al., 2000; Oppong & de Bruyn, 2010).

One can distinguish two main families of microrheological experiments: One type of experiments focuses on the object itself; for example, the study of motor proteins aims at understanding the mechanical motions of the protein associated with enzymatic activities on the molecular level (Ou-Yang & Wei, 2010). The other type of experiment aims at understanding the local environment of the probe by observing changes in its random movements (Crocker & Grier, 1996; MacKintosh & Schmidt, 1999). Fundamentally different from relaxation kinetics, microrheology measures spontaneous thermal fluctuations without introducing major external perturbations into the systems being investigated. Other well-established methods in this family are dynamic light scattering (Dasgupta et al., 2002; Alexander & Dalgleish, 2007; Tassieri et al. 2010), and fluorescence correlation spectroscopy (Borsali & Pecora, 2008; Wöll et al., 2009). With recent advancement in spatial and temporal resolution to subnanometer and submillisecond, particle tracking experiments are now applicable to study of macromolecules (Pan et al., 2009) and intracellular components such as cytoskeletal networks (Cicuta & Donald, 2007). Detailed descriptions of the methods and applications of microrheology to the study of bulk systems have been given in review articles published in recent years (Crocker & Grier 1996; MacKintosh & Schmidt, 1999; Mukhopadhyay & Granick, 2001; Waigh, 2005; Gardel et al., 2005; Cicuta & Donald, 2007).

Interfaces play a dominant role in the behavior of many complex fluids. Interfacial rheology has been found to be a key factor in the stability of foams and emulsions, compatibilization of polymer blends, flotation technology, fusion of vesicles, etc. (Langevin, 2000). Also, proteins, lipids, phase-separated domains, and other membrane-bound objects diffuse in the plane of an interface (Cicuta et al., 2007). Particle-laden interfaces have attracted much attention in recent years because of the tendency of colloidal particles to become (almost irreversibly) trapped at interfaces and their behavior once there has led to their use in a wide variety of systems including drug delivery, stabilization of foams and emulsions, froth, flotation, or ice cream production. There still is a need to understand the colloidal interactions to have control over the structure and therefore the properties of the particle assemblies formed, specially because it has been pointed out that the interactions of the particles at interfaces are far more complex than in the bulk (Binks & Horozov, 2006; Bonales et al., 2011). In recent years books and reviews of particles at liquid interfaces have been published (Kralchewski & Nagayama, 2001). The dynamic properties of particle-laden interfaces are strongly influenced by direct interparticle forces (capillary, steric, electrostatic, van der Waals, etc.) and complicated hydrodynamic interactions mediated by the surrounding fluid. At macroscopic scales, the rheological properties of particle-laden fluid interfaces can be viewed as those of a liquid-liquid interface with some effective surface viscoelastic properties described by effective shear and compressional complex viscoelastic moduli.

A significant fact is that for the simplest fluid-fluid interface, different dynamic modes have to be taken into account: the capillary (out of plane) mode, and the in-plane mode, which

contains dilational (or extensional) and shear contributions. For more complex interfaces, such as thicker ones, other dynamic modes (bending, splaying) have to be considered (Miller & Liggieri, 2009). Moreover, the coupling of the abovementioned modes with adsorption/desorption kinetics may be very relevant for interfaces that contain soluble or partially soluble surfactants, polymers or proteins (Miller & Liggieri, 2009; Muñoz et al., 2000; Díez-Pascual et al. 2007). In the case of surface shear rheology, most of the information available has been obtained using macroscopic interfacial rheometers which in many cases work at low Boussinesq numbers (Barentin et al., 2000; Gavranovic et. al., 2005; Miller & Liggieri, 2009; Maestro et al., 2011.a). Microrheology has been foreseen as a powerful method to study the dynamics of interfaces. In spite that the measurement of diffusion coefficients of particles attached to the interface is relatively straightforward with modern microrheological techniques, many authors have relied on hydrodynamic models of the viscoelastic surroundings traced by the particles in order to obtain variables such as interfacial elasticity or shear viscosity. The more complex the structure of the interface the stronger are the assumptions of the model, and therefore it is more difficult to check their validity. In the present work we will briefly review modern microrheology experimental techniques, and some of the recent results obtained for bulk and interfacial systems. Finally, we will summarize the theoretical models available for calculating the shear microviscosity of fluid monolayers from particle tracking experiments, and discuss the results for some systems.

2. Experimental techniques

For studying the viscoelasticity of the probe environment there are two broad types of experimental methods: active methods, which involve probe manipulation, and passive methods, that rely on thermal fluctuations to induce motion of the probes. Because thermal driving force is small, no sample deformation occurs that exceeds equilibrium thermal fluctuations. This virtually guarantees that only the linear viscoelastic response of the embedding medium is probed (Waigh, 2005). On the contrary, active methods allow the nonlinear response to be inferred from the relationship between driving force and probe velocity, in such cases the microstructure itself can be deformed significantly so that the material response differs from the linear case (Squires, 2008). As a consequence, passive techniques are typically more useful for measuring low values of predominantly viscous moduli, whereas active techniques can extend the measurable range to samples with significant elasticity modulus. Figure 1 shows the typical ranges of frequencies and shear moduli that can be studied with the different microrheological techniques.

2.1 Active techniques

2.1.1 Magnetic tweezers

This is the oldest implementation of an active microrheology technique, and it has been recently reviewed by Conroy (Conroy, 2008). A modern design has been described by Keller et al. (2001). The method combines the use of strong magnets to manipulate embedded super-paramagnetic or ferromagnetic particles, with video microscopy to measure the displacement of the particles upon application of constant or time-dependent forces. Strong magnetic fields are required to induce a magnetic dipole in the beads and magnetic field gradients are applied to produce a force. The force exerted is typically in the range of 10 pN to 10 nN depending on the experimental details (Keller et al. 2001). The spatial resolution is typically in the range of 10-20 nm, and the frequency range is 0.01 – 1000 Hz. Three modes

of operation are possible: a viscosimetry measurement after applying a constant force, a creep response experiment after applying a pulse excitation, and the measurement of the frequency dependent viscoelastic moduli in response to an oscillatory stress (Riande et al., 2000). This technique has been extensively applied to characterize the bulk viscoelasticity of systems of biological relevance (Wilson & Poon, 2011; Gardel et al., 2005). Moreover, real-time measurements of the local dynamics have also been reported for systems which change in response to external stimuli (Bausch et al., 2001), and rotational diffusion of the beads has also been used to characterize the viscosity of the surrounding fluid and to apply mechanical stresses directly to the cell surfaces receptors using ligand coated magnetic colloidal particles deposited onto the cell membrane (Fabry et al., 2001). Finally, this technique is well suited for the study of anisotropic systems by mapping the strain-field, and for studying interfaces (Lee et al., 2009). In recent years (Reynaert et al., 2008) have described a magnetically driven macrorheometer for studying interfacial shear viscosities in which one of the dimensions of the probe (a magnetic needle) is in the μm range. This has allowed the authors to work at rather high values of the Boussinesq number, which is one of the typical characteristics of the microrheology techniques.

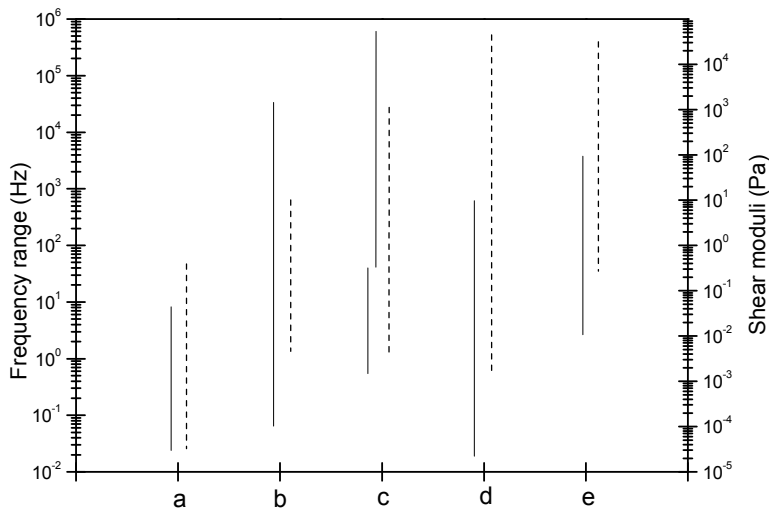


Fig. 1. Frequency and elasticity modulus range available to the different microrheological techniques. Continuous vertical represent the frequency range, and dashed arrows the range of shear moduli (G' , G'') that are accessible to each technique. a) Video particle tracking. b) Optical Tweezers. c) Diffusing wave spectroscopy: upper line for transmission geometry, lower line for back geometry. d) Magnetic microrheology. e) Atomic Force Microscopy (AFM). Adapted from Waigh (2005).

2.1.2 Optical tweezers

This technique uses a highly focused laser beam to trap a colloidal particle, as a consequence of the momentum transfer associated with bending light. The most basic design of an optical tweezer is shown in Figure 2.a: A laser beam (usually in the IR range) is focused by a high-quality microscope (high numerical aperture objective) to a spot in a plane in the fluid.

Figure 2.b shows a detailed scheme of how an optical trap is created. Light carries a momentum, in the direction of propagation, that is proportional to its energy. Any change in the direction of light, by reflection or refraction, will result in a change of the momentum of the light. If an object bends the light, conservation momentum requires that the object must undergo an equal and opposite momentum change, which gives rise to a force acting on the subject. In a typical instrument the laser has a Gaussian intensity profile, thus the intensity at the center is higher than at the edges. When the light interacts with a bead, the sum of the forces acting on the particle can be split into two components: F_{sc} , the scattering force, pointing in the direction of the incident beam, and F_g , the gradient force, arising from the gradient of the Gaussian intensity profile and pointing in the plane perpendicular to the incident beam towards the center of the beam. F_g is a restoring force that pulls the bead into the center of the beam. If the contribution to F_{sc} of the refracted rays is larger than that of the reflected rays then a restoring force is also created along the beam direction and a stable trap exists. A detailed description of the theoretical basis and of modern experimental setups has been given in Refs. (Ou-Yang & Wei, 2010; Borsali & Pecora, 2008; Resnick, 2003) that also include a review of applications of optical and magnetic tweezers to problems of biophysical interest: ligand-receptor interactions, mechanical response of single chains of biopolymers, force spectroscopy of enzymes and membranes, molecular motors, and cell manipulation. A recent application of optical tweezers to study the non-linear mechanical response of red-blood cells is given by Yoon et al. (2008). Finally, optical tweezers are also suitable for the study of interfacial rheology (Steffen et al., 2001).

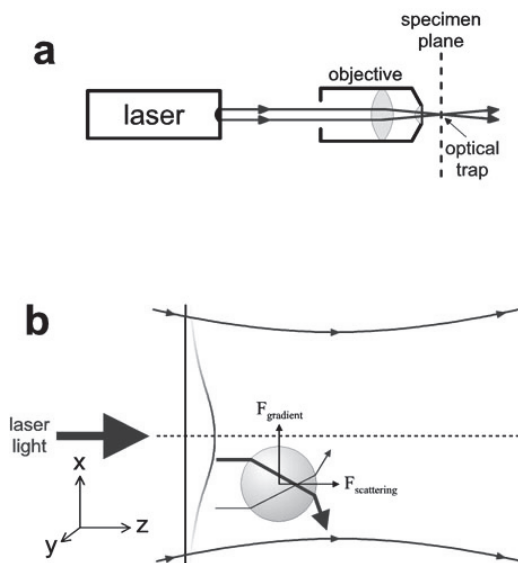


Fig. 2. a) Basic design of an optical tweezers instrument. b) Details of the physical principles leading to the optical trap.

2.2 Passive techniques

These techniques use the Brownian dynamics of embedded colloids to measure the rheology of the materials. Since passive methods use only the thermal energy of the beads, materials

must be sufficiently soft for the motion of the particles to be measured precisely. The resolution typically ranges from 0.1 to 10 nm and elastic modulus from 10 to 500 Pa can be measured with micron sized particles. Thermal fluctuations of particles in transparent bulk systems have traditionally been studied using light scattering techniques that allow one to measure the intensity correlation function from which the field correlation function $g_1(t)$ can be calculated, t being the time. For monodisperse particles $g_1(t)$ is directly related to the mean squared displacement of the particles, MSD, through

$$g_1(t) = \exp [-q^2 \langle \Delta r^2(t) \rangle / 6] \quad (1)$$

q being the scattering wave vector (Borsali & Pecora, 2008). Once $\langle \Delta r^2(t) \rangle$ is obtained, it is possible to calculate the real and imaginary components of the shear moduli, G' and G'' (Oppong & de Bruyn, 2010).

2.2.1 Diffusion wave spectroscopy

Diffusion wave spectroscopy, DWS, allows measurements of multiple scattering media, and therefore non-transparent samples can be studied. The output of the technique allows to calculate $\langle \Delta r^2(t) \rangle$, and because of the multiple scattering all q -dependent information is lost as photons average over all possible angles, thus resulting only in two possible scattering geometries: transmission and backscattering. The frequency range of both geometries is complementary (see Figure 1) spanning from 0.1 Hz to 1MHz. For bulk polymer solutions and gels excellent agreement of the G' and G'' values obtained by DWS and those obtained with conventional rheology has been found (Dasgupta et al., 2002; Dasgupta & Weitz, 2005). Even though these light scattering techniques are quite powerful tools for bulk microrheology, they have been scarcely used to probe the rheology of interfaces; in fact, as far as we know, only in old papers of Rice's group a set-up was described to measure dynamic light scattering of polymer monolayers using evanescent waves (Lin et al., 1993; Marcus et al., 1996).

2.2.2 Fluorescence correlation spectroscopy (FCS)

It is usually combined with optical microscopy, in particular confocal or two-photon microscopy. In these techniques light is focused on a sample and the fluorescence intensity fluctuations (due to diffusion, physical or chemical reactions, aggregations, etc.) can be measured in the form of a temporal correlation function. Similarly to what has been discussed in the light scattering technique, it is possible to obtain the MSD from the correlation function. In most experiments, Brownian motion drives the fluctuation of fluorescent-labeled molecules (or particles) within a well-defined element of the measurement cell. The samples have to be quite dilute, so that only few probes are within the focal spot (usually 1 - 100 molecules in one fL). Because of the tiny size of the confocal volume (approx. 0.2 fL), the measurements can be carried out in living cells or on cell membranes. In case that the interactions between two molecules wish to be studied, two options are available depending on their relative size. If their size is quite different, only one of them has to be labeled with a fluorescent dye (autocorrelation). If the diffusion coefficients of both molecules are similar, both have to be labeled with different dyes (cross-correlation). A detailed description of FCS techniques and of the data analysis has been recently given by Riegler & Elson (2001). Recent problems to which FCS has been applied include: dynamics of rafts in membranes and vesicles, dynamics of supramolecular

complexes, proteins, polymers, blends and micelles, electrically induced microflows, diffusion of polyelectrolytes onto polymer surfaces, normal and confined diffusion of molecules and polymers, quantum dots blinking, dynamics of polymer networks, enzyme kinetics and structural heterogeneities in ionic liquids (Winkler, 2007; Heuf et al., 2007; Ries & Schuille, 2008; Cherdhirankorn et al., 2009; Wöll et al., 2009; Guo et al., 2011). The use of microscopes makes FCS suitable for the study of the dynamics of particles at interfaces. Moreover, contrary to particle tracking techniques, it is not necessary to “see” the particles, thus interfaces with nanometer sized particles can be studied (Riegler & Elson, 2001).

2.2.3 Particle tracking techniques

The main idea in particle tracking is to introduce onto the interface a few spherical particles of micrometer size and follow their trajectories (Brownian motion) using videomicroscopy. The trajectories of the particles, either in bulk or on surfaces, allow one to calculate the mean square displacement, which is related to the diffusion coefficient, D , and the dimensions, d , in which the translational motion takes place by

$$\langle \Delta r^2(t) \rangle = \langle [\bar{r}(t_0 + t) - \bar{r}(t_0)]^2 \rangle = 2dDt^\alpha \quad (2)$$

where the brackets indicate the average over all the particles tracked, and t_0 the initial time. In case of diffusion in a purely viscous material or interface, α is equal to 1, and the usual linear relation is obtained between MSD and t . When the material or interface is viscoelastic, α becomes lower than 1 and this behavior is called sub-diffusive. It is worth noticing that sub-diffusivity can be found not only as a consequence of the elasticity of the material, but also due to particle interactions as concentration increases, an effect that is particularly important at interfaces. Anomalous diffusion is also found in many systems of biological interest where the Brownian motion of the particles is hindered by obstacles (Feder et al., 1996), or even constrained to defined regions (corralled motion) (Saxton & Jacobson, 1997). The diffusion coefficient is related to the friction coefficient, f , by the Einstein relation

$$D = \frac{k_B T}{f} \quad (3)$$

In 3D Stokes law, $f=6\pi\eta a$, applies and for pure viscous fluids the shear viscosity, η , can be directly obtained from the diffusion coefficient of the probe particle of radius a at infinite dilution. The situation is much more complex in the case of fluid interfaces, and it will be discussed in more detail in the next section.

Figure 3 shows a sketch of a typical setup for particle tracking experiments. A CCD camera (typically 30 fps) is connected to a microscope that permits to image either the interface prepared onto a Langmuir trough, or a plane into a bulk fluid. The series of images are transferred to a computer to be analyzed to extract the trajectories of a set of particles. Figure 4.a shows typical results of MSD obtained for a 3D gel, combining DWS and particle tracking techniques which shows a very good agreement between both techniques, and illustrates the broad frequency range that can be explored. Figure 4.b shows a typical set of results for the MSD of a system of latex particles (1 μm of diameter) spread at the water/*n*-octane interface. The analysis of MSD within the linear range in terms of Eq. (2) allows to obtain D .

One of the experimental problems frequently found in particle tracking experiments is that the linear behavior of the MSD vs. t is relatively short. This may be due to poor statistics in calculating the average in Eq.(2), or to the existence of interactions between particles. As it will be discussed below, this may be a problem in calculating the shear modulus from the MSD. An additional experimental problem may be found when the interaction of the particles with the fluid surrounding them is very strong, which may lead to changes in its viscoelastic modulus, or when the samples are heterogeneous at the scale of particle size, a situation rather frequent in biological systems, e.g. cells (Konopka & Weisshaar, 2004), or gels (Alexander & Dalglish, 2007), or solutions of rod-like polymers (Hasnain & Donald, 2006). In this case the so-called “two-point” correlation method is recommended (Chen et al., 2003). In this method the fluctuations of pairs of particles at a distance R_{ij} are measured for all the possible values of R_{ij} within the system. Vector displacements of individual particles are calculated as a function of lag time, t , and initial time, t_0 .

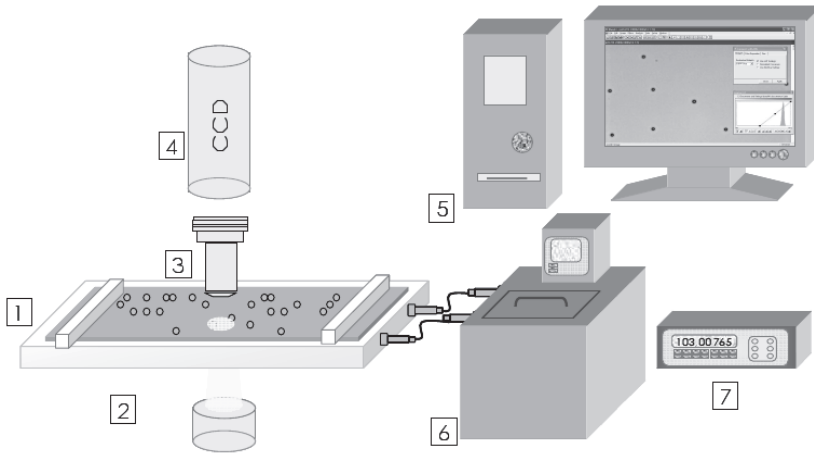


Fig. 3. Typical particle tracking setup for 2D microrheology experiments: 1: Langmuir trough; 2: illumination; 3: microscope objective; 4: CCD camera; 5: computer; 6: thermostat; 7: electronics for measuring the temperature and the surface pressure.

Then the ensemble averaged tensor product of the vector displacements is calculated (Chen et al., 2003):

$$D_{\alpha\beta}(r, \tau) = \left\langle \Delta r_{\alpha}^i(r, t) \Delta r_{\beta}^j(r, t) \delta[r - R_{ij}(t_0)] \right\rangle_{i \neq j, t} \quad (4)$$

where a and b are coordinate axes. The average corresponding to $i = j$ represents the one-particle mean-squared displacement.

Two-point microrheology probes dynamics at different length scales larger than the particle radius, although it can be extrapolated to the particle's size thus giving the MSD (Liu et al., 2006). In fact it has been found that for R_{ij} close to the particle radius, the two-point MSD matches the tendency of the MSD obtained by tracking single particles. However, both sets of results are different for R_{ij} 's much larger than the particle diameter. This is a consequence of the fact that single particle tracking reflects both bulk and local rheologies, and therefore

the heterogeneities of the sample. Figure 5 shows a comparison of the MSD obtained by single particle and two-point tracking for a solution of entangled F-actin solutions at different length scales from 1 to 100 μm (Liu et al., 2006). Both methods agree when the particle size is of the same order than the scale of the inhomogeneities of the system when the particle probes the average structure. Otherwise, the two methods lead to different results. In general, quite good agreement is found between two-point tracking experiments and macroscopic rheology experiments.

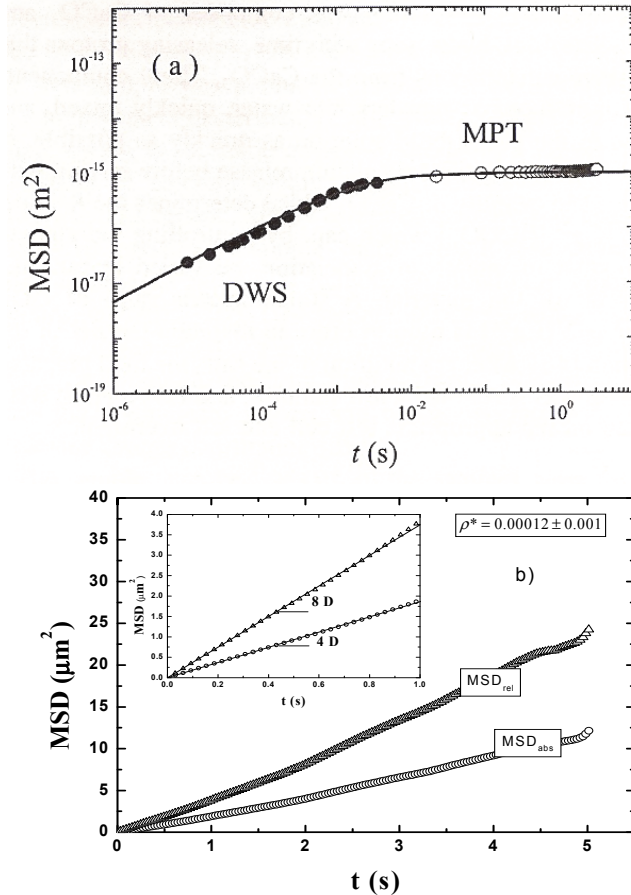


Fig. 4. a) Typical results of mean square displacement for a 3D gel made out of a polysaccharide in water [44]. Filled points are from DWS experiments, and open symbols are from particle tracking. The continuous line is an eye guide. b) Mean square displacement (MSD_{abs}), circles, and relative square displacement (MSD_{rel}), triangles, for latex particles at the water/n-octane interface. Experimental details: set of 300 latex particles of 1 μm of diameter, surface charge density: -5.8 mC cm^{-2} , and reduced surface density, $\rho^*=1.2 \cdot 10^{-3}$ ($\rho^*=\rho a^2$), 25 $^\circ\text{C}$. Figure 4.a is reproduced from Vincent et al. (2007). Inset corresponds to a smaller time interval.

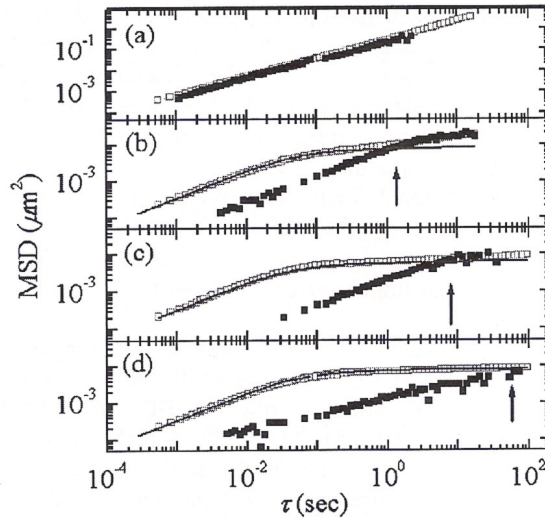


Fig. 5. Comparison of one-particle (open symbols) and two-particle (closed symbols) MSD for a solution of F-actin using particles of radius $0.42 \mu\text{m}$. Different average actin filaments are used: a) $0.5 \mu\text{m}$, b) $2 \mu\text{m}$, c) $5 \mu\text{m}$, d) $17 \mu\text{m}$. Notice that when the scale of the inhomogeneities of the solution is similar to the particle size both methods lead to the same results. The figure is reproduced from Liu et al. (2006).

For the case in which the particles are embedded in a viscoelastic fluid, particle tracking experiments allow one to obtain the viscoelastic moduli of the fluids. Manson & Weitz (1995) first in an ad-hoc way, and later Levine & Lubensky (2000) in a more rigorous way, proposed a generalization of the Stokes-Einstein (GSE) equation:

$$\langle \Delta \tilde{r}^2(s) \rangle = \frac{2k_B T}{3\pi a s \tilde{G}(s)} \quad (5)$$

where $\tilde{G}(s)$ is the Laplace transform of the stress relaxation modulus, s is the Laplace frequency, and a is the radius of the particles. An alternative expression for the GSE equation can be written in the Fourier domain as:

$$G^*(\omega) = \frac{k_B T}{\pi a i \omega \Im \langle \Delta r^2(t) \rangle} \quad (6)$$

where \Im represents a unilateral Fourier transform, which is effectively a Laplace transform generalized for a complex frequency $i\omega$. Different methods have been devised to obtain $\tilde{G}(s)$ from the experimental MSD including direct Laplace or Fourier transformations (Dasgupta et al., 2002; Evans et al., 2009), or analytical approximations (Mason, 2000; Wu & Dai, 2006). It must be stressed that the GSE equation is valid under the following approximations: (a) the medium around the sphere may be treated as a continuum material, which requires that the size of the particle be larger than any structural length scale of the

material, (b) no slip boundary conditions, (c) the fluid surrounding the sphere is incompressible, and (d) no inertial effects.

The application of the GSE is limited to a frequency range limited in the high frequency range by the appearance of inertial effects. The high frequency limit is imposed by the fact that the viscous penetration depth of the shear waves propagated by the particle motion must be larger than the particle size. The penetration depth is proportional to $(G^*/\rho\omega^2)^{1/2}$, where ρ is the density of the fluid surrounding the particles, and for micron-sized particles in water is of the order of 1 MHz. On the other hand, the lower limit is set by the time at which compressional modes become significant compared to the shear modes excited by the particle motion. An approximate value for the low frequency limit is given by

$$\omega_L \geq \frac{G' \xi^2}{\eta a} \tag{7}$$

ξ being the characteristic length scale of the elastic network in which the particles move. Again, for the same conditions mentioned above, the low-frequency limit is in the range of 0.1 to 10 Hz. Figure 6.a shows the frequency dependence of the shear modulus for a 3D gel using two passive techniques: DWS and particle tracking. As it can be observed the agreement is very good. It must be stressed that, in order to obtain reliable Laplace or Fourier transforms of the MSD, it is necessary to measure the particle trajectories over long t periods (minutes), which makes absolutely necessary to eliminate any collective drift in the system. Very recently Felderhof (2009) has presented an alternative method for calculating the shear complex modulus from the velocity autocorrelation function, VAF, that can be calculated from the particle trajectories. An experimental difficulty associated to this method is that the VAF decays very rapidly, and therefore it is difficult to obtain many experimental data in the decay region.

Under the same conditions assumed for the GSE equation, the creep compliance is directly related to the MSD by

$$J(t) = \frac{\pi a}{k_B T} \langle \Delta r^2(t) \rangle \tag{8}$$

Even though the GSE method has been applied to different bulk systems, few applications have been done for studying the complex shear modulus of interfaces and thin films (Wu & Dai, 2006; Prasad & Weeks, 2009; Maestro et al., 2011).

The two-point correlation method also provides information about the viscoelastic moduli of the fluid in which the particles are embedded. In effect, the ensemble averaged tensor product, Eq.(4), leads to (Chen et al., 2003)

$$\tilde{D}_{rr}(r,s) = \frac{k_B T}{2\pi r s \tilde{G}(s)}; \quad D_{\theta\theta} = D_{\phi\phi} = \frac{1}{2} D_{rr} \tag{9}$$

where $\tilde{D}_{rr}(r,s)$ is the Laplace transform of $D_{rr}(r,t)$ and the off-diagonal terms vanish. Figure 6.b compares the G' and G'' results calculated for a solution of F-actin (MSD data shown in Figure 4) using one- and two-particle tracking methods. The results agree with those obtained by single-particle methods as far as the scale of the inhomogeneities is similar to the particle size, otherwise the single particle method is affected both by local and global

rheology. Notice that the results of the two-point technique agree with those obtained with conventional macroscopic rheometers.

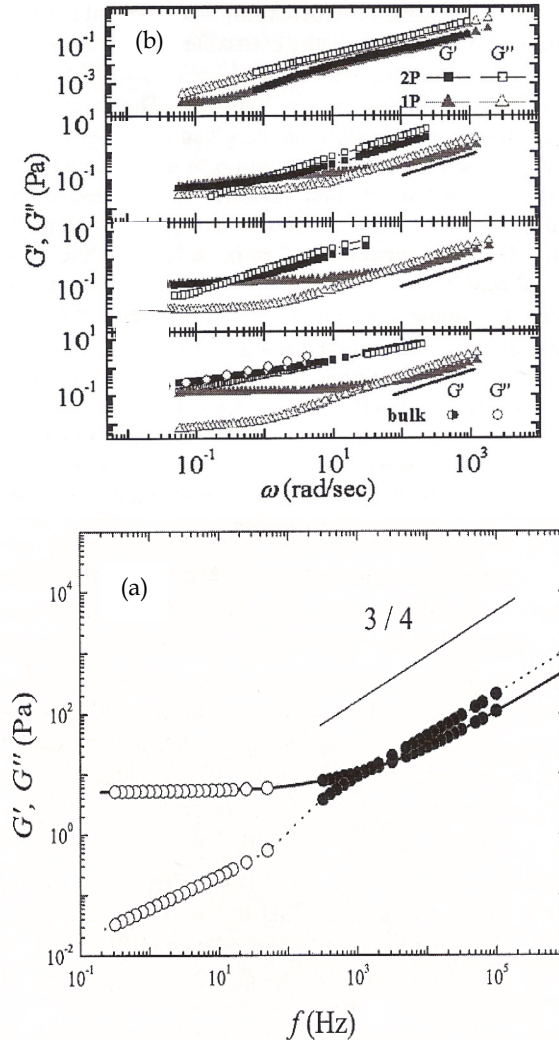


Fig. 6. Real and imaginary components calculated from the MSD shown in: a) the Figure 4.a, and b) Figure 5. Notice the good agreement between the results calculated from DWS (closed symbols) and single particle tracking (open symbols) in Figure 5.a. The solid and dotted lines are guides for G' and G'' results, respectively. In Figure 6.b the open symbols refer to G'' , and the full ones to G' . Triangles correspond to single particle tracking and squares to two-particle tracking. Circles correspond to conventional macro-rheology. Figure 6.a was taken from Vincent et al. (2007) and Figure 6.b from Cherdhirankorn et al. (2009).

3. Dynamics of particles at interfaces

For using particle tracking techniques to get insight of the interfacial microrheology it is first necessary to study the diffusion of particles in the bare interface. For an inviscid interface the drag comes entirely from the upper and lower fluid phases (in the usual air-water interface only from the water subphase). The MSD of particles trapped at fluid interfaces depends on the surface concentration, and for very low surface concentration it is linear with time, thus the diffusion coefficients, D_0 , can be easily obtained. However, for high surface concentrations, even below the threshold of aggregation or fluid-solid phase transitions (Bonales et al., 2011), the MSD is no longer linear with time, but shows a sub-diffusive behavior, $MSD(t) \sim t^\alpha$ with $\alpha < 1$, hence D_0 must be obtained from the time dependence of the MSD in the limit of short times.

3.1 Shear micro-rheology of monolayers at fluid interfaces

In the case of particles trapped at interfaces Einstein’s equation, Eq.(3), is still valid. However, one cannot calculate the friction coefficient using Stokes equation and directly substituting the interfacial shear viscosity. Instead, f is a function of the viscosities of the phases (η ’s), the geometry of the particle (the radius “ a ” for spheres), the contact angle between the probe particle and the interface (θ), etc. For a pure 2D system there is no solution for the slow viscous flow equations for steady translational motion of a sphere in a 2D fluid (Stokes paradox).

3.1.1 Motion of a disk in and incompressible membrane of arbitrary viscosity

Saffman & Delbrück (1975) and Hughes et al. (1981) have solved the problem of the motion of a thin disk immersed in a membrane of arbitrary viscosity, η_L separating two phases of viscosities η_1 and η_2 . The height of the disk is assumed to be equal to the membrane thickness, h . They obtained the following expression for the translational mobility,

$$b_T = \frac{1}{f} = \frac{1}{4\pi(\eta_1 + \eta_2)R\Lambda(\epsilon)} \tag{10}$$

Where $\Lambda(\epsilon)$ is non-linear function of ϵ , $\left[\epsilon = \frac{R}{h} \left(\frac{\eta_1 + \eta_2}{\eta_L} \right) \right]$. $\Lambda(\epsilon)$ cannot be expressed analytically except for two limit cases,

$$\Lambda(\epsilon) = \left\{ \epsilon \left(\ln \left(\frac{2}{\epsilon} \right) - \gamma + \frac{4}{\pi} \epsilon - \frac{1}{2} \epsilon^2 \ln \left(\frac{2}{\epsilon} \right) + O(\epsilon^2) \right) \right\}^{-1} \quad (\text{Highly viscous membranes, } \epsilon < 1)$$

$$\Lambda(\epsilon) = \frac{2}{\pi} \quad (\text{Low viscous membranes, } \epsilon > 1)$$

These works have been generalized by Stone & Adjari (1998) and by Barentin et al. (2000).

3.1.2 Danov’s model for a sphere in a compressible surfactant layer

The above theories are limited to non protruding particles (or high membrane viscosities). In particle tracking experiments spherical particles are used that are partially immersed in both

fluid phases separating the interface. Danov et al. (1995) and Fischer et al. (2006) have made numerical calculations of the drag coefficient of spherical microparticles trapped at fluid-fluid interfaces. While Danov considered the interface as compressible, Fischer assumed that the interface is incompressible, both authors predicted the dynamics of the particles adsorbed on bare fluid interfaces, i.e. with no surfactant monolayers (the so-called the limit of zero surface viscosity). The predictions of their theories are different, and will be discussed in detail below. More recently, Reynaert et al. (2007) and Madivala et al. (2009) have studied the dynamics of spherical, weakly aggregated, and of non-spherical particles at interfaces, though using macroscopic rheometers.

Danov et al. (1995) have calculated the hydrodynamic drag force and the torque acting on a micro spherical particle trapped at the air-liquid interface (they consider the viscosity of air to be zero) interface, and moving parallel to it. This model was later extended by Dimova et al. (2000) and by Danov et al. (2000) to particles adsorbed to flat or curved (spherical) interfaces separating two fluids of non vanishing viscosity. The interface was modeled as a compressible, 2D fluid characterized by two dimensionless parameters K and E defined as $E = \eta_{sh}/(\eta a)$ and $K = \eta_d/(\eta a)$, being η_{sh} and η_d the surface shear and dilational viscosity respectively (Note that E is the inverse of ε used by Hughes). Danov et al. made the following assumptions: 1) The movement implies a low Reynolds number, thus they ignored any inertial term; 2) the moving particle is not affected by capillarity or electro-dipping; 3) the contact line does not move to respect to the particle surface, and 4) they considered $E=K$, i.e. the interface is compressible. With these assumptions they solved numerically the Navier-Stokes equation to obtain the values of the drag coefficient f as a function the contact angle and of E (or K). They presented their results in graphical form, and their results are reproduced in Figure 7.

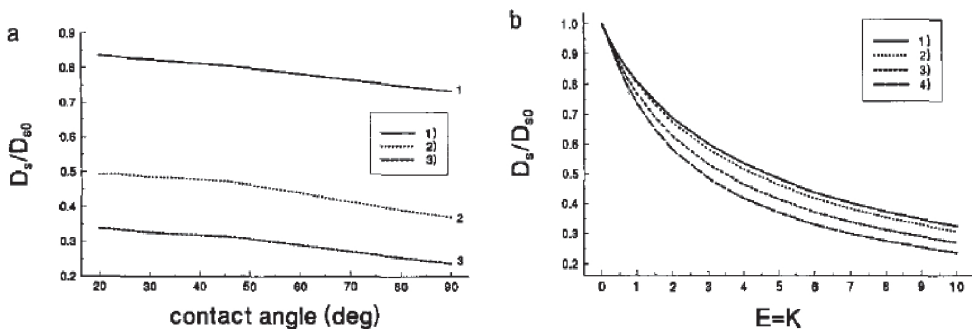


Fig. 7. Left: Effect of contact angle on the diffusion coefficient of a particle trapped at a fluid interface according to Danov's theory. D_{s0} is the diffusion coefficient for the bare interface. The different lines correspond to the following values of $E (=K)$: 1) 0; 2) 1; 3) 5. Right: Effect of the surface to bulk shear viscosity on the diffusion coefficient. The different lines correspond to the following values of $E (=K)$: 1) 0; 2) 1; 3) 5; 4) 10. Figures reproduced from Dimova et al. (2000).

These curves can be used to obtain the shear viscosity of compressible surfactant layer once one has obtained the diffusion coefficient from particle tracking experiments, D_0 , for a free interface and in the presence of a surfactant layer. It must be stressed that, from a strict

theoretical point of view, the results presented by Danov are valid only in the limit $E \gg 1$, and for arbitrary values of the contact angle. Sickert & Rondelez (2003) were the first to applied Danov's ideas to obtain the surface shear viscosity by particle tracking using spherical microparticles trapped at the air-water interface, which was covered with Langmuir films. They have measured the surface viscosity of three monolayers formed by pentadecanoic acid (PDA), L- α -dipalmitoylphosphatidylcholine (DPPC) and N-palmitoyl-6-n-penicillanic acid (PPA) respectively. The values of the shear viscosities for PDA, DPPC and PPA reported were in the range of 1 to $11 \cdot 10^{-10} \text{ N} \cdot \text{s} \cdot \text{m}^{-1}$ in the liquid expanded region of the monolayer. These values are beyond the range that can be reached by macroscopic mechanical methods, that usually have a lower limit in the range of $10^{-7} \text{ N} \cdot \text{s} \cdot \text{m}^{-1}$.

Fischer considered that a monolayer cannot be considered as compressible. Due to the presence of a surfactant, Marangoni forces (forces due to surface tension gradients) strongly suppress any motion at the surface that compress or expands the interface. Any gradient in the surface pressure is almost instantly compensated by the fast movement of the surfactant at the interface given a constant surface pressure, behaving thus as a incompressible monolayer (Fischer assumed that the velocity of the 2D surfactant diffusion is faster than the movement of the beads). The fact that the drag on a disk in a monolayer is that of an incompressible surface has been verified experimentally by Fischer (2004). In the case of Langmuir films of polymers, the monolayer could be considered as compressible or incompressible depending on the rate of the polymer dynamics at the interface compared to the velocity of the beads probes. Bonales et al. (2007) have calculated the shear viscosity of two polymer Langmuir films using Danov's theory, and compared these values with those obtained by canal viscosimetry. Video Particle tracking and Danov's theory were used by Maestro et al. (2011.a) to show the glass transition in Langmuir films. Figure 8 shows the results obtained for a monolayer of poly(4-hydroxystyrene) onto water. For all the monolayers reported by Bonales et al. (2007) and Maestro et al. (2011.b) the surface shear viscosity calculated from Danov's theory was lower than that measured with the macroscopic canal surface viscometer. Similar qualitative conclusions were reached at by Sickert et al. (2007) for monolayers of fatty acids and phospholipids in the liquid expanded region.

3.1.3 Fischer's theory for a sphere in a incompressible surfactant layer

Fischer et al. (2006) have numerically solved the problem of a sphere trapped at an interface with a contact angle θ moving in an *incompressible* surface. They showed that contributions due to Marangoni forces account for a significant part of the total drag. This effect becomes most pronounced in the limit of vanishing surface compressibility. In this limit the Marangoni effects are simply incorporated to the model by approximating the surface as incompressible. They solved the fluid dynamics equations for a 3D object moving in a monolayer of surface shear viscosity, η_s between two infinite viscous phases. The monolayer surface is assumed to be flat (no electrocapillary effects). Then the translational drag coefficient, k_T , was expressed as a series expansion of the Boussinesq number, $B = \eta_s / ((\eta_1 + \eta_2) a)$, a being the radius of the spherical particle:

$$k_T = k_T^0 + Bk_T^1 + O(B^2) \tag{11}$$

For $B=0$, and for an air-water interface ($\eta_1, \eta_2=0$), the numerical results for k_T are fitted with an accuracy of 3% by the formula,

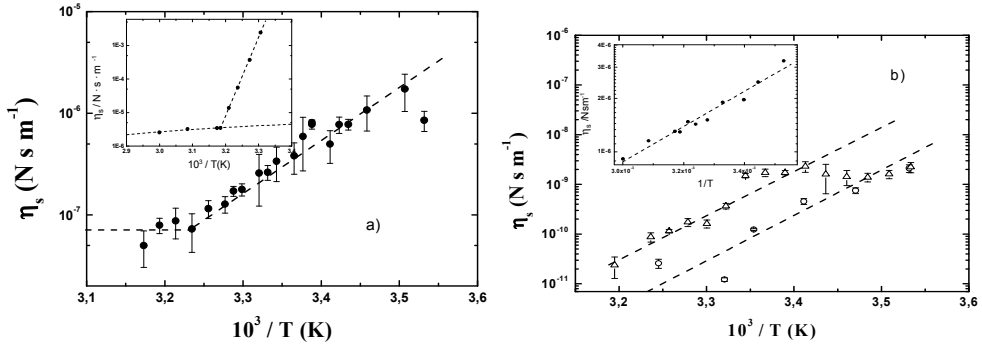


Fig. 8. Temperature dependence of the surface shear viscosity of a monolayer of poly(4-hydroxystyrene) at the air-water interface obtained by particle tracking (the insets show the corresponding values measured with a macroscopic canal viscometer. Left: experiments done at $\Pi=8 \text{ mN m}^{-1}$. Right: triangles correspond to $\Pi=3 \text{ mN m}^{-1}$ and circles to $\Pi=2 \text{ mN m}^{-1}$. Notice that the results obtained by particle tracking are much smaller than those obtained with the canal viscometer. Data taken from Hilles et al. (2009).

$$k_T^0 \approx 6\pi \sqrt{\tanh\left(32\left(\frac{d}{R} + 2\right)\right) / (9\pi^2)} \quad (12)$$

where d is the distance from the apex of the bead to the plane of the interface (which defines the contact angle). Note that if d goes to infinity, $k_T^0 = 6\pi$, which is the correct theoretical value for a sphere in bulk (Stokes law). The translational drag in a half immersed sphere in a non viscous monolayer is $k_T^0 \approx 11$ which is about 25% higher than the drag on a sphere trapped at a free surface, $k_T = 3\pi$. This means that even in the absence of any appreciable surface viscosity the drag coefficient of an incompressible monolayer is higher than that of a free interface, and the data cannot be used to extract the surface shear viscosity using Danov's theory especially in the limit of low surface viscosities.

The numerical results for $k_T^{(1)}$ are fitted within an accuracy of 3% to,

$$k_T^{(1)} \approx \begin{cases} -4\ln\left(\frac{2}{\pi} \arctan\left(\frac{2}{3}\right)\right) \left(\frac{a^{3/2}}{(d+3a)^{3/2}}\right) & (d/a > 0) \\ -4\ln\left(\frac{2}{\pi} \arctan\left(\frac{d+2a}{3a}\right)\right) & (d/a < 0) \end{cases} \quad (13)$$

Sickert & Rondelez (2003) have introduced in an ad-hoc way the incompressibility effect in Danov's theory by renormalizing his master curve (Figure 7 above) by the empirical value of 1.2, and they have later reanalyzed their data by combining the Danov's and Fischer's theories (Sickert et al., 2007). First they used the value determined by Danov et al. (2000) for the resistance coefficient of a sphere at a clean, compressible surface and at the contact angle of their experiments (50°). Afterwards, they used the predictions of Fischer et al. (2006) for a sphere in a surfactant monolayer (incompressible) with the contact angle corrected by the change in the surface tension, and in the case of $E \ll 1$ (notice that this is the opposite E -limit than for the original Danov's theory),

$$\frac{D_0}{D_{\rightarrow 0}} = \frac{\xi_0^{(Danov)}(\theta)}{\xi^{(Fischer)}(\theta)} = \frac{\xi_0^{(Danov)}(\theta)}{k_1^0(\theta) + Ek_1^1(\theta)} \tag{14}$$

D_0 being the diffusion coefficient of the beads at a free surface (compressible), and $D_{\rightarrow 0}$ is the value of an incompressible monolayer which surface concentration is tending to zero. They found that this relation is not equal to 1 but to 0.84 for their systems and experimental conditions which confirms the observation of Barentin et al. (2000).

Figure 9 shows the friction coefficient for latex particles at the water-air interface obtained from particle tracking for polystyrene latex particles. It also shows the values calculated from Danov's and from Fischer's theories (notice that for the bare interface $E = B = 0$). The figure clearly shows that both theories underestimate the experimental values over the whole θ range. An empirical factor of $\eta(\theta)_{exp}/\eta(\theta)_{Fischer} = 1.8 \pm 0.2$ brings the calculated values in good agreement with the experiments at all the contact angle values. A similar situation was found for the water-n-octane interface.

The values of the shear viscosities calculated by Sickert & Rondelez (2003) by using the modified-Fisher theory are 2 or 3 times higher than the previous values. Sickert et al. (2007) also refers to a model developed by Stone which would be valid over the whole range of E , although only for a contact angle of 90° . Figure 10 shows clearly the large difference found between micro- and macrorheology for monolayers of poly(t-butyl acrylate) at the so-called Γ^{**} surface concentration (Muñoz et al., 2000). The macrorheology results have been obtained using two different oscillatory rheometers. The huge difference cannot be attributed to specific interactions between the particles and the monolayer.

In effect, Figure 11 shows that the values obtained are the same for particles of rather different surface characteristics. Moreover, the values calculated from the modified-Fisher's theory or by direct application of the GSE equation lead to almost indistinguishable surface shear viscosities. It must be stressed that in all the cases the contact angle used is the experimentally measured using the gel-trapping technique described by Paunov et al.

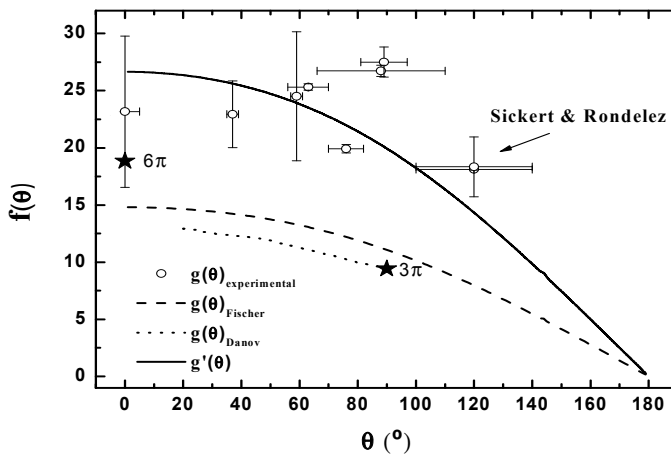


Fig. 9. Friction coefficients calculated from the experimental diffusion coefficients measured by particle tracking experiments (symbols), by Danov's theory (dotted line), by Fischer's theory (dashed line), and by the corrected Fischer's theory (continuous line).

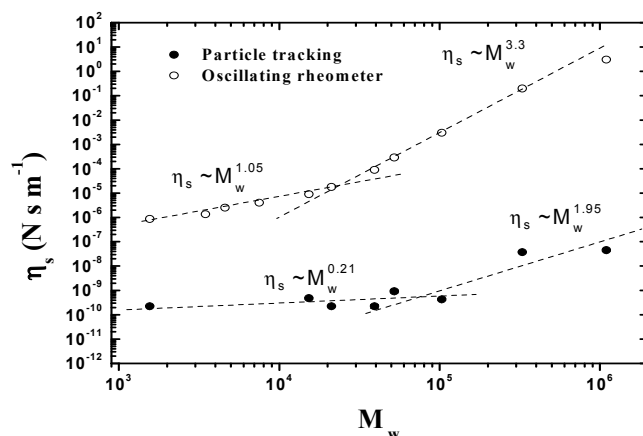


Fig. 10. Surface shear viscosity for monolayers of poly(t-butyl acrylate) as a function of the molecular weight and for a surface pressure of 16 mN m^{-1} . The lower curve corresponds to data obtained from particle tracking. The upper curve was obtained from conventional oscillatory rheometers.

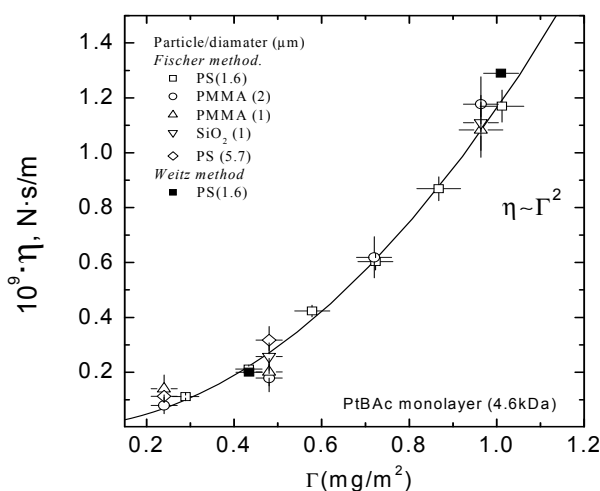


Fig. 11. Surface shear viscosity of a monolayer of poly(t-butyl acrylate) (molecular weight 4.6 kDa) measured by particle tracking. Different microparticles were used: poly(styrene) of 1.6 and 5.7 μm (stabilized by sulfonate groups); poly(methylmethacrylate) stabilized by Coulombic repulsions (PMMA1), or by steric repulsions (PMMA2); Silica particles stabilized by Coulombic repulsions. Empty symbols: the viscosities were calculated using Fischer theory. Full symbols: calculated by the GSE equation.

(2003). This discrepancy between micro- and macrorheology in the study of monolayers seems to be a rather general situation (Schmidt et al., 2000; Khair & Brady, 2005; Oppong & de Bruyn, 2010; Lee et al., 2010) and no clear theoretical answer has been found so far.

4. Conclusions

The set of microrheological techniques offer the possibility of studying the rheology of very small samples, of systems which are heterogeneous, and facilitate to measure the shear modulus over a broad frequency range. Particle tracking techniques are especially well suited for the study of the diffusion of microparticles either in the bulk or at fluid interfaces. Different types of mean squared displacements, MSD, (one-particle, two-particle) allow one to detect spatial heterogeneities in the samples. Even though good agreement has been found between micro- and macrorheology (at least when two-particle MSD is used) in bulk systems, the situation is still not clear for the case of fluid interfaces, where the shear surface microviscosity is much smaller than the one measured with conventional surface rheometers.

5. Acknowledgments

This work has been supported in part by MICIN under grant FIS2009-14008-C02-01, by ESA under grant FASES MAP-AO-00-052, and by U.E. under grant Marie-Curie-ITN "MULTIFLOW". L.J. Bonales and A. Maestro are grateful to MICINN for their Ph.D. fellowships. We are grateful to Th.M. Fisher, R. Miller and L. Liggieri for helpful discussions.

6. References

- Alexander M., Dalgleish D.G., 2007, Diffusing wave spectroscopy of aggregating and gelling systems. *Curr. Opinion Colloid Interf. Sci.* 12 (4-5) 179-186, ISSN: 1359-0294
- Barentin C., Muller, P., Ybert, C., Joanny J.-F., di Meglio J.-M., 2000, Shear viscosity of polymer and surfactant monolayers. *Eur. Phys. J. E.* 2 (2) 153-159, ISSN: 1292-8941
- Bausch A.R., Hellerer U., Essler M., Aepfelbacher M., Sackmann E., 2001, Rapid stiffening of integrin receptor-actin linkages in endothelial cells stimulated with thrombin: A magnetic bead microrheometry study. *Biophys. J.* 80 (6) 2649-2657, ISSN: 0006-3495
- Binks B., Horozov S., (Eds.), 2006, *Colloidal particles at liquid interfaces*. Cambridge Univ. Press, ISBN: 9780521848466, Cambridge.
- Bonales L.J., Ritacco H., Rubio J.E.F., Rubio R.G., Monroy F., Ortega F., 2007. Dynamics in ultrathin films: Particle tracking microrheology of Langmuir monolayers. *Open Phys. Chem. J.* 1 (1) 25-32; ISSN: 1874-0677
- Bonales L.J., Rubio J.E.F., Ritacco H., Vega C., Rubio R.G., Ortega F., 2011. Freezing transition and interaction potential in monolayers of microparticles at fluid interfaces. *Langmuir* 27 (7) 3391-3400, ISSN: 0743-7463.
- Borsali R., Pecora R., (Eds.), 2008. *Soft-matter characterization*. Vol. 1., Springer, ISBN: 978-1-4020-8290-0, Berlin.
- Breedveld V., Pine D.J., 2003, Microrheology as a tool for high-throughput screening. *J. Mater. Sci.* 38 (22), 4461-4470, ISSN: 002-2461
- Chen D.T., Weeks E.R., Crocker J.C., Islam M.F., Verma R., Gruber J., Levine A.J., Lubensky T.C., Yodh A.G., 2003, Rheological microscopy. Local mechanical properties from microrheology. *Phys. Rev. Lett.* 90 (10) 108301, ISSN: 0031-9007

- Cherdhirankorn T., Harmandaris V., Juhari A., Voudouris P., Fytas G., Kremer K., Koynov K., 2009, Fluorescence correlation spectroscopy study of molecular probe diffusion in polymer melts. *Macromolecules* 42 (13) 4858-4866, ISSN: 0024-9297
- Cicuta P., Donald A.M., 2007, Microrheology: a review of the method and applications. *Soft Matter* 3 (12) 1449-1455, ISSN: 1744-683X
- Cicuta P., Keller S.L., Veatch S.L., 2007, Diffusion of Liquid Domains in Lipid Bilayer Membranes, *J. Phys. Chem. B* 111 (13) 3328-3331, ISSN:1520-6106
- Conroy R., 2008, Force spectroscopy with optical and magnetic tweezers. In *Handbook of molecular force spectroscopy*. Noy A. (Ed.), Springer, ISBN: 978-0-387-49987-1, Berlin.
- Crocker J.C., Grier D.G., 1996, Methods of digital video microscopy for colloidal studies. *J. Colloid Interf. Sci.* 179 (1), 298-310, ISSN: 0021-9797
- Danov K., Aust R., Durst F., Lange U. 1995. Influence of the surface viscosity on the hydrodynamic resistance and surface diffusivity of a large Brownian particle. *J. Colloid Int. Sci.*, 175 (1), 36-45, ISSN: 0021-9797
- Danov K.D., Dimova R., Pouligny B. 2000. Viscous drag of a solid sphere straddling a spherical or flat surface. *Physics of Fluids*, 12 (11) 2711-2722, ISSN: 0899-8213
- Dasgupta B.R., Tee S.Y., Crocker J.C., Frisken B.J., Weitz D.A., 2002, Microrheology of polyethylene oxide using diffusing wave spectroscopy and single scattering. *Phys. Rev. E* 65 (5) 051505, ISSN: 1539-3755
- Dasgupta B.R., Weitz D.A., 2005, Microrheology of cross-linked polyacrylamide networks. *Phys. Rev. E* 71 (2) 021504, ISSN: 1539-3755
- Diez-Pascual A.M., Monroy F., Ortega F., Rubio R.G., Miller R., Noskov B.A., 2007, Adsorption of water-soluble polymers with surfactant character. Dilational viscoelasticity. *Langmuir* 23 (7) 3802-3808, ISSN: 0743-7463
- Dimova R., Danov K., Pouligny B., Ivanov I.B. 2000. Drag of a solid particle trapped in a thin film or at an interface: Influence of surface viscosity and elasticity. *J. Colloid Interf. Sci.* 226 (1) 35-43, ISSN: 0021-9797
- Evans R.M., Tassieri M., Auhl D., Waigh Th.A., 2009, Direct conversion of rheological compliance measurements into storage and loss moduli. *Phys. Rev. E* 80 (1) 012501, ISSN: 1539-3755
- Fabry B., Maksym G.N., Butler J.P., Glogauer M., Navajas D., Fredberg JJ. 2001, Scaling the microrheology of living cells. *Phys. Rev. Lett.* 87 (14) 148102, ISSN: 0031-9007
- Feder T.J., Brust-Mascher I., Slattery J.P., Barid B., Webb W.W., 1996, Constrained diffusion or immobile fraction on cell surfaces: A new interpretation. *Biophys. J.* 70 (6) 2767-2773, ISSN: 0006-3495
- Felderhof B.U., 2009, Estimating the viscoelastic moduli of a complex fluid from observation of Brownian motion. *J. Chem. Phys.* 131 (16) 164904, ISSN: 0021-9606
- Fischer Th.M. 2004. Comment on "Shear viscosity of Langmuir Monolayers in the Low Density Limit". *Phys. Rev. Lett.* 92 (13) 139603, ISSN: 0031-9007
- Fischer Th. M., Dhar P., Heinig P. 2006. The viscous drag of spheres and filaments moving in membranes or monolayers, *J. Fluid Mech.* 558 (1) 451-475, ISSN: 0022-1120
- Gardel M.L., Valentine M.T., Weitz D.A., 2005, Microrheology. In *Microscale diagnostic techniques*. Brauer K., ed. Springer, ISBN: 978-3-540-23099-1, Berlin.

- Gavranovic G.T., Deutsch J.M., Fuller G.G., 2005, Two-dimensional melts: Chains at the air-water interface. *Macromolecules*, 38 (15) 6672-6679, ISSN: 0024-9297
- Guo J., Baker G.A., Hillesheim P.C., Dai S., Shaw R.W., Mahurin S.M. 2011. Fluorescence correlation spectroscopy evidence for structural heterogeneity in ionic liquids. *Phys. Chem. Chem. Phys.* 13 (27), 12395-12398, ISSN: 1463-9076
- Hasnain I., Donald A.M., 2006, Microrheology characterization of anisotropic materials. *Phys. Rev. E* 73 (3) 031901, ISSN: 1539-3755
- Heuf R.F., Swift J.L., Cramb D.T., 2007, Fluorescence correlation spectroscopy using quantum dots: Advances, challenges and opportunities. *Phys. Chem. Chem. Phys.* 9 (16) 1870-1880, ISSN: 1463-9076
- Hilles H.M., Ritacco H., Monroy F., Ortega F., Rubio R.G. 2009. Temperature and concentration effects on the equilibrium and dynamic behavior of a Langmuir monolayer: From fluid to gel-like behavior. *Langmuir* 25 (19) 11528-11532, ISSN: 0743-7463
- Hughes B.D., Pailthorpe P.A., White L.P. 1981. The translational and rotational drag of a cylinder moving in a membrane. *J. Fluid Mechanics* 110 (1) 349-372, ISSN: 0022-1120
- Kahir, A.S., Brady, J.F., 2005, "Microviscoelasticity" of colloidal dispersions, *J. Rheol.*, 49 (6) 1449-1481; ISSN: 0148-6055
- Keller M., Schilling J., Sackmann E., 2001, Oscillatory magnetic bead rheometer for complex fluid microrheometry. *Rev. Sci. Instrum.* 72 (9) 3626-3634, ISSN: 0034-6748
- Konopka M.C., Weisshaar J.C., 2004, Heterogeneous motion of secretory vesicles in the actin cortex of live cells: 3D tracking to 5-nm accuracy. *J. Phys. Chem. A* 108 (45) 9814-9826, ISSN: 1520-6106
- Kralchewski P., Nagayama K., 2001, Particles at fluid interfaces, attachment of colloid particles and proteins to interfaces and formation of two-dimensional arrays. In *Studies in interfacial science*, Vol. 10., Möbius D., Miller R., (Eds.), Elsevier, ISBN: 978-0-444-52180-4, Amsterdam.
- Langevin D., 2000, Influence of interfacial rheology on foam and emulsion properties. *Adv. Colloid Interf. Sci.* 88 (1-2) 209-222, ISSN: 0001-8686
- Larson R.G., 1999, *The structure and rheology of complex fluids*. Oxford University Press, ISBN: 978-0195121971, New York.
- Lee M.H., Lapointe C.P., Reich D.H., Steebe K.J., Leheny R., 2009, Interfacial hydrodynamic drag on nanowires embedded in thin oil films and protein layers, *Langmuir* 25 (14) 7976-7982, ISSN: 0743-7463
- Lee M.H., Reich D.H., Steebe K.J., Leheny R.L., 2010, Combined passive and active microrheology study of protein-layer formation at an air-water interface, *Langmuir* 26 (4) 2650-2658, ISSN: 0743-7463
- Levine A.J., Lubensky T.C., 2000, One- and two-particle microrheology. *Phys. Rev. Lett.* 85 (8) 1774-1777, ISSN: 0031-9007
- Lin B., Rice S.A., Weitz D.A., 1993, Static and dynamic evanescent wave light scattering studies of diblock copolymers adsorbed at the air/water interface. *J. Chem. Phys.*, 99 (10) 8308-8324, ISSN: 0021-9606

- Liu J., Gardel M.L., Kroy K., Frey E., Hoffman B.D., Crocker J.C., Bausch A.R., Weitz D.A., 2006, Microrheology probes length scale dependent rheology. *Phys. Rev. Lett.* 96 (11) 118104, ISSN: 0031-9007
- MacKintosh F.C., Schmidt C.F., 1999, Microrheology. *Curr. Opinion Colloid Interf. Sci.* 4 (4), 300-307, ISSN: 1359-0294
- Madivala B., Fransaeer J., Vermant J. 2009. Self-assembly and rheology of ellipsoidal particles at interfaces. *Langmuir* 25 (5) 2718-2728, ISSN: 0743-7463
- Maestro A., Guzmán E., Chuliá R., Ortega F., Rubio R.G., Miller R. 2011.a. Fluid to soft-glass transition in a quasi-2D system: Thermodynamic and rheological evidences for a Langmuir monolayer. *Phys. Chem. Chem. Phys.* 13 (20) 9534-9539, ISSN: 1463-9076
- Maestro A., Bonales L.J., Ritacco H., Fischer Th.M., Rubio R.G., Ortega, F., 2011.b. Surface rheology: Macro- and microrheology of poly(tert-butyl acrylate) monolayers. *Soft Matter*, in press, ISSN: 1744-683X
- Marcus A.H., Lin B., Rice S.A., 1996, Self-diffusion in dilute quasi-two-dimensional hard sphere suspensions: Evanescent wave light scattering and video microscopy studies. *Phys. Rev. E* 53 (2) 1765-1776, ISSN: 1539-3755
- Mason T.G., Weitz D.A., 1995, Optical measurements of frequency-dependent linear viscoelastic moduli of complex fluids. *Phys. Rev. Lett.* 74 (7) 1250-1253, ISSN: 0031-9007
- Mason Th.G., 2000, Estimating the viscoelastic moduli of complex fluids using the generalized Stokes-Einstein equation. *Rheol. Acta*, 39 (4) 371-378, ISSN: 0035-4511
- Miller R., Liggieri L., (Eds.), 2009, *Interfacial rheology*. Brill, ISBN: 9789004175860, Leiden.
- Mukhopadhyay A., Granick S., 2001, Micro- and nanorheology, *Curr. Opinion Colloid Interf. Sci.* 6 (5-6), 423-429, ISSN: 1359-0294
- Muñoz M.G., Monroy, F., Ortega F., Rubio R.G., Langevin D., 2000, Monolayers of symmetric triblock copolymers at the air-water interface. 2. Adsorption kinetics. *Langmuir* 16 (3) 1094-1101, ISSN: 0743-7463
- Oppong F.K., de Bruyn J.R., 2010, Microrheology and dynamics of an associative polymer, *Eur. Phys. J. E* 31 (1) 25-35, ISSN: 1292-8941
- Ou-Yang H.D., Wei M.T., 2010, Complex fluids: Probing mechanical properties of biological systems with optical tweezers, *Ann. Rev. Phys. Chem.*, 61, 421-440, ISSN: 0066-426X
- Pan W., Filobelo L., Phan N.D.Q., Galkin O., Uzunova V.V., Vekilov P.G., 2009, Viscoelasticity in homogeneous protein solutions, *Phys. Rev. Lett.* 102 (5) 058101, ISSN: 0031-9007
- Paunov V.N. 2003. Novel Method for Determining the Three-Phase Contact Angle of Colloid Particles Adsorbed at Air-Water and Oil-Water Interfaces. *Langmuir* 19 (19) 7970-7976, ISSN: 0743-7463
- Prasad V., Weeks E.R., 2009, Two-dimensional to three-dimensional transition in soap films demonstrated by microrheology, *Phys. Rev. Lett.* 102 (17) 178302, ISSN: 0031-9007
- Resnick A., 2003, Use of optical tweezers for colloid science, *J. Colloid Interf. Sci.* 262 (1) 55-59, ISSN: 0021-9797
- Reynaert S., Moldenaers P., Vermant J. 2007. Interfacial rheology of stable and weakly aggregated two-dimensional suspensions. *Phys. Chem. Chem. Phys.* 9 (48) 6463-6475, ISSN: 1463-9076

- Reynaert S., Brooks C.F., Moldanaers P., Vermant J., Fuller G.G., 2008. Analysis of the magnetic rod interfacial stress rheometer. *52* (1), 261-285, ISSN: 0148-6055
- Riande E., Diaz-Calleja R., Prolongo M.G., Masegosa R.M., Salom C., 2000, *Polymer viscoelasticity. Stress and strain in practice*. Marcel Dekker, ISBN: 0-8247-7904-5, New York.
- Ries J., Schwille P., 2008, New concepts for fluorescence correlation spectroscopy on membranes. *Phys. Chem. Chem. Phys.* 10 (24) 3487-3497, ISSN: 1463-9076
- Riegler R., Elson E.S., 2001, *Fluorescence correlation spectroscopy: Theory and applications*. Springer-Verlag, ISBN: 978-3540674337, Berlin.
- Saffman P-G., Delbrück M. 1975. Brownian Motion in Biological Membranes. *Proc. Nat. Acad. Sci. USA* 72 (8) 3111-3113, ISSN: 1091-6490
- Saxton M.J., Jacobson K., 1997, Single-particle tracking: Applications to membrane dynamics. *Annu. Rev. Biophys. Biomol Struct.* 26 (1) 373-399, ISSN: 1056-8700
- Schmidt F.G., Hinner B., Sackmann E., 2000, Microrheometry underestimates the values of the viscoelastic moduli in measurements on F-actin solutions compared to macrorheometry, *Phys. Rev. E* 61 (5) 5646-5652, ISSN: 1539-3755
- Sickert M., Rondelez F. 2003. Shear viscosity of Langmuir monolayers in the low density limit. *Phys. Rev. Lett.* 90 (12) 126104, ISSN: 0031-9007
- Sickert M., Rondelez F., Stone H.A. 2007. Single-particle Brownian dynamics for characterizing the rheology of fluid Langmuir monolayers. *Eur. Phys. Lett.* 79 (6) 66005, ISSN: 0295-5075
- Squires T.M., 2008, Nonlinear microrheology: Bulk stresses versus direct interactions. *Langmuir* 24 (4) 1147-1159, ISSN: 0743-7463
- Squires T.M., Mason Th.G., 2010, Fluid mechanics of microrheology, *Ann. Rev. Fluid Mechanics*, 42 (1) 413-438, ISSN: 0066-4189
- Steffen P., Heinig P., Wurlitzer S., Khattari Z., Fischer Th.M., 2001, The translational and rotational drag on Langmuir monolayer domains, *J. Chem. Phys.* 115 (2) 994-997, ISSN: 0021-9606
- Stone H., Adjari A. 1998. Hydrodynamics of particles embedded in a flat surfactant layer overlying a subphase of finite depth. *J. Fluid Mech.* 369 (1) 151-173, ISSN: 0022-1120
- Tassieri M., Gibson G.M., Evans R.M.L., Yao A.M., Warren R., Padgett M.J., Cooper J.M., 2010, Optical tweezers. Broadband microrheology, *Phys. Rev. E* 81 (2) 026308, ISSN: 1539-3755
- Vincent R.R., Pinder D.N., Hemar Y., Williams M.A.K., 2007, Microrheological studies reveal semiflexible networks in gels of a ubiquitous cell wall polysaccharide. *Phys. Rev. E* 76 (3) 031909, ISSN: 1539-3755
- Waigh T.A., 2005, Microrheology of complex fluids. *Rep. Prog. Phys.* 68 (3) 685-742, ISSN: 0034-4885
- Wilson L.G., Poon W.C.K., 2011, Small-world rheology: An introduction to probe-based active microrheology, *Phys. Chem. Chem. Phys.* 13 (22) 10617-10630, ISSN: 1463-9076
- Winkler R.G., 2007, Diffusion and segmental dynamics of rodlike molecules by fluorescence correlation spectroscopy. *J. Chem. Phys.* 127 (5) 054904, ISSN: 0021-9606

- Wöll D., Braeken E., Deres A., de Schryver F.C., Uji-I H., Hofkens J., 2009. Polymers and single molecule fluorescence spectroscopy, what can we learn? *Chem. Soc. Rev.* 38 (2), 313-328, ISSN: 0306-0012
- Wu J., Dai L.L., 2006, One-particle microrheology at liquid-liquid interfaces. *Appl. Phys. Lett.*, 89 (9) 094107, ISSN: 0003-6951
- Yoon Y-Z., Kotar J., Yoon G., Cicuta P., 2008, The nonlinear mechanical response of the red blood cell. *Phys. Biol.* 5 (3) 036007, ISSN: 1478-3975

Hydrodynamics Influence on Particles Formation Using SAS Process

A. Montes, A. Tenorio, M. D. Gordillo,
C. Pereyra and E. J. Martinez de la Ossa
*Department of Chemical Engineering and Food Technology,
Faculty of Science, UCA
Spain*

1. Introduction

Particle size and particle size distribution play an important role in many fields such as cosmetic, food, textile, explosives, sensor, catalysis and pharmaceuticals among others. Many properties of industrial powdered products can be adjusted by changing the particle size and particle size distribution of the powder. The conventional methods to produce microparticles have several drawbacks: wide size distribution, high thermal and mechanical stress, environmental pollution, large quantities of residual organic solvent and multistage processes are some of them.

The application of supercritical fluids (SCF) as an alternative to the conventional precipitation processes has been an active field of research and innovation during the past two decades (Jung & Perrut, 2001; Martín & Cocero, 2008; Shariati & Peters, 2003). Through its impact on health care and prevention of diseases, the design of pharmaceutical preparations in nanoparticulate form has emerged as a new strategy for drug delivery. In this way, the technology of supercritical fluids allows developing micronized drugs and polymer-drug composites for controlled release applications; this also meets the pharmaceutical requirements for the absence of residual solvent, correct technological and biopharmaceutical properties and high quality (Benedetti et al., 1997; Elvassore et al., 2001; Falk & Randolph, 1998; Moneghini et al., 2001; Reverchon & Della Porta, 1999; Reverchon, 2002; Subramaniam et al., 1997; Yeo et al., 1993; Winters et al., 1996), as well as giving enhanced therapeutic action compared with traditional formulations (Giunchedi et al., 1998; Okada & Toguchi, 1995).

The revised literature demonstrates that there are two principal ways of micronizing and encapsulating drugs with polymers: using supercritical fluid as solvent, the RESS technique (Rapid Expansion of Supercritical Solutions); or using it as antisolvent, the SAS technique (Supercritical AntiSolvent); the choice of one or other depends on the high or low solubility, respectively, of the polymer and drug in the supercritical fluid.

Although the experimental parameters influence on the powder characteristic as particle size and morphologies is now qualitatively well known, the prediction of the powder characteristics is not feasible yet. This fact is due to different physical phenomena involved in the SAS process. In most cases, the knowledge of the fluid phase equilibrium is

necessary but not sufficient since for similar thermodynamic conditions, different hydrodynamics conditions can lead to different powder characteristics (Carretier et al., 2003).

So, the technical viability of the SAS process requires knowledge of the phase equilibrium existing into the system; the hydrodynamics: the disintegration regimes of the jet; the kinetics of the mass transfer between the dispersed and the continuous phase; and the mechanisms and kinetics of nucleation and crystal growth.

From the point of view of thermodynamics, the SAS process must satisfy the requirements outlined below. The solute must be soluble in an organic solvent but insoluble in the SCF. The solvent must also be completely miscible with the SCF, or two fluid phases would form and the solute would remain dissolved or partly dissolved in the liquid-rich phase. Thus, the SAS process exploits both the high power of supercritical fluids to dissolve organic solvents and the low solubility of pharmaceutical compounds in supercritical fluids to cause the precipitation of these materials once they are dissolved in an organic solvent, and thus spherical microparticles can be obtained.

On the other hand, characterization of hydrodynamics is relevant because of it is an important step for the success or the failure of the entire process, but with only some exception (Dukhin et al., 2005; Lora et al., 2000; Martín & Cocero, 2004), in the models developed for the SAS process, the hydrodynamics step received only limited consideration. For these reasons, the present review is focused on the investigation of the disintegration regime of the liquid jet into the supercritical (SC) CO₂. There are many works where correlations between the morphologies of the particles obtained in the drug precipitation assays and the estimated regimes were established (Carretier et al., 2003; Reverchon et al., 2010; Reverchon & De Marco, 2011; Tenorio et al., 2009). It was demonstrated that there are limiting hydrodynamic conditions that must be overcome to achieve a dispersion of the liquid solution in the dense medium; this dispersion must be sufficiently fine and homogeneous to direct the process toward the formation of uniform spherical nanoparticles and to the achievement of higher yields (Tenorio et al., 2009).

In this way, Reverchon et al. (Reverchon et al., 2010, Reverchon & De Marco, 2011) tried to find a correlation between particle morphology and the observed jet, concluding that expanded microparticles were obtained working at subcritical conditions; whereas spherical microparticles were obtained operating at supercritical conditions up to the pressure where the transition between multi- and single-phase mixing was observed. Nanoparticles were obtained operating far above the mixture critical pressure. However, the observed particle morphologies have been explained considering the interplay among high-pressure phase equilibria, fluid dynamics and mass transfer during the precipitation process, because in some cases the hydrodynamics alone is not able to explain the obtained morphologies, demonstrating the complexity of SAS processes. Moreover, the kinetics of nucleation and growth must also be considered.

2. Supercritical fluids

A supercritical fluid can be defined as a substance above its critical temperature and pressure. At this condition the fluid has unique properties, where it does not condense or evaporate to form a liquid or gas. A typical pressure-temperature phase diagram is shown in Figure 1. Properties of SCFs (solvent power and selectivity) can also be adjusted continuously by altering the experimental conditions (temperature and pressure). Moreover,

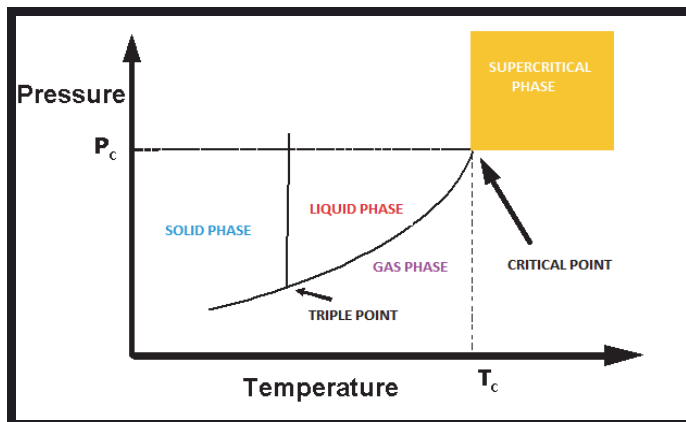


Fig. 1. Pressure-temperature phase diagram

these supercritical fluids have diffusivities that are two orders of magnitude larger than those of typical liquids, resulting in higher mass-transfer rates. Supercritical fluids show many exceptional characteristics, such as singularities in compressibility and viscosity, diminishing the differences between the vapor and liquid phases, and so on. Although a number of substances are useful as supercritical fluids, carbon dioxide has been the most widely used. Supercritical CO_2 avoids water discharge; it is low in cost, non-toxic and non-flammable. It has low critical parameters (304 K, 73.8 bar) and the carbon dioxide can also be recycled (Özcan et al., 1998).

3. Precipitation with SCF

The supercritical fluid technology has emerged as an important alternative to traditional processes of generation of micro and nanoparticles, offering opportunities and advantages such as higher product quality in terms of purity, more uniform dimensional characteristics, a variety of compounds to process and a substantial improvement on environmental considerations, among others.

Previously, it was discussed that the different particle formation processes using SCF are classified depending on how the SCF behaves, i.e., the supercritical CO_2 can play the role as antisolvent (AntiSolvent Supercritical process, SAS) or solvent (RESS process).

In the facilities of University of Cádiz, amoxicillin and ampicillin micronization have been carried out by SAS process (Montes et al., 2010, 2011a; Tenorio et al., 2007a, 2007b, 2008). Several experiments designs to evaluate the operating conditions influences on the particle size (PS) and particle size distribution (PSD) have been made. Pressures till 275 bar and temperatures till 338K have been used and antibiotic particle sizes have been reduced from 5-60 μm (raw material) to 200-500 nm (precipitated particles) (Figure 2).

The concentration was the factor that had the greatest influence on the PS and PSD. An increase in the initial concentration of the solution led to larger particles sizes with a wider distribution. Moreover, ethyl cellulose and amoxicillin co-precipitation has been carried out by SAS process (Montes et al., 2011b). SEM images of these microparticles are shown in Figure 3. It was noted that increasing temperature particle sizes were increased. Anyway, SEM images are not accurate enough to observe the distribution of both compounds

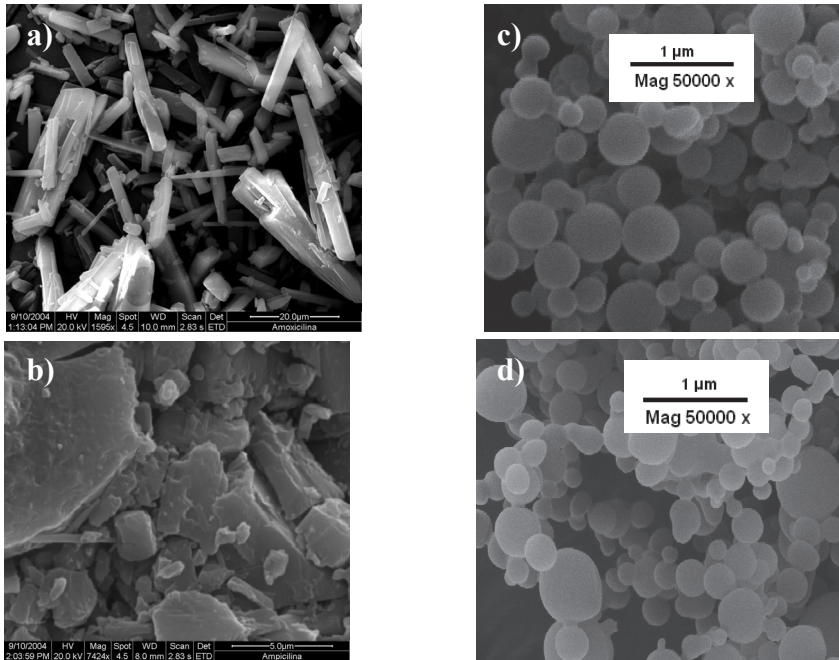


Fig. 2. SEM images of commercial a) amoxicillin and b) ampicillin, c) precipitated amoxicillin (Montes et al., 2010) and d) precipitated ampicillin (Montes et al., 2011a)

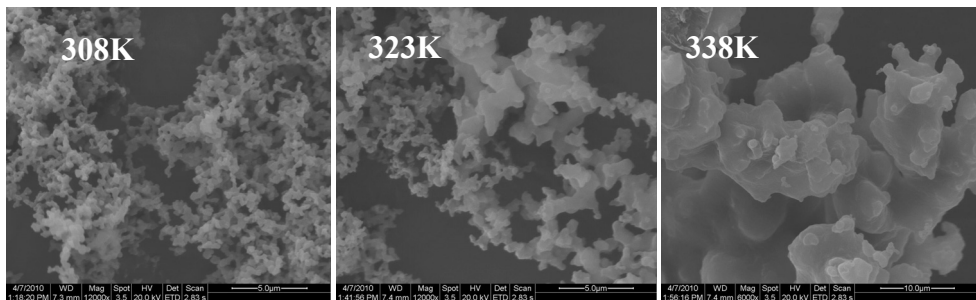


Fig. 3. SEM images of amoxicillin ethyl cellulose co-precipitated (Montes et al., 2011b).

because all the active substance could be situated on the surface of these microspheres and/or into the core. So, X-ray photoelectron spectroscopy (XPS) was used to determine the success of the encapsulation process by the chemical analysis of the particles on the precipitated surface (Morales et al., 2007). In this case, the elements that differentiate amoxicillin from ethyl cellulose are sulphur (S) and nitrogen (N) atoms. Therefore, these elements could indicate the location of the drug in the precipitated powders. On the other hand, amoxicillin delivery studies in simulated fluids from the co-precipitated obtained were carried out. The XPS spectra results were related to these drug delivery experiments and it was probed that the release of amoxicillin from precipitates in which N and S were

present on the surface is faster than in cases these elements were not. Anyway, all the co-precipitated materials allowed a slower drug release rate than pure drug.

On the other hand, in the RESS method, the sudden expansion of supercritical solution (solute dissolved in supercritical carbon dioxide) via nozzle and the rapid phase change at the exit of the nozzle cause a high super-saturation, thus causing very rapid nucleation of the substrate in the form of very small particles that are collected from the gas stream. Hence, the conditions inside the expansion chamber are a key factor to control particle size and the particles grow inside the expansion chamber to their final size. This result clarifies the influence of two important process parameters on particle size. Both, a shorter residence time and, hence, less time available for particle growth as well as a higher dilution of the particles in the expansion chamber result in smaller particles.

3.1 Parameters influence on hydrodynamic

Mass transfer is one of the key factors that control the particle size in the SAS process. This is influenced by both the spray hydrodynamics of the organic solution and the thermodynamic properties of the supercritical fluid phase.

In the last years, the hydrodynamic of the SAS process has been the subject of several papers. Most authors face up to this problem considering that the jet of organic solvent behaves like a liquid jet injected into a gas, allowing to apply the classic theory of jet break-up. This theory could be applied successfully at subcritical conditions, below the mixture critical point solvent-CO₂, where there is surface tension. The mixture critical point denotes the limit of the two-phase region of the phase diagram. In other words, this is the point at which an infinitesimal change in some thermodynamic variable such as temperature or pressure will lead to separation of the mixture into two distinct phases.

However, in supercritical conditions, above the critical point of the mixture organic solvent and CO₂, it is not possible to distinguish droplets nor interfaces between the liquid solution and the phase of dense CO₂ gas. Surface tension decreases to zero in a shorter distance than characteristic break-up lengths. Thus, the jet spreads forming a gaseous plume and will be characterized by the degree of turbulence associated with the vortices produced in the SC CO₂ (Chehroudi et al., 2002; Kerst et al., 2000; Reverchon et al., 2010). Lengsfeld et al. were the first group that investigated fluid dynamics of the SAS process, studying the evolution and disappearance of the liquid surface tension of fluids injected in supercritical carbon dioxide. They concluded that a gas-like jet is formed after the jet break-up (Lengsfeld et al., 2000). In this way, Kerst et al. determined the boundaries between the different modes and they noted a strong interdependence between mass transfer and fluid dynamics (Kerst et al., 2000).

In the SAS related literature there is a general agreement about the flow regimes observable when a liquid is injected in a vessel. The way in which the liquid solution is dispersed in the CO₂ when the operating conditions are below the mixture critical point (MCP), which is strongly influenced by the operating pressure and the flow rate of liquid solution at fixed temperature, can be described according to one of the following four regimes: 1) the dripping mode, which requires lower flow speed so that drops can detach themselves from the orifice, 2) the Rayleigh break up regime, which is characterized by a rupture of the jet in the form of monodisperse droplets, 3) the sine wave break up regime, in which a helicoidal oscillation of the jet occurs, leading to its rupture into droplets with a polydisperse distribution, and 4) atomization, in which the jet is smooth when it leaves the orifice, until it reaches the zone of highly chaotic rupture where a cone of atomized liquid is formed.

When SAS is performed at supercritical conditions a transition between multi-phase and single-phase mixing is observed by increasing the operating pressure. Single-phase mixing is due to the very fast disappearance of the interfacial tension between the liquid solvent and the fluid phase in the precipitator. The transition between these two phenomena depends on the operating pressure, but also on the viscosity and the surface tension of the solvent. Reverchon et al. demonstrates that in the case of dimethyl sulfoxide (DMSO) at pressures larger than the MCP a progressive transition exists between multi-phase and single-phase mixing, but is not observed, even for pressures very close to the MCP, in the case of acetone (Reverchon et al., 2010). In the dripping mode, the droplet size decrease with increase in pressure operation due to a corresponding decrease in the interface tension, so the initial droplet size can be manipulated by small changes in the pressure of CO₂ (Lee et al., 2008).

However, in the Rayleigh disintegration mode, the droplet size is weakly dependent on the interface tension of the system and is proportional to the diameter of the jet. In the dripping mode, the size and shape of the drops become highly dependent on the nozzle exit condition.

Sometimes, the transition between multi-phase (formation of droplets after jet break-up) and single-phase mixing (no formation of droplets after jet break-up) could not be located at the pressure of the mixture critical point. Dukhin et al. (Dukhin et al., 2003) and Gokhale et al. (Gokhale et al., 2007) found that jet break-up into droplets still takes place at pressures slightly above the MCP. Due to the non-equilibrium conditions during mixing, there is a dynamic (transient) interfacial tension that decreases between the inlet of the liquid and its transformation to a gas-like mixture. The transition between these multi-phase and single-phase mixing depends on the operating pressure, but also on the viscosity and the surface tension of the solvent.

Not only the thermodynamics but also the nozzle device or liquid solution flow rate will influence on the observed regime. The kind of injection device and its orifices diameter will determine the chosen liquid solution flow rate to get a successful jet break up. In this way, in a previous work, when the 200 μm diameter nozzle was used with a liquid flow rate of 1mL/min, the solution was not atomized, and we did not obtain any precipitation (Tenorio et al., 2009).

A lot of parameters control the precipitation process and many particle morphologies have been observed. As it was commented before, the kind of injection device used (and its efficiency), can strongly influence the precipitation process. The objective of these devices in SAS processing is to produce a very large contact surface between the liquid and the fluid phase, to favour the mass transfer between the antisolvent and the liquid solvent inducing jet break-up and atomization of the liquid phase.

Various injection devices to produce liquid jet break-up have been proposed in the literature. Yeo et al. (Yeo et al., 1993) proposed the adoption of a nozzle and tested various nozzle diameters ranging from 5 to 50 μm . Moussa et al. (Moussa et al., 2005) showed that the pressure distribution during the expansion of the supercritical fluid is a function of the nozzle length and diameter. Other authors used small internal diameter capillaries (Dixon et al., 1993; Randolph et al., 1993). Coaxial devices have also been proposed: in the SEDS process (solution enhanced dispersion by supercritical fluids) a coaxial twin-fluid nozzle to co-introduce the SCF antisolvent and solution is used (Bałdyga et al., 2010; He et al., 2010; Mawson et al., 1997; Wena et al., 2010). Complex nozzles geometries have also been tested carrying out a comparative study of the nozzle by computational fluid dynamics (Balabel et

al., 2011; Bouchard et al., 2008). Petit-Gas et al. found that for the lowest capillary internal diameter studied, there were particles with differences morphologies according to the jet velocity. For the lowest jet velocity, irregular morphology was obtained, and for highest jet velocity spherical morphology was obtained (Petit-Gas et al., 2009). However, for the highest capillary internal diameter experiments, particles morphology difference was less important. Particles were quasi-spherical, to a lesser extent for the smallest jet velocity. Once more time it was demonstrated the parameters interrelation in SAS process and its great complexity. Not only the kind of nozzle but also the nozzle relative position to CO₂ inlet must be taken into account. In this way, Martin & Cocero studied the differences on hydrodynamics and mixing when CO₂ is not introduced through the concentric annulus, but through a different nozzle, which is placed relatively far from the nozzle of the organic solution. Since the inlet velocity of CO₂ is much lower than the inlet velocity of the solution, this flow has a relatively small influence on hydrodynamics and mixing. However, if CO₂ is not introduced through the annulus, the fluid that diffuses into the jet is no longer almost pure CO₂, but fluid from the bulk fluid phase, which has some amount of organic solvent. This greatly reduces the supersaturation and bigger particles are formed (Martin & Cocero, 2004).

Moreover, these different unstable modes (Rayleigh break up, sine wave break up and atomization) are controlled by several competing effects: capillary, inertial, viscous, gravity and aerodynamic effects (Petit-Gas et al., 2009). The predominance of each effect has been discussed in several works (Badens et al., 2005; Carretier et al., 2003; Kerst et al., 2000). Reynolds number gives a measure of the ratio of inertial forces to viscous forces. For the lower Reynolds numbers, Rayleigh regime is observed and surface tension is the chief force controlling the break-up of an axisymmetrical jet. For higher Reynolds numbers, the inertial forces compete with the capillary forces. There is a lateral motion in the jet break-up zone which leads to the formation of an asymmetrical jet, which can be either sinuous or helicoidal. Finally, when the flow rate goes beyond a certain value, the aerodynamic effects become quite strong and the jet is atomised. Another dimensionless number frequently used to describe jet fluid dynamics is the Ohnesorge (Oh) number that relates the viscous and the surface tension force by dividing the square root of Weber number by Reynolds number (Badens et al., 2005; Czerwonatis, 2001; Kerst et al., 2000).

In this way, taking into account the critical atomization velocity defined as the velocity corresponding to the boundary between the asymmetrical mode and the atomization mode, it is possible to tune the process towards one or another regime. Moreover this critical velocity seems to be dependent on CO₂ density. Badens et al. observed a decrease in this critical jet velocity when the CO₂ continuous phase density increases (Badens et al., 2005). Badens et al. and Czerwonatis et al. found out the predominant effect of the continuous phase properties on jet break-up, especially in the asymmetrical and direct atomization modes because of the aerodynamic forces preponderance (Badens et al., 2005; Czerwonatis et al., 2001). However Petit-Gas et al. concluded that variations of the continuous phase properties had no effects on the transition velocity in the studied conditions (Petit-Gas et al., 2009).

3.2 Morphology

Some authors attempted to connect the observed flow or mixing regimes to the morphology of the precipitated particles. Lee et al. injected a solution of dichloromethane (DCM) and poly lactic acid (PLA) at subcritical conditions in the dripping and in the Rayleigh

disintegration regimes and observed the formation of uniform PLA microparticles (Lee et al., 2008). Other authors (Chang et al., 2008; Gokhale et al., 2007; Obrzut et al., 2007; Reverchon et al., 2008) did not find relevant differences in the various precipitates obtained. Particularly, PLA morphologies showed to be insensitive to the SAS processing conditions (Randolph et al., 1993). This characteristic fact could be assigned to the high molecular weights and the tendency to form aggregated particles because of the reduction of the glass transition temperature in SC-CO₂.

At subcritical conditions the interfacial tension between the injected liquid and the bulk phase never goes to zero and a supercritical mixture is not formed between the liquid solvent and CO₂. The droplets formed during atomization are subjected to a very fast internal formation of a liquid/CO₂ mixture. Due to a high solubility of CO₂ in pressurized organic liquids and a very poor evaporation of organic solvents into the bulk CO₂, the droplets expand. During these processes, the interfacial tension allows the droplets to maintain its spherical shape, even when the solute is precipitated within the droplet. Saturation occurs at the droplet surface and solidification takes place with all solutes progressively condensing on the particle internal surface. The final result is the formation of a solid shell.

This kind of particles has also been observed in other SAS works (Reverchon et al., 2008). It has been also obtained expanded hollow particle at same conditions. The different surface morphologies can depend on different controlling mass transfer mechanisms, as suggested by Duhkin et al. (Duhkin et al., 2005).

Operating conditions above the MCP, from a thermodynamic point of view, are characterized by zero interfacial tension. But, the liquid injected into the precipitator, before equilibrium conditions are obtained, experiences the transition from a pure liquid to a supercritical mixture. Therefore, interfacial tension starts from the value typical of the pure liquid and progressively reduces to zero. This fact means that droplets formed after jet break-up (whose presence indicates in every case the existence of an interfacial tension) are formed before the disappearance of the interfacial tension. In other words, the time of equilibration is longer than the time of jet break-up and spherical microparticles instead of nanoparticles can be obtained.

3.3 Visualization techniques

Many researchers have used imaging and visualization techniques to study jet flows, atomization, and droplets; a number of systems are reviewed in the literature (Bell et al., 2005; Chigier et al., 1991). Jet lengths and spray widths ranging to millimeters and drop and particle sizes ranging to micrometers must be taking into account in order to select imaging system components.

Several studies used particle and droplet visualization in supercritical fluids (Badens et al., 2005; Gokhale et al., 2007; Kerst et al., 2000; Lee et al., 2008; Mayer & Tamura, 1996; Obrzut et al., 2007; Randolph, et al., 1993; Shekunov et al., 2001).

The optical technique described in these works provides the ability to visualize mixing occurring between two fluids with different refractive indices. For instance, shadowgraphy is an optical method to obtain information on non-uniformities in transparent media, independently if they arise by temperature, density or concentration gradients. All of these inhomogeneities refract light which causes shadows.

Although for SAS precipitation, microscopy-base imaging offers the advantage of examining the dynamic process that leads to particle formation, the presence of particles smaller than two microns complicates an already difficult task of imaging an injection process.

The ability to identify and characterize these small formations drives future system improvements, including lighting enhancements laser-induced fluorescence, and higher spatial resolution cameras. In this way Reverchon et al. used light scattering technique to clearly differentiate between an atomized very droplet laden spray and a dense "gas-plume", limitation which cannot be gained by applying optical techniques due to the fact that both the droplet laden spray and the dense "gas-plume" result in a dark shadow (Reverchon et al., 2010).

On the other hand, extensive research has been done using scanning electron microscopy (SEM) to evaluate the size and morphology of particles formed under supercritical conditions (Armellini & Tester, 1994; Bleich et al., 1994; Mawson et al. 1997; Randolph et al., 1993; Shekunov et al., 2001). A limitation of SEM analysis is that it is applied to particles after they have been removed from the dynamic system.

4. A particular case: Ampicillin SAS precipitation

In our research group a study was carried out to establish a correlation between the morphologies of the particles obtained in the ampicillin precipitation assays and the estimated regimes. This correlation would be an ideal tool to establish the limiting hydrodynamic conditions for the success of the test in order to define the successful experiments; that is, the appropriate conditions to orientate the process toward the formation of uniform spherical nanoparticles instead of irregular and larger-sized particles, for the solute-solvent-SC CO₂ system studied (Tenorio et al., 2009).

A series of ampicillin precipitation experiments by the SAS technique, utilizing N-methylpyrrolidone (NMP) as the solvent and CO₂ as the antisolvent, under different operating conditions were carried out. Two nebulizers, with orifice diameters of 100 and 200 μm, respectively were used.

A pilot plant, developed by Thar Technologies® (model SAS 200) was used to carry out all the experiments. A schematic diagram of this plant is shown in Figure 4. The SAS 200 system comprises the following components: two high-pressure pumps, one for the CO₂ (P1) and the other for the solution (P2), which incorporate a low-dead-volume head and check valves to provide efficient pumping of CO₂ and many solvents; a stainless steel precipitator vessel (V1) with a 2L volume consisting of two parts, the main body and the frit, all surrounded by an electrical heating jacket (V1-HJ1); an automated back-pressure regulator (ABPR1) of high precision, attached to a motor controller with a position indicator; and a jacketed (CS1-HJ1) stainless steel cyclone separator (CS1) with 0.5L volume, to separate the solvent and CO₂ once the pressure was released by the manual back-pressure regulator (MBPR1). The following auxiliary elements were also necessary: a low pressure heat exchanger (HE1), cooling lines, and a cooling bath (CWB1) to keep the CO₂ inlet pump cold and to chill the pump heads; an electric high-pressure heat exchanger (HE2) to preheat the CO₂ in the precipitator vessel to the required temperature quickly; safety devices (rupture discs and safety valve MV2); pressure gauges for measuring the pump outlet pressure (P1, PG1), the precipitator vessel pressure (V1, PG1), and the cyclone separator pressure (CS1, PG1); thermocouples placed inside (V1-TS2) and outside (V1-TS1) the precipitator vessel, inside the cyclone separator (CS1-TS1), and on the electric high pressure heat exchanger to obtain continuous temperature measurements; and a FlexCOR Coriolis mass flowmeter (FM1) to measure the CO₂ mass flow rate and another parameters such as total mass, density, temperature, volumetric flow rate, and total volume.

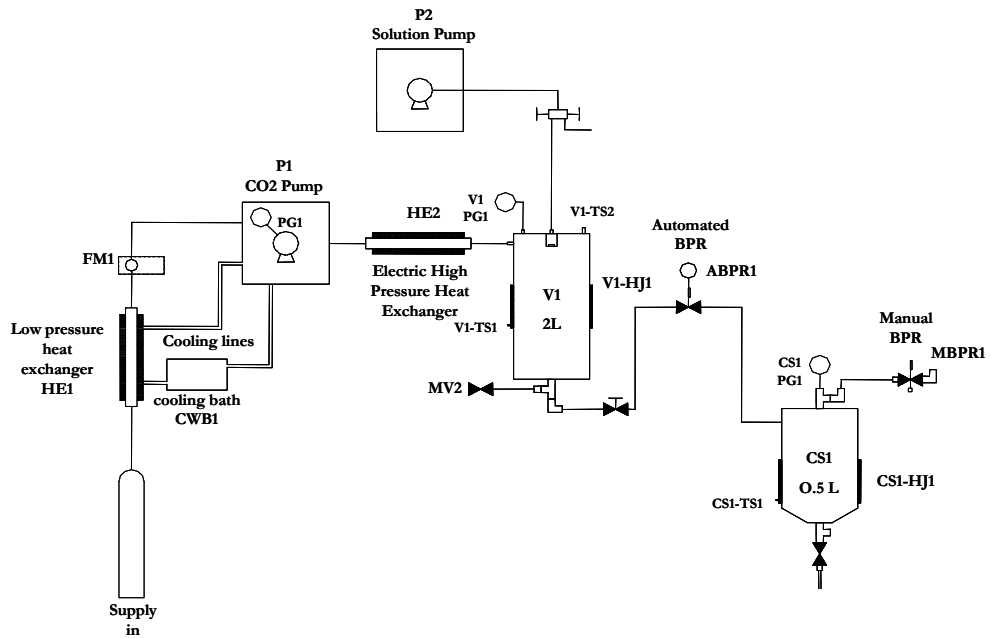


Fig. 4. Schematic diagram of the pilot plant

The pendant droplet method, as introduced by Andreas and Tucker, was used to determine the interfacial tension between NMP and SC CO₂ (Andreas&Tucker, 1938). This method, and its application to high pressures and temperatures, are comprehensively described by Jaeger (Jaeger et al., 1996). A commercial CCD video technique allows recording of droplet shapes for subsequent video image processing.

Rayleigh breakup, sinusoidal wave break up, and atomization regimes are seen to be clearly differentiated by representing graphically the Reynolds number against Ohnesorge number. Here, the forces of inertia of the liquid phase (pressure gradient), the forces of capillarity (surface tension), and those of viscosity of the liquid phase (friction) are taken into account, but the force of gravity is considered to be negligible.

Two differentiated types of morphology can be identified in the precipitated experiments: spherical nanoparticles of ampicillin that are obtained from a fine precipitate with foamy texture, and particles of ampicillin with irregular forms and larger size, which are characteristic of the precipitate formed by aggregates, compact films, and rods (Figure 5). The aim of the work is to explain, from the estimation of the different disintegration regimes as a function of the physicochemical properties and of the velocity of the jet, the two different morphologies obtained in the ampicillin precipitation experiments for a specific range of operating conditions. Thus it should be possible to specify the hydrodynamic conditions for orientating the process toward the formation of uniform spherical nanoparticles rather than larger size irregular particles.

The morphology of the precipitate obtained at low pressure was supposed to be in accordance with the Rayleigh estimated regime, since droplets with a diameter of approximately twice the diameter of the orifice would be produced; (Badens et al., 2005)

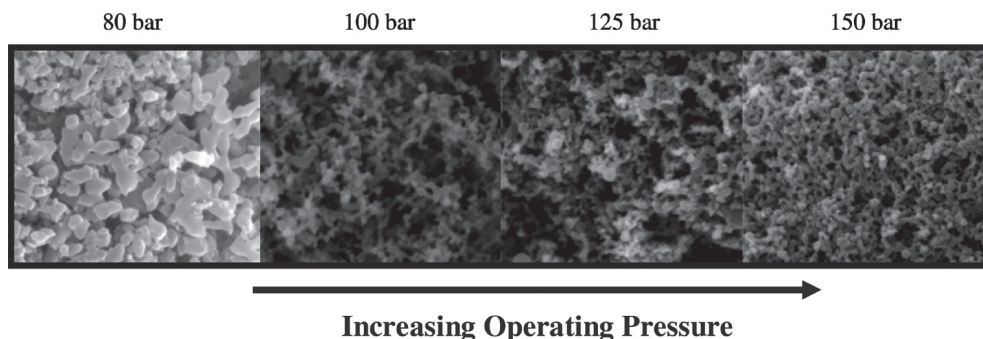


Fig. 5. Effect of operating pressure on microstructure of ampicillin powder obtained by the SAS experiments (Tenorio et al., 2009).

then, because sufficient contact area would not be generated, the liquid phase does not evaporate in the dense phase of the CO_2 . Instead, the liquid droplets accumulate in the filter, where the precipitate is obtained by the drying action of the CO_2 .

In contrast, for higher pressures, the presence of a precipitate occurring as aggregates in the filter may be explained by the existence of significant mechanisms that stabilize the liquid jet. These important mechanisms of stabilization may be associated with the existence of the dynamic interfacial tension (Dukhin et al., 2003). Therefore, the so-called “gaseous plume” or “gas-like jet”, which is characteristic of states of complete miscibility of mixtures (above their MCP), would not be produced, even at 150 bar.

The influence of the mean velocity of the jet of liquid solution was also analyzed. The liquid solution flow rate from 1 mL/min to 5 mL/min causes the jet to disintegrate, passing through the three possible regimes: Rayleigh, sine wave break-up and atomization. The lowest flow rate tested (1 mL/min), which is equivalent to a jet velocity of 0.5 m/s (200 μm nozzle diameter), led to an unsatisfactory test result, which may be in agreement with the Rayleigh-type estimated regime; this is because the droplets that formed would not generate sufficient contact area to produce saturation while they are in motion, and, consequently, ampicillin is not precipitated. When the liquid solution flow rate is increased to 2 mL/min a dispersion of the sine wave breakup type is estimated. Considering that a polydisperse

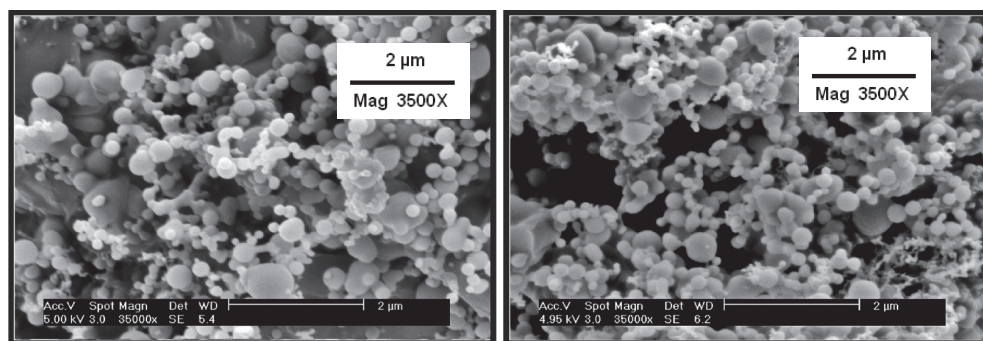


Fig. 6. SEM images showing the microstructure of the ampicillin powder obtained by SAS experiment with 5ml/min (at 180 bar, 328 K, and 200 μm) (Tenorio et al., 2009).

distribution of droplets is produced in this regime, it is very well correlated with the experimental obtained results (Tenorio et al., 2009).

When the flow rate is increased to 3 mL/min, it is estimated that the transition is complete, and the liquid is atomized. The large quantity of fine precipitate with foamy texture obtained both on the walls and accumulated in the filter (characteristic of nanoparticles) would have originated from the fully atomized and homogeneous dispersion that is occurring in the precipitation chamber. With 5 mL/min it was obtained similar results in accordance with the estimated atomization regime (Figure 6).

5. Conclusions

The hydrodynamics of the SAS process has been revised. Nozzle device, liquid flow rate and pressure effects on hydrodynamics have been taken into account. Flow regimes observable in the SAS related literature have been described. Dripping mode is simply due to the use of liquid flow rates that are too low to produce a continuous liquid flow and do not produce atomization. Rayleigh breakup, sinusoidal wave break up, and atomization regimes and, particularly their competition at some process conditions require a detailed analysis. The ability to identify and characterize these regimes drives future system improvements, including lighting enhancements laser-induced fluorescence, and higher spatial resolution cameras.

Morphology of the precipitated particles can be related to flow or mixing regimes. In the ampicillin case, two differentiated types of morphology can be identified in the precipitated experiments: spherical nanoparticles of ampicillin that are obtained from a fine precipitate with foamy texture, and particles of ampicillin with irregular forms and larger size, which are characteristic of the precipitate formed by aggregates, compact films, and rods. It has been correlated the morphologies of the particles obtained in the ampicillin precipitation assays and the estimated regimes as a function of the physicochemical properties and of the velocity of the jet, for a specific range of operating conditions.

However, the results from the application of these correlations cannot explain the morphologies of the precipitates obtained in some experiments. This fact can be due to important stabilization mechanisms as dynamic interfacial tension

Due to the great complexity of the SAS process, factors such as the ternary phase equilibrium, matter transfer between the phases, and the kinetics of nucleation and growth need to be considered, in addition to the limiting hydrodynamic conditions.

6. Acknowledgment

We are grateful to the Spanish Ministry of Education and Science (Project No. CTQ2010-19368) for financial support.

7. References

- Andreas, J. M.; Tucker, W. B. (1938). Boundary Tension by Pendant Drop. *J. Phys. Chem.*, 42, pp. 1001-1019.
- Armellini, F.J., Tester, J.W. (1994). Precipitation of sodium chloride and sodium sulfate in water from sub- to supercritical conditions: 150 to 550°C, 100 to 300 bar. *J. Supercrit. Fluids*, 7, pp. 147-158.

- Badens, E., Boutin, O., Charbit, G. (2005). Laminar jet dispersion and jet atomization in pressurized carbon dioxide, *J. Supercrit. Fluids*, 36, pp. 81-90.
- Balabel, A., Hegab, A.M., Nasr, M., El-Behery, S. M. (2011). Assessment of turbulence modeling for gas flow in two-dimensional convergent-divergent rocket nozzle. *Appl. Math. Model.*, 35, pp. 3408-3422.
- Baldyga, J., Kubicki, D., Shekunov, B.Y., Smith, K.B. (2010). Mixing effects on particle formation in supercritical fluids, *Chem. Eng. Res. Des.*, 88, pp. 1131-1141.
- Bell, P. W., Stephens, A. P., Roberts, C. B., Duke, S. R. (2005). High-resolution imaging of the supercritical antisolvent process, *Experiments in Fluids*, 38, pp. 708-719.
- Benedetti, L., Bertucco, A., Pallado, P. (1997). Production of micronic particles of biocompatible polymer using supercritical carbon dioxide, *Biotechnol. Bioeng.*, 53, pp. 232-237.
- Bleich, J., Cleinebudde, P., Muller, B.W. (1994). Influence of gas density and pressure on microparticles produced with the ASES process, *Int. J. Pharm.*, 106, pp. 77-84.
- Bouchard, A., Jovanovic, N., A. H. de Boer, Martín, A., Jiskoot, W., Crommelin, D. J.A. , Hofland, G.W., Witkamp, G.-J. (2008). Effect of the spraying conditions and nozzle design on the shape and size distribution of particles obtained with supercritical fluid drying, *Eur. J. Pharm. Biopharm.*, 70, pp. 389-401.
- Carretier, E., Badens, E., Guichardon, P., Boutin, O., Charbit, G. (2003). Hydrodynamics of supercritical antisolvent precipitation: characterization and influence on particle morphology, *Ind. Eng. Chem. Res.*, 42, pp. 331-338.
- Czerwonat, N., Eggers, R., Charbit, G. (2001). Disintegration of liquid jets and drop drag coefficients in pressurized nitrogen and carbon dioxide, *Chem. Eng. Tech.*, 24, pp. 619-624.
- Chang, S.-C., Lee, M.-J., Lin, H.-M. (2008). Role of phase behavior in micronization of lysozyme via a supercritical anti-solvent process, *Chem. Eng. J.*, 139, pp. 416-425.
- Chehroudi, B., Cohn, R., Talley, D. (2002). Cryogenic shear layers: experiments and phenomenological modelling of the initial growth rate under subcritical and supercritical conditions, *Int. J. Heat Fluid Flow*, 23, pp. 554-563.
- Chigier, N. (1991). Optical imaging of sprays. *Prog. Energy Combust. Sci.*, 17, pp.211-262
- Dixon, D.J., Johnston, K.P., Bodmeier, R.A. (1993). Polymeric materials formed by precipitation with a compressed fluid antisolvent, *AIChE J.*, 39 (1), pp. 127-139.
- Dukhin, S.S., Zhu, C., Pfeffer, R., Luo, J.J., Chavez, F., Shen, Y. (2003). Dynamic interfacial tension near critical point of a solvent-antisolvent mixture and laminar jet stabilization, *Physicochem. Eng. Aspects*, 229, pp. 181-199.
- Dukhin, S. S., Shen, Y., Dave, R., Pfeffer, R. (2005). Droplet mass transfer, intradroplet nucleation and submicron particle production in two-phase flow of solvent-supercritical antisolvent emulsion. *Colloids Surf. A*, 261, pp. 163-176.
- Elvassore, N., Bertucco, A., Caliceti, P. (2001). Production of insulin-loaded poly(ethylene glycol)/poly(L-lactide) (PEG/PLA) nanoparticles by gas antisolvent techniques, *J. Pharm. Sci.*, 90, pp. 1628-1636.
- Falk, R.F., Randolph, T.W. (1998). Process variable implications for residual solvent removal and polymer morphology in the formation of gentamycin-loaded poly (L-lactide) microparticles, *Pharm. Res.*, 15, pp. 1233-1237.
- Giunchedi, P., Genta, I., Conti, B., Conte, U., Muzzarelli, R.A.A. (1998). Preparation and characterization of ampicillin loaded methylpyrrolidinone chitosan and chitosan microspheres, *Biomat.*, 19, pp.157-161.

- Gokhale, A., Khusid, B., Dave, R.N., Pfeffer, R. (2007). Effect of solvent strength and operating pressure on the formation of submicrometer polymer particles in supercritical microjets, *J. Supercrit. Fluids*, 43, pp 341-356.
- He, W., Jiang, Z., Suo, Q., Li, G. (2010). Mechanism of dispersing an active component into a polymeric carrier by the SEDS-PA process, *J. Mater. Sci.*, 45, pp. 467-474.
- Jaeger, Ph T.; Schnitzler, J. V.; Eggers, R. (1996). Interfacial Tension of Fluid Systems Considering the Non-Stationary Case with Respect to Mass Transfer. *Chem. Eng. Technol.*, 19, pp.197.
- Jung, J., Perrut, M. (2001). Particle design using supercritical fluids: Literature and patentsurvey. *J. Supercrit. Fluids*, 20 (3), pp. 179-219.
- Kerst, A.W., Judat, B., Schlünder, E.U. (2000). Flow regimes of free jets and falling films at high ambient pressure, *Chem. Eng. Sci.*, 55, pp. 4189-4208.
- Lee, L.Y., Lim L. K., Hua, J., Wang, C.-H. (2008). Jet breakup and droplet formation in near-critical regime of carbon dioxide-dichloromethane system, *Chem. Eng. Sci.*, 63, pp. 3366-3378.
- Lengsfeld, C.S., Delplanque, J.P., Barocas, V.H., Randolph, T.W. (2000). Mechanism governing microparticle morphology during precipitation by a compressed antisolvent: atomization vs nucleation and growth, *J. Phys. Chem. B*, 104, pp. 2725-2735.
- Lora, M., Bertucco, A., Kikic, I. (2000). Simulation of the Semicontinuous Supercritical Antisolvent Recrystallization Process. *Ind. Eng. Chem. Res.*, 39, pp. 1487-1496.
- Martín, A., Cocero, M.J. (2004). Numerical modeling of jet hydrodynamics, mass transfer, and crystallization kinetics in the supercritical antisolvent (SAS) process *J. Supercrit. Fluids*, 32, pp. 203-219.
- Martín, A., Cocero, M.J. (2008). Precipitation processes with supercritical fluids: patents review, *Recent Patents Eng.* 2, pp.9 -20.
- Mawson S, Kanakia S, Johnston KP. (1997). Coaxial nozzle for control of particle morphology in precipitation with a compressed fluid antisolvent, *J. Appl. Polym. Sci.*, 64:, pp. 2105-2118.
- Mayer, W., Tamura, H. (1996). Propellant injection in a liquid oxygen/ gaseous hydrogen rocket engine. *J. Propul. Power*, 12(6), pp.1137-1147.
- Moneghini, M., Kikic I., Voinovich, D., Perissutti, B., Filipovic-Grcic, J. (2001). Processing of carbamazepine - PEG 4000 solid dispersions with supercritical carbon dioxide: Preparation, characterisation, and in vitro dissolution, *Int. J. Pharm.*, 222, pp.129-138.
- Montes, A., Tenorio, A., Gordillo, M.D., Pereyra, C., Martínez de la Ossa, E. (2010). Screening design of experiment applied to supercritical antisolvent precipitation of amoxicillin: exploring new miscible conditions. *J. Supercrit. Fluids*, 51, pp. 399-403.
- Montes, A., Tenorio, A., Gordillo, M.D., Pereyra, C., Martínez de la Ossa, E. (2011a). Supercritical Antisolvent Precipitation of Ampicillin in Complete Miscibility Conditions. *Ind. Eng. Chem. Res.*, 50, pp. 2343-2347.
- Montes, A., Gordillo, M.D., Pereyra, C., Martínez de la Ossa, E. (2011b). Co-precipitation of amoxicillin and ethylcellulose microparticles by supercritical antisolvent process *J. Supercrit. Fluids* (in press).
- Morales, M. E., Ruiz, M. A., Oliva, I., Oliva, M., Gallardo, V. (2007). Chemical characterization with XPS of the surface of polymer microparticles loaded with morphine. *Int. J. Pharm.*, 333, pp. 162-166.

- Moussa, A. B., Ksibi, H., Tenaud, C., Baccar, M. (2005). Parametric study on the nozzle geometry to control the supercritical fluid expansion, *Int. J. Thermal Sciences*, 44, pp. 774-786.
- Obrzut, D.L., Bell, P.W., Roberts, C.B., Duke, S.R. (2007). Effect of process conditions on the spray characteristics of a PLA plus methylene chloride solution in the supercritical antisolvent precipitation process, *J. Supercrit. Fluids*, 42, pp. 299-309.
- Okada, H., Toguchi, H. (1995). Biodegradable microspheres in drug delivery, *Crit. Rev. in Ther. Drug Carrier Syst.*, 12, pp. 1-99.
- Ozcan, A.S.; Clifford, A.A.; Bartle, K.D. and Lewis, D.M. (1998). Dyeing of cotton fibres with disperse dyes in supercritical carbon dioxide, *Dyes and Pigments*, 36(2), pp. 103-110.
- Petit-Gas, T., Boutin, O., Raspo, I., Badens, E. (2009). Role of hydrodynamics in supercritical antisolvent processes, *J. Supercrit. Fluids*, 51, pp. 248-255.
- Randolph, T.W., Randolph, A.D., Mebes, M., Yeung, S. (1993). Sub-micrometer-sized biodegradable particles of poly(L- lactic acid) via the gas antisolvent spray precipitation process, *Biotechnol. Progress*, 9, pp. 429-435.
- Reverchon, E., Della Porta, G. (1999). Production of antibiotic micro- and nano-particles by supercritical antisolvent precipitation, *Powder Technol.*, 106, pp. 23-29.
- Reverchon, E. (2002). Supercritical-assisted atomization to produce micro- and/or nanoparticles of controlled size and distribution, *Ind. Eng. Chem. Res.*, 41, pp. 2405-2411.
- Reverchon, E., Adami, R., Caputo, G., De Marco, I. (2008). Expanded microparticles by supercritical antisolvent precipitation: interpretation of results. *J. Supercrit. Fluids*, 44(1), pp. 98-108.
- Reverchon, E.; Torino, E.; Dowy, S.; Braeuer, A.; Leipertz, A. (2010). Interactions of phase equilibria, jet dynamics and mass transfer during supercritical antisolvent micronization. *Chem. Eng. J.*, 156, pp. 446-458.
- Reverchon, E., De Marco, I. (2011). Mechanisms controlling supercritical antisolvent precipitate morphology. *Chem. Eng. J.* (In press).
- Shariati, A., Peters. C. J. (2003). Recent developments in particle design using supercritical fluids, *Curr. Opin. Solid State Mater. Sci.*, 7, (4-5) pp. 371-383.
- Shekunov, B. Yu., Baldyga, J., York, P. (2001). Particle formation by mixing with supercritical antisolvent at high Reynolds numbers. *Chem. Eng. Sci.*, 56, pp. 2421-2433.
- Subramaniam, B., Snavely, K., Rajewski, R.A. (1997). Pharmaceutical processing with supercritical carbon dioxide, *J. Pharm. Sci.*, 86, pp. 885-890.
- Tenorio, A., Gordillo, M. D., Pereyra, C.M., Martínez de la Ossa, E.J. (2007a). Controlled submicro particle formation of ampicillin by supercritical antisolvent precipitation, *J. Supercrit. Fluids*, 40, pp. 308-316.
- Tenorio, A.; Gordillo, M. D.; Pereyra, C. M.; Martínez de la Ossa, E. M. (2007b). Relative importance of the operating conditions involved in the formation of nanoparticles of ampicillin by supercritical antisolvent precipitation. *Ind. Eng. Chem. Res.*, 46, pp. 114-123.
- Tenorio, A., Gordillo, M. D., Pereyra, C.M., Martínez de la Ossa, E.J. (2008). Screening design of experiment applied to supercritical antisolvent precipitation of amoxicillin, *J. Supercrit. Fluids*, 44, pp. 230-237.
- Tenorio, A., Jaeger, P., Gordillo, M.D., Pereyra, C.M., Martínez de la Ossa, E.J. (2009). On the selection of limiting hydrodynamic conditions for the SAS process, *Ind. Eng. Chem. Res.*, 48 (20), pp. 9224-9232.

- Wena, Z., Liua, B., Zhenga, Z., Youa, X., Pua, Y., Li, Q. (2010). Preparation of liposomes entrapping essential oil from *Atractylodes macrocephala* Koidz by modified RESS technique, *Chem. Eng. Res. Des.*, 88, pp. 1102-1107.
- Winters, M.A., Knutson, B.L., Debenedetti, P.G., Sparks, H.G., Przybycien, T.M., Stevenson, C.L., Prestrelski, S.J. (1996). Precipitation of proteins in supercritical carbon dioxide, *J. Pharm. Sci.*, 85, pp. 586-594.
- Yeo, S.-D., Lim, G.-B., Debenedetti, P.G., Bernstein, H. (1993). Formation of microparticulate protein powders using a supercritical fluid antisolvent, *Biotechnol. Bioeng.*, 41, pp. 341-346.

Rotational Dynamics of Nonpolar and Dipolar Molecules in Polar and Binary Solvent Mixtures

Sanjeev R. Inamdar
*Laser Spectroscopy Programme,
 Department of Physics,
 Karnatak University, Dharwad
 India*

1. Introduction

The absorption of photons by a molecule leads to its excitation. An electronically excited molecule can lose its energy by emission of ultraviolet, visible, infrared radiation or by collision with the surrounding matter. Luminescence is thus the emission of photons from excited electronic energy levels of molecules. The energy difference between the initial and the final electronic states is emitted as fluorescence or phosphorescence (Lakowicz, 2006). Fluorescence is a spin-allowed radiative transition between two states of the same multiplicity (e.g., $S_1 \rightarrow S_0$) whereas; phosphorescence is a spin-forbidden radiative transition between two states of different multiplicity (e.g., $T_1 \rightarrow S_0$).

The mechanisms by which electronically excited molecules relax to ground state are given by the Jablonski diagram as shown in Fig. 1. The absorption of a photon takes a molecule from ground state (singlet state, S_0) to either first excited state (singlet state, S_1) or second

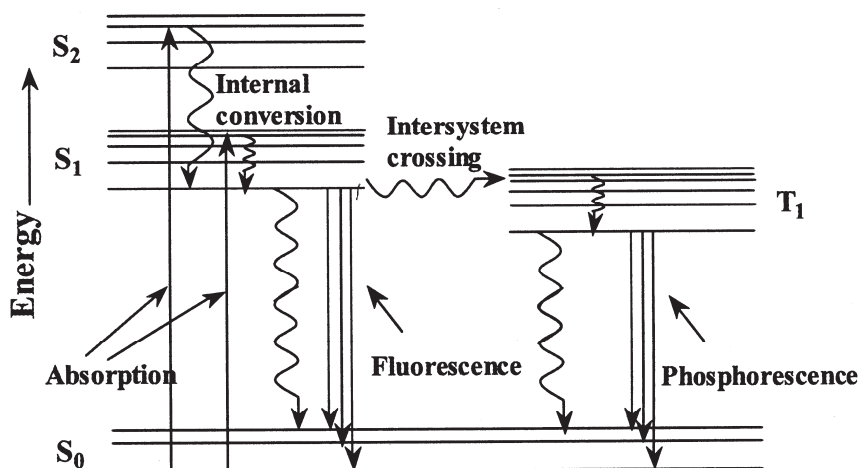


Fig. 1. Jablonski diagram of transitions among various electronic energy levels

excited state (S_2). The excited molecule then relaxes to the lowest vibronic level of the first excited state through internal conversion (IC), which generally occurs within 10^{-12} s or less. Since fluorescence lifetimes are typically near 10^{-8} s, IC is generally complete prior to emission. Now it can relax from the singlet excited state to the ground state via three mechanisms. First by emitting a photon (radiative process), second without emitting photon (nonradiative mechanism) and third it goes to a triplet state (T_1) by intersystem crossing (ISC) which also is a nonradiative process. The transition from triplet (T_1) to ground singlet state is forbidden and hence is a very slow process relative to fluorescence. Emission from T_1 is called phosphorescence and generally is shifted to longer wavelength relative to the fluorescence.

In fluorescence spectroscopy the observed spectral intensity is a function of two variables: the excitation wavelength (λ_{ex}) and the emission wavelength (λ_{em}). The fluorescence property of a compound is conventionally studied by examining both the excitation spectrum and the emission spectrum. The intensity vs. wavelength plot of the fluorescence spectrum obtained is characteristic of a fluorophore and sensitive to its local surrounding environment. It is consequentially used to probe structure of the local environment. Generally, the wavelength of maximum fluorescence intensity is shifted to longer wavelength relative to the wavelength of its absorption maximum. The difference between these two wavelengths, known as Stokes' shift, arises because of the relaxation from the initially excited state to the 'ground' vibronic level of S_1 which involves a loss of energy. Further loss of energy is due to the transitions from S_1 to higher vibrational levels of the ground state S_0 . The Stokes' shift further increases because of general solvent effects. The energy difference between the absorption maximum (ν_a) and the emission maximum (ν_f) is given by Lippert equation (Birks, 1970) in which the energy difference ($\nu_a - \nu_f$) of a fluorophore as a function of the refractive index (n) and dielectric constant (ϵ) of the solvent is related as

$$\nu_a - \nu_f \approx \frac{2}{hc} \left[\frac{\epsilon - 1}{2\epsilon + 1} - \frac{n^2 - 1}{2n^2 + 1} \right] \frac{(\mu^* - \mu)^2}{a^3} + const \quad (1)$$

where h is the Planck's constant, c the velocity of light and a is the radius of the cavity in which the fluorophore resides. Also, μ and μ^* are the ground and excited state dipole moments, respectively.

Fluorescence emission is generally independent of excitation wavelength. This is because of the rapid relaxation to the lowest vibrational level of S_1 prior to emission, irrespective of excitation to any higher electronic and vibrational levels. Excitation on the extreme red edge of the absorption spectrum frequently results in a red-shifted emission. The red-shift occurs because red-edge excitation selects those fluorophores which are more strongly interacting with the solvent (solvation dynamics) (Demchenko, 2002). The red-edge effect can also be thought as ground state heterogeneity, which is common in most complex systems like a probe distribution in microheterogeneous media. In the case of ground state heterogeneity or the presence of multiple species in the ground state, the fluorescence emission spectrum is dependent on the excitation wavelength and the fluorescence excitation spectrum is dependent on the emission wavelength. Also fluorescence excitation spectrum observed for a given emission wavelength differs from that of the absorption spectrum for heterogeneous system. The large spectral width of the emission spectrum compared to absorption spectral width is also due to the presence of multiple species in the excited state. Fluorescence

emission spectrum is generally a mirror image of the absorption spectrum (S_0 to S_1 transition).

1.1 Steady-state and time resolved fluorescence

Fluorescence measurements can be broadly classified into two types of measurements: steady-state and time-resolved. Steady-state measurements, the most common type, are those performed with constant illumination and observation. The sample is illuminated with a continuous beam of light, and the intensity or emission spectrum is recorded as function of wavelength. When the sample is first exposed to light steady state is reached almost immediately. Because of the ns timescale of fluorescence, most measurements employ steady-state method. The second type of measurement is time-resolved method which is used for measuring intensity decays or anisotropy decays. For these measurements the sample is exposed to a pulse of light, where the pulse width is typically shorter than the decay time of the sample. The intensity decay is recorded with a high-speed detection system that permits the intensity or anisotropy to be measured on the ns timescale.

1.2 Fluorescence anisotropy

The photoselection of fluorescent probe by polarized light offers the opportunity to study some relevant processes occurring at molecular level in heterogeneous systems. The fluorescence, emitted from the samples excited with polarized light, is also polarized. This polarization is due to the photoselection of the fluorophores according to their orientation relative to the direction of the polarized excitation. This photoselection is proportional to the square of the cosine of the angle between the absorption dipole of the fluorophore and the axis of polarization of the excitation light. The orientational anisotropic distribution of the excited fluorophore population relaxes by rotational diffusion of the fluorophores and excitation energy transfer to the surrounding acceptor molecule. The polarized fluorescence emission becomes depolarized by such processes. The fluorescence anisotropy measurements reveal the average angular displacement of the fluorophore, which occurs between absorption and subsequent emission of a photon. The degree of polarization, P , and steady state fluorescence anisotropy r , are thus respectively given by equations (Lakowicz, 2006)

$$P = \frac{I_{||} - I_{\perp}}{I_{||} + I_{\perp}} \quad (2)$$

$$r = \frac{I_{||} - I_{\perp}}{I_{||} + 2I_{\perp}} \quad (3)$$

where $I_{||}$ and I_{\perp} represent the fluorescence intensities when the orientation of the emission polarizer is parallel and perpendicular to the orientation of the excitation polarizer, respectively. The fluorescence anisotropy (r) is a measure of the average depolarization during the lifetime of the excited fluorophore under steady-state conditions. A steady-state observation is simply an average of the time-resolved phenomena over the intensity decay of the sample. But the time resolved measurements of fluorescence anisotropy using ultrafast polarized excitation source (laser) give an insight into the time dependent depolarization. The time dependent fluorescence anisotropy decay, $r(t)$, is defined as

$$r(t) = \frac{I_{||}(t) - I_{\perp}(t)}{I_{||}(t) + 2I_{\perp}(t)} \quad (4)$$

where $I_{||}(t)$ and $I_{\perp}(t)$ are the fluorescence intensity decays collected with the polarization of the emission polarizer maintained parallel and perpendicular to the polarization of the excitation source, respectively. For a fluorophore in a sample solvent, the fluorescence depolarization is simply due to rotational motion of the excited fluorophore and the decay parameters depend on the size and shape of the fluorophore. For spherical fluorophores, the anisotropy decay is a single exponential with a single rotational correlation time and is given by (Lakowicz, 2006)

$$r(t) = r_0 \exp(-t / \tau_r) \quad (5)$$

where r_0 is the initial anisotropy (anisotropy at time $t=0$ or anisotropy observed in the absence of any depolarizing processes) and τ_r is the rotational correlation time. The initial anisotropy r_0 is related to the angle (θ) between the absorption and emission dipoles of the fluorophore under study as

$$r_0 = \frac{2}{5} \left(\frac{3 \cos^2(\theta) - 1}{2} \right) \quad (6)$$

where the value r_0 can vary between 0.4 and -0.2 as the angle (θ) varies between 0° and 90° respectively. The rotational correlation times τ_r of the fluorophore is governed by the viscosity (η), temperature (T) of the solution and the molecular volume (V) of the fluorophore. This is given by Stokes-Einstein relation (Fleming, 1986) as shown below:

$$\tau_r = \frac{\eta V}{kT} \quad (7)$$

where k is the Boltzmann constant.

The relation between the steady-state anisotropy (r), initial anisotropy (r_0), rotational correlation time (τ_r) and fluorescence lifetime (τ_f) is given by Perrin equation as follows (Lackowicz, 1983)

$$\frac{r_0}{r} = 1 + \frac{\tau_f}{\tau_r} \quad (8)$$

The Perrin equation is very useful in obtaining the correlation time without the measurement of polarization dependent fluorescence decays [$I_{||}(t)$ and $I_{\perp}(t)$]. The theory developed for more complicated shapes of the fluorophore show that a maximum of five exponentials are enough to explain the fluorescence anisotropy decay (Steiner, 1991).

2. Introduction to rotational dynamics

Understanding solute-solvent interaction has been of great relevance in physico-chemical processes due to the importance of these interactions in determining properties such as chemical reaction yield and kinetics or the ability to isolate one compound from another. Interactions between the solutes and their surrounding solvent molecules are difficult to

resolve because, unlike in solids, the spatial relationship between the molecules are not fixed on time scales that can be accessed using structural measurements such as X-ray diffraction or multidimensional NMR spectrometry. Intermolecular interactions in the liquid phase are more complex than those in gas phase because of their characteristic strength, the property that gives rise to the liquid phase and at the same time prevents a simple statistical description of collisional interactions from providing adequate insight (Fleming, 1986).

Regardless of almost three and a half decades of continuous investigation, the details of solute-solvent interactions, particularly in polar solvent systems, remain to be understood in detail. Most investigations of intermolecular interactions in solution have used a "probe" molecule present at low concentration in neat or binary solvent systems. Typically, a short pulse of light is shone to establish some non-equilibrium condition in the ensemble of probe molecules, with the object of the experiment being to monitor the return to equilibrium. These studies have included fluorescence lifetime, molecular reorientation (Eisenthal, 1975; Shank and Ippen, 1975; von Jena and Lessing, 1979a; Sanders and Wirth, 1983; Templeton et al., 1985; Blanchard and Wirth, 1986; Templeton and Kenney-Wallace, 1986; Blanchard, 1987, 1988, 1989; Blanchard and Cihal, 1988; Hartman et al., 1991; Srivastava and Doraiswamy, 1995; Imeshev and Khundkar, 1995; Dutt, et al., 1995; Chandrashekhar et al., 1995; Levitus et al., 1995; Backer et al., 1996; Biasutti et al., 1996; Horng et al., 1997; Hartman et al., 1997; Laitinen et al., 1997; Singh, 2000; Dutt and Raman, 2001; Gustavsson et al., 2003; Dutt and Ghanty, 2004; Kubinyi et al., 2006), vibrational relaxation (Heilweil et al., 1986, 1987, 1989; Lingle Jr. et al., 1990; Anfinrud et al., 1990; Elsaesser and Kaiser, 1991; Hambir et al., 1993; Jiang and Blanchard, 1994a & b, 1995; McCarthy and Blanchard, 1995, 1996) and time-delayed fluorescence Stokes shift (Shapiro and Winn, 1980; Maroncelli and Fleming, 1987; Huppert et al. 1989, 1990; Chapman et al., 1990; Wagener and Richert, 1991; Fee et al., 1991; Jarzaba et al., 1991; Yip et al., 1993; Fee and Maroncelli, 1994; Inamdar et al., 1995) measurements. Of these, molecular reorientation of molecules in solution has been an important experimental and theoretical concept for probing the nature of liquids and the interactions of solvents with molecules. This has proven to be among the most useful because of the combined generality of the effect and the well-developed theoretical framework for the interpretation of the experimental data (Debye, 1929; Perrin, 1936; Chuang and Eisenthal, 1972; Hu and Zwanzig, 1974; Youngren and Acrivos, 1975; Zwanzig and Harrison, 1985). Though, the effect of solute-solvent interactions on the rotational motion of a probe molecule in solution has been extensively studied, these interactions are generally described as friction to probe rotational motion and can be classified into three types. The first category includes short-range repulsive forces, which dominate intermolecular dynamics during molecular collisions. These interactions are present in all liquids and lead to viscous dissipation, which is well described by hydrodynamic theories (Fleming, 1986). The second category includes long-range electrostatic interactions between a charged or dipolar probe and polar solvent molecules. As the solute turns, the induced solvent polarization can lag behind rotation of the probe, creating a torque, which systematically reduces the rate of rotational diffusion. This effect, termed dielectric friction, arises from the same type of correlated motions of solvent molecules, which is responsible for the time dependent Stokes' shift (TDSS) dynamics of fluorescent probes (van der Zwan and Hynes, 1985; Barbara and Jarzaba, 1990; Maroncelli, 1993). The third category includes specific solute-solvent interactions. Hydrogen bonding is probably the most frequently encountered example of this kind. Strong hydrogen bonds will lead to the formation of

solute-solvent complexes of well-defined stoichiometry. These new, larger species can persist in solution for fairly long times and will rotate more slowly than the bare solute. Formation and breakage of weak H binds occurring on time scales faster than probe rotation will provide a channel for rotational energy dissipation giving rise to additional friction.

The theoretical interest in the study of rotational reorientation kinetics of molecules in liquids arises from the fact that it provides information about the intermolecular interaction in the condensed phase. However, the theoretical modeling of molecular reorientation in liquids and its correlation with experimental data is still far from satisfactory. Thus far, two kinds of approaches have been employed in understanding the rotational dynamics. In the first approach, binary collision approximation has been used to explain the rotational dynamics. With this approach, kinetic theory model for rotational relaxation has been employed for rough sphere fluids (Widom, 1960; Rider and Fixman, 1972; Chandler, 1974) and for smooth convex bodies (Evans et al., 1982; Evans and Evans, 1984; Evans, 1988). Evans model along with Enskog equation for viscosity has been employed to express rotational reorientation time (τ_r) as a function of the solvent viscosity. However, explaining rotational dynamics from such a molecular point of view is severely constrained on account of multibody interaction in a fluid. For real systems the quantitative predictions can be made about the variation of τ_r with solvent viscosity. The second approach is the macroscopic approach of understanding the rotational dynamics, where the solvent is assumed to be a structureless continuum and the rotational motion of solutes is considered Markovian or diffusional. A considerable degree of success on the rotational dynamics arises from the Stokes-Einstein-Debye (SED) hydrodynamic theory, which forms the basis of understanding molecular rotations of medium sized molecules (few hundred \AA^3 volumes) in liquids (Einstein, 1906; Debye, 1929; Stokes, 1956), according to which the rotational reorientation time (τ_r) of a solute molecule is proportional to its volume (V), bulk viscosity (η) of the solvent and inversely related to its temperature (T).

Rotational dynamics of number of nonpolar and polar solutes have been carried out in homologous series of polar and nonpolar solvents. In general, the experimentally measured reorientation times of most of the nonpolar probes could be described by the SED theory with slip boundary condition. In some cases the reorientation times were found to be faster than predicted by the slip boundary condition, a situation termed as subslip behavior. However, for a given probe in a homologous series of solvents (alkanes or alcohols) the normalized reorientation times (i.e., reorientation times at unit viscosity) decrease as the size of the solvent increased. In other words, the reorientation times did not scale linearly with solvent viscosity. This behavior, known as the size effects, could not be explained with SED theory. Another observation, which the SED theory failed to explain, is that the experimentally measured reorientation times of nonpolar probes are faster in alcohols than in alkanes of similar viscosity. To explain the observed size effects two quasihydrodynamics theories have been used. The first one is a relatively old theory proposed by Geirer and Wirtz (GW) (1953), which takes into account both the size of the solute as well as that of the solvent while calculating the boundary condition. This theory visualizes the solvent to be made up of concentric shells of spherical particles surrounding the spherical probe molecule at the center. Each shell moves at a constant angular velocity and the velocity of successive shells decreases with the distance from the surface of the probe molecule, as though the flow between the shells is laminar. As the shell number increases, i.e., at large distances, the angular velocity vanishes. Although, the GW theory is successful in predicting the observed

size effects in a qualitative way, it could not explain the faster rotation of nonpolar probes in alcohols compared to alkanes. The second relatively new quasihydrodynamic theory was proposed by Dote, Kivelson and Schwartz (DKS) (1981). The DKS theory not only takes into consideration the relative sizes of the solvent and the probe but also the cavities or free spaces created by the solvent around the probe molecule. If the size of the solute is comparable to the free volumes of the solvent, the coupling between the solute and the solvent will become weak which results in reduced friction experienced by the probe molecule.

On the other hand, rotational dynamics of small and medium sized polar solutes dissolved in polar solvents experiences more friction than predicted by the hydrodynamic theories. This 'additional friction' is attributed to the solute-solvent hydrogen bonding. The first and the oldest concept of dielectric friction invoked by chemists is the 'solvent-berg' model, in which it is assumed that there is a solute-solvent interaction causing increase in the volume of the solute. Such an enhancement of the volume automatically causes the molecule to rotate slower. However, reservations against such an explanation have also been expressed (Chuang and Eisenthal, 1972; Horng et al., 1997). Objections to this kind of interpretations arise from the fact that in bulk solution, the solvent molecules are expected to exchange (solute-solvent hydrogen bonding dynamics) on a much faster time scale compared to the rotational dynamics. Later, the slower reorientation times of polar molecules in polar solvents have been interpreted using dielectric friction theories (Phillips et al., 1985; Dutt et al., 1990; Alavi et al., 1991b,c; Dutt and Raman, 2001; Gustavsson et al., 2003). Dielectric friction on a rotating solute arises because the polar molecule embedded in a dielectric medium polarizes the surrounding dielectric. As the solute tries to rotate, the polarization of the medium cannot instantaneously keep in phase with the new orientation of the probe molecule and this lag exerts a retarding force on the probe molecule, giving rise to rotational dielectric friction. Although molecular theories of dielectric friction are available, at present these theories are difficult to apply because they require some knowledge of the intermolecular potential or some unavailable properties of the solvent. Continuum theories offer advantages of simplicity and the calculation of molecular friction in terms of easily accessible bulk properties of the solvent.

The SED theory has been found to describe the rotational dynamics of medium sized molecules fairly well when the coupling between the solute and solvent is purely mechanical or hydrodynamic in nature. It is documented that the SED model correctly predicts the linear dependence of the rotational reorientation times on the solvent viscosity for polar and cationic dyes dissolved in polar and non polar solvents (Chuang and Eisenthal, 1971; Fleming et al., 1976; 1977; Porter et al., 1977; Moog et al., 1982; Spears and Cramer, 1978; Millar et al., 1979; von Jena and Lessing, 1979a, b; 1981; Rice and Kenney-Wallace, 1980; Waldeck and Fleming, 1981; Dutt et al., 1990; Alavi et al., 1991a, b, c; Krishnamurthy et al., 1993; Dutt et al., 1998) that have been interpreted using dielectric friction theories. The dielectric friction can be modeled using continuum theories of Nee-Zwanzig (NZ) (Nee and Zwanzig, 1970), which treats the solute as a point dipole rotating in a spherical cavity, Alavi-Waldeck (AW) (Alavi and Waldeck, 1991b; 1993) model which is an extension of the NZ theory where the solute is treated as a distribution of charges instead of point dipole and the semiempirical approach of van der Zwan and Hynes (vdZH) (van der Zwan and Hynes, 1985) in which fluorescence Stokes shift of the solute in a given solvent is related to dielectric friction. Conversely, the results of neutral and nonpolar solutes deviate

significantly from the hydrodynamic predictions at higher viscosities (Waldeck et al., 1982; Canonica et al., 1985; Phillips et al., 1985; Courtney et al., 1986; Ben Amotz and Drake, 1988; Roy and Doraiswamy, 1993; Williams et al., 1994; Jiang and Blanchard, 1994; Anderton and Kauffman, 1994; Brocklehurst and Young, 1995; Benzler and Luther, 1997; Dutt et al., 1999; Ito et al., 2000; Inamdar et al., 2006). These probes rotate much faster than predicted by the SED theory with stick boundary condition and are described by either slip boundary condition or by quasihydrodynamic theories. Slip boundary condition (Hu and Zwanzig, 1974) assumes the solute-solvent coupling parameter to be less than unity, contrary to the stick boundary condition. Quasihydrodynamic theories of Gierer and Wirtz (GW) (Gierer and Wirtz, 1953) and Dote, Kivelson and Schwartz (DKS) (Dote, Kivelson and Schwartz, 1981) attempt to improve upon SED theory by taking into consideration not only the size of the solute but also that of the solvent molecule, thereby modifying the boundary conditions. It has been argued (Ben Amotz and Drake, 1988; Roy and Doraiswamy, 1993) that as the size of the solute molecule becomes much larger than the size of the solvent molecule, the observed reorientation times approach the SED theory with the stick boundary condition.

Based on the above description, we have chosen two kinds of solutes categorized as nonpolar and polar to study their rotational reorientation dynamics in nonpolar, polar and binary mixtures of solvents. In the first case, where the nonpolar probes embedded in polar or nonpolar solvents to examine the influence of solute to solvent size ratio and the shape of the solute on the friction experienced by the probe molecule which in turn enables to test the validity of hydrodynamic and quasihydrodynamic theories. The friction experienced by these probes is purely hydrodynamic or mechanical in nature since it is dominated by short-range repulsive forces. Polar probes used in charged polar solvents with an intention of understanding how the long-range electrostatic interactions between the solute and the solvent, which are charge-dipole or dipole-dipole in nature, influence the rotational dynamics of the probe molecules. Dielectric friction on a rotating solute arises because of the polar molecule entrenched in a dielectric medium polarizes the surrounding dielectric. As the solute tries to rotate, the polarization of the medium cannot instantaneously keep in phase with the new orientation of the probe molecule and this lag exerts a retarding force on the probe molecule, giving rise to rotational dielectric friction.

2.1 Theoretical background

Among the many proposed models for the study of rotational motion, the most commonly employed is the rotational diffusion model outlined by Debye (Debye, 1929), in which the reorientation is assumed to occur in small angular steps. On account of high frequency collisions, a molecule can rotate through a very small angle before undergoing another reorienting collision. The rotational diffusion equation solved to obtain the rotational correlation time τ_r of the density function $\rho(\theta, \phi)$ is given by (Lackowicz, 2006)

$$\frac{\partial \rho}{\partial t} = D \frac{1}{\sin \theta} \frac{\partial}{\partial \theta} \left[\frac{1}{\sin \theta} \frac{\partial \rho}{\partial \theta} + \frac{1}{\sin^2 \theta} \frac{\partial^2 \rho}{\partial \phi^2} \right] \quad (9)$$

where D is the rotational diffusion coefficient. For spherical particles ρ satisfies the form $C_1(t) Y_{l,m}(\theta, \phi)$ in isotropic liquids, where $Y_{l,m}(\theta, \phi)$ are the Legendre polynomials and the coefficient $C_1(t)$ is essentially the same as the correlation function. Substitution of $\rho = C_1(t) Y_{l,m}(\theta, \phi)$ gives an ordinary differential equation for C as

$$\frac{dC_1}{dt} = -Dl(l+1)C_1 \quad (10)$$

This implies that the correlation function decays exponentially, $e^{-t/\tau}$ and the correlation time $\tau_l = [l(l+1)D]^{-1}$. In fluorescence depolarization experiments, one measures the anisotropy decay which is $l=2$ correlation and hence $\tau_r = (6D)^{-1}$.

The rotational diffusion co-efficient of a solute is given by the Stokes-Einstein model (Lakowicz, 2006) as

$$D = \frac{kT}{\zeta} \quad (11)$$

where ζ is the friction coefficient and kT is the thermal energy. It is this friction, which is of great importance in theoretical as well as experimental studies. A molecule rotating in liquid experiences friction on account of its continuous interaction with its neighbors and the desire to understand has been a motivating force in carrying the experimental measurements of rotational reorientation in liquids.

2.1.1 Hydrodynamic theory

Mechanical friction on a rotating solute in solvent is computed employing hydrodynamic theory by treating the solute as a smooth sphere rotating in a continuum fluid, which is characterized by a shear viscosity. If ' a ' is the radius of the molecule and ' η ' the viscosity of the liquid, then according to Stokes law (Stokes, 1956)

$$\zeta = 8\pi a^3 \eta \quad (12)$$

Eqn. (11) reduces to

$$D = \frac{kT}{8\pi\eta a^3} \quad (13)$$

The rotational correlation time (τ_r) is given by

$$\tau_r = \frac{1}{6D} = \frac{\zeta}{6kT} \quad (14)$$

substitution of Eqn. (12) in (14) gives

$$\tau_r = \frac{\eta V}{kT} \quad (15)$$

where V is the molecular volume. The most widely used Stokes-Einstein-Debye (SED) hydrodynamic equation for the description of rotational dynamics of spherical molecule is given by

$$\tau_r = \frac{\eta V}{kT} + \tau_0 \quad (16)$$

where τ_0 is the rotational reorientation time at zero viscosity. It is known that spherical approximation embedded in a SED is glossy in error and the shape of the probes is however,

more important. In reality, the exact shape of the solute molecule is need not be a spherical and there is a necessary to include a parameter, which should describe the exact shape of nonspherical probes. Hence, the equation for nonspherical molecule proposed by Perrin (Perrin, 1936) is given as follows

$$\tau_r = \frac{\eta V}{kT} (fC) \quad (17)$$

where f is shape factor and is well specified, C is the boundary condition parameter dependent strongly on solute, solvent and concentration. The shapes of the solute molecules are usually incorporated into the model by treating them as either symmetric or asymmetric ellipsoids. For nonspherical molecules, $f > 1$ and the magnitude of deviation of f from unity describes the degree of the nonspherical nature of the solute molecule. C , signifies the extent of coupling between the solute and the solvent and is known as the boundary condition parameter (Barbara and Jarzeba, 1990). In the two limiting cases of hydrodynamic stick and slip for a nonspherical molecule, the value of C follows the inequality, $0 < C \leq 1$ and the exact value of C is determined by the axial ratio of the probe.

It is observed that the experimentally measured rotational reorientation times of number of the nonpolar solutes (Waldeck et al., 1982; Canonica et al., 1985; Phillips et al., 1985; Courtney et al., 1986; Ben Amotz and Drake, 1988; Roy and Doraiswamy, 1993; Williams et al., 1994; Jiang and Blanchard, 1994; Anderton and Kauffman, 1994; Brocklehurst and Young, 1995; Benzler and Luther, 1997; Dutt et al., 1999; Ito et al., 2000; Inamdar et al., 2006) could be described by the SED theory with slip boundary condition (subslip behavior). For a homologous series of solvents such as alcohols or alkanes, the normalized reorientation times decreased as the size of the solvent is increased. In other words, the reorientation times did not scale linearly with solvent viscosity.

2.1.2 Quasihydrodynamic theories

While the SED hydrodynamic theory takes only the size of the solute molecule into account leaving solvent size aside, one needs to consider the size of the solute as well as solvent molecules. Quasihydrodynamic theories consider these and modify the boundary condition accordingly. To explain such observation of size effects, two quasihydrodynamic theories by Gierer and Wirtz (GW) and Dote, Kivelson and Schwartz (DKS) have been used.

i. Gierer and Wirtz theory (GW)

The first and the relatively old theory proposed by Gierer and Wirtz (GW) in 1953, takes into account both the size of the solute as well as that of the solvent while calculating the boundary condition. It visualizes the solvent to be made up of concentric shells of spherical particles surrounding the spherical probe molecule at the center. Each shell moves at a constant angular velocity and the velocity of successive shells decreases with the distance from the surface of the probe molecule, as though the flow between the shells is laminar. As the shell number increase, i.e., at large distances, the angular velocity vanishes. The angular velocity ω_1 of the first solvation shell is related to the angular velocity ω_0 of the probe molecule by means of a sticking factor σ .

$$\omega_1 = \sigma \omega_0 \quad (18)$$

When $\sigma = 1$, it gives the stick boundary condition and σ is related to the ratio of the solute to solvent size, as

$$\sigma = \left[1 + 6 \left(\frac{V_s}{V_p} \right)^{\frac{1}{3}} C_0 \right]^{-1} \quad (19)$$

where

$$C_0 = \left\{ \frac{6(V_s/V_p)^{1/3}}{\left[1 + 2(V_s/V_p)^{1/3} \right]^4} + \frac{1}{\left[1 + 4(V_s/V_p)^{1/3} \right]^3} \right\}^{-1} \quad (20)$$

V_s and V_p are the volumes of the solvent and probe, respectively. The expression for C_{GW} is given by

$$C_{GW} = \sigma C_0 \quad (21)$$

C in Eqn. (17) should be replaced with C_{GW} obtained from Eqn. (21) for calculating the reorientation times with GW theory. When the ratio V_s/V_p is very small C_{GW} reduces to unity and the SED equation with stick boundary condition is obtained.

ii. The Dote-Kivelson-Schwartz theory (DKS)

Although, the GW theory is successful in predicting the observed size effects in a qualitative way, it could not explain the faster rotation of nonpolar probes in alcohols compared to alkanes. Hence, the second relatively new quasihydrodynamic theory, was proposed by Dote, Kivelson and Schwartz (DKS) in 1981. This theory not only takes into consideration the relative sizes of the solvent and the probe but also the cavities or free spaces created by the solvent around the probe molecule. If the size of the solute is comparable to the free volumes of the solvents, the coupling between the solute and the solvent will become weak which results in reduced friction experienced by the probe molecule. According to DKS theory the solute-solvent coupling parameter, C_{DKS} is given by (Dote, Kivelson and Schwartz, 1981)

$$C_{DKS} = (1 + \gamma/\phi)^{-1} \quad (22)$$

where γ/ϕ is the ratio of the free volume available for the solvent to the effective size of the solute molecule, with

$$\gamma = \frac{\Delta V}{V_p} \left[4 \left(\frac{V_p}{V_s} \right)^{2/3} + 1 \right], \quad (23)$$

and ϕ is the ratio of the reorientation time predicted by slip hydrodynamics to the stick prediction for the sphere of same volume. ΔV is the smallest volume of free space per solvent molecule and some discretion must be applied while calculating this term (Dutt et al., 1988; Anderton and Kauffman, 1994; Dutt and Rama Krishna, 2000). ΔV is empirically related to the solvent viscosity, the Hilderbrand-Batchinsky parameter B and the isothermal compressibility k_T of the liquid by

$$\Delta V = Bk_T\eta kT \quad (24)$$

Since the Frenkel hole theory and the Hilderbrand treatment of solvent viscosity were developed for regular solutions (Anderton and Kauffman, 1994), Equation (24) may not be a valid measure of the free space per solvent molecule for associative solvents like alcohols and polyalcohols. Hence, for alcohols ΔV is calculated using

$$\Delta V = V_m - V_s \quad (25)$$

where V_m is the solvent molar volume divided by the Avogadro number.

2.1.3 Dielectric friction theories

The simple description of hydrodynamic friction arising out of viscosity of the solvent becomes inadequate when the motion concerning rotations of polar and charged solutes desired to be explained. A polar molecule rotating in a polar solvent experiences hindrance due to dielectric friction (ζ_{DF}), in addition to, the mechanical (ζ_M) or hydrodynamic friction. In general, the dielectric and mechanical contributions to the friction are not separable as they are linked due to electrohydrodynamic coupling (Hubbard and Onsager, 1977; Hubbard, 1978; Dote et al., 1981; Felderhof, 1983; Alavi et al., 1991c; Kumar and Maroncelli, 2000). Despite this nonseparability, it is common to assume that the total friction experienced by the probe molecule is the sum of mechanical and dielectric friction components, i.e.,

$$\zeta_{Total} = \zeta_M + \zeta_{DF} \quad (26)$$

Mechanical friction can be modeled using both hydrodynamic (Debye, 1929) and quasihydrodynamic (Gierer and Wirtz, 1953; Dote et al., 1981) theories, whereas, dielectric friction is modeled using continuum theories.

The earliest research into dielectric effects on molecular rotation took place in the theoretical arena. Initial investigations were closely intertwined with the theories of dielectric dispersion in pure solvents (Titulaer and Deutch, 1974; Bottcher and Bordewijk, 1978; Cole, 1984). Beginning with the first paper to relate the dielectric friction to rotational motion published by Nee and Zwanzig in 1970, a number of studies have made improvements to the Nee-Zwanzig approach (Tjai et al, 1974; Hubbard and Onsager, 1977; Hubbard and Wolynes, 1978; Bordewijk, 1980; McMahan, 1980; Brito and Bordewijk, 1980; Bossis, 1982; Madden and Kivelson, 1982; Felderhof, 1983; Nowak, 1983; van der Zwan and Hynes, 1985; Alavi et al, 1991a,b,c; Alavi and Waldeck, 1993). These have included the electrohydrodynamic treatment which explicitly considers the coupling between the hydrodynamic (viscous) damping and the dielectric friction components.

i. The Nee-Zwanzig theory

Though not the first, the most influential early treatment of rotational dielectric friction was made by Nee and Zwanzig (NZ) (1970). These authors examined rotational dynamics of the same solute/solvent model in the simple continuum (SC) description i.e., they assumed an Onsager type cavity dipole with dipole moment μ and radius a embedded in a dielectric continuum with dispersion $\epsilon(\omega)$. Motion was assumed to be in the purely-diffusive (or Smoluchowski) limit. Using a boundary condition value calculation of the average reaction field, Nee and Zwanzig obtained their final result linking the dielectric friction contribution in the spherical cavity as

$$\tau_{DF}^{NZ} = \frac{\mu^2}{9a^3kT} \frac{(\epsilon_\infty + 2)^2(\epsilon_0 - \epsilon_\infty)}{(2\epsilon_0 + \epsilon_\infty)^2} \tau_D \quad (27)$$

where ϵ_0 , ϵ_∞ and τ_D are the zero frequency dielectric constant, high-frequency dielectric constant and Debye relaxation time of the solvent, respectively.

If one assumes that the mechanical and dielectric components of friction are separable, then

$$\tau_r^{obs} = \tau_{SED} + \tau_{DF} \quad (28)$$

Therefore, the observed rotational reorientation time (τ_r^{obs}) is given as the sum of reorientation time calculated using SED hydrodynamic theory and dielectric friction theory.

$$\tau_r^{obs} = \frac{\eta V f C}{kT} + \frac{\mu^2}{9a^3kT} \frac{(\epsilon + 2)^2(\epsilon_0 - \epsilon_\infty)\tau_D}{(2\epsilon_0 + \epsilon_\infty)^2} \quad (29)$$

It is clear from the above equation that for a given solute molecule, the dielectric friction contribution would be significant in a solvent of low ϵ and high τ_D . However, if the solute is large, the contribution due to dielectric friction becomes small and the relative contribution to the overall reorientation time further diminishes due to a step increase in the hydrodynamic contribution. Hence, most pronounced contribution due to dielectric friction could be seen in small molecules with large dipole moments especially in solvents of low ϵ and large τ_D .

ii. The van der Zwan-Hynes theory (vdZH)

A semiempirical method for finding dielectric friction proposed by van der Zwan and Hynes (1985), an improvement over the Nee and Zwanzig model, provides a prescription for determining the dielectric friction from the measurements of response of the solute in the solvent of interest. It relates dielectric friction experienced by a solute in a solvent to solvation time, τ_s , and solute Stokes shift, S . According to this theory the dielectric friction is given by (van der Zwan and Hynes, 1985)

$$\tau_{DF} = \frac{\mu^2}{(\Delta\mu)^2} \frac{S\tau_s}{6kT} \quad (30)$$

where $\Delta\mu$ is the difference in dipole moment of the solute in the ground and excited states and

$$S = hv_a - hv_f \quad (31)$$

where hv_a and hv_f are the energies of the 0-0 transition for absorption and fluorescence, respectively. The solvation time is approximately related to the solvent longitudinal relaxation time, $\tau_L = \tau_D(\epsilon_\infty / \epsilon_0)$ and is relatively independent of the solute properties. Hence, τ_L can be used in place of τ_s in Eqn. (30).

Assuming the separability of the mechanical and dielectric friction components, the rotational reorientation time can be expressed as

$$\tau_r^{obs} = \frac{\eta V f C}{kT} + \frac{\mu^2}{(\Delta\mu)^2} \frac{hc \Delta\nu}{6kT} \tau_s \quad (32)$$

where the first term represents the mechanical contribution and the second the dielectric contribution.

iii. The Alavi and Waldeck theory (AW)

Alavi and Waldeck theory (Alavi and Waldeck, 1991a), proposes that it is rather the charge distribution of the solute than the dipole moment that is used to calculate the friction experienced by the solute molecule. Not only the dipole moment of the solute, but also the higher order moments, contribute significantly to the dielectric friction. In other words, molecules having no net dipole moment can also experience dielectric friction. AW theory has been successful compared to NZ and ZH theories in modeling the friction in nonassociative solvents (Dutt and Ghanty, 2003). The expression for the dielectric friction according to this model is given by (Alavi and Waldek, 1991a)

$$\tau_{DF} = P \frac{(\epsilon_0 - 1)}{(2\epsilon_0 + 1)^2} \tau_D \quad (33)$$

where

$$P = \frac{4}{3akT} \sum_{j=1}^N \sum_{i=1}^N \sum_{L=1}^{L_{\max}} \sum_{M=1}^L \left(\frac{2L+1}{L+1} \right) \frac{(L-M)!}{(L+M)!} \times$$

$$M^2 q_i q_j \left(\frac{r_i}{a} \right)^L \left(\frac{r_j}{a} \right)^L P_L^M(\cos \theta_i) P_L^M(\cos \theta_j) \cos M \phi_{ji} \quad (34)$$

where $P_L^M(x)$ are the associated Legendre polynomials, a is the cavity radius, N is the number of partial charges, q_i is the partial charge on atom i , whose position is given by (r_i, θ_i, ϕ_i) , and $\phi_{ji} = \phi_j - \phi_i$. Although the AW theory too treats solvent as a structureless continuum like the NZ and vdZH theories, it provides a more realistic description of the electronic properties of the solute.

3. Experimental methods

The experimental techniques used for the investigation of rotational reorientation times mainly consist of steady-state fluorescence spectrophotometer and time resolved fluorescence spectrometer employing time correlated single photon counting (TCSPC).

3.1a Steady-state measurements

For vertical excitation, the steady-state fluorescence anisotropy can be expressed as (Dutt et al., 1999; Lakowicz, 1983)

$$\langle r \rangle = \frac{I_{||} - GI_{\perp}}{I_{||} + 2GI_{\perp}} \quad (35)$$

where $I_{||}$ and I_{\perp} denote the fluorescence intensities parallel and perpendicular polarized components with respect to the polarization of the exciting beam. G ($= 1.14$) is an instrumental factor that corrects for the polarization bias in the detection system (Inamdar et al., 2006) and is given by

$$G = \frac{I_{HV}}{I_{HH}} \quad (36)$$

where I_{HV} is the fluorescence intensity when the excitation polarizer is kept horizontal and the emission polarizer vertical and I_{HH} is the fluorescence intensity when both the polarizers are kept horizontal.

3.1b Time-resolved fluorescence measurements

The fluorescence lifetimes of all the probes were measured with time correlated single photon counting technique (TCSPC) using equipment described in detail elsewhere (Selvaraju and Ramamurthy, 2004). If the decay of the fluorescence and the decay of the anisotropy are represented by single exponential, then the reorientation time τ_r is given by (Lakowicz, 1983)

$$\tau_r = \frac{\tau_f}{(r_0 / \langle r \rangle - 1)} \quad (37)$$

where r_0 is the limiting anisotropy when all the rotational motions are frozen and τ_f is the fluorescence lifetime.

In case of a prolate-ellipsoid model, the parameter f_{stick} is given by (Anderton and Kauffman, 1994)

$$f_{stick} = \frac{2(\rho^2 + 1)(\rho^2 - 1)^{3/2}}{3\rho [(2\rho^2 - 1) \ln\{\rho + (\rho^2 - 1)^{1/2}\} - \rho(\rho^2 - 1)^{1/2}]} \quad (38)$$

where ρ is the ratio of major axis (a) to the minor axis (b) of the ellipsoid. This expression is valid for stick boundary condition.

3.2 Fluorescent probes used in the study

Nonpolar probes

A variety of the nonpolar fluorescent probe molecules have been studied extensively in the recent past. Most of the nonpolar probes so far studied have the radii of 2.5 Å to 5.6 Å (Inamdar et al., 2006) and a transition towards stick boundary condition is evident with increase in size of the solute. Most of the medium sized neutral nonpolar molecules rotate faster in alcohols compared to alkanes, which is in contrast to that of smaller neutral solutes. It is also noted that the quasihydrodynamic description is adequate for small solutes of 2-3 Å radius in case of GW theory whereas, the DKS model with experimental value in alcohols fail beyond the solute radius of 4.2 Å. Our earlier work on rotational dynamics of exalite probes E392A ($r = 5.3$ Å), and E398 ($r = 6.0$ Å), yielded striking results (Inamdar et al., 2006), in that, these large probes rotated much faster than slip hydrodynamics and followed subslip trend in alcohols.

The quest to understand the influence of size of solute on rotational dynamics is continued with three nonpolar solutes viz., Exalite 404 (E404), Exalite 417 (E417) and Exalite 428 (E428), which may further fill the gap between the existing data. These probes have an anisotropic shape and a dipole emission along their long rod-like backbones. The rod like or cylinder shape is a macromolecular model of great relevance. A number of biopolymers including

some polypeptides, proteins, nucleic acids and viruses, under certain conditions exhibit the typical rod-like conformation and their hydrodynamic properties can therefore be analyzed in terms of cylindrical models. Surprisingly, not much is studied about the motion of these highly anisotropic rod-like molecules in liquids, neither experimentally nor by any simulation studies. These exalite dyes have found applications in many areas of research. When pumped by XeCl-excimer laser, Ar⁺ and Nd:YAG laser, provide tunable lasers in the ultraviolet-blue range (Valenta et al., 1999). E428 has been used to generate circularly polarized light in glassy liquid crystal films (Chen et al., 1999). Exalites are mixed with plastic scintillators (PS) to form new scintillaors, which are for superficial and diagnostic applications (Kirov et al., 1999).

Polar probes

Rotational diffusion of medium-sized molecules provides a useful means to probe solute-solvent interactions and friction. By modeling this friction using various continuum-based theories (NZ, AW and ZH) one can get better insight into the nature of solute-solvent interactions. In order to understand the effect of polar solvents on the reorientational dynamics of the polar solutes, one must unravel the effects of mechanical friction, dielectric friction and specific short-range solute-solvent interactions. To address this issue, rotational dynamics of three polar laser dyes: coumarin 522B (C522B), coumarin 307 (C307) and coumarin 138 (C138) having identical volumes and distinct structures have been carried out in series of alcohols and alkanes. These coumarins are an important class of oxygen heterocycles, which are widespread in plant kingdom and have been extensively used as laser dyes. Their chemical structures can be looked upon as arising out of the fusion of a benzene ring to pyran-2-one, across the 5- and 6-positions in skeleton. In the present coumarins, the two free substituents at 6 and 7 positions, ethylamino and methyl for C307 in comparison with the analogous model substrate C522B wherein, there is no free substituent rather they are joined by ends to obtain piperidino moiety. These two probes are looked upon as polar due to the presence of electron donating amino group and electron withdrawing CF₃ group. In C138, this CF₃ group is replaced by an alkyl group making it less polar compared to C522B and C307.

The rotational diffusion studies of the following two sets of structurally similar molecules dyes: (i) coumarin-440 (C440), coumarin-450 (C450), coumarin 466 (C466) and coumarin-151 (C151) and (ii) fluorescein 27 (F27), fluorescein Na (FNa) and sulforhodamine B (SRB) in binary mixtures of dimethyl sulphoxide + water and propanol + water mixtures, respectively. Among coumarins, C466 possess N-diethyl group at the fourth position whereas, other three dyes possess amino groups at the seventh position in addition to carbonyl group. This structure is expected to influence molecular reorientation due to possible hydrogen bonding with the solvent mixture. The spectroscopic properties of fluorescein dyes are well known with the dyes having applications ranging from dye lasers to tracers in flow visualization and mixing studies. SRB has been used to measure drug-induced cytotoxicity and cell proliferation for large-scale drug-screening applications (Koochesfahani and Dimotakis, 1986; Dahm et al., 1991; Karasso and Mungal, 1997; Voigt, 2005). Both F27 and FNa are neutral polar molecules each containing one C = O group, F-27 has two Cl and FNa has two Na groups. The anionic probe SRB possesses N (C₂H₅), N⁺ (C₂H₅) groups and sulfonic groups SO₃Na and SO₃ at positions 3, 6, 4' and 2', respectively. The laser grade nonpolar probes Exalites (E404, E417 and E428), nonpolar probes (i) coumarin derivatives (C522B, C307 and C138) and (ii) F27, FNa and SRB (all from Exciton Chemical Co., USA) were used as received. For steady-state experiments, all the samples

were excited at 375 nm and the emission was monitored from 403-422 nm from alkanes to alcohols for Exalites. All the solvents (Fluka, HPLC grade) were used without further purification. The concentration of all the solutions was kept sufficiently low in order to reduce the effects of self-absorption. All the measurements were performed at 298 K.

3.2.1 Rotational dynamics of non-polar probes

The molecular structures of the non-polar probes exalite 404 (E404), exalite 417 (E417) and exalite 428 (E428) chosen for the study are shown in Fig.2. The absorption and fluorescence spectra of the probes in methanol are shown in Fig.3. These probes are approximated as prolate ellipsoids (Inamdar et al., 2006) with molecular volumes 679, 837 and 1031 Å³, respectively, for E404, E417 and E428. The rotational reorientation times (τ_r) calculated using Eqn. (4.43), are tabulated in Table 1 and 2, respectively.

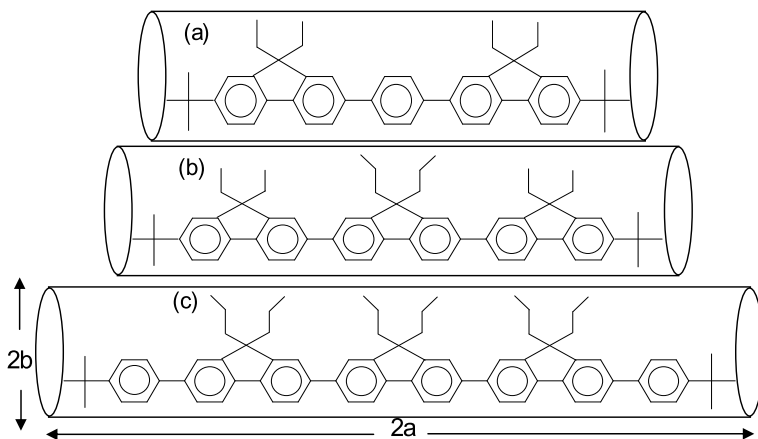


Fig. 2. Molecular structures of (a) E404, (b) E417 and (c) E428

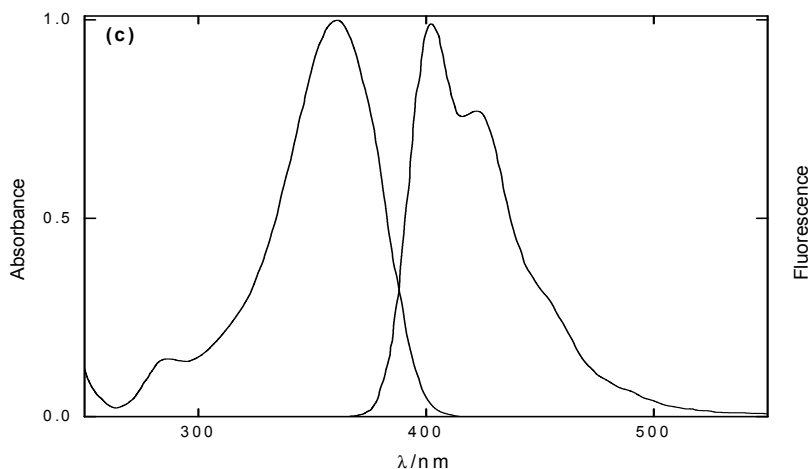


Fig. 3. Absorption and Fluorescence spectra of E404

Solvents	η / mPa s ^a	E404	E417	E428
		τ_r / ps	τ_r / ps	τ_r / ps
Pentane	0.23	114±10	169±14	315±28
Hexane	0.29	153±14	223±18	413±40
Heptane	0.41	199±16	319±22	517±50
Octane	0.52	275±25	401±30	687±65
Nonane	0.66	322±25	523±45	814±78
Decane	0.84	417±35	677±55	1060±101
Dodecane	1.35	634±55	1002±88	1493±141
Tridecane	1.55	718±60	1137±100	1726±155
Pentadecane	2.81	1262±115	1740±120	2261±200
Hexadecane	3.07	1362±113	2080±140	2520±220

^a Viscosity data is from Inamdar et al., 2006

Table 1. Rotational reorientation times (τ_r) of Exalites in alkanes at 298K

Solvents	η / mPa s ^a	E404	E417	E428
		τ_r / ps	τ_r / ps	τ_r / ps
Methanol	0.55	319±32	675±54	694±63
Ethanol	1.08	494±48	860±70	1244±110
Propanol	1.96	896±73	1153±99	1890±172
Butanol	2.59	1008±89	1710±150	2223±220
Pentanol	3.55	1185±100	1815±155	2750±225
Hexanol	4.59	1514±120	2244±201	3178±300
Heptanol	5.87	2070±182	2363±210	3627±345
Octanol	7.63	2669±255	2859±250	4130±380
Nonanol	9.59	3879±315	3099±292	4541±410
Decanol	11.80	4038±330	3702±340	4800±400

^a Viscosity data is from Inamdar et al., 2006

Table 2. Rotational reorientation times (τ_r) of Exalites in alcohols at 298K

i. Rotational reorientation times of Exalite 404 (E404)

Fig. 4 gives the plot of τ_r vs η in alkanes and alcohols for E404 shows that τ_r values increase linearly with η both in alkanes and alcohols, following slip hydrodynamic and subslip behavior, respectively. This clearly indicates that the rotational dynamics of E404 follows SED hydrodynamics with slip boundary condition. Further, E404 rotates slower in alkanes compared to alcohols by a factor of 1 to 1.3. It may be recalled that E392A followed SED hydrodynamics near stick limit in alkanes (Inamdar et al., 2006). E404 is larger than E392A by a factor of 1.1, and exhibits an opposite behavior to that of E392A following slip behavior in alkanes. Interestingly, the rotational dynamics of both these probes follow subslip behavior in higher alcohols.

Theoretical justification for this approach is provided by the microfriction theories of Geirer-Wirtz (GW) and Dote-Kivelson-Schwartz (DKS) wherein the solvent size as well as free spaces is taken into account. However, there is a large deviation of experimentally measured reorientation times from those calculated theoretically.

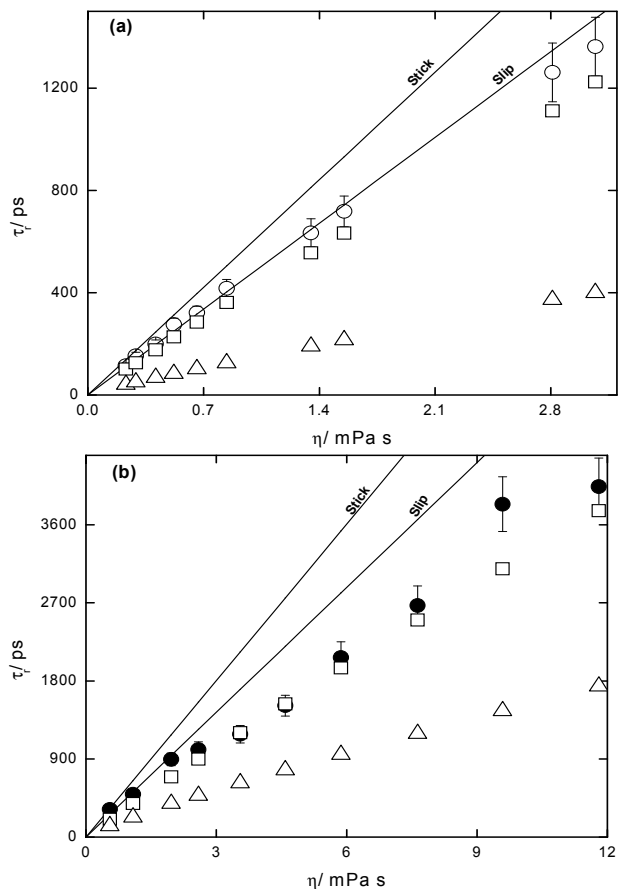


Fig. 4. Plot of rotational reorientation times of E404 as function of viscosity in (a) alkanes and (b) alcohols. The symbols (\circ , \bullet) represent experimentally measured reorientation times. The stick and slip lines calculated using hydrodynamic theory are represented by solid lines. GW and DKS theories are represented using the symbols Δ and \square respectively.

ii. Rotational reorientation times of Exalite 417 (E417)

The rotational reorientation times of E417 scale linearly with η (Fig. 5) and exhibits subslip behavior in alcohols. A large nonlinearity is observed on increasing solvent viscosity. In alkanes, the rotational reorientation times follow slip hydrodynamic boundary condition, similar to E404. GW theory is unable to explain experimental results while DKS theory is in fairly good agreement with experiment and slip hydrodynamics in case of alkanes.

iii. Rotational reorientation times of Exalite 428 (E428)

E428 is the largest probe studied so far in literature. In alcohols the τ_r values for E428 increase linearly with η from methanol to butanol and follows slip boundary condition, and from pentanol to decanol a large deviation from the linearity is observed resulting in subslip behavior (Fig. 6). However, in alkanes the measured reorientation times, clearly follow slip hydrodynamics up to tridecane, whereas in higher alkanes pentadecane and hexadecane

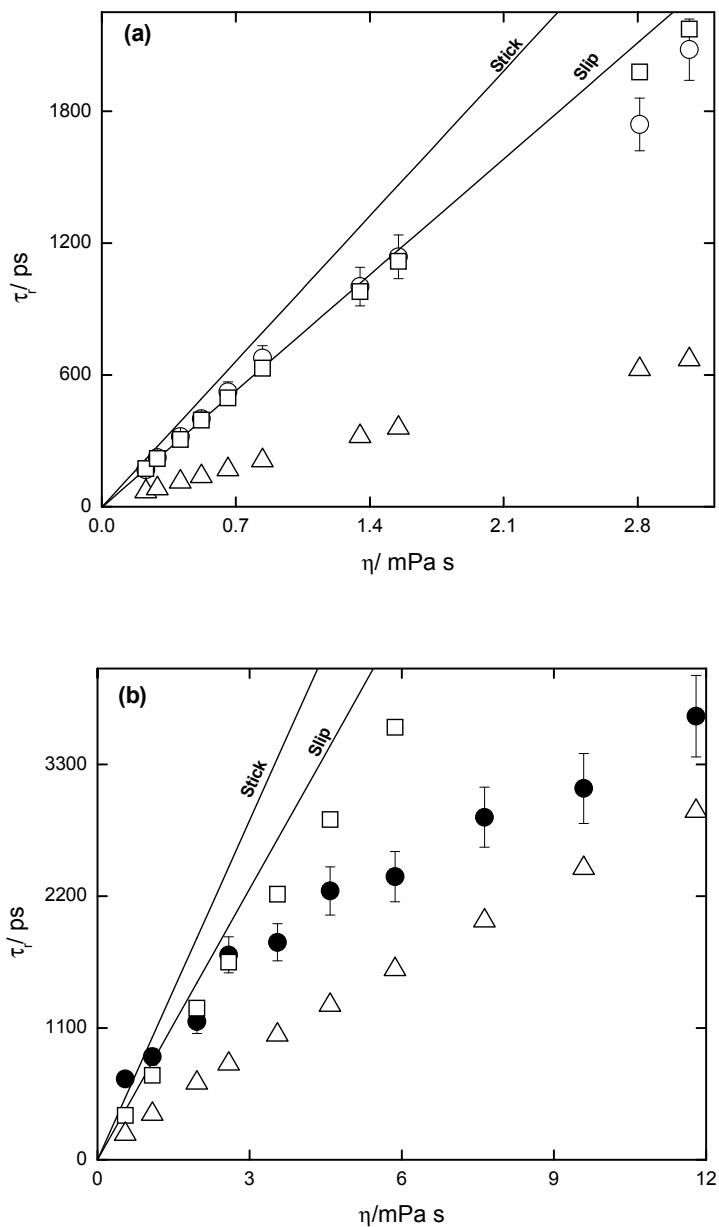


Fig. 5. Plot of rotational reorientation times of E417 as function of viscosity in (a) alkanes and (b) alcohols. The symbols (\circ , \bullet) represent experimentally measured reorientation times. The stick and slip lines calculated using hydrodynamic theory are represented by solid lines. GW and DKS quasihydrodynamic theories are represented using the symbols Δ and \square respectively.

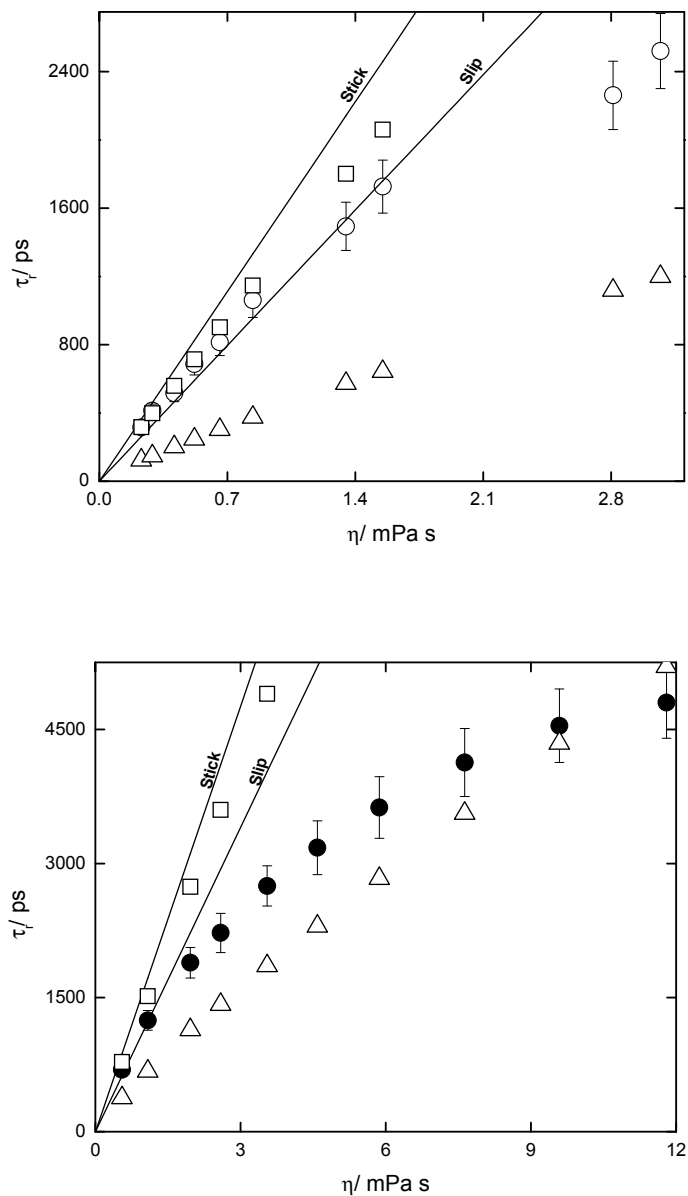


Fig. 6. Plot of rotational reorientation times of E428 as function of viscosity in (a) alkanes and (b) alcohols. The symbols (\circ, \bullet) represent experimentally measured reorientation times. The stick and slip lines calculated using hydrodynamic theory are represented by solid lines. GW and DKS quasihydrodynamic theories are represented using the symbols Δ and ∇ respectively.

subslip behavior is observed. It is interesting to note that, all the three probes rotate much faster in alcohols compared to alkanes. This can be explained as due to large interstitial gaps that may be formed in the solvent medium and because of the possible elastic nature of the spatial H-bonding network of large alcohol molecules constituting a supramolecular structure. The elasticity of the spatial network is a driving force for solvophobic interaction, which is important for the larger probes. Presumably these exalite molecules will be located mainly in these solvophobic regions. The probe molecules, thus, can rotate more freely in these gaps as they experience reduced friction due to a decreased viscosity at the point of contact. This actual viscosity is highly localized and cannot be measured easily. In such a situation the coupling parameter C can be much smaller than C_{slip} predicted by slip hydrodynamic boundary condition. One of the plausible reasons is also due to the Brownian motion, which results from the fluctuating forces in the liquid, is behind and diffusive process.

Ben-Amotz and Scott (1987) opined that processes, which are slow compared to solvent fluctuations, would see the full spectrum of the fluctuations and thus the shear viscosity of the solvent. For example, the fluctuations in n -alcohols occur roughly on the 100 ps/mPa s time scale – precisely the time scale of the Debye absorption in these solvents. On the other hand, processes, which are extremely fast, do not experience Brownian fluctuating force and are not viscously damped. Thus one expects a reduction in microscopic friction for probe molecules, which diffuse at a rate comparable to or faster than the solvent fluctuations. This is exactly the type of effect, which could explain the faster rotational diffusion of exalites in n -alcohols than in n -alkanes. Further, the subslip behavior observed for these probes in polar solvents indicates the existence the nonhydrodynamic forces and the straightforward relation between the probe size and the nature of their behavior may not be appropriate.

Table 3 and 4 contain selected data for various neutral solute molecules (including exalites), whose rotational times in alkanes and alcohols have been measured experimentally. There are many reports on rotational diffusion of small neutral molecules which follow subslip behavior. Garg and Smyth (1965) have attributed these alcohol molecules to be associated

Solute	Volume (Å ³)	Radius (Å)	Axial ratio	T_r (ps/ cP)	T_{slip} (ps/ cP)	T_{stick} (ps/ cP)	T_r/T_{stick}	References
Biphenyl	152	3.31	2.26	24	20	63	0.38	Bauer et al., 1974
Stilbene	180	3.50	2.82	38	41	94	0.40	Courtney et al., 1986
DPB	208	3.38	3.40	66	71	140	0.47	Waldeck et al., 1982
PTP	224	3.77	3.03	54	59	128	0.42	Philips et al., 1985; Kim et al., 1989
Binaphthyl	237	3.84	2.36	51	35	102	0.50	Bowman et al., 1988
PQP	296	4.13	3.77	112	124	226	0.50	Ben Amotz & Scott, 1987
DPA	312	4.15	2.55	78	56	147	0.53	Ben Amotz & Scott, 1987
BMQ	325	4.27	2.65	131	95	241	0.54	Roy and Doraiswamy, 1993
TMQ	359	4.41	2.10	149	71	265	0.56	Roy and Doraiswamy, 1993
DMQ	376	4.48	1.82	194	54	282	0.68	Roy and Doraiswamy, 1993
TMI	429	4.68	2.43	294	145	416	0.71	Roy and Doraiswamy, 1993
E392A	609	5.26	3.59	384	347	435	0.88	Inamdar et al., 2006
QUI	639	5.38	2.09	454	147	554	0.82	Roy and Doraiswamy, 1993
E404	679	5.45	4.21	437	362	601	0.73	Present work
BTBP	733	5.59	3.50	430	269	507	0.85	Ben Amotz & Drake, 1988
E417	837	5.85	5.00	636	623	944	0.67	Present work
E428	1031	6.27	6.18	749	1134	1587	0.47	Present work

Table 3. List of normalized rotational diffusion parameters of neutral nonpolar solutes in alkanes, at 25±5°C

Solute	τ_r (ps/ cP)	τ_r/τ_{stick}	References
Stilbene	10	0.10	Courtney et al., 1986
PTP	39	0.30	Ben Amotz & Scott, 1987
Binaphthyl	36	0.35	Bowman et al., 1988
DPA	50	0.34	Ben Amotz & Scott, 1987
BMQ	87	0.36	Roy and Doraiswamy, 1993
TMQ	117	0.44	Roy and Doraiswamy, 1993
DMQ	137	0.49	Roy and Doraiswamy, 1993
TMI	194	0.47	Roy and Doraiswamy, 1993
E392A	196	0.45	Inamdar et al., 2006
QUI	436	0.79	Roy and Doraiswamy, 1993
E404	349	0.58	Present work
BTBP	430	0.85	Ben Amotz & Drake, 1988
E417	259	0.27	Present work
E428	357	0.22	Present work

Table 4. List of normalized rotational diffusion parameters of neutral nonpolar solutes in alcohols, at $25 \pm 5^\circ \text{C}$

with hydrogen bridges in temporary microcrystalline structures. These structures are in fact not stable, and at a given instant each of these has a finite length. At each instance some hydrogen bonds are ruptured and others are formed.

The first dispersion region is connected with the molecules in these microcrystalline structures. The dielectric relaxation process involves the breaking and reforming of the hydrogen bonds with the orientation of dipole moment, and the rate of breaking off is a determining factor for the relaxation time. In order to check whether there is any dielectric friction on these large nonpolar probes in alcohols, we have also calculated dielectric friction contribution to the rotating probe molecule. The dipole moment values in the excited states were obtained using solvatochromic shift method (Inamdar et al., 2003; Nadaf et al., 2004; Kawski et al., 2005). It is noted that summing up the contribution due to hydrodynamic and dielectric friction will not affect the subslip trend exhibited by the rotational reorientation times. Hence, we attribute this unhindered faster rotation due to strong hydrogen bonding among the solvent molecules leading to supramolecular structures.

There are several reports in literature where the reorientation times of neutral nonpolar solutes have been measured as a function of solute size and the transition from slip to stick hydrodynamics has been observed experimentally. Ben-Amotz and Drake (Ben-Amotz and Drake, 1988) have reported the rotational dynamics of the neutral large sized probe BTBP ($V=733 \text{ \AA}^3$) in series of alcohols and alkanes, and observed that rotational correlation times followed stick boundary condition. Though, BTBP contain the electronegative groups like -O and -N, which are capable of forming hydrogen bond with any solvent, they attributed, stick condition to its volume which is much larger than that of all the solvent molecules studied. Later, Roy and Doraiswamy (Roy and Doraiswamy, 1993) have studied the rotational dynamics of series of nonpolar solutes, which do not contain any electronegative groups like -O or -N. They observed transition towards the stick boundary condition on increasing the solute size from BMQ ($V = 325 \text{ \AA}^3$) to QUI ($V = 639 \text{ \AA}^3$). It is clear from the above two findings that a stick transition arises due to increase in the solute size, when compared to that of the solvent. Thus, one can expect stick or superstick behavior in case of exalites (E404, E417 and E428) as these are larger than QUI by a factor of 1.1, 1.3 and 1.6, respectively. The present situation, where the largest probe E428 follows subslip in alcohols

is surprising in the light of above studies. In such a situation the microscopic friction of the solvent molecules reduces well below the macroscopic value, which may result from either dynamic or structural features of the macroscopic solvation environment-giving rise to faster rotation in hydrogen bonding solvents.

On the other hand, rotational reorientation times of these exalite nonpolar probes bequeath interesting results following slip boundary condition in alkanes. It is observed from the Table 5 that there is a difference in slope for the two solvent types. Therefore, it is evident that the rotational reorientation times of these exalites are shorter in alcohols than alkanes of comparable viscosity. This difference is an indication of nonhydrodynamic effects in one or both of the solvents. It is unlikely that nonhydrodynamic behavior resulting from frequency dependence of the solvent friction occurs in alkanes on the 100 ps to 1 ns time scale (Hynes, 1986). These times are much longer than dynamic memory effects in the solvent arising from molecular collisions. These collisional events manifest themselves in the viscoelastic relaxation time, which for an *n*-alkane is estimated to lie in the subpicosecond to single picosecond time domain (Hynes, 1986).

Solutes	Alcohols	Alkanes
Slope	Slope (ps/ mPa s)	(ps/ mPa s)
E404	349	437
	360*	454*
E417	259	636
	362*	677*
E428	357	749
	510*	901*

* Second entry for solute is a slope of the best fit line made to pass through the origin.

Table 5. Linear regression results of rotational reorientation of exalites in series of alcohols, alkanes and binary mixture

Thus one would expect rotational times to be well described by the SED relation with the appropriate boundary condition and the solute shape factor (Ben Amotz and Scott, 1987) in *n*-alkanes. The internal mobility also allows the solute molecule to slip better through the surrounding solvent molecules than for a rigid molecular backbone (Alavi et al., 1991b,c). Waldeck et al. (1982) have also argued for the probe DPB, that the slip boundary condition is entirely reasonable for an uncharged nonpolar molecule in nonpolar solvents. E428 is about 5 times larger than DPB and from the Table 3; it is evident that τ_r/τ_{stick} ratio is same for both these probes in alkanes, which suggests the fact that the rotation of these probes can be well explained by slip hydrodynamics. Similarly, the studies of the neutral dye BBOT (Fleming et al., 1977), an approximate prolate top, found that this molecule followed slip boundary condition. It was anticipated that neutrals would not strongly interact with the solvent, and slip boundary condition were thus more appropriate. Others have argued (Porter et al., 1977) that the faster rotation observed for BBOT might also be due to the internal mobility of the dye. This may be one of the possible reasons for the faster rotation observed for the large exalite probes. Both GW and DKS models were tested for a quantitative prediction of τ_r of solutes in alkanes. The GW model predicts very low τ_r values in alkanes as well as in the case of alcohols and fails to satisfactorily explain the observed results. Also, the *C* values are nearly invariant of the size of the solute. It has

been evidenced that the GW theory correctly predicts the observed results for a solute with ~ 2.5 Å radius. Therefore, the GW model is adequate for very small solutes that show subslip behavior, viz., I_2 and NCCCCN (Goulay, 1983). Though, DKS theory is found to be in good agreement with the experimentally observed trend up to decane in case of E404 and up to nonane for E428, a better agreement is found in alkanes for E417. It has been noted that the rotational reorientation times in alkanes is reproduced quantitatively for solutes with radius up to 4.2 Å only, beyond which the theory tends to show poor agreement with experimental values [93]. Our experimental results are indicative of the fact the DKS theory also holds well even for larger probes up to a radius of 6.3 Å in alkanes and brings out the subtle variations in the observed data.

3.2.2 Rotational dynamics of polar probes

The rotational dynamics studies using polar solutes in polar solvents have shed lights on concepts such as dielectric friction and solute-solvent hydrogen bonding. In addition to viscous drag, polar-polar interaction between a polar solute and a polar solvent gives rise to an additional retarding force often termed as dielectric friction. This arises because of the inability of the solvent molecules, encircling the polar solute probe, to rotate synchronously with the probe. The result of this effect is the creation of an electric field in the cavity, which exerts a torque opposing the reorientation of the probe molecule. Under such circumstances, the observed friction, which is proportional to the measured reorientation time, has been explained as a combination of mechanical and dielectric frictions. However, many experimental investigations of reorientation dynamics have indicated that there is another source of drag on a rotating probe molecule due to hydrogen bonding between the solute and the solvent molecules. A solute molecule can form hydrogen bond with the solvent molecule depending on the nature of the functional groups on the solute and the solvent which enhances the volume of the probe molecule. This further impedes the rotational motion and thus the observed reorientation time becomes longer than that observed with the bare solute molecule.

Molecular structures of the three coumarin dyes chosen under the category of polar probes are shown in Fig. 7. The reorientation times of C522B, C307 in alcohols and alkanes and C138 in alcohols (Mannekutla et al., 2010) are summarized in Tables 6 and 7. The τ_r values obtained in alkanes clearly show that C522B rotates faster compared to C307. In alcohols, it is interesting to note that, the probe C138 rotates faster almost by a factor of 1:2 from propanol to decanol compared to C522B and C307, respectively. In other words, C138 experiences a reduced mechanical friction i.e., almost same as C522B and twice as C307 from propanol to decanol. This is because C307 shows greater interaction owing to its greater polarity.

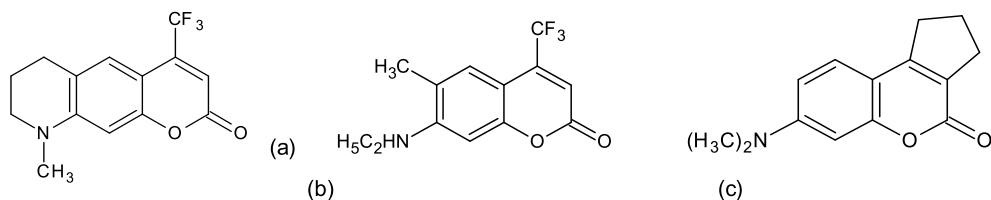


Fig. 7. Molecular structures of (a) C522B, (b) C307 and (c) C138

Solvents	η (mPa s ^a)	C522B			C307			C138		
		$\langle r \rangle$	τ_f (ns)	τ_r (ps)	$\langle r \rangle$	τ_f (ns)	τ_r (ps)	$\langle r \rangle$	τ_f (ns)	τ_r (ps)
Methanol	0.55	0.004±0.001	4.87	53±13	0.003±0.001	5.10	42±14	0.003±0.001	3.63	30±10
Ethanol	1.08	0.006±0.001	5.02	83±14	0.006±0.001	5.12	84±14	0.006±0.002	3.63	61±20
Propanol	1.95	0.009±0.001	5.05	126±14	0.011±0.002	5.13	157±29	0.009±0.002	3.64	92±20
Butanol	2.59	0.011±0.002	5.08	156±28	0.016±0.002	5.14	232±29	0.011±0.001	3.64	113±10
Pentanol	3.51	0.013±0.002	5.09	186±29	0.021±0.003	5.14	309±44	0.015±0.003	3.64	156±31
Hexanol	4.57	0.017±0.002	5.09	246±29	0.027±0.002	5.14	405±30	0.020±0.002	3.65	212±21
Heptanol	5.97	0.022±0.003	5.10	323±44	0.034±0.003	5.15	521±46	0.025±0.002	3.65	268±21
Octanol	7.63	0.027±0.002	5.10	403±30	0.041±0.003	5.15	642±47	0.035±0.004	3.68	390±45
Nonanol	9.59	0.033±0.003	5.10	501±46	0.051±0.003	5.18	828±49	0.037±0.002	3.74	422±23
Decanol	11.74	0.042±0.003	5.12	658±47	0.065±0.002	5.18	1104±34	0.047±0.003	3.77	477±35

^a Viscosity data is from Inamdar et al., 2006

Table 6. Steady-state anisotropy ($\langle r \rangle$), fluorescence lifetime (τ_f) and rotational reorientation time (τ_r) of coumarins in alcohols at 298K (the maximum error in the fluorescence life times is less than ±50 ps) (Mannekutla et al., 2010)

Solvents	η / mPa s ^a	C522B			C307		
		$\langle r \rangle$	τ_f / ns	τ_r / ps	$\langle r \rangle$	τ_f / ns	τ_r / ps
Pentane	0.23	-	-	-	0.003±0.001	4.23	35±12
Hexane	0.29	-	-	-	0.003±0.001	4.28	35±12
Heptane	0.41	0.002±0.001	3.98	22±11	0.004±0.001	4.37	48±12
Octane	0.52	0.003±0.001	4.11	34±11	0.004±0.001	4.51	49±12
Nonane	0.66	0.004±0.001	4.17	46±12	0.005±0.001	4.63	63±13
Decane	0.84	0.005±0.001	4.20	58±12	0.006±0.001	4.60	76±13
Dodecane	1.35	0.006±0.001	4.26	70±12	0.007±0.002	4.79	92±26
Tridecane	1.55	0.007±0.001	4.31	83±12	0.008±0.002	4.80	106±27
Pentadecane	2.81	0.009±0.001	4.38	110±12	0.009±0.002	4.80	120±27
Hexadecane	3.07	0.010±0.001	4.52	126±13	0.010±0.002	4.86	135±27

^a Viscosity data is from Inamdar et al., 2006

Table 7. Steady-state anisotropy ($\langle r \rangle$), fluorescence lifetime (τ_f) and rotational reorientation time (τ_r) of coumarins in alkanes at 298K for C522B and C307 (the maximum error in the fluorescence life times is less than ±50 ps) (Mannekutla et al., 2010)

The probes C522B and C138 have shown coincidentally similar interactions. In C138, aminomethyl group being free contributes more to the charge separation through resonance- whereas in C522B this resonance contribution is sluggish, comparatively. However, the presence of -CF₃ in C522B increases the charge separation, which leads to better interaction with the hydrogen bonding solvents. Replacement of -CF₃ by cyclic alkyl group in C138 would not have any great contribution towards its polarity. Hence, the presence of two different groups with contradicting properties leads to the coincidental similarities in reorientation dynamics of C522B and C138.

The normalized rotational reorientation times (at unit viscosity) are smaller in alkanes compared to alcohols, which indicates that the probes C522B and C307 rotate faster in alkanes compared to alcohols. The reorientation times of the three probes thus obtained in alcohols follow the trend: $\tau_r^{C307} > \tau_r^{C522B} \geq \tau_r^{C138}$.

Fig. 8 gives a typical plot of τ_r vs η for all the three probes in alcohols and in alkanes along with the stick and slip lines. Note that the experimentally measured reorientation times lie between slip and stick hydrodynamic in case of alcohols. However, in alkanes we observe, as the size of the solvent molecule becomes equal to and bigger than the size of the solute molecule, the probe molecule experiences a reduced friction. Benzler and Luther (1977) measured the reorientation time of biphenyl ($V=150 \text{ \AA}^3$) and *p*-terphenyl ($V=221 \text{ \AA}^3$) in *n*-alkanes. For biphenyl a nonlinearity was observed in the plot of τ_r vs η from decane and from tetradecane, in case of *p*-terphenyl. Singh [24] studied reorientation times of the probe neutral red ($V=234 \text{ \AA}^3$) which experienced a reduced friction from tetradecane to hexadecane following subslip behavior. C522B (223 \AA^3) and C307 (217 \AA^3) have nearly identical volumes as compared to neutral red and *p*-terphenyl and thus a similar rotational relaxation in alkanes may be expected.

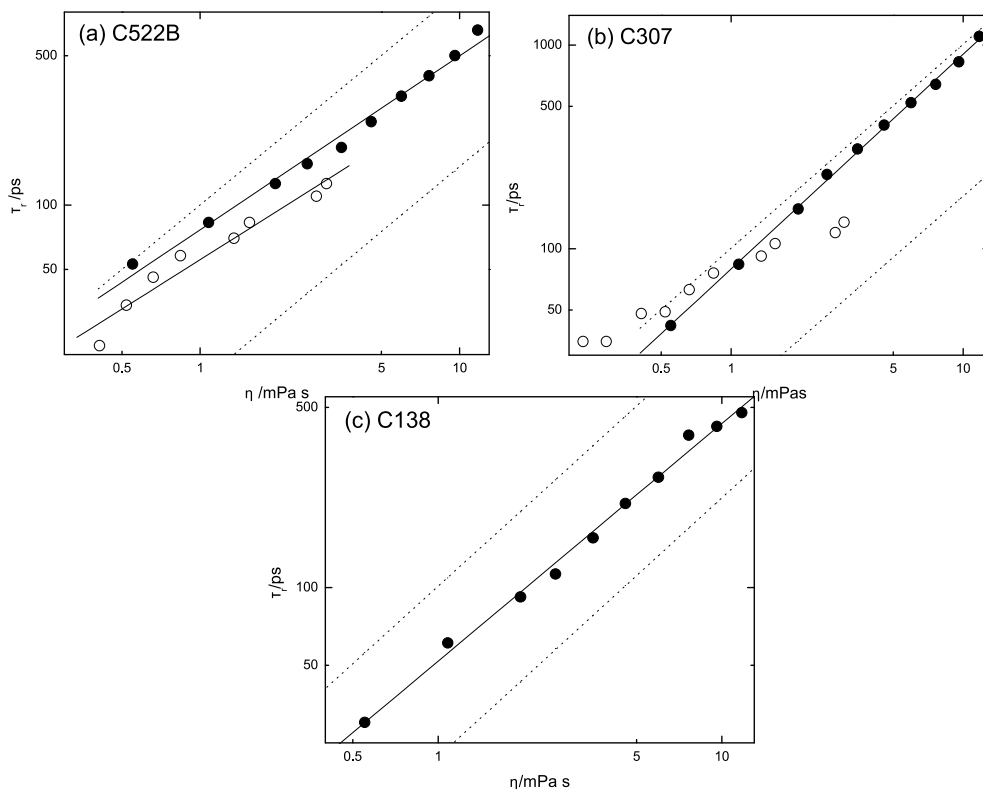


Fig. 8. Plots of τ_r vs η for the three coumarins in alcohols (\circ), and alkanes (\bullet) in case of C522B and C307

Note that the probes experience reduced friction as the size of the solvent increases. A number of probes have been studied (Phillips et al., 1985; Courtney et al., 1986; Ben Amotz and Drake, 1988; Roy and Doraiswamy, 1993; Williams et al., 1994; Jiang and Blanchard, 1994; Anderton and Kauffman, 1994; Brocklehurst and Young, 1995) in alcohols and alkanes, wherein faster rotation of the probe in alcohols is observed compared to alkanes, which has been explained as due to higher free volume in alcohols compared to alkanes with the help of DKS theory. If there were no electrical interaction between the coumarins and alcohols, a faster rotation of the coumarins would have been observed in alcohols compared to alkanes, but an opposite trend has been observed that indicates the presence of electrical friction (Dutt and Raman, 2001). Before evaluating the amount of dielectric friction, the contribution due to mechanical friction must be estimated with a reasonable degree of accuracy. SED theory with a slip hydrodynamic boundary condition is often used to calculate the mechanical friction in case of medium-sized solute molecules. However, in the present study the solvent size increases by more than 5 times in alcohols from methanol to decanol. Hence, DKS quasihydrodynamic theory is found to be more appropriate, when size effect is taken into account as compared with GW. Eqn. 25 is used to calculate ΔV in associative solvents like alcohols, because C_{DKS} obtained in this manner gave a better agreement with the experimental results (Hubbard and Onsager, 1977; Anderton and Kauffman, 1996; Dutt et al., 1999; Dutt and Raman, 2001).

In summary, a faster rotation of the probes is observed in case of C522B and C138 in alcohols compared to C307. In spite of the distinct structures, almost similar rotational reorientation times are observed for C522B and C138 in alcohols from propanol to decanol. Further studies of dielectric friction in alcohols, the observed reorientation times of these coumarins could not follow the trend predicted by the theories of Nee-Zwanzig and van der Zwan-Hynes. Dielectric frictions obtained experimentally and theoretically using NZ and ZH theories, do not agree well.

3.2.3 Rotational dynamics of polar probes in binary solvents

Binary mixtures of polar solvents represent an important class of chemical reaction media because their polarity can be controlled through changes in composition. In a binary mixture, altering the composition of one of the ingredients can lead to a change in solubility, polarizability, viscosity and many other static and dynamic properties. Yet, it is often found that the dielectric properties of polar mixtures depart significantly from what one might expect on the basis of ideal mixing. In hydrogen-bonding systems, such as alcohol-water mixtures, intermolecular correlations are strong, and consequently, the dielectric properties of the mixture are usually not simply related to those of the separated components. Recently, the properties of some binary solutions were studied using theoretical calculations and molecular dynamics (MD) simulations (Chandra and Bagchi, 1991; Chandra, 1995; Skaf and Ladanyi, 1996; Day and Patey, 1997; Yoshimori et al., 1998; Laria and Skaf, 1999). The results showed that the dynamical features of binary solutions are very much different from those of neat solutions, and the dynamics can be strongly affected by the properties of the solute probe. The binary mixtures show exotic features which pose interesting challenges to both theoreticians and experimentalists. Amongst them, the extrema observed in the composition dependence of excess viscosity (Qunfang and Yu-Chun, 1999; Pal and Daas, 2000) and the anomalous viscosity dependence of the rotational relaxation time (Beddard et al., 1981) are significant. The anomalous features in the complex systems arise from specific

intermolecular interactions due to structural heterogeneities. In DMSO+water mixture, the partial negative charge on the oxygen atom of the dimethyl sulphoxide molecule forms hydrogen bonds with water molecules, giving rise to a non-ideal behavior of the mixture. The non-ideality of mixtures depends on the nature of interaction between the different species constituting the mixture. Traube suggested that the anomalous behavior of viscosity in binary mixtures arises from the formation of clusters (Traube, 1886). The prominent hydrophilic nature of DMSO renders it capable of forming strong and persistent hydrogen bonds with water through its oxygen atom (Safford et al., 1969; Martin and Hanthall, 1975; De La Torre, 1983; Luzar and Chandler, 1993). This leads to the formation of DMSO-water molecular aggregates of well-defined geometry which are often responsible for the strong nonideal behavior manifested as maxima or minima (Cowie and Toporowski, 1964; Packer and Tomlinson, 1971; Fox and Whittingham, 1974; Tokuhiko et al., 1974; Gordalla and Zeidler, 1986; 1991; Kaatz et al., 1989). The largest deviations from the ideal mixing occur around 33% mole of DMSO, thus suggesting the existence of stoichiometrically well defined 1DMSO:2water complexes. Recently, a number of MD simulations (Vaisman and Berkowitz, 1992; Soper and Luzar, 1992; 1996; Luzar and Chandler, 1993; Borin and Skaf, 1998; 1999) and neutron diffraction experiments have indeed identified the structure of the 1DMSO:2water complex and linked many of the structural and dynamical features of DMSO water mixtures to the presence of such aggregates. Of late, Borin and Skaf (Borin and Skaf, 1998; 1999) have found from MD simulations, another distinct type of aggregate consisting of two DMSO molecules linked by a central water molecule through H-bonding, which is expected to be the predominant form of molecular association between DMSO and water in DMSO-rich mixtures. This H-bonded complex is referred to as 2DMSO:1water aggregate.

The rotational diffusion studies of the following two sets of structurally similar molecules dyes: coumarin-440 (C440), coumarin-450 (C450), coumarin 466 (C466) and coumarin-151 (C151) and fluorescein 27 (F27), fluorescein Na (FNa) and sulforhodamine B (SRB) (Fig. 9) in binary mixtures of dimethyl sulphoxide + water and propanol + water mixtures, respectively. Among coumarins, C466 possess N-diethyl group at the fourth position whereas, other three dyes possess amino groups at the seventh position in addition to carbonyl group. This structure is expected to affect the reorientation times due to the formation of hydrogen bond with the solvent mixture.

The photo-physics of fluorescent molecules in solvent mixtures has not been studied as extensively as those in neat solvents. Thus the structure and structural changes in the solvent environment around the solute in the mixed solvents have not been fully understood. It is therefore important to investigate the photophysical characteristics that are unique to the binary solvent mixtures.

DMSO is miscible with water in all proportions and aqueous DMSO solutions are quite interesting systems, as there exists a nonlinear relationship between the bulk viscosity and the composition of the solvent mixture. In DMSO-water binary mixture, there is a rapid rise in viscosity with a small addition of DMSO to water and viscosity decay profile after the post peak point is gradual. The sharp increase in the viscosity of the binary mixture with increasing DMSO concentration may be attributed to significant hydrogen bonding effects between water and DMSO molecules. Beyond around 15% composition of DMSO, there exist two DMSO compositions for which viscosity is same. This dual valuedness should manifest in reasonable mirror symmetry of the rotational reorientation time (τ_r) about the

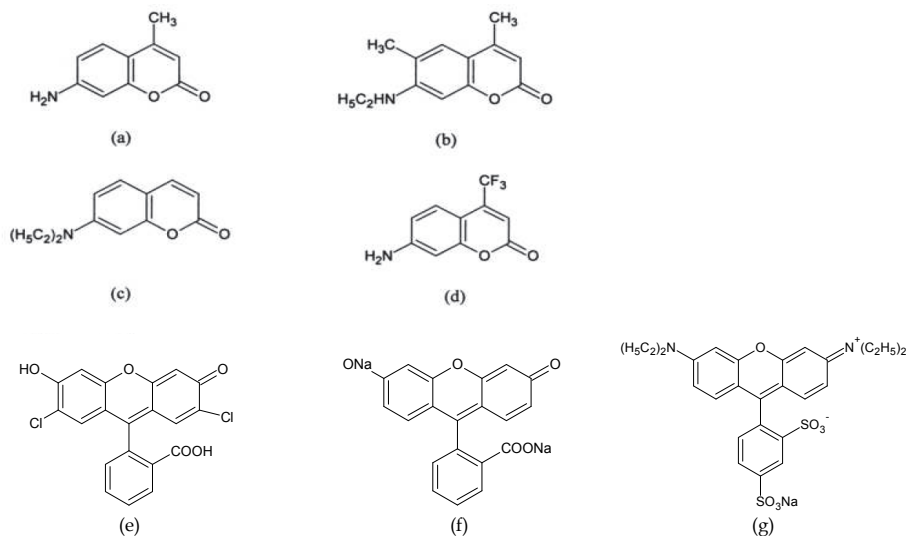


Fig. 9. The molecular structures of (a) C440, (b) C450, (c) C466, (d) C151, (e) F27, (f) FNa and (g) SRB.

viscosity peak point. The viscosity of DMSO is slightly more than twice that of water. At about 40% mole composition of DMSO, the solvent mixture has a maximum value of viscosity of 3.75 m Pas which is 1.87 times that of DMSO and nearly 4 times that of water. From the viscosity profile it may be seen that there are four distinct compositions of DMSO for which the viscosity is nearly the same and as per hydrodynamic theory the friction experienced by a rotating probe molecule is expected to be the same.

Fig. 10 (a and b) represent the variation of τ_r with η along with theoretical profile including the viscous and the dielectric contribution for all the probes, which clearly indicates a non-hydrodynamic behavior. The rotational reorientation time of a solute in a solvent is in a way an index of molecular friction. Experimentally obtained results of all the probes under study show a hairpin profiles bent upwards. The reorientation times gradually increases as a function of viscosity up to the peak viscous value and interestingly these values further increase even after the solvent mixture exhibits reduction in viscosity after the peak value. Thus all the probes exhibit different rotational reorientation values for isoviscous points. Note that, reorientation times are longer in the DMSO region compared to the water rich zone. The studies of the rotational diffusion of the dye molecules in binary solvents showed that the rotational relaxation time does not necessarily scale linearly with viscosity when the solvent composition is changed. These observations have been interpreted as a manifestation of solvent structure on time scales similar to or longer than the time scale of solute rotation or as resulting from a change in the dielectric friction through the solvent mixture. In some cases these observations have been interpreted as a breakdown of the hydrodynamic approximation. The rotational diffusion studies of the dye molecule oxazine 118 in two binary solvent systems as a function of temperature showed a nonlinear dependence of the rotational diffusion on the solvent viscosity when the solvent composition is changed (Williams et al., 1994).

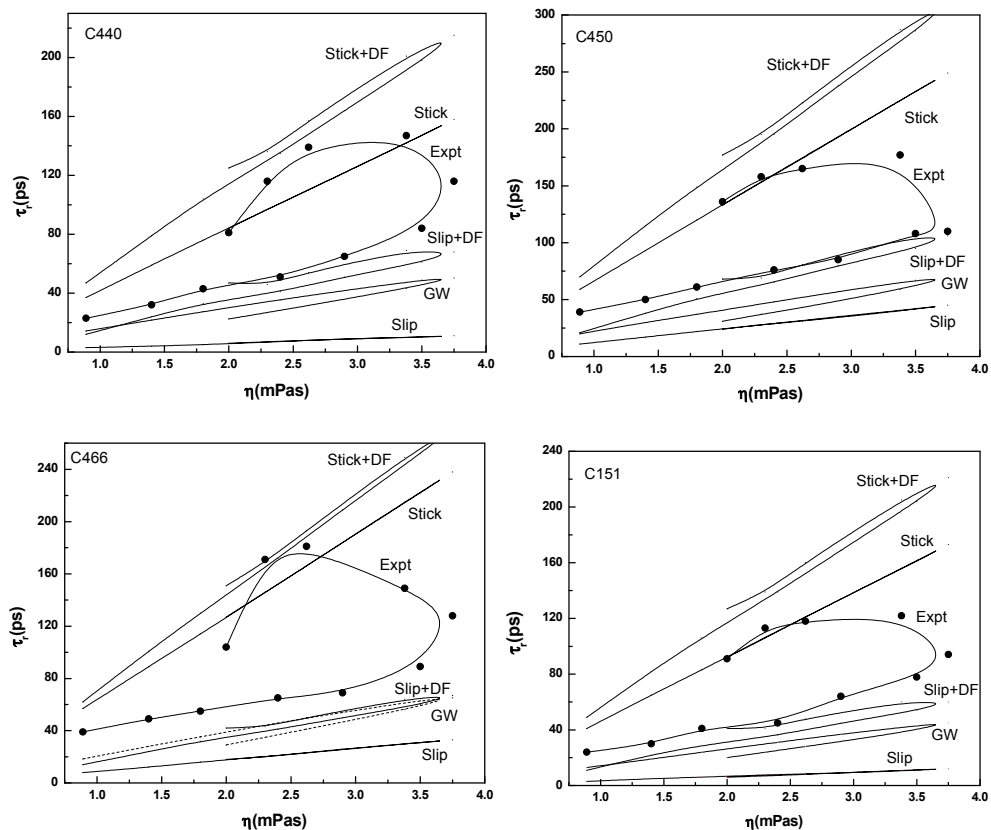


Fig. 10. Plot of rotational reorientation time with viscosity along with theoretical profile including the viscous and the dielectric contribution for C440, C450, C466 and C151 probes (Inamdar et al., 2009)

The linear variation of the τ_r as a function of η from pure water to the composition of the binary mixture when the viscosity reaches its peak is in accordance with the SED theory, though it does not account for the large curvature in the profile. The theoretical SED stick line shows a sharp hairpin profile. Incorporation of the dielectric friction contribution qualitatively mimics the observed profile, with the τ_r being slightly larger in the post peak viscosity DMSO rich zone. The fact, that a continuum theory without the consideration of any molecular features could reproduce the gross features of the observed profile of τ_r vs. η is noteworthy. The experimentally observed profile bent upwards yields considerably higher τ_r in the DMSO rich zone than the corresponding isoviscous point in the water rich zone. This is also reproduced by the theoretical models qualitatively. The pronounced difference in the rotational reorientation times at the isoviscous points can be explained only on the basis of solvation. It is possible that at the isoviscous points the microstructural features in the binary mixture could be different. The dual values of τ_r at isoviscous points in the DMSO rich zone are also due to the contributions of dielectric friction at these two points being different.

Beddard et al. (1981) reported different rotational relaxation times of the dye cresyl violet in ethanol water mixture by varying the ethanol water composition i.e., at the same viscosity but at different compositions. The observed re-entrance type behavior of the orientational relaxation time when plotted against viscosity could not be explained only in terms of non-ideality in viscosity exhibited in a binary mixture. Beddard et al. also reported that the re-entrance behavior is strongly dependent on the specific interaction of the solute with the solvents. This is because in a system where solute interacts with few different species in a binary mixture in a different manner, its rotational relaxation will depend more on the composition than on the viscosity of the binary mixture. The role of specific interaction on the orientational dynamics has often been discussed in relation to changing boundary conditions (Fleming, 1986). We find that the orientational relaxation time of the probe molecules when plotted against the solvent viscosity does indeed show re-entrance. Our study here re-affirms that for a solute dissolved in a binary mixture, its rotational relaxation will depend more on the composition than on the viscosity of the binary mixture and thus the re-entrant type behaviour is strongly dependent on the interactions of the solute with the two different species in the solvent.

The rotational dynamics of two kinds of medium sized three dyes-Fluorescein 27(F27) and Fluorescein Na(FNa) (both neutral but polar), and Sulforhodamine B(SRB) (anion) has been studied in binary mixtures comprising of 1-Propanol and water at room temperature using both steady-state and time resolved fluorescence depolarization techniques. Alcohols have both a hydrogen-bonding -OH group and a hydrophobic alkyl group. The latter affects the water structure. The objective in studying two neutral and an anion dyes is to compare and contrast the rotational dynamics as a function of charge. A nonlinear hook-type profile of rotational reorientation times of the probe (τ_r) as a function of viscosity (η) is observed for all three dyes in this binary system, with the rotational reorientation times being longer in organic solvent rich zone, compared to the corresponding isoviscous point in water rich zone. This is attributed to strong hydrogen bonding between the solute and propanol molecules.

The increase in viscosity as 1-propanol is added to water is sharp with the peak value of 2.70 mPa s being reached at about 30% mole composition of 1-propanol. The viscosity of 1-propanol is 1.96 mPa s, the decrease after the post peak point is linear but gradual. The dielectric friction contribution in water, amides, and dipolar aprotics is minimal while it goes on increasing in alcohols (Krishnamurthy et al, 1993).

At isoviscous points there are two different τ_r values and this duality results from different values of dielectric frictions at the isoviscous points (Fig. 11). It is seen that both the neutral dyes F27 and FNa clearly produce the hook-type profile bent upwards and qualitatively mimic the nonhydrodynamic behavior. The reorientation times gradually increase as a function of viscosity up to the peak viscous value. τ_r values decrease after the solvent mixture exhibits a reduction in viscosity after the peak value. Note that the reorientation times are longer in propanol rich region compared to the water rich zone. In case of SRB though it exhibits hook type profile, surprisingly τ_r values longer in water rich zone in the beginning and later probe rotates faster in the intermediate viscous region. In propanol rich zone SRB shows similar τ_r values as those of water rich zone. This may be due to both amino groups of SRB are ethylated and the rotational diffusion of this dye was slightly more rapid than predicted. Theoretical models mimic this trend qualitatively, though GW & DKS models invariably predict a reduced friction and illustrate a hairpin - bending downwards. Thus, these models underestimate the friction experienced by the probe. The dual

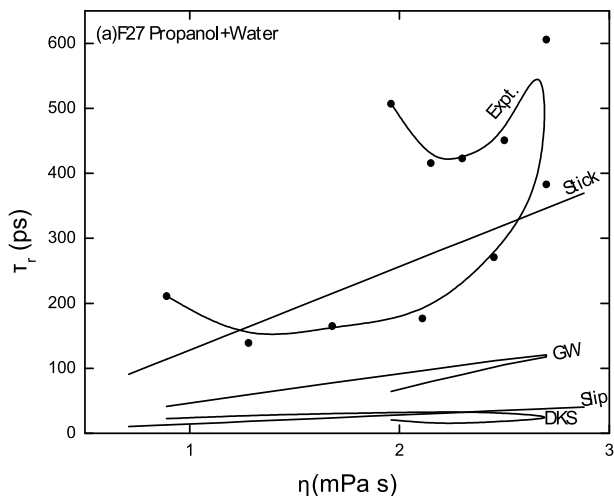


Fig. 11. Plot of rotational reorientation time with viscosity along with theoretical profile including viscous contribution for F27

valuedness of τ_r at isoviscous points near the organic solvent rich zone were attributed to different contributions of dielectric friction at these compositions and to strong hydrogen bonding.

General conclusion and summary

In this article, an attempt has been made to understand solute-solvent interactions in various situations using the powerful fluorescence spectroscopic techniques. The interesting observation of faster rotation of nonpolar probes in alcohols compared to alkanes can be attributed to large interstitial gaps that may be formed in the solvent medium and because of the possible elastic nature of the spatial H-bonding network of large alcohol molecules constituting a supramolecular structure. Presumably the exalite molecules will be located mainly in these solvophobic regions and thus, can rotate more freely in these gaps and experience reduced friction due to decreased viscosity at the point of contact. This actual viscosity is highly localized and cannot be measured easily. In such a situation the coupling parameter C can be much smaller than C_{slip} predicted by slip hydrodynamic boundary condition. Also, the largest probe E428 following subslip trend in alcohols is surprising. In such a situation the microscopic friction of the solvent molecules reduces well below the macroscopic value, which may result from either dynamic or structural features of the macroscopic solvation environment-giving rise to faster rotation in hydrogen bonding solvents. The experimental results indicate that DKS theory also holds well even for larger probes up to a radius of 6.3 Å in alkanes.

In case of polar probes, a faster rotation of the probes is observed for C522B and C138 in alcohols compared to C307. In spite of the distinction in structure a coincidental similar rotational reorientation times is observed in case of C522B and C138 in alcohols from propanol to decanol. Further studies of dielectric friction in alcohols, the observed reorientation times of these coumarins could not follow the trend predicted by the theories of Nee-Zwanzig and van der Zwan-Hynes. Experimentally and theoretically obtained dielectric frictions using NZ and ZH theories, do not agree well.

A nonlinear hook-type profile of rotational reorientation times of the probe as a function of viscosity is observed for all the dyes in binary mixtures, with the rotational reorientation times being longer in organic solvent rich zone, compared to the corresponding isoviscous point in water rich zone. This is attributed to strong hydrogen bonding between the solutes and DMSO or propanol molecules. Theoretical models mimic this trend qualitatively, though GW & DKS models invariably predict a reduced friction and illustrate a hairpin profile bending downwards. Thus they underestimate the friction experienced by the probe. The dual valuedness of τ_r at isoviscous points near the organic solvent rich zone were attributed to different contributions of dielectric friction at these compositions and to strong hydrogen bonding.

In general, the theoretical models: hydrodynamic as well as those based on dielectric friction do not adequately and precisely describe the experimental observations. The theoretical description of solute-solvent interaction to explain the experimental observations is yet to evolve. The failure of the theoretical models, to explain the experimental results quantitatively in specific cases, calls for the formulation of molecular based theories.

4. Acknowledgment

The author acknowledges the encouragement and support of Profs. M.I. Savadatti and B.G. Mulimani. Thanks are also due to Dr. James R.M., K.H. Nagachandra and M.A. Shivkumar for their timely help and financial support from Council of Scientific & Industrial Research and University Grants Commission, New Delhi.

5. References

- Alavi, D.S., Hartman, R.S. & Waldeck, D.H., 1991a, A test of continuum models for dielectric friction. Rotational diffusion of phenoxazine dyes in dimethylsulfoxide *J. Chem. Phys.* 94, 4509-20
- Alavi, D.S. & Waldeck, D.H., 1991b, Rotational dielectric friction on a generalized charge distribution *J. Chem. Phys.* 94, 6196-6202
- Alavi, D.S., Hartman, R.S. & Waldeck, D.H., 1991c, The influence of wave vector dependent dielectric properties on rotational friction. Rotational diffusion of phenoxazine dyes *J. Chem. Phys.* 95, 6770-83
- Alavi, D.S. & Waldeck, D.H., 1993, Erratum: Rotational dielectric friction on a generalized charge distribution *J. Chem. Phys.* 98, 3580-82
- Anderton, R.M. & Kauffman, J.F., 1994, Temperature-Dependent Rotational Relaxation of Diphenylbutadiene in n-Alcohols: A Test of the Quasihydrodynamic Free Space Model *J. Phys. Chem.* 98, 12117-12124
- Anfinrud, P.A., C. Han, T. Lian and R. M. Hochstrasser, 1990, Evolution of the transient vibrational spectrum following short-pulse excitation *J. Phys. Chem.* 94, 1180-84
- Backer, S.D., Dutt, G.B., Ameloot, M., Schryver, F.C.D., Müllen, K. & Holtrup, F., 1996, Fluorescence Anisotropy of 2,5,8,11-Tetra-tert-butylperylene and 2,5,10,13-Tetra-tert-butylterrylene in Alkanes and Alcohols *J. Phys. Chem.* 100, 512-518
- Barbara, P.F. & Jarzeba, W., 1990, Ultrafast Photochemical Intramolecular Charge and Excited State Solvation in *Adv. in Photochem.* Vol.15, pp. 1-68, Eds: D.H. Volman, G.S. Hammond, K. Gollnick, John Wiley & Sons, Inc., USA

- Bauer, D.R., I.I. Brauman & Pecora, R., 1974, Molecular reorientation in liquids. Experimental test of hydrodynamic models *J. Am. Chem. Soc.* 96, 6840-43
- Beddard, G.S., Doust, T. & Hudales, J. 1981, Structural features in ethanol-water mixtures revealed by picoseconds fluorescence anisotropy *Nature* 294,145-46
- Ben Amotz, D. & Scott, T.W., 1987, Microscopic frictional forces on molecular motion in liquids. Picosecond rotational diffusion in alkanes and alcohols *J. Chem. Phys.* 87, 3739-48
- Ben Amotz, D. & Drake, J.M., 1988, The solute size effect in rotational diffusion experiments: A test of microscopic friction theories *J. Chem. Phys.* 89, 1019-29
- Benzler, J. & Luther, L., 1997, Rotational relaxation of biphenyl and *p*-terphenyl in *n*-alkanes: the breakdown of the hydrodynamic description *Chem. Phys. Lett.* 279, 333-38
- Biasutti, M.A., Feyter, S.D., Backer, S.D., Dutt, G.B., Schryver, F.C.D., Ameloot, M., Schlichting P. & Müllen K., 1996, *Chem. Phys. Lett.* 248, 13-19
- Birks, J.B., 1970, *Photophysics of Aromatic Molecules*, John Wiley & Sons, New York
- Blanchard, G.J. & Wirth, M.J., 1986, Anomalous temperature-dependent reorientation of cresyl violet in 1-dodecanol *J. Phys. Chem.* 90, 2521-25
- Blanchard, G.J., 1987, Picosecond spectroscopic measurement of a solvent dependent change of rotational diffusion rotor shape *J. Chem. Phys.* 87, 6802-08
- Blanchard, G.J. & Cihal, C.A. 1988, Orientational relaxation dynamics of oxazine 118 and resorufin in the butanols. Valence- and state-dependent solvation effects *J. Phys. Chem.* 92, 5950-54
- Blanchard, G.J. 1988, A study of the state-dependent reorientation dynamics of oxazine 725 in primary normal aliphatic alcohols *J. Phys. Chem.* 92, 6303-07
- Blanchard, G.J. 1989, State-dependent reorientation characteristics of Methylene Blue: the importance of dipolar solvent-solute interactions *J. Phys. Chem.* 93, 4315-19
- Blanchard, G.J. 1989, Detection of a transient solvent-solute complex using time-resolved pump-probe spectroscopy *Anal. Chem.* 61, 2394-98
- Bordewijk, P., 1980, *Z. Naturforsch.* 35A, 1207-17
- Borin, I.A. & Skaf, M.S., 1998, *Chem. Phys. Lett.* 296, 125-30; 1999, Molecular association between water and dimethyl sulfoxide in solution: A molecular dynamics simulation study *J. Chem. Phys.* 110, 6412-20
- Bossis, G., 1982, The dynamical Onsager cavity model and dielectric friction *Mol. Phys.* 46, 475-80
- Bottcher, C.F.J. & Bordewijk, P., 1978, *Theory of Electric polarization*, 78th Edn., Vol. 11, Elsevier, Amsterdam
- Bowman, R.M., Eissenthal, K.B. & Millar, D.P., 1988, Frictional effects on barrier crossing in solution: Comparison with the Kramers' equation *J. Chem. Phys.* 89, 762
- Brito, P. & Bordewijk, P., 1980, Influence of dielectric friction on molecular reorientations *Mol. Phys.* 39, 217-226
- Brocklehurst, B. & Young, R.N., 1995, Rotation of Perylene in Alkanes: Nonhydrodynamic Behavior *J. Phys. Chem.* 99, 40-43
- Canonica, S., Schmid, A. & Wild, U.P., 1985, The rotational diffusion of *p*-terphenyl and *p*-quaterphenyl in non-polar solvents *Chem. Phys. Lett.* 122, 529-34
- Chandler, D., 1974, Translational and rotational diffusion in liquids. I. Translational single-particle correlation functions *J. Chem. Phys.* 60, 3500-07; Translational and rotational diffusion in liquids. II. Orientational single-particle correlation functions *ibid* 3508-12

- Chandra, A. & Bagchi, B., 1991, Molecular theory of solvation and solvation dynamics in a binary dipolar liquid *J. Chem. Phys.* 94, 8367-77
- Chandra, A., 1995, Ion solvation dynamics in binary dipolar liquids: theoretical and simulation results for mixtures of Stockmayer liquids *Chem. Phys. Lett.* 235, 133-39
- Chandrashekhar, K., Inamdar, S.R., Patil, D.C. & Math, N.N., 1993, Orientational relaxation of aminocoumarins by time-resolved dichroism with picosecond pulses *Spectrosc. Lett.* 28, 153-65
- Chapman, C.F., Fee, R.S. & Maroncelli, M., 1990, Solvation dynamics in N-methylamides *J. Phys. Chem.* 94, 4929-35
- Chen, S.H., Katsis, D., Schmid, A.W., Mastrangelo, J.C., Tsutsui, T. & Blanton, T.N., 1999, Circularly polarized light generated by photoexcitation of luminophores in glassy liquid-crystal films *Nature*, 397, 506
- Chuang, J.T. & Eiselthal, K.B., 1971, Studies of effects of hydrogen bonding on orientational relaxation using picosecond light pulses *Chem. Phys. Lett.* 11, 368-70
- Chuang, T.J. & Eiselthal, K.B., 1972, Theory of Fluorescence Depolarization by Anisotropic Rotational Diffusion *J. Chem. Phys.* 57, 5094-97
- Cole, R.H., 1984, in *Molecular Liquids-Dynamics and Interactions*, Eds: A. J. Barnes, W. J. Orville-Thomas and J. Yarwood, pp. 59-100, Reidel, Dordrecht
- Courtney, S.H., Kim, S.K., Canonica, S. & Fleming, G.R., 1986, Rotational diffusion of stilbene in alkane and alcohol solutions *J. Chem. Soc. Faraday Trans.* 82, 2065-72
- Cowie, M.G. & Toporowski, P.M., 1961, Association in the binary liquid system dimethyl sulphoxide - water *Can. J. Chem.* 39, 2240-43
- Dahm, W.J.A., Southerland, K.B. & Buch, K.A. 1991, Direct, high resolution, four-dimensional measurements of the fine scale structure of $Sc \gg 1$ molecular mixing in turbulent flows *Phys Fluids A.3*, 1115-1127
- Day, T.J.F. & Patey, G.N., 1997, Ion solvation dynamics in binary mixtures *J. Chem. Phys.* 106, 2782-91
- De la Torre, J.C., 1983, Biological actions and medical applications of dimethyl sulfoxide *Ann. N.Y. Acad. Sci.* 411, xi-xi
- Debye, P., 1929, *Polar molecules*, Dover Publications, London
- Demchenko, A.P., 2002, The red-edge effects: 30 years of exploration *Luminescence* 17, 19-42
- Dote, J.L., Kivelson, D. & Schwartz, R.N., 1981, A molecular quasi-hydrodynamic free-space model for molecular rotational relaxation in liquids *J. Phys. Chem.* 85, 2169-80
- Dutt, G.B., Doraiswamy, S., Periasamy, N. & Venkataraman, B., 1990, Rotational reorientation dynamics of polar dye molecular probes by picosecond laser spectroscopic technique *J. Chem. Phys.* 93, 8498-8513
- Dutt, G.B. Konitsky, W. & Waldeck, D.H., 1995, Nonradiative relaxation of 2-phenylindene in solution and its implications for isomerization of stilbenes *Chem. Phys. Lett.* 245, 437-40
- Dutt, G.B., Singh, M.K. & Sapre, A.V., 1998, Rotational dynamics of neutral red: Do ionic and neutral solutes experience the same friction? *J. Chem. Phys.* 109, 5994-5603
- Dutt, G.B., Srivatsavoy, V.J.P. & Sapre, A.V., 1999, Rotational dynamics of pyrrolopyrrole derivatives in alcohols: Does solute-solvent hydrogen bonding really hinder molecular rotation? *J. Chem. Phys.* 110, 9623-29
- Dutt, G.B. & Rama Krishna, G., 2000, Temperature-dependent rotational relaxation of nonpolar probes in mono and diols: Size effects versus hydrogen bonding *J. Chem. Phys.* 112, 4676-82

- Dutt, G.B. & Raman, S., 2001, Rotational dynamics of coumarins: An experimental test of dielectric friction theories *J. Chem. Phys.* 114, 6702-13
- Dutt, G.B. & Ghanty, T.K. 2003, Rotational Diffusion of Coumarins in Electrolyte Solutions: The Role of Ion Pairs *J. Phys. Chem B.* 107, 3257-64
- Dutt, G.B. & Ghanty, T.K., 2004, Is molecular rotation really influenced by subtle changes in molecular shape? *J. Chem. Phys.* 121, 3625-31
- Einstein, A., 1906, On the Theory of Brownian Motion (Zur Theorie der Brownschen Bewegung) *Ann. Phys.* 19, 371-81
- Eisenthal, K. B. 1975, Studies of chemical and physical processes with picosecond lasers *Acc. Chem. Res.* 8, 118-24
- Elsaesser, T. & Kaiser, W., 1991, Vibrational and Vibronic Relaxation of Large Polyatomic Molecules in Liquids *Annu. Rev. Phys. Chem.* 42, 83-107
- Evans, G.T., Cole, R.G. & Hoffman, D.K., 1982, A kinetic theory calculation of the orientational correlation time of a rotorlike molecule in a dense fluid of spheres *J. Chem. Phys.* 77, 3209-20
- Evans, G.T. & Evans, D.R., 1984, Kinetic theory of rotational relaxation in liquids: Smooth spherocylinder and rough sphere models *J. Chem. Phys.* 81, 6039-43
- Evans, G.T., 1988, Translational and rotational dynamics of simple dense fluids *J. Chem. Phys.* 88, 5035-41
- Fee, R.S. & Maroncelli, M., 1994, Estimating the time-zero spectrum in time-resolved emission measurements of solvation dynamics *Chem. Phys.* 183, 235-47
- Fee, R.S., Milsom, J.A. & Maroncelli, M., 1991, Inhomogeneous decay kinetics and apparent solvent relaxation at low temperatures *J. Phys. Chem.* 95, 5170-81
- Felderhof, B.U., 1983, Dielectric friction on a polar molecule rotating in a fluid *Mol. Phys.* 48, 1269-81; Dielectric friction on an ion rotating in a fluid *Mol. Phys.* 48, 1283-88
- Fleming, G.R., Morris, J.M. & Robinson, G.W., 1976, Direct observation of rotational diffusion by picosecond spectroscopy *Chem. Phys.* 17, 91-100
- Fleming, G.R., Knight, A.E.W., Morris, J.M., Robbins, R.J. & Robinson, G.W., 1977, Rotational diffusion of the mode-locking dye dodci and its photoisomer *Chem. Phys. Lett.* 49, 1-7
- Fleming, G.R., 1986, *Chemical Applications of Ultrafast Spectroscopy*, Oxford University Press: New York
- Fox, F. & Whittingham, K.P., 1974, Component interactions in aqueous dimethyl sulphoxide *J. Chem. Soc., Faraday Trans.* 75, 1407-12
- Garg, S.K. & Smyth, C.P., 1965, Microwave Absorption and Molecular Structure in Liquids. LXII. The Three Dielectric Dispersion Regions of the Normal Primary Alcohols *J. Phys. Chem.* 69, 1294-1301
- Geirer, A. & Wirtz, K., 1953, Molecular theory of microfriction *Z. Naturforsch.* A8, 532-38
- Gordalla, B.C. & Zeidler, M.D., 1986; Molecular dynamics in the system water-dimethylsulphoxide *Mol. Phys.* 59, 817-28; 1991, NMR proton relaxation and chemical exchange in the system H16 2O/H17 2O-[2H6]dimethylsulphoxide, *Mol. Phys.* 74, 975-84
- Goulay, A.M., 1983, Rotational relaxation of OCS in n-alkanes: Collective and collisional effects *J. Chem. Phys.* 79, 1145-53
- Gustavsson, T., Cassara, L., Marguet, S., Gurzadyan, G., van der Meulen, P., Pommeret, S. & Mialocq, J.-C., 2003, *Photochem. Photobiol. Sci.* 2, 329

- Hambir, S.A., Y. Jiang & Blanchard, G.J., 1993, Ultrafast stimulated emission spectroscopy of perylene in dilute solution: Measurement of ground state vibrational population relaxation *J. Chem. Phys.* 98, 6075-82
- Hartman, R.S., Alavi, D.S. and Waldeck, D.H., 1991, An experimental test of dielectric friction models using the rotational diffusion of aminoanthraquinones *J. Phys. Chem.* 95, 7872-80
- Hartman, R.S., Konitsky, W.M., Waldeck, D.H., Chang, Y.J. & Castner, Jr, E.W., 1997, Probing solute-solvent electrostatic interactions: Rotational diffusion studies of 9,10-disubstituted anthracenes *J. Chem. Phys.* 106, 7920-30
- Heilweil, E.J., Casassa, M.P., Cavanagh, R.R. & Stephenson, J.C., 1986, Population lifetimes of OH($v=1$) and OD($v=1$) stretching vibrations of alcohols and silanols in dilute solution *J. Chem. Phys.* 85, 5004-18
- Heilweil, E.J., R. R. Cavanagh and J. C. Stephenson, 1987, Population relaxation of CO($v = 1$) vibrations in solution phase metal carbonyl complexes *Chem. Phys. Lett.* 134, 181-88
- Heilweil, E.J., Casassa, M.P., Cavanagh, R.R. & Stephenson, J.C. 1989, Picosecond Vibrational Energy Transfer Studies of Surface Adsorbates *Annu. Rev. Phys. Chem.* 40, 143-71
- Heilweil, E.J., Cavanagh, R.R. & Stephenson, J.C., 1989, CO($v=1$) population lifetimes of metal-carbonyl cluster compounds in dilute CHCl₃ solution *J. Chem. Phys.* 89, 230-39
- Hornig, M.-L., Gardecki, J.A. & Maroncelli, M., 1997, Rotational Dynamics of Coumarin 153: Time-Dependent Friction, Dielectric Friction, and Other Nonhydrodynamic Effects *J. Phys. Chem. A* 101, 1030-47
- Hu, C.M. & Zwanzig, R., 1974, Rotational friction coefficients for spheroids with the slipping boundary condition *J. Chem. Phys.* 60, 4354-57
- Hubbard, J.B. & Onsager, L., 1977, Dielectric dispersion and dielectric friction in electrolyte solutions. I. *J. Chem. Phys.* 67, 4850-57
- Hubbard, J.B., 1978, Friction on a rotating dipole *J. Chem. Phys.* 69, 1007-09
- Hubbard, J.B. & Wolynes, P.G., 1978, Dielectric friction and molecular reorientation *J. Chem. Phys.* 69, 998-1006
- Huppert, D., Ittah, V. & E. Kosower, 1989, Static and dynamic electrolyte effects on excited-state behavior *Chem. Phys. Lett.* 159, 267-75
- Huppert, D., Ittah, V. & Kosower, E., 1990, Static and dynamic electrolyte effects on excited large dipole solvation: high dielectric constant solvents *Chem. Phys. Lett.* 173, 496-502
- Hynes, J.T., 1986, Chemical reaction rates and solvent friction *J. Stat. Phys.* 42, 149-168 and references therein
- Imeshev, G. & Khundkar, L.R., 1995, Inhomogeneous rotational dynamics of a rodlike probe in 1-propanol *J. Chem. Phys.* 103, 8322-28
- Inamdar, S.R., Chandrashekhara, K., Patil, D.C., Math, N.N. & Savadatti, M.I., 1995, Picosecond time-resolved laser emission of coumarin 102: Solvent relaxation, *Pramana, J. Phys.*, 45, 279-290
- Inamdar, S.R., Nadaf, Y.F. & Mulimani, B.G., 2003, Ground and excited state dipole moments of exalite 404 and exalite 417 uv laser dyes determined from solvatochromic shift of absorption and fluorescence spectra *J. Mol. Struct. (Theochem)*, 624, 47-51
- Inamdar, S.R., Mannekutla, J.R., Mulimani, B.G. & Savadatti, M.I., 2006, Rotational dynamics of nonpolar laser dyes *Chem. Phys. Lett.* 429, 141- 46
- Inamdar, S.R., Gayathri, B.R. & Mannekutla, J.R., 2009, Rotational diffusion of coumarins in aqueous DMSO *J. Fluoresc.* 19, 693-703

- Ito, N., Kajimoto, O. & K. Hara, 2000, Picosecond time-resolved fluorescence depolarization of *p*-terphenyl at high pressures *Chem. Phys. Lett.* 318, 118-24
- Jarzeba, W., Walker, G.C., Johnson, A.E. & Barbara, P.F., 1991, Nonexponential solvation dynamics of simple liquids and mixtures *Chem. Phys.* 152, 57-68
- Jiang, J. & Blanchard, G.J., 1994, Rotational Diffusion Dynamics of Perylene in n-Alkanes. Observation of a Solvent Length-Dependent Change of Boundary Condition *J. Phys. Chem.* 98, 6436-40; Vibrational Population Relaxation of Perylene in n-Alkanes. The Role of Solvent Local Structure in Long-Range Vibrational Energy Transfer, *ibid*, 9411-16; Vibrational Population Relaxation of Perylene in Its Ground and Excited Electronic States *ibid*, 9417-21
- Jiang Y. & Blanchard, G.J., 1995, Vibrational Population and Orientational Relaxation Dynamics of 1-Methylperylene in n-Alkanes. The Effective Range of Dipolar Energy Relaxation in Solution *J. Phys. Chem.* 99, 7904-12
- Kaatze, K., Pottel, R. & Schaefer, M., 1989, Dielectric spectrum of dimethyl sulfoxide/water mixtures as a function of composition *J. Phys. Chem.* 93, 5623-27
- Karasso, P.S. & Mungal, M.G., 1997, PLIF measurements in aqueous flows using the Nd:YAG laser *Exp Fluids* 23, 382-387
- Kawski, A., Kuklinski, B. & Bojarski, P., 2005, Dipole moment of aniline in the excited S₁ state from thermochromic effect on electronic spectra *Chem. Phys. Lett.* 415, 251-55
- Kirov, A.S., Hurlbut, C., Dempsey, J.F., Shrinivas, S.B., Epstein, J.W., Binns, W.R., Dowkontt, P.F. & Williamson, J.F., 1999, Radiation Therapy Physics: Towards two-dimensional brachytherapy dosimetry using plastic scintillator: New highly efficient water equivalent plastic scintillator materials *Med. Phys.* 26, 1515-23
- Koochesfahani, M.M. & Dimotakis, P.E., 1986, Mixing and chemical reactions in a turbulent liquid mixing layer *J Fluid Mech.* 170, 83-112
- Krishnamurthy, M., Khan, K.K. & Doraiswamy, S., 1993, Rotational diffusion kinetics of polar solutes in hexamethylphosphoramide-water systems *J. Chem. Phys.* 98, 8640-47
- Kubinyi, M., Grofcsik, A., Kárpáti, T. & Jones, W.J., 2006, Rotational reorientation dynamics of ionic dye solutes in polar solvents with the application of a general model for the solvation shell *Chem. Phys.* 322, 247-54
- Kumar, P.V. & Maroncelli, M., 2000, The non-separability of "dielectric" and "mechanical" friction in molecular systems: A simulation study *J. Chem. Phys.* 112, 5370-81
- Lakowicz, J.R., 1983, *Principles of Fluorescence Spectroscopy*, Plenum Press, New York
- Lakowicz, J. R., 2006, *Principles of fluorescence spectroscopy*, Springer: New York
- Laitinen, E., Korppi-Tommola, J. & Linnanto, J., 1997, Dielectric friction effects on rotational reorientation of three cyanine dyes in n-alcohol solutions *J.Chem.Phys.* 107, 7601-12
- Laria, D. & Skaf, M., 1999, Solvation response of polar liquid mixtures: Water-dimethylsulfoxide *J. Chem. Phys.* 111, 300-09
- Levitus, M, Negri, R.M. & Aramenda, P.F., 1995, Rotational Relaxation of Carbocyanines. Comparative Study with the Isomerization Dynamics *J. Phys. Chem.* 99, 14231-39
- Lingle Jr. R., Xu, X., Yu, S.C., Zhu, H. & Hopkins, J.B., 1990, Ultrafast investigation of condensed phase chemical reaction dynamics using transient vibrational spectroscopy: Geminate recombination, vibrational energy relaxation, and electronic decay of the iodine A' excited state *J. Chem. Phys.* 93, 5667-80
- Luzar, A. & Chandler, D., 1993, Structure and hydrogen bond dynamics of water-dimethyl sulfoxide mixtures by computer simulations *J. Chem. Phys.*, 98, 8160-73

- Madden, P. & Kivelson, D., 1982, Dielectric friction and molecular orientation *J. Phys. Chem.* 86, 4244-56
- Mannektla, J.R., Ramamurthy, P., Mulimani, B.G. & S.R. Inamdar, 2007, Rotational dynamics of UVITEX-OB in alkanes, alcohols and binary mixtures *Chem. Phys.*, 340, 149-57
- Mannektla, J.R., S. R. Inamdar, B. G. Mulimani and M. I. Savadatti, 2010, Rotational diffusion of coumarins: A Dielectric friction study *J Fluoresc.* 20, 797-808
- Maroncelli, M., 1993, The dynamics of solvation in polar liquids. *J. Molec. Liq.* 57, 1-37
- Maroncelli, M. & Fleming, G.R., 1987, Picosecond solvation dynamics of coumarin 153: The importance of molecular aspects of solvation *J. Chem. Phys.* 86, 6221-39
- Martin, D. & Hanthall, H., 1975, *Dimethyl Sulfoxide*; John Wiley & Sons, Inc., New York
- McCarthy, P.K. & Blanchard, G.J., 1995, Vibrational Population Relaxation of Tetracene in n-Alkanes. Evidence for Short-Range Molecular Alignment *J. Phys. Chem.* 99, 17748-53
- McCarthy, P.K. and Blanchard, G.J., 1996, Solvent Methyl Group Density Dependence of Vibrational Population Relaxation in 1-Methylperylene: Evidence for Short-Range Organization in Branched Alkanes *J. Phys. Chem.* 100, 5182-87
- McMahon, D.R.A., 1980, Dielectric friction and polar molecule rotational relaxation *J. Chem. Phys.* 72, 2411-24
- Millar, D.P., Shah, R. & Zewail, A.H., 1979, Picosecond saturation spectroscopy of cresyl violet: rotational diffusion by a "sticking" boundary condition in the liquid phase *Chem. Phys. Lett.* 66, 435-40
- Moog, R.S., Ediger, M.D., Boxer, S. G. & Fayer, M.D., 1982, Viscosity dependence of the rotational reorientation of rhodamine B in mono- and polyalcohols. Picosecond transient grating experiments *J. Phys. Chem.* 86, 4694-4700
- Nadaf, Y.F., Mulimani, B.G., Gopal, M. & Inamdar, S.R., 2004, Ground and excited state dipole moments of some exalite dyes from solvatochromic method using solvent polarity parameters *J. Mol. Struct. (Theochem)* 678, 177-81
- Nee, T.W. & Zwanzig, R., 1970, Theory of Dielectric Relaxation in Polar Liquids *J. Chem. Phys.* 52, 6353-63
- Nowak, E., 1983, Dielectric friction and energy dissipation in polar fluids *J. Chem. Phys.* 79, 976-81
- Packer, K.J. & Tomlinson, D.J., 1971, Nuclear spin relaxation and self-diffusion in the binary system, dimethyl sulphoxide (DMSO)+ water *J. Chem. Soc., Trans. Faraday* 67, 1302-14
- Pal, A. & Daas, G., 2000, Excess molar volumes and viscosities of binary mixtures tetraethylene glycol dimethyl ether (tetraglyme) with chloroalkanes at 298.15K *J. Mol. Liq.* 84, 327-37
- Papazyan, A. & Maroncelli, M., 1995, Rotational dielectric friction and dipole solvation: Tests of theory based on simulations of simple model solutions *J. Chem. Phys.* 102, 2888-2919
- Perrin, F., 1936, Mouvement brownien d'un ellipsoïde (II). Rotation libre et depolarisation des fluorescences. Translation et diffusion de molécules ellipsoïdales, *J. Phys. Radium* 7, 1-11
- Phillips, L.A., Webb, S.P. & Clark, J.H., 1985, High-pressure studies of rotational reorientation dynamics: The role of dielectric friction *J. Chem. Phys.* 83, 5810-21
- Porter, G., Sadkowski, P.J. & Tredwell, C.J., 1977, Picosecond rotational diffusion in kinetic and steady state fluorescence spectroscopy *Chem. Phys. Lett.* 49, 416-20

- Qunfang, L. & Yu-Chun, H., 1999, Correlation of viscosity of binary liquid mixtures. *Fluid Phase Equilibria* 154, 153-163 and references therein
- Rice, S.A. & Kenney-Wallace, G.A., 1980, Time-resolved fluorescence depolarization studies of rotational relaxation in viscous media *Chem. Phys.* 47, 161-70
- Rider, K.L. & Fixman, M., 1972, Angular Relaxation of the Symmetrical Top. II. The Rough Sphere *J. Chem. Phys.* 57, 2548-59
- Roy, M. & Doraiswamy, S., 1993, Rotational dynamics of nonpolar solutes in different solvents: Comparative evaluation of the hydrodynamic and quasihydrodynamic models *J. Chem. Phys.* 98, 3213-23
- Sanders, M.J. & Wirth, M.J., 1983, Evidence for solvation structural dependence of rotational diffusion anisotropy *Chem. Phys. Lett.* 101, 361-66
- Safford, G.J., Schaffer, P.C., Leung, P.S., Doebbler, G.F., Brady G.W. & Lyden, E.F.X. 1969, Neutron Inelastic Scattering and X-Ray Studies of Aqueous Solutions of Dimethylsulphoxide and Dimethylsulphone *J. Chem. Phys.* 50, 2140-59
- Shapiro, S.L. & Winn, K.R., 1980, Picosecond time-resolved spectral shifts in emission: dynamics of excited state interactions in coumarin 102 *Chem. Phys. Lett.* 71, 440-44
- Sceats, M.G. & Dawes, J.M., 1985, On the viscoelastic properties of n-alkane liquids *J. Chem. Phys.* 83, 1298-1304
- Selvaraju, C. & Ramamurthy, P., 2004, Excited-State Behavior and Photoionization of 1,8-Acrindinedione Dyes in Micelles *Chem. Eur. J.* 10, 2253-62
- Shank, C.V. & Ippen, E.P., 1975, Anisotropic absorption saturation with picosecond pulses *Appl. Phys. Lett.* 26, 62-63
- Singh, M.K., 2000, Rotational Relaxation of Neutral Red in Alkanes: Effect of Solvent Size on Probe Rotation *Photochem. Photobiol.* 72, 438-43
- Skaf, M. & Ladanyi, B.M., 1996, Molecular Dynamics Simulation of Solvation Dynamics in Methanol-Water Mixtures *J. Phys. Chem.* 100, 18258-68
- Soper, A.K. & Luzar, A., 1996, Orientation of Water Molecules around Small Polar and Nonpolar Groups in Solution: A Neutron Diffraction and Computer Simulation Study *J. Phys. Chem.* 100, 1357-67
- Soper, A.K. & Luzar, A., 1992, A neutron diffraction study of dimethyl sulphoxide-water mixtures *J. Chem. Phys.* 97, 1320-31
- Spears, K.G. and L. E. Cramer, 1978, Rotational diffusion in aprotic and protic solvents *Chem. Phys.* 30, 1-8
- Srivastava, A. & Doraiswamy, S., 1995, Rotational diffusion of rose bengal *J. Chem. Phys.* 103, 6197-6205
- Steiner, R.F., 1991, in *Topics in Fluorescence Spectroscopy*, Vol. 2., J. R. Lakowicz (Ed.), Plenum Press, New York
- Stokes, G., 1856, *Trans. Cambridge Philos. Soc.* 9, 5
- Templeton, E. F. G., Quitevis, E. L. & Kenney-Wallace, G. A., 1985, Picosecond reorientational dynamics of resorufin: correlations of dynamics and liquid structure *J. Phys. Chem.* 89, 3238-43
- Templeton, E.F.G. & Kenney-Wallace, G.A., 1986, Picosecond laser spectroscopic study of orientational dynamics of probe molecules in the dimethyl sulfoxide-water system *J. Phys. Chem.* 90, 2896-2900
- Titulaer, U.M. & Deutch, J.M., 1974, Analysis of conflicting theories of dielectric relaxation *J. Chem. Phys.* 60, 1502-13

- Tjai, T.H., Bordewijk P. & Bottcher, C.F.J., 1974, On the notion of dielectric friction in the theory of dielectric relaxation *Adv. Mol. Relax. Proc.* 6, 19-28
- Tokuhiro, T., Menafrá L. & Szmant, H.H., 1974, Contribution of relaxation and chemical shift results to the elucidation of the structure of the water-DMSO liquid system *J. Chem. Phys.* 61, 2275-82
- Traube, J., 1886, *Ber. Dtsch Chem. Ges.* B.19, 871-892
- Vaisman, I.I. & Berkowitz, M.L., 1992, Local structural order and molecular associations in water-DMSO mixtures. Molecular dynamics study *J. Am. Chem. Soc.* 114, 7889-96
- van der Zwan, G. & Hynes, J.T., 1985, Time-dependent fluorescence solvent shifts, dielectric friction, and nonequilibrium solvation in polar solvents *J. Phys. Chem.* 90, 4181-88
- Valenta, J., Dian, J., Hála, J., Gilliot, P. & Lévy, R., 1999 Persistent spectral hole-burning and hole-filling in CuBr semiconductor nanocrystals *J. Chem. Phys.* 111, 9398-403
- Voigt, W., 2005, Sulforhodamine B assay and chemosensitivity *Methods Mol. Med.* 110, 39-48
- von Jena, A. & Lessing, H. E., 1979a, Rotational-diffusion anomalies in dye solutions from transient-dichroism experiments *Chem. Phys.* 40, 245-56
- von Jena, A. & Lessing, H. E., 1979b, Rotational Diffusion of Prolate and Oblate Molecules from Absorption Relaxation *Ber. Bunsen-Ges. Phys. Chem.* 83, 181-91
- von Jena, A. & Lessing, H.E., 1981, Rotational diffusion of dyes in solvents of low viscosity from transient-dichroism experiments *Chem. Phys. Lett.* 78, 187-93
- Wagener, A. & Richert, R., 1991, Solvation dynamics versus inhomogeneity of decay rates as the origin of spectral shifts in supercooled liquids *Chem. Phys. Lett.* 176, 329-34
- Waldeck, D.H. and G. R. Fleming, 1981, Influence of viscosity and temperature on rotational reorientation. Anisotropic absorption studies of 3,3'-diethyloxadicarbocyanine iodide *J. Phys. Chem.* 85, 2614-17
- Waldeck, D.H., Lotshaw, W.T., McDonald, D.B. & Fleming, G.R., 1982, Ultraviolet picosecond pump-probe spectroscopy with a synchronously pumped dye laser. Rotational diffusion of diphenyl butadiene *Chem. Phys. Lett.* 88, 297-300
- Widom, B., 1960, Rotational Relaxation of Rough Spheres, *J. Chem. Phys.* 32, 913-23
- Wiemers, K. & Kauffman, J. F., 2000, Dielectric Friction and Rotational Diffusion of Hydrogen Bonding Solutes *J. Phys. Chem. A* 104, 451-57
- Williams, A.M., Jiang, Y. & Ben-Amotz, D., 1994, Molecular reorientation dynamics and microscopic friction in liquids *Chem. Phys.* 180, 119-29
- Yip, R.W., Wen, Y. X. & Szabo, A.G., 1993, Decay associated fluorescence spectra of coumarin 1 and coumarin 102: evidence for a two-state solvation kinetics in organic solvents *J. Phys. Chem.* 97, 10458-62
- Yoshimori, A., Day, T.J.F. & Patey, G.N., Theory of ion solvation dynamics in mixed dipolar solvents *J. Chem. Phys.* 109, 3222-31
- Youngren, G.K. & Acrivos, A., 1975, Rotational friction coefficients for ellipsoids and chemical molecules with the slip boundary condition *J. Chem. Phys.* 63, 3846-48
- Zwanzig, R. & Harrison, A.K., 1985, Modifications of the Stokes-Einstein formula *J. Chem. Phys.* 83, 5861- 62

Flow Instabilities in Mechanically Agitated Stirred Vessels

Chiara Galletti and Elisabetta Brunazzi
*Department of Chemical Engineering,
Industrial Chemistry and Materials Science, University of Pisa
Italy*

1. Introduction

A detailed knowledge of the hydrodynamics of stirred vessels may help improving the design of these devices, which is particularly important because stirred vessels are among the most widely used equipment in the process industry.

In the last two decades there was a change of perspective concerning stirred vessels. Previous studies were focused on the derivation of correlations able to provide global performance indicators (e.g. impeller flow number, power number and mixing time) depending on geometric and operational parameters. But recently the attention has been focused on the detailed characterization of the flow field and turbulence inside stirred vessels (Galletti et al., 2004a), as only such knowledge is thought to improve strongly the optimization of stirred vessel design.

The hydrodynamics of stirred vessels has resulted to be strongly three dimensional, and characterised by different temporal and spatial scales which are important for the mixing at different levels, i.e. micro-mixing and macro-mixing.

According to Tatterson (1991) the hydrodynamics of a mechanically agitated vessel can be divided at least into three flow systems:

- *impeller flows* including discharge flows, trailing vortices behind the blades, etc.;
- *wall flows* including impinging jets generated from the impeller, boundary layers, shed vortices generated from the baffles, etc.;
- *bulk tank flows* such as large recirculation zones.

Trailing vortices originating behind the impeller blades have been extensively studied for a large variety of impellers. For instance for a Rushton turbine (RT) they appear as a pair, behind the lower and the upper sides of the impeller blade, and provide a source of turbulence that can improve mixing. Assirelli et al. (2005) have shown how micro-mixing efficiency can be enhanced when a feeding pipe stationary with the impeller is used to release the fed reactant in the region of maximum dissipation rate behind the trailing vortices. Such trailing vortices may also play a crucial role in determining gas accumulation behind impeller blades in gas-liquid applications, thus affecting pumping and power dissipation capacity of the impeller.

But in the last decade lots of investigations have pointed out that there are other important vortices affecting the hydrodynamics of stirred vessels. In particular it was found that the flow inside stirred vessels is not steady but characterised by different flow instabilities,

which can influence the flow motion in different manners. Their knowledge and comprehension is still far from complete, however the mixing optimisation and safe operation of the stirred vessel should take into account such flow variations.

The present chapter aims at summarizing and discussing flow instabilities in mechanically agitated stirred vessels trying to highlight findings from our research as well as from other relevant works in literature. The topic is extremely wide as flow instabilities have been detected with different investigation techniques (both experimental and numerical) and analysis tools, in different stirred vessel/impeller configurations.

Thus investigation techniques and related analysis for the flow instability detection will be firstly overviewed. Then a possible classification of flow instabilities will be proposed and relevant studies in literature will be discussed. Finally, examples of findings on different flow instabilities and their effects on the mixing process will be shown.

2. Investigation techniques

Researchers have employed a large variety of investigation techniques for the detection of flow instabilities. As such techniques should allow identifying flow instabilities, they should be able to detect a change of the flow field (or other relevant variables) with time. Moreover a good time resolution is required to allow an accurate signal processing. Regarding this point, actually flow instabilities in stirred vessels are generally low frequencies phenomena as their frequency is much smaller than the impeller rotational frequency N ; so, effectively, the needed temporal resolution is not so high. Anyway the acquisition frequency should at least fulfil the Nyquist criterion.

The graph of Fig. 1a summarises the main techniques, classified as experimental and numerical, employed so far for the investigation of flow instabilities. A brief description of the techniques will be given in the following text in order to highlight the peculiarities of their applications to stirred vessels.

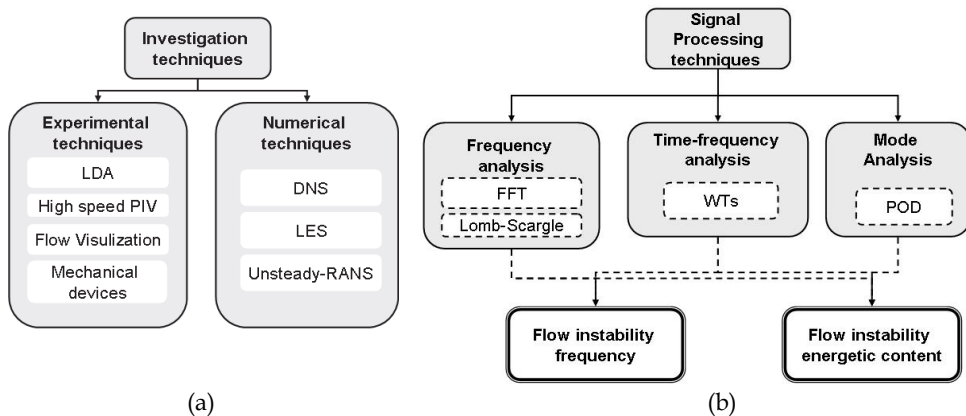


Fig. 1. Overview of investigation (a) and analysis (b) techniques for flow instability characterization in stirred vessels.

2.1 Experimental techniques

Laser Doppler anemometry (LDA) is one of the mostly used experimental technique for flow instability detection. LDA is an optical non-intrusive technique for the measurement of

the fluid velocity. It is based on the Doppler shift of the light scattered from a 'seeding' particle, which is chosen to be nearly neutrally buoyant and to efficiently scatter light. LDA does not need any calibration and resolves unambiguously the direction of the velocity. Moreover it provides high spatial and temporal resolutions. These are very important for flow instability detection. In addition, more than one laser Doppler anemometer can be combined to perform multi-component measurements. The application of LDA to cylindrical stirred vessels requires some arrangement in order to minimize refraction effects at the tank walls, so often the cylindrical vessel is placed inside a square trough.

Particle Image Velocimetry (PIV) is also an optical technique which allows the velocity of a fluid to be simultaneously measured throughout a region illuminated by a two-dimensional light sheet, thus enabling the instantaneous measurements of two velocity components. However recently the use of a stereoscopic approach allows all three velocity components to be recorded. So far the temporal resolution of PIV measurements has been limited because the update rate of velocity measurements, governed by the camera frame rate and the laser pulse rate, was too low. Thus PIV was not suited for the investigation of flow instabilities. However recently, high-frame rate PIV systems have been developed allowing flow measurements with very high update rates (more than 10 kHz); thus its use for the analysis of flow instabilities in stirred vessels has been explored by some investigators. Similarly to LDA, also PIV requires the fluid and vessel walls to be transparent as well as actions to minimize refraction effects at the tank curvature.

Different flow visualization techniques have also been used to help clarifying the mechanism of flow instabilities. Such flow visualization techniques may simply consist of tracing the fluid with particles and recording with a camera a region of the flow illuminated by a laser sheet. More sophisticated techniques are able of providing also concentration distribution: for example Laser Induced Fluorescence, LIF, uses a fluorescent marker and a camera (equipped with a filter corresponding to the wave of fluorescence) which detects the fluorescence levels in the liquid.

In addition to such optical instruments, different mechanical devices have been used in literature for the detection of flow instabilities. Such devices are based on the measurements of the effect of flow instabilities on some variables. Bruha et al. (1995) employed a "tornadometer", that is a device which allows measuring the temporal variation of the force acting on a small target placed into the flow where instabilities are thought to occur. Paglianti et al. (2006) proved that flow instabilities in stirred vessels could be detected by pressure transducers positioned at the tank walls. The pressure transducers provided time series of pressure with a temporal resolution suited for the flow instability detection. Such a technique is particularly interesting as it is well suited for industrial applications. Haam et al. (1992) identified flow instabilities from the measurement of heat flux and temperature at the walls through heat flux sensors and thermocouples. Hasal et al. (2004) measured the tangential force acting on the baffles as a function of time by means of mechanical devices. Also power number measurements (as for instance through strain gauge techniques) have been found to give an indication of flow instabilities related to change in the circulation loop (Distelhoff et al., 1995).

2.2 Numerical techniques

Numerical models have also been used for the investigation of flow instabilities in stirred vessels, especially because of the increasing role of Computational Fluid Dynamics (CFD). Logically, since the not steady nature of such instabilities, transient calculation techniques

have to be employed. These may be classified in: Unsteady Reynolds-averaged Navier-Stokes equations (URANS), Large Eddy Simulation (LES) and Direct Numerical Simulation (DNS)

URANS employs the usual Reynolds decomposition, leading to the Reynolds-averaged Navier-Stokes equations, but with the transient (unsteady) term retained. Subsequently the dependent variables are not only a function of the space coordinates, but also a function of time. Moreover, part of the turbulence is modelled and part resolved. URANS have been applied to study stirred vessels by Torr e et al. (2007) who found indications on the presence of flow instabilities from their computations; however their approach was not able to identify precessional flow instabilities.

LES consists of a filtering operation, so that the Navier-Stokes are averaged over the part of the energy spectrum which is not computed, that is over the smaller scales. Since the remaining large-scale turbulent fluctuations are directly resolved, LES is well suited for capturing flow instabilities in stirred vessels, although it is very computationally expensive. This has been shown for both single-phase (for example Roussinova et al., 2003, Hartmann et al., 2004, Nurtono et al. 2009) and multi-phase (Hartmann et al., 2006) flows.

DNS consists on the full resolution of the turbulent flow field. The technique has been applied by Lavezzo et al. (2009) to an unbaffled stirred vessel with $Re = 1686$ providing evidence of flow instabilities.

3. Analysis techniques

The above experimental or modelling investigations have to be analysed with suited tools in order to get information on flow instabilities. These consist mainly of signal processing techniques, which are applied to raw data, such as LDA recordings of the instantaneous velocity, in order to gain information on the characteristics of flow instabilities.

Two kinds of information have been extracted so far:

- frequency of the flow instabilities as often they appear as periodic phenomena;
- relevance of flow instabilities on the flow motion.

Among the techniques which have been employed in literature for the characterization of flow instabilities in stirred vessels, there are (see Fig. 1b):

- frequency analysis techniques (the Fast Fourier Transforms and the Lomb-Scargle periodogram method);
- time-frequency analysis techniques (Wavelet Transforms);
- principal component analysis (Proper Orthogonal Decomposition).

Whereas the first two techniques have been largely used for the determination of the flow instability frequency, the latter has been used to evaluate the impact of flow instabilities on the motion through the analysis of the most energetic modes of the flow.

3.1 Frequency analysis

The Fast Fourier Transform (FFT) decomposes a signal in the time domain into sines and cosines, i.e. complex exponentials, in order to evaluate its frequency content. Specifically the FFT was developed by Cooley & Tukey (1965) to calculate the Fourier Transform of a K samples series with $O(K \log_2 K)$ operations. Thus FFT is a powerful tool with low computational demand, but it can be performed only over data evenly distributed in time. In case of LDA recordings, these should be resampled and the original raw time series replaced with series uniform in time. As for the resampling techniques, simple methods like

the "Nearest Neighbour" or the "Sample and Hold" should be preferred over complex methods (e.g. "Linear Interpolation", "Spline Interpolation"), because the latter bias the variance of the signal. It should be noticed that the resampled series contains complete information about the spectral components up to the Nyquist critical frequency $f_c=1/2\Delta$ where Δ is the sampling interval. At frequencies larger than the Nyquist frequency the information on the spectral components is aliased.

The Lomb-Scargle Periodogram (LSP) method (Lomb, 1976, Scargle, 1982) performs directly on unevenly sampled data. It allows analysing frequency components larger than the Nyquist critical frequency: this is possible because in irregularly spaced series there are a few data spaced much closer than the average sampling rate, removing ambiguity from any aliasing. The method is much more computational expensive than FFTs, requiring $O(10^2K^2)$ operations.

It is worthwhile discussing the suitability of the analysis techniques described above for the investigation of flow instabilities and what are the main parameters to be considered. Flow instabilities are low frequency phenomena, therefore we are interested in the low frequency region of the frequency spectrum. The lowest frequency which can be resolved with both the FFT and Lomb-Scargle method is inversely related to the acquisition time; hence longer sampling times yield better frequency resolutions. This explains the long observations made for flow instabilities detection in stirred vessels. In our works on flow instabilities we have used typically LDA recordings at least 800 s long. In other words the sampling time should be long enough to cover a few flow instabilities cycles. As the time span covered by a series is proportional to the number of samples, the application of the LSP to long series requires strong computational effort.

A benchmark between the two methods is provided in Galletti (2005) and shown in Fig. 2.

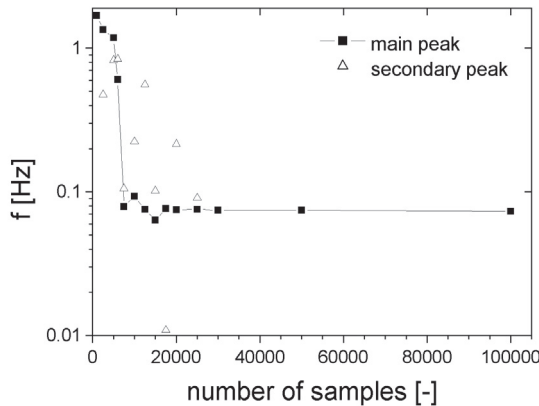


Fig. 2. Frequency of the main and the secondary peak in the low frequency region of the spectrum calculated with the Lomb-Scargle method as a function of the number of samples. $RT, D/T = 0.33, C/T = 0.5, Re = 27,000$. Galletti (2005).

The solid squares show the frequency f of the main peak identified in the spectrum calculated with the LSP as function of the number of samples used for the analysis. It can be observed that f is scattered for low numbers of samples, and it approaches asymptotically the value of $f = 0.073$ Hz (the same of the FFT analysis over the whole acquisition time of 800 s with 644,000

samples) as the number of samples increases. The empty triangles indicate the presence of further low frequency peaks. The main fact to be aware of is that low time intervals conceal the flow instabilities by covering only a portion of the fluctuations.

3.2 Time-frequency analysis

Both FFT and LSP inform how much of each frequency component exists in the signal, but they do not tell us when in time these frequencies occur in the signal. For transient flows it may be of interest the time localisation of the spectral component. The Wavelet Transform (WT) is capable of providing the time and frequency information simultaneously, hence it gives a time-frequency representation of the signal (Daubechies, 1990, Torrence and Compo, 1998). The WT breaks the signal into its "Wavelets", that are functions obtained from the scaling and the shifting of the "mother Wavelet" ψ . The WT has been proposed for the investigation of stirred vessels by Galletti et al. (2003) and subsequently applied by Roy et al. (2010).

3.3 Proper orthogonal decomposition

POD is a linear procedure, based on temporal and spatial correlation analysis, which allows to decompose a set of signals into a modal base, with the first mode being the most energetic (related to large-scale structures thus trailing vortices and flow instabilities) and the last being the least energetic (smaller scales of turbulence). It was first applied for MI characterisation by Hasal et al. (2004) and latterly by Ducci & Yianneskis (2007). An in-depth explanation of the methodology is given in Berkooz et al. (1993).

4. Classification of flow instabilities

A possible classification of flow instabilities in stirred vessels is reported in Fig. 3. The graph is not aimed at imposing a classification of flow instabilities, however it suggests a way of interpretation which may be regarded as a first effort to comprehend all possible instabilities.

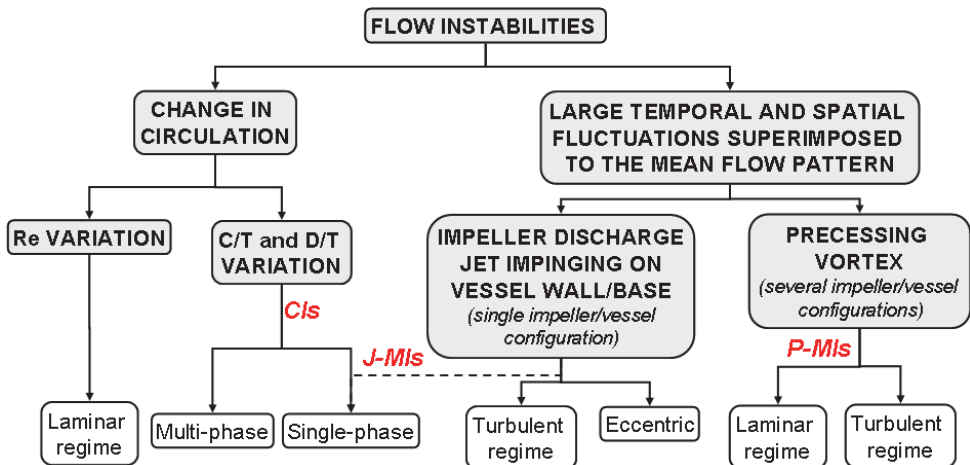


Fig. 3. Possible classification of flow instabilities in stirred vessels.

4.1 Change in circulation pattern

A first kind of flow instability (see left-hand side of the diagram of Fig. 3) manifests as a real change in the circulation pattern inside the tank. Two main sources of such a change have been identified: a variation of the Reynolds number (Re) or a variation of the impeller/vessel geometrical configuration.

In relation to the former source, Nouri & Whitelaw (1990) reported a transition due to Re variations in the flow pattern induced by a 60° PBT with $D = T/3$ set at $C = T/3$ in a vessel of $T = 0.144$ m. For non-Newtonian fluids a flow pattern transition from a radial to an axial flow was observed as the Re was increased up to $Re = 4,800$. For Newtonian fluids the authors observed that the flow pattern transition occurred at about $Re = 650$. This value was also confirmed by the power number measurements through strain-gauges carried out by Distelhoff et al. (1995). Similar investigations on such transition may be found in the works of Hockey (1990) and Hockey & Nouri (1996).

Schäfer et al. (1998) observed by means of flow visualisation the flow discharged by a 45° PBT to be directed axially at higher Re and radially at lower Re . The flow stream direction was unstable, varying from radial to axial, for $Re = 490$ - 510 . A similar flow transition was also indicated by Bakker et al. (1997) who predicted with CFD techniques the flow pattern generated from a 4-bladed 45° PBT of diameter $D = T/3$ and set at $C = T/3$ inside a tank of $T = 0.3$ m. The regime was laminar, the Reynolds number being varied between 40 and 1,200. The impeller discharge stream was directed radially for low Re numbers, however for Re larger than 400 the flow became more axial, impinging on the vessel base rather than on the walls.

A second source of instabilities, manifesting as a flow pattern change, is associated with variations of the impeller/vessel geometrical configuration, which means either variations of the distance of the impeller from the vessel bottom (C/T) or variation of the impeller diameter (D/T) or a combination of both variations.

This kind of instabilities were firstly noticed by Nienow (1968) who observed a dependency on the clearance of the impeller rotational speed required to suspend the particles (N_{js}) in a solid-liquid vessel equipped with a $D = 0.35T$ RT. He observed that for $C < T/6$ the pattern was different (the discharge stream was directed downwards towards the vessel corners) from the typical radial flow pattern, providing low N_{js} values. Baldi et al. (1978) also observed a decrease of the N_{js} with the impeller off-bottom clearance for a 8-bladed turbine. Conti et al. (1981) found a sudden decrease of the power consumption associated with the change in the circulation pattern when lowering the impeller clearance of a 8-bladed turbine. The aforementioned authors concluded that the equation given by Zwietering (1958) for the calculation of the N_{js} should be corrected in order to take into account the dependency on C/T .

The dependency of the power number on the impeller off-bottom clearance was also observed by Tiljander & Theliander (1993), who measured the power consumption of two PBT of different sizes, i.e. $D = T/3$ and $D = T/2$, and a high flow impeller of $D = T/2$. The visual observation of the flow pattern revealed that at the transition point between the axial and the radial flow patterns, the circulation inside the vessel appears chaotic.

Ibrahim & Nienow (1996) investigated the efficiency of different impellers, i.e. a RT, a PBT pumping either upwards or downwards, a Chemineer HE3 and a Lightnin A310 hydrofoil pumping downwards and a Ekato Intermig agitator, for solids suspension. For the RT, the aforementioned authors observed a sudden decrease of both the impeller speed and the mean dissipation rate required to just suspend the particles as the clearance was decreased

from $C = T/3$ down to $C = T/6$ for the impeller having $D = T/3$; such a clearance corresponded to the transition from the radial flow pattern to the axial.

Subsequently, a strong influence of the clearance on the suspension of particles was confirmed also by Myers et al. (1996) for three axial impellers. If the clearance was sufficiently high the discharge flow impinged on the vessel wall rather than the base, leading to a secondary circulation loop which was directed radially inward at the vessel base and returned upwards to the impeller at the centre of the vessel. Such a reversed flow occurred for $C > 0.45T$ for a PBT of diameter $D = 0.41T$ and for $C > 0.25T$ for a straight-blade turbine of the same diameter, whereas only for very high clearances ($C > 0.95T$) for a high efficiency Chemineer impeller having the same diameter.

Bakker et al. (1998) reported that the flow pattern generated by either a PBT or a three-blade high efficiency impeller depended on C/T and D/T , influencing the suspension of the particles.

Armenante & Nagamine (1998) determined the N_{js} and the power consumption of four impellers set at low off-bottom clearances, typically $C < T/4$. For radial impellers, i.e. a RT and a flat blade turbine, they observed that the clearance at which the change in the flow pattern from a radial to an axial type occurred was a function of both impeller type and size, i.e. D/T . In particular the flow pattern changed at lower C/T for larger impellers. This was in contrast with previous works (see for example Conti et al., 1981) which reported a clearance of transition independent on D/T . For instance Armenante & Nagamine (1998) found the flow pattern transition to occur at $0.16 < C/T < 0.19$ for a Rushton turbine with a diameter $D = 0.217T$ and at $0.13 < C/T < 0.16$ for a $D = 0.348T$ RT. For the flat blade turbine the clearances at which the transition took places were higher, being of 0.22-0.24 and 0.19-0.21 for the two impeller sizes $D = 0.217T$ and $D = 0.348T$, respectively.

Sharma & Shaikh (2003) provided measurements of both N_{js} and power consumption of solids suspension in stirred tanks equipped with 45° PBT with 4 and 6 blades. They plotted the critical speed of suspension N_{js} as a function of C/T distinguishing three regions, according to the manner the critical suspension speed varied with the distance of the impeller from the vessel base. As the impellers were operating very close to the vessel base, the N_{js} was observed to be constant with C/T (first region); then for higher clearances N_{js} increased with C/T because the energy available for suspension decreased when increasing the distance of the impeller from the vessel base (second region), and finally (third region) for high clearances the N_{js} increased with C/T with a slope higher than that of the second region. The onset of third region corresponded to the clearance at which the flow pattern changed from the axial to the radial flow type. In addition the aforementioned authors observed that as the flow pattern changed the particles were alternatively collected at the tank base in broad streaks and then suddenly dispersed with a certain periodicity. They concluded that a kind of instabilities occurred and speculated that maybe the PBT behaved successively as a radial and axial flow impellers.

The influence of C on the flow pattern has been intensively studied also for single-phase flow in stirred tanks. Yianneskis et al. (1987) showed that the impeller off-bottom clearance affects the inclination of the impeller stream of a Rushton turbine of diameter $D = T/3$. In particular the discharge angle varied from 7.5° with respect to the horizontal plane for $C = T/4$ down to 2.5° for $C = T/2$.

Jaworski et al. (1991) measured with LDA the flow patterns of a 6-bladed 45° PBT having a diameter $D = T/3$ for two impeller clearances, $C = T/4$ and $C = T/2$. For the lower impeller clearance, the impeller stream impinged on the vessel base and generated an intensive radial

circulation from the vessel axis towards the walls. For the higher clearance the impeller stream turned upwards before reaching the base of the vessel, generating also a reverse flow directed radially from the walls towards the vessel axis at the base of the vessel.

Kresta & Wood (1993) measured the mean flow field of a vessel stirred with a 4-bladed 45° PBT for two impeller sizes, i.e. $D = T/3$ and $D = T/2$, and varying the impeller clearance systematically from $T/20$ up to $T/2$. They observed that the circulation pattern underwent a transition at $C/D = 0.6$, and for the larger impeller ($D = T/2$) such a transition was accompanied by a deflection of the inclination of the discharge stream toward the horizontal.

Ibrahim & Nienow (1995) measured the power number of different impellers for a wide range of Reynolds number, i.e. $40 < Re < 50,000$, in Newtonian fluids. For a $D = T/3$ RT they observed that the power numbers with clearances of $C = T/3$ and $C = T/4$ was the same for all Re ; however for $C = T/6$ the discharge flow was axial rather than radial and the associated power number was considerably lower (by about 25%) for all the range of Re investigated. For a $D = T/2$ RT a radial discharge flow was still observed at $C = T/6$ for all Re except for those with the highest viscosity (1 Pa·s).

Rutherford et al. (1996a) investigated the flow pattern generated by a dual Rushton impeller and observed different circulation patterns depending on the impeller clearance of the lower impeller and the separations between the two impellers, observing three stable flow patterns: "parallel flow", "merging flow" and "diverging flow" patterns.

Mao et al. (1997) measured with LDA the flow pattern generated from various PBT of different sizes in the range of $0.32 < D/T < 0.6$ and number of blades varying from 2 to 6 in a stirred vessel in turbulent regime ($Re > 20,000$). They used two impeller off-bottom clearances, $C = T/3$ and $C = T/2$, observing a secondary circulation loop with the higher clearance.

Montante et al. (1999) provided a detailed investigation of the flow field generated by $D = T/3$ RT placed at different off-bottom clearances varying from $C = 0.12T$ to $C = 0.33T$. They found that the conventional radial flow pattern (termed "double-loop" pattern) occurred for $C = 0.20T$, but it was replaced by an axial flow pattern (termed "single loop" pattern) as the clearance was decreased to $C = 0.15T$. A reduction of the power number from 4.80-4.85 for $C/T = 0.25-0.33$ down to 3.80 as the clearance was decreased to $C/T = 0.12-0.15$ was reported, so that the power consumption was reduced by about 30% as the flow underwent a transition from the double- to the single-loop pattern.

4.1.1 Clearance instabilities (CIs)

Galletti et al. (2003, 2005a, 2005b) studied the flow pattern transition for a $D = T/3$ RT and identified a kind of flow instabilities, which will be denoted as CIs (clearance instability). The authors found that the flow pattern transition (single- to double-loop pattern) occurred for $C/T = 0.17-0.2$, thus within an interval of clearances of about $0.03T$. Such C interval was dependent on the fluid properties, lower clearances being observed for more viscous fluids. At clearances of flow pattern transition the velocity time series indicated flow pattern instabilities as periods of double-loop regime, single-loop regime and "transitional" state that followed each other. When the flow underwent a change from one type of circulation to another, the transitional state was always present and separated in time the single- from the double-loop flow regime. Nevertheless, a flow pattern could change firstly into the transitional state and afterwards revert to the original flow regime, without changing the type of circulation. The occurrence of the three flow regimes was shown to be random, and

their lifetimes could be significant, often of the order of few minutes. The time duration of the three flow regimes depended on the impeller clearance, higher clearances promoting the double-loop regime. Moreover the time duration of the three flow regimes depended on the impeller rotational speed, higher impeller rotational speeds promoting the double-loop regime.

An example of flow pattern transition is shown in the LDA time series of Fig. 4a which indicated different regimes, that can be attributed to the double-loop, transitional and single-loop patterns. The most surprising finding was that within the transitional state an instability was manifested as a periodic fluctuation of the flow between the double and the single-loop regimes, characterised by a well-defined frequency f . Such frequency was linearly dependent on the impeller speed according to $f' = f/N = 0.12$.

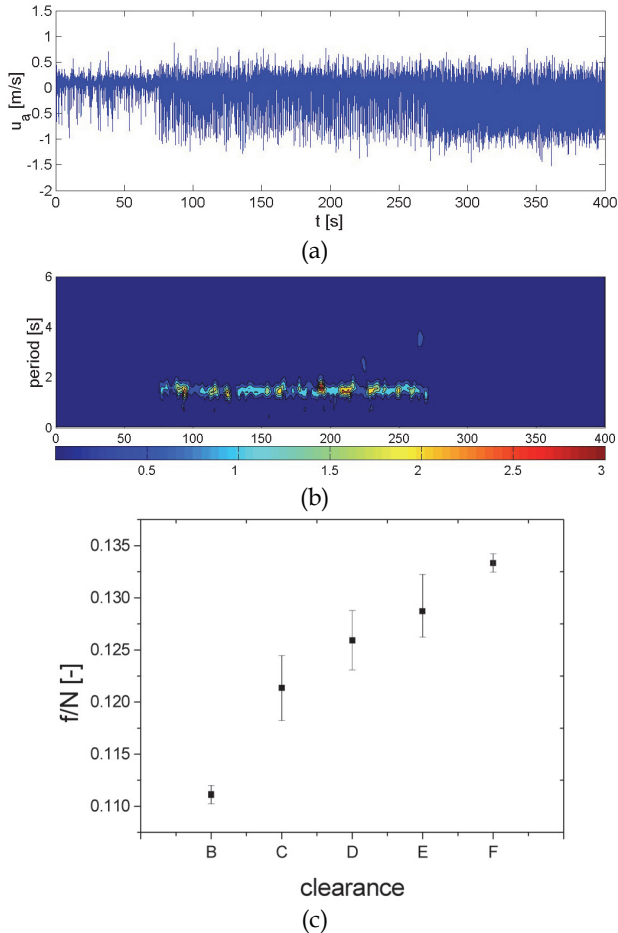


Fig. 4. Wavelet power analysis of axial velocity data: (a) time series; (b) Wavelet power spectrum; (c) dependence of frequency on impeller clearance (B is the highest, F the lowest clearance). Taken from Galletti et al. (2003).

Therefore the flow pattern transition which occurs for a RT when changing the impeller position is governed by two types of instability. The first one manifests as a random succession of double-loop regime, single-loop regime and transitional state over large time intervals. The second one is the instability encountered during the transitional state, characterised by a well-defined periodicity of the order of few seconds.

The exact nature of the clearance-related instabilities is not fully understood, but it is not likely to be related to the turbulence content of the flows, as the phenomenon is characterised by a single frequency even for the lowest Re range studied with the most viscous fluid, for which Re is around 5,200 and the corresponding flows should be mostly laminar. Some evidences as the increase of f' with lowering C/T (or increasing the impeller stream mean velocity by reducing the impeller blade thickness to diameter ratio t_b/D) may confirm that it is the interaction between the impeller discharge stream and the vessel base/walls to play a major role in the formation of such instability.

4.2 Macro-instabilities

Another kind of instability (see the right-hand side of the diagram of Fig. 3) manifests itself as large temporal and spatial variations of the flow superimposed to the mean flow patterns, thus such flow instabilities are called "macro-instabilities". On the basis of results achieved during our work and from other works in literature it was chosen to divide this kind of flow instability into two subgroups, because we think that there were two different underlying mechanisms driving such instabilities.

4.2.1 Precessional macro-instabilities (P-MIs)

The first subgroup comprehends flow instabilities which seem to be associated with a vortex moving about the shaft. The first evidence of this vortex was provided by Yianneskis et al. (1987) who noticed that the vortex motion produced large temporal and spatial fluctuations superimposed on the mean flow pattern. A similar vortex was also observed by Haam et al. (1992) cited earlier.

Precessional MIs were investigated by Nikiforaki et al. (2003), who used two different impellers (RT and PBT) having the same diameter $D = T/3$ for $Re > 20,000$. The frequency of the macro-instabilities was found to be linearly related to the impeller speed with $f' = f/N = 0.015-0.020$, independently on impeller clearance and design. In a more recent work Nikiforaki et al. (2004) studied the effect of operating parameters on macro-instabilities. In particular they observed the presence of other frequencies varying from $f' = 0.04-0.15$, as the Reynolds number was reduced.

Hartmann et al. (2004) performed a LES simulation of the turbulent flow ($Re = 20,000$ and $30,000$) in a vessel agitated with a $D = T/3$ RT set at $C = T/2$. The geometries of the vessel and impeller were identical to those used for the experiments of Nikiforaki et al. (2003). The simulation indicated the presence of a vortical structure moving round the vessel centreline in the same direction as the impeller. Such structure was observed both below and above the impeller (axial locations of $z/T = 0.12$ and $z/T = 0.88$ were monitored), however the two vortices were moving with a mutual phase difference. The frequency associated with the vortices was calculated to be $f' = 0.0255$, therefore slightly higher than the $0.015-0.02$ reported by Nikiforaki et al. (2003). The authors concluded that this may encourage an improvement of the sub-scale grid and/or the numerical settings.

Importantly, the presence of a phase shift between the precessing vortices below and above the impeller was confirmed by the LDA experiments of Micheletti & Yianneskis (2004).

These authors used a cross-correlation method between data taken in the upper and lower parts of the vessel, and estimated a phase difference between the vortices in the two locations of approximately 180° .

The presence of the precessing vortex was assessed also in a solid-liquid system by the LES simulation of Derksen (2003).

Hasal et al. (2004) investigated flow instabilities with a Rushton turbine and a pitched blade turbine, both of $D = T/3$ with the proper orthogonal decomposition analysis. They confirmed the presence of the precessing vortex, however they found different f' values depending on the Re . In particular f' values akin to those of Nikiforaki et al. (2003) were observed for high Re , whereas higher values, i.e. $f' = 0.06$ - 0.09 were found for low Re .

Galletti et al. (2004b) investigated macro-instabilities stemming from the precessional motion of a vortex about the shaft for different impellers, geometries and flow regimes. The authors confirmed that the P-MI frequency is linearly dependent on the impeller rotational speed, however they indicated that different values of the proportionality constant between MI frequency and impeller rotational speed were found for the laminar and turbulent flow regimes, indicating different behaviour of MIs depending on the flow Re (see Fig. 5a). For intermediate (transitional) regions two characteristic frequencies were observed, confirming the presence of two phenomena. In particular in the laminar flow region P-MIs occurred with a non-dimensional frequency f' about 7-8 times greater than that observed for the turbulent region. This was proved for two RTs ($D/T = 0.33$ and 0.41 RT) as well as for a $D/T = 0.46$ PBT. Thus the impeller design does not affect P-MIs for both laminar and turbulent regions. The impeller off-bottom clearance does not affect significantly the P-MI frequency for the Rushton turbine and the pitched blade turbine (see for instance Fig. 5b). However differences in the regions where P-MIs are stronger may be found, as for instance lower impeller clearances originated weaker P-MIs near the liquid surface.

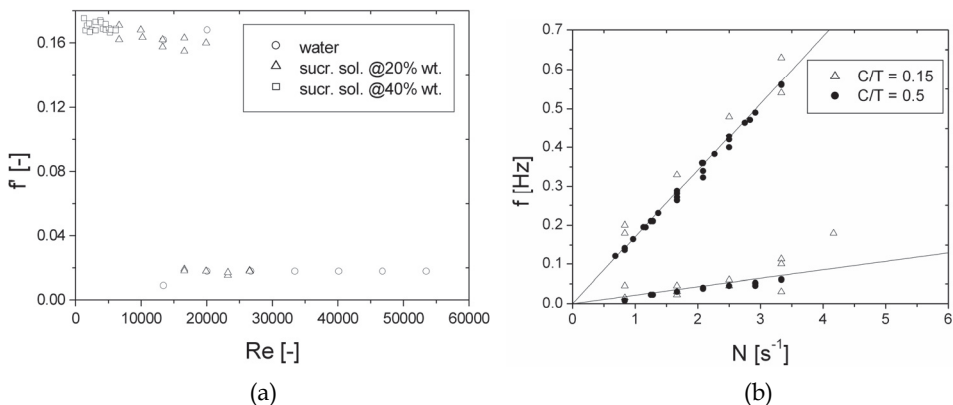


Fig. 5. (a) Non-dimensional macro-instability frequency as a function of the impeller Reynolds number. RT, $D/T = 0.41$, $C/T = 0.5$. (b) Macro-instability frequency as a function of the impeller rotational speed for different clearances. RT, $D/T = 0.41$. Galletti (2005).

Importantly, Galletti et al. (2004b) found that the MI frequency is affected by the impeller diameter. For the laminar regime a linear dependence of the non-dimensional macro-instability frequency on the impeller to tank diameter ratio was established:

$$f' = a \cdot \left(\frac{D}{T} \right) + b \quad (1)$$

A deep clarification of precessional MIs triggering mechanism in both laminar and turbulent regimes was provided by Ducci & Yianneskis (2007) for a $D = T/3$ RT placed at $C = T/2$. The authors used 2-point LDA and a 2-D PIV with a 13kHz camera. Through a vortex identification and tracking technique, the authors showed that P-MIs stem from a precessional vortex moving around the vessel axis with $f' = 0.0174$ for the turbulent regime. In laminar regime the frequency corresponding to a precession period was higher, of about $f' = 0.13$. The slight differences on the frequencies with the work of Galletti et al. (2004b) may be imputed to the different spectral analysis. For instance in the vortex tracking method the frequency was evaluated from the time needed to a vortex to complete 360° , whereas the FFT analysis of Galletti et al. (2004b) covered several MI cycles. But importantly Ducci & Yianneskis (2007) showed that in the laminar regime the vortex precessional motion was much closer to the axis than in turbulent regime (for which the vortex tends to stay rather far from the axis). In addition to that the authors showed a change in the flow pattern between the laminar and turbulent conditions, which affects the precessional MI frequency.

In a later work Ducci et al. (2008) investigated also the transitional regime showing the interaction between the two frequency instabilities ($f' = 0.1$ and $f' = 0.02$ of the laminar and turbulent regime, respectively). They found that the two simultaneous instabilities are associated to two different types of perturbation of the main mean flow: an off-centering instability that results in a precession of the vortex core centre with a $f' = 0.02$ and a stretching instability that induces an elongation of the vortex core along a direction that is rotating with $f' = 0.1$ around the vessel axis. For higher Re, the authors identified an interaction between the perturbations of the mean vortex core associated to $f' = 0.02$ off-centering structures and a $f' = 0.04$ stretching/squeezing instability.

A deep investigation of precessional MIs was also carried out by the same group (Doulgerakis et al., 2011) for an axial impeller (PBT) with $D = T/2$ placed at $C = T/2$ with $Re = 28,000$. The MI frequency distribution across the vessel indicated the presence of many frequencies reported before in literature. However the two dominant frequencies were $f' = 0.1$ and $f' = 0.2$. The POD analysis showed that the first mode can be seen as a radial off-center perturbation of the mean flow that results in a precession of the vortex core around the impeller axis with $f' = 0.1$. The second mode is an instability which stretches/squeezes the vortex core in a direction that is rotating with $f' = 0.1$. Importantly also for the PBT, the higher frequency was exactly double than the lower one as for the RT case. This would be also in agreement with many spectral analysis reported in Galletti (2005) which showed the presence of an additional peak frequency about the double of the P-MI frequency.

Kilander et al. (2006) identified through LSP analysis of LDA data frequencies with $f' = 0.025$ for the turbulent regime (thus in fully agreement with the work by Hartman et al., 2006) in a vessel agitated by a $D = T/3$ RT.

Lately, many other computational methods confirmed also the presence of precessional MIs. Nurtono et al. (2009) obtained from LES simulations a frequency $f' = 0.0125$ for a $D=T/3$ RT placed at $C = T/2$ for $Re = 40,000$.

The DNS simulations of Lavezzo et al. (2009) for an unbaffled vessel equipped with a 8-blade paddle impeller indicated the presence of a spiralling vortex with $f' = 0.162$ for $Re = 1686$. The application of Eq. [1] developed by Galletti et al. (2004b) to the above case would

give a higher frequency $f' = 0.24$, however it should be pointed out that the equation was developed for baffled configurations.

4.2.2 Jet impingement macro-instabilities (J-MIs)

Other evidence of large temporal and spatial variations of the flow macro-instabilities have been reported in the last decade and they not always seem to be related to a precessional vortex.

Bruha et al. (1995) used a device called "tornadometer" to estimate the flow instabilities induced by a 6-bladed 45° PBT of $D = 0.3T$ set at $C = 0.35T$. The target was axially located above the impeller at $z/C = 1.2$ and 1.4 and at radial distance equal to the impeller radius. The aforementioned authors found a linear relation between the instability frequency f and the impeller rotational speed N , according to $f = -0.040 N + 0.50$. In a later work (Bruha et al., 1996) the same authors reported a linear dependence of the MI frequency on N ($f' = 0.043-0.0048$) for Re values above 5,000. No flow-instabilities were noted for $Re < 200$ and an increase in f' was observed for $200 < Re < 5,000$.

Montes et al. (1997) studied with LDA the flow instabilities in the vicinity of the impeller, induced by a 6-bladed 45° PBT of $D = 0.33T$ set at $C = 0.35T$ and observed different values for f' depending on the Reynolds number: $f' = 0.09$ for $Re = 1140$ and $f' = 0.0575$ for $Re = 75,000$. They suggested that macro-instabilities appear as the switching between one loop and two or many loops, taking place between the impeller and the free surface and they are able to alter this surface. This leads to different flow patterns in front of the baffles or between two adjacent baffles. The mechanism is complex and three-dimensional but the large vortices clearly appear in a regular way, with a well defined frequency. Hasal et al. (2000) used the proper orthogonal decomposition to analyse LDA data observed for a PBT and found a $f' = 0.087$ for $Re = 750$ and $Re = 1,200$, and a value of 0.057 for $Re = 75,000$. In addition they noticed that the fraction of the total kinetic energy carried by the flow instabilities (relative magnitude) varied with the location inside the stirred vessel, they being stronger in the central and wall regions below the impeller but weaker in the discharge flow from the impeller.

Myers et al. (1997) used digital PIV to investigate flow instabilities in a stirred tank equipped with two different impellers: a 4-bladed 45° PBT of $D = 0.35T$ and a Chemineer HE-3 of $D = 0.39T$. The PBT was set at $C = 0.46T$ and $0.33T$, whereas the Chemineer HE-3 was set at $C = 0.33T$. The Reynolds number was ranging between 6,190 and 13,100. For the higher clearance, i.e. $C = 0.46T$, the PBT showed flow fluctuations of about 40 s for an impeller rotational speed $N = 60$ rpm, therefore $f' = 0.025$. The same impeller set at the lower clearance, $C = 0.33T$, showed more stable flow fields, with not very clear peaks in the low frequency region of the spectra, at around $f' = 0.07-0.011$. The Chemineer HE-3 impeller showed fluctuations of much longer periods than those of the PBT.

Roussinova et al. (2000, 2001) performed LDA measurements in two tank sizes ($T = 0.24$ and 1.22 m), using various impeller types, impeller sizes, clearances, number of baffles (2 and 4) and working fluids in fully turbulent regime. For a 45° PBT of $D = T/2$ they observed a macro-instability non-dimensional frequency of $f' = 0.186$. Such frequency was coherent as the PBT was set at $C = 0.25T$, and such a configuration was called "resonant" geometry, whereas a broad low frequency band was observed for different clearances. The same authors performed also a LES of the vessel stirred by a PBT and confirmed the above non dimensional frequency value. In a later work Roussinova et al. (2003) identified three possible mechanisms triggering the above flow instabilities: the impingement of the jet-like

impeller stream on either the vessel walls or bottom, converging radial flow at the vessel bottom from the baffles and shedding of trailing vortices from the impeller blades. For the resonant geometry, the first mechanism coincided with the impingement of the discharge stream on the vessel corner, generating pressure waves reflected back towards the impeller. The impingement jet frequency was approached with a dimensional analysis based on the Strouhal number. We will denote such flow instabilities as jet impingement instabilities (J-MIs). In a later investigation Roussinova et al. (2004) extended the analysis to different axial impellers. In such work the authors used the LSP method for the spectral analysis.

Paglianti et al. (2006) analysed literature data on MIs as well as comprehensive data obtained from measurements of wall pressure time series, and develop a simple model (based on a flow number) for predicting the MI frequency due to impinging jets (J-MI).

Also Galletti et al. (2005b) investigated flow instability for a PBT and detected a $f' = 0.187$ (thus akin the Roussinova et al., 2003). Such instabilities were found to prevail in the region close to the impeller (just above it and below it in the discharged direction).

Nurtono et al. (2009) found a similar frequency $f' = 0.185$ from LES modelling of a $D=T/3$ PBT placed at $C = T/2$ at $Re = 40,000$.

The LES results on different impellers (DT, PBTD60, PBTD45, PBTD30 and HF) from Murthy & Joshi (2008) showed the presence of J-MIs with $f' = 0.13-0.2$. Moreover they observed a frequency $f' = 0.04-0.07$, which lies in between the precessional and the jet instability; such frequency was attributed to the interaction of precessing vortex instability with either the mean flow or jet/circulation instabilities.

Roy et al. (2010) investigated through both experimental (PIV) and numerical (LES) techniques, the flow induced by a PBT impeller at different Reynolds numbers ($Re = 44,000$, $88,000$ and $132,000$). They found low frequency flow instabilities with frequencies of about $f' = 0.2$. They could not resolve lower frequencies because of the short observation (due to computational cost of LES models) of their simulations. The authors showed changes in the three-dimensional flow pattern during different phases of the macro-instability cycle. They concluded that one mechanism driving flow instabilities was the interaction of the impeller jet stream with the tank baffles. The flow-instabilities were also observed to affect the dynamics of trailing edge vortices.

More recently Galletti & Brunazzi (2008) investigated through LDA and flow visualisation the flow features of an unbaffled vessel stirred by an eccentrically positioned Rushton turbine. The flow field evidenced two main vortices: one departing from above the impeller towards the top of the vessel and one originating from the impeller blades towards the vessel bottom. The former vortex was observed to dominate all vessel motion, leading to a strong circumferential flow around it.

The frequency analysis of LDA data indicated the presence of well defined peaks in the frequency spectra of velocity recordings. In particular three characteristic frequencies were observed in different locations across the vessel: $f' = 0.105$, 0.155 and 0.94 . Specifically, the $f' = 0.155$ and 0.105 frequencies were related to the periodic movements of the upper and lower vortices' axis, respectively, which are also well visible from flow visualization experiments (see Fig. 6a and Fig. 6b, respectively). The $f' = 0.94$ frequency was explained by considering the vortical structure – shaft interaction, which occurs in eccentric configuration and leads to vortex shedding phenomena. The authors provided an interpretation based on the Strouhal number.

In a later work (Galletti et al., 2009) the effect of blade thickness t_b was investigated, finding that for a thicker impeller ($t_b/D = 0.05$) the frequency of the upper vortex movement was

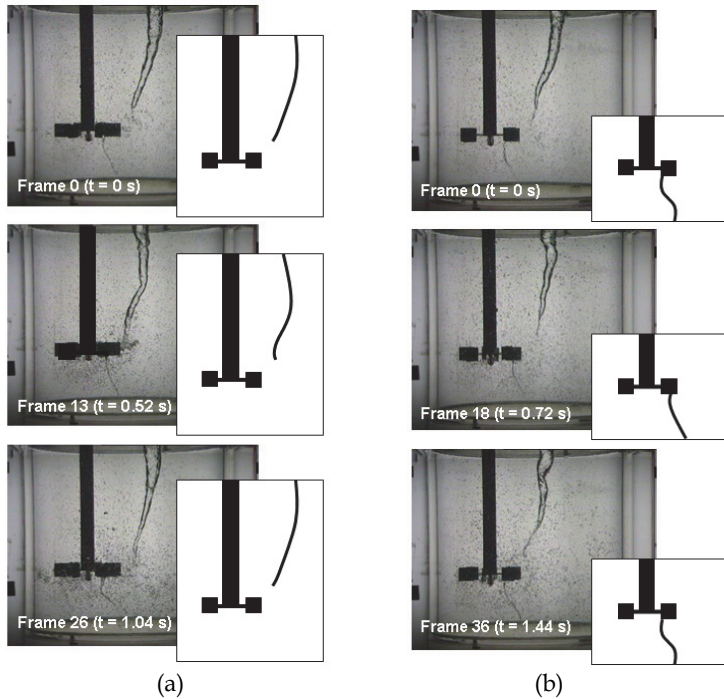


Fig. 6. Frames taken from flow visualisation experiments with sketches at $N = 400$ rpm (from Galletti & Brunazzi, 2008). Unbaffled vessel, RT, eccentricity $E/T = 0.21$, $C/T = 0.33$, $D/T = 0.33$, $t_b/D = 0.01$.

lower, i.e. $f' = 0.143$ than for the thinner one ($f' = 0.155$ for $t_b/D = 0.01$). The origin of the above instabilities is not fully clarified. The frequencies are one order of magnitude higher than the P-MIs frequencies. The values of f' found are more similar to frequencies typical of J-MIs. Actually the eccentric position of the shaft and the consequently reduced distance between the impeller blade tip and the vessel boundaries, is likely to enhance the strength of the impeller discharged stream – wall interaction. In such a case, resulting flow instabilities will show a frequency which is expected to increase with increasing the velocity of the impeller discharged stream (see the flow-instability analysis in terms of pumping number by Paglianti et al., 2006, and/or peak velocity by Roussinova et al., 2003), thus with decreasing the blade thickness (Rutherford et al., 1996b).

5. Effect of flow instabilities

Flow instabilities may affect mixing operations in mechanically agitated vessels in different manners.

Since the energetic content of J-MIs may be significant, they can exert strong forces on the solid surfaces immersed in the stirred tank, i.e. the shaft, baffles, heating and cooling coils, etc. (Hasal et al., 2004). These forces may cause mechanical failure of the equipment and therefore they should be taken into account in the design of industrial-scale stirred vessels.

However except for such drawbacks, MIs may be beneficially utilized to improve mixing, provided that their phenomenology is well understood.

It has been proved than flow instabilities in stirred vessels can have a direct effect on overall parameters, which are fundamental for the design practice. The different studies on the change of circulation pattern (mentioned in section 4.1) have evidenced that such change is accompanied by a change of power number. In case of solid suspension, changes in the N_{js} is observed. Thus the knowledge of parameters affecting the circulation change may help optimising solid-liquid operations. Moreover, the heat flux studies of Haam et al. (1992) showed that precessional MIs may induce a variation of the heat transfer coefficient up to 68% near the surface.

Macro-instabilities may have beneficial implications for mixing process operation and efficiency as such flow motions can enhance mixing through mean-flow variations. For example, the associated low-frequency, high-amplitude oscillatory motions in regions of low turbulence in a vessel, have the capability of transporting substances fed to a mixing process over relatively long distances, as demonstrated by Larsson et al. (1996). These authors measured glucose concentration in a cultivation of *Saccharomyces Cerevisiae* and observed fluctuations of glucose concentration which were more pronounced as the feed was located in a stagnant area rather than in the well-mixed impeller area. Therefore flow instabilities may help destroying segregated zones inside the tank. Ducci & Yianneskis (2007) showed that the mixing time could be reduced even by 30% if the tracer is inserted at or near the MI vortex core. Houcine et al. (1999) reported with LIF a feedstream jet intermittency in a continuous stirred tank reactor due to MIs. Recently also Galletti et al. (2009) observed from decolourisation experiments in an eccentrically agitated unbaffled vessel that the flow instability oscillations help the transport of reactants far away if these are fed in correspondence of the vortices shown in Fig. 6.

Subsequently MIs have similar effects to those reported for laminar mixing in stirred tanks by Murakami et al. (1980), who observed that additional raising and lowering of a rotating impeller produced unsteady mean flow motions that either destroyed segregated regions or prevented them from forming, and could produce desired mixing times with energy savings of up to 90% in comparison to normal impeller operation. Later Nomura et al. (1997) observed that the reversal of the rotational direction of an impeller could also decrease mixing times as the additional raising or lowering of the impeller.

For a solid-liquid system (solid volume fractions up to 3.6%) agitated by a $D = T/3$ RT in turbulent regime ($Re = 100,000$ and $150,000$) Derksen (2003) showed that the precessing vortex may help the resuspension of particles lying on the bottom of the tank, thus enhancing the mass transfer.

Guillard et al. (2000a) carried out LIF experiments on a stirred tank equipped with two RT observing large time scale oscillations of the concentration, induced by an interaction between the flows from the impeller and a baffle. They argued that circulation times can be altered when the flow direction changes, the turbulence levels measured with stationary probes can be significantly broadened and thus can provide an erroneous interpretation of the true levels of turbulence in a tank, and mixing in otherwise quiescent regions can be significantly enhanced due to the presence of flow variations (Guillard et al., 2000b). Knowledge of true levels of turbulence is needed for the optimum design of micro-mixing operations (as in cases of chemical reactions). Also Nikiforaki et al. (2003) observed that P-MIs can broaden real turbulence levels up to 25% for a PBT.

Actually the problem is rather complex as Galletti et al. (2005b) as well other investigators (e.g. Ducci & Yianneskis, 2007, Roussinova et al., 2004) showed that different kinds of macro-instabilities may be present simultaneously in stirred vessels. For instance Galletti et al. (2005b) studied simultaneously with 2-point LDA the combined effect of precessional MIs and flow instabilities stemming from impeller clearance variations (CIs) in different regions of a vessel stirred with a RT. Table 1 summarizes the flow instability characteristics. The authors removed from the total energetic content of a LDA signal, the contribution of blade passage, P-MIs and CIs, evaluating the real turbulent energy. They found that the occurrence and energetic content of P-MIs and CIs depend on both measurement location and flow regime. In particular, near the vessel surface P-MIs are stronger, with energetic contents that reach 50% of the turbulent energy, meaning that they can broaden turbulence levels up to 22%. In the vicinity of the impeller the energetic content of the P-MIs is smaller, whereas CIs contribute strongly to the fluid motion with average energetic contents of about 21% of the turbulent energy for the transitional regime. Results are summarised in Table 2.

Rushton turbine		
Flow instability	CIs	P-MIs
How they manifest	change in circulation	large temporal and spatial fluctuation superimposed on the mean flow pattern
Impeller/vessel configuration	specific configuration ($C/T = 0.17-0.2$ with $D/T = 0.33$)	several configurations (different impeller types $D/T, C/T$)
Temporal appearance	intermittently present	continuously present
Non-dimensional frequency	$f' = 0.13$	$f' = 0.015$
Possible origin	interaction between impeller discharged stream and vessel base/walls	precessional motion of a vortex about the shaft

Table 1. Characteristics of CIs and MIs investigated with the Rushton turbine. Galletti (2005).

	Near the surface		Impeller region	
	E_{MI}/E_{TUR}	E_{CI}/E_{TUR}	E_{MI}/E_{TUR}	E_{CI}/E_{TUR}
double-loop	up to 50%	~4%	~5%	~3%
transitional state	up to 25%	up to 25%	negligible	~ 21%
single-loop	~ 12 %	~ 3%	negligible	negligible

Table 2. Relative energy of MIs and CIs with respect to the turbulent energy for the double-, single- and transitional patterns. Galletti (2005).

A similar analysis was carried out for a PBT: in this case the P-MIs and J-MIs were studied (see Table 3). The authors found the presence of both instabilities, indicating that the occurrence and magnitude, i.e. energetic content, of MIs and JIs vary substantially from one region of a vessel to another. P-MIs affect strongly the region of the vessel near the surface and around the shaft, whereas the bulk of the vessel is dominated more by J-MIs generated from the interaction of the impeller discharged stream and the vessel boundaries. J-MIs are also stronger upstream of the baffles and near the walls, which may confirm their origin. Table 4 reports the energetic contribution of the different macro-instabilities at different axial location in the vessel.

Pitched Blade Turbine		
Flow instability	J-MIs	P-MIs
How they manifest	large temporal and spatial fluctuation superimposed on the mean flow pattern	large temporal and spatial fluctuation superimposed on the mean flow pattern
Impeller/vessel configuration	specific configuration ($C/T = 0.25$ with $D/T = 0.5$)	several configurations (different impeller types $D/T, C/T$)
Temporal appearance	continuously present	continuously present
Non-dimensional frequency	$f' = 0.186$	$f' = 0.015$
Possible origin	interaction between impeller discharged stream and vessel base/walls	precessional motion of a vortex about the shaft

Table 3. Characteristics of JIs and MIs investigated with the pitched blade turbine. Galletti (2005).

Location of the horizontal plane	P-MIs		J-MIs	
	Max E_{MI}/E_{TUR}	Average E_{MI}/E_{TUR}	Max E_{JI}/E_{TUR}	Average E_{JI}/E_{TUR}
$z/T = 0.05$	1.9%	5.7%	2.7%	6.3%
$z/T = 0.6$	6.2%	12%	10.1%	20%
$z/T = 0.93$	14.6%	39.8%	1.7%	7%

Table 4. Average and maximum relative energy of MIs and JIs with respect to the turbulent energy, for different horizontal planes. Galletti (2005).

For the eccentric agitation in an unbaffled vessel, Galletti & Brunazzi (2008) showed that the flow instability related to the movement of the two vortices described in section 4.2.2. was very strong, as its energetic contribution was evaluated to be as high as 52% of the turbulent kinetic energy. Also the shedding vortices from flow-shaft interaction considerably affected the turbulence levels (energetic contribution of 82%), hence they should be considered in evaluating the micro-mixing scales.

6. References

- Armenante, P.M. & Nagamine, E.U. (1998). Effect of low off-bottom impeller clearance on the minimum agitation speed for complete suspension of solids in stirred tanks. *Chemical Engineering Science*, Vol. 53, pp. 1757-1775.
- Assirelli, M.; Bujalski, W.; Eaglesham, A. & Nienow, A.W. (2005). Intensifying micromixing in a semi-batch reactor using a Rushton turbine. *Chemical Engineering Science*, Vol. 60, pp.2333-2339.
- Bakker, A.; Fasano, J.B. & Myers, K.J. (1998). Effects of flow pattern on the solid distribution in a stirred tank, Published in "The online CFM Book" at <http://www.bakker.org.cfm>.
- Bakker, A.; La Roche, R.D.; Wang, M. & Calabrese, R. (1997). Sliding mesh simulation of laminar flow in stirred reactors. *Transactions IChemE, Chemical Engineering Research and Design*, Vol. 75, pp. 42-44.
- Baldi, G.; Conti, R. & Alaria, E. (1978). Predicting the minimum suspension speeds in agitated tanks. *Chemical Engineering Science*, Vol. 33, pp. 21-25.
- Berkooz, G.; Holmes, P. & Lumley, J.L. (1993). The proper orthogonal decomposition in the analysis of turbulent flows. *Annual Review of Fluid Mechanics*, Vol. 25, pp. 539-576.
- Bruha, O.; Fort, I. & Smolka, P. (1995). Phenomenon of turbulent macro-instabilities in agitated systems. *Collection of Czechoslovak Chemical Communications*, Vol. 60, pp. 85-94.
- Bruha, O.; Fort, I.; Smolka, P. & Jahoda, M. (1996). Experimental study of turbulent macroinstabilities in an agitated system with axial high-speed impeller and with radial baffles. *Collection of Czechoslovak Chemical Communications*, Vol. 61, pp. 856-867.
- Conti, R.; Sicardi, S. & Specchia, V. (1981). Effect of the stirrer clearance on suspension in agitated vessels. *Chemical Engineering Journal*, Vol. 22, pp. 247-249.
- Cooley, J.W. & Tukey, J.W. (1965). An algorithm for the machine calculation of complex Fourier series. *Mathematical Computation*, Vol. 19, pp. 297-301.
- Daubechies, I. (1990). The Wavelet transform time-frequency localization and signal analysis. *IEEE Transactions on Information Theory*, Vol. 36, pp. 961-1005.
- Derksen, J.J. (2003). Numerical simulation of solids suspension in a stirred tank, *AIChE Journal*. Vol. 49, pp. 2700-2714.
- Distelhoff, M.F.W.; Laker, J.; Marquis, A.J. & Nouri, J. (1995). The application of a strain-gauge technique to the measurement of the power characteristics of 5 impellers. *Experiments in Fluids*, Vol. 20, pp. 56-58.
- Doulgerakis, Z.; Yianneskis, M.; Ducci, A. (2011). On the interaction of trailing and macro-instability vortices in a stirred vessel-enhanced energy levels and improved mixing potential. *Chemical Engineering Research and Design*, Vol. 87, pp. 412-420.
- Ducci, A. & Yianneskis, M. (2007). Vortex tracking and mixing enhancement in stirred processes. *AIChE Journal*, Vol. 53, pp. 305-315.
- Ducci, A.; Doulgerakis, Z. & Yianneskis, M. (2008). Decomposition of flow structures in stirred reactors and implications for mixing enhancement. *Industrial and Engineering Chemistry Research*, Vol. 47, pp. 3664-3676.
- Galletti, C. & Brunazzi, E. (2008). On the main flow features and instabilities in an unbaffled vessel agitated with an eccentrically located impeller. *Chemical Engineering Science*, Vol 63, pp. 4494-4505

- Galletti, C. (2005). *Experimental analysis and modeling of stirred vessels*. Ph.D. thesis, University of Pisa, Pisa, Italy.
- Galletti, C.; Brunazzi, E.; Pintus, S.; Paglianti, A. & Yianneskis, M. (2004a). A study of Reynolds stresses, triple products and turbulence states in a radially stirred tank with 3-D laser anemometry. *Transactions IChemE, Chemical Engineering Research and Design*, Vol. 82, pp. 1214-1228.
- Galletti, C.; Brunazzi, E.; Yianneskis, M. & Paglianti, A. (2003). Spectral and Wavelet analysis of the flow pattern transition with impeller clearance variations in a stirred vessel. *Chemical Engineering Science*, Vol. 58, pp. 3859-3875.
- Galletti, C.; Lee, K.C.; Paglianti, A. & Yianneskis, M. (2005a). Flow instabilities associated with impeller clearance changes in stirred vessels. *Chemical Engineering Communications*, Vol. 192, pp. 516-531.
- Galletti, C.; Lee, K.C.; Paglianti, A. & Yianneskis, M. (2004b). Reynolds number and impeller diameter effects on instabilities in stirred vessels, *AIChE Journal*, Vol. 50, 2050-2063.
- Galletti, C.; Paglianti, A. & Yianneskis, M. (2005b). Observations on the significance of instabilities, turbulence and intermittent motions on fluid mixing processes in stirred reactors. *Chemical Engineering Science*, Vol. 60, pp. 2317-2331.
- Galletti, C.; Pintus, S. & Brunazzi, E. (2009). Effect of shaft eccentricity and impeller blade thickness on the vortices features in an unbaffled vessel. *Chemical Engineering Research and Design*, Vol. 87, pp. 391-400.
- Guillard, F.; Trägårdh, C. & Fuchs, L. (2000a). A study of turbulent mixing in a turbine-agitated tank using a fluorescence technique. *Experiments in Fluids*, Vol. 28, pp. 225-235.
- Guillard, F.; Trägårdh, C. & Fuchs, L. (2000b). A study on the instability of coherent mixing structures in a continuously stirred tank. *Chemical Engineering Science*, Vol. 55, pp. 5657-5670.
- Haam, S.; Brodkey, R.S. & Fasano, J.B. (1992). Local heat-transfer in a mixing vessel using heat-flux sensors. *Industrial and Engineering Chemistry Research*, Vol. 31, 1384-1391.
- Hartmann, H.; Derksen, J.J. & van den Akker H.E.A. (2006). Numerical simulation of a dissolution process in a stirred tank reactor. *Chemical Engineering Science*. Vol 61 , pp. 3025 - 3032
- Hartmann, H.; Derksen, J.J. & van den Akker, H.E.A. (2004). Macroinstability uncovered in a Rushton turbine stirred tank by means of LES. *AIChE Journal*, Vol. 50, pp. 2383-2393.
- Hasal, P.; Fort, I. & Kratena, J. (2004). Force effects of the macro-instability of flow pattern on radial baffles in a stirred vessel with pitched-blade and Rushton turbine impeller. *Transactions IChemE, Chemical Engineering Research and Design*, Vol. 82, pp. 1268-1281.
- Hasal, P.; Montes, J.L.; Boisson, H.C. & Fort, I. (2000). Macro-instabilities of velocity field in stirred vessel: detection and analysis. *Chemical Engineering Science*, Vol. 55, pp. 391-401.
- Hockey, R. M. & Nouri, M. (1996). Turbulent flow in a baffled vessel stirred by a 60° pitched blade impeller. *Chemical Engineering Science*, Vol. 51, pp. 4405-4421.
- Hockey, R.M. (1990). *Turbulent Newtonian and non-Newtonian flows in a stirred reactor*, Ph.D. thesis, Imperial College, London.

- Houcine, I.; Plasari, E.; David, R. & Villermaux, J. (1999). Feedstream jet intermittency phenomenon in a continuous stirred tank reactor. *Chemical Engineering Journal*, Vol. 72, pp. 19-29.
- Ibrahim, S. & Nienow, A.W. (1995). Power curves and flow patterns for a range of impellers in Newtonian fluid: $40 < Re < 5 \times 10^5$. *Transactions IChemE, Chemical Engineering Research and Design*, Vol. 73, pp. 485-491.
- Ibrahim, S. & Nienow, A.W. (1996). Particle suspension in the turbulent regime: the effect of impeller type and impeller/vessel configuration. *Transactions IChemE, Chemical Engineering Research and Design*, Vol. 74, pp. 679-688.
- Jaworski, Z.; Nienow, A.W.; Koutsakos, E.; Dyster, K. & Bujalski, W. (1991). An LDA study of turbulent flow in a baffled vessel agitated by a pitched blade turbine. *Transactions IChemE, Chemical Engineering Research and Design*, Vol. 69, pp. 313-320.
- Kilander, J; Svensson, F.J.E. & Rasmuson, A. (2006). Flow instabilities, energy levels, and structure in stirred tanks. *AIChE Journal*, Vol. 52, pp. 3049-4051.
- Kresta, S.M. & Wood, P.E. (1993). The mean flow field produced by a 45° pitched-blade turbine: changes in the circulation pattern due to off bottom clearance. *Canadian Journal of Chemical Engineering*, Vol. 71, pp. 42-53.
- Larsson G.; Toˆrnkvist M.; Ståhl Wernersson E.; Traˆgårdh ,C.; Noorman, H. & Enfors, S.O. (1996). Substrate gradients in bioreactors: origin and consequences. *Bioprocess Engineering*, Vol. 14, pp. 281-289.
- Lavezzo, V.; Verzicco, R. & Soldati, A. (2009). Ekman pumping and intermittent particle resuspension in a stirred tank reactor. *Chemical Engineering Research and Design*. Vol. 87, pp. 557-564.
- Lomb, N.R. (1976). Least-squares frequency analysis of unequally spaced data, *Astrophysics and Space Science*. Vol. 39, pp. 447-462.
- Mao, D.; Feng, L.; Wang, K. & Li, Y. (1997). The mean flow generated by a pitched-blade turbine: changes in the circulation pattern due to impeller geometry, *Canadian Journal of Chemical Engineering*, Vol. 75, pp. 307-316.
- Micheletti, M. & Yianneskis, M. (2004). Precessional flow macro-instabilities in stirred vessels: study of variations in two locations through conditional phase-averaging and cross-correlation approaches, *Proceedings 11th International Symposium on Applications of Laser Techniques to Fluid Mechanics*, Lisbon, Portugal.
- Montante, G.; Lee, K.C.; Brucato, A. & Yianneskis, M. (1999). Double- to single- loop flow pattern transition in stirred vessels. *Canadian Journal of Chemical Engineering*, Vol. 77, pp. 649-659.
- Montes, J.L.; Boisson H.C.; Fort, I. & Jahoda, M. (1997). Velocity field macro-instabilities in an axially agitated mixing vessel. *Chemical Engineering Journal*, Vol. 67, pp. 139-145.
- Murakami, Y.; Hirose, T.; Yamato, T.; Fujiwara, H. & Ohshima, M. (1980). Improvement in mixing of high viscosity liquid by additional up-and-down motion of a rotating impeller. *Journal of Chemical Engineering of Japan*, Vol. 13, pp. 318-323.
- Murthy, B.N. & Joshi, J.B. (2008). Assessment of standard k- ϵ , RSM and LES turbulence models in a baffled stirred vessel agitated by various impeller designs. *Chemical Engineering Science*, Vol. 63, pp. 5468-5495
- Myers, K.J.; Bakker, A. & Corpstein, R.R. (1996). The effect of flow reversal on solids suspension in agitated vessels. *Canadian Journal of Chemical Engineering* 74, pp. 1028-1033.

- Myers, K.J.; Ward, R.W. & Bakker, A. (1997). A digital particle image velocimetry investigation of flow field instabilities of axial-flow impellers. *Journal of Fluid Engineering*, Vol. 119, pp. 623-632.
- Nienow, A. W. (1968). Suspension of solid particles in turbine agitated baffled vessels. *Chemical Engineering Science*, Vol. 23, pp. 1453-1459.
- Nikiforaki, L.; Montante, G.; Lee, K.C.; Yianneskis, M. (2003). On the origin, frequency and magnitude of macro-instabilities of the flows in stirred vessels. *Chemical Engineering Science*, Vol. 58, pp. 2937-2949.
- Nikiforaki, L.; Yu, J.; Baldi, S.; Genenger, B.; Lee, K.C.; Durst, F. & Yianneskis, M. (2004). On the variation of precessional flow instabilities with operational parameters in stirred vessels. *Chemical Engineering Journal*, Vol. 102, pp. 217-231.
- Nomura, T.; Uchida, T. & Takahashi, K. (1997). Enhancement of mixing by unsteady agitation of an impeller in an agitated vessel. *Journal of Chemical Engineering of Japan*, Vol. 30, pp. 875-879.
- Nouri, J.M. & Whitelaw, J.H. (1990). Flow characteristics of stirred reactors with Newtonian and non-Newtonian fluids. *AIChE Journal*, Vol. 36, pp. 627-629.
- Nurtono T.; Setyawan; H. Altway A. & Winardi, S. (2009) Macro-instability characteristic in agitated tank based on flow visualization experiment and large eddy simulation. *Chemical Engineering Research and Design*, Vol. 87, pp. 923-942.
- Paglianti, A.; Montante, G. & Magelli, F. (2006). Novel experiments and a mechanistic model for macroinstabilities in stirred tanks. *AIChE Journal*, Vol. 52, pp. 426-437.
- Roussinova, V.T.; Grgic, B. and Kresta, S.M. (2000). Study of macro-instabilities in stirred tanks using a velocity decomposition technique. *Transactions IChemE, Chemical Engineering Research and Design*, Vol. 78, 1040-1052.
- Roussinova, V.T.; Kresta, S.M. & Weetman, R. (2003). Low frequency macroinstabilities in a stirred tank: scale-up and prediction based on large eddy simulations. *Chemical Engineering Science*, Vol. 58, pp. 2297-2311.
- Roussinova, V.T.; Kresta, S.M. & Weetman, R. (2004). Resonant geometries for circulation pattern macroinstabilities in a stirred tank. *AIChE Journal*, Vol. 50, pp. 2986-3005.
- Roussinova, V.T.; Weetman, R. & Kresta, S.M. (2001). Large eddy simulation of macro-instabilities in a stirred tank with experimental validation at two scales. *North American Mixing Forum 2001*.
- Roy, S.; Acharya, S. & Cloeter, M. (2010). Flow structure and the effect of macro-instabilities in a pitched-blade stirred tank. *Chemical Engineering Science*, Vol. 65, pp. 3009-3024.
- Rutherford, K.; Lee, K.C.; Mahmoudi, S.M.S. & Yianneskis, M. (1996a). Hydrodynamic characteristics of dual Rushton impeller stirred vessels. *AIChE Journal*, Vol. 42, pp. 332-346.
- Rutherford, K.; Mahmoudi, S.M.S.; Lee, K.C. & Yianneskis, M. (1996b). The Influence of Rushton impeller blade and disk thickness on the mixing characteristics of stirred vessels. *Transactions IChemE, Chemical Engineering Research and Design*, Vol. 74, pp. 369-378.
- Scargle, J. (1982). Studies in astronomical time series analysis. II Statistical aspect of spectral analysis of unevenly spaced data. *Astrophysical Journal*, Vol. 263, pp. 835-853.
- Schäfer, M.; Yianneskis, M.; Wächter, P. & Durst, F. (1998). Trailing vortices around a 45° pitched-blade impeller. *AIChE Journal*, Vol. 44, pp. 1233-1246.

- Sharma, R.N. & Shaikh, A.A. (2003). Solids suspension in stirred tanks with pitched blade turbines. *Chemical Engineering Science*, Vol. 58, pp. 2123-2140.
- Tatterson, G.B. (1991). *Fluid mixing and gas dispersion in agitated tanks*, McGraw-Hill Inc., New York.
- Tiljander, P. & Theliander, H. (1993). Power-consumption and solid suspension in completely filled vessels. *Chemical Engineering Communications*, Vol. 124, pp. 1-14.
- Torré, J.P.; Fletcher, D.F; Lasuye T. & Xuereb, C. (2007) Single and multiphase CFD approaches for modelling partially baffled stirred vessels: Comparison of experimental data with numerical predictions. *Chemical Engineering Science*, Vol. 62, pp. 6246-6262
- Torrence, C. & Compo, P. (1998). A practical guide to Wavelet analysis. *Bulletin of the American Meteorological Society*, Vol. 79, pp. 61-78.
- Yianneskis, M.; Popiolek, Z. & Whitelaw, J.H. (1987). An experimental study of the steady and unsteady flow characteristics of stirred reactors. *Journal of Fluid Mechanics*, Vol. 175, pp. 537-555.
- Zwietering, T.N. (1958). Suspending of solid particles in liquid by agitators. *Chemical Engineering Science*, Vol. 8, pp. 244-253.

Hydrodynamic Properties of Aggregates with Complex Structure

Lech Gmachowski
Warsaw University of Technology
Poland

1. Introduction

Hydrodynamic properties of fractal aggregates and polymer coils, such as sedimentation velocity, permeability, translational and rotational diffusion coefficients and intrinsic viscosity, are of great interest in hydrodynamics, engineering, colloid and polymer science and biophysics. The hydrodynamic properties of aggregates are closely connected to their structure.

Aggregates - the clusters of monomers - usually have a fractal structure which means that parts of the object are similar to the whole. The self-similar structure is characterized by the fractal dimension which is a measure of how the aggregate fills the space it occupies. The fractal dimension can be calculated by analyzing the mass-radius relation for a series of similar aggregates, since the mass of an aggregate scales as a power of the size.

The fractal dimension can be also determined by covering the aggregate with spheres of changing radius (Fig. 1). Then plotting the number of spheres $N(\rho)$ versus their radius ρ in a log-log coordinate system, one determines the fractal dimension as the negative slope of the obtained line.

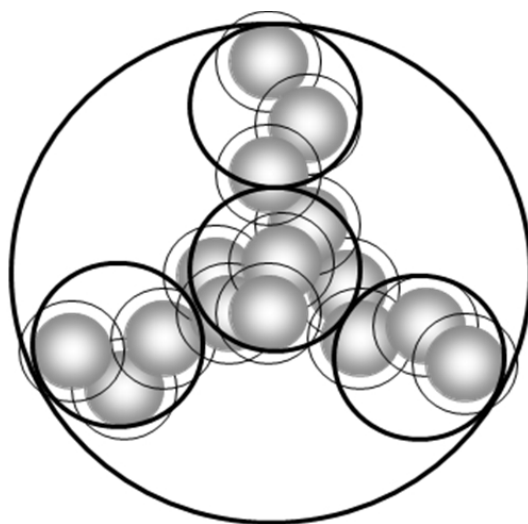


Fig. 1. Aggregate covering with spheres of changing radius.

The Hausdorff dimension (Hausdorff, 1919) is the critical exponent for which the Hausdorff measure M_d , being proportional to the product of number of spheres and a power of their radius, changes from zero to infinity when the size of covering elements tends to zero

$$M_d \propto N(\rho) \cdot \rho^d \xrightarrow{\rho \rightarrow 0} \begin{cases} 0, & d > D \\ \infty, & d < D \end{cases} \quad (1)$$

In practice each monomer has its size. It is thus generally accepted the constancy of Hausdorff measure in a finite range of size to be sufficient to characterize the aggregate structure. The constancy of the Hausdorff measure for two limiting sizes of spheres, written for an aggregate containing i monomers, can be expressed as

$$1 \cdot R^D = i \cdot R_1^D \quad (2)$$

where R is the radius of the sphere circumscribed on the aggregate and R_1 is the radius of envelope surrounding one monomer, for which the similarity to the aggregate still exists (Gmachowski, 2002).

The structure of aggregates is permeable which means that a fluid flows not only around but also through the aggregate. It is analyzed by taking into account the internal permeability of aggregates, either directly or by replacing a given aggregate by a smaller impermeable sphere of the same hydrodynamic properties. In this way the hydrodynamic radius is defined.

The structure of fractal aggregate can be related to the possibility to penetrate its interior by a fluid, well represented by internal permeability. The translational friction coefficient of a particle of radius R can be written in the following form

$$f_T = 6\pi\eta_0 R \cdot \frac{r}{R} \quad (3)$$

where the hydrodynamic radius r is introduced to take into account its dependence on the internal permeability of the aggregate. Such relation gave Brinkman for translational friction factor (Brinkman, 1947)

$$\frac{r}{R} = \frac{1 - \frac{\tanh \sigma}{\sigma}}{1 + \frac{3}{2\sigma^2} \left(1 - \frac{\tanh \sigma}{\sigma}\right)} \quad (4)$$

where $\sigma = R / \sqrt{k}$ is the reciprocal square root of dimensionless internal permeability of a sphere of uniform structure modeling the fractal aggregate. The analogous relations of the normalized hydrodynamic radius for the rotational friction coefficient and the intrinsic viscosity are slightly different, but all the three give the results which are very close to one another (Gmachowski, 2003).

For a homogeneous porous medium, being an arrangement of monosized particles, the permeability is proportional to the square of the characteristic pore size (Dullien, 1979) which is closely correlated to the size of constituents. In the case of fractal aggregate, which is not homogeneous, the fluid flow occurs mainly in the large pores. Hence their size determines the aggregate permeability.

For similar aggregates the size of large pores scales as the size of the whole aggregate. Therefore the ratio of the internal permeability and the square of aggregate radius is expected to be constant for aggregates of the same fractal dimension and to decrease with increasing fractal dimension due to the increment of the aggregate compactness (Gmachowski, 1999; Woodfield & Bickert, 2001; Bushell et al., 2002). This means that $\sigma = R / \sqrt{k}$ is a unique function of the fractal dimension of an aggregate and hence the ratio r/R is determined by D (Eq. 4). A formula

$$\frac{r}{R} = \sqrt{1.56 - \left(1.728 - \frac{D}{2}\right)^2} - 0.228 \quad (5)$$

has been derived from analysis of permeability of aggregated system (Gmachowski, 2000) and is confirmed by different hydrodynamic properties of fractal aggregates (Gmachowski, 2003).

This means that the hydrodynamic radius is proportional to aggregate radius for a given fractal dimension. The covering can be thus performed not only in the range of radii, but also in the range of hydrodynamic radii. The hydrodynamic radius of a solid monomer is its geometrical radius. For fractal aggregate the mass-hydrodynamic radius relation has the following form

$$i = \left(\frac{r}{a}\right)^D \quad (6)$$

since the hydrodynamic radius r converges to the primary particle radius a for the number of constituent particles equal to unity (Gmachowski, 2008). The mass-radius relation reads

$$i = \left(\frac{r}{R}\right)^D \left(\frac{R}{a}\right)^D \quad (7)$$

which reduces to the previous one if the aggregation number is related to the hydrodynamic radius instead to the radius. The full form of mass-radius relation has the form

$$i = \left[\sqrt{1.56 - \left(1.728 - \frac{D}{2}\right)^2} - 0.228 \right]^D \left(\frac{R}{a}\right)^D \quad (8)$$

Plotting in a log-log system the aggregation number against radius for several similar aggregates, one can determine a best fit straight line whose slope is the fractal dimension and the location makes it possible to determine the monomer radius.

If the aggregate is composed of smaller aggregates instead of solid monomers, their number is correlated to the hydrodynamic radius of smaller aggregates according to the mass-radius relation of the form similar to Eq. (8).

2. Aggregates with complex structure

An aggregate has a complex structure if it consists of smaller aggregates instead of solid monomers (Fig. 2) and their fractal dimension is different from that of the whole aggregate.

In opposite, the constancy of Hausdorff measure would take place in the range of the whole aggregate hydrodynamic size down to the solid monomer size. An aggregate with complex structure is termed as aggregate with mixed statistics, since it has different fractal dimensions on different length scales. The constituent aggregates are known as blobs.

The knowledge of the hydrodynamic radius in relation to the radius of fractal aggregate of a given fractal dimension, utilized for blobs, makes it possible to replace the blobs by their hydrodynamic equivalents. In this way an aggregate with mixed statistics is reduced to fractal aggregate with the Hausdorff measure constant in the range of the whole aggregate hydrodynamic size down to the hydrodynamic size of blobs.

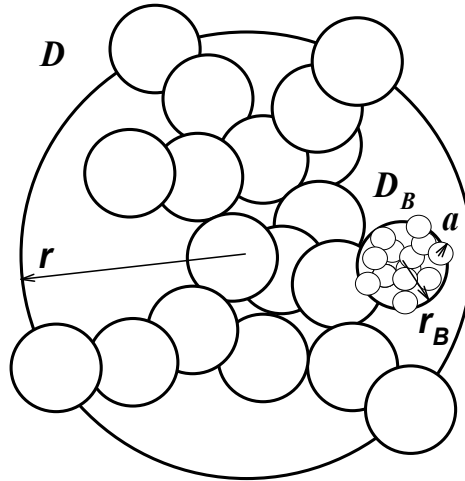


Fig. 2. Graphical representation of an aggregate with mixed statistics. The aggregate fractal dimension is a result of the spatial arrangement of blobs.

An aggregate with mixed statistics of hydrodynamic radius r and fractal dimension D consists of I blobs of hydrodynamic radius r_B and fractal dimension D_B , each containing i_B solid monomers of radius a . The mass-hydrodynamic radius relations are

$$i_B = \left(\frac{r_B}{a} \right)^{D_B} \quad (9)$$

$$I = \left(\frac{r}{r_B} \right)^D \quad (10)$$

Let us imagine an aggregate of the same mass and fractal dimension composed of monomers instead of blobs. Then the total number of monomers can be expressed as

$$Ii_B = \left(\frac{r_0}{a} \right)^D \quad (11)$$

Combining the last three equations, one gets the expression for the change of hydrodynamic radius caused by the presence of blobs

$$\frac{r}{r_0} = i_B^{1/D_B - 1/D} \quad (12)$$

The corresponding mass-radius relation for an aggregate with mixed statistics reads

$$I = \left[\sqrt{1.56 - \left(1.728 - \frac{D}{2}\right)^2} - 0.228 \right]^D \left(\frac{R}{r_B}\right)^D \quad (13)$$

which makes it possible to determine the blob hydrodynamic radius by plotting in a log-log system the number of blobs against the aggregate radius for several similar aggregates with mixed statistics and then deducing the slope and location of the best fit straight line obtained.

3. Asphaltene aggregates

The aggregate of mixed statistics can be obtained by shearing the crude oil (Gmachowski & Paczuski, 2011). Asphaltenes, a part of petroleum, are aromatic multicyclic molecules surrounded and linked by aliphatic chains and heteroatoms, of the molar mass in the range 500-50000 u. As a result of shearing, they aggregate to form blobs of a size of several micrometers, which join to form aggregates with mixed statistics. If the crude oil is mixed with toluene and n-heptane in different proportions, the range of aggregate size becomes wider.



Fig. 3. Typical microscope image of asphaltene aggregate.

It is possible to estimate the size and number of blobs for several images (Fig. 3) to identify the form of mass-radius relation of asphaltene aggregates by plotting the data in a log-log system. This is presented in Fig. 4.

The fractal dimension determined by this method for aggregates of mixed statistics investigated was $D=1.5$, whereas the hydrodynamic radius of blobs $r_B \cong 3\mu\text{m}$. Two additional lines are drawn in Fig. 4, representing Eq. (13) for the same fractal dimension and two values of the blob hydrodynamic radius, namely $r_B = 2\mu\text{m}$ and $r_B = 4\mu\text{m}$. Their locations do not correspond to points representing the experimental data, which confirms the rationality of the method of mass-radius relation for aggregates with mixed statistics. Moreover, the size estimated (blob hydrodynamic radius $r_B = 3\mu\text{m}$) is close to that observed in the image (blob radius), which suggests very compact structure of blobs formed by asphaltenes.

4. Free settling velocity

Free settling velocity of an aggregate with mixed statistics can be determined by equating the gravitational force allowing for the buoyancy of the surrounding fluid with the opposing

hydrodynamic force which depends on the aggregate size and its permeability. The use of hydrodynamic radius which is the radius of an impermeable sphere of the same mass

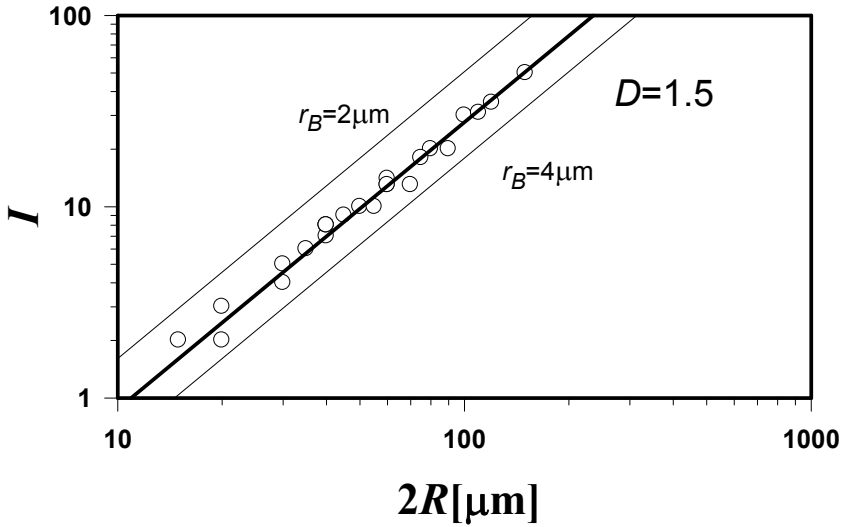


Fig. 4. Graphical representation of the mass-radius relation for asphaltene aggregates.

having the same dynamic properties, instead of the aggregate radius, makes it possible to neglect the internal permeability. For an aggregate of hydrodynamic radius r composed of $i = li_B$ primary particles of radius a the force balance is

$$\frac{4}{3} \pi a^3 li_B (\rho_s - \rho_f) g = 6 \pi \eta_0 r u \tag{14}$$

Using the mass-hydrodynamic radius relations for blob and aggregate (Eqs. 9,10), one gets

$$\frac{u}{u_a} = I^{1-1/D} i_B^{1-1/D_B} \tag{15}$$

where

$$u_a = \frac{2}{9 \eta_0} (\rho_s - \rho_f) g a^2 \tag{16}$$

is the Stokes falling velocity of primary particle.

Alternatively, using the expression for the hydrodynamic radius changed by the presence of blobs (Eq. 12), one obtains

$$\frac{u}{u_a} = \left(\frac{r_0}{a} \right)^{D-1} / \frac{r_0}{r} \tag{17}$$

If the blobs of the fractal dimension different from that of the aggregate are not present ($D = D_B$ and $r_0 = r$), the corresponding dependences reduce to the following relations

$$\frac{u_0}{u_a} = i^{1-1/D} \quad (18)$$

$$\frac{u_0}{u_a} = \left(\frac{r_0}{a} \right)^{D-1} \quad (19)$$

characteristic for fractal aggregates with one-level structure. Hence the following formulae

$$\frac{u}{u_0} = i_B^{1/D-1/D_B} \quad (20)$$

$$\frac{u}{u_0} = \frac{r_0}{r} \quad (21)$$

describe the free settling velocity of aggregates with mixed statistics.

5. Intrinsic viscosity of macromolecular coils and the thermal blob mass

A macromolecular coil in a solution is modeled as an aggregate with mixed statistics consisting of I thermal blobs of $D_B = 2$, each containing i_B solid monomers of radius a and mass M_a . To calculate the intrinsic viscosity

$$[\eta] \equiv \lim_{c \rightarrow 0} \frac{\eta - \eta_0}{\eta_0 c} \quad (22)$$

one has to define the mass concentration c of a macromolecular solution analyzed. The mass concentration in the coil, represented by the equivalent impermeable sphere, can be calculated as the product of the total number of non-porous monomers li_B multiplied by their mass $4/3\pi a^3 \rho_s$ and divided by the hydrodynamic volume of the coil $4/3\pi r^3$. This concentration multiplied by the volume fraction of equivalent aggregates φ gives the overall polymer mass concentration in the solution.

$$c = \varphi \rho_s \frac{li_B a^3}{r^3} \quad (23)$$

Mass-radius relations are then employed. The thermal blob mass related to that of nonporous monomer is the aggregation number of the thermal blob

$$i_B = \frac{M_B}{M_a} = \left(\frac{r_B}{a} \right)^2 \quad (24)$$

whereas the macromolecular mass related to that of thermal blob is the aggregation number of aggregate equivalent to coil

$$I = \frac{M}{M_B} = \left(\frac{r}{r_B} \right)^D \quad (25)$$

Taking into account that the volume fraction of polymer in an aggregate equivalent to polymer coil can be rearranged as follows

$$\frac{li_B a^3}{r^3} = I \left(\frac{r_B}{r} \right)^3 i_B \left(\frac{a}{r_B} \right)^3 \quad (26)$$

finally one gets

$$c = \varphi \rho_s \left(\frac{M_B}{M_a} \right)^{-1/2} \left(\frac{M}{M_B} \right)^{1-3/D} \quad (27)$$

or

$$c = \varphi \rho_s \left(\frac{M_B}{M_a} \right)^{-1/2} \left(\frac{M}{M_B} \right)^{-a_{MHS}} \quad (28)$$

if the fractal dimension D is replaced by the Mark-Houwink-Sakurada exponent a_{MHS} , characterizing the thermodynamic quality of the solvent, where

$$a_{MHS} = 3 / D - 1 \quad (29)$$

The structure of a dissolved macromolecule depends on the interaction with solvent and other macromolecules. The resultant interaction determines whether the monomers effectively attract or repel one another. Chains in a solvent at low temperatures are in collapsed conformation due to dominance of attractive interactions between monomers (poor solvent). At high temperatures, chains swell due to dominance of repulsive interactions (good solvent). At a special intermediate temperature (the theta temperature) chains are in ideal conformations because the attractive and repulsive interactions are equal. The exponent a_{MHS} changes from 1/2 for theta solvents to 4/5 for good solvents, which corresponds to the fractal dimension range of from 2 to 5/3.

The viscosity of a dispersion containing impermeable spheres present at volume fraction φ can be described by the Einstein equation (Einstein, 1956)

$$\eta = \eta_0 \left(1 + \frac{5}{2} \varphi \right) \quad (30)$$

from which

$$\frac{\eta - \eta_0}{\eta_0} = \frac{5}{2} \varphi \quad (31)$$

The intrinsic viscosity can be thus calculated as

$$[\eta] \equiv \lim_{c \rightarrow 0} \frac{\eta - \eta_0}{\eta_0 c} = \lim_{c \rightarrow 0} \frac{5}{2} \frac{\varphi}{c} \quad (32)$$

Utilizing the expression for the mass concentration, one gets

$$[\eta] \equiv \lim_{c \rightarrow 0} \frac{\eta - \eta_0}{\eta_0 c} = \lim_{c \rightarrow 0} \frac{5}{2} \frac{\varphi}{c} = \lim_{c \rightarrow 0} \frac{5}{2} \frac{\varphi}{\varphi \rho_s \left(\frac{M_B}{M_a}\right)^{-1/2} \left(\frac{M}{M_B}\right)^{-a_{MHS}}} = \frac{5}{2\rho_s} \left(\frac{M_B}{M_a}\right)^{1/2} \left(\frac{M}{M_B}\right)^{a_{MHS}} \quad (33)$$

The obtained equation can be also derived in terms of complex structure aggregate parameters for any blob fractal dimension to get

$$[\eta] = \frac{5}{2\rho_s} i_B^{3/D_B - 1} I^{3/D - 1} \quad (34)$$

which is equivalent to

$$[\eta] = \frac{5}{2\rho_s} \left(\frac{r_0}{a}\right)^{3-1/D} \left(\frac{r}{r_0}\right)^3 \quad (35)$$

Equation derived for polymer coil can be compared to the empirical Mark-Houwink-Sakurada expression relating the intrinsic viscosity to the polymer molecular mass

$$[\eta] = K_\eta M^{a_{MHS}} \quad (36)$$

For the theta condition the formulae (Eq. 33) read

$$[\eta]_\theta = \frac{5}{2\rho_s} \left(\frac{M_B}{M_a}\right)^{1/2} \left(\frac{M}{M_B}\right)^{1/2} = \frac{5}{2\rho_s} \left(\frac{M}{M_a}\right)^{1/2} \quad (37)$$

and

$$[\eta]_\theta = K_\theta M^{1/2} \quad (38)$$

The Mark-Houwink-Sakurada expressions are presented in Fig. 5.

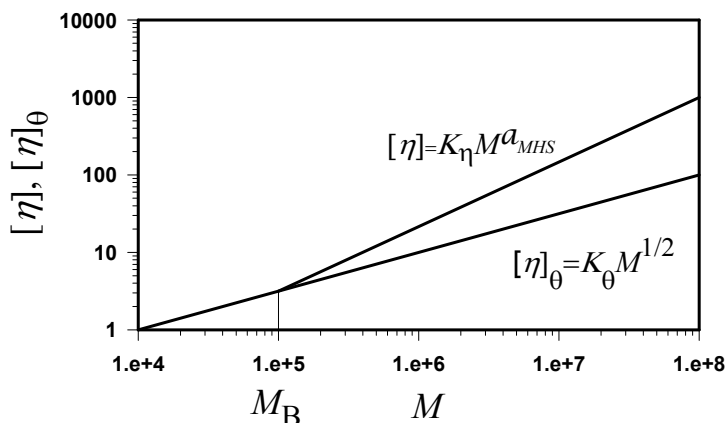


Fig. 5. Graphical representation of the Mark-Houwink-Sakurada expressions.

There is a lower limit of the Mark-Houwink-Sakurada expression applicability. Intrinsic viscosity of a given polymer in a solvent crosses over to the theta result at a molecular mass which is the thermal blob molecular mass. This means that

$$K_\eta M_B^{a_{MHS}} = K_\theta M_B^{1/2} \quad (39)$$

from which

$$M_B = \left(\frac{K_\theta}{K_\eta} \right)^{1/(a_{MHS}-1/2)} \quad (40)$$

The thermal blob mass depends on the Mark-Houwink-Sakurada constant at the theta temperature, characteristic for a given polymer-solvent system, as well as the constant and the Mark-Houwink-Sakurada exponent valid at a given temperature. The form of this dependence is strongly influenced by the mass of non-porous monomer M_a of thermal blobs, which is different for different polymers. The thermal blob mass normalized by the mass of non-porous monomer M_B / M_a , however, is the number of non-porous monomers in one thermal blob and therefore it expected to be a unique function of the solvent quality. This function, determined (Gmachowski, 2009a) from many experimental data measured for different polymer-solvent systems, reads

$$i_B = \frac{M_B}{M_a} = \left\{ \exp \left[0.9 \cdot (2a_{MHS} - 1)^{1/3} \right] \right\}^{a_{MHS}/(a_{MHS}-0.5)} \quad (41)$$

The thermal blob aggregation number can be also calculated from the theoretical model of internal aggregation based on the cluster-cluster aggregation act equation (Gmachowski, 2009b)

$$i + i \sim \left[\frac{r}{R}(D) \right]^D \left(i^{1/D_i} + i^{1/D_i} \right)^D \quad (42)$$

being an extension of the mass-radius relation for single aggregate

$$i = \left(\frac{r}{a} \right)^D = \left[\frac{r}{R}(D) \right]^D \left(\frac{R}{a} \right)^D \quad (43)$$

assuming it is a result of joining to two identical sub-clusters and its radius R is proportional to the sum of hydrodynamic radii $a \cdot (i^{1/D_i} + i^{1/D_i})$, where the normalized hydrodynamic radius is described by Eq. (5). Aggregation act equation can be specified to the form of an equality

$$i_B + i_B = 2^{1-D} \left[\frac{r}{R}(D) / \frac{r}{R}(D_{lim}) \right]^D \left(i_B^{1/D_i} + i_B^{1/D_i} \right)^D \quad (44)$$

for which D tends to D_{lim} if i_B tends to infinity.

Let us imagine a coil consisting of one thermal blob. This is in fact a thermal blob of the structure of a large coil. Such rearranged blobs can join to another one to produce an object of double mass. The model makes it possible to calculate the fractal dimension D of the coil after each act of aggregation of two smaller identical coils of fractal dimension D_i changing with the aggregation progress.

Using the model for $D_{\text{lim}} = 2$ (the fractal dimension of thermal blobs), the dependences $i_B(D)$ have been calculated using CCA simulation, starting from both good and poor solvent regions. The aggregates growing by consecutive CCA events restructured to get a limiting fractal dimension D_{lim} in an advanced stage of the process. Starting from $i_B = 8$ and $D_i = 5/3$, the result is $D = 1.8115$. The second input to the model equation is thus $i_B = 16$ and $D_i = 1.8115$. Finally, the calculation results are presented in Fig. 6, where they are compared to the dependence deduced from the empirical data.

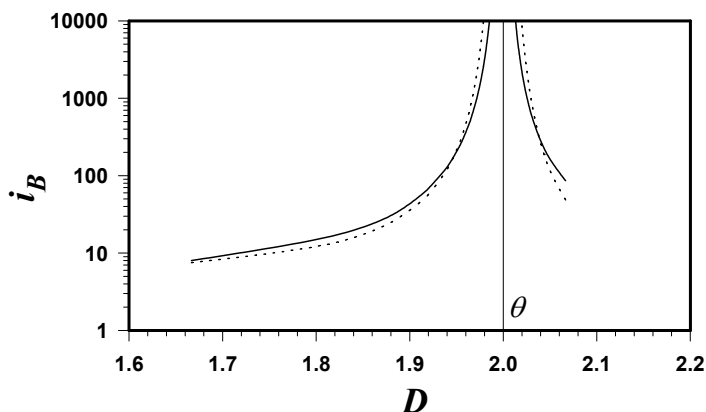


Fig. 6. Comparison of the model fractal dimension dependence of the thermal blob aggregation number (solid lines) to the representation of the experimental data measured for different polymer-solvent systems (Eq. 41), depicted as dashed lines.

6. Hydrodynamic structure of fractal aggregates

As discussed earlier, the ratio of the internal permeability and the square of aggregate radius is expected to be constant for aggregates of the same fractal dimension. Consider an early stage of aggregate growth in which the constancy of the normalized permeability is attained. At the beginning the aggregate consists of two and then several monomers. The number of pores and their size are of the order of aggregation number and monomer size, respectively. At a certain aggregation number, however, the size of new pores formed starts to be much larger than that formerly created. This means that the hydrodynamic structure building has been finished and the smaller pores become not active in the flow and can be regarded as connected to the interior of hydrodynamic blobs.

A part of the aggregate interior is effectively excluded from the fluid flow, so one can consider this part as the place of existence of impermeable objects greater than the monomers. Since both the impermeable object size and the pore size are greater than formerly, the real permeability is bigger than that calculated by a formula valid for a

uniform packing of monomers. So this point can be considered as manifested by the beginning of the decrease of the normalized aggregate permeability calculated. During the aggregate growth the number of large pores tends to a value which remains unchanged during the further aggregation. The self-similar structure exists, which can be described by an arrangement of pores and effective impermeable monomers (hydrodynamic blobs) of the size growing proportional to the pore size. According to the above considerations one can expect effective aggregate structure such that the normalized aggregate permeability k/R^2 attains maximum. To determine the hydrodynamic structure of fractal aggregate the aggregate permeability is estimated by the Happel formula

$$\frac{k}{a^2} = \frac{2}{9\varphi} \cdot \frac{3 - 4.5\varphi^{1/3} + 4.5\varphi^{5/3} - 3\varphi^2}{3 + 2\varphi^{5/3}} \tag{45}$$

where the volume fraction of solid particles in an aggregate is described as

$$\varphi = i \cdot \left(\frac{a}{R}\right)^3 \tag{46}$$

The normalized aggregate permeability is calculated as

$$\frac{k}{R^2} = \frac{k}{a^2} \frac{a^2}{R^2} = \frac{k}{a^2} \left(\frac{i}{\varphi}\right)^{-2/3} \tag{47}$$

The results are presented in Fig. 7.

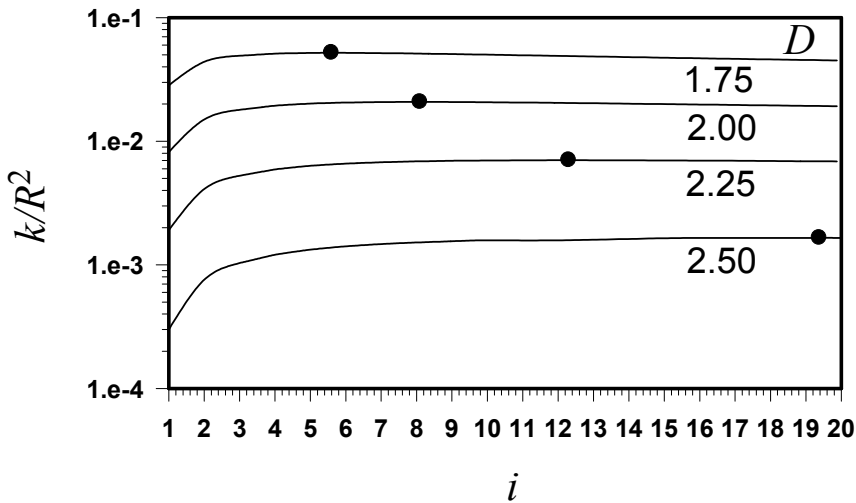


Fig. 7. Normalized aggregate permeability calculated by the Happel formula for different fractal dimensions. The maxima (indicated) determine the number of hydrodynamic blobs in aggregate.

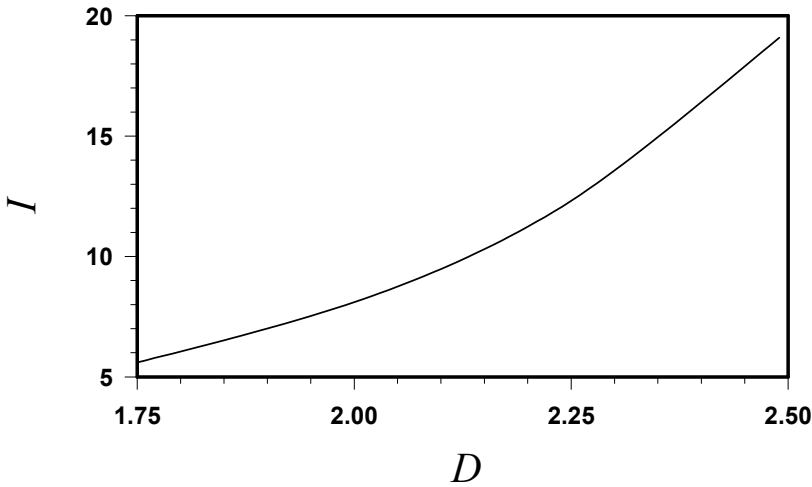


Fig. 8. Number of hydrodynamic blobs as dependent on fractal dimension.

Due to self-similarity, the number of monomers deduced from Fig. 8 is the number of hydrodynamic blobs which are the fractal aggregates similar to the whole aggregate. Hydrodynamic picture of a growing aggregate is such that after receiving a given number of monomers the number of hydrodynamic blobs becomes constant and further growth causes the increase in blob mass not their number.

As this estimation shows, the number of hydrodynamic blobs rises with the aggregate fractal dimension. The knowledge of this number makes it possible to estimate the aggregate permeability in the slip regime where the free molecular way of the molecules of the dispersing medium becomes longer than the aggregate size. In this region the dynamics of the continuum media is no longer valid.

The permeability of a homogeneous arrangement of solid particles of radius a , present at volume fraction φ , can be calculated (Brinkman, 1947) as

$$\frac{k}{a^2} = \frac{2}{9\varphi} \cdot \frac{6\pi\eta_0 a}{f_{packing}} \quad (48)$$

The friction factor of a particle in a packing can be presented as the friction factor of individual particle multiplied by a function of volume fraction of particles

$$f_{packing} = f \cdot S(\varphi) \quad (49)$$

In the continuum regime

$$f = f_{continuum} = 6\pi\eta_0 a \quad (50)$$

whereas in the slip one (Sorensen & Wang, 2000)

$$f = f_{slip} = 6\pi\eta_0 a / \left(1 + 1.612 \frac{\lambda}{a} \right) \quad (51)$$

where λ is the gas mean free path.

For a given structure of arrangement (a, φ) it possible to calculate the permeability coefficient in the slip regime from that valid in the continuum regime (Gmachowski, 2010)

$$k_{slip} = k \frac{f_{continuum}}{f_{slip}} = \left(1 + 1.612 \frac{\lambda}{a} \right) \cdot k \quad (52)$$

in which the monomer size should be replaced by the hydrodynamic blob radius rising such as the growing aggregate. So large differences in permeabilities at the beginning diminish when the aggregate mass increases and disappear when the aggregate size greatly exceeds the gas mean free path.

Calculated mobility radius r_m , representing impermeable aggregate in the slip regime, is smaller than the hydrodynamic one because of higher permeability and tends to the hydrodynamic size when the difference in permeabilities becomes negligible. At an early stage of the growth of aerosol aggregates it can be approximated as a power of mass (Cai & Sorensen, 1994)

$$r_m = a \cdot i^{1/2.3} \quad (53)$$

in which the number 2.3 greatly differs from the fractal dimension equal to 1.8.

7. Discussion

Covering the aggregate with spheres of a given size, one defines the blobs which are the units in which the monomers present in aggregates are grouped. Changing the size of the spheres we can increase or decrease the blob size. If the blobs have the same structure as the whole aggregate, the aggregate is the self-similar object.

Otherwise the object is a structure of mixed statistics with the hydrodynamic properties described in this chapter. There were analyzed aggregates containing monosized blobs of a given fractal dimension. The blobs of asphaltene aggregates are dense, probably of fractal dimension close to three. The thermal blobs - the constituents of polymer coils - have constant fractal dimension of two, independently of the thermodynamic quality of the solvent and hence the coil fractal dimension.

The determination of the hydrodynamic radius of hydrodynamic blobs in fractal aggregates, despite the same fractal structure as for the whole aggregate, serves to estimate the size of large pores through the fluid can flow. It makes it possible to model the fluid flow through the aggregate in terms of both the continuum and slip regimes.

8. References

- Brinkman, H. C. (1947). A calculation of the viscosity and the sedimentation velocity for solutions of large chain molecules taking into account the hampered flow of the solvent through each chain molecule. *Proceedings of the Koninklijke Nederlandse Akademie van Wetenschappen*, Vol. 50, (1947), pp. 618-625, 821, ISSN: 0920-2250

- Bushell, G. C., Yan, Y. D., Woodfield, D., Raper, J., & Amal, R. (2002). On techniques for the measurement of the mass fractal dimension of aggregates. *Advances in Colloid and Interface Science*, Vol. 95, No.1, (January 2002), pp. 1-50, ISSN 0001-8686
- Cai, J., & Sorensen, C. M. (1994). Diffusion of fractal aggregates in the free molecular regime. *Physical Review E*, Vol. 50, No. 5, (November 1994), pp. 3397-3400, ISSN 1539-3755
- Dullien, F. A. L. (1979). *Porous media. Fluid transport and pore structure*, Academic Press, ISBN 0-12-223650-5, New York
- Einstein, A. (1956). *Investigations on the Theory of the Brownian Movement*, Dover Publications, ISBN 0-486-60304-0, Mineola, New York
- Gmachowski, L. (1999). Comment on „Hydrodynamic drag force exerted on a moving floc and its implication to free-settling tests” by R. M. Wu and D. J. Lee, *Wat. Res.*, 32(3), 760-768 (1998). *Water Research*, Vol. 33, No. 4, (March 1999), pp. 1114-1115, ISSN 0043-1354
- Gmachowski, L. (2000). Estimation of the dynamic size of fractal aggregates. *Colloids and Surfaces A: Physicochemical and Engineering Aspects*, Vol. 170, No. 2-3, (September 2000), pp. 209-216, ISSN 0927-7757
- Gmachowski, L. (2002). Calculation of the fractal dimension of aggregates. *Colloids and Surfaces A: Physicochemical and Engineering Aspects*, Vol. 211, No. 2-3, (December 2002), pp. 197-203, ISSN 0927-7757
- Gmachowski, L. (2003). Fractal aggregates and polymer coils: Dynamic properties of. In: *Encyclopedia of Surface and Colloid Science*, P. Somasundaran (Ed.), 1-10, ISBN 978-0-8493-9615-1, Marcel Dekker, New York
- Gmachowski, L. (2008). Free settling of aggregates with mixed statistics. *Colloids and Surfaces A: Physicochemical and Engineering Aspects*, Vol. 315, No. 1-3, (February 2008), pp. 57-60, ISSN 0927-7757
- Gmachowski, L. (2009a). Thermal blob size as determined by the intrinsic viscosity. *Polymer*, Vol. 50, No. 7, (March 2009), pp. 1621-1625, ISSN 0032-3861
- Gmachowski, L. (2009b). Aggregate restructuring by internal aggregation. *Colloids and Surfaces A: Physicochemical and Engineering Aspects*, Vol. 352, No. 1-3, (December 2009), pp. 70-73, ISSN 0927-7757
- Gmachowski, L. (2010). Mobility radius of fractal aggregates growing in the slip regime. *Journal of Aerosol Science*, Vol. 41, No. 12, (December 2010), pp. 1152-1158, ISSN 0021-8502
- Gmachowski, L., & Paczuski, M. (2011). Fractal dimension of asphaltene aggregates determined by turbidity. *Colloids and Surfaces A: Physicochemical and Engineering Aspects*, Vol. 384, No. 1-3, (July 2011), pp. 461-465, ISSN 0927-7757
- Hausdorff, F. (1919). Dimension und äußeres Maß. *Mathematische Annalen*, Vol. 79, No. 2, (1919), pp. 157-179, ISSN 1432-1807
- Sorensen, C. M., & Wang, G. M. (2000). Note on the correction for diffusion and drag in the slip regime. *Aerosol Science and Technology*, Vol. 33, No. 4, (October 2000) pp. 353-356, ISSN 0278-6826

Woodfield, D., & Bickert, G. (2001). An improved permeability model for fractal aggregates settling in creeping flow. *Water Research*, Vol. 35, No. 16, (November 2001), pp. 3801- 3806, ISSN 0043-1354

Part 4

Radiation-, Electro-, Magnetohydrodynamics and Magnetorheology

Electro-Hydrodynamics of Micro-Discharges in Gases at Atmospheric Pressure

O. Eichwald, M. Yousfi, O. Ducasse, N. Merbahi,
J. P. Sarrette, M. Meziane and M. Benhenni
*University of Toulouse, University Paul Sabatier,
LAPLACE Laboratory,
France*

1. Introduction

Micro-discharges are specific cold filamentary plasma that are generated at atmospheric pressure between electrodes stressed by high voltage. As cold plasma or non-thermal plasma, we suggest that the energy of electrons inside the conductive plasma is much higher than the energy of the heaviest particles (molecules and ions). In such kind of plasma, the temperature of the gas remains cold (i.e. more or less equal to the ambient temperature) unlike in the field of thermal plasmas where the gas temperature can reach some thousands of Kelvin. This high level of temperature can be measured for example in plasma torch or in lightning.

The conductive channels of micro-discharges are very thin. Their diameters are estimated around some tens of micrometers. This specificity explains their name: micro-discharge. Another of their characteristic is their very fast development. In fact, micro-discharges propagate at velocity that can attain some tens of millimetres per nanosecond i.e. some 10^7 cm.s⁻¹. This very fast velocity is due to the propagation of space charge dominated streamer heads. The space charge inside the streamer head creates a very high electric field in which the electrons are accelerated like in an electron gun. These electrons interact with the gas and create mainly ions and radicals. In fact, the energy distribution of electrons inside streamer heads favours the chemical electron-molecule reactions rather than the elastic electron-molecule collisions. Therefore, micro-discharges are mainly used in order to activate chemical reactions either in the gas volume or on a surface (Penetrante & Schultheis, 1993, Urashima & Chang, 2010, Foest et al. 2005, Clement, 2001).

Several designs of plasma reactors are able to generate micro-discharges. The most convenient and the well known is probably the corona discharge reactor (Loeb, 1961&1965, Winands, 2006, Ono & Oda a, 2004, van Veldhuizen & Rutgers, 2002, Briels et al., 2006). Corona micro-discharges reactor has at least two asymmetric electrodes i.e. with one of them presenting a low curvature that introduces a pin effect where the geometric electric field is enhanced. The corona micro-discharges are initiated from this high geometric field area. Some samples of corona reactor geometries are shown in Fig. 1.

The transient character and the small dimensions make some micro-discharges parameters, like charged and radical densities, electron energy or electric field strength, difficult to be accessible to measurements. Therefore, the complete simulation of the discharge reactor, in complement to experimental study can lead to a better understanding of the physico-

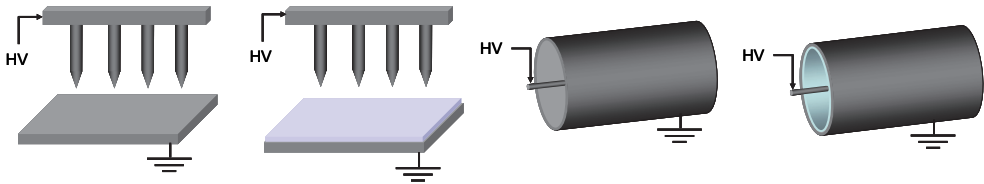


Fig. 1. Sample of pin-to-plane and wire-to-cylinder corona discharge reactors. The light blue material corresponds to a dielectric material. Depending on applications, design and reactor efficiency, the High Voltage (HV) shape can be DC, pulsed, AC or a combination of them.

chemical activity triggered by the micro-discharge during the plasma process. All these information can be used in order to improve the reactor design and to achieve the best operating conditions (such as the reactor geometry, the flue gas resident time, the applied voltage shape and magnitude, among others) as a function of the chosen applications.

The present chapter is devoted to description of the main electro-hydrodynamics phenomena that take place in non-thermal plasma reactors at atmospheric pressure activated by corona micro-discharges. The first section describes the micro-discharges characteristics using the experimental results obtained in a mono pin-to-plane reactor stressed by either DC or pulsed high voltage. The physics of the micro-discharges development is explained and a complete hydrodynamics model is proposed based on the moments of Boltzmann equations for charged and neutral particles. Then before to conclude, the previous described model is used in order to simulate the strongly coupled chemical and hydrodynamics phenomena generated by micro-discharges in a non thermal plasma reactor.

2. Description of positive corona micro-discharges

2.1 Introduction

In this first section, we describe the main characteristics of the corona micro-discharge formation and development as a function of several operating parameters such as the geometry of electrodes or the shape and magnitude of applied high voltage. Then, based on Boltzmann kinetic theory, we describe the strongly coupled electrical, hydrodynamics and chemical phenomena that take place in a compressible gas crossed by micro-discharges.

2.2 Positive corona micro-discharge under DC voltage condition

Let consider a mono pin-to-plane electrode corona reactor filled with dry air at atmospheric pressure and ambient temperature (Dubois et al., 2007). A DC high voltage supply is connected to the pin through a mega ohm resistor. When the applied voltage is raised gradually there is no sustained discharge current as much as the electrical gap field remains less than the onset one. Then, a sudden current pulse appears marking the beginning of the self sustained onset streamer regime. The associated current pulses occur intermittently and randomly and the mean current is very low (of few μA). Using a CCD camera with a large time shutter, we can observe a low intensity spot light just around the pin (see Fig. 2a). If we continue to increase the DC voltage, the current pulses vanish. However, the spot light near the point is always observed but with a quite higher intensity (see Fig. 2b). This regime corresponds to the classical glow corona discharge which is characterised by a drift of charged particles in the inter-electrode gap. The average current can reach some tens of μA .

For a high voltage threshold value, some regular repetitive current pulses appear with a repetition frequency of some tens of kHz and a magnitude of some tens to hundred of mA. Each current pulse lasts some hundred of nanoseconds and corresponds to the propagation of a mono-filament corona micro-discharge shown in Fig. 2c.

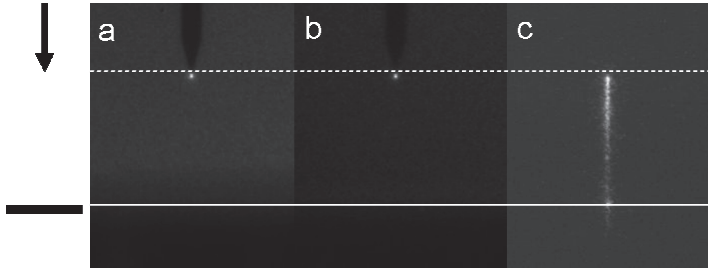


Fig. 2. Photography of the different corona discharge regimes under positive DC voltage condition (inter-electrode distance = 7mm, pin radius = 20 μm , dry air, atmospheric pressure). a: onset streamer, DC voltage magnitude = 3.2kV, time camera shutter = 1s, b: glow discharge, DC voltage magnitude = 5kV, time camera shutter = 10ms, c: streamer micro-discharge, DC voltage magnitude = 7.2kV, time camera shutter = 10 μs (Eichwald et al., 2008).

More detailed information on the spatio-temporal evolution of the micro-discharge can be obtained thanks to the analysis of the streak camera picture shown in Fig. 3 and the corresponding current pulse shown in Fig. 4 (Eichwald et al., 2008, Marode, 1975). In Fig. 3, the X-axis is the time axis while the Y-axis is the inter-electrode distance. The electrode location is shown in the drawing at the left side of Fig. 3. For a given time on the X-axis, the light emission of the micro-discharge filament at each position is focused along the corresponding Y-axis coordinate. When 8.2kV is applied to the pin, three main phases can be distinguished in the corona micro-discharge development. The first one corresponds to the primary streamer propagation from the anode pin towards the cathode plane. The primary streamer propagates a luminous spot (called streamer head) which leaves the first narrow luminous trail shown on the streak picture of Fig. 3. During this first phase, the current rapidly increases as shown in Fig. 4 between 50ns and 75ns. The second phase

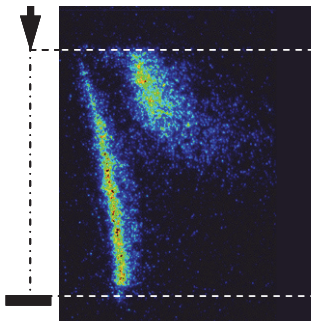


Fig. 3. Streak camera picture of a corona micro-discharge: Inter-electrode distance = 7mm, pin radius = 20 μm , dry air, atmospheric pressure, DC voltage magnitude = 8.2kV

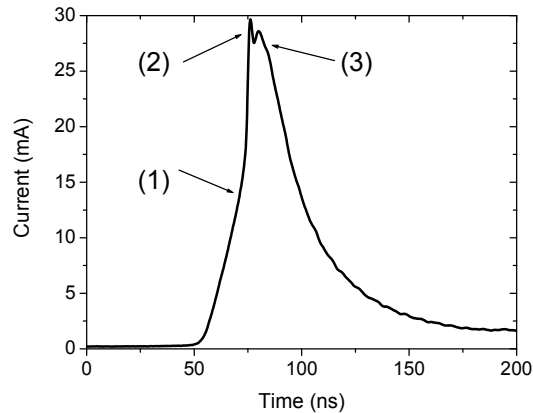


Fig. 4. Instantaneous micro-discharge current (inter-electrode distance = 7mm, pin radius = 20 μm , dry air, atmospheric pressure, DC voltage magnitude = 8.2kV)

corresponds to the arrival of the primary streamer at the cathode. It is associated to both the sudden increase of the current pulse at around 75ns (see Fig. 4) and the first current peak. In the present experimental conditions, the current pulse magnitude reaches a maximum of 30mA. On the current curve of Fig. 4, we also observe that the primary streamer needs about 25ns to cross the inter electrode gap and to reach the cathode plane 7mm underneath the pin. Thereby, the mean primary streamer velocity can be estimated of about $3 \times 10^7 \text{cm s}^{-1}$. We also observe in Fig. 3 the development of a secondary streamer (Sigmond, 1984) starting from the point when the primary streamer arrives at the cathode plane. The associated light emission is more diffuse on the streak picture because the radiative species are distributed along the pre-ionized channel. The development and propagation of the secondary streamer induce a second current peak (see Fig. 4). Finally, each current pulse is characterised by the propagation of primary and secondary streamers which in turn create the thin ionized channels of the micro-discharge shown in Fig. 2c.

2.3 Positive corona micro-discharge under pulsed voltage condition

The morphology of micro-discharges under pulse voltage condition is quite different from the case of DC voltage condition (van Veldhuizen & Rutgers, 2002, Abahazem et al. 2008). However, we will see at the end of the present section the correspondence between both regimes using a large voltage pulse width. Fig. 5 shows a sample of a high voltage pulse applied on the pin of a pin-to-plane corona reactor and the resulting measured current pulse. The pulse voltage width is first chosen in order to obtain only one micro-discharge per pulse. The experimental conditions are very similar to those used for the DC voltage study described in previous section 2.2. In Fig. 5, the two current peaks superposed with the increasing and decreasing fronts of the pulse voltage are two capacitive current pulses generated by the equivalent capacitance of the pin-to-plane electrode configuration. The micro-discharge current pulse is positioned at time $t=0\text{ns}$ in Fig. 5. A detailed description of this peculiar current pulse can be seen in Fig. 6. A rapid comparison with the DC current pulse in Fig. 4 indicates that the current pulse magnitude under pulse voltage condition is much higher ($\sim 175\text{mA}$) than in the DC voltage case ($\sim 30\text{mA}$). In fact, the ICCD time

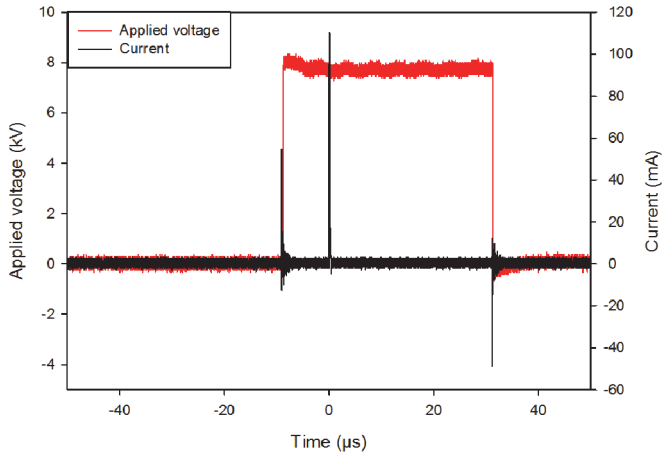


Fig. 5. Instantaneous measured current for pulsed voltage conditions: Maximum voltage magnitude=8kV, pulse voltage width=40 μ s, inter-electrode distance=8mm, pin radius=25 μ m, dry air at atmospheric pressure.

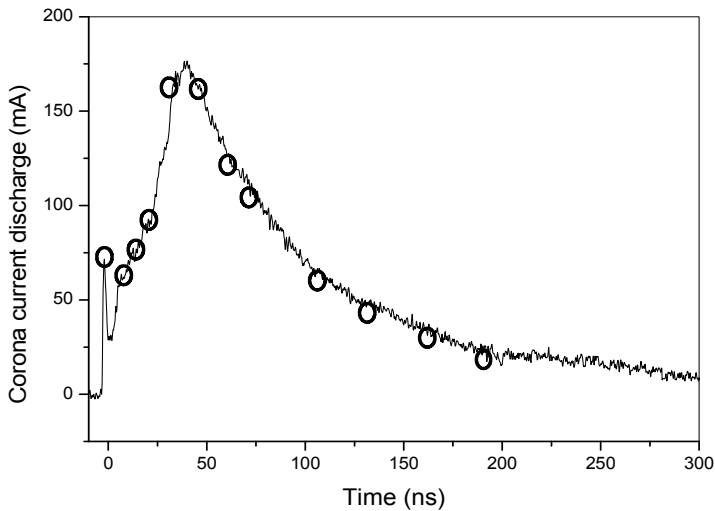


Fig. 6. Instantaneous corona current for pulsed voltage conditions: Maximum voltage magnitude=8kV, pulse voltage width=40 μ s, inter-electrode distance=8mm, pin radius=25 μ m, dry air at atmospheric pressure.

integrated picture of Fig. 7 clearly shows that there are several streamers starting from the pin towards the plane. This branching mechanism occurs in pulsed voltage conditions and therefore gives a higher discharge current than in the case of DC voltage.

The evolution of the corona current in Fig. 6 is characterized by a first peak of about 70mA with a short duration (around 4ns) corresponding to the discharge ignition due to the

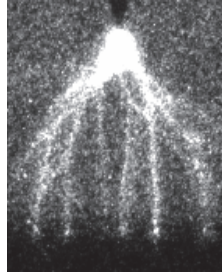


Fig. 7. Time integrated picture of corona discharge in dry air at atmospheric pressure for a time exposure of 10ms: Maximum voltage magnitude=8kV, pulse voltage width=40 μ s, inter-electrode distance=8mm and pin radius=25 μ m.

intense ionization processes generated by the high geometric electric field near the pin. This phenomenon can be seen in the first picture of Fig. 8 which shows an intensive spot light around the pin. After this first current peak, as soon as the electron avalanches reach a critical size, the accumulated charge space splits into several streamer heads that begin to propagate towards the cathode (see Fig. 8). During this primary streamer propagation, the corona current begins to steeply increase up to reach a peak value of about 175mA at the streamers arrival at the cathode for a time around 50ns (see Fig. 6). The streamer branches arrive separately at the cathode with an average propagation velocity of about 2.7×10^7 cm.s⁻¹. Above this instant, the corona current peak, after a first decrease due to transition between displacement and conduction currents, slows down during a short duration (around 70ns) corresponding to the secondary streamer propagation. This is then followed by a slower and monotonic fall of the corona current corresponding to the relaxation time that lasts above the 300ns displayed in the time axis of Fig. 6.

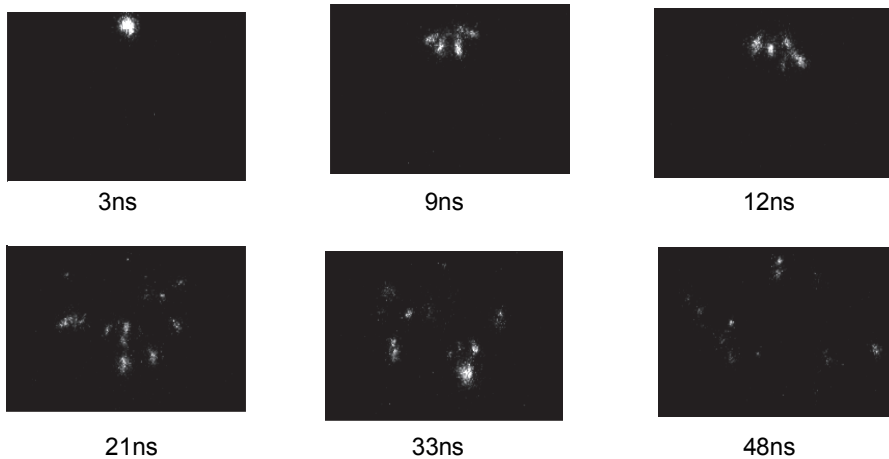


Fig. 8. Time resolved corona discharge pictures at different instants for dry air at atmospheric pressure: Maximum voltage magnitude=8kV, pulse voltage width=40 μ s, inter-electrode distance=8mm and pin radius=25 μ m, exposure time = 3ns, reference intensity image=21ns

To summarize, the voltage pulsed corona micro-discharges are characterized by a streamer branching structure and the propagation of multiple primary and secondary streamers. Relations between pulsed and DC voltage conditions can be pointed out using a large width voltage pulse. In this case, several micro-discharges are able to cross the inter-electrode gap during a single voltage pulse. Fig. 9 shows the morphology of the first the 18 corona micro-discharges generated between a pin and a plane using a high voltage pulse of 20ms of duration.

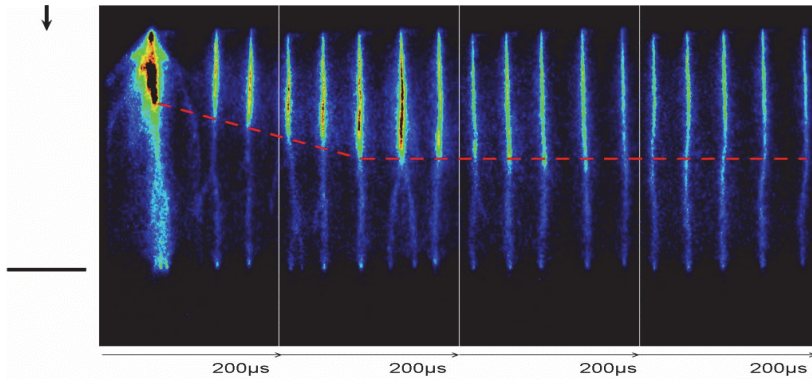


Fig. 9. Streak pictures of the successive corona micro-discharges induced in dry air by a pulse voltage of 20 ms duration and 7.2 kV magnitude (Abahazem et al. 2008).

The branching phenomenon is clearly observed in the first corona micro-discharge with the simultaneous development of a high number of filaments (see the first corona micro-discharge in Fig. 9). Then, during about $400\mu\text{s}$, the following discharges present a trunk expansion (shown by the red line in Fig. 9) in front of which a low number of filaments develop. A complete mono-filament structure appears after tens of discharges. Their characteristics are the same as those observed under DC high voltage condition. Thus, the more luminous trails in the discharge pictures of Fig. 9 correspond in fact to the development of the secondary streamers which extend gradually from the point towards the plane. Therefore, the formation of the mono-filament structure can be explained as a result of complex thermal and kinetics memory effects induced in the secondary streamer between each successive discharge.

2.4 Induced neutral gas perturbations

Even if micro-discharges are non thermal plasmas, their propagation can affect the neutral background gas (Eichwald et al. 1997, Ono & Oda b, 2004, Batina et al, 2002). In all cases, the micro-discharges modify the chemical composition of the medium (Kossyi et al. 1992, Eichwald et al. 2002, Dorai & Kushner 2003). In fact, the streamer heads propagate high energetic electrons that create radicals, dissociated, excited and ionized species by collision with the main molecule of the gas. Indeed, we have to keep in mind the low proportion of electrons and more generally of charged particles present in non-thermal plasma. At atmospheric pressure, and in the case of corona micro-discharge, we have about one million of neutral particles surrounding every charged species. Therefore, the collisions charged-neutral particles are predominant. During the discharge phase (which is associated to the

current pulse), the radical and excited species are created inside the micro-discharge volume. But during the post-discharge phase (i.e. between two successive current pulses) these active species react with the other molecules and atoms and diffuse in the whole reactor volume. If a gas flow exists, they are also transported by the convective phenomena. However, convective transport can also be induced by the micro-discharges themselves. Indeed, the momentum transfers between heavy charged particles and background gas are able to induce the so called “electric wind”. The random elastic collisions between charged and neutral particles directly increase the gas thermal energy. Furthermore, the inelastic processes modify the internal energy of some molecules thus leading to rotational, vibrational and electronic excitations, ionisation and also dissociation of molecular gases. After a certain time, the major part of these internal energy components relaxes into random thermal energy. However, during the lifetime of micro-discharges (some hundred of nanoseconds), only a fraction of this energy, which in fact corresponds mainly to the rotational energy and electronic energy of the radiative excited states, relaxes into thermal form. The other fraction of that energy, which is essentially energy of vibrational excitation, relaxes more slowly (after 10^{-5} s up to 10^{-4} s). The thermal shock during the discharge phase can induce pressure waves and a diminution of the gas density and the vibrational energy relaxation can increase the mean gas temperature (Eichwald et al. 1997). All these complex phenomena induce memory effects between each successive micro-discharge. In fact, the modification of the chemical composition of the gas can favour stepwise ionisation with the pre-excited molecule (like metastable and vibrational excited species), the gas density modification influences all the discharge parameters which are function of the reduced electric field E/N (E being the total electric field and N the background gas density) and the three body reaction that are also function of the gas density. Furthermore, the local temperature increase also modifies the gas reactivity because the efficiency of some reactions depends on the gas temperature following Arrhenius law. Therefore, the complete simulation of micro-discharges has to take into account all these complex phenomena of discharge and gas dynamics.

2.5 The complete micro-discharge model in the hydrodynamics approximation

The complete simulation of the discharge reactor, in complement to experimental studies can lead to a better understanding of the physico-chemical activity triggered during micro-discharge development and relaxation. Nowadays, in order to take into account the complex energetic, hydrodynamics and chemical phenomena that can influence the corona plasma process, the full simulation of the non thermal plasma reactor can be undertaken by coupling the following models:

- The external electric circuit model,
- the electro-hydrodynamics model,
- the background gas hydrodynamics model including the vibrational excited state evolution,
- the chemical kinetics model,
- and the basic data model which gives the input data for the whole previous models.

Each model gives specific information to the others. For example, the electro-hydrodynamics model gives the morphology of the micro-discharge, the electron density and energy as well as the energy dissipated in the ionized channel by the main charged-neutral elastic and inelastic collision processes. This information is coupled with the external

electric circuit model to calculate the micro-discharge impedance needed to follow the inter-electrode voltage evolution. On the other hand, the calculated dissipated energy and momentum transfer are included as source terms in the background gas model in order to simulate the induced hydrodynamics phenomena like electric wind, pressure wave propagation, neutral gas temperature increase, etc. The neutral gas hydrodynamics influences both the discharge dynamics and the chemical kinetics results. For example, the charged transport coefficients depend on the neutral gas density and some main chemical reactions involving neutral species (like the three body reactions) are very dependant on both the gas temperature and density. Finally, the basic data models (Yousfi & Benabdessadok, 1996, Bekstein et al. 2008, Yousfi et al. 1998, Nelson et al. 2003) give the necessary parameters (such as the convective and diffusive charged and neutral transport coefficients, the charged-neutral and neutral-neutral chemical reaction coefficients, the fraction of the energy transferred to the gas from the elastic and inelastic processes, among others) needed to close the total equation systems.

The electro-hydrodynamics model is an approximation of a more rigorous model. The kinetic description based on Boltzmann equations for the charged particles is probably the more rigorous theoretical approach. However the main drawback of the kinetics approach is linked to the treatment of the high number of electrons coming from ionization processes which involves huge computation times especially at atmospheric pressure. Therefore, the classical mathematical model used for solving the micro-discharge dynamics is the macroscopic fluid one also called the hydrodynamics electric model. Up to now, the most commonly used fluid model is the hydrodynamics first order model which involves the first two moments of Boltzmann equation (i.e the density and the momentum transfer conservation equation) for each charged specie coupled with Poisson equation for the space charged electric field calculation (Eichwald et al. 1996). In all cases, the momentum equation can be simplified into the classical drift-diffusion approximation. The obtained system of hydrodynamics equations is then closed by the local electric field approximation which assumes that the transport and reaction coefficients of charged particles depend only on the local reduced electric field E/N . The hydrodynamics approximation is valid as long as the relaxation time for achieving a steady state electron energy distribution function is short compared to the characteristic time of the discharge development. At atmospheric pressure and because of the high number of collisions, the momentum and energy equilibrium times are generally small compared to any macroscopic scale variations of the system. In the hydrodynamics approximation, the coupled set of equations that govern the micro-discharge evolution is the following:

$$\frac{\partial n_c}{\partial t} + \vec{\nabla} \cdot n_c \vec{v}_c = S_c \quad \forall c \quad (1)$$

$$n_c \vec{v}_c = \mu_c \vec{E} - \vec{D}_c \cdot \vec{\nabla} n_c \quad \forall c \quad (2)$$

$$\epsilon_0 \Delta V = -\sum_c q_c n_c \quad (3)$$

$$\vec{E} = -\vec{\nabla} V \quad (4)$$

These first four equations allow to simulate the behaviour of each charge particle “c” in the micro-discharge (like for example e, N₂⁺, O₂⁺, O₄⁺, O⁻, O₂⁻, among others). n_c , \vec{v}_c , S_c , μ_c , \vec{D}_c , q_c are respectively the density, the velocity, the source term, the mobility, the diffusive tensor and the charge of each charge specie “c” involved in the micro-discharge. V and \vec{E} are the potential and the total electric field. The source terms S_c represent for each charge specie the chemical processes (like ionization, recombination, attachment, dissociative attachment, among others) as well as the secondary emission processes (like photo-ionisation and photo-emission from the walls (Kulikovsky, 2000, Hallac et al. 2003, Segur et al. 2006)). The transport equations of charged particles are not only strongly coupled through the plasma reactivity but also through the potential and electric field equations. Indeed, in equation (3) the potential and therefore the electric field in equation (4) are directly dependant on the variation of the density of the charged species, obtained from solution of equations (1)-(2) requiring the knowledge of transport and reaction coefficients that in turn have a direct dependence on the local reduced electric field E/N. Therefore the simulation of micro-discharge dynamics needs fast and accurate numerical solver to calculate the electric field at each time step (especially in regions with high field gradients like near the streamer head and the electrode pin) and also to propagate high density shock wave.

Even if the solution of the first order hydrodynamics model allows a better understanding of the complex phenomena that govern the dynamics of charged particles in micro-discharges, the experimental investigations clearly show that the micro-discharges have an influence on the gas dynamics that can in turn modify the micro-discharge characteristics. It is therefore necessary to couple the electro-hydrodynamics model with the classical Navier-Stokes equations of a compressible and reactive background neutral gas coupled with the conservation equation of excited vibrational energy (Byron et al. 1960, Eichwald et al. 1997).

$$\frac{\partial \rho m_i}{\partial t} + \vec{\nabla} \cdot \rho m_i \vec{v} + \vec{\nabla} \cdot \vec{J}_i = S_i + S_{ic} \quad \forall i \quad (5)$$

$$\frac{\partial \rho}{\partial t} + \vec{\nabla} \cdot \rho \vec{v} = 0 \quad (6)$$

$$\frac{\partial \rho \bar{v}}{\partial t} + \vec{\nabla} \cdot \rho \bar{v} \vec{v} = -\vec{\nabla} P - \vec{\nabla} \cdot \vec{\tau} + \vec{S}_{qm} \quad (7)$$

$$\frac{\partial \rho h}{\partial t} + \vec{\nabla} \cdot \rho h \vec{v} = \vec{\nabla} \cdot (k \vec{\nabla} T) + \frac{\partial P}{\partial t} + \vec{v} \cdot \vec{\nabla} P + \vec{\tau} : \vec{\nabla} \vec{v} - \vec{\nabla} \cdot \sum_i \vec{J}_i h_i + S_h + \frac{\mathcal{E}_v}{\tau_v} \quad (8)$$

$$\frac{\partial \mathcal{E}_v}{\partial t} + \vec{\nabla} \cdot \mathcal{E}_v \vec{v} = S_v - \frac{\mathcal{E}_v}{\tau_v} \quad (9)$$

The set of equations (5) to (9) are used to simulate the neutral gas behavior and to follow each neutral chemical species “i” (like N, O, O₃, NO₂, NO, N₂ (A³Σ_u⁺), N₂ (a¹Σ_u⁻), O₂ (a¹Δg), among others) that are created during the micro-discharge phase. In equations (5) to (9), ρ is the mass density of the background neutral gas, \vec{v} the gas velocity, P the static pressure and

\Rightarrow τ the stress tensor. For each chemical species "i", m_i is the mass fraction, \bar{j}_i the diffusive flux due to concentration and thermal gradients, S_i the net rate of production per unit volume (due to chemical reactions between neutral species) and S_{ic} simulates the creation of new neutral active species during the discharge phase by electron or ion impacts with the main molecules of the gas. h is the static enthalpy, T the temperature, k the thermal conductivity and ε_v the vibrational energy. S_h and S_v are the fraction of the total electron power $\bar{j} \cdot \vec{E}$ transferred during the discharge phase into thermal and vibrational energy. It is generally assumed that the translational, rotational and electronic excitation energies relax quasi immediately into thermal form and that the vibrational energy stored during the discharge phases relaxes after a mean delay time τ_v of some tens of micro-seconds. \bar{S}_{qm} is the total momentum transferred from charged particles to the neutral ones. As already explained, all the discharge parameters (S_c , μ_c , \vec{D}_c , S_{ic} , \bar{S}_{qm} , S_h and S_v) are strongly dependent on the reduced electric field (E/N). Therefore the coupling of all the set of equations (1) to (9) for each charged and neutral chemical species will considerably enhance the complexity of the global hydrodynamics model. In fact, each gas density variation can directly affect the development of micro-discharges through the reduced electric field variation.

Finally, the modelling of complex phenomena occurring inside non-thermal reactor filled with complex gas mixtures needs the knowledge of the electron, the ion and the neutral transport and reaction coefficients. The charged and neutral particles kinetics model is therefore one of the method in complement to the experimental one that can be used to calculate or complete the set of basic data. Concerning the charged particles, the more appropriate method to obtain the unknown swarm data is to use a microscopic approach (e.g. a Boltzmann's equation solution for the electron data and a Monte Carlo simulation for the ion data) based on collision cross sections (Yousfi & Benabdessadok, 1996, Bekstein et al. 2008, Yousfi et al. 1998, Nelson et al. 2003). On the other hand the most commonly used method to calculate the neutral swarm data in a gas mixture is the use of the classical kinetic theory of neutral gas mixture (Hirschfelder et al. 1954). The macroscopic charged particles swarm data are given over a large range of either the reduced electric field or the mean electron energy. The whole set of data includes:

- The macroscopic transport coefficients like mobility, longitudinal and transversal diffusion coefficients,
- the reaction coefficients like ionization, attachment, dissociation, radiative or metastable electronic excitation coefficients,
- the mean electron energy exchange frequencies of the elastic, inelastic and super-elastic processes,
- and the mean electron momentum exchange frequency (if the classical drift diffusion approximation is not assumed valid)

The calculation of the scalar (e.g. ionization or attachment frequencies), vectorial (drift velocity), and tensorial (diffusion coefficients) hydrodynamics electron and ion swarm parameters in a gas mixture, needs the knowledge of the elastic and inelastic electron-molecule and ion-molecule set of cross sections for each pure gas composing the mixture. Each collision cross section set involves the most important collision processes that either

affect the charged species transport coefficients or are needed to follow the charged species chemical kinetics and energy or momentum exchange. For example, in order to calculate the macroscopic electron swarm parameters in water vapor, 21 collision cross sections must be known involving the rotational, the vibrational and the electronic excitation processes as well as the ionization, the dissociative attachment and the superelastic processes.

One of the main difficulties is to validate for each pure gas that compose the mixture the chosen set of cross sections. To do that, a first reliable set of electron-molecule and ion-molecule cross section for each individual neutral molecule in the gas mixture must be known. Then, in order to obtain the complete and coherent set of cross sections, it is necessary to adjust this first set of cross sections so as to fit experimental macroscopic coefficients with the calculated ones estimated from either a Boltzmann's equation solution or a Monte Carlo simulation. The obtained solution is certainly not unique but as the comparisons concern several kinds of swarm macroscopic parameters having different dependencies on cross sections (ionization or attachment coefficient, drift velocity, transverse or longitudinal diffusion coefficient) over a wide range of reduced electric field or mean electron energy, most of the incoherent solutions are rejected. Finally, when the sets of cross section are selected for each pure gas, they can be used to calculate with a Boltzmann's equation solution or a Monte Carlo simulation the macroscopic charged species transport and reaction parameters whatever the proportion of the pure gas in the background gas mixture.

2.6 Summary

Micro-discharges are characterized by the development of primary and secondary streamers. As a function of the high voltage applied on the small curvature electrode (DC or pulse), the micro-discharges show either a mono-filament or a large branching structure. The passage from multi-filaments to mono-filament structure can be observed if a sufficiently large high voltage pulse is applied. The transition can be explained through the memory effects accumulated during the previous discharge. The primary streamers propagate fast ionization waves characterized by streamer heads in which the electric field is high enough to generate high energetic electrons like in an electron gun. The streamer head propagates a high charge quantity toward the inter-electrode gap. The micro-plasmas are generated behind the streamer heads. They are small conductive channels that connect the streamer head to the electrode stressed by the high voltage. The primary streamers are then followed by a secondary streamer which is characterized by an electric field extension that ensures the transition between the displacement current and the conductive one when the primary streamer arrives on the cathode. Both primary and secondary streamers create radicals and excited species by electron-molecule impacts. The elastic and inelastic energy transfers generate a chemical activity, a thermal energy increase of the gas and a neutral gas dynamics. To better understand all these complex phenomena, a hydrodynamics model can be used based on conservation equations of charged and neutral particles coupled to Poisson equation for the electric field calculation.

3. Chemical and hydrodynamics activation of gases using corona micro-discharge

3.1 Introduction

During the past two decades several studies have shown that non-thermal plasmas reactor working in ambient air are very efficient sources of active species like charged particles,

radicals and excited species. In fact, and as already explained in the previous sections, in the non-thermal plasma reactor, the majority of the injected electrical energy goes into the generation of energetic electrons, rather than into gas heating. The energy in the micro-plasma is thus directed preferentially to electron-impact dissociation, excitation and ionization of the background gas to generate active species that, in turn, induce the chemical activation of the medium. As a consequence, the non-thermal plasma reactors at atmospheric pressure are used in many applications such as flue gas pollution control (Fridman et al., 2005, Urashima et Chang, 2010), ozone production (Ono & Oda b, 2004), surface decontamination (Clement et al., 2001, Foest et al., 2005) and biomedical field (Laroussi, 2002, Villeger et al., 2008, Sarrette et al., 2010). For many applications, particularly in the removal of air pollutants, decontamination or medicine field, the non-thermal plasma approach would be most appropriate because of its energy selectivity and its capability for simultaneous treatment of pollutants, bacteria or cells for example.

In micro-discharges the active species are created by energetic electrons during the primary and the secondary streamer propagation that last some hundred of nanoseconds. Despite these very fast phenomena, the energy transferred to the gas can initiate shock waves starting from the stressed high voltage electrodes. Furthermore, a part of the electronic energy is stored in the vibrational energy that relaxes in thermal form after some tens of microseconds. Anyway, it is worth to notice, that all the initial energy (chemical, thermal, among others) is transferred inside a very thin discharge filament i.e. in a very small volume compared with the volume of the plasma reactor. Therefore, the efficiency of the processes is correlated to the radical production efficiency during the discharge phase, the number of micro-discharges that cross the inter-electrode gap, the repetition frequency of the discharge and how the radicals are diffused and transported from the micro-discharge towards the whole reactor volume.

In the following sections, the discharge and the post-discharge phase are simulated using the hydrodynamics models presented in section 2.5 in the case of a DC positive pin-to-plan corona reactor in dry air at atmospheric pressure.

3.2 Discharge phase simulation

The simulation conditions are described in detail in reference (Eichwald et al. 2008) as well as the used numerical methods and boundary conditions. To summarize, a DC high voltage of 7.2kV is applied on the pin of a pin-to-plane reactor filled with dry air at atmospheric pressure. The inter-electrode gap is of 7mm, the pin radius is equal to 25 μ m and photo-ionisation phenomenon is taken into account in the simulation. Results in Fig. 10 and 11 are obtained by coupling equations (1) to (4) for electrons, two negative ions (O^- and O_2^-), four positive ions (N_2^+ , O_2^+ , N^+ and O^+) and two radical atoms (O , N) reacting following 10 selected reactions. Because of the time scale of the discharge phase (some hundred of nanoseconds), the radical atoms and the main neutral molecules (N_2 and O_2) are supposed to remain static during the discharge phase simulation. Fig. 10 shows the reduced electric field (E/N) expressed in Td (1Td=10⁻²¹ Vm² so that 500Td at atmospheric pressure is equivalent to an electric field of 12MVm⁻¹). When the high voltage is applied to the pin, some seed electrons are accelerated in the high geometric electric field around the pin. A luminous spot is observed experimentally near the pin thus indicating the formation of excited species due to a high electronic energy. One can notice that the electrons move towards the pin. Furthermore, the electrons gain sufficient energy to perform electronic

avalanches and a plasma spot is created just around the pin. The plasma is a quasi neutral electric gas in which the quantity of negative and positive species is quasi similar. Nevertheless, as the mobility of electrons is much higher than those of positive ions, the electric neutrality of the initial plasma spot is perturbed just in front of the pin. Indeed, the electrons are absorbed by the positive anodic pin while the positive ions remain quasi static due to their mass inertia. A positive charged space is formed and the electric field is no more at his maximum on the pin but just in front of it. This situation can be seen at time $t=20\text{ns}$ in the first picture of Fig. 10.

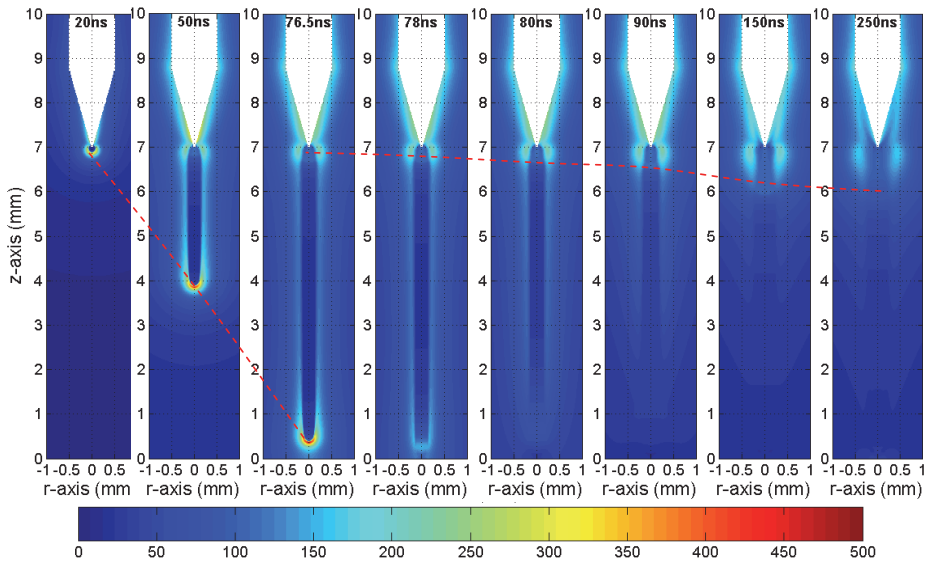


Fig. 10. Reduced electric field profile ($500\text{Td}=12\text{MVm}^{-1}$) in function of time

A streamer head is created that propagates from the pin towards the plane. This streamer head can be interpreted as the propagation of a positive charge space shock wave. At each time of its propagation, new seed electrons are created in front of the streamer head by photo-ionisation processes. These electrons are accelerated in the high electric field and their energy is high enough to ionize, dissociate and excite the main molecules of the gas. When the electrons have crossed the streamer head they drift towards the pin inside a small conductive plasma channel that connects the streamer head to the pin. A micro-plasma is formed behind the streamer head and is constricted by a cylinder of space charged electric field. A quasi-homogeneous small value of electric field is maintained inside the micro-plasma in order to allow the drift of electrons from the streamer head to the pin that ensures the continuity of the total current density. The time laps needed for the streamer head to cross the inter-electrode gap is associated with the primary streamer propagation of the micro-discharge phase. The streamer head propagates a charge quantity which is absorbed by the cathode plane as soon as it arrives on the cathode plane. It results to the first current peak observed in Fig. 4 for a high voltage DC condition. The first red dashed curve in Fig. 10 follows the trail left by the high electric field of the streamer head. Its shape corresponds to the luminous trail observed by streak camera shown in Fig. 3. When the primary streamer

arrives at the cathode plane, a secondary streamer starts its propagation from the pin. The secondary streamer is an electric field plateau extension of value of about 100Td. This extension ensures the continuity of the total current when the total charge space transported by the streamer head is absorbed at the cathode (Eichwald et al. 2008, Bastien & Marode, 1985). The second red dashed curve follows the plateau extension. The evolution of the luminous trail left by the secondary streamer shown in Fig. 3 is due to the excited species created by the energetic electrons inside the secondary streamer expansion. Fig. 11 shows the radical O density after 150ns. The simulation indicates that about 70% of the radical O is produced inside the secondary streamer by dissociative collisions between electrons and O₂ molecules in reaction $e + O_2 \rightarrow O + O$. The concentration of O radical is also high near the cathode plane due to a higher electric field magnitude inside the streamer head when it reaches the cathode.

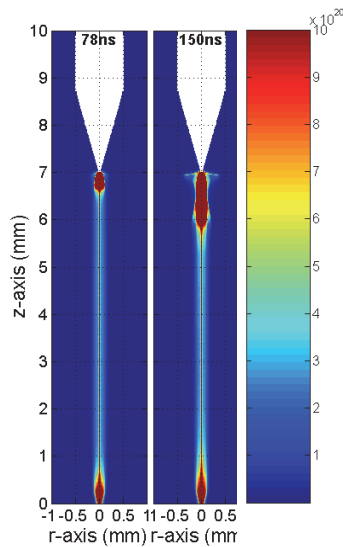


Fig. 11. O radical profile (m^{-3})

The effect on the neutral gas dynamics induced by the micro-discharge propagation is shown in Fig. 12 and 13. Fig. 12 shows the temperature profile of the background neutral gas at $0.1\mu s$ ($=100ns$) and $0.3\mu s$ ($=300ns$). Fig. 13 shows the pressure profile from $0.1\mu s$ to $4\mu s$. The gas temperature just on the pin reaches some thousands of Kelvin but a mean value of about $700^\circ K$ is obtained around the point. This value is coherent with experimental results obtained under very similar condition (Spyrou et al., 1992). The thermal shock creates high pressure gradients (see Fig. 13 at $0.1\mu s$) and induces the gas expansion (see Fig. 13). Due to the inertia principle, the mass density near the point decreases more gradually in a time scale greater than the temperature increase. The gas expansion is characterised by a cylindrical and a spherical shock wave (see Fig. 13 from 0.3 to $0.9\mu s$). Indeed, the initial pressure gradients (which induced the gas motion) follow the temperature ones which are constricted along the axis and inside the micro-plasma channel. We therefore observe a cylindrical pressure wave (represented by two vertical lines in the flat pressure mappings of Fig. 13) that propagates from the streamer axis towards the whole domain. The complex

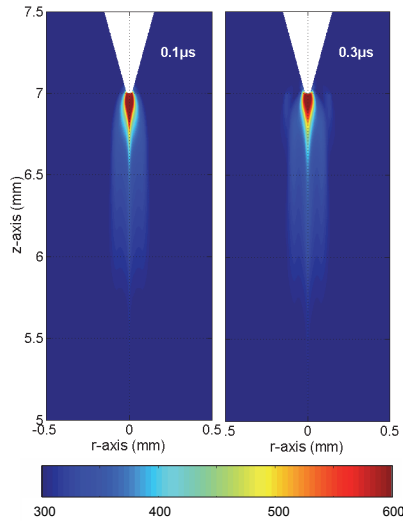


Fig. 12. Gas temperature ($^{\circ}\text{K}$) profile near the point

structure of the pressure gradients near the point induces a spherical pressure wave superimposed to the cylindrical one. Such kind of spherical pressure waves were already observed experimentally (Ono & Oda b, 2004) using the laser Schlieren method. Furthermore, the simulation shows that the spherical shock wave propagates at the speed of sound as in the case of experimental work (Ono & Oda b, 2004).

In this kind of simulation the effects of temperature and gas density variations on the streamer development are not taken into account. However, it should be in further works because if the gas density varies it will modify the reduced electric field (E/N) and therefore the behaviour of the charged particles whose properties (like mobility, ionisation frequency,...) completely depend on the reduced electric field. Nevertheless, the previous results are able to give the initial profiles of all the source terms needed to simulate the post-discharge phase evolution.

3.3 Post-discharge phase simulation

The discharge phase simulation gives very clear information on the gas dynamics and the spatio-temporal evolution of each active species of the background gas mixture. However, the time and space scales between the discharge phase and the post-discharge phase are completely different. Indeed, the micro-discharge generated micro-plasma in some hundred of nanoseconds while post-discharge phase must be considered with centimetre scale and milliseconds time laps. A complete simulation of both coupled phenomena for multi-pin reactor needs therefore adaptive meshes from micrometer to centimetre scale and also adaptive time scale from picoseconds (in order to follow the nano-scale discharge phenomena) up to fraction of milliseconds. This means a large number of discrete spatial cells and a huge computing time. In order to overcome these difficulties, one can assume that the effects of the discharges on the background gas can be simulated by locally injected inside the micro-discharge volumes and only during the discharge phase, average source terms estimated from the complete discharge phase model.

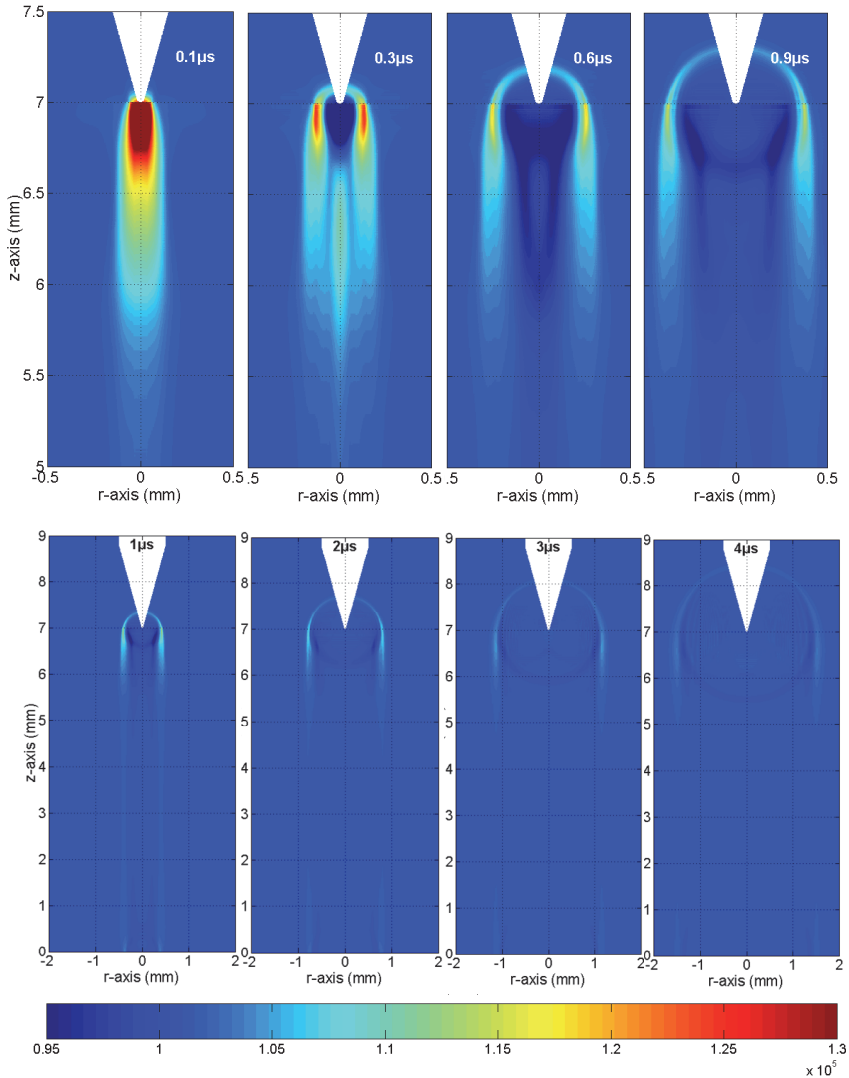


Fig. 13. Pressure wave (Pa) near the point (from 0.1 to 0.9 μs) and in the whole domain (from 1 to 4 μs)

As an example, let us suppose the multi-pin reactor described in Fig. 14. The domain is divided with square structured meshes of $50\mu\text{m}\times 50\mu\text{m}$ size. A DC high voltage of 7.2kV is applied on the pins. During each discharge phase, monofilament micro-discharges are created between each pin and the plane with a natural frequency of 10kHz. The micro-discharges have an effective diameter of $50\mu\text{m}$ which correspond to the size of the chosen cells. Therefore, it is possible to inject in the cells located between each pin and the plane specific profiles of active source species and energy that will correspond the micro-discharge effects.

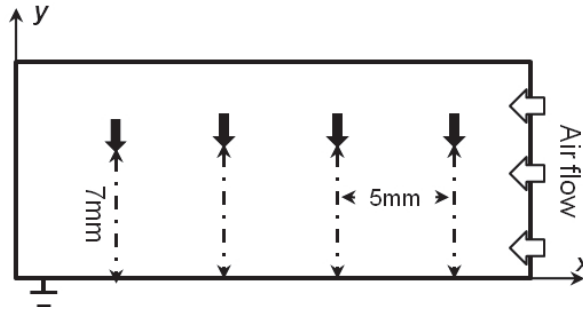


Fig. 14. 2D Cartesian simulation domain of the multi-pin to plane corona discharge reactor.

As an example, consider equation (5) of section 2.5 applied to O radical atoms ($i''=O$).

$$\frac{\partial \rho m_O}{\partial t} + \vec{\nabla} \cdot \rho m_O \vec{v} + \vec{\nabla} \cdot \vec{J}_O = S_O + S_{O_c}$$

The challenge is to correctly estimate the source term S_{O_c} inside the volume of each micro-discharge. As the radial extension of the micro-discharges is equal to the cell size, the source term between each pin and the plane depends only on variable z . The average source term responsible of the creation of O radical during the discharge phase is therefore expressed as follow:

$$S_{O_c}(z) = \frac{1}{r_d} \frac{1}{t_d} \int_0^{r_d} \int_0^{t_d} s_{O_c}(t, r, z) dt dr \quad (10)$$

t_d is the effective micro-discharge duration, r_d the effective micro-discharge radius and $s_{O_c}(t, r, z)$ the source terms ($m^{-3}s^{-1}$) of radical production during the discharge phase (i.e. $k(E/N)n_e n_{O_2}$ for reaction $e + O_2 \rightarrow O + O$ where $k(E/N)$ is the corresponding reaction coefficient). All the data in equation (10) come from the complete simulation of the discharge phase. In the present simulation conditions, specific source terms are calculated for 5 actives species that are created during the discharge phase ($N_2(A^3\Sigma_u^+)$, $N_2(a^1\Sigma_u^-)$, $O_2(a^1\Delta_g)$, N and O).

The energy source terms in equations (8) and (9) are estimated using equations (11) and (12):

$$S_h(z) = \rho C_p \frac{1}{r_d} \frac{1}{t_p^2} \int_0^{r_d} \int_0^{t_p} T(t_p, r, z) dt dr \quad (11)$$

$$S_v(z) = \frac{1}{r_d} \frac{1}{t_d} \int_0^{r_d} \int_0^{t_d} f_v \vec{j} \cdot \vec{E} dt dr \quad (12)$$

In equation (12), $\vec{j} \cdot \vec{E}$ is the total electron density power gained during the discharge phase and f_v the fraction of this power transferred into vibrational excitation state of background gas molecules. One can notice the specificity of equation (11) related with the estimation of the direct random energy activation of the gas. In this equation, t_p is the time scale of the pressure wave generation rather than the micro-discharge duration t_d . In fact, during the

post-discharge phase, the size of discrete cells is not sufficiently small to follow the gradients of pressure wave generated by thermal shock near the point (see Fig. 13). However, pressure waves transport a part of the stored thermal energy accumulated around each pin. From $0.1\mu\text{s}$ to $0.3\mu\text{s}$, the gas temperature on the pins decreases from about 3000°K down to about 1200°K . After this time, the temperature variation in the micro-discharge volume is less affected by the gas dynamics. The diffusive phenomena become predominant. Therefore, taken into account the mean energy source term at time t_d will overestimate the temperature enhancement on the pins during the post-discharge phase simulation. As a consequence, the time t_p is chosen equal to 300ns i.e. after the pressure waves have left the micro-discharge volume.

As an example, Fig. 15 shows the temperature profile obtained at $t=t_p$ just after the first discharge phase. The results were obtained using the Fluent Software in the simulation conditions described in Fig. 14. As expected and just after the first discharge phase, the enhancement of the gas temperature is confined only inside the micro-plasma filaments located between each pin and the plane. The temperature profile along the inter-electrode gap is very similar to the one obtained by the complete discharge phase simulation (see Fig. 12). It is also the case for the active source terms species. Fig. 16 shows at time $t=t_d$, the axial profile of some active species that are created during the discharge phase. The curves of the discharge model represent the axial profile density averaged along the radial direction. In

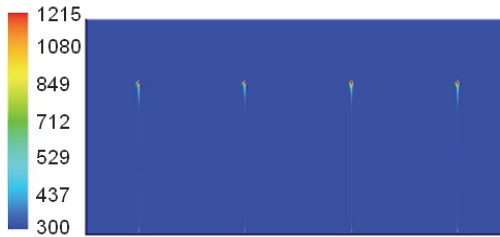


Fig. 15. Gas temperature profile after the first discharge phase at $t=t_p = 300\text{ns}$.

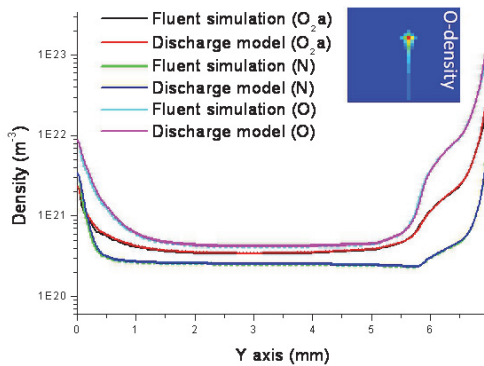


Fig. 16. Comparison of numerical solutions given by the completed discharge and Fluent models at $t_d=150\text{ ns}$ for O, N and O_2 ($\text{a}^1\Delta\text{g}$) densities. The zoom box shows, as an example, the O radical profile near a pin.

the case of the O radical, the density profile of Fig. 11 was averaged along the radial direction until $r_d=50\mu\text{m}$ and drawn in Fig. 16 with the magenta color. The light blue color curve represents the O radical profile obtained with the Fluent Software when the specific source term profile $S_{O_c}(z)$ is injected between a pin and the cathode plane in the simulation conditions of Fig. 14.

In the following results, the complete simulation of the successive discharge and post-discharge phases involves 10 neutral chemical species (N, O, O₃, NO₂, NO, O₂, N₂, N₂ ($A^3\Sigma_u^+$), N₂ ($a^1\Sigma_u^+$) and O₂ ($a^1\Delta_g$)) reacting following 24 selected chemical reactions. The pin electrodes are stressed by a DC high voltage of 7.2kV. Under these experimental conditions the current pulses appear each 0.1ms (i.e. with a repetition frequency of 10KHz). It means that the previous described source terms are injected every 0.1ms during laps time t_d or t_p and only locally inside the micro-plasma filament located between each pin and the plane. The lateral air flow is fixed with a neutral gas velocity of $5\text{m}\cdot\text{s}^{-1}$.

Pictures in Fig. 17 show the cartography of the temperature and of the ozone density after 1ms (i.e. after 10 discharge and post-discharge phases). One, two, three or four pins are stressed by the DC high voltage. Pictures (a) show that for the mono pin case, the lateral air flow and the memory effect of the previous ten discharges lead to a wreath shape of the space distribution of both the temperature and the ozone density.

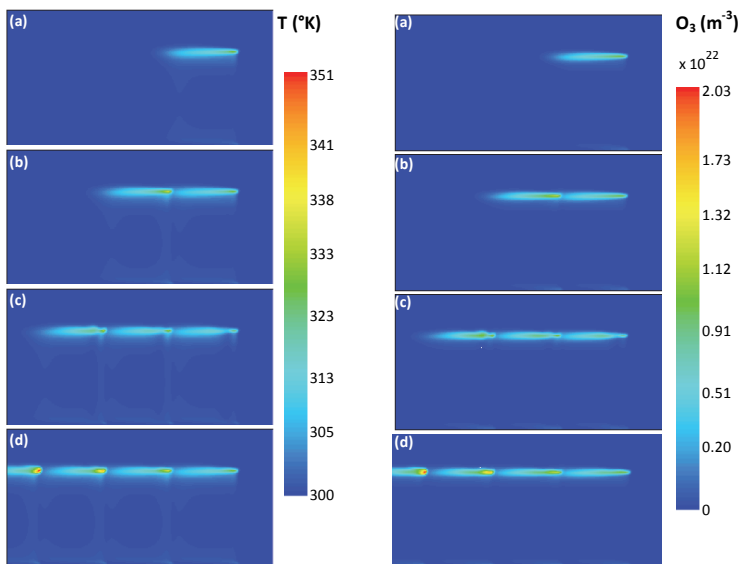


Fig. 17. Temperature and ozone density profile at 1ms i.e. after ten discharge and post-discharge phases. The number of high voltage pin is respectively (a) one, (b) two, (c) three and (d) four. The lateral air flow is $5\text{m}\cdot\text{s}^{-1}$.

The temperature and the ozone maps are very similar. Indeed, both radical and energy source terms are higher near the pin (i.e. inside the secondary streamer area expansion as it was shown in section 3.2). Furthermore, the production of ozone is obviously sensitive to the gas temperature diminution since it is mainly created by the three body reaction $O + O_2 + M \rightarrow O_3 + M$ (having a reaction rate inversely proportional to gas temperature).

For more than one pin, the temperature and ozone wreaths interact each other and their superposition induce locally a rise of both the gas temperature and ozone density (see Fig. 17). The local maximum of temperature is around 325K for one pin case and increases up to 350K for four anodic pins.

The average temperature in the whole computational domain remains quasi constant and the small variations show a linear behavior with the number of anodic pins. The same linear tendency is observed for the ozone production in Fig. 18. After 1ms, and for the four pins case, the mean total density inside the computational domain reaches $4 \times 10^{14} \text{ cm}^{-3}$.

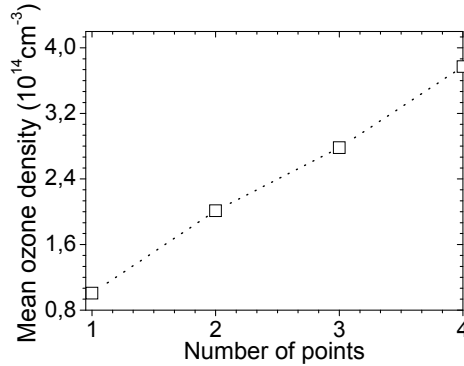


Fig. 18. Mean ozone density increase inside the computational domain of Fig. 14 as a function of the number of pins

3.4 Summary

The complete simulation of all the complex phenomena that are triggered by micro-discharges in atmospheric non thermal plasma was found to be possible not as usually done in the literature only for 0D geometry but also in multidimensional geometry. In DC voltage conditions, a specific first order electro-hydrodynamics model was used to follow the development of the primary and secondary streamers in mono pin-to-plane reactor. The simulation results reproduce qualitatively the experimental observations and are able to give a full description of micro-discharge phases. Further works, already undertaken in small dimensions or during the first instants of the micro-discharge development (Pancheshnyi 2005, Papageorgiou et al. 2011), have to be achieved in 3D simulation in order to describe the complex branching structure for pulsed voltage conditions. Nevertheless, the micro-discharge phase simulation gives specific information about the active species profiles and density magnitude as well as about the energy transferred to the background gas. All these parameters were introduced as initial source terms in a more complete hydrodynamics model of the post-discharge phase. The first obtained results show the ability of the Fluent software to solve the physico-chemical activity triggered by the micro-discharges.

4. Conclusion

The present chapter was devoted to the description of the hydrodynamics generated by corona micro-discharges at atmospheric pressure. Both experimental and simulation tools have to be exploited in order to better characterise the strongly coupled behaviour of micro-

discharges dynamics and background gas dynamics. The experimental devices have to be very sensitive and precise in order to capture the main characteristics of nanosecond phenomena located in very thin filaments of micro scale extension. However, the recent evolution of experimental devices (ICCD or streak camera, DC and pulsed high voltage supply, among others) allow to better understand the physics of the micro-discharge. Furthermore, recent simulation of the micro-discharges involving the discharge and post-discharge phase in multidimensional dimension was found to give precise information about the chemical and hydrodynamics activation of the background gas in an atmospheric non-thermal plasma reactor. These kinds of simulation results, coupled with experimental investigation, can be used in future works for the development of new design of plasma reactor very well adapted to the studied application either in the environmental field or biomedical one.

5. Acknowledgment

All the simulations were performed using the HPC resources from CALMIP (Grant 2011-[P1053] - www.calmip.cict.fr/spip/spip.php?rubrique90)

6. References

- Abahazem, A.; Merbahi, N.; Ducasse, O.; Eichwald, O. & Yousfi, M. (2008), Primary and secondary streamer dynamics in pulsed positive corona discharges, *IEEE Transactions on Plasma Science*, Vol. 36, No. 4, pp. 924-925
- Bastien, F. & Marode, E. (1985), Breakdown simulation of electronegative gases in non-uniform field, *Journal of Physics D: Applied Physics*, Vol. 18, pp. 377-393
- Batina, J.; Noel, F.; Lachaud, S.; Peyrous, R. & Loiseau, J. F. (2001) Hydrodynamical simulation of the electric wind in a cylindrical vessel with positive point-to-plane device, *Journal of Physics D: Applied Physics*, Vol. 34, pp. 1510-1524
- Bekstein, A.; Benhenni, M.; Yousfi, M.; Ducasse, O. & Eichwald, O. (2008), Ion swarm data of N_4^+ in N_2 , O_2 , and dry air for streamer dynamics simulation, *European Physics Journal Applied Physics*, Vol. 42, pp. 33-40
- Briels, T. M. P.; Kos J.; van Veldhuizen E. M. & Ebert, U. (2006), Circuit dependence of the diameter of pulsed positive streamers in air, *Journal of Physics D: Applied Physics*, Vol. 39, pp. 5201-5210
- Byron, R.; Stewart, W. E.; Lightfoot E. N. (1960) *Transport Phenomena*, John Wiley & Sons
- Clement, F.; Held, B.; Soulem N. & Spyrou N. (2001). Polystyrene thin films treatment under DC pulsed discharges conditions in nitrogen, *The European Physical Journal, Applied Physics*, Vol. 13, pp. 67-75
- Dubois, D.; Merbahi, N.; Eichwald, O.; Yousfi, M.; Ducasse, O. & Benhenni, M. (2007), Electrical analysis of DC positive corona discharge in air and N_2 , O_2 and CO_2 mixtures, *Journal of Applied Physics*, Vol. 101, Issue 5, pp. 053304-053304-9
- Dorai R. & Kushner M. (2003) Consequences of unburned hydrocarbons on microstreamer dynamics and chemistry during plasma remediation of NO_x using dielectric barrier discharges *Journal of Physics D: Applied Physics*, Vol. 36, pp. 1075-1083
- Eichwald, O.; Ducasse, O.; Merbahi, N.; Yousfi, M. & Dubois, D. (2006), Effect of order fluid models on flue gas streamer dynamics", *Journal of Physics D: Applied Physics*, Vol. 39, pp. 99-107

- Eichwald, O.; Yousfi M.; Hennad A. & Benabdessadok M. D. (1997) Coupling of chemical kinetics, gas dynamics, and charged particle kinetics models for the analysis of NO reduction from flue gases, *Journal of Applied Physics*, Vol. 82, No. 10, pp. 4781-4794
- Eichwald, O.; Ducasse, O.; Dubois, D.; Abahazem, A.; Merbahi, N.; Benhenni M. & Yousfi, M. (2008) Experimental analysis and modelling of positive streamer in air: towards an estimation of O and N radical production, *J. Phys. D: Appl. Phys.*, Vol. 41 234002 (11pp)
- Eichwald, O., Guntoro, N. A.; Yousfi, M. & Benhenni M. (2002) Chemical kinetics with electrical and gas dynamics modelization for NO_x removal in an air corona discharge *Journal of Physics D: Applied Physics*, Vol. 35, pp. 439-450
- Foest, R.; Kindel, E.; Ohl, A.; Stieber, M. & Weltmann, K. D. (2005) Non-thermal atmospheric pressure discharges for surface modification *Plasma Physics Controlled Fusion*, Vol. 47, B525-B536
- Fridman A.; Chirokov, A. & Gutsol, A. (2005), TOPICAL REVIEW, Non-thermal atmospheric pressure discharges, *Journal of Physics D: Applied Physics*, Vol. 38, R1-R24
- Hallac, A.; Georghiou, G. E. & Metaxas, A; C. (2003) Secondary emission effects on streamer branching in transient non-uniform short-gap discharges, *Journal Of Physics D: Applied Physics*, Vol. 36 pp. 2498-2509
- Hirschfelder, J. O.; Curtiss, F. E. and Bird R. B. (1954) *Molecular theory of gases and liquids*, Wiley, New York
- Kossyi, I. A. ; Yu Kostinsky, A. ; Matveyev A. A. & Silakov V. P., (1992), Kinetic scheme of the non equilibrium discharge in nitrogen-oxygen mixtures, *Plasma Sources Sciences and Technologies*, Vol.1, pp. 207-220
- Kulikovskiy, A. A. (2000), The role of photoionisation in positive streamer dynamics, *Journal of Physics D: Applied Physics*, Vol. 33, pp. 1514-1524
- Laroussi, M. (2002). Nonthermal decontamination of biological media by atmospheric-pressure plasmas: review, analysis and prospects, *IEEE Transactions on Plas. Science*, Vol. 30, No.4, pp. 1409-1415
- Loeb, L. B. (1961) *Basic processes of gaseous electronics*, University of California Press, Berkeley.
- Loeb, L. B. (1965) *Electrical coronas*, University of California Press, Berkeley.
- Marode, E. (1975), The mechanism of spark breakdown in air at atmospheric pressure between a positive point and a plane. I. Experimental: Nature of the streamer track, *Journal of Applied Physics*, Vol. 46, No. 5, pp. 2005-2015
- Nelson, D.; Benhenni, M.; Eichwald, O. & Yousfi, M. (2003), Ion swarm data for electrical discharge modeling in air and flue gas, *Journal of Applied Physics*, Vol. 94, pp. 96-103
- Ono, R. & Oda, T. a (2004). Spatial distribution of ozone density in pulsed corona discharges observed by two-dimensional laser absorption method, *Journal of Physics D: Applied Physics*, Vol. 37, pp. 730-735.
- Ono, R. & Oda, T. b (2004) Visualization of Streamer Channels and Shock Waves Generated by Positive Pulsed Corona Discharge Using Laser Schlieren Method, *Japanese Journal of Applied Physics*, Vol. 43, No. 1, 2004, pp. 321-327
- Pancheshnyi, S. (2005), Role of electronegative gas admixtures in streamer start, propagation and branching phenomena, *Plasma Sources Science and Technology*, Vol. 14, pp. 645-653

- Papageorgiou, L., Metaxas, A. C. & Georghiou, G. E. (2011), Three-dimensional numerical modelling of gas discharges at atmospheric pressure incorporating photoionization phenomena, *Journal of Physics D: Applied Physics*, Vol. 44, 045203 (10pp).
- Penetrante, B. M. & Schultheis, S. E. (1993), Nonthermal Plasma Techniques for Pollution Control, Part A&B, Editors, NATO ASI Series Vol. G 34, Springer-Verlag, Karlsruhe.
- Sarrette, J. P.; Cousty, S.; Merbahi, N.; Nègre-Salvayre, A. & F. Clément (2010), Observation of antibacterial effects obtained at atmospheric and reduced pressures in afterglow conditions, *European Physical Journal. Applied. Physics*, Vol. 49 13108
- Segur, P.; Bourdon, A.; Marode, E., Bessieres D. & Paillol J. H. (2006) The use of an improved Eddington; approximation to facilitate the calculation of photoionization in streamer discharges, *Plasma Sources Sciences and Technologies*, Vol. 15, pp. 648–660
- Sigmond, R. S. (1984), The residual streamer channel: Return strokes and secondary streamers, *Journal of Applied Physics*, Vol. 56, No. 5, pp. 1355-1370
- Spyrou, N.; Held, B.; Peyrous, R.; Manassis, Ch. & Pignolet, P. (1992) Gas temperature in a secondary streamer discharge: an approach to the electric wind, *Journal of Physics D: Applied Physics*, Vol. 25, pp. 211-216
- van Veldhuizen, E. M. & Rutgers, W. R. (2002), Pulsed positive corona streamer propagation and branching, *Journal of Physics D: Applied Physics*, Vol. 35, pp. 2169-2179
- Urashima K. & J. S. Chang (2010) Removal of Volatile Organic Compounds from Air Streams and Industrial Flue Gases by Non-Thermal Plasma Technolog, *IEEE Transactions on Dielectrics and Electrical Insulation*, Vol. 7 No. 5, pp. 602-614
- Villeger, S.; Sarrette, J. P.; Rouffet, B.; Cousty S. & Ricard A. (2008), Treatment of flat and hollow substrates by a pure nitrogen flowing post discharge: Application to bacterial decontamination in low diameter tubes, *European Physical Journal. Applied. Physics*, Vol. 42, pp. 25-32.
- Winands, G.; Liu, Z.; Pemen, A.; van Heesch, E.; Yan, K. & van Veldhuizen, E. (2006), Temporal development and chemical efficiency of positive streamers in a large scale wire-plate reactor as a function of voltage waveform parameters, *Journal of Physics D: Applied Physics*, Vol. 39, pp. 3010-3017
- Yousfi, M. & Benabdessadok, M. D. (1996), Boltzmann equation analysis of electron-molecule collision cross sections in water vapor and ammonia, *Journal of Applied Physics*, Vol. 80, pp. 6619-6631
- Yousfi, M.; Hennad, A. & Eichwald, O. (1998), Improved Monte Carlo method for ion transport in ion-molecule asymmetric systems at high electric fields, *Journal of Applied Physics*, Vol. 84, No. 1, pp. 107-104

An IMEX Method for the Euler Equations That Posses Strong Non-Linear Heat Conduction and Stiff Source Terms (Radiation Hydrodynamics)

Samet Y. Kadioglu¹ and Dana A. Knoll²

¹*Idaho National Laboratory, Fuels Modeling and Simulation Department, Idaho Falls*

²*Los Alamos National Laboratory, Theoretical Division, Los Alamos
USA*

1. Introduction

Here, we present a truly second order time accurate self-consistent IMEX (IMplicit/EXplicit) method for solving the Euler equations that posses strong nonlinear heat conduction and very stiff source terms (Radiation hydrodynamics). This study essentially summarizes our previous and current research related to this subject (Kadioglu & Knoll, 2010; 2011; Kadioglu, Knoll & Lowrie, 2010; Kadioglu, Knoll, Lowrie & Rauenzahn, 2010; Kadioglu et al., 2009; Kadioglu, Knoll, Sussman & Martineau, 2010). Implicit/Explicit (IMEX) time integration techniques are commonly used in science and engineering applications (Ascher et al., 1997; 1995; Bates et al., 2001; Kadioglu & Knoll, 2010; 2011; Kadioglu, Knoll, Lowrie & Rauenzahn, 2010; Kadioglu et al., 2009; Khan & Liu, 1994; Kim & Moin, 1985; Lowrie et al., 1999; Ruuth, 1995). These methods are particularly attractive when dealing with physical systems that consist of multiple physics (multi-physics problems such as coupling of neutron dynamics to thermal-hydrolic or to thermal-mechanics in reactors) or fluid dynamics problems that exhibit multiple time scales such as advection-diffusion, reaction-diffusion, or advection-diffusion-reaction problems. In general, governing equations for these kinds of systems consist of stiff and non-stiff terms. This poses numerical challenges in regards to time integrations, since most of the temporal numerical methods are designed specific for either stiff or non-stiff problems. Numerical methods that can handle both physical behaviors are often referred to as IMEX methods. A typical IMEX method isolates the stiff and non-stiff parts of the governing system and employs an explicit discretization strategy that solves the non-stiff part and an implicit technique that solves the stiff part of the problem. This standard IMEX approach can be summarized by considering a simple prototype model. Let us consider the following scalar model

$$u_t = f(u) + g(u), \quad (1)$$

where $f(u)$ and $g(u)$ represent non-stiff and stiff terms respectively. Then the IMEX strategy consists of the following algorithm blocks:

Explicit block solves:

$$\frac{u^* - u^n}{\Delta t} = f(u^n), \quad (2)$$

Implicit block solves:

$$\frac{u^{n+1} - u^*}{\Delta t} = g(u^{n+1}). \quad (3)$$

Here, for illustrative purposes we used only first order time differencing. In literature, although the both algorithm blocks are formally written as second order time discretizations, the classic IMEX methods (Ascher et al., 1997; 1995; Bates et al., 2001; Kim & Moin, 1985; Lowrie et al., 1999; Ruuth, 1995) split the operators in such a way that the implicit and explicit blocks are executed independent of each other resulting in non-converged non-linearities therefore time inaccuracies (order reduction to first order is often reported for certain applications). Below, we illustrate the interaction of an explicit and an implicit algorithm block based on second order time discretizations of Equation(1) in classical sense,

Explicit block:

$$\begin{aligned} u^1 &= u^n + \Delta t f(u^n) \\ u^* &= (u^1 + u^n)/2 + \Delta t/2 f(u^1) \end{aligned} \quad (4)$$

Implicit block:

$$u^{n+1} = u^* + \Delta t/2 [g(u^n) + g(u^{n+1})]. \quad (5)$$

Notice that the explicit block is based on a second order TVD Runge-Kutta method and the implicit block uses the Crank-Nicolson method (Gottlieb & Shu, 1998; LeVeque, 1998; Thomas, 1999). The major drawback of this strategy as mentioned above is that it does not preserve the formal second order time accuracy of the whole algorithm due to the absence of sufficient interactions between the two algorithm blocks (refer to highlighted terms in Equation (4)) (Bates et al., 2001; Kadioglu, Knoll & Lowrie, 2010).

In an alternative IMEX approach that we have studied extensively in (Kadioglu & Knoll, 2010; 2011; Kadioglu, Knoll & Lowrie, 2010; Kadioglu, Knoll, Lowrie & Rauen Zahn, 2010; Kadioglu et al., 2009), the explicit block is always solved inside the implicit block as part of the nonlinear function evaluation making use of the well-known Jacobian-Free Newton Krylov (JFNK) method (Brown & Saad, 1990; Knoll & Keyes, 2004). We refer this IMEX approach as a *self-consistent IMEX method*. In this strategy, there is a continuous interaction between the implicit and explicit blocks meaning that the improved solutions (in terms of time accuracy) at each nonlinear iteration are immediately felt by the explicit block and the improved explicit solutions are readily available to form the next set of nonlinear residuals. This continuous interaction between the two algorithm blocks results in an implicitly balanced algorithm in that all nonlinearities due to coupling of different time terms are consistently converged. In other words, we obtain an IMEX method that eliminates potential order reductions in time accuracy (the formal second order time accuracy of the whole algorithm is preserved). Below, we illustrate the interaction of the explicit and implicit blocks of the self-consistent IMEX method for the scalar model in Equation (1). The interaction occurs through the highlighted terms in Equation (6).

Explicit block:

$$\begin{aligned} u^1 &= u^n + \Delta t f(u^n) \\ u^* &= (u^1 + u^n)/2 + \Delta t/2 f(u^{n+1}) \end{aligned} \quad (6)$$

Implicit block:

$$u^{n+1} = u^* + \Delta t/2 [g(u^n) + g(u^{n+1})]. \quad (7)$$

Remark: We remark that another way of achieving a self-consistent IMEX integration that preserves the formal numerical accuracy of the whole system is to improve the lack of influence of the explicit and implicit blocks on one another by introducing an external iteration procedure wrapped around the both blocks. More details regarding this methodology can be found in (Kadioglu et al., 2005).

2. Applications

We have applied the above described self-consistent IMEX method to both multi-physics and multiple time scale fluid dynamics problems (Kadioglu & Knoll, 2010; 2011; Kadioglu, Knoll, Lowrie & Rauenzahn, 2010; Kadioglu et al., 2009; Kadioglu, Knoll, Sussman & Martineau, 2010). The multi-physics application comes from a multi-physics analysis of fast burst reactor study (Kadioglu et al., 2009). The model couples a neutron dynamics that simulates the transient behavior of neutron populations to a mechanics model that predicts material expansions and contractions. It is important to introduce a second order accurate numerical procedure for this kind of nonlinearly coupled system, because the criticality and safety study can depend on how well we predict the feedback between the neutronics and the mechanics of the fuel assembly inside the reactor. In our second order self-consistent IMEX framework, the mechanics part is solved explicitly inside the implicit neutron diffusion block as part of the nonlinear function evaluation. We have reported fully second order time convergent calculations for this model (Kadioglu et al., 2009).

As part of the multi-scale fluid dynamics application, we have solved multi-phase flow problems which are modeled by incompressible two-phase Navier-Stokes equations that govern the flow dynamics plus a level set equation that solves the inter-facial dynamics between the fluids (Kadioglu, Knoll, Sussman & Martineau, 2010). In these kinds of models, there is a strong non-linear coupling between the interface and fluid dynamics, e.g, the viscosity coefficient and surface tension forces are highly non-linear functions of interface variables, on the other hand, the fluid interfaces are advected by the flow velocity. Therefore, it is important to introduce an accurate integration technique that converges all non-linearities due to the strong coupling. Our self-consistent IMEX method operates on this model as follows; the interface equation together with the hyperbolic parts of the fluid equations are treated explicitly and solved inside an implicit loop that solves the viscous plus stiff surface tension forces. More details about the splitting of the operators of the Navier-Stokes equations in a self-consistent IMEX manner can be found in (Kadioglu & Knoll, 2011).

Another multi-scale fluid dynamics application comes from radiation hydrodynamics that we will be focusing on in the remainder of this chapter. Radiation hydrodynamics models are commonly used in astrophysics, inertial confinement fusion, and other high-temperature flow systems (Bates et al., 2001; Castor, 2006; Dai & Woodward, 1998; Drake, 2007; Ensmann, 1994; Kadioglu & Knoll, 2010; Lowrie & Edwards, 2008; Lowrie & Rauenzahn, 2007; Mihalas & Mihalas, 1984; Pomraning, 1973). A commonly used model considers the compressible Euler equations that contains a non-linear heat conduction term in the energy part. This model is relatively simple and often referred to as a *Low Energy-Density Radiation Hydrodynamics (LERH)* in a diffusion approximation limit (Kadioglu & Knoll, 2010). A more complicated model is referred to as a *High Energy-Density Radiation Hydrodynamics (HERH)* in a diffusion approximation limit that considers a combination of a hydrodynamical model resembling the compressible Euler equations and a radiation energy model that contains a separate radiation energy equation with nonlinear diffusion plus coupling source terms to

materials (Kadioglu, Knoll, Lowrie & Rauenzahn, 2010). Radiation Hydrodynamics problems are difficult to tackle numerically since they exhibit multiple time scales. For instance, radiation and hydrodynamics process can occur on time scales that can differ from each other by many orders of magnitudes. Hybrid methods (Implicit/Explicit (IMEX) methods) are highly desirable for these kinds of models, because if one uses all explicit discretizations, then due to very stiff diffusion process the explicit time steps become often impractically small to satisfy stability conditions (LeVeque, 1998; Thomas, 1999). Previous IMEX attempts to solve these problems were not quite successful, since they often reported order reductions in time accuracy (Bates et al., 2001; Lowrie et al., 1999). The main reason for time inaccuracies was how the explicit and implicit operators were split in which explicit solutions were lagging behind the implicit ones. In our self-consistent IMEX method, the hydrodynamics part is solved explicitly making use of the well-understood explicit schemes within an implicit diffusion block that corresponds to radiation transport. Explicit solutions are obtained as part of the non-linear functions evaluations withing the JFNK framework. This strategy has enabled us to produce fully second order time accurate results for both LERH and more complicated HERH models (Kadioglu & Knoll, 2010; Kadioglu, Knoll, Lowrie & Rauenzahn, 2010).

In the following sections, we will go over more details about the LERH and HERH models and the implementation/implications of the self-consistent IMEX technology when it is applied to these models. We will also present a mathematical analysis that reveals the analytical convergence behavior of our method and compares it to a classic IMEX approach.

2.1 A Low Energy Density Radiation Hydrodynamics Model (LERH)

This model uses the following system of partial differential equations formulated in spherically symmetric coordinates.

$$\frac{\partial \rho}{\partial t} + \frac{1}{r^2} \frac{\partial}{\partial r} (r^2 \rho u) = 0, \quad (8)$$

$$\frac{\partial}{\partial t} (\rho u) + \frac{1}{r^2} \frac{\partial}{\partial r} (r^2 \rho u^2) + \frac{\partial p}{\partial r} = 0, \quad (9)$$

$$\frac{\partial E}{\partial t} + \frac{1}{r^2} \frac{\partial}{\partial r} [r^2 u (E + p)] = \frac{1}{r^2} \frac{\partial}{\partial r} (r^2 \kappa \frac{\partial T}{\partial r}), \quad (10)$$

where ρ , u , p , E , and T are the mass density, flow velocity, fluid pressure, total energy density of the fluid, and the fluid temperature respectively. κ is the coefficient of thermal conduction (or diffusion coefficient) and in general is a nonlinear function of ρ and T . In this study, we will use an ideal gas equation of state, i.e. $p = R\rho T = (\gamma - 1)\rho\epsilon$, where R is the specific gas constant per unit mass, γ is the ratio of specific heats, and ϵ is the internal energy of the fluid per unit mass. The coefficient of thermal conduction will be assumed to be written as a power law in density and temperature, i.e. $\kappa = \kappa_0 \rho^a T^b$, where κ_0 , a and b are constants (Marshak, 1958). This simplified radiation hydrodynamics model allows one to study the dynamics of nonlinearly coupled two distinct physics; compressible fluid flow and nonlinear diffusion.

2.2 A High Energy Density Radiation Hydrodynamics Model (HERH)

In general, the radiation hydrodynamics concerns the propagation of thermal radiation through a fluid and the effect of this radiation on the hydrodynamics describing the fluid motion. The role of the thermal radiation increases as the temperature is raised. At low

temperatures the radiation effects are negligible, therefore, a low energy density model (LERH) that limits the radiation effects to a non-linear heat conduction is sufficient. However, at high temperatures, a more complicated high energy density radiation hydrodynamics (HERH) model that accounts for more significant radiation effects has to be considered. Accordingly, the governing equations of the HERH model consist of the following system

$$\frac{\partial \rho}{\partial t} + \frac{1}{r^2} \frac{\partial}{\partial r}(r^2 \rho u) = 0, \quad (11)$$

$$\frac{\partial}{\partial t}(\rho u) + \frac{1}{r^2} \frac{\partial}{\partial r}(r^2 \rho u^2) + \frac{\partial}{\partial r}(p + p_v) = 0, \quad (12)$$

$$\frac{\partial E}{\partial t} + \frac{1}{r^2} \frac{\partial}{\partial r}[r^2 u(E + p)] = -c\sigma_a(aT^4 - E_v) - \frac{1}{3}u \frac{\partial E_v}{\partial r}, \quad (13)$$

$$\frac{\partial E_v}{\partial t} + \frac{1}{r^2} \frac{\partial}{\partial r}[r^2 u(E_v + p_v)] = \frac{1}{r^2} \frac{\partial}{\partial r}(r^2 c D_r \frac{\partial E_v}{\partial r}) + c\sigma_a(aT^4 - E_v) + \frac{1}{3}u \frac{\partial E_v}{\partial r}, \quad (14)$$

where the flow variables and parameters that also occur in the LERH model are described above. Here, more variable definitions come from the radiation physics, i.e, E_v is the radiation energy density, $p_v = \frac{E_v}{3}$ is the radiation pressure, c is the speed of light, a is the Stephan-Boltzmann constant, σ_a is the macroscopic absorption cross-section, and D_r is the radiation diffusion coefficient. From the simple diffusion theory, D_r can be written as

$$D_r(T) = \frac{1}{3\sigma_a}. \quad (15)$$

We note that we solve a non-dimensional version of Equations (11)-(14) in order to normalize large digit numbers (c, σ_a, a etc.) and therefore improve the performance of the non-linear solver. The details of the non-dimensionalization procedure are given in (Kadioglu, Knoll, Lowrie & Rauenzahn, 2010). The non-dimensional system is the following,

$$\frac{\partial \rho}{\partial t} + \frac{1}{r^2} \frac{\partial}{\partial r}(r^2 \rho u) = 0, \quad (16)$$

$$\frac{\partial}{\partial t}(\rho u) + \frac{1}{r^2} \frac{\partial}{\partial r}(r^2 \rho u^2) + \frac{\partial}{\partial r}(p + \mathcal{P} p_v) = 0, \quad (17)$$

$$\frac{\partial E}{\partial t} + \frac{1}{r^2} \frac{\partial}{\partial r}[r^2 u(E + p)] = -\mathcal{P}\sigma_a(T^4 - E_v) - \frac{1}{3}\mathcal{P}u \frac{\partial E_v}{\partial r}, \quad (18)$$

$$\frac{\partial E_v}{\partial t} + \frac{1}{r^2} \frac{\partial}{\partial r}[r^2 u(E_v + p_v)] = \frac{1}{r^2} \frac{\partial}{\partial r}(r^2 \kappa \frac{\partial E_v}{\partial r}) + \sigma_a(T^4 - E_v) + \frac{1}{3}u \frac{\partial E_v}{\partial r}, \quad (19)$$

where $\mathcal{P} = \frac{aT_0^4}{\rho_0 c_{s,0}}$ is a non-dimensional parameter that measures the radiation effects on the flow and is roughly proportional to the ratio of the radiation and fluid pressures.

3. Numerical procedure

Here, we present the numerical procedure for the LERH model. The extension to the HERH model is straight forward. First, we split the operators of Equations (8)-(10) into two pieces one being the pure hydrodynamics part (hyperbolic conservation laws) and the other

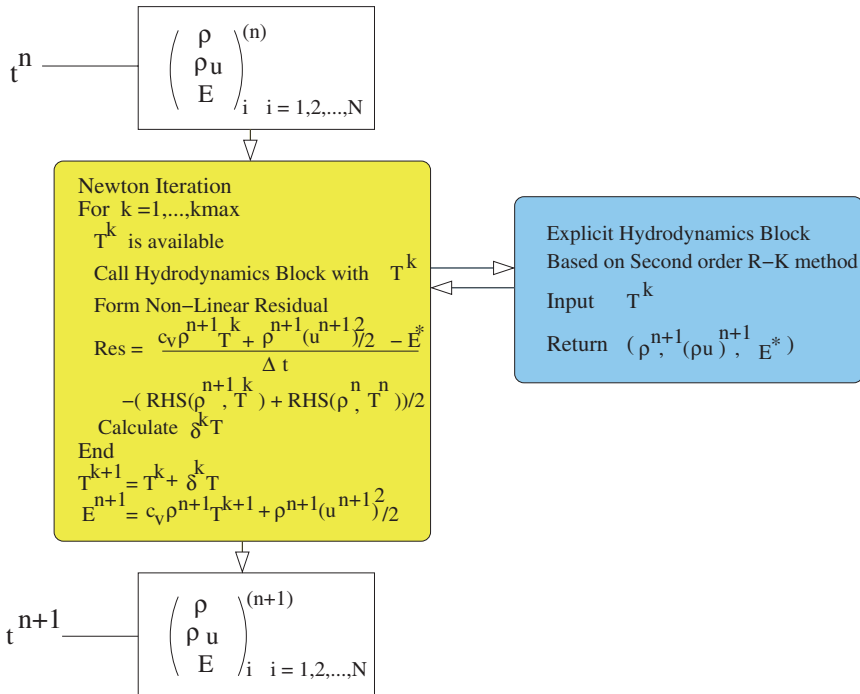


Fig. 1. Flowchart of the second order self-consistent IMEX algorithm

accounting for the effects of radiation transport (diffusion equation). For instance, the pure hydrodynamics equations can be written as

$$\frac{\partial \mathbf{U}}{\partial t} + \frac{\partial (A\mathbf{F})}{\partial V} + \frac{\partial \mathbf{G}}{\partial r} = 0, \tag{20}$$

where $\mathbf{U} = (\rho, \rho u, E)^T$, $\mathbf{F}(\mathbf{U}) = (\rho u, \rho u^2, u(E + p))^T$, and $\mathbf{G}(\mathbf{U}) = (0, p, 0)^T$. Then the diffusion equation becomes

$$\frac{\partial E}{\partial t} = \frac{\partial}{\partial V} (A\kappa \frac{\partial T}{\partial r}), \tag{21}$$

where $V = \frac{4}{3}\pi r^3$ is the generalized volume coordinate in one-dimensional spherical geometry, and $A = 4\pi r^2$ is the associated cross-sectional area. Notice that the total energy density, E , obtained by Equation (20) just represents the hydrodynamics component and it must be augmented by Equation (21).

Our algorithm consists of an explicit and an implicit block. The explicit block solves Equation (20) and the implicit block solves Equation (21). We will briefly describe these algorithm blocks in the following subsections. However, we note again that the explicit block is embedded within the implicit block as part of a nonlinear function evaluation as it is depicted in Fig. 1. This is done to obtain a nonlinearly converged algorithm that leads to second order calculations. We also note that similar discretizations, but without converging nonlinearities, can lead to order reduction in time convergence (Bates et al., 2001). Before we go into details of the individual algorithm blocks, we would like to present a flow diagram that illustrates the

execution of the whole algorithm in the self-consistent IMEX sense (refer to Fig. 1). According to this diagram, at beginning of each Newton iteration, we have the temperature values based on the current Newton iterate. This temperature is passed to the explicit block that returns the updated density, momentum, and a prediction to total energy. Then we form the non-linear residuals (e.g, forming the IMEX function in Section 3.3) for the diffusion equation out of the updated and predicted values. With the IMEX function in hand, we can execute the JFNK method. After the Newton method convergences, we get second order converged temperature and total energy density field.

3.1 Explicit block

Our explicit time discretization is based on a second order TVD Runge-Kutta method (Gottlieb & Shu, 1998; Gottlieb et al., 2001; Shu & Osher, 1988; 1989). The main reason why we choose this methodology is that it preserves the strong stability properties of the explicit Euler method. This is important because it is well known that solutions to the conservation laws usually involve discontinuities (e.g, shock or contact discontinuities) and (Gottlieb & Shu, 1998; Gottlieb et al., 2001) suggest that a time integration method which has the strong stability preserving property leads to non-oscillatory calculations (especially at shock or contact discontinuities).

A second order two-step TVD Runge-Kutta method for (20) can be cast as

Step-1 :

$$\begin{aligned} \rho^1 &= \rho^n - \Delta t \frac{1}{r^2} \frac{\partial}{\partial r} (r^2 \rho u)^n, \\ (\rho u)^1 &= (\rho u)^n - \Delta t \left[\frac{1}{r^2} \frac{\partial}{\partial r} (r^2 \rho u^2) + \frac{\partial p}{\partial r} \right]^n, \\ E^1 &= E^n - \Delta t \left\{ \frac{1}{r^2} \frac{\partial}{\partial r} [r^2 u (E + p)] \right\}^n, \end{aligned} \tag{22}$$

Step-2 :

$$\begin{aligned} \rho^{n+1} &= \frac{\rho^n + \rho^1}{2} - \frac{\Delta t}{2} \frac{1}{r^2} \frac{\partial}{\partial r} (r^2 \rho u)^1, \\ (\rho u)^{n+1} &= \frac{(\rho u)^n + (\rho u)^1}{2} - \frac{\Delta t}{2} \left\{ \frac{1}{r^2} \frac{\partial}{\partial r} (r^2 \rho u^2)^1 + \frac{\partial}{\partial r} (\rho^1 R \mathbf{T}^{n+1}) \right\}, \\ E^* &= \frac{E^n + E^1}{2} - \frac{\Delta t}{2} \left\{ \frac{1}{r^2} \frac{\partial}{\partial r} [r^2 u^1 (c_v \rho^1 \mathbf{T}^{n+1} + \frac{1}{2} \rho^1 (u^1)^2 + \rho^1 R \mathbf{T}^{n+1})] \right\}. \end{aligned} \tag{23}$$

We used the following equation of state relations in (22)- (23);

$$p = \rho R T E = c_v \rho T + \frac{1}{2} \rho u^2, \tag{24}$$

where $c_v = \frac{R}{\gamma-1}$ is the fluid specific heat with R being the universal gas constant. This explicit algorithm block interacts with the implicit block through the highlighted T^{n+1} terms in Equation (23). We can observe that the implicit equation (21) is practically solved for T by using the energy relation. Therefore, the explicit block is continuously impacted by the

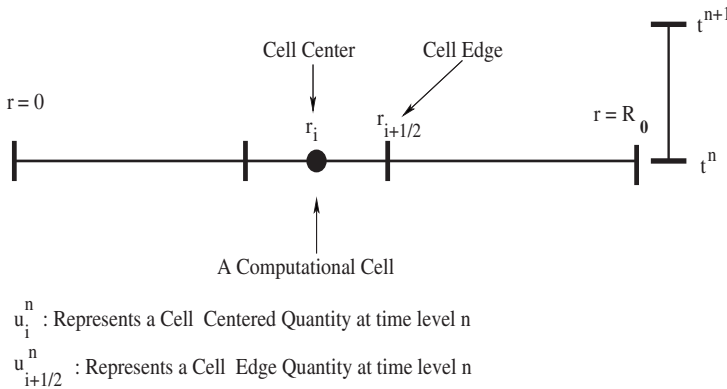


Fig. 2. Computational Conventions.

implicit T^{n+1} solutions at each non-linear Newton iteration. This provides the tight nonlinear coupling between the two algorithm blocks. Notice that the k^{th} nonlinear Newton iteration of the implicit block corresponds to $T^{n+1} \leftarrow T^k$ and $k \rightarrow (n+1)$ upon the convergence of the Newton method (refer to Fig. 1). Also, the $*$ values in Equation (23) are predicted intermediate values and later they are corrected by the implicit block which is given in the next subsection. One observation about this algorithm block is that some calculations are redundant related to Equation (22). In other words, Equation (22) can be computed only once at the beginning of each Newton iteration, because the non-linear iterations do not impact (22). This can lead overall less number of function evaluations.

Now we shall describe how we evaluate the numerical fluxes needed by Equations (22) and (23). For simplicity, we consider (20) to describe our fluxing procedure. Basically, it is based on the Local Lax Friedrichs (LLF) method (we refer to (LeVeque, 1998; Thomas, 1999) for the details of the LLF method and for more information in regards to the explicit discretizations of conservation laws). For instance, if we consider the following simple discretization for Equation (20),

$$\mathbf{U}_i^1 = \mathbf{U}_i^n - \frac{\Delta t}{\Delta V_i} (A_{i+1/2} F_{i+1/2}^n - A_{i-1/2} F_{i-1/2}^n) - \frac{\Delta t}{\Delta r} (G_{i+1/2}^n - G_{i+1/2}^n), \quad (25)$$

where $\Delta V_i = V(r_{i+1/2}) - V(r_{i-1/2})$, $A_{i\pm 1/2} = A(r_{i\pm 1/2})$, and indices i and $i+1/2$ represent cell center and cell edge values respectively (refer to Fig. 2), then the *Local Lax Friedrichs method* defines $F_{i+1/2}$ and $G_{i+1/2}$ as

$$F_{i+1/2} = \frac{F(\mathbf{U}_{i+1/2}^R) + F(\mathbf{U}_{i+1/2}^L)}{2} - \alpha_{i+1/2} \frac{\mathbf{U}_{i+1/2}^R - \mathbf{U}_{i+1/2}^L}{2}, \quad (26)$$

$$G_{i+1/2} = \frac{G(\mathbf{U}_{i+1/2}^R) + G(\mathbf{U}_{i+1/2}^L)}{2}, \quad (27)$$

where $\alpha = \max\{|\lambda_1^L|, |\lambda_1^R|, |\lambda_2^L|, |\lambda_2^R|, |\lambda_3^L|, |\lambda_3^R|\}$ in which $\lambda_1 = u - c$, $\lambda_2 = u$, $\lambda_3 = u + c$, and c is the sound speed. The sound speed is defined by

$$c = \sqrt{\frac{\partial p}{\partial \rho}}, \quad (28)$$

where $\frac{\partial p}{\partial \rho} = RT$ in this study. $\mathbf{U}_{i+1/2}^R$ and $\mathbf{U}_{i+1/2}^L$ are the interpolated values at $(i + 1/2)^{th}$ cell edge from the right and left side, i.e.,

$$\begin{aligned} \mathbf{U}_{i+1/2}^R &= \mathbf{U}_{i+1} - \frac{\Delta r}{2} \mathbf{U}_{r,i+1}, \\ \mathbf{U}_{i+1/2}^L &= \mathbf{U}_i + \frac{\Delta r}{2} \mathbf{U}_{r,i}, \end{aligned} \tag{29}$$

where

$$\mathbf{U}_{r,i} = \text{minmod}(a, b) = \begin{cases} a & \text{if } |a| < |b| \text{ and } ab > 0, \\ b & \text{if } |b| < |a| \text{ and } ab > 0, \\ 0 & \text{if } ab \leq 0, \end{cases} \tag{30}$$

where

$$a = \frac{\mathbf{U}_{i+1} - \mathbf{U}_i}{\Delta r}, \tag{31}$$

$$b = \frac{\mathbf{U}_i - \mathbf{U}_{i-1}}{\Delta r}. \tag{32}$$

3.2 Implicit block

The explicit block produces the following solution vector

$$\mathbf{U}^n \rightarrow \mathbf{U}^* = \begin{pmatrix} \rho^{n+1} \\ (\rho u)^{n+1} \\ E^* \end{pmatrix}.$$

This information is used to discretize Equation (21) as follows,

$$\frac{(c_v \rho^{n+1} T^{n+1} + \frac{1}{2} \rho^{n+1} (u^{n+1})^2 - E^*)_i}{\Delta t} = \frac{1}{2} \frac{\partial}{\partial V} (A \kappa^{n+1} \frac{\partial T^{n+1}}{\partial r})_i + \frac{1}{2} \frac{\partial}{\partial V} (A \kappa^n \frac{\partial T^n}{\partial r})_i, \tag{33}$$

where

$$\frac{\partial}{\partial V} (A \kappa \frac{\partial T}{\partial r})_i = \frac{A_{i+1/2} \kappa_{i+1/2} (T_{i+1} - T_i) / \Delta r}{\Delta V_i} - \frac{A_{i-1/2} \kappa_{i-1/2} (T_i - T_{i-1}) / \Delta r}{\Delta V_i}. \tag{34}$$

Notice that this implicit discretization resembles to the *Crank-Nicolson method* (Strikwerda, 1989; Thomas, 1998). We solve Equation (33) iteratively for T^{n+1} . The nonlinear solver needed by Equation (33) is based on the Jacobian-Free Newton Krylov method which is described in the next subsection. When the Newton method converges all the nonlinearities in this discretization, we obtain the following fully updated solution vector,

$$\mathbf{U}^* \rightarrow \mathbf{U}^{n+1} = \begin{pmatrix} \rho^{n+1} \\ (\rho u)^{n+1} \\ E^{n+1} \end{pmatrix}.$$

3.3 The Jacobian-Free Newton Krylov method and forming the IMEX function

The Jacobian-Free Newton Krylov method (e.g. refer to (Brown & Saad, 1990; Kelley, 2003; Knoll & Keyes, 2004)) is a combination of the Newton method that solves a system of nonlinear equations and a Krylov subspace method that solves the Newton correction equations. With this method, Newton-like super-linear convergence is achieved in the nonlinear iterations, without the complexity of forming or storing the Jacobian matrix. The effects of the Jacobian matrix are probed only through approximate matrix-vector products required in the Krylov iterations. Below, we provide more details about this technique. The Newton method solves $\mathbf{F}(T) = 0$ (e.g. assume Equation (33) is written in this form) iteratively over a sequence of linear system defined by

$$\begin{aligned} \mathbf{J}(T^k)\delta T^k &= -\mathbf{F}(T^k), \\ T^{k+1} &= T^k + \delta T^k, \quad k = 0, 1, \dots \end{aligned} \quad (35)$$

where $\mathbf{J}(T^k) = \frac{\partial \mathbf{F}}{\partial T}$ is the Jacobian matrix and δT^k is the update vector. The Newton iteration is terminated based on a required drop in the norm of the nonlinear residual, i.e.

$$\|\mathbf{F}(T^k)\|_2 < tol_{res}\|\mathbf{F}(T^0)\|_2 \quad (36)$$

where tol_{res} is a given tolerance. The linear system, Newton correction equation (35), is solved by using the Arnoldi based Generalized Minimal RESidual method (GMRES)(Saad, 2003) which belongs to the general class of the Krylov subspace methods(Reid, 1971). We note that these subspace methods are particularly suitable choice when dealing with non-symmetric linear systems. In GMRES, an initial linear residual, \mathbf{r}_0 , is defined for a given initial guess δT_0 ,

$$\mathbf{r}_0 = -\mathbf{F}(T) - \mathbf{J}\delta T_0. \quad (37)$$

Here we dropped the index k convention since the Krylov (GMRES) iteration is performed at a fixed k . Let j be the Krylov iteration index. The j^{th} Krylov iteration minimizes $\|\mathbf{J}\delta T_j + \mathbf{F}(T)\|_2$ within a subspace of small dimension, relative to n (the number of unknowns), in a least-squares sense. δT_j is drawn from the subspace spanned by the Krylov vectors, $\{\mathbf{r}_0, \mathbf{J}\mathbf{r}_0, \mathbf{J}^2\mathbf{r}_0, \dots, \mathbf{J}^{j-1}\mathbf{r}_0\}$, and can be written as

$$\delta T_j = \delta T_0 + \sum_{i=0}^{j-1} \beta_i (\mathbf{J})^i \mathbf{r}_0, \quad (38)$$

where the scalar β_i minimizes the residual. The Krylov iteration is terminated based on the following inexact Newton criteria (Dembo, 1982)

$$\|\mathbf{J}\delta T_j + \mathbf{F}(T)\|_2 < \gamma \|\mathbf{F}(T)\|_2, \quad (39)$$

where the parameter γ is set in terms of how tight the linear solver should converge at each Newton iteration (we typically use $\gamma = 10^{-3}$). One particularly attractive feature of this methodology is that it does not require forming the Jacobian matrix. Instead, only matrix-vector multiplications, $\mathbf{J}v$, are needed, where $v \in \{\mathbf{r}_0, \mathbf{J}\mathbf{r}_0, \mathbf{J}^2\mathbf{r}_0, \dots\}$. This leads to the so-called *Jacobian-Free* implementations in which the action of the Jacobian matrix can be approximated by

$$\mathbf{J}v = \frac{\mathbf{F}(T + \epsilon v) - \mathbf{F}(T)}{\epsilon}, \quad (40)$$

where $\epsilon = \frac{1}{n\|v\|_2} \sum_{i=1}^n b|u_i| + b$, n is the dimension of the linear system and b is a constant whose magnitude is within a few orders of magnitude of the square root of machine roundoff (typically 10^{-6} for 64-bit double precision).

Here, we briefly describe how to form the IMEX function $F(T)$. We refer $F(T)$ as the IMEX function, since it uses both explicit (hydrodynamics) and implicit (diffusion) information. Notice that for a method that uses all implicit information, $F(T)$ would correspond to a regular nonlinear residual function. The following pseudo code describes how to form $F(T)$ (we also refer to Fig. 1).

Evaluating $F(T^k)$:

Given T^k where k represents the current Newton iteration.
Call Hydrodynamics block with (ρ^n, u^n, E^n, T^k) to compute ρ^{n+1}, u^{n+1}, E^* .
Form $F(T^k)$ based on the Crank-Nicolson method,

$$F(T^k) = \frac{[c_v \rho^{n+1} T^k + \frac{1}{2} \rho^{n+1} (u^{n+1})^2 - E^*]}{\Delta t} - \frac{1}{2} \frac{\partial}{\partial V} (A \kappa^k \frac{\partial T^k}{\partial r}) - \frac{1}{2} \frac{\partial}{\partial V} (A \kappa^n \frac{\partial T^n}{\partial r}).$$

It is important to note that we are not iterating between the implicit and explicit blocks. Instead we are executing the explicit block inside of a nonlinear function evaluation defined by $F(T^k)$. The unique properties of JFNK allow us to perform a Newton iteration on this IMEX function, and thus JFNK is a required component of this nonlinearly converged IMEX approach.

3.4 Time step control

In this section, we describe two procedures to determine the computational time steps that are used in our test calculations. The first one was originally proposed by (Rider & Knoll, 1999). The idea is to estimate the dominant wave propagation speed in the problem. In one dimension this involves calculating the ratio of temporal to spatial derivatives of the dependent variables. In principle, it is sufficient to consider the following hyperbolic equation rather than using the entire system of the governing equations

$$\frac{\partial E}{\partial t} + v_f \frac{\partial E}{\partial r} = 0, \tag{41}$$

where the unknown v_f represents the front velocity. This gives

$$v_f = - \frac{\partial E / \partial t}{\partial E / \partial r}. \tag{42}$$

As noted in Rider & Knoll (1999), to avoid problems from lack of smoothness the following numerical approximation is used to calculate v_f

$$v_f^n = \frac{\sum (|E_i^n - E_i^{n-1}| / \Delta t)}{\sum (|E_{i+1}^n - E_{i-1}^n| / 2 \Delta r)}. \tag{43}$$

Then the new time step is determined by the Courant-Friedrichs-Lewy (CFL) condition

$$\Delta t^{n+1} = C \frac{\| \Delta r \|}{v_f^n}, \tag{44}$$

where $\|\Delta r\|$ uses the L_1 norm as in Equation (43). We can further simplify Equation (44) by using Equation (43), i.e.,

$$\Delta t^{n+1} = \frac{1}{2} \frac{\sum |E_{i+1}^n - E_{i-1}^n|}{\sum (|E_i^n - E_i^{n-1}|/\Delta t)}. \quad (45)$$

We remark that the time steps determined by this procedure is always compared with the pure hydrodynamics time steps and the most restrictive ones are selected. The hydrodynamics time steps are calculated by

$$\Delta t^{Hydro,n+1} = CFL \times \frac{\Delta r}{\max_i |u + c|_i}, \quad (46)$$

where u is the fluid velocity and c is the sound speed (e.g, refer to Equation (28)). The coefficient CFL is set to 0.5. Alternative time step control criterion are used for radiation hydrodynamics problems (Bowers & Wilson, 1991). One commonly used approach is based on monitoring the maximum relative change in E . For instance,

$$\Delta t^{n+1} = \Delta t^n \sqrt{\frac{(\Delta E/E)^{n+1}}{(\Delta E/E)_{max}}}, \quad (47)$$

where

$$\left(\frac{\Delta E}{E}\right)^{n+1} = \max_i \left(\frac{|E_i^{n+1} - E_i^n|}{E_i^{n+1} + E_0}\right), \quad (48)$$

where the parameter E_0 is an estimate for the lower bound of the energy density. Comparing Equation (47) to (45) we observed that Equation (45) is computationally more efficient. Therefore, we use Equation (45) in our numerical test problems.

4. Computational results

4.1 Smooth problem test

We use the LERH model to produce numerical results for this test problem. In this test, we run the code until a particular final time so that the computational solutions are free of shock waves and steep thermal fronts. The problem is to follow the evolution of the nonlinear waves that results from an initial energy deposition in a narrow region. The initial total energy density is given by

$$E(r, 0) = \frac{\varepsilon_0 \exp(-r^2/c_0^2)}{(c_0 \sqrt{\pi})^3}, \quad (49)$$

where c_0 is a constant and set to 1/4 for this test. Note that $c_0 \rightarrow 0$ gives a delta function at origin. We use the cell averaged values of E as in (Bates et al., 2001), i.e., we integrate (49) over the i^{th} cell from $r_{i-1/2}$ to $r_{i+1/2}$ so that

$$E_i = \frac{\varepsilon_0 [erf(r_{i+1/2}/c_0) - erf(r_{i-1/2}/c_0)] - 2\pi c_0^2 [r_{i+1/2} E(r_{i+1/2}) - r_{i-1/2} E(r_{i-1/2})]}{\Delta V_i}, \quad (50)$$

where the symbol erf denotes the error function. The initial density is set to $\rho = 1/r$. The initial temperature is calculated by using $E = c_v \rho T + \frac{1}{2} \rho u$ where $u = 0$ initially. The boundary

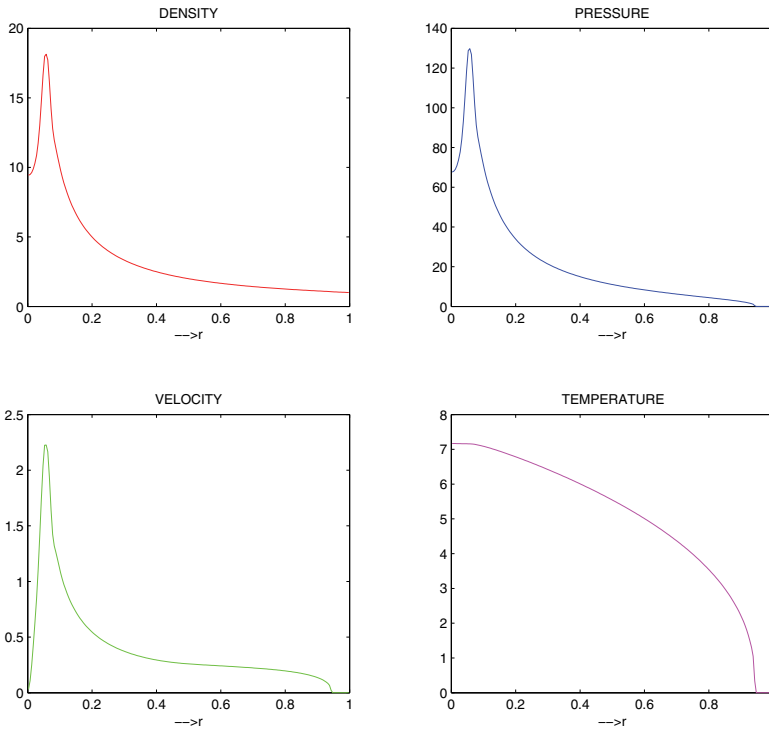


Fig. 3. Solution profiles resulting from the smooth problem test. The solutions are calculated for $t_{final} = 0.01$ with $M = 200$ cell points.

conditions for the hydrodynamics variables are *reflective* and *outflow* boundary conditions at the left and right ends of the computational domain respectively. The zero-flux boundary conditions are used for the temperature at both ends (e.g, $\partial T / \partial r|_{r=0} = 0$). The coefficient of thermal conduction is set to $\kappa(T) = T^{5/2}$.

We run the code until $t = 0.01$ with $\epsilon_0 = 100$ using 200 cell points. The size of the computational domain is set to 1 (e.g, $R_0 = 1$ in Fig. 2). Fig. 3 shows the computed solutions for density, pressure, velocity, and temperature. As can be seen, there is no shock formation or steep thermal fronts occurred around this time. Fig. 4 shows our numerical time convergence analysis. To measure the rate of time convergence, we run the code with a fixed mesh (e.g, $M = 200$ cell points) and different time step refinements to a final time (e.g, $t = 0.01$). This provides a sequence of solution data ($E^{\Delta t}, E^{\Delta t/2}, E^{\Delta t/4}, \dots$). Then we measure the L_2 norm of errors between *two* consecutive time step solutions ($\|E^{\Delta t} - E^{\Delta t/2}\|_2, \|E^{\Delta t/2} - E^{\Delta t/4}\|_2, \dots$) and plot these errors against to a second order line. It is clear from Fig. 4 that we achieve second order time convergence unlike (Bates et al., 2001) fails to provide second order accurate results for the same test.

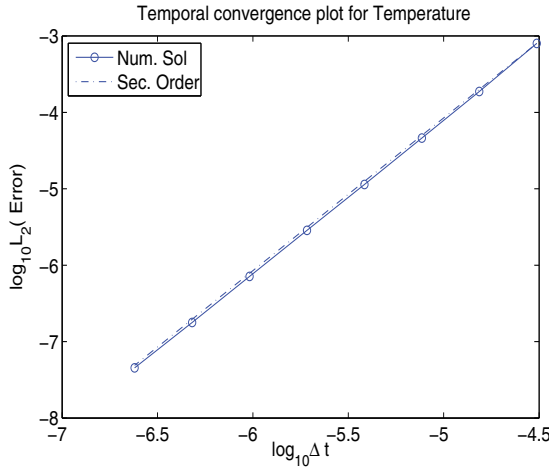


Fig. 4. Temporal convergence plot for the smooth problem test. $t_{final} = 0.01$ with $M = 200$ cell points.

4.2 Point explosion test

We use the HERH model for this test. We note that we have studied this test by using both of the LERH and HERH models and reported our results in two consecutive papers (Kadioglu & Knoll, 2010; Kadioglu, Knoll, Lowrie & Rauenzahn, 2010). This section reviews our numerical findings from (Kadioglu, Knoll, Lowrie & Rauenzahn, 2010). In this test, important physics such as the propagation of sharp shock discontinuities and steep thermal fronts occur. This is important, because this test enables us to study/determine the time accuracy of the strong numerical coupling of two distinct physical processes.

Typically a point explosion is characterized by the release of large amount of energy in a small region of space (few cells near the origin). Depending on the magnitude of the energy deposition, weak or strong explosions take place. If the initial explosion energy is not large enough, the diffusive effect is limited to region behind the shock. However, if the explosion energy is large, then the thermal front can precede the hydrodynamics front. Both weak and strong explosions are studied in (Kadioglu & Knoll, 2010) where the LERH model is considered. Here, we solve/recast the strong explosion test by using the HERH model. The problem setting is as follows. The initial total energy density is given by

$$E_0 = \frac{\varepsilon_0 \exp(-r^2/c_0^2)}{(c_0 \sqrt{\pi})^3}, \quad (51)$$

where $\varepsilon_0 = 235$ and $c_0 = 1/300$. The initial fluid and radiation energies are set to $E(r, 0) = E_v(r, 0) = E_0/2$. The fluid density is initialized by $\rho(r, 0) = r^{-19/9}$. The initial temperature is calculated by using $E = c_v \rho T / \gamma + \frac{1}{2} \rho u^2$ with the initial $u = 0$. The radiation diffusivity (κ in Equation (19)) is calculated by considering the LERH model and comparing it with the sum of Equation (18) plus \mathcal{P} times Equation (19). For instance

$$\frac{\partial}{\partial t}(E + \mathcal{P}E_v) + \frac{1}{r^2} \frac{\partial}{\partial r} [r^2 u (E + p + \mathcal{P}(E_v + p_v))] = \frac{1}{r^2} \frac{\partial}{\partial r} (r^2 \mathcal{P} \kappa \frac{\partial E_v}{\partial r}), \quad (52)$$

is compared to Equation (6) of (Kadioglu & Knoll, 2010). Then κ becomes

$$\kappa(\rho, T) = \kappa_0 \frac{\rho^a T^b}{4\mathcal{P}T^3}, \tag{53}$$

where $\kappa_0 = 10^2$, $a = -2$ and $b = 13/2$ as in (Kadioglu & Knoll, 2010). We set $\mathcal{P} = 10^{-4}$ and $\sigma_a = 10^8$ that appear in Equations (18) and (19).

We compute the solutions until $t = 0.02$ using 400 cell points. Fig. 5 shows fluid density, fluid pressure, flow velocity, fluid energy, fluid temperature, and radiation temperature profiles. At this time ($t = 0.02$), hydrodynamical shocks are depicted near $r = 0.2$. In this test case, the thermal front (located near $r = 0.8$) propagates faster than the hydrodynamical shocks due to large initial energy deposition. Fig. 6 shows the time convergence analysis for different field variables. Clearly, we have obtained second order time accuracy for all variables. This convergence result is important, because this problem is a difficult one meaning that the coupling of different physics is highly non-linear and it is a challenge to produce fully second order convergence from an operator split method for these kinds of problems. One comment that can be made about our spatial discretization (LLF method), though it is not the primary focus of this study, is that our numerical results (figures in Fig. 5) indicate that the LLF fluxing procedure provides very good shock capturing with no spurious oscillations at or near the discontinuities.

4.3 Radiative shock test

The problem settings for this test are similar to (Drake, 2007; Lowrie & Edwards, 2008) where more precise physical definitions can be found. Radiative shocks are basically strong shock waves that the radiative energy flux plays essential role in the governing dynamics. Radiative shocks occur in many astrophysical systems where they move into an upstream medium leaving behind an altered downstream medium. In this test, we assume that a simple planar radiative shock exists normal to the flow as it is illustrated in Fig. 7. The initial shock profiles are determined by considering the given values in Region-1 and finding the values in Region-2 of Fig. 7. To find the values in Region-2, we use the so-called Rankine-Hugoniot relations or jump conditions (LeVeque, 1998; Smoller, 1994; Thomas, 1999). A general formula for the radiation hydrodynamics jump conditions is given in (Lowrie & Edwards, 2008). For instance

$$s(\rho_2 - \rho_1) = \rho_2 u_2 - \rho_1 u_1, \tag{54}$$

$$s(\rho_2 u_2 - \rho_1 u_1) = (\rho_2 u_2^2 + p_2 + \mathcal{P}p_{v,2}) - (\rho_1 u_1^2 + p_1 + \mathcal{P}p_{v,1}), \tag{55}$$

$$s(E_2 - E_1) = u_2(E_2 + p_2 + \mathcal{P}p_{v,2}) - u_1(E_1 + p_1 + \mathcal{P}p_{v,1}), \tag{56}$$

$$s(E_{v,2} - E_{v,1}) = u_2(E_{v,2}) - u_1(E_{v,1}), \tag{57}$$

where s is the propagation speed of the shock front. In our test problem, we assume that the radiation temperature is smooth. Therefore, it is sufficient to use the jump conditions for the compressible Euler equations to initiate hydrodynamics shock profiles. The Euler jump conditions can be easily obtained by dropping the radiative terms in Equations (54), (55), (56), and (57). Then the necessary formulae to initialize the shock solutions are

$$s = u_1 + c_1 \sqrt{1 + \frac{\gamma + 1}{2\gamma} \left(\frac{p_2}{p_1} - 1 \right)}, \tag{58}$$

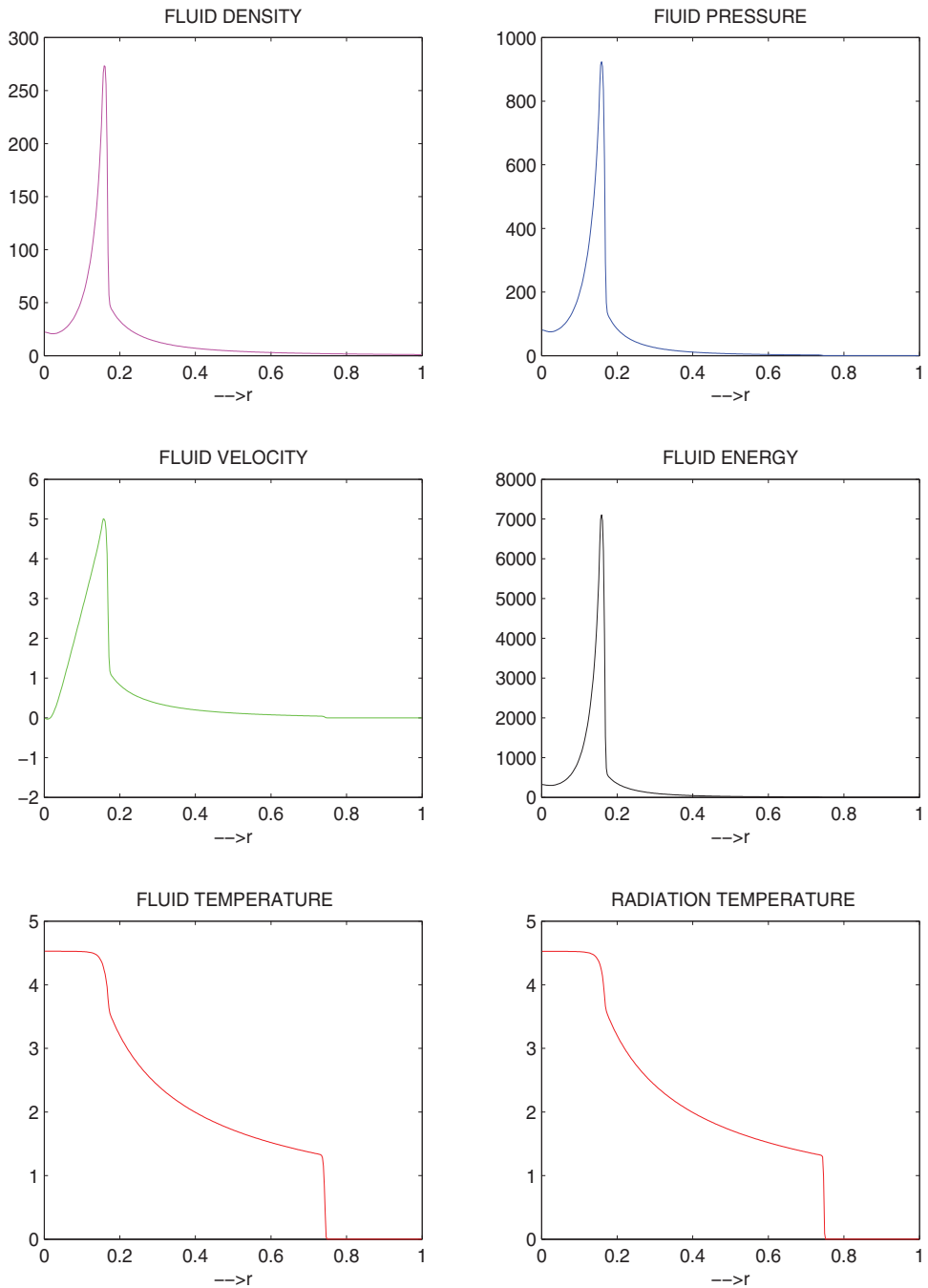


Fig. 5. Point explosion test with $t = 0.02$ and $M = 400$ cell points.

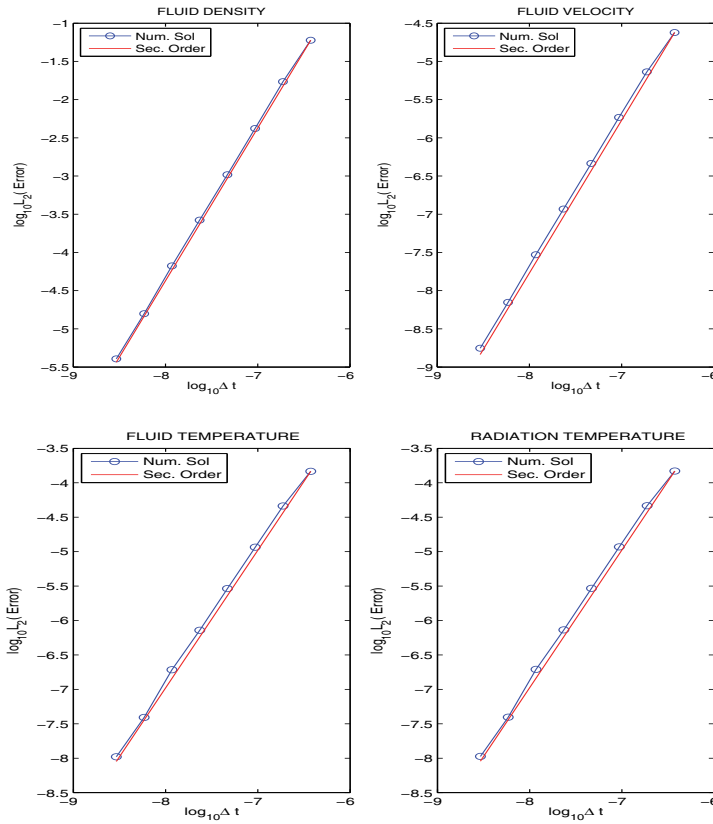


Fig. 6. Temporal convergence plot for various field variables from the point explosion test. $t = 0.001$ and 400 cell points are used.

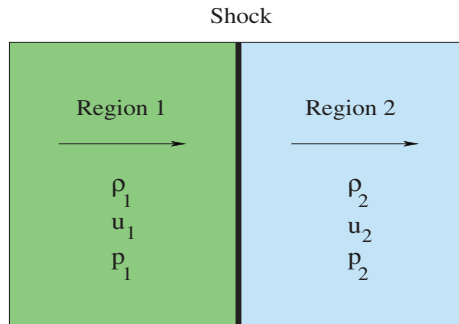


Fig. 7. A schematic diagram of a shock wave situation with the indicated density, velocity, and pressure for each region.

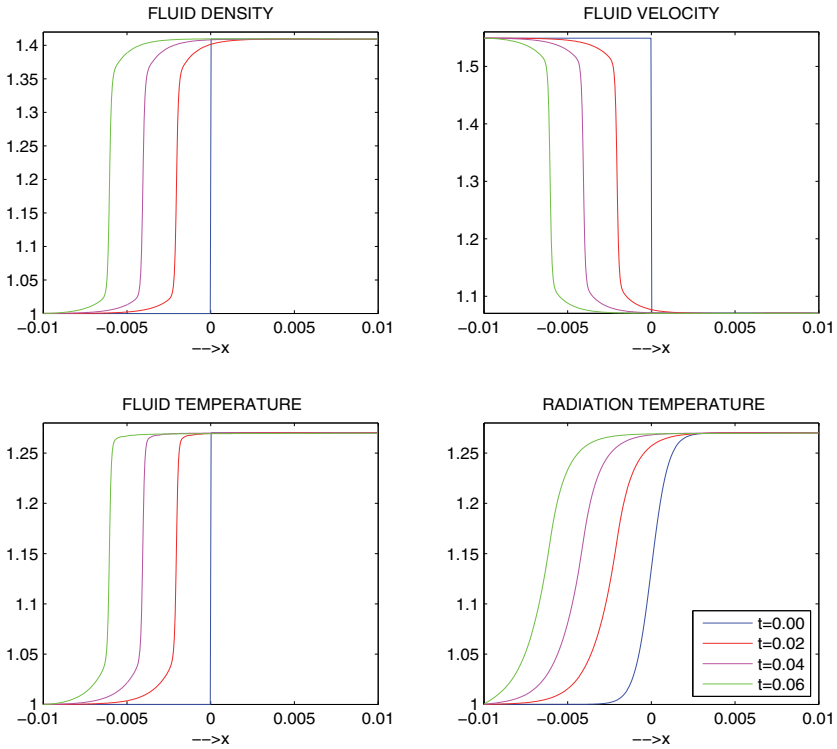


Fig. 8. Time evolution of the left moving radiative shock.

$$\frac{p_2}{p_1} = 1 + \frac{2\gamma}{\gamma + 1} \left[\left(\frac{s - u_1}{c_1} \right)^2 - 1 \right], \tag{59}$$

$$u_2 = u_1 + \frac{p_2 - p_1}{\rho_1(s - u_1)}, \tag{60}$$

$$\frac{\rho_2}{\rho_1} = \frac{s - u_1}{s - u_2}, \tag{61}$$

where $c_1 = \sqrt{\gamma \frac{p_1}{\rho_1}}$ is the speed of sound in the fluid at upstream conditions. More details regarding the derivation of Equations (58)-(61) can be found in (Anderson, 1990; LeVeque, 1998; Smoller, 1994; Thomas, 1999; Wesseling, 2000).

We are interested in solving a left moving radiative shock problem. To achieve this, we set the initial shock speed $s = -0.1$ in Equation (58). Other upstream flow variables are set as follows; $\rho_1 = 1.0$, $T_1 = 1.0$, and $M_1 = u_1/c_1 = 1.2$ as the upstream Mach number. Then we calculate the pressure from a calorically perfect gas relation ($p_1 = R\rho_1 T_1$). Using p_1 and ρ_1 , we calculate the upstream sound speed $c_1 = \sqrt{\gamma p_1/\rho_1}$ together with $u_1 = M_1 c_1$. With these information in hand, we can easily calculate the downstream values using Equations (58)-(61). The total fluid energies in both upstream and downstream directions are calculated

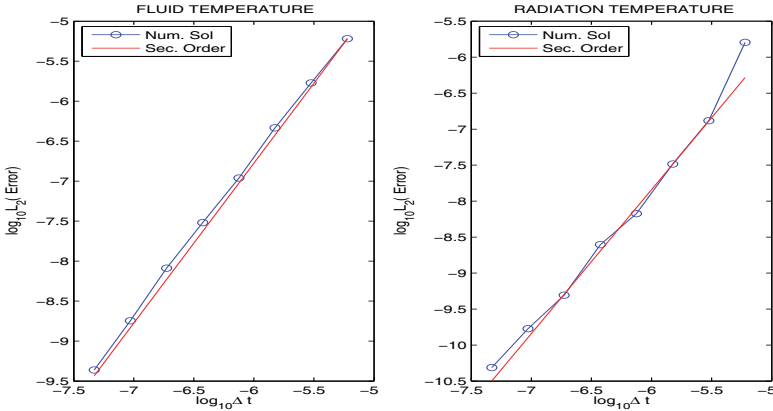


Fig. 9. Temporal convergence plot for the material and radiation temperature from the radiative shock test. $t = 0.02$ and 400 cell points are used.

by using the energy relation $E = c_v \rho T + \frac{1}{2} \rho u^2$. The radiation temperature is assumed to be a smooth function across the shock and equal to T_1 and T_2 on the left and right boundary of the computational domain, i.e., we choose

$$T_v(x, 0) = \frac{(T_2 - T_1)}{2} \tanh(1000x) + \frac{(T_2 + T_1)}{2}. \tag{62}$$

The initial radiation energy is calculated by $E_v = T_v^4$. Other parameters that appear in Equations (16)-(19) are set as $\mathcal{P} = 10^{-4}$, $\sigma_a = 10^6$, and $\kappa = 1$. These parameters are chosen to be consistent with (Lowrie & Edwards, 2008). We solve Equations (16)-(19), the HERH model, in Cartesian coordinates with the above initial conditions. The solutions use fixed boundary conditions at both ends. In other words, at each time step, the solutions are reset to the initial boundary values. The numerical calculations are carried out with 400 cell points and $\Delta t = 10^{-6}$. Fig. 8 shows the time history of the solutions. Notice that the solutions are highly transient, therefore it is a good test to carry out a time convergence study. Fig. 9 shows time convergence analysis for the fluid and the radiation temperature. Second order time convergence can be clearly seen in both fields.

5. Convergence analysis

In this section, we present a mathematical analysis (modified equation analysis) to study the analytical convergence behavior of our self-consistent IMEX method and compare it to a classic IMEX method. The modified equation analysis (truncation error analysis) is performed by considering the LERH model (Equations (8)-(10) or (20)-(21)). Also, for simplicity, we assume that the system given by Equations (20)-(21) is written in cartesian coordinates. In the introduction, we first described a classic IMEX approach then presented our self-consistent IMEX method. Therefore, we shall follow the same order in regards to below mathematical analysis.

5.1 A classic IMEX method

The classic IMEX method operates on Equations (20)-(21) as follows.

Explicit block:

Step-1:

$$\begin{aligned}\rho^1 &= \rho^n - \Delta t \frac{\partial}{\partial x} (\rho u)^n, \\ (\rho u)^1 &= (\rho u)^n - \Delta t \frac{\partial}{\partial x} [(\rho u^2)^n + p^n], \\ E^1 &= E^n - \Delta t \frac{\partial}{\partial x} \{u^n [E^n + p^n]\},\end{aligned}\quad (63)$$

Step-2:

$$\begin{aligned}\rho^{n+1} &= \frac{\rho^1 + \rho^n}{2} - \frac{\Delta t}{2} \frac{\partial}{\partial x} (\rho u)^1, \\ (\rho u)^{n+1} &= \frac{(\rho u)^1 + (\rho u)^n}{2} - \frac{\Delta t}{2} \frac{\partial}{\partial x} [\rho^1 (u^2)^1 + R\rho^1 \mathbf{T}^n], \\ E^* &= \frac{E^n + E^1}{2} - \frac{\Delta t}{2} \frac{\partial}{\partial x} \{u^1 [c_v \rho^1 \mathbf{T}^n + \frac{1}{2} \rho^1 (u^1)^2 + R\rho^1 \mathbf{T}^n]\},\end{aligned}\quad (64)$$

Implicit block:

$$\frac{E^{n+1} - E^*}{\Delta t} = \frac{1}{2} \frac{\partial}{\partial x} (\kappa^{n+1} \frac{\partial T^{n+1}}{\partial x}) + \frac{1}{2} \frac{\partial}{\partial x} (\kappa^n \frac{\partial T^n}{\partial x}),\quad (65)$$

where we incorporated with the equation of states relations plus we assume that the explicit block is based on a second order TVD Runge-Kutta method and the implicit block is similar to the Crank-Nicolson method. Notice that the classic IMEX method is executed in such a way that the implicit temperature does not impact the explicit block (refer to the highlighted terms in Equation (64)). We carry out the modified equation analysis for the energy part of Equations (63)-(65), but the same procedure can easily be extended to the whole system. We consider

$$E^1 = E^n - \Delta t \frac{\partial}{\partial x} \{u^n [E^n + p^n]\},\quad (66)$$

$$E^* = \frac{E^n + E^1}{2} - \frac{\Delta t}{2} \frac{\partial}{\partial x} \{u^1 [c_v \rho^1 T^n + \frac{1}{2} \rho^1 (u^1)^2 + R\rho^1 T^n]\},\quad (67)$$

Substituting Equation (66) into (67), we get

$$E^* = E^n - \frac{\Delta t}{2} \frac{\partial}{\partial x} \{u^n [E^n + p^n]\} - \frac{\Delta t}{2} \frac{\partial}{\partial x} \{u^1 [c_v \rho^1 T^n + \frac{1}{2} \rho^1 (u^1)^2 + R\rho^1 T^n]\}.\quad (68)$$

We let $L(E^n) = -\frac{\partial}{\partial x} \{u^n [E^n + p^n]\}$ and use $T^n = T^1 - \Delta t T_i^n + O(\Delta t^2)$, then (68) becomes

$$\begin{aligned}E^* &= E^n + \frac{\Delta t}{2} L(E^n) - \frac{\Delta t}{2} \frac{\partial}{\partial x} \{u^1 [c_v \rho^1 (T^1 - \Delta t \frac{\partial T^n}{\partial t} + O(\Delta t^2)) \\ &\quad + \frac{1}{2} \rho^1 (u^1)^2 + R\rho^1 (T^1 - \Delta t \frac{\partial T^n}{\partial t} + O(\Delta t^2))]\}.\end{aligned}\quad (69)$$

Carrying out the necessary algebra, Equation (69) becomes

$$E^* = E^n + \frac{\Delta t}{2}L(E^n) + \frac{\Delta t}{2}L(E^1) + \frac{\Delta t^2}{2}\rho^1 u^1 \frac{\partial T^n}{\partial t}(c_v + R) + O(\Delta t^3), \quad (70)$$

where $L(E^1) = -\frac{\partial}{\partial x}\{u^1[c_v \rho^1 T^1 + \frac{1}{2}\rho^1(u^1)^2 + R\rho^1 T^1]\} = -\frac{\partial}{\partial x}\{u^1[E^1 + p^1]\}$. Further simplification comes from the following identity

$$L(E^1) = L(E^n) + \Delta t \frac{\partial L}{\partial t} + O(\Delta t^2). \quad (71)$$

Inserting Equation (71) into (70), we get

$$E^* = E^n + \Delta t L(E^n) + \frac{\Delta t^2}{2} \frac{\partial L}{\partial t} + \frac{\Delta t^2}{2} \rho^1 u^1 \frac{\partial T^n}{\partial t}(c_v + R) + O(\Delta t^3). \quad (72)$$

Now, we consider the following Taylor series for the implicit block (Equation (65))

$$E^{n+1} = E^n + \Delta t \frac{\partial E^n}{\partial t} + \frac{\Delta t^2}{2} \frac{\partial^2 E^n}{\partial t^2} + O(\Delta t^3), \quad (73)$$

$$T^{n+1} = T^n + \Delta t \frac{\partial T^n}{\partial t} + \frac{\Delta t^2}{2} \frac{\partial^2 T^n}{\partial t^2} + O(\Delta t^3), \quad (74)$$

$$\kappa^{n+1} = \kappa^n + \Delta t \frac{\partial \kappa^n}{\partial t} + \frac{\Delta t^2}{2} \frac{\partial^2 \kappa^n}{\partial t^2} + O(\Delta t^3). \quad (75)$$

Substituting Equations (73), (74), (75), and (72) into Equation (65), we form the truncation term as

$$\begin{aligned} \tau^n = & E^n + \Delta t \frac{\partial E^n}{\partial t} + \frac{\Delta t^2}{2} \frac{\partial^2 E^n}{\partial t^2} - [E^n + \Delta t L(E^n) + \frac{\Delta t^2}{2} \frac{\partial L(E^n)}{\partial t} \\ & + \frac{\Delta t^2}{2} \rho^1 u^1 \frac{\partial T^n}{\partial t}(c_v + R)] - \Delta t \frac{1}{2} \frac{\partial}{\partial x} [(\kappa^n + \Delta t \frac{\partial \kappa^n}{\partial t} + \frac{\Delta t^2}{2} \frac{\partial^2 \kappa^n}{\partial t^2}) \\ & \frac{\partial}{\partial x} (T^n + \Delta t \frac{\partial T^n}{\partial t} + \frac{\Delta t^2}{2} \frac{\partial^2 T^n}{\partial t^2})] - \Delta t \frac{1}{2} \frac{\partial}{\partial x} (\kappa^n \frac{\partial T^n}{\partial x}) + O(\Delta t^3). \end{aligned} \quad (76)$$

Cancelling the opposite sign common terms and grouping the other terms together, we get

$$\begin{aligned} \tau^n = & \Delta t \left[\frac{\partial E^n}{\partial t} - L(E^n) \right] + \frac{\Delta t^2}{2} \frac{\partial}{\partial t} \left[\frac{\partial E^n}{\partial t} - L(E^n) \right] \\ & - \left[\frac{\Delta t}{2} \frac{\partial}{\partial x} (\kappa^n \frac{\partial T^n}{\partial x}) + \frac{\Delta t}{2} \frac{\partial}{\partial x} (\kappa^n \frac{\partial T^n}{\partial x}) \right] \\ & - \left[\frac{\Delta t^2}{2} \frac{\partial}{\partial x} (\kappa^n \frac{\partial T_t^n}{\partial x}) + \frac{\Delta t^2}{2} \frac{\partial}{\partial x} (\kappa_t^n \frac{\partial T^n}{\partial x}) \right] \\ & + \frac{\Delta t^2}{2} \rho^1 u^1 \frac{\partial T^n}{\partial t}(c_v + R) + O(\Delta t^3). \end{aligned} \quad (77)$$

This further simplifies by using

$$\frac{\partial}{\partial t} \left[\frac{\partial}{\partial x} (\kappa^n \frac{\partial T^n}{\partial x}) \right] = \frac{\partial}{\partial x} (\kappa_t^n \frac{\partial T^n}{\partial x}) + \frac{\partial}{\partial x} (\kappa^n \frac{\partial T_t^n}{\partial x}). \quad (78)$$

Then we have

$$\begin{aligned}\tau^n &= \Delta t \left[\frac{\partial E^n}{\partial t} - L(E^n) - \frac{\partial}{\partial x} \left(\kappa^n \frac{\partial T^n}{\partial x} \right) \right] \\ &+ \frac{\Delta t^2}{2} \frac{\partial}{\partial t} \left[\frac{\partial E^n}{\partial t} - L(E^n) - \frac{\partial}{\partial x} \left(\kappa^n \frac{\partial T^n}{\partial x} \right) \right] \\ &+ \frac{\Delta t^2}{2} \rho^1 u^1 \frac{\partial T^n}{\partial t} (c_v + R) + O(\Delta t^3).\end{aligned}\quad (79)$$

From the energy equation (Equation (10)) we have $\frac{\partial E^n}{\partial t} - L(E^n) - \frac{\partial}{\partial x} \left(\kappa^n \frac{\partial T^n}{\partial x} \right) = 0$, thus Equation (79) becomes

$$\tau^n = \frac{\Delta t^2}{2} \rho^1 u^1 \frac{\partial T^n}{\partial t} (c_v + R) + O(\Delta t^3).\quad (80)$$

This shows that the classic IMEX method carries first order terms in the resulting truncation error. This conclusion will be verified by our numerical computations (refer to Fig. 10).

5.2 A self-consistent IMEX method

We have already described how the self-consistent IMEX method operates on Equations (20)-(21) in Section 3.1. However, to be able to easily follow the analysis, we repeat the self-consistent operator splitting below.

Explicit block:

Step-1:

$$\begin{aligned}\rho^1 &= \rho^n - \Delta t \frac{\partial}{\partial x} (\rho u)^n, \\ (\rho u)^1 &= (\rho u)^n - \Delta t \frac{\partial}{\partial x} [(\rho u^2)^n + p^n], \\ E^1 &= E^n - \Delta t \frac{\partial}{\partial x} \{u^n [E^n + p^n]\},\end{aligned}\quad (81)$$

Step-2:

$$\begin{aligned}\rho^{n+1} &= \frac{\rho^1 + \rho^n}{2} - \frac{\Delta t}{2} \frac{\partial}{\partial x} (\rho u)^1, \\ (\rho u)^{n+1} &= \frac{(\rho u)^1 + (\rho u)^n}{2} - \frac{\Delta t}{2} \frac{\partial}{\partial x} [\rho^1 (u^2)^1 + R \rho^1 \mathbf{T}^{n+1}], \\ E^* &= \frac{E^n + E^1}{2} - \frac{\Delta t}{2} \frac{\partial}{\partial x} \{u^1 [c_v \rho^1 \mathbf{T}^{n+1} + \frac{1}{2} \rho^1 (u^1)^2 + R \rho^1 \mathbf{T}^{n+1}]\},\end{aligned}\quad (82)$$

Implicit block:

$$\frac{E^{n+1} - E^*}{\Delta t} = \frac{1}{2} \frac{\partial}{\partial x} \left(\kappa^{n+1} \frac{\partial T^{n+1}}{\partial x} \right) + \frac{1}{2} \frac{\partial}{\partial x} \left(\kappa^n \frac{\partial T^n}{\partial x} \right).\quad (83)$$

Notice that the implicit temperature impacts the explicit block in this case (refer to the highlighted terms in Equation (82)). Again, we perform the modified equation analysis on the energy part of Equations (81)-(83). Substituting E^1 into E^* , we get

$$E^* = E^n - \frac{\Delta t}{2} \frac{\partial}{\partial x} \{u^n [E^n + p^n]\} - \frac{\Delta t}{2} \frac{\partial}{\partial x} \{u^1 [c_v \rho^1 T^{n+1} + \frac{1}{2} \rho^1 (u^1)^2 + R \rho^1 T^{n+1}]\}.\quad (84)$$

We let $L(E^n) = -\frac{\partial}{\partial x}\{u^n[E^n + p^n]\}$ and use Equation (74) in (84) to get

$$E^* = E^n + \frac{\Delta t}{2}L(E^n) - \frac{\Delta t}{2}\frac{\partial}{\partial x}\{u^1[c_v\rho^1(T^n + \Delta t\frac{\partial T^n}{\partial t} + O(\Delta t^2)) + \frac{1}{2}\rho^1(u^1)^2 + R\rho^1(T^n + \Delta t\frac{\partial T^n}{\partial t} + O(\Delta t^2))]\}. \tag{85}$$

Now, we insert $T^n = T^1 - \Delta t\frac{\partial T^n}{\partial t} + O(\Delta t^2)$ in Equation (85) and perform few algebra to get

$$E^* = E^n + \frac{\Delta t}{2}L(E^n) + \frac{\Delta t}{2}L(E^1) + O(\Delta t^3), \tag{86}$$

where $L(E^1) = -\frac{\partial}{\partial x}\{u^1[c_v\rho^1T^1 + \frac{1}{2}\rho^1(u^1)^2 + R\rho^1T^1]\}$. Equation (86) can be further simplified by using (71),

$$E^* = E^n + \Delta tL(E^n) + \frac{\Delta t^2}{2}\frac{\partial L}{\partial t} + O(\Delta t^3). \tag{87}$$

Making use of the Taylor series given in Equations (73), (74), (75), and Equation (87) in the implicit discretization (83), we form the truncation error term as

$$\begin{aligned} \tau^n &= E^n + \Delta t\frac{\partial E^n}{\partial t} + \frac{\Delta t^2}{2}\frac{\partial^2 E^n}{\partial t^2} - (E^n + \Delta tL(E^n) + \frac{\Delta t^2}{2}\frac{\partial L(E^n)}{\partial t}) \\ &\quad - \Delta t\frac{1}{2}\frac{\partial}{\partial x}[(\kappa^n + \Delta t\frac{\partial \kappa^n}{\partial t} + \frac{\Delta t^2}{2}\frac{\partial^2 \kappa^n}{\partial t^2})\frac{\partial}{\partial x}(T^n + \Delta t\frac{\partial T^n}{\partial t} + \frac{\Delta t^2}{2}\frac{\partial^2 T^n}{\partial t^2})] \\ &\quad - \Delta t\frac{1}{2}\frac{\partial}{\partial x}(\kappa^n\frac{\partial T^n}{\partial x}) + O(\Delta t^3). \end{aligned} \tag{88}$$

Cancelling the opposite sign common terms, grouping the other terms together, and making use of Equation (78), we get

$$\tau^n = \Delta t [\frac{\partial E^n}{\partial t} - L(E^n) - \frac{\partial}{\partial x}(\kappa^n\frac{\partial T^n}{\partial x})] + \frac{\Delta t^2}{2}\frac{\partial}{\partial t}[\frac{\partial E^n}{\partial t} - L(E^n) - \frac{\partial}{\partial x}(\kappa^n\frac{\partial T^n}{\partial x})] + O(\Delta t^3) \tag{89}$$

Again from the energy equation, we know that $\frac{\partial E^n}{\partial t} - L(E^n) - \frac{\partial}{\partial x}(\kappa^n\frac{\partial T^n}{\partial x}) = 0$, thus Equation (89) becomes

$$\tau^n = O(\Delta t^3), \tag{90}$$

clearly proving that the self-consistent IMEX method is second order.

Here, we numerically verify our analytical findings about the two IMEX approaches. We solve the point explosion problem studied in (Kadioglu & Knoll, 2010) by using the LERH model and $M = 200$ cell points until the final time $t = 0.02$. We note that we ran the code twice as longer final time than the original test in order to allow the numerical methods to depict more accurate time behaviors. In Fig. 10, we plot the L_2 -norm of errors for variety of flow variables committed by the both approaches. Fig. 10 clearly shows that the classic IMEX method suffers from order reductions as predicted by our mathematical analysis. We present more detailed analysis regarding more general IMEX methods (e.g., Strang splitting type methods (Knoth & Wolke, 1999; Strang, 1968)) in our forthcoming paper (Kadioglu, Knoll & Lowrie, 2010).

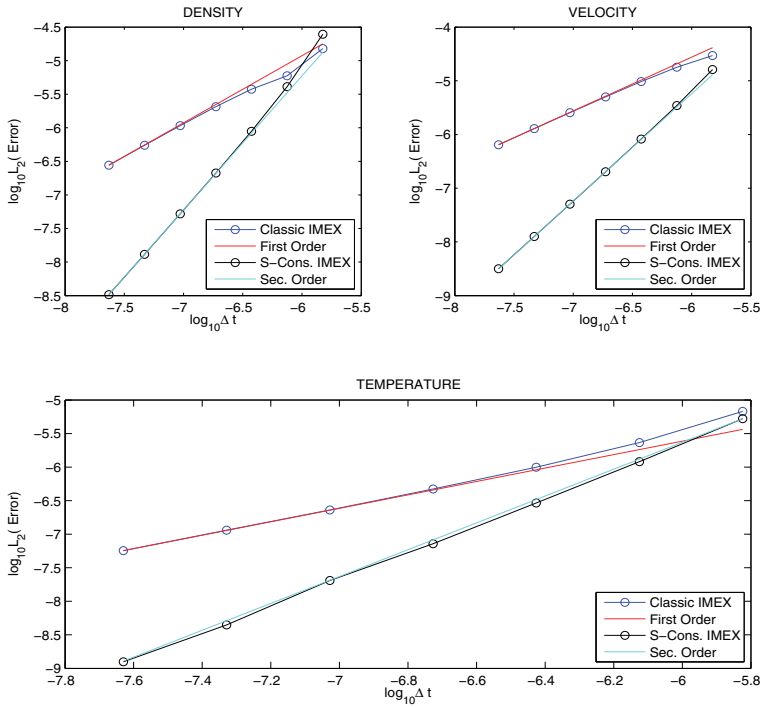


Fig. 10. The self-consistent IMEX method versus a classic IMEX method in terms of the time convergence.

6. Conclusion

We have presented a self-consistent implicit/explicit (IMEX) time integration technique for solving the Euler equations that possess strong nonlinear heat conduction and very stiff source terms (Radiation hydrodynamics). The key to successfully implementing an implicit/explicit algorithm in a self-consistent sense is to carry out the explicit integrations as part of the non-linear function evaluations within the implicit solver. In this way, the improved time accuracy of the non-linear iterations is immediately felt by the explicit algorithm block and the more accurate explicit solutions are readily available to form the next set of non-linear residuals. We have solved several test problems that use both of the low and high energy density radiation hydrodynamics models (the LERH and HERH models) in order to validate the numerical order of accuracy of our scheme. For each test, we have established second order time convergence. We have also presented a mathematical analysis that reveals the analytical behavior of our method and compares it to a classic IMEX approach. Our analytical findings have been supported/verified by a set of computational results. Currently, we are exploring more about our multi-phase IMEX study to solve multi-phase flow systems that possess tight non-linear coupling between the interface and fluid dynamics.

7. Acknowledgement

The submitted manuscript has been authored by a contractor of the U.S. Government under Contract No. DEAC07-05ID14517 (INL/MIS-11-22498). Accordingly, the U.S. Government retains a non-exclusive, royalty-free license to publish or reproduce the published form of this contribution, or allow others to do so, for U.S. Government purposes.

8. References

- Anderson, J. (1990). *Modern Compressible Flow.*, Mc Graw Hill.
- Ascher, U. M., Ruuth, S. J. & Spiteri, R. J. (1997). Implicit-explicit Runge-Kutta methods for time-dependent partial differential equations., *Appl. Num. Math.* 25: 151–167.
- Ascher, U. M., Ruuth, S. J. & Wetton, B. T. R. (1995). Implicit-explicit methods for time-dependent pde's., *SIAM J. Num. Anal.* 32: 797–823.
- Bates, J. W., Knoll, D. A., Rider, W. J., Lowrie, R. B. & Mousseau, V. A. (2001). On consistent time-integration methods for radiation hydrodynamics in the equilibrium diffusion limit: Low energy-density regime., *J. Comput. Phys.* 167: 99–130.
- Bowers, R. & Wilson, J. (1991). *Numerical Modeling in Applied Physics and Astrophysics.*, Jones & Bartlett, Boston.
- Brown, P. & Saad, Y. (1990). Hybrid Krylov methods for nonlinear systems of equations., *SIAM J. Sci. Stat. Comput.* 11: 450–481.
- Castor, J. (2006). *Radiation Hydrodynamics.*, Cambridge University Press.
- Dai, W. & Woodward, P. (1998). Numerical simulations for radiation hydrodynamics. i. diffusion limit., *J. Comput. Phys.* 142: 182.
- Dembo, R. (1982). Inexact newton methods., *SIAM J. Num. Anal.* 19: 400–408.
- Drake, R. (2007). Theory of radiative shocks in optically thick media., *Physics of Plasmas* 14: 43301.
- Ensman, L. (1994). Test problems for radiation and radiation hydrodynamics codes., *The Astrophysical Journal* 424: 275–291.
- Gottlieb, S. & Shu, C. (1998). Total variation diminishing Runge-Kutta schemes., *Mathematics of Computation* 221: 73–85.
- Gottlieb, S., Shu, C. & Tadmor, E. (2001). Strong stability-preserving high-order time discretization methods., *Siam Review* 43-1: 89–112.
- Kadioglu, S. & Knoll, D. (2010). A fully second order Implicit/Explicit time integration technique for hydrodynamics plus nonlinear heat conduction problems., *J. Comput. Phys.* 229-9: 3237–3249.
- Kadioglu, S. & Knoll, D. (2011). Solving the incompressible Navier-Stokes equations by a second order IMEX method with a simple and effective preconditioning strategy., *Appl. Math. Comput. Sci.* Accepted.
- Kadioglu, S., Knoll, D. & Lowrie, R. (2010). Analysis of a self-consistent IMEX method for tightly coupled non-linear systems., *SIAM J. Sci. Comput.* to be submitted.
- Kadioglu, S., Knoll, D., Lowrie, R. & Rauen Zahn, R. (2010). A second order self-consistent IMEX method for Radiation Hydrodynamics., *J. Comput. Phys.* 229-22: 8313–8332.
- Kadioglu, S., Knoll, D. & Oliveria, C. (2009). Multi-physics analysis of spherical fast burst reactors., *Nuclear Science and Engineering* 163: 1–12.
- Kadioglu, S., Knoll, D., Sussman, M. & Martineau, R. (2010). A second order JFNK-based IMEX method for single and multi-phase flows., *Computational Fluid Dynamics, Springer-Verlag* DOI 10.1007/978 - 3 - 642 - 17884 - 9_69.

- Kadioglu, S., Sussman, M., Osher, S., Wright, J. & Kang, M. (2005). A Second Order Primitive Preconditioner For Solving All Speed Multi-Phase Flows., *J. Comput. Phys.* 209-2: 477–503.
- Kelley, C. (2003). *Solving Nonlinear Equations with Newton's Method.*, Siam.
- Khan, L. & Liu, P. (1994). An operator-splitting algorithm for coupled one-dimensional advection-diffusion-reaction equations., *Computer Meth. Appl. Mech. Eng.* 127: 181–201.
- Kim, J. & Moin, P. (1985). Application of a fractional-step method to incompressible navier-stokes equations., *J. Comput. Phys.* 59: 308–323.
- Knoll, D. A. & Keyes, D. E. (2004). Jacobian-free Newton Krylov methods: a survey of approaches and applications., *J. Comput. Phys.* 193: 357–397.
- Knoth, O. & Wolke, R. (1999). Strang splitting versus implicit-explicit methods in solving chemistry transport models., *Transactions on Ecology and the Environment* 28: 524–528.
- LeVeque, R. (1998). *Finite Volume Methods for Hyperbolic Problems.*, Cambridge University Press, Texts in Applied Mathematics.
- Lowrie, R. B., Morel, J. E. & Hittinger, J. A. (1999). The coupling of radiation and hydrodynamics., *Astrophys. J.* 521: 432.
- Lowrie, R. & Edwards, J. (2008). Radiative shock solutions with grey nonequilibrium diffusion., *Shock Waves* 18: 129–143.
- Lowrie, R. & Rauenzahn, R. (2007). Radiative shock solutions in the equilibrium diffusion limit., *Shock Waves* 16: 445–453.
- Marshak, R. (1958). Effect of radiation on shock wave behavior., *Phys. Fluids* 1: 24–29.
- Mihalas, D. & Mihalas, B. (1984). *Foundations of Radiation Hydrodynamics.*, Oxford University Press, New York.
- Pomraning, G. (1973). *The Equations of Radiation Hydrodynamics.*, Pergamon, Oxford.
- Reid, J. (1971). *On the methods of conjugate gradients for the solution of large sparse systems of linear equations.*, Large Sparse Sets of Linear Equations, Academic Press, New York.
- Rider, W. & Knoll, D. (1999). Time step size selection for radiation diffusion calculations., *J. Comput. Phys.* 152-2: 790–795.
- Ruuth, S. J. (1995). Implicit-explicit methods for reaction-diffusion problems in pattern formation., *J. Math. Biol.* 34: 148–176.
- Saad, Y. (2003). *Iterative Methods for Sparse Linear Systems.*, Siam.
- Shu, C. & Osher, S. (1988). Efficient implementation of essentially non-oscillatory shock capturing schemes., *J. Comput. Phys.* 77: 439.
- Shu, C. & Osher, S. (1989). Efficient implementation of essentially non-oscillatory shock capturing schemes II., *J. Comput. Phys.* 83: 32.
- Smoller, J. (1994). *Shock Waves And Reaction-diffusion Equations.*, Springer.
- Strang, G. (1968). On the construction and comparison of difference schemes., *SIAM J. Numer. Anal.* 8: 506–517.
- Strikwerda, J. (1989). *Finite Difference Schemes Partial Differential Equations.*, Wadsworth & Brooks/Cole, Advance Books & Software, Pacific Grove, California.
- Thomas, J. (1998). *Numerical Partial Differential Equations I (Finite Difference Methods).*, Springer-Verlag New York, Texts in Applied Mathematics.
- Thomas, J. (1999). *Numerical Partial Differential Equations II (Conservation Laws and Elliptic Equations).*, Springer-Verlag New York, Texts in Applied Mathematics.
- Wesseling, P. (2000). *Principles of Computational Fluid Dynamics.*, Springer Series in Computational Mathematics.

Hydrodynamics on Charged Superparamagnetic Microparticles in Water Suspension: Effects of Low-Confinement Conditions and Electrostatics Interactions

P. Domínguez-García¹ and M.A. Rubio²

¹*Dep. Física de Materiales, UNED, Senda del Rey 9, 28040. Madrid*

²*Dep. Física Fundamental, UNED, Senda del Rey 9, 28040. Madrid
Spain*

1. Introduction

The study of colloidal dispersions of micro-nano sized particles in a liquid is of great interest for industrial processes and technological applications. The understanding of the microstructure and fundamental properties of this kind of systems at microscopic level is also useful for biological and biomedical applications.

However, a colloidal suspension must be placed somewhere and the dynamics of the micro-particles can be modified as a consequence of the confinement, even if we have a low-confinement system. The hydrodynamics interactions between particles and with the enclosure's wall which contains the suspension are of extraordinary importance to understanding the aggregation, disaggregation, sedimentation or any interaction experienced by the microparticles. Aspects such as corrections of the diffusion coefficients because of a hydrodynamic coupling to the wall must be considered. Moreover, if the particles are electrically charged, new phenomena can appear related to electro-hydrodynamic coupling.

Electro-hydrodynamic effects (Behrens & Grier (2001a,b); Squires & Brenner (2000)) may have a role in the dynamics of confined charged submicron-sized particles. For example, an anomalous attractive interaction has been observed in suspensions of confined charged particles (Grier & Han (2004); Han & Grier (2003); Larsen & Grier (1997)). The possible explanation of this observation could be related with the distribution of surface's charges of the colloidal particles and the wall (Lian & Ma (2008); Odriozola et al. (2006)). This effect could be also related to an electrostatic repulsion with the charged quartz bottom wall or to a spontaneous macroscopic electric field observed on charged colloids (Rasa & Philipse (2004)). In this work, we are going to describe experiments performed by using magneto-rheological fluids (MRF), which consist (Rabinow (1948)) on suspensions formed by water or some organic solvent and micro or nano-particles that have a magnetic behaviour when an external magnetic field is applied upon them. Then, these particles interact between themselves forming aggregates with a shape of linear chains (Kerr (1990)) aligned in the direction of the magnetic field. When the concentration of particles inside the fluid is high enough, this microscopic behaviour turns to significant macroscopic

consequences, as an one million-fold increase in the viscosity of the fluid, leading to practical and industrial applications, such as mechanical devices of different types (Lord Corporation, <http://www.lord.com/> (n.d.); Nakano & Koyama (1998); Tao (2000)). This magnetic particle technology has been revealed as useful in other fields such as microfluidics (Egatz-Gómez et al. (2006)) or biomedical techniques (Komeili (2007); Smirnov et al. (2004); Vuppu et al. (2004); Wilhelm, Browaeys, Ponton & Bacri (2003); Wilhelm et al. (2005)).

In our case, we investigate the dynamics of the aggregation of magnetic particles under a constant and uniaxial magnetic field. This is useful not only for the knowledge of aggregation properties in colloidal systems, but also for testing different models in Statistical Mechanics. Using video-microscopy (Crocker & Grier (1996)), we have measured the different exponents which characterize this process during aggregation (Domínguez-García et al. (2007)) and also in disaggregation (Domínguez-García et al. (2011)), i.e., when the chains vanishes as the external field is switched off. These exponents are based on the temporal variation of the aggregates' representative quantities, such as the size s or length l . For instance, the main dynamical exponent z is obtained through the temporal evolution of the chains length $s \sim t^z$. Our experiments analyse the microstructure of the suspensions, the aggregation of the particles under external magnetic fields as well as disaggregation when the field is switched off. The observations provide results that diverge from what a simple theoretical model says. These differences may be related with some kind of electro-hydrodynamical interaction, which has not been taken into account in the theoretical models.

In this chapter, we would like first to summarize the basic theory related with our system of magnetic particles, including magnetic interactions and Brownian movement. Then, hydrodynamic corrections and the Boltzmann sedimentation profile theory in a confined suspension of microparticles will be explained and some fundamentals of electrostatics in colloids are explained. In the next section, we will summarize some of the most recent remarkable studies related with the electrostatic and hydrodynamic effects in colloidal suspensions. Finally, we would like to link our findings and investigations on MRF with the theory and studies explained herein to show how the modelization and theoretical comprehension of these kind of systems is not perfectly understood at the present time.

2. Theory

In this section, we are going to briefly describe the theory related with the main interactions and effects which can be suffered by colloidal magnetic particles: magnetic interactions, Brownian movement, hydrodynamic interactions and finally electrostatic interactions.

2.1 Magnetic particles

By the name of "colloid" we understand a suspension formed by two phases: one is a fluid and another composed of mesoscopic particles. The mesoscopic scale is situated between the tens of nanometers and the tens of micrometers. This is a very interesting scale from a physical point of view, because it is a transition zone between the atomic and molecular scale and the purely macroscopic one.

When the particles have some kind of magnetic property, we are talking about magnetic colloids. From this point of view, two types of magnetic colloids are usually considered: ferromagnetic and magneto-rheologic. The ferromagnetic fluids or ferrofluids (FF) are colloidal suspensions composed by nanometric mono-domain particles in an aqueous or organic solvent, while magneto-rheological fluids (MRF) are suspensions of paramagnetic micro or nanoparticles. The main difference between them is the permanent magnetic moment

of the first type: while in a FF, magnetic aggregation is possible without an external magnetic field, this does not occur in a MRF. The magnetic particles of a MRF are usually composed by a polymeric matrix with small crystals of some magnetic material embedded on it, for example, magnetite. When the particles are superparamagnetic, the quality of the magnetic response is improved because the imanation curve has neither hysteresis nor remanence.

Another point of view for classifying these suspensions is the rheological perspective. By rheology, we name the discipline which study deformations and flowing of materials when some stress is applied. In some ranges, it is possible to consider the magnetic colloids as Newtonian fluids because, when an external magnetic field is applied, the stress is proportional to the velocity of the deformation. On a more global perspective, these fluids can be immersed on the category of complex fluids (Larson (1999)) and are studied as complex systems (Science. (1999)).

Now we are going to briefly provide some details about magnetic interactions: magnetic dipolar interaction, interaction between chains and irreversible aggregation.

2.1.1 Magnetic dipolar interaction

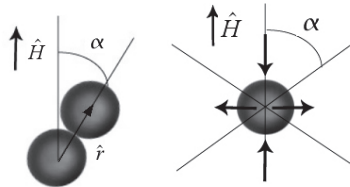


Fig. 1. Left: Two magnetic particles under a magnetic field \vec{H} . The angle between the field direction and the line that join the centres of the particles is named as α . Right: The attraction cone of a magnetic particle. Top and bottom zones are magnetically attractive, while regions on the left and on the right have repulsive behaviour.

As it has been said before, the main interest of MRF are their properties in response to external magnetic fields. These properties can be optical (birefringence (Bacri et al. (1993)), dichroism (Melle (2002))) or magnetical or rheological. Under the action of an external magnetic field, the particles acquire a magnetic moment and the interaction between the magnetic moments generates the particles aggregation in the form of chain-like structures. More in detail, when a magnetic field \vec{H} is applied, the particles in suspension acquire a dipolar moment:

$$\vec{m} = \frac{4\pi a^3}{3} \vec{M} \tag{1}$$

where $\vec{M} = \chi \vec{H}$ and a are respectively the particle's imanation and radius, whereas χ is the magnetic susceptibility of the particle.

The most simple way for analysing the magnetic interaction between magnetic particles is through the dipolar approximation. Therefore, the interaction energy between two magnetic dipoles \vec{m}_i and \vec{m}_j is:

$$U_{ij}^d = \frac{\mu_0 \mu_s}{4\pi r^3} \left[(\vec{m}_i \cdot \vec{m}_j) - 3(\vec{m}_i \cdot \hat{r})(\vec{m}_j \cdot \hat{r}) \right] \tag{2}$$

where \vec{r}_i is the position vector of the particle i , $\vec{r} = \vec{r}_j - \vec{r}_i$ joins the centre of both particles and $\hat{r} = \vec{r}/r$ is its unitary vector.

Then, we can obtain the force generated by \vec{m}_i under \vec{m}_j as:

$$\vec{F}_{ij}^d = \frac{3\mu_0\mu_s}{4\pi r^4} \left\{ \left[(\vec{m}_i \cdot \vec{m}_j) - 5(\vec{m}_i \cdot \hat{r})(\vec{m}_j \cdot \hat{r}) \right] \hat{r} + (\vec{m}_j \cdot \hat{r})\vec{m}_i + (\vec{m}_i \cdot \hat{r})\vec{m}_j \right\} \quad (3)$$

If both particles have identical magnetic properties and knowing that the dipole moment aligns with the field, we obtain the following two expressions for potential energy and force:

$$U_{ij}^d = \frac{\mu_0\mu_s m^2}{4\pi r^3} (1 - 3\cos^2 \alpha) \quad (4)$$

$$\vec{F}_{ij}^d = \frac{3\mu_0\mu_s m^2}{4\pi r^4} \left[(1 - 3\cos^2 \alpha)\hat{r} - \sin(2\alpha)\hat{a} \right] \quad (5)$$

where α is the angle between the direction of the magnetic field \hat{H} , and the direction set by \hat{r} and where \hat{a} is its unitary vector.

From the above equations, it follows that the radial component of the magnetic force is attractive when $\alpha < \alpha_c$ and repulsive when $\alpha > \alpha_c$, where $\alpha_c = \arccos \frac{1}{\sqrt{3}} \simeq 55^\circ$, so that the dipolar interaction defines an hourglass-shaped region of attraction-repulsion in the complementary region (see Fig.1). In addition, the angular component of the dipolar interaction always tends to align the particles in the direction of the applied magnetic field. Thus, the result of this interaction will be an aggregation of particles in linear structures oriented in the direction of \hat{H} .

The situation depicted here is very simplified, especially from the viewpoint of magnetic interaction itself. In the above, we have omitted any deviations from this ideal behaviour, such as multipole interactions or local field (Martin & Anderson (1996)). Multipolar interactions can become important when $\mu_p/\mu_s \gg 1$. The local field correction due to the magnetic particles themselves generate magnetic fields that act on other particles, increasing the magnetic interaction. For example, when the magnetic susceptibility is approximately $\chi \sim 1$, this interaction tends to increase the angle of the cone of attraction from 55° to about 58° and also the attractive radial force in a 25% and the azimuth in a 5% (Melle (2002)).

One type of fluid, called electro-rheological (ER fluids) is the electrical analogue of MRF. This type of fluid is very common in the study of kinematics of aggregation. Basically, the ER fluids consist of suspensions of dielectric particles of sizes on the order of micrometers (up to hundreds of microns) in conductive liquids. This type of fluid has some substantial differences with MRF, especially in view of the ease of use. The development of devices using electric fields is more complicated, requiring high power voltage; in addition, ER fluids have many more problems with surface charges than MRF, which must be minimized as much as possible in aggregation studies. However, basic physics, described above, are very similar in both systems, due to similarities between the magnetic and electrical dipolar interaction.

2.1.2 Magnetic interaction between chains

Chains of magnetic particles, once formed, interact with other chains in the fluid and with single particles. In fact, the chains may laterally coalesce to form thicker strings (sometimes called columns). This interaction is very important, especially when the concentration of particles in suspension is high. The first works that studied the interaction between chains of particles come from the earliest studies of external field-induced aggregation (Fermigier & Gast (1992); Fraden et al. (1989))

Basically, the aggregation process has two stages: first, the chains are formed on the basis of the aggregation of free particles, after that, more complex structures are formed when chains aggregate by lateral interaction. When the applied field is high and the concentration of particles in the fluid is low, the interactions between the chains are of short range. Under this situation, there are two regions of interaction between the chains depending on the lateral distance between them: when the distance between two strings is greater than two diameters of the particle, the force is repulsive; if the distance is lower, the resultant force is attractive, provided that one of the chains is moved from the other a distance equal to one particle's radius in the direction of external field (Furst & Gast (2000)). In this type of interactions, the temperature fluctuations and the defects in the chains morphology are particularly important. Indeed, variations on these two aspects generate different types of theoretical models for the interaction between chains. The model that takes into account the thermal fluctuations in the structure of the chain for electro-rheological fluids is called *HT* (Halsey & Toor (1990)), and was subsequently extended to a modified HT model (MHT) (Martin et al. (1992)) to include dependence on field strength. The latter model shows that only lateral interaction occurs between the chains when the characteristic time associated with their thermal relaxation is greater than the characteristic time of lateral assembling between them. Possible defects in the chains can vary the lateral interaction, mainly through perturbations in the local field.

2.1.3 Irreversible aggregation

The irreversible aggregation of colloidal particles is a phenomenon of fundamental importance in colloid science and its applications. Basically, there are two basic scenarios of irreversible colloidal aggregation. The first, exemplified by the model of Witten & Sander (1981), is often referred to as Diffusion-Limited Aggregation (DLA). In this model, the particles diffuse without interaction between them, so that aggregation occurs when they collide with the central cluster. The second scenario is when there is a potential barrier between the particles and the aggregate, so that aggregation is determined by the rate at which the particles manage to overcome this barrier. The second model is called Colloid Reaction-Limited Aggregation (RLCA). These two processes have been observed experimentally in colloidal science (Lin et al. (1989); Tirado-Miranda (2001)).

These aggregation processes are often referred as fractal growth (Vicsek (1992)) and the aggregates formed in each process are characterized by a concrete fractal dimension. For example, in DLA we have aggregates with fractal dimension $D_f \sim 1.7$, while RLCA provides $D_f \sim 2.1$. A very important property of these systems is precisely that its basic physics is independent of the chemical peculiarities of each system colloidal i.e., these systems have universal aggregation. Lin et al. (1989) showed the universality of the irreversible aggregation systems performing light scattering experiments with different types of colloidal particles and changing the electrostatic forces in order to study the RLCA and DLA regimes in a differentiated way. They obtained, for example, that the effective diffusion coefficient (Eq.28) did not depend on the type of particle or colloid, but whether the process aggregation was DLA or RLCA.

The DLA model was generalized independently by Meakin (1983) and Kolb et al. (1983), allowing not only the diffusion of particles, but also of the clusters. In this model, named Cluster-Cluster Aggregation (CCA), the clusters can be added by diffusion with other clusters or single particles. Within these systems, if the particles are linked in a first touch, we obtain the DCLA model. The theoretical way to study these systems is to use the theory of von Smoluchowski (von Smoluchowski (1917)) for cluster-cluster aggregation among Monte Carlo

simulations (Vicsek (1992)). This theory considers that the aggregation kinetics of a system of N particles, initially separated and identical, aggregate; and these clusters join themselves to form larger objects. This process is studied through the distribution of cluster sizes $n_s(t)$ which can be defined as the number of aggregates of size s per unit of volume in the system at a time t . Then, the temporal evolution is given by the following set of equations:

$$\frac{dn_s(t)}{dt} = \frac{1}{2} \sum_{i+j=s} K_{ij} n_i n_j - n_s \sum_{j=1} K_{sj} n_j, \quad (6)$$

where the kernel K_{ij} represents the rate at which the clusters of size i and j are joined to form a cluster of size $s = i + j$. All details of the physical system are contained in the kernel K_{ij} , so that, for example, in the DLA model, the kernel is proportional to the product of the cross-section of the cluster and the diffusion coefficient. Eq.6 has certain limitations because only allows binary aggregation processes, so it is just applied to processes with very low concentration of particles.

A scaling relationship for the cluster size distribution function in the DCLA model was introduced by Vicsek & Family (1984) to describe the results of Monte Carlo simulations. This scaling relationship can be written as:

$$n_s \sim s^{-2} g(s/S(t)) \quad (7)$$

where $S(t)$ is the average cluster size of the aggregates:

$$S(t) \equiv \frac{\sum_s s^2 n_s(t)}{\sum_s s n_s(t)} \quad (8)$$

and where the function $g(x)$ is in the form:

$$g(x) \begin{cases} \sim x^\Delta & \text{if } x \ll 1 \\ \ll 1 & \text{if } x \gg 1 \end{cases}$$

One consequence of the scaling 7 is that a temporal power law for the average cluster size can be deduced:

$$S(t) \sim t^z \quad (9)$$

Calculating experimentally the average cluster size along time, we can obtain the kinetic exponent z . Similarly to $S(t)$ is possible to define an average length in number of aggregates $l(t)$:

$$l(t) \equiv \frac{\sum_s s n_s(t)}{\sum_s n_s(t)} = \frac{1}{N(t)} \sum_s s n_s(t) = \frac{N_p}{N(t)} \quad (10)$$

where $N(t) = \sum n_s(t)$ is the total number of cluster in the system at time t and $N_p = \sum s n_s(t)$ is the total number of particles. Then, it is expected that N had a power law form with exponent z' :

$$N(t) \sim t^{-z'} \quad (11)$$

$$l(t) \sim t^{z'} \quad (12)$$

2.2 Brownian movement and microrheology

Robert Brown¹ (1773-1858) discovered the phenomena that was denoted with his name in 1827, when he studied the movement of pollen in water. The explanation of Albert Einstein in 1905 includes the named Stokes-Einstein relationship for the diffusion coefficient of a particle of radius a immersed in a fluid of viscosity η at temperature T :

$$D = \frac{k_B T}{6\pi a \eta} \tag{13}$$

where k_B is the Boltzmann constant. This equation can be generalized for an object (an aggregate) formed by a number of particles N :

$$D = \frac{k_B T}{6\pi \eta R_g}$$

where R_g is the radius of gyration defined as $R_g(N) = \sqrt{1/N \sum_{i=1}^N r_i^2}$, where r_i is the distance between the i particle to the centre of mass of the cluster. If $R_g = a$, we recover the Stokes-Einstein expression.

Let's see how to calculate the diffusion coefficient D from the observation of individual particles moving in the fluid. The diffusion equation says that:

$$\frac{\partial \rho}{\partial t} = D \nabla^2 \rho$$

where ρ is here the probability density function of a particle that spreads a distance Δr at time t . This equation has as a solution:

$$\rho(\Delta r, t) = \frac{1}{(4\pi Dt)^{3/2}} e^{-\Delta r^2/4Dt} \tag{14}$$

If the Brownian particle moves a distance Δr in the medium on which is immersed after a time δt , then the mean square displacement (MSD) weighted with the probability function given by Eq.14 is given by:

$$\langle (\Delta r)^2 \rangle = \langle |r(t + \delta t) - r(t)|^2 \rangle = 6Dt \tag{15}$$

The diffusion coefficient can be obtained by 15 and observing the displacement Δr of the particle for a fixed δt . In two dimensions, the equations 14 and 15 are:

$$\rho(\Delta r, t) = \frac{1}{(4\pi Dt)} e^{-\Delta r^2/4Dt} \tag{16}$$

$$\langle |r(t + \delta t) - r(t)|^2 \rangle = 4Dt \tag{17}$$

The equations 13 and 15 are the basis for the development of a experimental technique known as microrheology (Mason & Weitz (1995)). This technique consists of measuring viscosity and other mechanical quantities in a fluid by monitoring, using video-microscopy, the movement

¹ Literally: *While examining the form of these particles immersed in water, I observed many of them very evidently in motion [...]. These motions were such as to satisfy me, after frequently repeated observation, that they arose neither from currents in the fluid, nor from its gradual evaporation, but belonged to the particle itself.* (Edinburgh New Philosophical Journal, Vol. 5, April to September, 1828, pp. 358-371)

of micro-nano particles (regardless their poralization). Thus, it is possible to obtain the viscosity of the medium simply by studying the displacement of the particle in the fluid. The microrheology has been widely used since the late nineties of last century (Waigh (2005)). Due to microrheology needs and for the sake of the analysis of the thermal fluctuation spectrum of probe spheres in suspension, the generalized Stokes-Einstein equation (Mason & Weitz (1995)) was developed. This expression is similar to Eq.13, but introducing Laplace transformed quantities:

$$\tilde{D}(s) = \frac{k_B T}{6\pi a s \tilde{\eta}_s} \quad (18)$$

where s is the Laplace frequency, and $\tilde{\eta}_s$ and $\tilde{D}(s)$ are the Laplace transformed viscosity and diffusion coefficient. The dynamics of the Brownian particles can be very different depending on the mechanical properties of the fluid. This equation is the base for the rheological study, by obtaining its viscoelastic moduli (Mason (2000)), of the complex fluid in which the particles are immersed.

If we only track the random motion of colloidal spheres moving freely in the fluid, we are talking of “passive” microrheology, but there are variations on this technique named “active” microrheology, for example, using optical tweezers (Grier (2003)). This technique allows to study the response of colloidal particles in viscoelastic fluids and the structure of fluids in the micro-nanometer scales (Furst (2005)), measure viscoelastic properties of biopolymers (like DNA) and the cell membrane (Verdier (2003)). Other useful methodologies are the two-particles microrheology (Crocker et al. (2000)) which allows to accurately measure rheological properties of complex materials, the use of rotating chains following an external rotating magnetic field (Wilhelm, Browaeys, Ponton & Bacri (2003); Wilhelm, Gazeau & Bacri (2003)) or magnetic bead microrheometry (Keller et al. (2001)).

2.3 Hydrodynamics

When we are talking about hydrodynamics in a colloidal suspension of particles we need to introduce the Reynolds number, Re , defined as:

$$Re \equiv \frac{\rho_r v a}{\eta} \quad (19)$$

where ρ_r is the relative density, a is the particle radius, v is the velocity of the particle in the fluid which has a viscosity η . This number reflects the relation between the inertial forces and the viscous friction. If we are in a situation of low Reynolds number dynamics, as it usually happens in the physical situation here studied, the inertial terms in the Newton equations can be neglected, and $m\ddot{x} \cong 0$.

However, even in the case of low Reynolds number, the diffusion coefficient of particles in a colloidal system may have certain deviations from the expressions explained above. The diffusion coefficient can vary due to hydrodynamic interactions between particles, the morphology of the clusters, or because of the enclosure containing the suspension. When a particle moves near a “wall”, the change in the Brownian dynamics of the particle is remarkable. The effective diffusion coefficient then varies with the distance of the particle from the wall (Russel et al. (1989)), the closer is the particle to the wall, the lower the diffusion coefficient. The interest of the modification on Brownian dynamics in confinement situations is quite large, for example to understand how particles migrate in porous media, how the macromolecules spread in membranes, or how cells interact with surfaces.

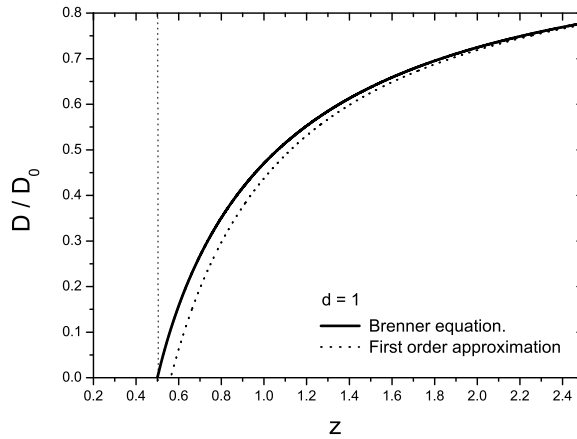


Fig. 2. Comparative analysis between the relative diffusion coefficient for the Brenner equation (Eq.20) and the first order approximation (Eq.21), as a function of the distance to the wall z for a particle of diameter 1 (z -unit are in divided by the diameter of the particle). These two expressions are practically equal when $z \geq 1.5$.

2.3.1 Particle-wall interaction

When a particle diffuses near a wall, thanks to the linearity of Stokes equations, the diffusion coefficient can be separated into two components, one parallel to the wall $D_{||}$ and the other perpendicular D_{\perp} . In the literature, several studies in this regard can be found (Crocker (1997); Lin et al. (2000); Russel et al. (1989)). One particularly important is the study of Fauchaux & Libchaber (1994) where measurements of particles confined between two walls are reported. This work provides a table with the diffusion coefficients obtained (theoretical and experimental) for different samples (different radius and particles) and different distances from the wall, from 1 to 12 μm . For example, for a particle diameter 2.5 μm , a distance of 1.3 μm from the wall and with a density 2.1 times that of water, a diffusion coefficient $D/D_0 = 0.32$ is obtained, where D_0 is the diffusion coefficient given by Eq.13.

There are no closed analytical solutions for this type of problem, with the exception of that obtained for a sphere moving near a flat wall in the direction perpendicular to it (Brenner (1961)):

$$\frac{D_{\perp}(z)}{D_0} = \left\{ \frac{4}{3} \sinh \alpha \sum_{n=1}^{\infty} \frac{n(n+1)}{(2n-1)(2n+3)} \left[\frac{2 \sinh[(2n+1)\alpha] + (2n+1) \sinh[2\alpha]}{4 \sinh^2[(n+1/2)\alpha] - (2n+1)^2 \sinh^2[\alpha]} - 1 \right] \right\}^{-1} \quad (20)$$

where $\alpha \equiv \text{arccosh}(z/a)$ and a is the radius particle and z is the distance between the centre of the particle and the wall.

Theoretical calculations in this regard are generally based on the methods of reflections, which involves splitting the hydrodynamic interaction between the wall and the particle in a linear superposition of interactions of increasing order. Using this method, it is possible to obtain a iterative solution for this problem in power series of (a/z) . In the case of the perpendicular direction it is found:

$$\frac{D_{\perp}(z)}{D_0} \cong 1 - \frac{9}{8} \left(\frac{a}{z}\right) + O\left(\frac{a}{z}\right)^3 \quad (21)$$

In the Fig.2 a comparison between the exact equation 20 and this first order expression 21 is plotted. These two expressions provide similar results when $z \geq 1.5$.

In the case of the parallel direction to the wall we have the following approximation :

$$\frac{D_{||}(z)}{D_0} \cong 1 - \frac{9}{16} \frac{a}{z} + \frac{1}{8} \frac{a^3}{z^3} - \frac{45}{256} \frac{a^4}{z^4} - \frac{1}{16} \frac{a^5}{z^5} + \dots \quad (22)$$

which is commonly used in their first order:

$$\frac{D_{||}(z)}{D_0} \cong 1 - \frac{9}{16} \left(\frac{a}{z}\right) + O\left(\frac{a}{z}\right)^3 \quad (23)$$

If we are thinking about one particle between two close walls, Dufresne et al. (2001) showed how it is possible to deduce, using the Stokeslet method (Liron & Mochon (1976)), a very complicated closed expression for the diffusion coefficients when $a \ll h$, being h the distance between the two walls. However, the method of reflections gives approximated theoretical expressions. Basically, there are three approximations that provide good results and which are different because of small modifications in the drag force. The first of these methods is the Linear Superposition Approximation (LSA) where the drag force over the sphere is chosen as the sum of the force that makes all the free fluid over the sphere. A second method is the Coherent Superposition Approximation (CSA) whose modification proposed by Bensech & Yiacoumi (2003) was named as Modified Coherent Superposition Approximation (MCSA) and gives the following expression:

$$\begin{aligned} \frac{D(z)}{D_0} = & \left\{ 1 + [C(z) - 1] + [C(h - z) - 1] + \sum_{n=1}^{\infty} (-1)^n \frac{nh - z - a}{nh - z} [C(nh + z) - 1] \right. \\ & \left. + \sum_{n=1}^{\infty} (-1)^n \frac{(n-1)h + z - a}{(n-1)h + z} [C((n+1)h - z) - 1] \right\}^{-1} \quad (24) \end{aligned}$$

where the function $C(z)$ is the inverse of the normalized diffusion coefficient ($D_0/D(z)$) in the only one wall situation.

Another interesting physical configuration is the hydrodynamic coupling of two Brownian spheres near to a wall. Dufresne et al. (2000) showed that the collective diffusion coefficients in the directions parallel and perpendicular to the surface are related by a hydrodynamical coupling because of the fact that the surrounded fluid moved by one of the particles affects the other. This wall-induced effect may have an influence in the origin of some anomalous effects in experiments of confined microparticles in suspension.

2.3.2 Particle-particle interaction

Another effect of considerable importance, or at least, that we must take into account, is the hydrodynamic interaction between two particles. This effect is quantified by the parameter $\rho = r/a$ where r is the radial distance between the centres of the particles and a is their radius. Crocker (1997) showed how the modification of the diffusion coefficient due to the mutual hydrodynamic interaction between the two particles varies in the directions parallel or perpendicular to the line joining the centres of mass. Finally, they obtained that the predominant effect is the one that occurs in the radial direction and which is given by:

$$\frac{D}{D_0} \cong -\frac{15}{4\rho^4} \quad (25)$$

The effect in the perpendicular direction is much lower and negligible ($O(\rho^{-6})$).

2.3.3 Anisotropic friction

When the aggregates are formed in the suspensions, their way of spreading in the fluid is expected to change. By analogy with the Stokes-Einstein equation, in which the diffusion coefficient depends on the inverse of particle diameter ($D \sim a^{-1}$), Miyazima et al. (1987) suggested that the diffusion coefficient depends on the inverse cluster size s in the form $D(s) \sim s^\gamma$, where γ is the coefficient that marks the degree of homogeneity of the kernel of the Smoluchowski equation (Eq. 6). The result for the diffusion coefficient $\gamma = -1$ is considered to be strictly valid for spherical particles that not interact hydrodynamically among them. However, in the case of an anisotropic system, as is the case of chain aggregates, the diffusion coefficient varies due to the hydrodynamic interaction in the direction parallel and perpendicular to the axis of the chain, as follows (Doi & Edwards (1986)):

$$D_{\parallel} = \frac{k_B T}{2\pi\eta a} \frac{\ln s}{s} \quad (26)$$

$$D_{\perp} = D_{\parallel}/2 \quad (27)$$

This result is based assuming point particles, but similar expressions are obtained by modelling the aggregates in the form of cylinders of length L and diameter $d = 2a$. Tirado & García (1979; 1980) provide diffusion coefficients for this objects in the directions perpendicular, parallel and rotational to the axis of the chains ($D_{\parallel}, D_{\perp}, D_r$).

By using measurements of Dynamic Light Scattering (DLS), an effective diffusion coefficient, D_{eff} , of the aggregates can be extracted (Koppel (1972)). This effective coefficient is related to the others mentioned above by means of the relationship:

$$D_{\text{eff}} = D_{\perp} + \frac{L^2}{12} D_r \quad (28)$$

which is correct if $qL \gg 1$ where q is the scattering wave vector defined as: $q = 4\pi/\lambda_l \sin(\theta/2)$, λ_l is the wave length of the laser over the suspension and θ is the scattering angle.

2.3.4 Cluster sedimentation

A particularly important effect is the sedimentation of the clusters or aggregates. It is essential, when a colloidal system is studied, determine the position of the aggregates from the wall, as well as knowing what the deposition rate by gravity is and when the equilibrium in a given layer of fluid is reached. The velocity v_c experienced by a cluster composed of N identical spherical particles of radius a and mass M falling by gravity in a fluid without the presence of walls is (González et al. (2004)):

$$v_c = \frac{MgN}{\gamma_0} \left(1 - \frac{\rho}{\rho_p}\right) = \frac{MgDN}{k_B T} \left(1 - \frac{\rho}{\rho_p}\right)$$

where g is the value of the gravity acceleration, ρ is the fluid density, ρ_p is the density of the particles, γ_0 is the drag coefficient and D the diffusion coefficient. If we have only one spheric particle, the last equation yields the classic result for the sedimentation velocity:

$$v_p = \frac{2a^2 g \Delta \rho}{9\eta}$$

with $\Delta\rho = \rho_p - \rho$. We can define the Péclet number as the ratio between the sedimentation time t_s and diffusion t_d using a fixed distance, for instance, $2a$:

$$P_e \equiv \frac{t_d}{t_s} = \frac{Mga}{k_B T} \left(1 - \frac{\rho}{\rho_p}\right) = \frac{4\pi a^4 g \Delta\rho}{3k_B T} \quad (29)$$

Then, the vertical distance travelled by gravity for a cluster in a time equal to that a particle spread a distance equal to the diameter of the particle d is $d_c = v_c t_d = P_e N d$.

The above expressions are satisfied when sedimentation occurs in an unconfined fluid. If there is a bottom wall, then it provides a spatial distribution of particles ρ which depends on the relative height with respect to the bottom wall. If the system is in an equilibrium state and with low concentration of particles, we can use the Boltzmann density profile, which measures the balance on the thermal forces and gravity:

$$\ln \rho(z) \propto -\frac{z}{L_G} \quad (30)$$

where $L_G \sim k_B T / Mg$. As mentioned, this density profile is valid when the interactions between the colloidal particles are neglected. However, experimental situations can be much more complicated, resulting in deviations from this profile, so theoretical research is still in development about this question (Chen & Ma (2006); Schmidt et al. (2004)). In fact, it has been discovered experimentally that the influence of the electric charge of silica nanoparticles in a suspension of ethanol may drastically change the shape of the density profile (Rasa & Philipse (2004)). We will here assume the expression 30 to be correct, so that the average height z_m of a particle of radius a , between two walls separated by a distance h , can be determined by the Boltzmann profile as Faucheux & Libchaber (1994) showed:

$$P_B(z) = \frac{1}{L} \left(\frac{e^{-z/L}}{e^{-a/L} - e^{(a-h)/L}} \right) \quad (31)$$

where z is the position of the particle between the two walls, where the bottom wall is at $z = 0$ and the top is located at $z = h$, L is the characteristic Boltzmann length defined as $L \equiv k_B T (g \Delta M)^{-1}$ where $\Delta M \equiv (4/3)\pi a^3 (\rho_p - \rho)$.

Therefore, the mean distance z_m can be calculated:

$$\begin{aligned} z_m &= \int_a^{h-a} z P_B(z) dz = \\ &= \frac{e^{-a/L} [aL + L^2] - e^{(a-h)/L} [(h-a)L + L^2]}{L [e^{-a/L} - e^{(a-h)/L}]} \end{aligned} \quad (32)$$

With that expression and the equations for the diffusion coefficient near a wall (Eqs. 20 to 25) we can estimate the effective diffusion coefficient of a sedimented particle. However, when we have a set of particles, clusters or aggregates near the walls of the enclosure, the evaluation of hydrodynamic effects on the diffusion coefficient and their dynamics is not an easy problem to evaluate theoretically or experimentally. In fact, this problem is very topical, for example, focused on polymer science (Hernández-Ortiz et al. (2006)) or more specifically, in the case of biopolymers, such as DNA strands, moving by low flows in confined enclosures (Jendrejack et al. (2003)). Kutthe (2003) performed Stokesian dynamics simulations (SD) of chains, clusters and aggregates in various situations in which hydrodynamic interactions

are not negligible. Specifically, they calculated the friction coefficient γ_N depending on N (number of particles) for linear chains located at a distance z of the wall and applying a transverse velocity $V_x = 0.08$ diameters per second. The friction coefficient γ_N , to reach a velocity V_x in the transverse direction was obtained as:

$$\gamma_N = \frac{F_x}{3\pi\eta d V_x}$$

where F_x is the force over the chain and d the diameter of the particle. Then, they obtain that, far away from the wall, $\gamma_{30} \sim 6$ for a chain formed by 30 particles. But, near enough from the wall, the friction coefficient grows to a value $\gamma_{30} \sim 200$. Recently, Paddinga & Briels (2010) showed simulation results for translational and rotational friction components of a colloidal rod near to a planar hard wall. They obtained an enhancement friction tensor components because of the hydrodynamic interactions between the rod and the wall.

In any case, when we are thinking on one spherical Brownian particle, we can estimate the diffusion coefficient using the Boltzmann profile by calculating the mean position of the particle using Eq.32. Then, if we can calculate the experimental diffusion coefficient when sedimentation affects to the particles, we can employ the following expression (Domínguez-García, Pastor, Melle & Rubio (2009); Fauchoux & Libchaber (1994)):

$$D_{||}^\delta = \int_0^L P_B(z) \left[\int_{z-\delta(z,\eta)}^{z+\delta(z,\eta)} D_{||}(z',\eta) \frac{P_B(z')}{N_B(z',\eta)} dz' \right] dz$$

where $P_B(z)$ is the Boltzmann probability distribution, $N_B(z)$ is the normalization of that function, $D_{||}(z',\eta)$ is the corrected diffusion coefficient of the particle for the motion parallel to the wall. This expression introduces a correction because of the vertical movement: during each time window of span τ , the particle typically explores a region of size 2δ with $\delta(z,\eta) = \frac{1}{2}\sqrt{2\tau D_\perp(z,\eta)}$, where D_\perp is the diffusion coefficient for the motion normal to the wall. The height of the particle from the bottom, z , is calculated by assuming the Boltzmann probability distribution.

2.4 Electrostatics

In a colloidal system, there are usually present not only external forces or hydrodynamic interaction of particles with the fluid, but also electrostatic interactions of various kinds. Moreover, as we shall see, many of the commercial micro-particles have carboxylic groups ($-COOH$) to facilitate their possible use, for example, in biological applications. These groups provide for electrolytic dissociation, a negative charge on the particle surface, so that we can see their migration under a constant and uniaxial electric field using the technique of electrophoresis. Therefore, these groups generate an electrostatic interaction between the particles.

2.4.1 DLVO theory

DLVO theory (Derjaguin & Landau (1941); Verwey & Overbeek (1948)) is the commonly used classical theory to explain the phenomena of aggregation and coagulation in colloidal particle systems without external fields applied. Roughly speaking, the theory considers that the colloidal particles are subject to two types of electrical forces: repulsive electrostatic forces due to same-sign charged particles and, on the other hand, Van der Waals forces which are of attractive nature and appear due to the interaction between the molecules that form the colloid. According to the intensity relative to each other, the particles will aggregate or repel.

Thus, the method to control the aggregation is to vary the ionic strength of medium, i.e., the pH. In most applications in colloids, it is enormously important to control aggregation of particles, for example, for purification treatments of water.

The situation around a negatively charged colloidal particle is approximately described by the double layer model. This model is used to display the ionic atmosphere in the vicinity of the charged colloid and explain how the repulsive electrical forces act. Around the particle, the negative charge forms a rigid layer of positive ions from the fluid, usually called Stern layer. This layer is surrounded by the diffuse layer that is formed by positive ions seeking to approach the colloidal particle and that are rejected by the Stern layer. In the diffuse layer there is a deficit of negative ions and its concentration increases as we left the colloidal particle. Therefore, the diffuse layer can be viewed as a positively charged atmosphere surrounding the colloid.

The two layers, the Stern layer and diffuse layer, form the so-called double layer. Therefore, the negative particle and its atmosphere produce a positive electrical potential associated with the solution. The potential has its maximum value on the surface of the particle and gradually decreases along the diffuse layer. The value of the potential that brings together the Stern layer and the diffuse layer is known as the Zeta potential, whose interest mainly lies in the fact that it can be measured. This Zeta potential measurement, is commonly referred as ζ and measured in mV. The Zeta potential is usually measured using the Laser Doppler Velocimeter technique. This device applies an electric field of known intensity of the suspension, while this is illuminated with a laser beam. The device measures the rate at which particles move so that the Zeta potential, ζ , can be calculated by several equations that relate the Zeta potential electrophoretic mobility, μ_e .

In a general way, it is possible to use the following expression, known as the Hückel equation:

$$\mu_e = \frac{2}{3} \frac{\varepsilon \zeta}{\eta} f(\kappa a) \quad (33)$$

where ε is the dielectric constant of the medium, η its viscosity, a the radius of the particle and where $1/\kappa$ is the width of the double layer, known as the Debye screening length and where $f(\kappa a)$ is the named Henry function. In the case of $1 < \kappa a < 100$, the Zeta potentials can be calculated by means of some analytic expression of the Henry function (Otterstedt & Brandreth. (1998)). Summarising, the higher is the Zeta potential, the more intense will be the Coulombian repulsion between the particles and the lower will be the influence of the Van der Waals force in the colloid.

The Van der Waals potential, which can provide a strong attractive interaction, is usually neglected because its influence is limited to very short surface-to-surface distances in the order of 1 nm. Therefore, the DLVO electrostatic potential between two particles located a radial distance r one from the other is usually given by the classical expression:

$$U(r) = \frac{(Z^*e)^2}{\varepsilon} \frac{\exp(2a\kappa)}{(1+a\kappa)^2} \frac{\exp(-\kappa r)}{r} \quad (34)$$

where Z^* is the effective charge of the particles and $\sigma_{\text{eff}} = Z^*e/4\pi a^2$ is their density of effective charge. Therefore, in this theory, two spherical like-charged colloidal particles suffered a purely electrostatic repulsion between them. The colloidal particle can have carboxylic groups (COOH) attached to their surfaces, creating a layer of negative charge of length δ in the order of nanometers surrounding the colloidal particles (Shen et al. (2001)).

The presence of this layer modifies the equation of the double-layer potential (Reiner & Radke (1993); Shen et al. (2001)):

$$U_{dl}(s) = 2\pi\epsilon(\psi)^2 \frac{2}{2 + s'/a} \exp(-\kappa s') \tag{35}$$

where $s' = s - 2\delta$.

2.4.2 Ornstein-Zernike equation

For calculating the electrostatic potential in a colloidal suspension, we can use the following methodology. This approach involves using the radial distribution function of the particles, $g(r)$, knowing that it is related with the interaction energy of two particles in the limit of infinite dilution by means of the Boltzmann distribution:

$$\lim_{n \rightarrow 0} g(r) = e^{-\beta U(r)} \tag{36}$$

where n is the particle density and $\beta \equiv 1/k_B T$. However, for finite concentrations, $g(r)$ is influenced by the proximity between particles, so we can calculate the mean force potential, $w(r)$:

$$w(r) = -\frac{1}{\beta} \ln g(r) \tag{37}$$

But we do not know the relation between $w(r)$ and $U(r)$. Here, is usually defined a total correlation function $h(r) \equiv g(r) - 1$ and is used the Ornstein-Zernike (O-Z) equation for two particles in a two-dimensional fluid:

$$h(r) = c(r) + n \int c(r') h(|\mathbf{r}' - \mathbf{r}|) dr' \tag{38}$$

The $c(r)$ function is the direct correlation function between two particles. Now, it is necessary to close the integral equation by linking $h(r)$, $c(r)$ and $U(r)$. For that, one of the following assumptions is employed:

$$c(r) = \begin{cases} -\beta U(r) & \text{MSA} \\ -\beta U(r) + h(r) - \ln g(r) & \text{HNC} \\ (1 - e^{\beta U})(1 + h(r)) & \text{PY} \end{cases} \tag{39}$$

named Mean Spherical Approximation (MSA), Hypernetted Chain (HNC) and Percus-Yevick (PY).

In the case of video-microscopy experiments, a more practical methodology is explained by Behrens & Grier (2001b) for obtaining the electrostatic potential. More explicitly, with the PY approximation we have:

$$U(r) = w(r) + \frac{n}{\beta} I(r) = -\frac{1}{\beta} [\ln g(r) - nI(r)], \tag{40}$$

and with the HC:

$$U(r) = w(r) + \frac{1}{\beta} \ln [1 + nI(r)] = -\frac{1}{\beta} \left[\ln \left(\frac{g(r)}{1 + nI(r)} \right) \right], \tag{41}$$

In both cases, $I(r)$ is the convolution integral defined as:

$$I(r) = \int [g(r') - 1 - nI(r')] [g(|\mathbf{r}' - \mathbf{r}|) - 1] d^2r', \tag{42}$$

which can be calculated numerically.

2.4.3 Anomalous effects

In order to understand the interactions in this kind of systems, we have to note that the standard theory of colloidal interactions, the DLVO theory, fails to explain several experimental observations. For example, an attractive interaction is observed between the particles when the electrostatic potential is obtained. This is an effect that has been previously observed in experiments on suspensions of confined equally-charged microspheres (Behrens & Grier (2001a,b); Grier & Han (2004); Han & Grier (2003); Larsen & Grier (1997)).

Grier and colleagues listed several experimental observations using suspensions of charged polystyrene particles with diameters around 0.65 microns at low ionic strength and strong spatial confinement. They note that such effects appear when a wall of glass or quartz is near the particles. Studying the $g(r)$ function and its relation to the interaction potential, given by expression 36, they showed the appearance of a minimum on the potential located at $z = 2.5$ microns of the wall and a distance between centres to be $r_{\min} = 3.5$ microns. This attraction cannot be a Van der Waals interaction, because for this type of particle and with separations greater than 0.1 micrometres, this force is less than $0.01 k_B T$ (Pailthorpe & Russel (1982)), while this attractive interaction is about $0.7 k_B T$.

The same group (Behrens & Grier (2001b)) extended this study using silica particle suspensions (silicon dioxide, SiO_2) of 1.58 microns in diameter, with a high density of 2.2 g/cm^3 , using a cell of thickness $h = 200 \mu\text{m}$. In this situation, even though the particles are deposited at a distance from the bottom edge of the particle to the bottom wall equal to $s = 0.11 \mu\text{m}$, no minimum in the interaction energy between pairs appears, being the interaction purely repulsive, in the classical form of DLVO given by Eq.34. In that work, a methodology is also provided to estimate the Debye length of the system and the equivalent load Z^* through a study of the presence of negative charge quartz wall due to the dissociation of silanol groups in presence of water (Behrens & Grier (2001a)). However, Han & Grier (2003) observed the existence of a minimum in the potential when they use polystyrene particles of 0.65 micron and density close to water, 1.05 g/cm^3 , with a separation between the walls of $h = 1.3$ microns. What is more, using silica particles from previous works, they observe a minimum separation between walls of $h = 9 \mu\text{m}$.

The physical explanation of this effect is not clear (Grier & Han (2004)), being the main question how to explain the influence on the separation of the two walls in the confinement cell. However, some criticism has appeared about this results. For example, about the employment of a theoretical potential with a DLVO shape. An alternative is using a Sogami-Ise (SI) potential (Tata & Ise (1998)). Moreover, Tata & Ise (2000) contend that both the DLVO theory and the SI theory are not designed for situations in confinement, so interpreting the experimental data using either of these two theories may be wrong. Controversy on the use of a DLVO-type or SI potentials appears to be resolved considering that the two configurations represent physical exclusive situations (Schmitz et al. (2003)). In fact, simulations have been performed to explore the possibility of a potential hydrodynamic coupling with the bottom wall generated by the attraction between two particles (Dufresne et al. (2000); Squires & Brenner (2000)). However, the calculated hydrodynamic effects do not seem to explain the experimental minimum on the potential (Grier & Han (2004); Han & Grier (2003)). Other authors argue that this kind of studies should be more rigorous in the analysis of errors when extracting data from the images (Savin & Doyle (2005; 2007); Savin et al. (2007)) and other authors claim that the effect on the electrostatic potential may be an artefact (Baumgart et al. (2006)) that occurs because of an incorrect extraction of the position of the particles (Gyger et al. (2008)).

Polin et al. (2007) realized that some minimums in the electrostatic potential can be eliminated by measuring the error on the displacement of the particles. However, this is not a double implication and other experimental minimums in the potential remain there. In that work, the authors take into account all the proposed artefacts to date for their measurements, demonstrating that charged glass surfaces really induce attractions between charged colloidal spheres. Moreover, Tata et al. (2008) claim that their observations using confocal laser scanning of millions of charged colloidal particles establish the existence of an attractive behaviour in the electrostatic potential.

Moreover, other possible electrostatic variations in these systems may appear for several reasons. For instance, the emergence of a spontaneous macroscopic electric field in charged colloids (Rasa & Philipse (2004)). Moreover, according to several studies, changes in the fluid due to, for example, environmental pollution with atmospheric CO₂, can be relatively easy and are not negligible at low concentrations, being able to radically change the electrical properties on the fluid (Carrique & Ruiz-Reina (2009)). Thus, interactions related to colloidal stability can produce anomalous effects and significant changes in, for example, sedimentation kinetics (Buzzaccaro et al. (2008)) or sedimentation-diffusion profiles (Philipse & Koenderink (2003)). Then, these electrostatic effects can affect the dynamics of aggregation and influence the mobility of the particles and clusters.

3. Results

Our experimental system is formed by a MRF composed of colloidal dispersions of superparamagnetic micron-sized particles in water. These particles have a radius of 485 nm and a density of 1.85 g/cm³, so they sediment to an equilibrium layer on the containing cell. They are composed by a polymer (PS) with nano-grains of magnetite dispersed into it, which provide their magnetic properties. The particles are also functionalized with carboxylic groups, so they have an electrical component, therefore, they repel each other, avoiding aggregation. This effect is improved by adding sodium dodecyl sulfate (SDS) in a concentration of 1 gr/l.

The containing cell consists on two quartz windows, one of them with a cavity of 100 μm. The cell with the suspension in it is located in an experimental setup that isolate thermically the suspension and allows to generate a uniform external magnetic field in the centre of the cell. The particles and aggregates are observed using video-microscopy (see details for this experimental setup on (Domínguez-García et al. (2007))). Images of the fluid are saved on the computer and then analysed for extracting the relevant data by using our own developed software (Domínguez-García & Rubio (2009)) based on *ImageJ* (U. S. National Institutes of Health, Bethesda, Maryland, USA, <http://rsb.info.nih.gov/ij/> (n.d.)). In Fig.3, we show an example of these microparticles and aggregates observed in our system.

The zeta potential of these particles is about -110 to -60 mV for a pH about 6 - 7. Therefore, the electrical content of the particles is relatively high and it is only neglected in comparison with the energy provided by the external magnetic field. However, the colloidal stability of these suspensions is not being controlled and it may have an effect on the dynamics of the clusters, specially when no magnetic field is applied. In any case, as we will see, even when a magnetic field is applied, it is observed a disagreement between theoretical aggregation times and experimental ones.

3.1 Control parameters

We have already defined some important parameters as the Péclet number, Eq.29, and the Reynolds number Eq.19. However, in our system we need to define some external parameters related with the concentration of particles and the intensity of the magnetic field. The concentration of volume of particles in the suspension, ϕ , is defined as the fraction of volume occupied by the spheres relative to the total volume of the suspension. In a quasi-2D video-microscopy system is useful to take into account the surface concentration ϕ_{2D} . For measuring the influence of the magnetic interaction we used the λ parameter, defined as:

$$\lambda \equiv \frac{W_m}{k_B T} = \frac{\mu_s \mu_0 m^2}{16\pi a^3 k_B T} \quad (43)$$

as the ratio of $W_m = U_{ij}^d(r = 2a, \alpha = 0)$, i.e., the magnetic energy, and the thermal fluctuations $k_B T$. Here, μ_s is the relative magnetic permeability of the solvent, μ_0 the magnetic permeability of vacuum and m the magnetic moment. The parameters λ y ϕ_{2D} allow to define a couple of characteristic lengths. First, we define a distance R_1 for which the energy of dipolar interaction is equal to thermal fluctuations:

$$R_1 \equiv 2a\lambda^{1/3} \quad (44)$$

Finally, we define a mean distance between particles:

$$R_0 \equiv \sqrt{\pi a \phi_{2D}^{-1/2}} \quad (45)$$

The comparative between these two quantities allows to distinguish between different aggregation regimes. When, $R_1 < R_0$, the thermal fluctuations prevail over the magnetic interactions so diffusion is the main aggregation process. If $R_1 > R_0$, the aggregation of the particles occurs mainly because of the applied magnetic field.

3.2 Aggregation and disaggregation

Studies about the dynamics of the irreversible aggregation of clusters under unidirectional constant magnetic fields have used a collection of experimental systems. For example, electro-rheological fluids (Fraden et al. (1989)), magnetic holes (non-magnetic particles in a ferrofluid) (Cernak et al. (2004); Helgesen et al. (1990; 1988); Skjeltorp (1983)), and magneto-rheological fluids and magnetic particles (Bacri et al. (1993); Bossis et al. (1990); Cernak (1994); Cernak et al. (1991); Fermigier & Gast (1992); Melle et al. (2001); Promislow et al. (1994)).

These studies focus their efforts in calculating the kinetic exponent z obtaining different values ranging $z \sim 0.4 - 0.7$. The different methodologies employed can be the origin of these dispersed values. However, more recent studies (Domínguez-García et al. (2007); Martínez-Pedrero et al. (2007)) suggest that this value is approximately $z \sim 0.6 - 0.7$ in accordance with experimental values reported for aggregation of dielectric colloids $z \sim 0.6$ (Fraden et al. (1989)) and with recent simulations of aggregation of superparamagnetic particles (Andreu et al. (2011)). Regarding hydrodynamics interactions Miguel & Pastor-Satorras (1999) proposed an effective expression for explaining the dispersed value of the kinetic exponent based on logarithmic corrections in the diffusion coefficient (Eqs. 26 and 27):

$$S(t) \sim (t \ln[S(t)])^{\xi}, \quad (46)$$

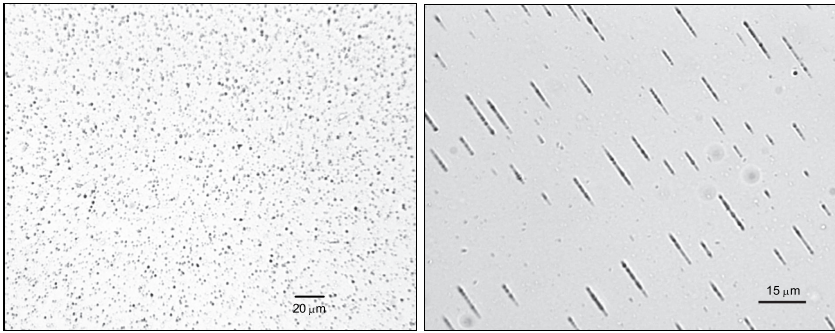


Fig. 3. Superparamagnetic microparticles observed when no external magnetic field is applied (Left) and when it is applied (Right).

where the exponent ζ is an exponent that depends on the dimensionality of the system, so if $d \geq 2$, $\zeta = 1/2$. Using Monte Carlo simulations they obtain that $\zeta \simeq 0.51$, and therefore that z is $z \simeq 0.61$.

In the case of our experiments, we have experimentally obtained that the z exponent in aggregation is contained in the range of $0.43 - 0.67$ (Domínguez-García et al. (2007)) with an average value of $z \sim 0.57 \pm 0.03$. These experimental values do not depend on the amplitude of the magnetic field nor on the concentration of particles, but they seem to depend on the ratio R_1/R_0 , which is a sign of the more important regime of aggregation. The dependency on this ratio also appears when the morphology of the chains is studied (Domínguez-García, Melle & Rubio (2009); Domínguez-García & Rubio (2010)). Besides, the scaling behaviour given by Eq.7 is experimentally observed and checked. We have compared our experimental results with Brownian dynamics simulations based on a simple model which only included dipolar interaction between the particles, hard-sphere repulsion and Brownian diffusion, neglecting inertial terms and effects related with sedimentation or electrostatics. The results of these simulations agree with the theoretical prediction, whereas the experimental aggregation time, t_{ag} , appears to be much longer than expected (Cernak et al. (2004); Domínguez-García et al. (2007)), about three orders of magnitude of difference. The formation of dimers (two-particles aggregates) in the experiments lapses $t \sim 10^2$ seconds, but Brownian simulations show that this lapse of time is about $t \sim 0.1$ s. This last value can be easily obtained by assuming that the equation for the movement between two particles with dipolar magnetic interaction is:

$$M\ddot{r} + \gamma_0\dot{r} + 3\mu\mu_0m^2r^{-4}\pi^{-1} = 0$$

where M is the mass of the particles. Because of Reynolds number (Eq.19) is very low, we neglect the inertial term on this equation. If the particles are separated a initial distance $d = R_0$ we can obtain that:

$$t_{ag} \cong \frac{32\pi\gamma_0a^5}{15\mu_s\mu_0m^2} \phi_{2D}^{-5/2}$$

If we express this equation in function of the λ parameter 43 and of the diffusion coefficient given by the Stokes-Einstein equation 13:

$$t_{ag} \cong \frac{2a^2}{15} \frac{1}{\lambda D} \phi_{2D}^{-5/2} \quad (47)$$

For example, the aggregation processes for $S(t)$ in the work of Promislow et al. (1994), show an aggregation time of 200 seconds. The paramagnetic particles used in that work have a diameter of $0.6 \mu\text{m}$ and a 27% of magnetite content. Using the Stokes-Einstein expression, $D = 0.86 \mu\text{m}^2/\text{s}$ is obtained, supposing that these particles do not sediment. Using $\phi = 0.0012$ and $\lambda = 8.6$, we can obtain that $t_{\text{ag}} \sim 122$ seconds, in the order of their experimental result. In the case of our experiments, we obtain the same values using Eq.47 that using Brownian simulations.

These discrepancies may be related with hydrodynamic interactions which should affect the diffusion of the particles. From Eq.47, we see that some variation on the diffusion coefficient of the particles can modify the expected aggregation time for two particles. For testing that, we made some microrheology measurements using different types of isolated particles according to the theory of sedimentation and with the corrections on the values of the diffusion coefficient. The experimental values agree very well with the theoretical ones calculated from the expression 2.3.4 (Domínguez-García, Pastor, Melle & Rubio (2009)) but they imply a reduction on the diffusion coefficient a factor of three as a maximum, no being sufficient for explaining the discrepancy in the aggregation times.

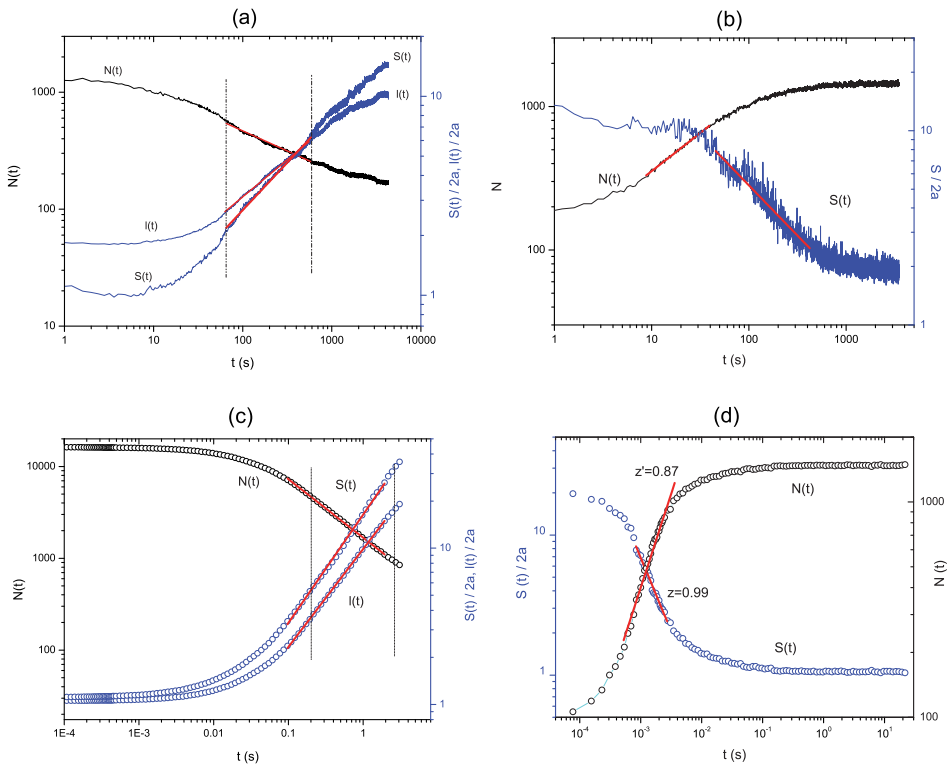


Fig. 4. Experiments of aggregation and disaggregation. The experimental process of aggregation (a) begins with $\lambda = 1718$, $\phi_{2D} = 0.088$ while disaggregation is shown in (b). Brownian dynamics simulations results with $\lambda = 100$, $\phi_{2D} = 0.03$ are shown for aggregation (c) and disaggregation (d). Data from Refs.(Domínguez-García et al. (2007; 2011))

For completing this study, we also have shown results of disaggregation, that is, the process that occurs when the external magnetic field is switched off and the clusters vanish. For this process we study the kinetics in the same way that in aggregation, by searching power laws behaviours and calculating the kinetic exponents z and z' (Domínguez-García et al. (2011)). We have also developed Brownian dynamics simulations to be compared with the experiments. The Fig.4 summarizes some of our results in aggregation and disaggregation. The experimental kinetic exponents during disaggregation range from $z = 0.44$ to 1.12 and $z' = 0.27$ to 0.67 , while simulations give very regular values, with z and $z' \sim 1$. Then, the kinetic exponents do not agree, being also the process of disaggregation much faster in simulations. From these results, we conclude that remarkable differences exist between a simple theoretical model and the interactions in our experimental setup, differences that are specially important when the influence of the applied magnetic field is removed. In all these experiments some data has been collected before any external field is applied. That allows us to study the microstructure of the suspensions by calculating the electrostatics potential using the methods previously explained. The inversion of the O-Z equation reveals an attractive well in the potential with a value in its minimum in the order of $-0.2 k_B T$, similar to other observations of attractive interactions of sedimented particles in confinement situations. Moreover, these values of the minimum in the potential seems to depend of the concentration of particles (Domínguez-García, Pastor, Melle & Rubio (2009)), something which is expected, if it is related in some way with the electrical charge contained in the suspension.

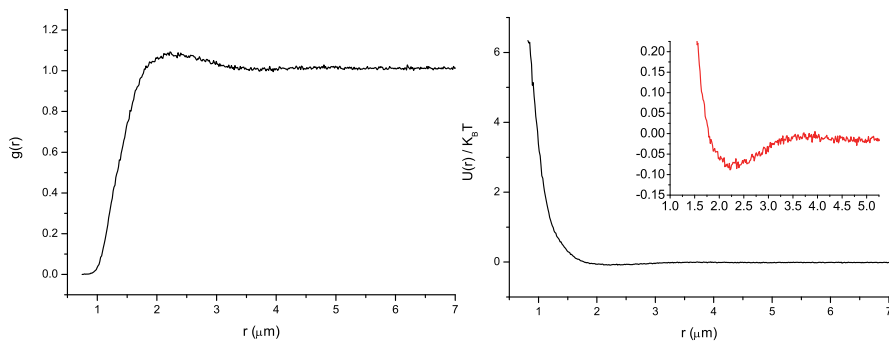


Fig. 5. Left: $g(r)$ function, Right: Electrostatic potential calculated by inverting the O-Z equation (all the approximations give the same result) Inset: a detail for $U(r)$ in the region of the minimum. Number density $n = 0.0009$

As a confirmation of these results, we show here a calculation of the electrostatic potential using a long set of images of charged superparamagnetic microparticles spreading in the experimental system described above. We have obtained images of the suspension during more than an hour, with a temporal lapse between images of 0.3 seconds. This data allow us to produce a very defined graph for the pair correlation function, showed in the Fig.5. In the right side of the Fig.5, we plot the electrostatic potential and in its inset we can see that the minimum has a value of about $-0.1 k_B T$, confirming the previous results obtained in this experimental setup.

However, this result may be an effect of an imaging artefact. About that question, some of the studies which use particle tracking only apply some filters to the images for detecting brightness points and then extracting the position of the particles. Our image analysis

software (Domínguez-García & Rubio (2009)) employs open-sourced algorithms for detecting the centres of mass of the particles by detecting the borders of each object and then obtaining its geometrical properties. As an example, we have tried to evaluate how this border detection can have an influence on the result of the electrostatic potential. A measured apparent displacement $\Delta(r) = r' - r$ should affect to the radial distribution function in the following form: $g(r) = g'(r + \Delta(r))(1 + d\Delta(r)/dr)$ (Polin et al. (2007)). From that expression, the variation in the electrostatic potential is:

$$\beta U'(r) - \beta U(r) \cong -\beta \frac{dU(r)}{dr} \Delta(r) + \frac{d\Delta(r)}{dr} \quad (48)$$

For obtaining $\Delta(r)$ we have extracted a typical particle image and we have composed some set of images which consist on separating the two particles a known distance (r) in pixels. Next, we apply our methods of image analysis for obtaining the position of those particles and calculate the distances (r'). Then, the apparent displacement, $\Delta(r) = r' - r$, is observed to grow when the particles are very near. In Fig.6, we display the results of our calculations on the possible artefact in the analysis of the position of the particles by image binarization and binary watershed, a method for automatically separating particles that are in contact. The figure reveals that the correction on the electrostatic potential for this cause is basically negligible, because the correction in the potential is zero for distances $r > 1.2 \mu\text{m}$. In the inset of the figure we can see some of the images we have employed for this calculation, showing the detected border of the particles among the images themselves.

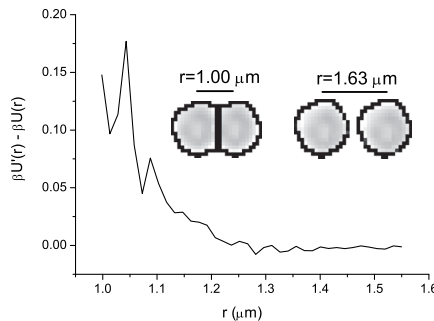


Fig. 6. Estimation of a possible artefact in the analysis of the position of the particles. In the inset we have included some examples of the images used for this calculation.

In any case, the possibility of an artifact can be the cause of these observations in the electrostatic potential cannot be discarded. However, the direct or indirect presence and influence of these attractive wells has been detected in many other situations in these experiments. For example, the attractive interaction disappears when we added a salt, in our case KCl, to the suspensions, confirming the electrostatic nature of the phenomena (Domínguez-García, Pastor, Melle & Rubio (2009)). In disaggregation it is observed how the particles move inside the chains without leaving them (Domínguez-García et al. (2011)). The lapse of time that the particles are in this situation depends on the initial morphology of the aggregates, something which has been observed to depend on the ratio R_1/R_0 (Domínguez-García, Melle & Rubio (2009); Domínguez-García & Rubio (2010)). Then, this effective lapse of time depends of how many particles are located near the other in a short distance. In that situation, the attractive interaction should play a role in disaggregation, as it

seems to be. Indeed, this “detaining” effect of the particles inside the clusters is not observed in experiments with added salt.

What is more, we have also observed that the kinetic exponents during aggregation are different and slower if we add salt to the suspension (Domínguez-García et al. (2011)). This last effect may be related with an unexpected interaction of the particles with the charged quartz bottom wall by means of a spontaneous macroscopic electric field. When the particles and clusters have no electrical component, they should be highly sedimented at the bottom of the quartz cell and the resistance to their the movement should be increased (Kutthe (2003)), generating that the kinetic exponents reduce their value.

4. Conclusions

In this chapter, we have reviewed the main interactions, with focus on hydrodynamics and from a experimental point of view, that can be important in a confined colloidal system at low concentration of microparticles. We have used charged superparamagnetic microparticles dispersed in water in low-confinement conditions by means of a glass cell for the study of irreversible field-induced aggregation and disaggregation, as well as the microstructure of the suspension. Regarding aggregation characteristic times and basic behaviour on the disaggregation of the particles, we have observed significant discrepancies between the experimental results and the theory. Moreover, anomalous effects in the electrostatic behaviour have been observed, showing that, in this kind of systems, the electro-hydrodynamics interactions are not well understood at present and deserve more theoretical and experimental investigations.

5. Acknowledgements

We wish to acknowledge Sonia Melle and J.M. Pastor for all the work done, J.M M. González, J.M. Palomares and F. Pigazo (ICMM) for the VSM magnetometry measurements and J.C. Gómez-Sáez for her proofreading of the English texts. This research has been partially supported by M.E.C. under Project No. FIS2006-12281-C02-02, M.C.I under FIS2009-14008-C02-02, C.A.M under S/0505/MAT/0227 and UNED by 2010V/PUNED/0010.

6. References

- Andreu, J. S., Camacho, J. & Faraudo, J. (2011). Aggregation of superparamagnetic colloids in magnetic fields: the quest for the equilibrium state, *7*: 2336.
- Bacri, J. C., Djerfi, K. & Neveu, S. (1993). Ferrofluid viscometer - transient magnetic birefringence in crossed fields, *J. Mag. Mat.* 123 (1-2): 67–73.
- Baumgart, J., Arauz-Lara, J. L. & Bechinger, C. (2006). Like-charge attraction in confinement: myth or truth?, *Soft Matter* 2: 631–635.
- Behrens, S. H. & Grier, D. G. (2001a). The charge of glass and silica surfaces, *J. Chem. Phys.* 115: 6716–6721.
- Behrens, S. H. & Grier, D. G. (2001b). Pair interaction of charged colloidal spheres near a charged wall, *Phys. Rev. E* 64: 050401(R).
- Bensech, T. & Yiacoymi, S. (2003). Brownian motion in confinement., *Phys. Rev. E* 68: 021401.
- Bossis, G., Mathis, C., Minouni, Z. & Paparoditis, C. (1990). Magnetoviscosity of micronic particles, *Europhys. Lett.* 11: 133.
- Brenner, H. (1961). The slow motion of a sphere through a viscous fluid towards a plane surface., *Phys. Rev. E* 68: 021401.

- Buzzaccaro, S., Tripodi, A., Rusconi, R., Vigolo, D. & Piazza, R. (2008). Kinetics of sedimentation in colloidal suspensions, *J. Phys. Condens. Matter* (20): 494219.
- Carrique, F. & Ruiz-Reina, E. (2009). Effects of water dissociation and CO₂ contamination on the electrophoretic mobility of a spherical particles in aqueous salt-free concentrated suspensions, *J. Phys. Chem. B* (113): 8613–8625.
- Cernak, J. (1994). Aggregation of needle-like macro-clusters in thin-layers of magnetic fluid, *J. Magn. Magn. Mater.* 132: 258.
- Cernak, J., Helgesen, G. & Skjeltorp, A. T. (2004). Aggregation dynamics of nonmagnetic particles in a ferrofluid, *Phys. Rev. E* 70 (3): 031504 Part 1.
- Cernak, J., Macko, P. & Kasparkova, M. (1991). Aggregation and growth-processes in thin-films of magnetic fluid, *J. Phys. D: Appl. Phys.* 24: 1609.
- Chen, H. & Ma, H. (2006). The density profile of hard sphere liquid system under gravity., *J. Chem. Phys.* 125: 024510.
- Crocker, J. C. (1997). Measurement of the hydrodynamic corrections of the Brownian motion of two colloidal spheres., *J. Chem. Phys.* 106: 2837–2840.
- Crocker, J. C. & Grier, D. G. (1996). Methods of digital video microscopy for colloidal studies, *J. Colloid Interface Sci.* 179: 298–310.
- Crocker, J. C., Valentine, M. T., Weeks, E. R., Gisler, T., Kaplan, P. D., Yodh, A. G. & Weitz, D. A. (2000). Two-point microrheology of inhomogeneous soft materials, *Phys. Rev. Lett.* 85: 888–891.
- Derjaguin, B. V. & Landau, L. (1941). Theory of the stability of strongly charged lyophobic sols and of the adhesion of strongly charged particles in solution of electrolytes., *Acta Physicochim. URSS* 14: 633.
- Doi, M. & Edwards, S. (1986). *The Theory of Polymer Dynamics.*, Clarendon Press, Oxford.
- Domínguez-García, P., Melle, S., Pastor, J. M. & Rubio, M. A. (2007). Scaling in the aggregation dynamics of a magneto-rheological fluid., *Phys. Rev. E* 76: 051403.
- Domínguez-García, P., Melle, S. & Rubio, M. A. (2009). Morphology of anisotropic chains in a magneto-rheological fluid during aggregation and disaggregation processes., *J. Colloid Interface Sci.* 333: 221–229.
- Domínguez-García, P., Pastor, J. M., Melle, S. & Rubio, M. A. (2009). Electrostatic and hydrodynamics effects in a sedimented magneto-rheological suspension, *Phys. Rev. E* 80: 0214095.
- Domínguez-García, P., Pastor, J. M. & Rubio, M. A. (2011). Aggregation and disaggregation dynamics of sedimented and charged superparamagnetic microparticles in water suspension, *Europhys. J. E. Soft. Matter.* 34: 36.
- Domínguez-García, P. & Rubio, M. A. (2009). Jchainsanalyser: an imagej-based stand-alone application for the study of magneto-rheological fluids., *Comput. Phys. Commun.* 80: 1956–1960.
- Domínguez-García, P. & Rubio, M. A. (2010). Three-dimensional morphology of field-induced chain-like aggregates of superparamagnetic micro-particles, *Colloids Surf., A* 358: 21–27.
- Dufresne, E. R., Altman, D. & Grier, D. G. (2001). Brownian dynamics of a sphere between parallel walls, *Europhys. Lett.* 53: 264–270.
- Dufresne, E. R., Squires, T. M., Brenner, M. P. & Grier, D. G. (2000). Hydrodynamic coupling of two brownian spheres to a planar surface, *Phys. Rev. Lett.* 85(15): 3317–3320.

- Egatz-Gómez, A., Melle, S., García, A. A., Lindsay, S. A., Márquez, M., Domínguez-García, P., Rubio, M. A., Picraux, S. T., Taraci, J. L., Clement, T., Yang, D., Hayes, M. A. & Gust, D. (2006). Discrete magnetic microfluidics, *Appl. Phys. Lett.* 89(3)(034106).
- Faucheux, L. P. & Libchaber, A. J. (1994). Confined brownian motion, *Phys. Rev. E* 49: 5158.
- Fermigier, M. & Gast, A. P. (1992). Structure evolution in a paramagnetic latex suspension, *J. Colloid Interface Sci.* 154: 522.
- Fraden, S., Hurd, A. J. & Meyer, R. B. (1989). Electric-field-induced association of colloidal particles, *Phys. Rev. Lett.* 63 (21): 2373–2376.
- Furst, E. M. (2005). Applications of laser tweezers in complex fluid rheology., *Curr. Opin. Colloid Interface Sci.* 10: 79–86.
- Furst, E. M. & Gast, A. P. (2000). Micromechanics of magnetorheological suspensions, *Phys. Rev. E* 61: 6732.
- González, A. E., Odriozola, G. & Leone, R. (2004). Colloidal aggregation with sedimentation: concentration effects., *Europhys. J. E. Soft. Matter.* 13: 165–178.
- Grier, D. G. (2003). A revolution in optical manipulation., *Nature* 424: 810–815.
- Grier, D. G. & Han, Y. (2004). Anomalous interactions in confined charge-stabilized colloid, *J. Phys. Condens. Matter* 16: 4145–4157.
- Gyger, M., Ruckerl, F., Käs, J. A. & Ruiz-García, J. (2008). Errors in two particle tracking at close distances, *J. Colloid Interface Sci.* 326: 382–386.
- Halsey, T. C. & Toor, W. (1990). Structure of electrorheological fluids, *Phys. Rev. Lett.* 65: 2820.
- Han, Y. & Grier, D. G. (2003). Confinement-induced colloidal attractions in equilibrium, *Phys. Rev. Lett.* 91(3): 038302.
- Helgesen, G., Pieranski, P. & Skjeltorp, A. T. (1990). Nonlinear phenomena in systems of magnetic holes, *Phys. Rev. Lett.* 64 (12): 1425–1428.
- Helgesen, G., Skjeltorp, A. T., Mors, P. M., Botet, R. & Jullien, R. (1988). Aggregation of magnetic microspheres: Experiments and simulations, *Phys. Rev. Lett.* 61(15): 1736–1739.
- Hernández-Ortiz, J. P., Ma, H., de Pablo, J. J. & Graham, M. D. (2006). Cross-stream-line migration in confined flowing polymer solutions: Theory and simulation., *Phys. Fluids* 18: 123101.
- Jendrejack, R. M., Schwartz, D. C., Graham, M. D. & de Pablo, J. J. (2003). Effect of confinement on DNA dynamics in microfluidic devices., *J. Chem. Phys.* 119(2): 1165–1173.
- Keller, M., Schilling, J. & Sackmann, E. (2001). Oscillatory magnetic bead rheometer for complex fluid microrheometry, *Rev. Sci. Instr.* 72(9): 3626.
- Kerr, R. A. (1990). *Science* 247: 050401.
- Kolb, M., Botet, R. & Jullien, R. (1983). Scaling of kinetically growing clusters, *Phys. Rev. Lett.* 51: 1121–1126.
- Komeili, A. (2007). Molecular mechanisms of magnetosome formation., *Annu. Rev. Biochem.* 76: 351–356.
- Koppel, D. E. (1972). Analysis of macromolecular polydispersity in intensity correlation spectroscopy: The method of cumulants., *J. Chem. Phys.* 57(11): 4814–4820.
- Kutthe, R. (2003). Stokesian dynamics of nonspherical particles, chains, and aggregates., *J. Chem. Phys.* 119(17): 9280–9294.
- Larsen, A. E. & Grier, D. G. (1997). Like-charge attraction in metastable colloidal crystallites, *Nature* 385(16): 230–233.
- Larson, R. G. (1999). *The Structure and Rheology of Complex Fluids*, Oxford University Press, New York.

- Lian, Z. & Ma, H. (2008). Electrostatic interaction between two nonuniformly charged colloid particles confined in a long charged cylinder wall., *J. Phys. Condens. Matter* 20: 035109.
- Lin, B., Yu, J. & Rice, S. A. (2000). Direct measurements of constrained Brownian motion of an isolated sphere between two walls., *Phys. Rev. E* 62 (3): 3909–3919.
- Lin, M. Y., Lindsay, H. M., Weitz, D. A., Ball, R. C., Klein, R. & Meakin, P. (1989). Universality in colloid aggregation, *Nature* 339(1): 360–362.
- Liron, N. & Mochon, S. (1976). Stokes flow for a stokeslet between two parallel flat plates., *J. Eng. Math.* 10 (4): 287–303.
- Lord Corporation, <http://www.lord.com/> (n.d.).
- Martin, J. E. & Anderson, R. A. (1996). Chain model of electrorheology, *J. Chem. Phys.* 104: 4814.
- Martin, J. E., Odinek, J. & Halsey, T. C. (1992). Evolution of structure in a quiescent electrorheological fluid, *Phys. Rev. Lett.* 69 (10): 1524–1527.
- Martínez-Pedrero, F., Tirado-Miranda, M., Schmitt, A. & Callejas-Fernández, J. (2007). Formation of magnetic filaments: A kinetic study., *Phys. Rev. E* 76: 011405.
- Mason, T. G. (2000). Estimating the viscoelastic moduli of complex fluid using the generalized stokes-einstein equation, *Rheol. Acta* 39: 371–378.
- Mason, T. G. & Weitz, D. A. (1995). Optical measurements of frequency-dependent linear viscoelastic moduli of complex fluids, *Phys. Rev. Lett.* 74: 1250 – 1253.
- Meakin, P. (1983). Formation of fractal clusters and networks by irreversible diffusion-limited aggregation, *Phys. Rev. Lett.* 51: 1119–1122.
- Melle, S. (2002). *Estudio de la dinámica de suspensiones magneto-reológicas sometidas a campos externos mediante el uso de técnicas ópticas. Procesos de agregación, formación de estructuras y su evolución espacio-temporal.*, PhD thesis, Universidad Nacional de Educación a Distancia.
- Melle, S., Rubio, M. A. & Fuller, G. G. (2001). Time scaling regimes in aggregation of magnetic dipolar particles: scattering dichroism results., *Phys. Rev. Lett.* 87(11): 115501.
- Miguel, M. C. & Pastor-Satorras, R. (1999). Kinetic growth of field-oriented chains in dipolar colloidal solutions, *Phys. Rev. E* 59 (1): 826–834.
- Miyazima, S., Meakin, P. & Family, F. (1987). Aggregation of oriented anisotropic particles, *Phys. Rev. A* 36 (3): 1421–1427.
- Nakano, M. & Koyama, K. (eds) (1998). *Proceedings of the 6th International Conferences on ER and MR fluids and their applications*, World Scientific, Singapore.
- Odriozola, G., Jiménez-Ángeles, F. & Lozada-Cassou, M. (2006). Effect of confinement on the interaction between two like-charged rods., *Phys. Rev. Lett.* 97: 018102.
- Otterstedt, J. & Brandreth., D. A. (1998). *Small Particles Technology.*, Springer.
- Paddinga, J. T. & Briels, W. J. (2010). Translational and rotational friction on a colloidal rod near a wall, *J. Chem. Phys.* 132: 054511.
- Pailthorpe, B. A. & Russel, W. B. (1982). The retarded van der Waals interaction between spheres, *J. Colloid Interface Sci.* 89(2): 563–566.
- Philipse, A. P. & Koenderink, G. H. (2003). Sedimentation-diffusion profiles and layered sedimentation of charged colloids at low ionic strength, *Adv. Colloid Interface Sci.* 100–102: 613–639.
- Polin, M., Grier, D. G. & Han, Y. (2007). Colloidal electrostatic interactions near a conducting surface., *Phys. Rev. E* 76: 041406.
- Promislow, J., Gast, A. P. & Fermigier, M. (1994). Aggregation kinetics of paramagnetic colloidal particles, *J. Chem. Phys.* 102(13): 5492–5498.
- Rabinow, J. (1948). The magnetic fluid clutch, *AIEE Trans.* 67: 1308.

- Rasa, M. & Philipse, A. P. (2004). Evidence for a macroscopic electric field in the sedimentation profiles of charged colloids, *Nature* 429(24): 857–860.
- Reiner, E. S. & Radke, C. J. (1993). Double layer interactions between charge-regulated colloidal surfaces: Pair potentials for spherical particles bearing ionogenic surfaces groups., *Adv. Colloid Interface Sci.* 47: 59–147.
- Russel, W. B., Saville, D. A. & Schowalter, W. R. (1989). *Colloidal Dispersions.*, Cambridge University Press.
- Savin, T. & Doyle, P. S. (2005). Static and dynamic error in particle tracking microrheology, *Biophysical Journal* 88: 623–638.
- Savin, T. & Doyle, P. S. (2007). Statistical and sampling issues when using multiple particle tracking, *Phys. Rev. E* 76: 021501.
- Savin, T., Spicer, P. T. & Doyle, P. S. (2007). A rational approach to noise characterization in video microscopy particle tracking, *Phys. Rev. E* 76: 021501.
- Schmidt, M., Dijkstra, M. & Hansen, J. P. (2004). Competition between sedimentation and phase coexistence of colloidal dispersions under gravity, *J. Phys. Condens. Matter* 16: S4185–S4194.
- Schmitz, K. S., Bhuiyan, L. B. & Mukherjee, A. K. (2003). On the grier-crocker/tata-ise controversy on the macroion-macroion pair potential in a salt-free colloidal suspension, *Langmuir* 19: 7160–7163.
- Science. (1999). Complex systems., *Science* 284(5411): 1–212.
- Shen, L., Stachowiak, A., Fateen, S. E. K., Laibinis, P. E. & Hatton, T. A. (2001). Structure of alkanolic acid stabilized magnetic fluids. A small-angle neutron and light scattering analysis, *Langmuir* 17: 288.
- Skjeltorp, A. T. (1983). One-dimensional and two-dimensional crystallization of magnetic holes, *Phys. Rev. Lett.* 51 (25): 2306–2309.
- Smirnov, P., Gazeau, F., Lewin, M., Bacri, J. C., Siauve, N., Vayssettes, C., Cuenod, C. A. & Clement, O. (2004). In vivo cellular imaging of magnetically labeled hybridomas in the spleen with a 1.5-t clinical mri system, *Magn. Reson. Med.* 52: 73–79.
- Squires, T. M. & Brenner, M. P. (2000). Like-charge attraction and hydrodynamic interaction, *Phys. Rev. Lett.* 85(23): 4976–4979.
- Tao, R. (ed.) (2000). *Proceedings of the 7th International Conferences on ER and MR fluids*, World Scientific, Singapore.
- Tata, B. V. R. & Ise, N. (1998). Monte carlo study of structural ordering in charged colloids using a long-range attractive interaction, *Phys. Rev. E* 58(2): 2237–2246.
- Tata, B. V. R. & Ise, N. (2000). Reply to “comment on ‘monte carlo study of structural ordering in charged colloids using a long-range attractive interaction’ ”, *Phys. Rev. E* 61(1): 983–985.
- Tata, B. V. R., Mohanty, P. S. & Valsakumar, M. C. (2008). Bound pairs: Direct evidence for long-range attraction between like-charged colloids, *Solid State Communications* 147: 360–365.
- Tirado, M. M. & García, J. (1979). Translational friction coefficients of rigid, symmetric top macromolecules. Application to circular cylinders., *J. Chem. Phys.* 71: 2581.
- Tirado, M. M. & García, J. (1980). Rotational dynamics of rigid symmetric top macromolecules. Application to circular cylinders., *J. Chem. Phys.* 73: 1986.
- Tirado-Miranda, M. (2001). *Agregación de Sistemas Coloidales Modificados Superficialmente.*, PhD thesis, Universidad de Granada.
- U. S. National Institutes of Health, Bethesda, Maryland, USA, <http://rsb.info.nih.gov/ij/> (n.d.).

- Verdier, C. (2003). Rheological properties of living materials., *J. Theor. Medic.* 5: 67–91.
- Verwey, E. J. W. & Overbeek, J. T. G. (1948). *Theory of the Stability of Lyophobic Colloids.*, Elsevier, Amsterdam.
- Vicsek, T. (1992). *Fractal Growth Phenomena*, 2 edn, World Scientific, Singapore.
- Vicsek, T. & Family, F. (1984). Dynamic scaling for aggregation of clusters, *Phys. Rev. Lett.* 52,19: 1669–1672.
- von Smoluchowski, M. (1917). *Z. Phys. Chem., Stoechiom. Verwandtschaftsl* 92: 129.
- Vuppu, A. K., García, A. A., Hayes, M. A., Booksh, K., Phelan, P. E., Calhoun, R. & Saha, S. K. (2004). Phase sensitive enhancement for biochemical detection using rotating paramagnetic particle chains, *J. Appl. Phys.* 96: 6831–6838.
- Waigh, T. A. (2005). Microrheology of complex fluids, *Rep. Prog. Phys.* 68: 685–742.
- Wilhelm, C., Browaeys, J., Ponton, A. & Bacri, J. C. (2003). Rotational magnetic particles microrheology: The maxwellian case, *Phys. Rev. E* 67: 011504.
- Wilhelm, C., Gazeau, F. & Bacri, J. C. (2003). Rotational magnetic endosome microrheology: Viscoelastic architecture inside living cells, *Phys. Rev. E* 67: 061908.
- Wilhelm, C., Gazeau, F. & Bacri, J. C. (2005). Magnetic micromanipulation in the living cell, *Europhys. news* 3: 89.
- Witten, T. A. & Sander, L. M. (1981). Diffusion-limited aggregation, a kinetic critical phenomenon, *Phys. Rev. Lett.* 47: 1400–1403.

Magnetohydrodynamics of Metallic Foil Electrical Explosion and Magnetically Driven Quasi-Isentropic Compression

Guiji Wang, Jianheng Zhao, Binqiang Luo and Jihao Jiang
*Institute of Fluid Physics, China Academy of Engineering Physics,
Mianyang City, Sichuan Province
China*

1. Introduction

The electrical explosion of conductors, such as metallic foils and wires, refers to rapid changes of physical states when the large pulsed current (tens or hundreds of kA or more, the current density $j \geq 10^6$ A/cm²) flows through the conductors in very short time (sub microsecond or several microseconds), which may produce and radiate shock waves, electrical magnetic waves, heat and so on. There are many applications using some characteristics of the electrical explosion of conductors.

The Techniques of metallic foil electrical explosion had been developed since 1961, which was first put forward by Keller, Penning^[1] and Guenther et al^[2]. However, it develops continually until now because of its wide uses in material science, such as preparation of nanometer materials and plating of materials^[3,4], shock wave physics^[5-7], high energy density physics^[8] and so on. Especially the techniques of metallic foil electrically exploding driving highvelocity flyers, are widely used to research the dynamics of materials, hypervelocity impact phenomena and initiation of explosives in weapon safety and reliability. Therefore, in this chapter we focus on the physical process of metallic foil explosion and the techniques of metallic foil electrically exploding driving highvelocity flyers. Here the explosion of metallic foils are caused by the large current flowing through in sub microsecond or 1~2 microsecond or less. During the whole physical process, not only does the temperature rising, melting, vaporizing and plasma forming caused by instantaneously large current, but also the electrical magnetic force exists and acts on. Because the whole process is confined by rigid face and barrel, and the time is very short of microsecond or sub microsecond or less, and the phenomena is similar to the explosion of explosives, we call the process electrical explosion of metallic foils. This process is a typically hydrodynamic phenomena. It is also a magnetohydrodynamic process because of the exist and action of the magnetic force caused by large current and self-induction magnetic field.

Magnetically driven quasi-isentropic compression is an relatively new topic, which was developed in 1972^[9]. At that time the technique of magnetically driven quasi-isentropic compression was used to produce high pressure and compress the cylindrical sample materials. Until 2000, the planar loading technique of magnetically driven quasi-isentropic

compression was firstly presented by J.R. Asay at Sandia National Laboratory^[10]. In last decade, this planar loading technique had being developed fastly and accepted by many researchers in the world, such as France^[11], United Kingdom^[12], and China^[13]. As J.R. Asay said, it will be a new experimental technique widely used in shock dynamics, astrophysics, high energy density physics, material science and so on. The process of magnetically driven quasi-isentropic compression is typical magnetodynamics^[14], which refers to dynamic compression, magnetic field diffusion, heat conduction and so on.

As described above, the electrical explosion of metallic foil and magnetically driven quasi-isentropic compression is typically magnetohydrodynamic problem. Although it develops fastly and maybe many difficulties and problems exist in our work, we present our important and summary understanding and results to everyone in experiments and simulations of electrical explosion of metallic foil and magnetically driven quasi-isentropic compression in last decade.

In the following discussions, more attentions are paid to the physical process, the experimental techniques and simulation of electrical explosion of metallic foil and magnetically driven quasi-isentropic compression.

2. Physical process of metallic foil electrical explosion and magnetically driven quasi-isentropic compression

2.1 Metallic foil electrical explosion

Here we introduce the model of metallic foil electrically exploding driving highvelocity flyers to describe the physical process of electrical explosion of metallic foil shown in Fig.1. A large pulsed current is released to the metallic foil of the circuit, which is produced by a typically pulsed power generator. The circuit can be described by R - C - L electrical circuit equations^[15]. During the circuit, the metallic foil is with larger resistance than that of other part, so the energy is mainly absorbed by the metallic foil, and then the physical states of metallic foil change with time. Fig.2 shows the typical current and voltage histories between metallic aluminum foil during the discharging process of pulsed power generator.

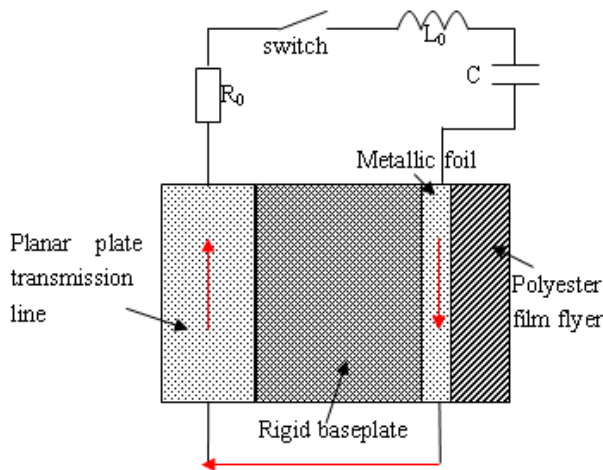


Fig. 1. The model of metallic foil electrically exploding driving highvelocity flyers.

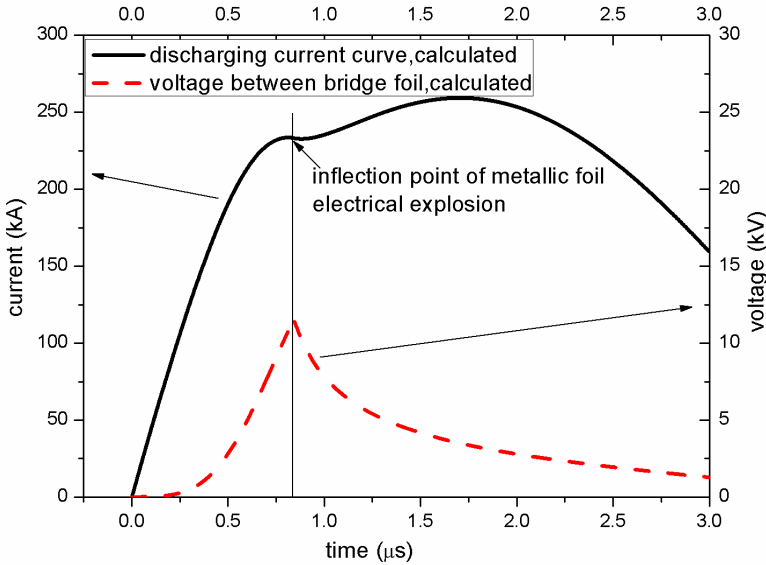


Fig. 2. The typically discharging current and voltage histories between bridge Aluminum foil.

According to the density changing extent of metallic foil when the first pulsed current flows through it, the whole process of electrical explosion of metallic foil can be classified to two stages. The initial stage includes the heating stage, the melting stage and the heating stage of liquid metal before vaporizing. During this process, the density of metallic foil changes relatively slow. The second stage includes the vaporizing stage and the following plasma forming. The typical feature of electrical explosion of metallic foil is that the foil expands rapidly and violently, and that the resistance increases to be two or more orders than that of initial time ($R/R_0 \sim 100$). The resistance increases to be maximum when the state of metallic foil is at the vaporizing stage. During this stage, the voltage of between foil also increases to be maximum, and then the breakdown occurs and the plasmas is forming. The inflection point of the discharging current shown in Fig.2 exhibits the feature.

At the initial stage, the expansion of metallic foil is not obvious, and the change of physical states can be described with one thermodynamic variable T (temperature) or specific enthalpy. The energy loss of the interaction between the foil and the ambient medium can be neglected when there is no surface voltaic arcs. Therefore, some assumptions can be used to simplify the problem. We can think that the heating of the metallic foil is uniform and the instability, heat conduction and skin effect can not be considered at initial stage. For this stage, the physical states of metallic foil vary from solid to liquid, and the model of melting phase transition can be used to described it well^[16].

For the second stage, the physical states varies from liquid to gas, and then from gas to plasma. There are several vaporizing mechanisms to describe this transition, such as surface evaporation and whole boil^[16]. The rapid vaporizing of liquid metal make its resistance increases violently, and the current decreases correspondingly. At this time, the induction voltage between bridge foil increases fastly. If the induction voltage can make the metallic vapor breakdown and the plasma is formed, the circuit is conducted again. Of course, the

breakdown of metallic vapor needs some time, which is called relaxation time as shown in Fig.3. For different charging voltages, the relaxation time varies, which can be seen from the experimental current histories in Fig.3.

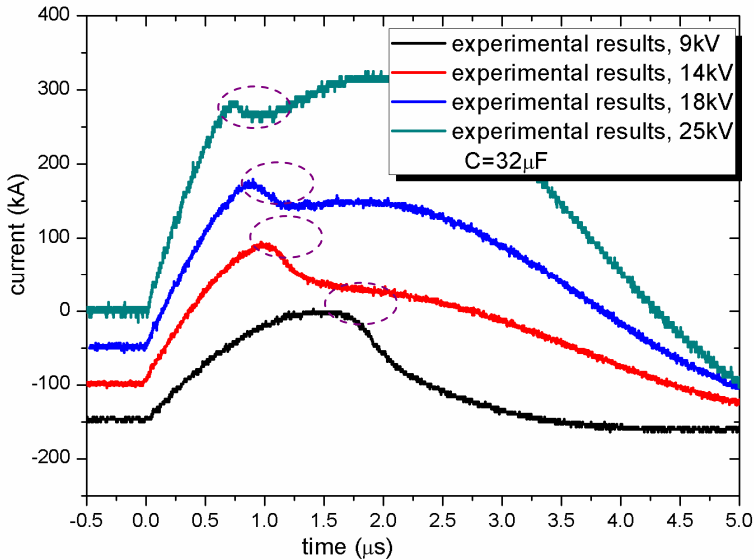


Fig. 3. The breakdown relaxation time shown in the discharging current histories at different charging voltage for the pulsed power generator.

One important application of the electrical explosion of metallic foil is to launch highvelocity flyers with the rapid expansion of the gas and plasma from electrical explosion of metallic foil. Some metallic materials are with good conductivity and explosion property, such as gold, silver, copper, aluminum and so on. The experimental results^[17] show that the aluminum foil is the best material for the application of metallic foil electrically exploding driven highvelocity flyers. There are many models used to describe the process, such as electrical Gurney model^[18], Schmidt model^[19] and one dimensional magnetohydrodynamic model^[20]. The electrical Gurney model and Schmidt model are two empirical models which are derived from energy conservation equation based on some assumptions. For a specific electrical parameters of the circuit of some apparatus, the electrical Gurney model can be used to predict the final velocity of the flyers when the Gurney parameters are determined based on some experimental results. And the Schmidt model can be used to predict the velocity history of the flyers because the Gurney energy part is substituted with an energy part with the function of time, which is depended on the measured current and voltage histories between bridge foil to correct the specific power coefficient. These two models can't reflect other physical variables of electrical explosion of metallic foil except the velocity of the flyer. Therefore, a more complex model is put forward based on magnetohydrodynamics, which considers heat conduction, magnetic pressure and electrical power. The magnetohydrodynamic model can well reflect the physical process of electrical explosion of metallic foil. The equations are given below^[16,20].

$$\left\{ \begin{array}{l} \dot{x} = u; \quad \dot{v} = \frac{\partial}{\partial q}(x^{\gamma-1}u) \\ \dot{u} + x^{\gamma-1} \frac{\partial}{\partial q}(p + p_{\omega} + \frac{B^2}{2\mu_0}) = 0 \\ \dot{\epsilon} + (p + p_{\omega})\dot{v} = Q_v \\ \frac{d}{dt}(x^{1-\gamma} v B) = \frac{\partial E}{\partial q} \\ E = \frac{1}{\mu_0 \sigma v} \frac{\partial}{\partial q}(x^{\gamma-1} B) \\ j = \sigma E; \quad Q_v = v j E \\ p = p(v, T); \quad \epsilon = \epsilon(v, T); \quad \sigma = \sigma(v, T) \end{array} \right. \quad (1)$$

Where, γ —symmetric exponent (for metallic wire or cylindrical foil $\gamma=2$, and for planar foil $\gamma=1$) ; $\partial/\partial q=x^{1-\gamma}v\partial/\partial x$; q —Lagrange mass coordinate; B —transverse component of magnetic field; E —axial component of electrical field; j —current density; Q_v —specific power of Joule heating; p_{ω} —artificial viscosity coefficient ; u —transverse moving velocity ; p —pressure; ϵ —internal energy; v —unit volume; σ —conductivity.

For this apparatus, the discharging circuit is a typical RCL circuit, which can be expressed by equation (2) below.

$$\left\{ \begin{array}{l} \frac{d}{dt}[(L_0 + L_{foil})I] + U_{foil} + R_0 I = U_c; \\ \frac{dU_c}{dt} = -\frac{I}{C_0}; \\ U_{foil} \simeq I_{foil} E[t, X(t)] \end{array} \right. , \quad (2)$$

In the equation (2), when the time $t=0$, the primary current and voltage $I(0) = 0$ and $U_c(0) = U_0$, C_0 and U_0 are the capacitance and charging voltage of capacitor or capacitor bank, L_0 and R_0 are the inductance and efficient resistance of circuit, U_{foil} is the voltage between the ends of metallic foil, which is related with the length l_{foil} of metallic foil and the magnetic field of the space around the foil. the dynamic inductance L_{foil} can be obtained by equation (3).

$$L_{foil}(t) = \mu_0 k (l_{foil} / b) [x_0' - X_0] \quad (3)$$

Where μ_0 is the vacuum magnetic permeability, k is a coefficient related with the length l and width b of metallic foil. x is the expanding displacement of metallic foil.

2.2 Magnetically driven quasi-isentropic compression

The concept of magnetically driven quasi-isentropic compression is illustrated in Fig.4. A direct short between the anode and cathode produces a planar magnetic field between the conductors when a pulsed current flows through the electrodes over a time scale of 300~800ns. The interaction between the current (density J) and the induction magnetic field

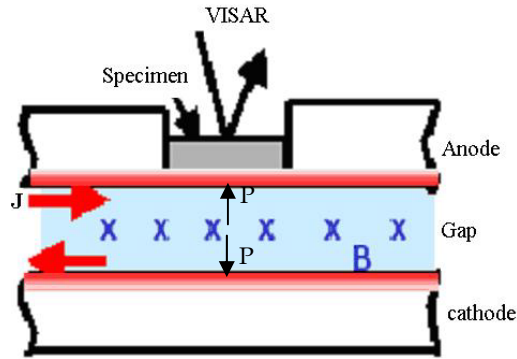


Fig. 4. The principle diagram of magnetically driven quasi-isentropic compression.

B produces the magnetic pressure ($\vec{J} \times \vec{B}$) proportional to the square of the field. The force is loaded to the internal surface that the current flows through. The loading pressure wave is a ramp wave, which is a continuous wave. Compared with the shock wave, the increment of temperature and entropy is very lower. However, because of the effects of viscosity and plastic work, the sample can't turn back to the original state after the loading wave. That is to say, in solids the longitudinal stress differs from the hydrostatic pressure because of resolved shear stresses that produce an entropy increase from the irreversible work done by deviator^[21, 22]. For this reason, the ramp wave loading process is usually assumed to be quasi-isentropic compression. Besides the loading force is magnetic pressure, it is called magnetically driven quasi-isentropic compression.

In order to produce high pressure, the amplitude of the current is usually up to several megamperes or tens of megamperes. Because of the effects of Joule heating and magnetic field diffusion, the physical states of the loading surface will change from solid to liquid, and to gas and plasma. And these changes will propagate along the thickness direction of the electrodes originated from the loading surface. These phenomena are typically magnetohydrodynamic problems. In order to describe the physical process, the equation of magnetic field diffusion is considered besides the equations of mass, momentum and energy. The magnetohydrodynamic equations are presented below.

$$\left\{ \begin{array}{l} \frac{\partial \rho_m}{\partial t} + \nabla \cdot (\rho_m \vec{u}) = 0 \\ \rho_m \frac{d\vec{u}}{dt} + \nabla(p+q) - \vec{J} \times \vec{B} = 0 \\ \frac{de}{dt} + (p+q) \frac{d(1/\rho_m)}{dt} - \dot{e}_D = 0 \\ \rho_m \frac{d}{dt} \left(\frac{\vec{B}}{\rho_m} \right) - (\vec{B} \cdot \nabla) \vec{u} = -\nabla \times \left[\frac{\eta}{\mu_0} (\nabla \times \vec{B}) \right] \\ \vec{J} = \sigma \vec{E} = \frac{1}{\mu_0} \nabla \times \vec{B} \\ \vec{u} = \frac{d\vec{x}}{dt}, \dot{e}_D = \kappa \nabla T \end{array} \right. \quad (4)$$

Where ρ_m is mass density of electrodes, u is velocity, J is current density, B is magnetic field, p is pressure, q is artificial viscosity pressure, e is specific internal energy, σ is electrical conductivity of electrodes and κ is thermal conductivity.

Similar to the technique of electrical explosion of metallic foil, the large current is also produced by some pulsed power generators, for example, the ZR facility at Sandia National Laboratory can produce a pulsed current with peak value from 16 MA to 26 MA and rising time from 600 ns to 100 ns^[23]. In the following part, we will introduce the techniques of magnetically driven quasi-isentropic compression based on the pulsed power generators developed by ourselves.

3. Techniques of metallic foil electrically exploding driving highvelocity flyers and magnetically driven quasi-isentropic compression

The techniques of metallic foil electrically exploding driving highvelocity flyers and magnetically driven quasi-isentropic compression have been widely used to research the dynamic properties of materials and highvelocity impact phenomena in the conditions of shock and shockless(quasi-isentropic or ramp wave) loading. By means of these two techniques, we can know the physical, mechanical and thermodynamic properties of materials over different state area (phase space), such as Hugoniot and off-Hugoniot states.

3.1 Metallic foil electrically exploding driving highvelocity flyers^[24,25,26]

As described above, the high pressure gas and plasma are used to launch highvelocity flyer plates, which are produced from the electrical explosion of metallic foil. The working principle diagram of the metallic foil electrically exploding driving highvelocity flyers is presented in Fig.5. Usually we choose the pure aluminum foil as the explosion material because of its good electrical conductivity and explosion property. The flyers may be polyester films, such as Mylar or Kapton, or complex ones consisted of polyester film and metallic foil. The material of barrel for accelerating the flyers may be metals or non-polyester films, such as Mylar or Kapton, or complex ones consisted of polyester film and metallic foil. The material of barrel for accelerating the flyers may be metals or non-metals, such as

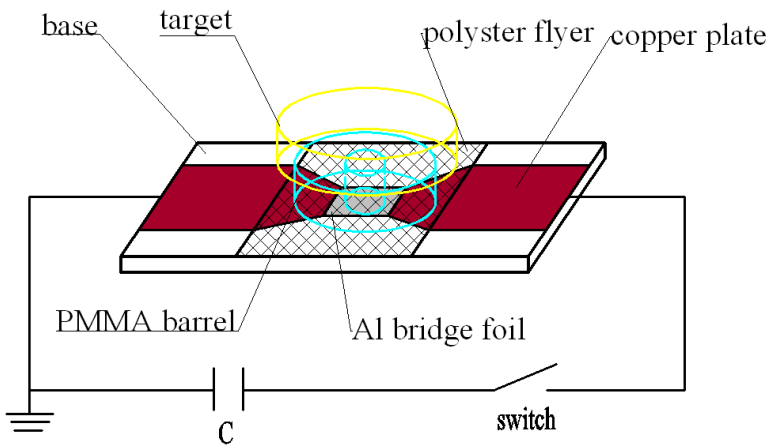


Fig. 5. The diagram of working principle of metallic foil electrically exploding driving flyer.

ceramics, steel or acryl glass. The base plate is used to confined the high pressure gas and plasma and reflect them to opposite direction to propel the flyers. The base plate also insulates the anode from the cathode transmission lines. So the material of base plate is non-metal and the ceramics is a good one.

The whole working process is that the large current flows through the metallic foil instantly and the metallic foil goes through from solid, to liquid, gas and plasma, and then the high pressure gases and plasmas expand to some direction to drive the polyester Mylar flyer to high velocity and impacts the targets.

Based on low inductance technologies of pulsed stored energy capacitor, detonator switch and parallel plate transmission lines with solid films insulation, two sets of experimental apparatuses with stored energy of 14.4 kJ and 40 kJ were developed for launching hypervelocity flyer. The first apparatus is only consisted of one stored energy pulsed capacitor with capacitance of 32 μF , inductance of 30 nH and rated voltage of 30 kV. The parallel plate transmission lines and solid insulation films are used, which are with very low inductance. The thickness of insulation films is no more than 1 mm, which is composed of several or ten pieces of Mylar films with thickness of 0.1 mm. The second apparatus is composed of two capacitors with capacitance of 16 μF and rated voltage of 50 kV in parallel. For two apparatuses, the detonator switch is used, which is with low inductance of about 7 nH and easy to connected with the parallel plate transmission lines.

Fig.6 shows the diagram of the detonator switch. The detonator is exploded and the explosion products make the aluminum ring form metallic jet and breakdown the insulation films between anode and negative electrodes, and then the stored energy is discharged to the load.

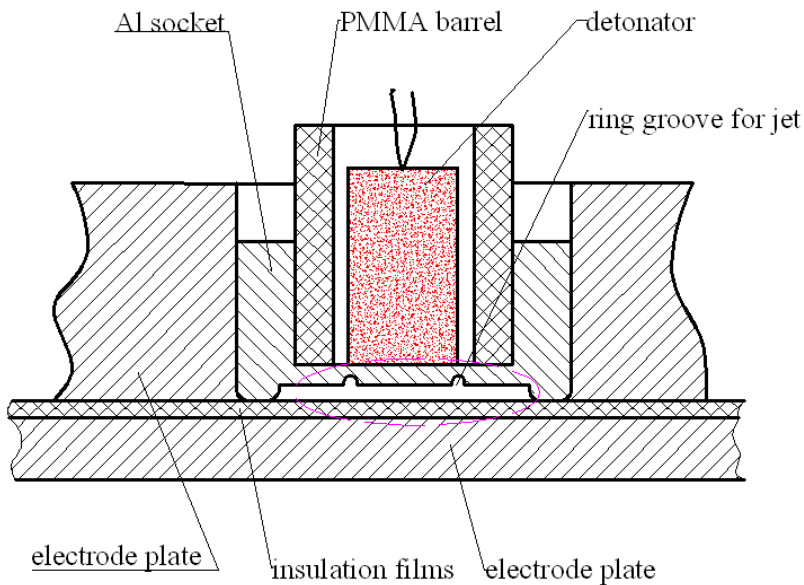
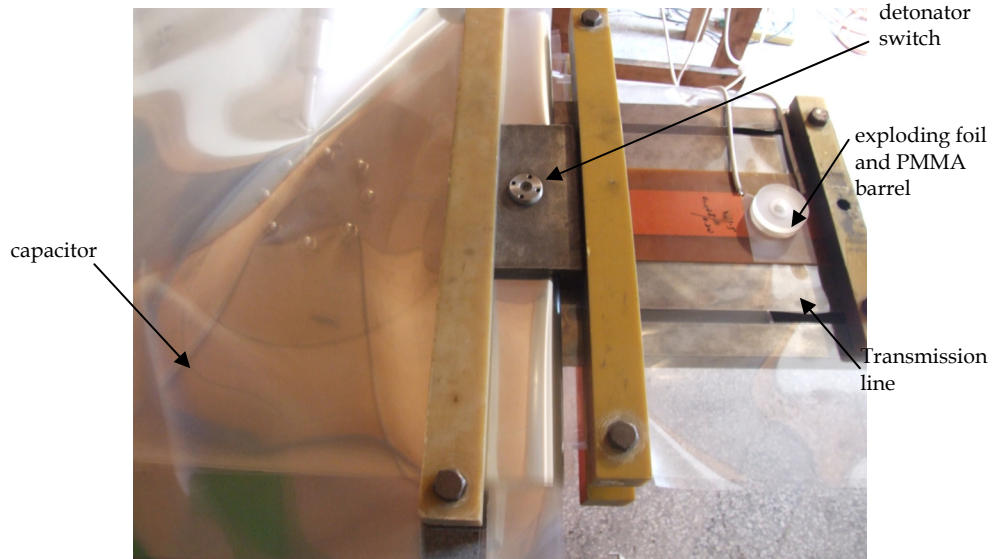
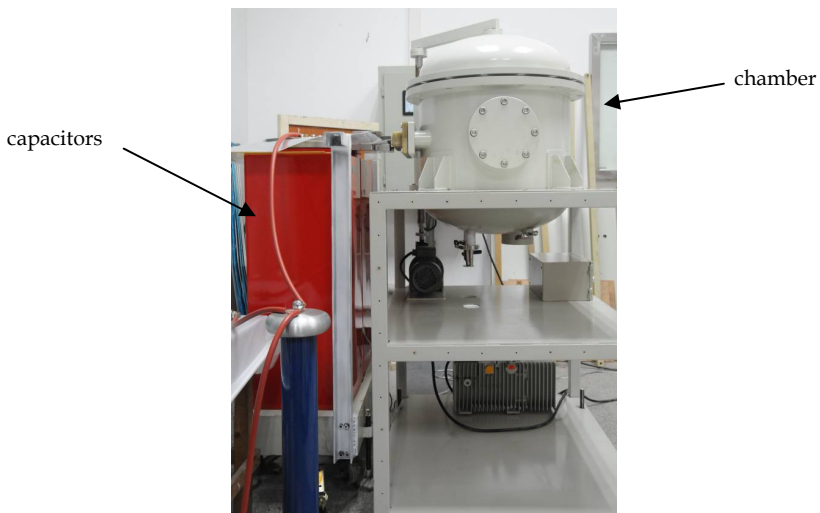


Fig. 6. Diagram of detonator switch

Fig. 7 shows the photos of two apparatuses and Table 1 gives the electrical parameters of these two apparatuses.



(a)



(b)

Fig. 7. Experimental apparatuses of metallic foil electrically exploding driving flyers. The apparatus with energy of 14.4 kJ (a) and the apparatus with energy of 40 kJ(b).

setup	$C/\mu\text{F}$	U_0/kV	E/kJ	$R/\text{m}\Omega$	L/nH	$T/\mu\text{s}$	$(dI/dt)_{t=0}/(\text{A/s})$	Remarks
1	32	30	14.4	14	40	7.1	7.5×10^{11}	Single capacitor
2	32	50	40	10	36	6.75	8.4×10^{11}	Two capacitors in parallel

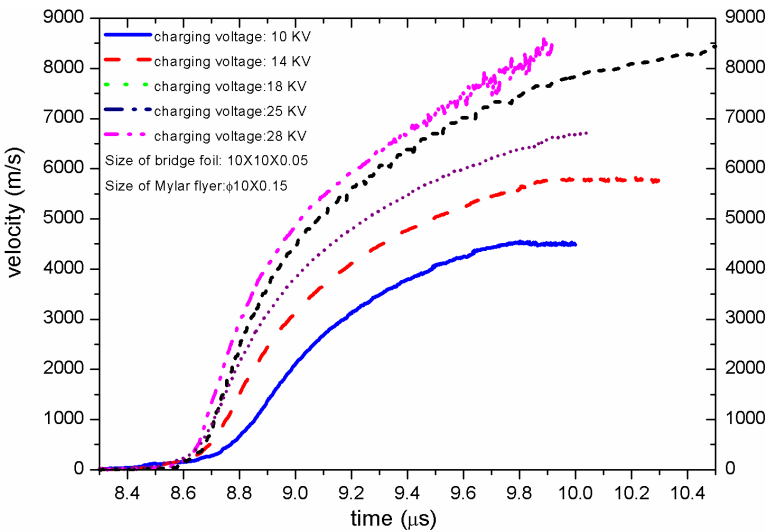
Table 1. Parameter Values of our two apparatuses

Table 2 gives the performance parameters of our two apparatuses of metallic foil electrically exploding driving flyers.

Parameters	Setup	
	1	2
Flyer—Mylar	$\phi(6\sim 20)\text{mm} \times (0.1\sim 0.2)\text{mm}$	$\phi(10\sim 30)\text{mm} \times (0.1\sim 0.3)\text{mm}$
Foil—Aluminum	$(6\sim 20)\text{mm} \times (6\sim 20)\text{mm} \times 0.028\text{mm}$	$(10\sim 30)\text{mm} \times (10\sim 30)\text{mm} \times 0.05\text{mm}$
Barrel—PMMA	$\phi(6\sim 20)\text{mm} \times (4\sim 15)\text{mm}$	$\phi(10\sim 30)\text{mm} \times (4\sim 15)\text{mm}$
Flyer velocity	$3\sim 10\text{km/s}$	$3\sim 15\text{km/s}$
Flyer Simultaneity at Impact	$\leq 25\text{ ns}$	$\leq 35\text{ ns}$

Table 2. The performance parameters of our two apparatuses

The typical velocity histories of the flyers are shown in Fig.8, which are measured by laser interferometer, such as VISAR (velocity interferometer system for any reflectors)^[27] or DISAR(all fibers displace interferometer system for any reflectors)^[28].



(a)

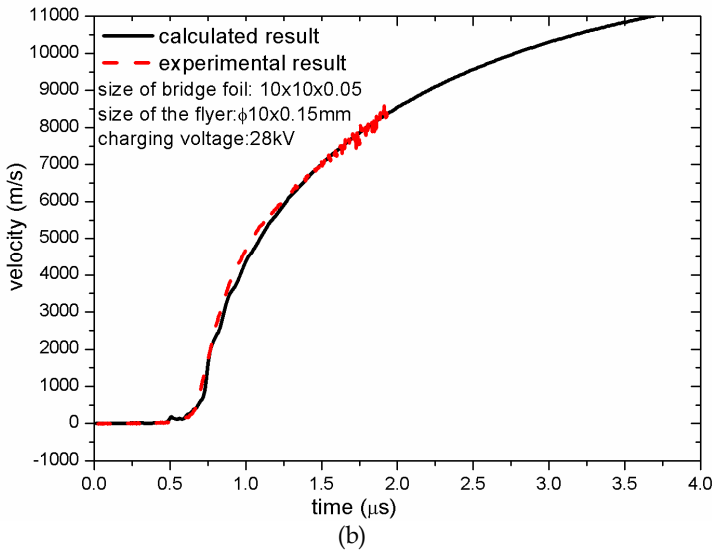


Fig. 8. The experimental results of the velocity of the flyer in different conditions. The velocities of the flyers vary from charging voltages (a) and the calculated and measured velocities of the flyers (b)

As described above, the apparatus of metallic foil electrically exploding driving flyers is a good plane wave generator for shock wave physics experiments. In the last part, we will introduce some important applications of this tool.

3.2 Magnetically driven quasi-isentropic compression

The techniques to realize magnetically driven quasi-isentropic compression are based on all kinds of pulsed power generators, such as ZR, Veloce^[29], Saturn^[30] facilities. As shown in Fig.9, Current \vec{j} flowing at the anode and cathode surfaces induces a magnetic field \vec{B} in

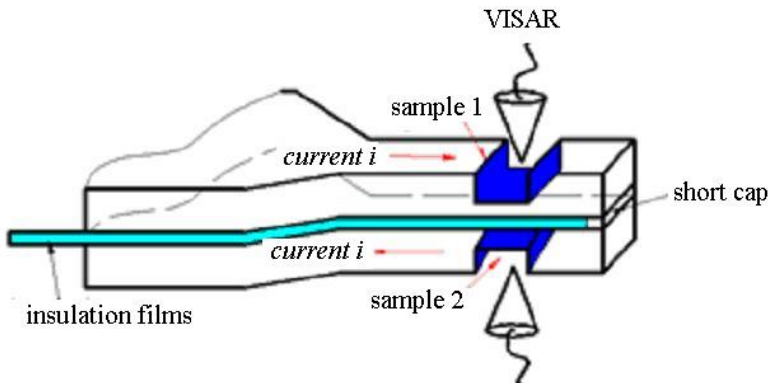


Fig. 9. Experimental configuration of samples for magnetically driven quasi-isentropic compression

the gap. The resulting $\vec{J} \times \vec{B}$ Lorentz force is transferred to the electrode material, and a ramp stress wave propagates into the samples. The stress normal to the inside surfaces of electrodes is $P_B = (1/2)\mu_0 J^2$, where J is the current per unit width. Two identical samples with a difference in thickness of h , are compressed by identical B-force and their particle velocity profiles $u(t)$ are measured by DISAR or VISAR.

An inverse analysis technique, i.e, the backward integration technique using difference calculation is developed to extract a compression isentrope from free-surface or window-interface velocity profiles^[31]. Different from Lagrangian wave analysis, inverse analysis can account for ramp-wave interactions that arise at free surfaces or window interfaces. In this method, the profiles of velocity and density are specified as an initial condition at the Lagrangian position of the measurement, then the equations of motion from equation (5) through equation (7) are integrated in the negative spatial direction to a position inside the material that is free of interaction effects during the time of interest. Assuming some parametric form shown in equation (8) for the mechanical isentrope of the material such as Murnaghan equation or others, the parameter values are found by iteratively performing backward integration on data from multiple thickness of the sample while minimizing the deviation between the results at a common position.

$$\sigma(h - dh, t) = \sigma(h, t) + \rho_0 [u(h, t + dt) - u(h, t - dt)] dh / (2dt) \quad (5)$$

$$\varepsilon(h - dh, t) = F[\sigma(h - dh, t)] \quad (6)$$

$$u(h - dh, t) = u(h, t) + [\varepsilon(h, t + dt) - \varepsilon(h, t - dt)] dh / (2dt) \quad (7)$$

$$B_s(V) = B_{s0} \left(\frac{V_0}{V} \right)^B \quad (8)$$

In order to do quasi-isentropic compression experiments, a compact capacitor bank facility CQ-1.5^[13] was developed by us, which can produce a pulsed current with peak value of about 1.5 MA and rising time of 500 ns~800 ns. The solid insulating films are used to insulate the anode electrode plates from the cathode ones. And the facility is used in the air. Fig.10 presents the picture of CQ-1.5. Based on CQ-1.5, about 50 GPa pressure is produced on the surface of steel samples. The parameter values of CQ-1.5 is given in Table 3.

performance parameters	values
total capacitance	15.88 μ F
period in short-circuit	3.40 μ s
rise time	500~800 ns
total inductance	about 18 nH
total resistance	~10 m Ω
charging voltage	75 kV~80 kV
peak current	\geq 1.5 MA

Table 3. The specifications of CQ-1.5

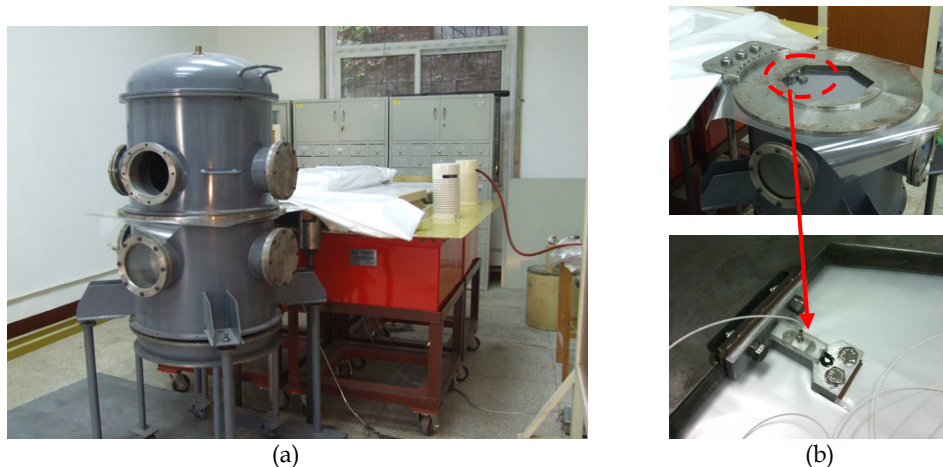


Fig. 10. The picture of experimental apparatus CQ-1.5 (a) and its load area including sample and measuring probe (b).

Fig. 11. shows the typical loading pressure histories. The pressure is a ramp wave.

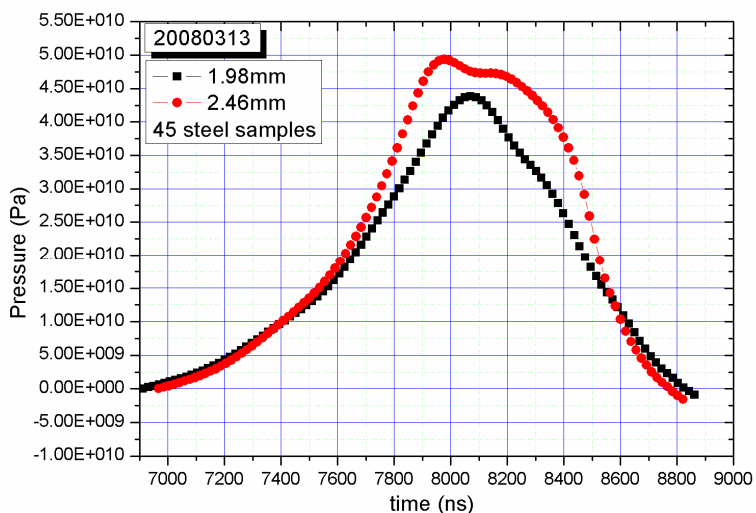


Fig. 11. The loading pressure histories of CQ-1.5

4. MHD simulation of metallic foil electrically exploding driving highvelocity flyers and magnetically driven quasi-isentropic compression

4.1 Metallic foil electrically exploding driving highvelocity flyers

The code used to simulate the electrical explosion of metallic foil is improved based our SSS code^[32], which is one dimensional hydrodynamic difference code based on Lagrange orthogonal coordinate. For the case of electrical explosion of metallic foil, the power of Joule

heating is increase into the energy equation, and the magnetic pressure part is considered. In order to calculate the power of Joule heating and magnetic pressure, the discharging current history is needed which is determined by the electric circuit equation (2) and equation (3). The resistance of foil varies from different phase states during discharging process, so a precisionly electrical resistivity model is needed to describe this change. The physical model is seen in Figure 1, and the Lagrange hydrodynamic equations are:

$$\left\{ \begin{array}{l} V = \frac{\partial X}{\partial M} \\ \frac{\partial U}{\partial t} = -\frac{\partial \sigma}{\partial M} + f_{EM} \\ \frac{\partial E}{\partial t} = -\frac{\partial(\sigma U)}{\partial M} + \frac{\partial(\Delta P)}{\partial M} + \lambda \frac{\partial}{\partial M} \left(\frac{\partial T}{\partial X} \right) \\ \Delta P = I^2 R_{foil} \\ f_{EM} = \vec{j}(X) \times \vec{B}(X) / M \end{array} \right. \quad (9)$$

Where, V is specific volume, M is mass, X is Lagrange coordinate, U is velocity, T is temperature, λ is thermal conductivity, σ is the total pressure and $\sigma=p+q$, p is heating pressure, q is artificial viscosity pressure, f_{EM} is magnetic pressure per mass, E is total specific energy and $E=e+0.5U^2$, e is specific internal energy, ΔP is power of Joule heating, B is magnetic flux density, μ is vacuum permeability, k is shape factor and $k=0.65$, R_{foil} is resistance of metallic foil and I is the current flowing through metallic foil in the circuit, which can be expressed with equation (10).

$$\left\{ \begin{array}{l} \frac{1}{C_0} \int_0^t I(t) dt + RI + L \frac{dI}{dt} = Vol_0 \\ L = L_s + L_d \\ R = R_s + R_{foil} \\ L_d = L(h + \Delta h) - L(h) = \frac{\mu l}{2\pi} \ln \frac{h + 1.23b}{h + \Delta h + 1.23b} \\ R_{foil}(t) = \frac{l}{b} \cdot \frac{1}{\int_0^h \frac{1}{\eta(X,t)} dX} \end{array} \right. \quad (10)$$

In the equation (10), C_0 is the capacitance of the experimental device, L is the total inductance of the circuit, L_s is the fixed inductance of the circuit, L_d is the variable inductance of the expansion of metallic foil caused by electrical explosion, R is the total resistance of the circuit, and R_s is the fixed resistance and R_{foil} is the dynamic resistance of the foil caused by electrical explosion, b, h and l is the width, thickness and length of the foil, η is the electrical resistivity, which is variable and can be expressed by the model put

forward by T.J. Burgess^[33]. The Burgess's model can describe the electrical resistivity of the foil at different phase states.

For solid state, there is

$$\eta_s = (C_1 + C_2 T^{C_3}) \cdot \left(\frac{V}{V_0} \right)^{F(\gamma)} \tag{11}$$

In equation (11), C_1 , C_2 and C_3 are fitting constants, γ is Gruneisen coefficient, for many materials $F(\gamma) = 2\gamma - 1$.

For liquid state, there is

$$\eta_L = \Delta\eta \cdot (\eta_s)_{T_m} \cdot \left(\frac{T}{T_m} \right)^{C_4} \tag{12}$$

In equation (12), for many materials, $\Delta\eta = k e^{0.069 L_F / T_m}$, k is a constant, L_F is the melting latent heat, T_m is melting point temperature and C_4 is fitting constant.

For gas state, the electrical resistivity is related with both the impact between electrons and ions and between electrons and neutrons. so,

$$\begin{cases} \eta_v = \eta_{ei} + \eta_{en} \\ \eta_{ei} = \frac{C_5}{T} [1 + \ln(1 + C_6 V T^{3/2})] \\ \eta = C_7 T^{1/2} [1 + \alpha_i^{-1}] \\ \partial_i = \left(1 + \frac{C_8 e^{C_9/T}}{V T^{3/2}} \right)^{-1/2} \end{cases} \tag{13}$$

In equation (13), α_i is the ionization fraction, C_5 , C_6 , C_7 , C_8 and C_9 are fitting constants.

In fact, there is mixed phase zone between liquid and gas states, a mass fraction m is defined. When $m=0$, all mass is condensed, and $m=1$, all mass is gas, and $0 < m < 1$, the mass is mixture states. Two mixture variants are also defined besides mass fraction.

$$\begin{cases} m = (V - V_0) \frac{C_{10}}{C_{11}} e^{-C_{12}/T} \\ X_c = (1 - m) / (V / V_0) \\ X_v = 1 - X_c \end{cases} \tag{15}$$

Where C_{10} , C_{11} and C_{12} are fitting constants.

The electrical resistivity of mixed phase zone can be expressed

$$\begin{cases} \eta_{mixed} = \left(\frac{X_c}{\eta_c} + \frac{X_v}{\eta_v} \right)^{-1} \\ \eta_c = \eta_l \end{cases} \tag{16}$$

Table 4 gives the parameters values of Burgess's model for Aluminum, which is used in our experiments.

C_1 (mΩ-cm)	C_2	C_3	C_4	C_5	C_6	γ_0	L_F (Mbar-cm ³ /mole)
-5.35e-5	0.233	1.210	0.638	1.5	1.20e-2	2.13	0.107
C_7	C_8	C_9	C_{10}	C_{11}	C_{12}	k	$T_{m,0}$ (ev)
3.80e-3	18.5	5.96	0.440	3.58e-2	3.05	0.878	0.0804

Table 4. The parameters values of Burgess’s model for Aluminum

The calculated results are presented in from Fig.12 through Fig.15. In Fig.14 and Fig.15, the experimental and calculated results are compared.

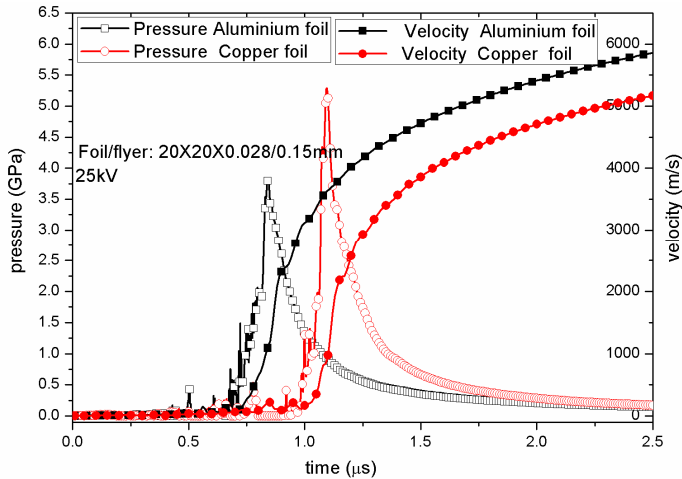


Fig. 12. The calculated pressure and flyer velocity history results of electrical explosion of Aluminum and Copper foils.

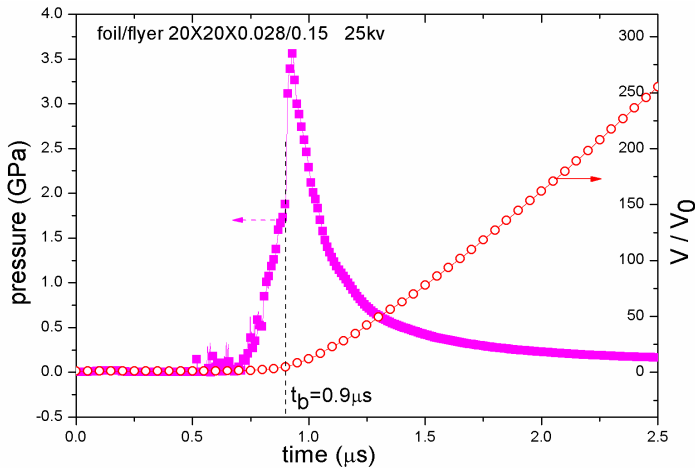


Fig. 13. The calculated results of pressure and specific volume of aluminum foil when exploding.

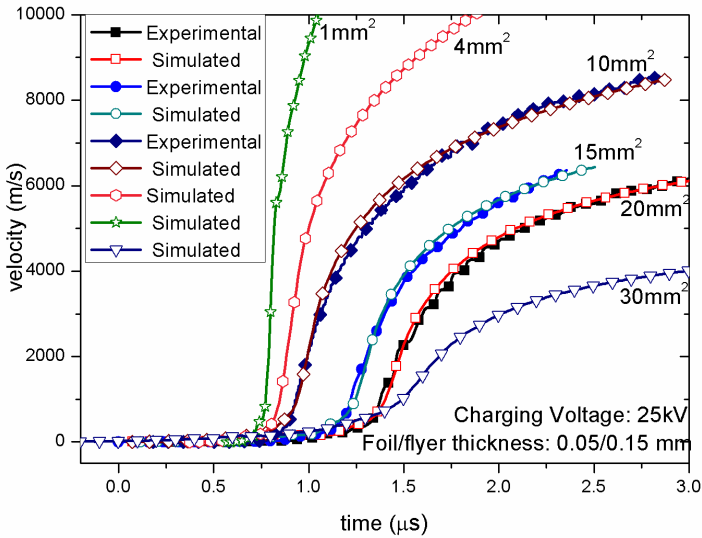


Fig. 14. The calculated and experimental results of flyer velocities for different flyer sizes.

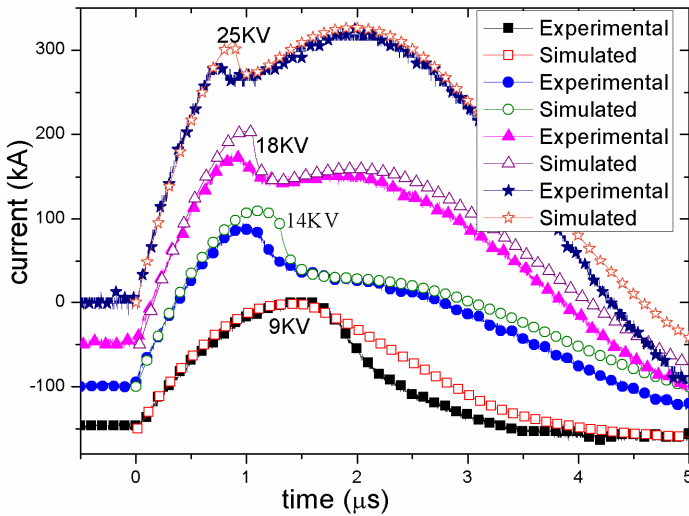


Fig. 15. The experimental and calculated results of discharging current.

The results presented in Fig.12 through Fig.15 show that the physical model here is appropriate to the electrical explosion of metallic foils.

4.2 Magnetically driven quasi-isentropic compression

In order to simplify the problem, the one dimensional model of magnetically driven quasi-isentropic compression can be described by the model shown in Fig.16. The changes of

electrical parameters caused by the motion of loaded electrode are not considered, and the heat conduction is neglected because it is slow in sub microsecond or one microsecond. A standardly discharging current in short circuit is as input condition presented in Fig.17. The relative magnetic permeability is supposed to be 1, that is to say, $\mu \approx \mu_0$.

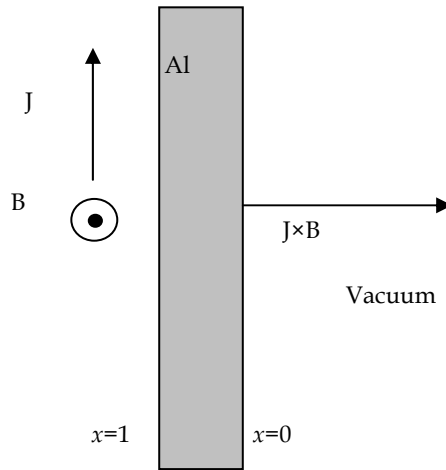


Fig. 16. Physical model of simulation

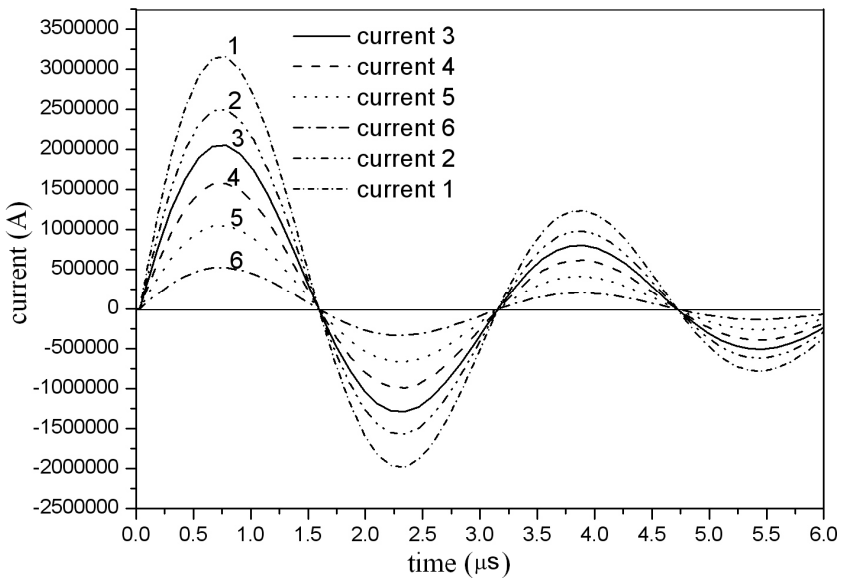


Fig. 17. Loading current curves

The controlling equations are one dimensionally magnetohydrodynamic ones, which include mass conservation equation, momentum conservation equation, energy conservation equation and magnetic diffusion equation, as shown in equation (4). The original boundary conditions are,

$$\text{For } t=0, \begin{cases} x=0: B=0, P=0 \\ x=1: B=0, P=0 \end{cases}, \text{ and for } t=t_n \text{ (at some time) }, \begin{cases} x=0: B=0, P=0 \\ x=1: B=\mu_0 J(t), P=0 \end{cases}$$

The calculation coordinate are Lagrangian ones, and for the Lagrangian coordinate, the equation (4) can be converted to equations from (17) through (19).

$$\rho_0 \frac{du}{dt} + \frac{\partial}{\partial x} \left(p + q + \frac{B^2}{2\mu_0} \right) = 0 \tag{17}$$

$$\rho_0 \frac{de}{dt} + (p + q) \frac{dV}{dt} - \rho_0 \dot{e}_D = 0 \tag{18}$$

$$\frac{\partial(VB)}{\partial t} = \frac{\partial}{\partial x} \left[\frac{\eta}{\mu_0 B} \frac{\partial(VB)}{\partial x} \right] \tag{19}$$

The equation of electrical resistivity is also very important for the case of magnetically driven quasi-isentropic compression. In order to simplify the problem, a simple model is considered.

$$\eta = \eta_0 (1 + \beta Q) \tag{20}$$

In equation (20), η_0 is the electrical resistivity of conductors at temperature of 0 °C, β is heating factor, Q is the heat capacity or increment of internal energy relative to that at temperature of 0 °C, which is related with temperature at the condensed states.

$$Q = c_v T \tag{21}$$

In equation (21), c_v is specific heat at constant volume, which is close to constant from 0 °C to the temperature of vaporization point.

For aluminum, β is $0.69 \times 10^{-9} \text{ m}^3/\text{J}$, η_0 is $2.55 \times 10^{-8} \text{ }\Omega\text{m}$. Before vaporization point, the equation (20) is suitable. After that, more complex electrical resistivity model is needed.

In this simulation, the stress wave front is defined when the amplitude of pressure reaches to 0.1 GPa, and the diffusion front of magnetic field is determined when the magnetic flux density is up to 0.2 T^[34].

Fig.18 gives the distribution of density and temperature of Aluminum sample along Lagrangian coordinates for different times in the condition of loading current density 1.5 MA/cm.

The results in Fig.18 show that the density and temperature of aluminum sample vary with the loading time along the direction of sample thickness because of the Joule heating and magnetic field diffusion.

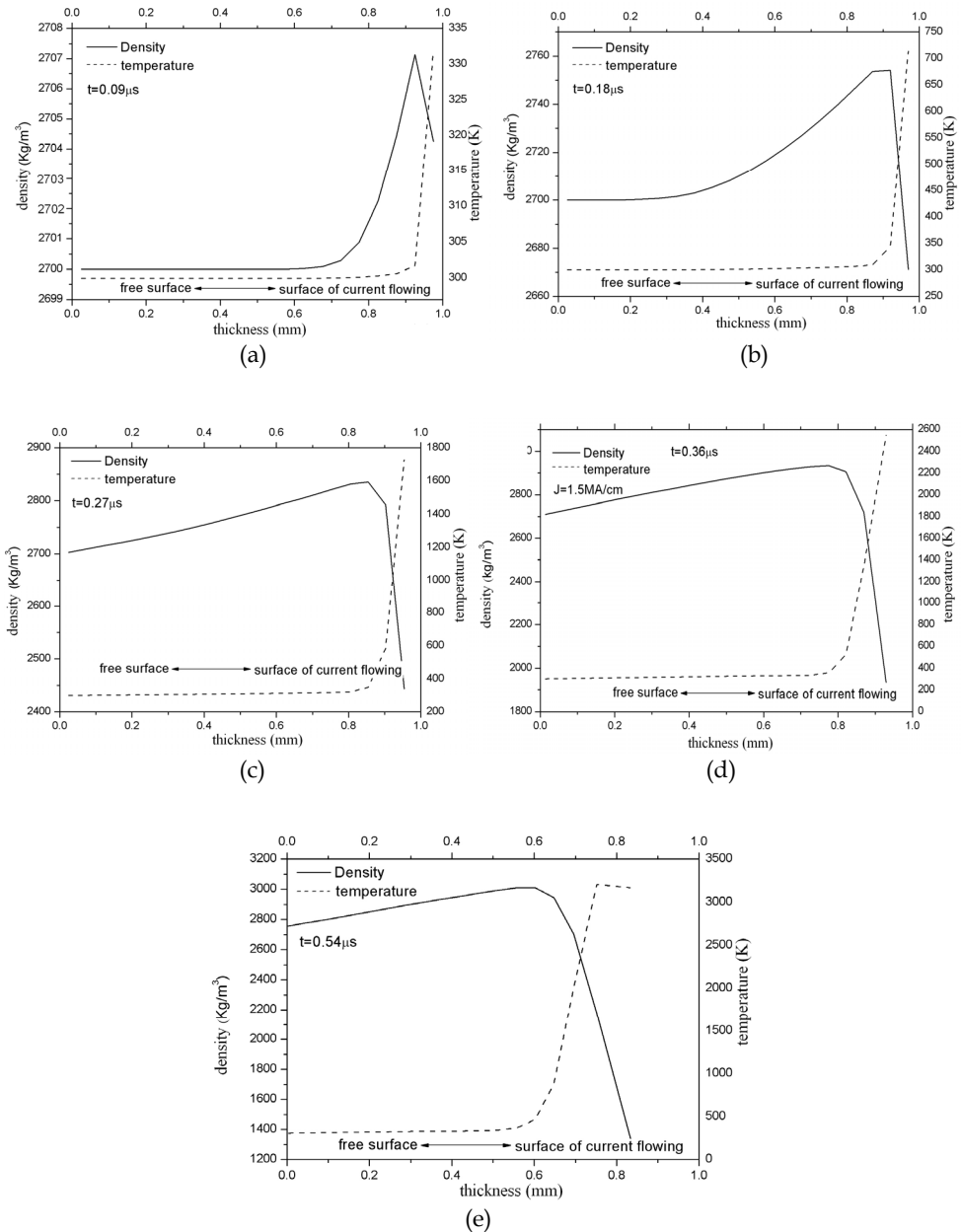


Fig. 18. Distribution of density and temperature of Aluminum sample along Lagrangian coordinates for different times under the condition of loading current density 1.5 MA/cm at time of 0.09 μs (a), 0.18 μs (b), 0.27 μs (c), 0.36 μs (d) and 0.54 μs (e)

Fig.19 gives the calculated results of distribution of magnetic induction strength along Lagrangian coordinates for different times in the condition of loading current density 1.5MA/cm.

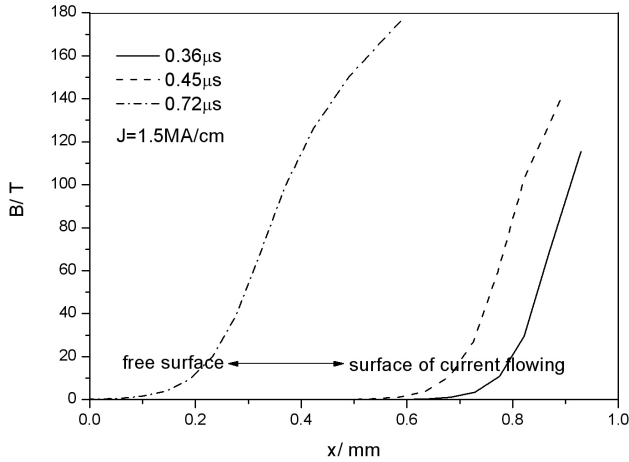


Fig. 19. Distribution of magnetic induction strength along Lagrangian coordinates for different times in the condition of loading current density 1.5MA/cm

And Fig.20 gives the physical characteristics of hydrodynamic stress wave front and magnetic diffusion front under the Lagrangian coordinates. The velocity of stress wave front is far more than that of the magnetic diffusion front, which is the prerequisite of magnetically driven quasi-isentropic compression. And the velocity of magnetic diffusion front increases gradually with the increasing of loading current density.

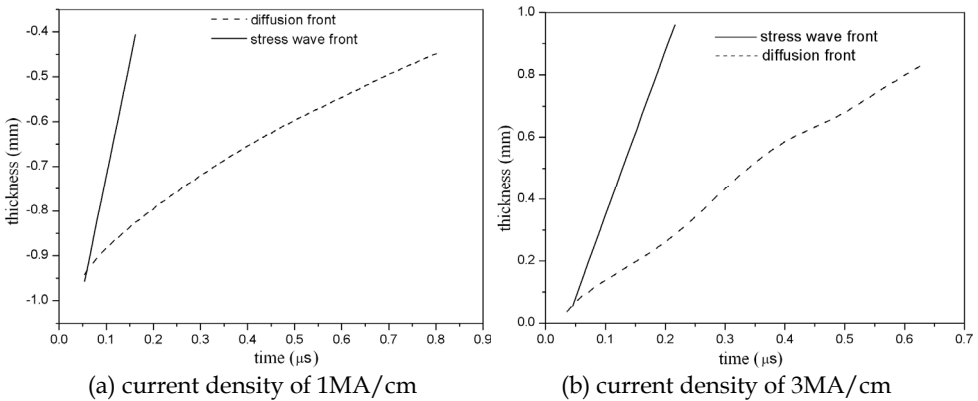


Fig. 20. Physical characteristics of hydrodynamic stress wave front and magnetic diffusion front under the Lagrangian coordinates

Fig.21 presents the relationships between the velocity of magnetic diffusion front and loading current density. The results show that an inflection point occurs at the loading current density of 1 MA/cm, and that the results can be expressed with two linear equations (22)

$$\begin{cases} D = 0.008 + 0.46J, & 1.0 < J \leq 3 \text{ MA/cm} \\ D = 0.36 + 0.06J, & 0.5 \leq J \leq 1.0 \text{ MA/cm} \end{cases} \quad (22)$$

In equation (22), D is the velocity of magnetic diffusion, and J is loading current density.

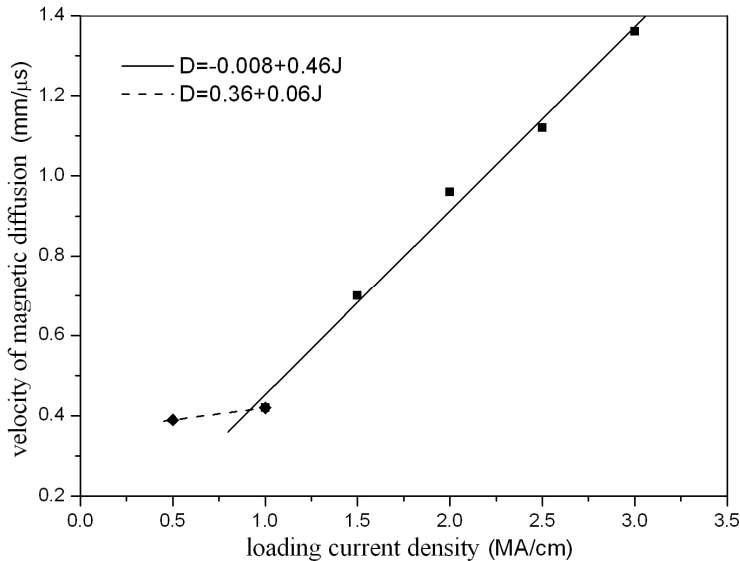


Fig. 21. The relationship of magnetic diffusion velocity varying with loading current densities.

Fig.22 is the case of copper samples under magnetically driven quasi-isentropic compression. The calculated results show that the particle velocity curves become steeper with the increasing of sample thickness, and that the shock is formed when the thickness is more than 2.5 mm for this simulating condition.

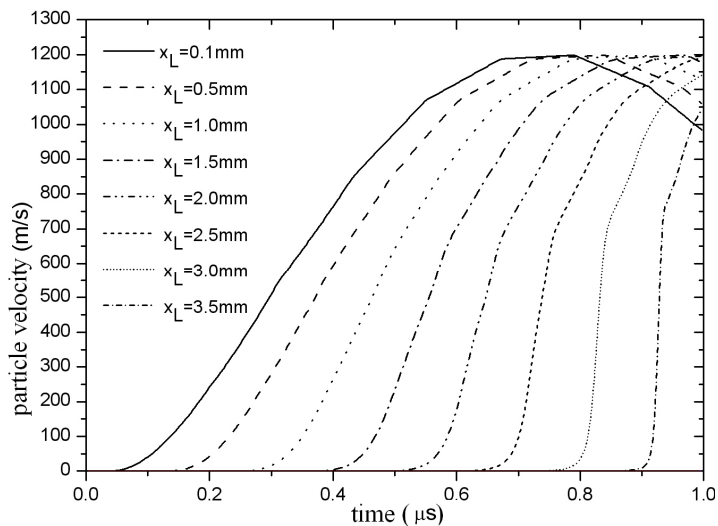


Fig. 22. The particle velocities of copper sample at different thickness in the condition of loading current density of 3 MA/cm.

5. Applications of metallic foil electrically exploding driving highvelocity flyers and magnetically driven quasi-isentropic compression

5.1 Metallic foil electrically exploding driving highvelocity flyers

5.1.1 Short-pulse shock initiation of explosive

The apparatus of metallic foil electrically exploding driving high velocity flyer offers an attractive means of performing shock initiation experiments. And the impact of an electrically exploding driven flyer produces a well-defined stimulus whose intensity and duration can be independently varied. Experiments are low-cost and there is fast turn-around between experiments.

Short-pulse shock initiation experiments will be very useful in developing more realistic theoretical shock initiation models. For the present, the models predicting shock initiation thresholds is short of, where very short pulses are employed. The technique can provide data to test the capability of improved models.

Based on our experimental apparatus, the shock initiation characteristics of TATB and TATB-based explosives are studied^[35,36]. Fig.23 and Fig.24 show the experimental results of shock initiation thresholds and run distance to detonation of a TATB-based explosive.

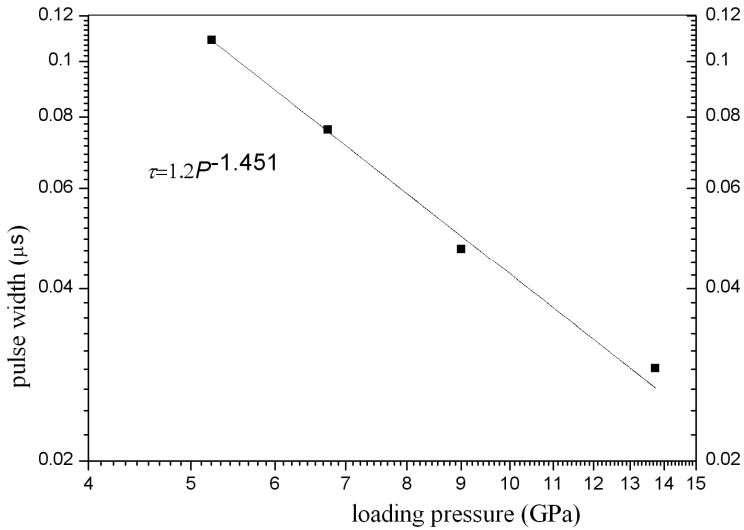


Fig. 23. Shock initiation threshold of 50% probability of initiation

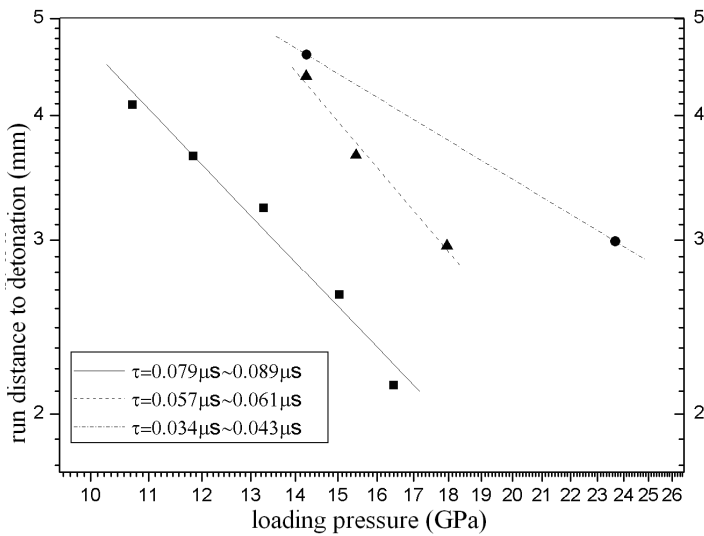


Fig. 24. Run distance to detonation in a TATB-based explosive

These experiments have the additional advantage of being applicable to relatively small explosive samples, an important consideration for evaluating and ranking new explosives.

5.1.2 Spallation experiments of materials

Compared with gas gun and explosively driven loading, The apparatus of metallic foil electrically exploding driving high velocity flyer is also a good tool used to research

dynamic behaviors of materials. The loading strain rates and stress duration vary easily. In order to study damage properties of materials using the apparatus of metallic foil electrically exploding driving high velocity flyer, a concept of two-stage flyer is put forward^[37]. The Mylar flyer flies some distance to impact a buffer plate such as PMMA or nylon with different thickness, and the pressure produced in the buffer is attenuated to the expected value, and then the attenuated pressure propels the impactor on the buffer to some velocity to impact the target. The impactor is the same material as the target. Fig.25 is the diagram of the two-stage flyer based on the apparatus of metallic foil electrically exploding driving high velocity flyer.

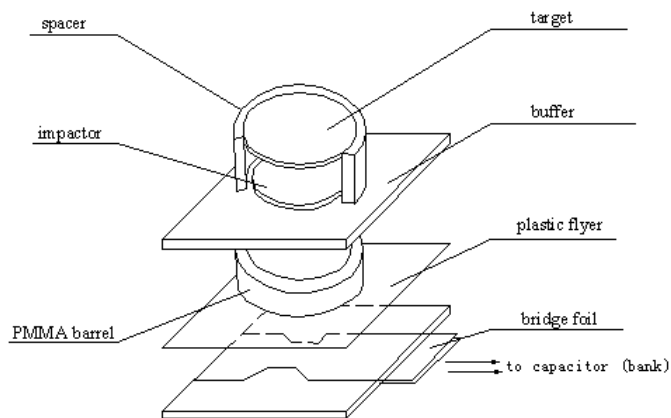


Fig. 25. Sketch of two-stage flyer based on the apparatus of metallic foil electrically exploding driving high velocity flyer

By means of the two-stage flyer, the spallations of steel and copper samples were researched. Fig.26 is the experimental results^[38].

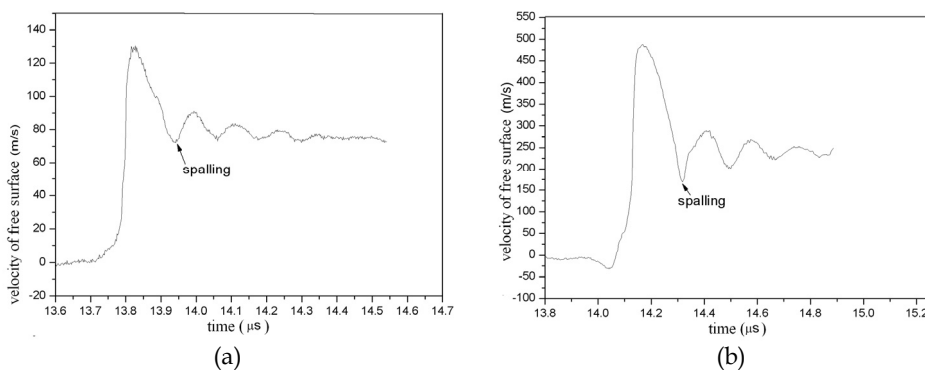


Fig. 26. Experimental results of spallation , steel target (a) and copper target (b).

It is also convenient to study other dynamic behaviors of materials using the electric gun. Further experimental researches about materials are being done by our research group.

5.1.3 Potential applications

Equation of state (EOS) measurement is an important potential application for our apparatus. In order to increase the loading pressure of this apparatus, two improvements should be done. Firstly, the flyer should be Mylar-metal foil laminate flyer. The metal layer increases the flyer's shock impedance and thus the pressure produced in the target. Secondly, the stored energy of apparatus should be increased. The expected pressure should be up to 200 GPa or more.

Impact experiment on the structure is also an important application for the apparatus of metallic foil electrically exploding driving high velocity flyer. For the apparatus of metallic foil electrically exploding driving high velocity flyer, its environment is well-controlled and instrumented, so it is suitable for studying impact phenomena in the fields of space science. Fig.27 shows a result of flyer of our apparatus impacting multi-layer structure.

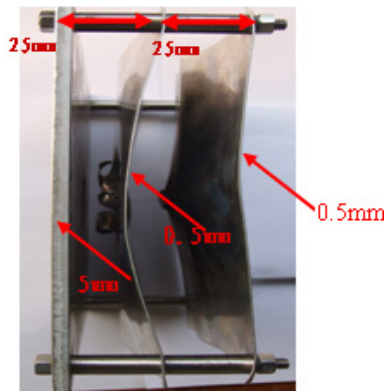


Fig. 27. Experimental result of flyer impact multi-layer structure

5.2 Magnetically driven quasi-isentropic compression

5.2.1 Compression isentropes of copper and aluminum

The experimental compression isentropes of T1 copper and L1 pure aluminum (Al content more than 99.7%) were measured on the CQ-1.5. The free-surface velocities were measured by DISAR, and the data were processed with the backward integration code developed by us. For the design of sample sizes, it is necessary that shock should not be formed in the samples and the side rarefaction wave should not affect the center regime to meet the requirements of one dimensional strain loading. Table 5 are the sizes of experimental samples.

Exp. Shot.	materials	thickness		width <i>w</i>
		<i>h</i> ₁	<i>h</i> ₂	
20070605	T1 copper	2.00 mm	1.58 mm	7 mm
20070608-1	T1 copper	2.08 mm	1.78 mm	5 mm
20070608-2	T1 copper	2.04 mm	1.52 mm	7 mm
20070705	L1 aluminum	2.60 mm	2.02 mm	5 mm

Table 5. Experimental conditions

Fig.28(a) are the typical free-surface velocity histories measured by DISAR, which show that the slope become steeper for thicker sample. The experimental compression isentropes, theoretical compression isentropes and shock Hugoniot data are presented in Fig.28(b) and Fig.28 (c).

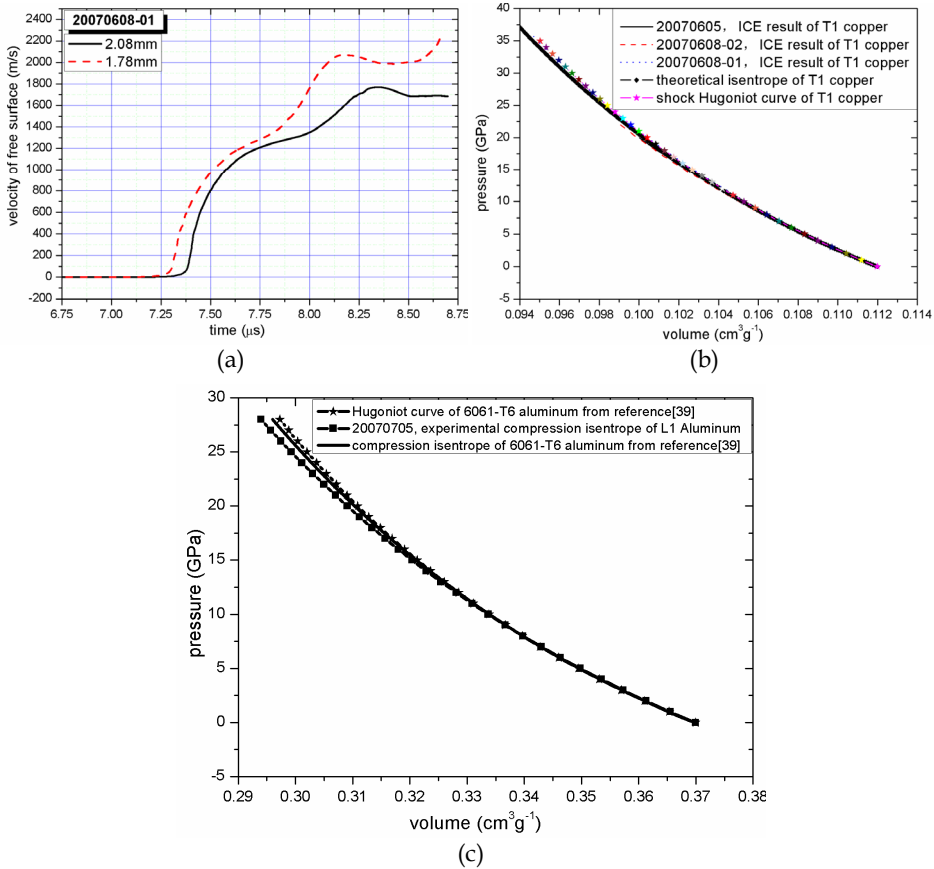


Fig. 28. Results of ICEs.(a) typical histories of free-surface velocity. (b) experimental, theoretical isentropes and Hugoniot data of T1 copper. (c) experimental isentrope of L1 pure aluminum, isentrope and Hugoniot data of 6061-T6 aluminum from reference [39].

The results show that the experimental compression isentropes are consistent with the theoretical ones within a deviation of 3%, and are close to the shock Hugoniot data under the pressure of 40GPa and lies under them. Different from the shock method, the whole isentrope can be obtained in one shot, and tens of shots are needed to gain one shock Hugoniot curve. The calculation results^[40] show that the compression isentropes gradually deviate from the shock Hugoniot with the increasement of loading pressure over 50 GPa. Therefore, the compression isentropes mainly reflect the off- Hugoniot properties of materials. Under 50 GPa, the compression isentropes are close to the shock Hugoniot, so we can use the isentrope data to check the validity or precision of shock Hugoniot.

5.2.2 Phase transition of 45 steel

Since the quasi-isentropic compression loading technique actually follows the P - v response of the material under investigation, the actual evolution of the phase transition can be observed. The classical polymorphic transition of iron at 13 GPa has been studied under quasi-isentropic compression. The two free-surface velocity profiles recorded in our experiments are shown in Fig.28. The elastic precursor wave is clearly seen in the lower pressure region of the two profiles. And the plastic wave and phase change wave occur, which show that the polymorphic transition ($\alpha \rightarrow \epsilon$) takes place. The velocity profiles in Fig.29 indicates that the onset of the phase transition is at velocity of 681 m/s, and the pressure of phase transition is also about 11.4 GPa.

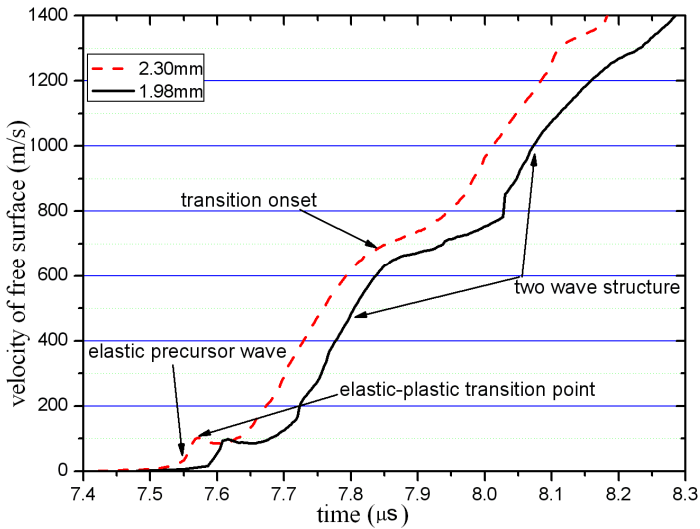


Fig. 29. Velocity profiles of 45 steel under quasi-isentropic compression

5.2.3 Spallation and elasto-plastic transition of pure tantalum

Fig.29 shows the results of the spalling experiments for pure tantalum (Ta contents 99.8%). The loading strain rate is 2.53×10^5 1/s. For the sample with thickness of 1.66 mm, the spallation is not obvious, perhaps the micro-damage occurs. For the sample with thickness of 1.06 mm, the spallation is obvious, and the pull-back velocity is 129.6 m/s. According to the formular (23), the spall strength is 4.49 GPa.

$$\sigma_{\text{spall}} = \frac{1}{2} \rho_0 C_1 \Delta U_{\text{pb}} \quad (23)$$

where ρ_0 is the initial density of sample, C_1 is the Larangian sound speed, ΔU_{pb} is the pull-back velocity as shown in Fig.4, and σ_{spall} is the spall strength of materials.

Under quasi-isentropic compression, the elasto-plastic transition are clearly shown in the velocity profiles of 45 steel and pure tantalum in Figure 28 and Fig.30. Here a concept of isentropic elastic limit (IEL, σ_{IEL}) is introduced. For the 45 steel sample, the σ_{IEL} is 2.26 GPa at the loading strain rate of 6.73×10^5 1/s, and for the pure tantalum sample, the σ_{IEL} is 2.42 GPa

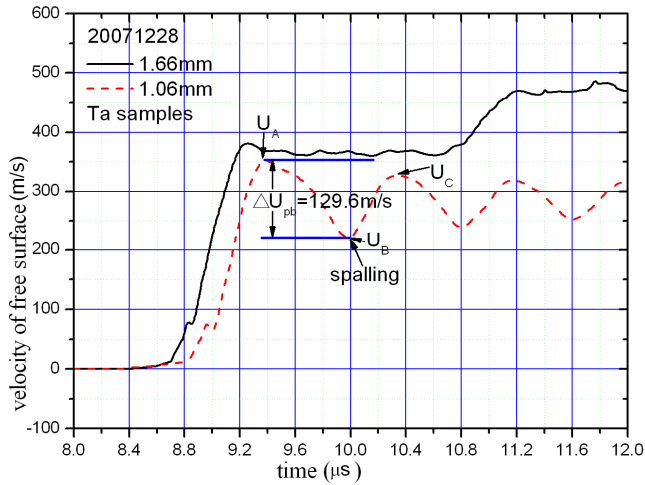


Fig. 30. Velocity profiles of Tantalum samples

at the loading strain rate of 2.53×10^5 1/s. Because of the difference of loading strain rates, the σ_{EL} ranges from 2.26 to 2.35 GPa for 45 steel, and from 2.42 to 2.70 GPa for pure tantalum in our experiments, correspondingly, the yield strength ranges from 1.29 to 1.34 GPa for 45 steel and from 1.12 to 1.25 GPa for pure tantalum.

5.2.4 Magnetically driven high-velocity flyers

It is an important application to launch high-velocity flyer plates using the techniques of magnetically driven quasi-isentropic compression. For the present, the researchers has launched the aluminum flyer plate with the size of 15 mm×11 mm×0.9 mm to the velocity of 43 km/s using this technique^[23], and can produce 1~2 TPa shock pressure on the heavy metallic or quartz samples. Based on CQ-1.5, the aluminum flyer plate with the size of 8 mm×6 mm×0.9 mm was launched to about 9 km/s by us. Figure 31 shows the experimental results of the velocities of the flyers.

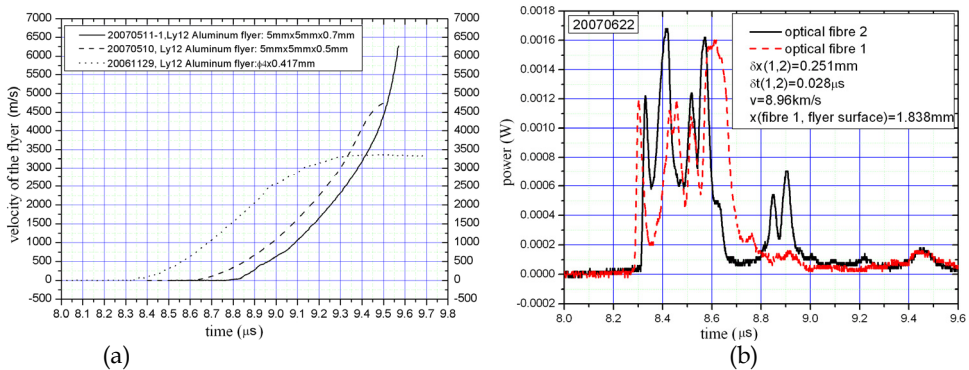


Fig. 31. The velocities of the aluminum flyer plates driven by magnetic pressure. The velocities measured by VISAR (a) and the averaged velocity measured by optical fibres pins (b)

6. Summary

The physical processes of electrical explosion of metallic foil and magnetically driven quasi-isentropic compression are very complex. This chapter discusses these problems simply from the aspect of one dimensionally magnetohydrodynamics. The key variable of electrical resistivity was simplified, which is very important. Especially for the problem of magnetically driven quasi-isentropic compression, only the resistivity is considered before the vaporization point of the matter. In fact, the phase states of the loading surface vary from solid to liquid, gas and plasma when the loading current density becomes more and more. In order to optimize the structural shapes of electrodes and the suitable sizes of samples and windows in the experiments of magnetically driven quasi-isentropic compression, two dimensionally magnetohydrodynamic simulations are necessary.

The applications of the techniques of electrical explosion of metallic foil and magnetically driven quasi-isentropic compression are various, and the word of versatile tools can be used to describe them. In this chapter, only some applications are presented. More applications are being done by us, such as the quasi-isentropic compression experiments of un-reacted solid explosives, the researches of hypervelocity impact phenomena and shock Hugoniot of materials at highly loading strain rates of $10^5 \sim 10^7$ 1/s.

7. Acknowledgements

The authors of this chapter would like to acknowledge Prof. Chengwei Sun and Dr. Fuli Tan, Ms. Jia He, Mr. Jianjun Mo and Mr. Gang Wu for the good work and assistance in our simulation and experimental work. We would also like to express our thanks to the referee for providing invaluable and useful suggestions. Of course, the work is supported National Natural Science Foundation of China under Contract NO. 10927201 and NO.11002130, and the Science Foundation of CAEP under Contract NO. 2010A0201006 and NO. 2011A0101001.

8. References

- [1] Keller D. V. and Penning R. J., Exploding foils—the production of plane shock waves and the acceleration of thin plates, *Exploding Wires*, W. G. Chase and H. K. Moore, Eds. Plenum Press, New York, Vol.2. 1962: 263
- [2] Guenther A. H., Wunsch D. C. and Soapes T. D., Acceleration of thin plates by exploding foil techniques, *Exploding Wires*, W. G. Chase and H. K. Moore, Eds. Plenum Press, New York, Vol.2. 1962: 279
- [3] Kotov Y A, Samatov O. M., Production of nanometer-sized AlN powders by the exploding wire method[J]. *Nanostructured Materials*, Vol.12(1-4),1999: 119
- [4] Suzuki T, Keawchai K, Jiang W H. Nanosize Al₂O₃ powder production by pulsed wire discharge[J]. *Jpn. J. Appl. Phys.*, Vol.40, 2001: 1073
- [5] Weingart R.C., *Electric gun: applications and potential*, UCRL-52000-80-2,1980
- [6] Steinberg D., Chau H., Dittbenner G. et al, The electric gun: a new method for generating shock pressure in excess of 1 TPa, UCI-17943, Sep. 1978
- [7] Weingart R.C., Chau H.H., Goosman D.R. et al, The electric gun: A new tool for ultrahigh-pressure research, UCRL-52752, April 1979
- [8] Sun Chengwei, Private Communications, 2004

- [9] Hawke R. S., Duerre D. E., Huebel J. G. et al, Electrical Properties of Al_2O_3 under Isentropic Compression up to 500Gpa(5Mbar)[J]. *J. Appl. Phys.*, Vol.49(6), June 1978: 3298~3303
- [10] Asay J. R., Isentropic Compression Experiments on the Z Accelerator. *Shock Compression of Condensed Matter-1999*, Edited by M. D. Furnish, L.C. Chhabildas and R. S. Hixson, 2000: 261~266
- [11] Avrillaud G., Courtois L., Guerre J. et al, GEPI: A Compact Pulsed Power Driver for Isentropic Compression Experiments and for Non Shocked High Velocity Flyer Plates. *14th IEEE Intl Pulsed Power Conf.*, 2003: 913~916
- [12] Rothman S. D., Parker K. W. et al, Isentropic compression of lead and lead alloy using the Z machine, *Shock Compression of Condensed Matter - 2003*, 1235-1238 · 2004
- [13] Wang Guji , Sun Chengwei, Tan Fuli et al, The compact capacitor bank CQ-1.5 employed in magnetically driven isentropic compression and high velocity flyer plate experiments, *REVIEW OF SCIENTIFIC INSTRUMENTS* 79, 053904 ,2008
- [14] Lemke R. W., Knudson M. D., Bliss D. E. et al, Magnetically accelerated, ultrahigh velocity flyer plates for shock wave experiments, *J. Appl. Phys.* 98, 2005:073530-1~9
- [15] Wang Guiji, Zhao Jianheng, Tang Xiaosong et al, Study on the technique of electric gun loading for one dimensionally planar strain, *Chinese Journal of High Pressure Physics*, Vol.19(3), 2005: 269-274
- [16] Brechov· Vladimir· Anatonievich, *Electrical explosion of conductors and its applications in electrically physical facilities(in Russian)*, 2000
- [17] Chau H.H., Dittbenner G., Hofer W.W. et al, Electric gun: a versatile tool for high-pressure shock wave research, *Rev. Sci. Instrum.* 51(12), Dec. 1980, P1676~1681
- [18] Tucker T.J. , Stanton P.L. , Electrical gurney energy: A new concept in modeling of energy transfer from electrically exploded conductors, SAND-75-0244, May 1975
- [19] Schmidt S.C., Seitz W.L., Wackerle Jerry, An empirical model to compute the velocity history of flyers driven by electrically exploding foils, LA-6809, July 1977
- [20] He Jia, Simulation on dynamic process of metallic foil electrical explosion driving multi-stage flyers, paper for Master degree, Institute of Fluid Physics, China Academy of Engineering Physics, Mianyang, Sichuan, China, 2007
- [21] Asay J.R. and Knudson M.D., Use of pulsed magnetic fields for quasi-isentropic compression experiments, *High-Pressure Shock Compression Solids VIII*, edited by L.C. Chhabildas, L. Davison and Y. Horie, Springer,2005:329
- [22] Davis J. P., Deeney C., Knudson M. D. et al, Magnetically driven isentropic compression to multimegabar pressures using shaped current pulses on the Z accelerator[J]. *Physics of Plasma*, 12, 2005:056310-1~056310-7
- [23] Savage Mark , The Z pulsed power driver since refurbishment, *The 13th International Conference on Megagauss Magnetic Field Generation and Related Topics*, July 2010.
- [24] Zhao Jianheng, Sun Chengwei, Tang Xiaosong et al, The Development of high performance electric gun facility, *Experimental Mechanics*, Vol.21(3), 2006
- [25] Wang Guiji, He Jia, Zhao Jianheng et al, The Techniques of Metallic Foil Electrically Exploding Driving Hypervelocity Flyer to more than 10km/s for Shock Wave Physics Experiments, submitted to *Rev. Scie. Instrum.*, 2011

- [26] Wang Guiji, Deng Xiangyang, Tan Fuli et al, Velocity measurement of the small size flyer of an exploding foil initiator, *Explosion and Shock Waves*, Vol.28(1),2008 : 28-32
- [27] Barker L.M. and Hollenback R.E., Laser interferometer for measuring high velocity of any reflecting surface. *J. Appl. Phys.*, Vol. 43(11),1972: 4669~4675
- [28] Weng Jidong , Tan Hua, Wang Xiang et al, Optical-fiber interferometer for velocity measurements with picosecond resolution, *Appl. Phys. Lett.* 89, 111101,2006
- [29] Ao T. , Asay J.R., Chantrenne S. et al., A compact strip-line pulsed power generator for isentropic compression experiments, *Rev. Scie. Instrum.*, 79(1), 013901, 2008
- [30] Furnish Michael D., Davis Jean-Paul, Knudson Marcus et al, Using the Saturn Accelerator for Isentropic Compression Experiments (ICE), SAND2001-3773, Sandia National Laboratories, 2001
- [31] Hayes D., Backward integration of the equations of motion to correct for free surface perturbation, SAND2001-1440, Sandia National Laboratories, 2001
- [32] Sun Chengwei, One dimensional shock and detonation wave computation code SSS, *Computation Physics*, No.3, 1986: 143-145
- [33] Burgess T.J., *Electrical resistivity model of metals*, 1986
- [34] Lemke R.W., Knudson M.D. et al., Characterization of magnetically accelerated flyer plates, *Phys. Plasmas* 10 (4), 1092-1099, 2003
- [35] Wang Guiji, Zhao Tonghu, Mo Jianjun et al., Short-duration pulse shock initiation characteristics of a TATB/HMX-based polymer bonded explosive, *Explosion and Shock Waves*, Vol.27(3), 2007:230-235
- [36] Wang Guiji, Zhao Tonghu, Mo Jianjun et al., Run distance to detonation in a TATB/HMX-based explosive, *Explosion and Shock Waves*, Vol.26(6), 2006:510-515
- [37] Sun Chengwei, Dynamic micro-fracture of metals under shock loading by electric gun, *J. Phys.*IV, Vol.4(8),1994:355-360
- [38] Xiong Xin, The spallation of ductile metals under loading of electric gun driven metallic flyer, paper for Master degree, Institute of Fluid Physics, China Academy of Engineering Physics, Mianyang, Sichuan, China, 2007
- [39] Hayes D. B., Hall C. A., Asay J. R. et al, Measurement of the Compression Isentrope for 6061-T6 Aluminum to 185 GPa and 46% Volumetric Strain Using Pulsed Magnetic Loading. *J. Appl. Phys.*, Vol.96(10),2004:5520~5527
- [40] Wang Ganghua, Experiments, simulation and data processing methods of magnetically driven isentropic compression and highvelocity flyer plates, paper for Ph.D degree, Institute of Fluid Physics, China Academy of Engineering Physics, Mianyang, Sichuan, China, 2008

Part 5

Special Topics on Simulations and Experimental Data

Hydrodynamics of a Droplet in Space

Hitoshi Miura

*Department of Earth Planetary Materials Science,
Graduate School of Science,
Tohoku University
Japan*

1. Introduction

1.1 Droplet in space

It is considered that our solar system 4.6 billion years ago was composed of a proto-sun and the circum-sun gas disk. In the gas disk, originally micron-sized fine dust particles accumulated by mutual collisions to be 1000 km-sized objects like as planets. Therefore, to understand the planet formation, we have to know the evolution of the dust particles in the early solar gas disk. One of the key materials is a millimeter-sized and spherical-shaped grain termed as "chondrule" observed in chondritic meteorites.

Chondrules are considered to have been formed from molten droplets about 4.6 billion years ago in the solar gas disk (Amelin et al., 2002; Amelin & Krot, 2007). Fig. 1 is a schematic of the formation process of chondrules. In the early solar gas disk, aggregation of the micron-sized dust particles took place before planet formation (Nakagawa et al., 1986). When the dust aggregates grew up to about 1 mm in size (precursor), some astrophysical process heated them to the melting point of about 1600 – 2100 K (Hewins & Radomsky, 1990). The molten dust aggregate became a sphere by the surface tension (droplet), and then cooled again to solidify in a short period of time (chondrule). The formation conditions of chondrules, such as heating duration, maximum temperature, cooling rate, and so forth, have been investigated experimentally by many authors (Blander et al., 1976; Fredriksson & Ringwood, 1963; Harold C. Connolly & Hewins, 1995; Jones & Lofgren, 1993; Lofgren & Russell, 1986; Nagashima et al., 2006; Nelson et al., 1972; Radomsky & Hewins, 1990; Srivastava et al., 2010; Tsuchiyama & Nagahara, 1981-12; Tsuchiyama et al., 1980; 2004; Tsukamoto et al., 1999). However, it has been controversial what kind of astronomical event could have produced chondrules in early solar system. The chondrule formation is one of the most serious unsolved problems in planetary science.

The most plausible model for chondrule formation is a shock-wave heating model, which has been tested by many theoreticians (Ciesla & Hood, 2002; Ciesla et al., 2004; Desch & Jr., 2002; Hood, 1998; Hood & Horanyi, 1991; 1993; Iida et al., 2001; Miura & Nakamoto, 2006; Miura et al., 2002; Morris & Desch, 2010; Morris et al., 2009; Ruzmaikina & Ip, 1994; Wood, 1984). Fig. 2 is a schematic of dust heating mechanism by the shock-wave heating model. Initially, the chondrule precursors were floating in the gas disk without any large relative velocity against the ambient gas (panel (a)). When a shock wave was generated in the gas disk, the gas behind the shock front was accelerated suddenly. On the other hand, the chondrule

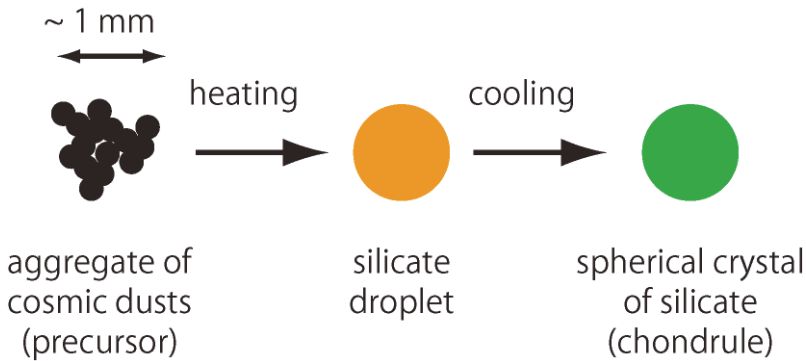


Fig. 1. Schematic of formation process of a chondrule. The precursor of chondrule is an aggregate of μm -sized cosmic dusts. The precursor is heated and melted by some mechanism, becomes a sphere by the surface tension, then cools to solidify in a short period of time.

precursors remain un-accelerated because of their inertia. Therefore, after passage of the shock front, the large relative velocity arises between the gas and dust particles (panel (b)). The relative velocity can be considered as fast as about 10 km s^{-1} (Iida et al., 2001). When the gas molecule collides to the surface of chondrule precursors with such large velocity, its kinetic energy thermalizes at the surface and heats the chondrule precursors, as termed as a gas drag heating. The peak temperature of the precursor is determined by the balance between the gas drag heating and the radiative cooling at the precursor surface (Iida et al., 2001). The gas drag heating is capable to heat the chondrule precursors up to the melting point if we consider a standard model of the early solar gas disk (Iida et al., 2001).

1.2 Physical properties of chondrules

The chondrule formation models, including the shock-wave heating model, are required not only to heat the chondrule precursors up to the melting point but also to reproduce other physical and chemical properties of chondrules recognized by observations and experiments. These properties that should be reproduced are summarized as observational constraints (Jones et al., 2000). The reference listed 14 constraints for chondrule formation. To date, there is no chondrule formation model that can account for all of these constraints.

Here, we review two physical properties of chondrules; size distribution and three-dimensional shape. The latter was not listed as the observational constraints in the literature (Jones et al., 2000), however, we would like to include it as an important constraint for chondrule formation. As discussed in this chapter, these two properties strongly relate to the hydrodynamics of molten chondrule precursors in the gas flow behind the shock front.

1.2.1 Size distribution

Fig. 3 shows the size distribution of chondrules compiled from measurement data in some literatures (Nelson & Rubin, 2002; Rubin, 1989; Rubin & Grossman, 1987; Rubin & Keil, 1984). The horizontal axis is the diameter D and the vertical axis is the cumulative fraction of

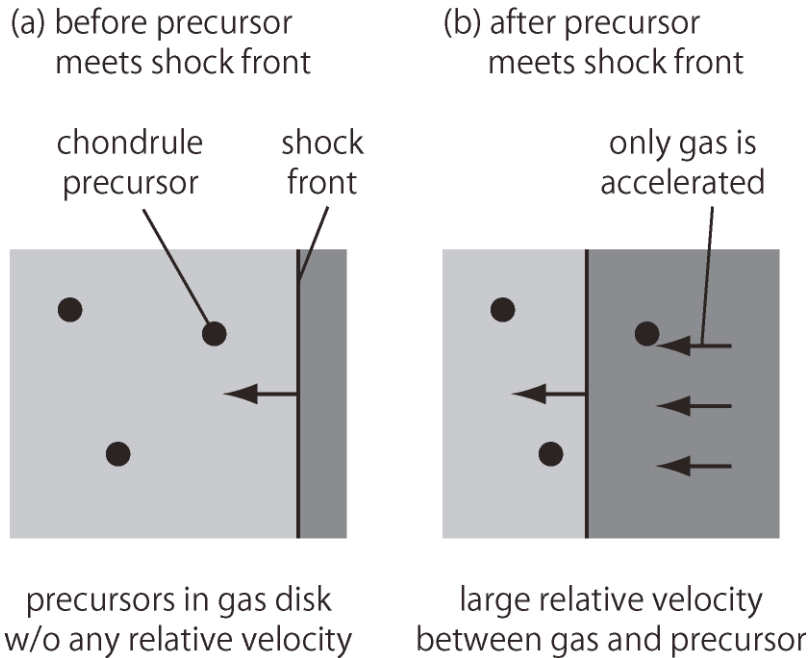


Fig. 2. Schematic of the shock-wave heating model for chondrule formation. (a) The precursors of chondrules are in a gas disk around the proto-sun 4.6 billion years ago. The gas and precursors rotate around the proto-sun with almost the same angular velocity, so there is almost no relative velocity between the gas and precursors. (b) If a shock wave is generated in the gas disk by some mechanism, the gas behind the shock front is suddenly accelerated. In contrast, the precursor is not accelerated because of its large inertia. The difference of their behaviors against the shock front causes a large relative velocity between them. The precursors are heated by the gas friction in the high velocity gas flow.

chondrules smaller than D in diameter. Table 1 shows the mean diameter and the standard deviation of each measurement. It is found that the chondrule sizes vary according to chondrite type. The mean diameters of chondrules in ordinary chondrites (LL3 and L3) are from $600\ \mu\text{m}$ to $1000\ \mu\text{m}$. In contrast, ones in enstatite chondrite (EH3) and carbonaceous chondrite (CO3) are from $100\ \mu\text{m}$ to $200\ \mu\text{m}$.

It should be noted that the true chondrule diameters are slightly larger than the data shown in Fig. 3 and Table 1 because of the following reason. This data was obtained by observations on thin-sections of chondritic meteorites. The chondrule diameter on the thin-section is not necessarily the same as the true one because the thin-section does not always intersect the center of the chondrule. Statistically, the mean and median diameters measured on the thin section are, respectively, $\sqrt{2}/3$ and $\sqrt{3}/4$ of the true diameters (Hughes, 1978). However, we do not take care the difference between true and measured diameters because it is not a substantial issue in this chapter.

It is considered that in the early solar gas disk the dust aggregates have the size distribution from $\approx\ \mu\text{m}$ (initial fine dust particles) to a few 1000 km (planets). In spite of the wide

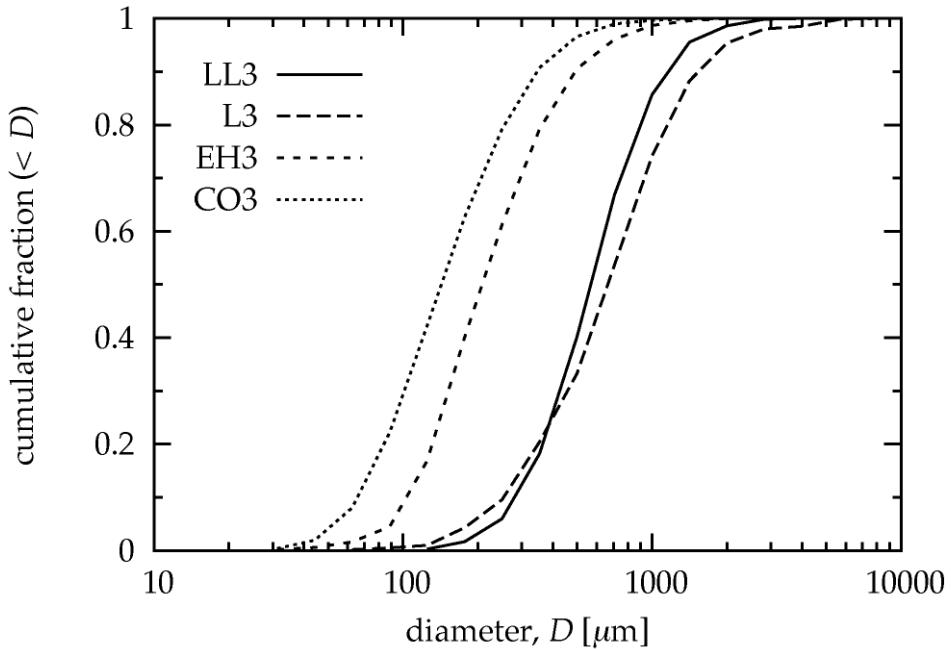


Fig. 3. Size distributions of natural chondrules in various types of chondritic meteorites (LL3, L3, EH3, and CO3). The vertical axis is the normalized cumulative number of chondrules whose diameters are smaller than that of the horizontal axis. Each data was compiled from the following literatures; LL3 chondrites (Nelson & Rubin, 2002), L3 chondrites (Rubin & Keil, 1984), EH3 chondrites (Rubin & Grossman, 1987), and CO3 chondrites (Rubin, 1989), respectively. The total number of chondrules measured in each literature is 719 for LL3, 607 for L3, 689 for EH3, and 2834 for CO3, respectively.

size range of solid materials, sizes of chondrules distribute in a very narrow range of about 100 – 1000 μm . Two possibilities for the origin of chondrule size distribution can be considered; (i) size-sorting prior to chondrule formation, and (ii) size selection during chondrule formation. In the case of (i), we need some mechanism of size-sorting in the early solar gas disk (Teitler et al., 2010, and references therein). In the case of (ii), the chondrule formation model must account for the chondrule size distribution. The latter possibility is what we investigate in this chapter.

1.2.2 Deformation from a perfect sphere

It is considered that spherical chondrule shapes were due to the surface tension when they melted. However, their shapes deviate from a perfect sphere and the deviation is an important clue to identify the formation mechanism. Tsuchiyama et al. (Tsuchiyama et al., 2003) measured the three-dimensional shapes of chondrules using X-ray microtomography. They selected 20 chondrules with perfect shapes and smooth surfaces from 47 ones for further analysis. Their external shapes were approximated as three-axial ellipsoids with axial radii of a , b , and c ($a \geq b \geq c$), respectively. Fig. 4 shows results of the measurement. The horizontal

chondrite type	meteorite type	chondrule number type*	diam. D [μm]	ref.
L3	Inman	BO	173	1038 ± 937 (Rubin & Keil, 1984)
L3	Inman	RP+C	201	852 ± 598 (Rubin & Keil, 1984)
L3	ALHA77011	BO	163	680 ± 625 (Rubin & Keil, 1984)
L3	ALHA77011	RP+C	70	622 ± 453 (Rubin & Keil, 1984)
LL3	total of 5 types	all	719	574^{+405}_{-237} (Nelson & Rubin, 2002)
EH3	total of 3 types	all	689	219^{+189}_{-101} (Rubin & Grossman, 1987)
CO3	total of 11 types	all	2834	148^{+132}_{-70} (Rubin, 1989)

Table 1. Diameters of chondrules from various types of chondritic meteorites and the standard deviations. *BO = barred olivine, RP = radial pyroxene, C = cryptocrystalline. all = all types are included.

and vertical axes are axial ratios of b/a and c/b , respectively. A point $(b/a, c/b) = (1, 1)$ means a perfect sphere because all of three axes have the same length. As going downward from the point, the shape becomes oblate (disk-like shape) because $a = b > c$. On the other hand, the shape becomes prolate (rugby-ball-like shape) as going leftward because $a > b = c$. The chondrule shapes in the measurement are classified into two groups: spherical chondrules in group-A and prolate chondrules in group-B. Chondrules in group-A have axial ratios of $c/b > \sim 0.9$ and $b/a > \sim 0.9$. In contrast, chondrules in group-B have smaller values of b/a as $\approx 0.7 - 0.8$.

It is considered that the deviation from a perfect sphere results from the deformation of a molten chondrule before solidification. For example, if the molten chondrule rotates rapidly, the shape becomes oblate due to the centrifugal force (Chandrasekhar, 1965). However, the shapes of chondrules in group-B are prolate rather than oblate. Tsuchiyama et al. (Tsuchiyama et al., 2003) proposed that the prolate chondrules in group-B can be explained by spitted droplets due to the shape instability with high-speed rotation. However, it is not clear whether the transient process such as the shape instability accounts for the range of axial ratio of group-B chondrules or not.

1.3 Hydrodynamics of molten chondrule precursors

If chondrules were melted behind the shock front, the molten droplet ought to be exposed to the high-velocity gas flow. The gas flow causes many hydrodynamics phenomena on the molten chondrule droplet as follows. (i) Deformation: the ram pressure deforms the droplet shape from a sphere. (ii) Internal flow: the shearing stress at the droplet surface causes fluid flow inside the droplet. (iii) Fragmentation: a strong gas flow will break the droplet into many tiny fragments. Hydrodynamics of the droplet in high-velocity gas flow strongly relates to the physical properties of chondrules. However, these hydrodynamics behaviors have not been investigated in the framework of the chondrule formation except of a few examples that neglected non-linear effects of hydrodynamics (Kato et al., 2006; Sekiya et al., 2003; Uesugi et al., 2005; 2003).

To investigate the hydrodynamics of a molten chondrule droplet in the high-velocity gas flow, we performed computational fluid dynamics (CFD) simulations based on cubic-interpolated propagation/constrained interpolation profile (CIP) method. The CIP method is one of the high-accurate numerical methods for solving the advection equation (Yabe & Aoki, 1991;

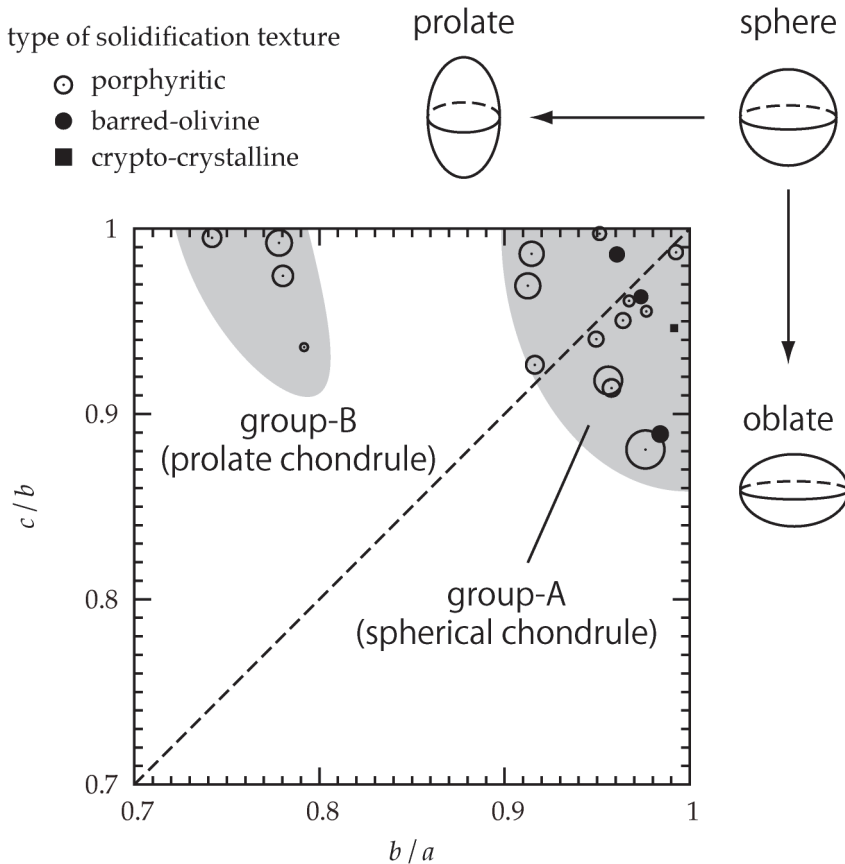


Fig. 4. Three-dimensional shapes of chondrules (Tsuchiyama et al., 2003, and their unpublished data). a , b , and c are axial radii of chondrules when their shapes are approximated as three-axial ellipsoids ($a \geq b \geq c$), respectively. The textures of these chondrules are 16 porphyritic (open circle), 3 barred-olivine (filled circle), and 1 crypto-crystalline (filled square). The radius of each symbol is proportional to the effective radius of each chondrule $r_* \equiv (abc)^{1/3}$; the largest circle corresponds to $r_* = 1129 \text{ }\mu\text{m}$. For the data of crypto-crystalline, $r_* = 231 \text{ }\mu\text{m}$. Chondrule shapes are classified into two groups: group-A shows the relatively small deformation from the perfect sphere, and group-B is prolate with axial ratio of $b/a \approx 0.7 - 0.8$.

Yabe et al., 2001). It can treat both compressible and incompressible fluids with large density ratios simultaneously in one program (Yabe & Wang, 1991). The latter advantage is important for our purpose because the droplet density ($\approx 3 \text{ g cm}^{-3}$) differs from that of the gas disk ($\approx 10^{-8} \text{ g cm}^{-3}$ or smaller) by many orders of magnitude.

In addition, we should pay a special attention how to model the ram pressure of the gas flow. The gas around the droplet is so rarefied that the mean free path of the gas molecules is an order of about 100 cm if we consider a standard gas disk model. The mean free path is much larger than the typical size of chondrules. This means that the gas flow around the droplet is a free molecular flow, so it does not follow the hydrodynamical equations. Therefore, in our model, the ram pressure acting on the droplet surface per unit area is explicitly given in the equation of motion for the droplet by adopting the momentum flux method as described in section 3.2.2.

1.4 Aim of this chapter

The hydrodynamical behaviors of molten chondrules in a high-velocity gas flow are important to elucidate the origin of physical properties of chondrules. However, it is difficult for experimental studies to simulate the high-velocity gas flow in the early solar gas disk, where the gas density is so rarefied that the gas flow around droplets does not follow the hydrodynamics equations. We developed the numerical code to simulate the droplet in a high-velocity rarefied gas flow. In this chapter, we describe the details of our hydrodynamics code and the results. We propose new possibilities for the origins of size distribution and three-dimensional shapes of chondrules based on the hydrodynamics simulations.

We describe the governing equations in section 2 and the numerical procedures in section 3. In section 4, we describe the results of the hydrodynamics simulations regarding the deformation of molten chondrules in the high-velocity rarefied gas flow and discuss the origin of rugby-ball-like shaped chondrules. In section 5, we describe the results regarding the fragmentation of molten chondrules and consider the relation to the size distribution of chondrules. We conclude our hydrodynamics simulations in section 6.

2. Governing equations

The governing equations are the equation of continuity and the Navier-Stokes equation as follows;

$$\frac{\partial \rho}{\partial t} + \vec{\nabla} \cdot (\rho \vec{u}) = 0, \quad (1)$$

$$\frac{\partial \vec{u}}{\partial t} + (\vec{u} \cdot \vec{\nabla}) \vec{u} = \frac{-\vec{\nabla} p + \mu \nabla^2 \vec{u} + \vec{F}_s + \vec{F}_g}{\rho} + \vec{g}, \quad (2)$$

where ρ is the density of fluid, \vec{u} is the velocity, p is the pressure, and μ is the viscosity. The ram pressure of the high-velocity gas flow, \vec{F}_g , is exerted on the surface of the droplet and given by (Sekiya et al., 2003)

$$\vec{F}_g = -p_{\text{fm}} (\vec{n}_i \cdot \vec{n}_g) \vec{n}_g \delta(\vec{r} - \vec{r}_i) \quad \text{for } \vec{n}_i \cdot \vec{n}_g \leq 0, \quad (3)$$

where \vec{n}_i is the unit normal vector of the surface of the droplet, \vec{n}_g is the unit vector pointing the direction in which the gas flows, and \vec{r}_i is the position of the liquid-gas interface. The delta function $\delta(\vec{r} - \vec{r}_i)$ means that the ram pressure works only at the interface. The ram

pressure does not work for $\vec{n}_i \cdot \vec{n}_g > 0$ because it indicates the opposite surface which does not face the molecular flow. The ram pressure causes the deceleration of the center of mass of the droplet. In our coordinate system co-moving with the center of mass, the apparent gravitational acceleration \vec{g} should appear in the equation of motion. The surface tension, \vec{F}_s , is given by (Brackbill et al., 1992)

$$\vec{F}_s = -\gamma_s \kappa \vec{n}_i \delta(\vec{r} - \vec{r}_i), \quad (4)$$

where γ_s is the fluid surface tension and κ is the local surface curvature. Finally, we consider the equation of state given by

$$\frac{dp}{d\rho} = c_s^2, \quad (5)$$

where c_s is the sound speed.

3. Numerical methods in hydrodynamics

To solve the equation of continuity (Eq. (1)) numerically, we introduce a color function ϕ that changes from 0 to 1 continuously. For incompressible two fluids, a density in each fluid is uniform and has a sharp discontinuity at the interface between these two fluids if the density of a fluid is different from another one. By using the color function, we can distinguish these two fluids as follows; $\phi = 1$ for fluid 1, $\phi = 0$ for fluid 2, and a region where $0 < \phi < 1$ for the interface. The density of a fluid element is given by

$$\rho = \phi \rho_1 + (1 - \phi) \rho_2, \quad (6)$$

where ρ_1 and ρ_2 are the inherent densities for fluid 1 and fluid 2, respectively. The governing equation for ϕ is given by

$$\frac{\partial \phi}{\partial t} + \vec{\nabla} \cdot (\phi \vec{u}) = 0. \quad (7)$$

The conservation equation for ϕ (Eq. (7)) is approximately equivalent to the original one (Eq. (1)) through the relationship between ρ and ϕ given by Eq. (6) (Miura & Nakamoto, 2007). Therefore, the problem to solve Eq. (1) results in to solve Eq. (7). We solve Eq. (7) using R-CIP-CSL2 method with anti-diffusion technique (sections 3.1.2 and 3.1.3).

In this study, the fluid 1 is the molten chondrule and the fluid 2 is the disk gas around the chondrule. The inherent densities are given by $\rho_1 = \rho_d$ and $\rho_2 = \rho_a$, where subscripts "d" and "a" mean the droplet and ambient gas, respectively. The other physical values of the fluid element (viscosity μ and sound speed c_s) are given in the same manner as the density ρ , namely, $\mu = \phi \mu_d + (1 - \phi) \mu_a$ and $c_s = \phi c_{s,d} + (1 - \phi) c_{s,a}$, respectively.

The Navier-Stokes equation (Eq. (2)) and the equation of state (Eq. (5)) are separated into two phases; the advection phase and the non-advection phase. The advection phases are written as

$$\begin{aligned} \frac{\partial \vec{u}}{\partial t} + (\vec{u} \cdot \vec{\nabla}) \vec{u} &= 0, \\ \frac{\partial p}{\partial t} + (\vec{u} \cdot \vec{\nabla}) p &= 0. \end{aligned} \quad (8)$$

Parameter	Sign	Value
Momentum of gas flow	p_{fm}	4000 dyn cm^{-2}
Surface tension	γ_s	400 dyn cm^{-1}
Viscosity of droplet	μ_d	$1.3 \text{ g cm}^{-1} \text{ s}^{-1}$
Density of droplet	ρ_d	3 g cm^{-3}
Sound speed of droplet	$c_{s,d}$	$2 \times 10^5 \text{ cm s}^{-1}$
Density of ambient	ρ_a	$10^{-6} \text{ g cm}^{-3}$
Sound speed of ambient	$c_{s,a}$	$10^{-5} \text{ cm s}^{-1}$
Viscosity of ambient	μ_a	$10^{-2} \text{ g cm}^{-1} \text{ s}^{-1}$
Droplet radius	r_0	$500 \mu\text{m}$

Table 2. Canonical input physical parameters for simulations of molten chondrules exposed to the high-velocity rarefied gas flow. We ought to use these parameters if there is no special description.

We solve above equations using the R-CIP method, which is the oscillation preventing method for advection equation (section 3.1.1). The non-advection phases can be written as

$$\begin{aligned}\frac{\partial \vec{u}}{\partial t} &= -\frac{\vec{\nabla} p}{\rho} + \frac{\vec{Q}}{\rho}, \\ \frac{\partial p}{\partial t} &= -\rho c_s^2 \vec{\nabla} \cdot \vec{u},\end{aligned}\quad (9)$$

where \vec{Q} is the summation of forces except for the pressure gradient. The problem intrinsic in incompressible fluid is in the high sound speed in the pressure equation. Yabe and Wang (Yabe & Wang, 1991) introduced an excellent approach to avoid the problem (section 3.2.1). It is called as the C-CUP method (Yabe & Wang, 1991). The numerical methods to calculate ram pressure of the gas flow and the surface tension of droplet in \vec{Q} are described in sections 3.2.2 and 3.2.3, respectively.

The input parameters adopted in this chapter are listed in Table 2.

3.1 Advection phase

3.1.1 CIP method

The CIP method is one of the high-accurate numerical methods for solving the advection equation (Yabe & Aoki, 1991; Yabe et al., 2001). In one-dimension, the advection equation is written as

$$\frac{\partial f}{\partial t} + u \frac{\partial f}{\partial x} = 0, \quad (10)$$

where f is a scalar variable of the fluid (e.g., density), u is the fluid velocity in the x -direction, and t is the time. When the velocity u is constant, the exact solution of Eq. (10) is given by

$$f(x; t) = f(x - ut; 0), \quad \text{when } u \text{ is constant}, \quad (11)$$

which indicates a simple translational motion of the spatial profile of f with the constant velocity u .

Let us consider that the values of f on the computational grid points x_{i-1} , x_i , and x_{i+1} are given at the time step n and denoted by f_{i-1}^n , f_i^n , and f_{i+1}^n , respectively. In Fig. 5, f^n are shown

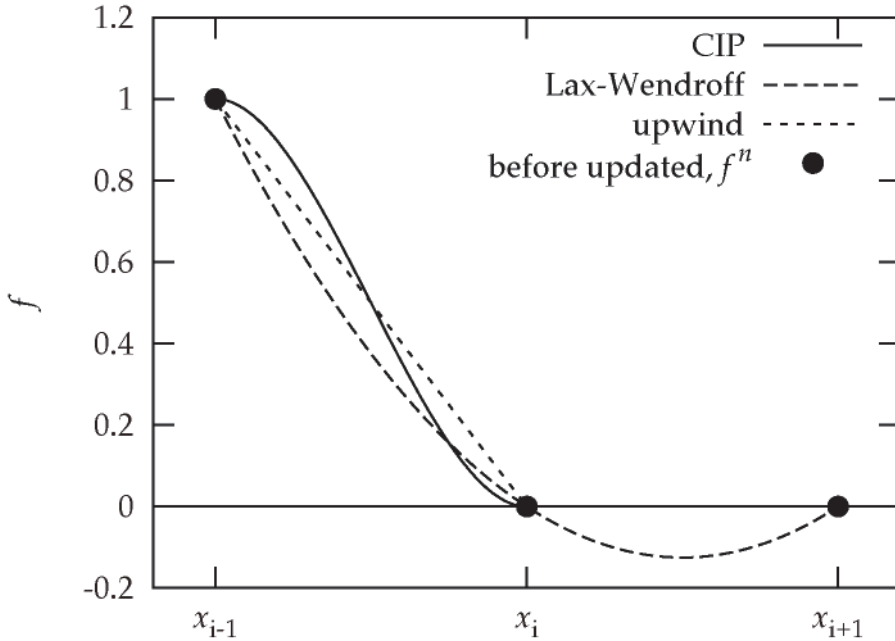


Fig. 5. Interpolate functions with various methods: CIP (solid), Lax-Wendroff (dashed), and first-order upwind (dotted). The filled circles indicate the values of f defined on the digitized grid points x_{i-1} , x_i , and x_{i+1} before updated.

by filled circles. From Eq. (11), we can obtain the values of f_i at the next time step $n + 1$ by just obtaining f_i^n at the upstream point $x = x_i - u\Delta t$, where Δt is the time interval between t^n and t^{n+1} . If the upstream point is not exactly on the grid points, which is a very usual case, we have to interpolate f_i^n with an appropriate mathematical function composed of f_{i-1}^n , f_i^n , and so forth. There are some variations of the numerical solvers by the difference of the interpolate function $F_i(x)$. One of them is the first-order upwind method, which interpolates f_i^n by a linear function and satisfies following two constraints; $F_i(x_{i-1}) = f_{i-1}^n$ and $F_i(x_i) = f_i^n$ (here we assume that $u > 0$ and the upstream point for f_i^n locates left-side of x_i). The other variation is the Lax-Wendroff method, which uses a quadratic polynomial satisfying three constraints; $F_i(x_{i-1}) = f_{i-1}^n$, $F_i(x_i) = f_i^n$, and $F_i(x_{i+1}) = f_{i+1}^n$. We show these interpolation functions in Fig. 5.

On the contrary, the CIP method interpolates using a cubic polynomial, which satisfies following four constraints; $F_i(x_{i-1}) = f_{i-1}^n$, $F_i(x_i) = f_i^n$, $\partial F_i/\partial x(x_{i-1}) = f_{x,i-1}^n$, and $\partial F_i/\partial x(x_i) = f_{x,i}^n$, where $f_x \equiv \partial f/\partial x$ is the spatial gradient of f . The interpolation function is given by

$$F_i(x) = a_i(x - x_i)^3 + b_i(x - x_i)^2 + c_i(x - x_i) + d_i, \tag{12}$$

where a_i , b_i , c_i , and d_i are the coefficients determined from f_{i-1}^n , f_i^n , $f_{x,i-1}^n$, and $f_{x,i}^n$. The expressions of these coefficients are shown in (Yabe & Aoki, 1991). We show the profile of $F_i(x)$ in Fig. 5 with $f_{x,i-1}^n = f_{x,i}^n = 0$. In the CIP method, therefore, we need the values of f_x^n in addition of f^n for solving the advection phase.

In the CIP method, f_x is treated as an independent variable and updated independently from f as follows. Differentiating Eq. (10) with respect to x , we obtain

$$\frac{\partial f_x}{\partial t} + u \frac{\partial f_x}{\partial x} = -f_x \frac{\partial u}{\partial x}, \quad (13)$$

where the second term of the left-hand side indicates the advection term and the right-hand side indicates the non-advection term. The interpolate function for the advection of f_x is given by $\partial F_i / \partial x$. The non-advection term can be solved analytically by considering that $\partial u / \partial x$ is constant.

Additionally, there is an oscillation preventing method in the concept of the CIP method, in which the rational function is used as the interpolate function. The rational function is written as (Xiao et al., 1996)

$$F_i(x) = \frac{a_i(x - x_i)^3 + b_i(x - x_i)^2 + c_i(x - x_i) + d_i}{1 + \alpha_i \beta_i (x - x_i)}, \quad (14)$$

where α_i and β_i are coefficients. The expressions of these coefficients are shown in (Xiao et al., 1996). Usually, we adopt $\alpha_i = 1$ to prevent oscillation. This method is called as the R-CIP method. The model with $\alpha_i = 0$ corresponds to the normal CIP method.

3.1.2 CIP-CSL2 method

The CIP-CSL2 method is one of the numerical methods for solving the conservative equation. In one-dimension, the conservative equation is written as

$$\frac{\partial f}{\partial t} + \frac{\partial (uf)}{\partial x} = 0. \quad (15)$$

Integrating Eq. (15) over x from x_i to x_{i+1} , we obtain

$$\frac{\sigma_{i+1/2}}{\partial t} + [uf]_{x_i}^{x_{i+1}} = 0, \quad (16)$$

where $\sigma_{i+1/2} \equiv \int_{x_i}^{x_{i+1}} f dx$. For f being density, $\sigma_{i+1/2}$ corresponds to the mass contained in a computational cell between i and $i + 1$, so it should be conserved during the time integration. Since the physical meaning of uf in the second term of the left-hand side is the flux of σ per unit area and per unit time, the time evolution of σ is determined by

$$\sigma_{i+1/2}^{n+1} = \sigma_{i+1/2}^n - J_{i+1} + J_i, \quad (17)$$

where $J_i \equiv \int_{t^n}^{t^{n+1}} u f dt$ is the transported value of σ from a region of $x < x_i$ to that of $x > x_i$ within Δt . The CIP-CSL2 method uses the integrated function $D_i(x) \equiv \int_{x_{i-1}}^x F_i(x) dx$ for the interpolation when $u_i > 0$. The function $D_i(x)$ is a cubic polynomial satisfying following four constraints; $D_i(x_{i-1}) = 0$, $D_i(x_i) = \sigma_{i-1/2}$, $\partial D_i / \partial x(x_{i-1}) = F_i(x_{i-1}) = f_{i-1}$, and $\partial D_i / \partial x(x_i) = F_i(x_i) = f_i$. Moreover, since Eq. (15) can be rewritten as the same form of Eq. (13), we can obtain the updated value f^{n+1} as well as f_x^{n+1} in the CIP method.

Additionally, there is an oscillation preventing method in the concept of the CIP-CSL2 method, in which the rational function is used for the function $D_i(x)$ (Nakamura et al., 2001). This method is called as the R-CIP-CSL2 method.

3.1.3 Anti-diffusion

To keep the sharp discontinuity in the profile of ϕ , we explicitly add an diffusion term with a negative diffusion coefficient α (anti-diffusion) to the CIP-CSL2 method (Miura & Nakamoto, 2007). In our model, we have an additional diffusion equation about σ as

$$\frac{\partial \sigma}{\partial t} = \frac{\partial}{\partial x} \left(\alpha \frac{\partial \sigma}{\partial x} \right). \quad (18)$$

Eq. (18) can be separated into two equations as

$$\frac{\partial \sigma}{\partial t} = -\frac{\partial J'}{\partial x}, \quad (19)$$

$$J' = -\alpha \frac{\partial \sigma}{\partial x}, \quad (20)$$

where J' indicates the anti-diffusion flux per unit area and per unit time. Using the finite difference method, we obtain

$$\sigma_{i+1/2}^{**} = \sigma_{i+1/2}^* - (\hat{J}'_{i+1} - \hat{J}'_i), \quad (21)$$

$$\hat{J}'_i = -\hat{\alpha}_i \times \text{minmod}(S_{i-1}, S_i, S_{i+1}), \quad (22)$$

where $\hat{J} \equiv J' / (\Delta x / \Delta t)$ is the mass flux which has the same dimension of σ , $\hat{\alpha} \equiv \alpha / (\Delta x^2 / \Delta t)$ is the dimensionless diffusion coefficient, and $S_i \equiv \sigma_{i+1/2} - \sigma_{i-1/2}$. The superscripts * and ** indicate the time step just before and after the anti-diffusion. The minimum modulus function (minmod) is often used in the concept of the flux limiter and has a non-zero value of $\text{sign}(a) \min(|a|, |b|, |c|)$ only when a , b , and c have the same sign. The value of the diffusion coefficient $\hat{\alpha}$ is also important. Basically, we take $\hat{\alpha} = -0.1$ for the anti-diffusion. Here, it should be noted that σ takes the limited value as $0 \leq \sigma \leq \sigma_m$, where σ_m is the initial value for inside of the droplet. The undershoot ($\sigma < 0$) or overshoot ($\sigma > \sigma_m$) are physically incorrect solutions. To avoid that, we replace $\hat{\alpha}_i = 0.1$ only when $\sigma_{i-1/2}$ or $\sigma_{i+1/2}$ are out of the appropriate range. We insert the anti-diffusion calculation after the CIP-CSL2 method is completed.

3.1.4 Test calculation

In order to demonstrate the advantage of the CIP method, we carried out one-dimensional advection calculations with various numerical methods. Fig. 6 shows the spatial profiles of f of the test calculations. The horizontal axis is the spatial coordinate x . The initial profile is given by the solid line, which indicates a rectangle wave. We set the fluid velocity $u = 1$, the intervals of the grid points $\Delta x = 1$, and the time step for the calculation $\Delta t = 0.2$. These conditions give the CFL number $\nu \equiv u \Delta t / \Delta x = 0.2$, which indicates that the profile of f moves 0.2 times the grid interval per time step. Therefore, the right side of the rectangle wave will reach $x = 80$ after 300 time steps and the dashed line indicates the exact solution. The filled circles indicate the numerical results after 300 time steps.

The upwind method does not keep the rectangle shape after 300 time steps and the profile becomes smooth by the numerical diffusion (panel a). In the Lax-Wendroff method, the numerical oscillation appears behind the real wave (panel b). Comparing with above two methods, the CIP method seems to show better solution, however, some undershoots ($f < 0$)

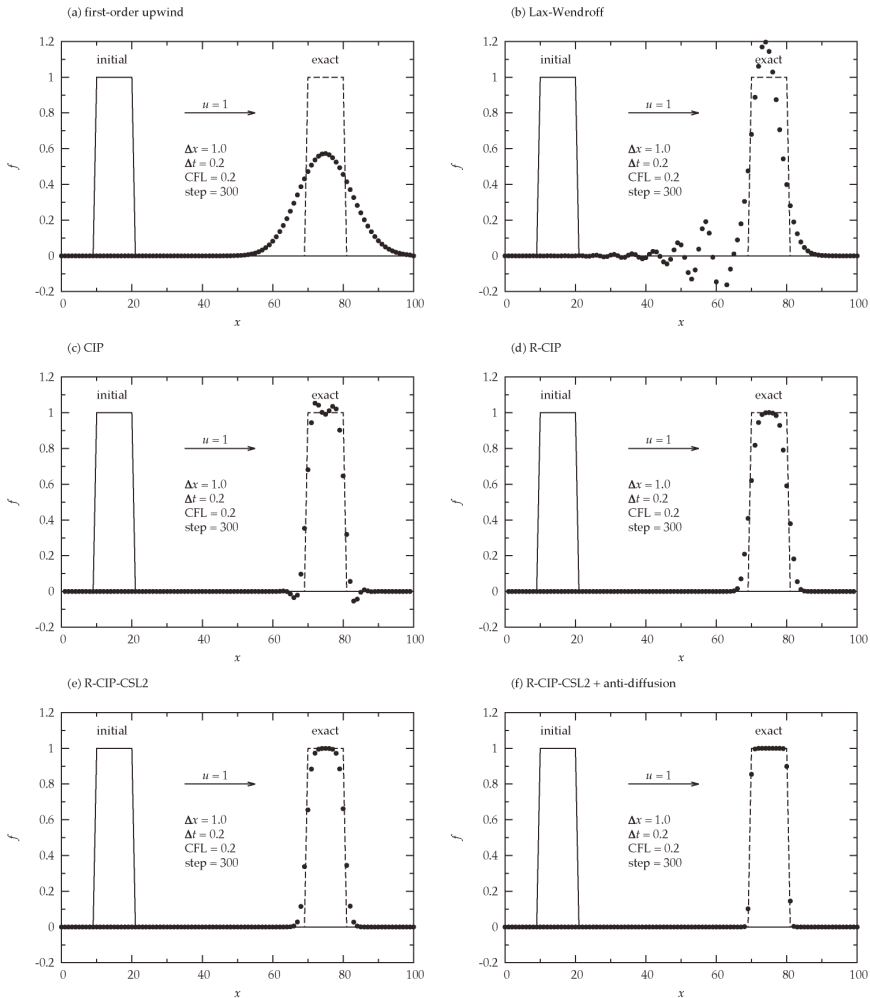


Fig. 6. Numerical solutions of the one-dimensional advection or conservation equation solved by various methods: (a) first-order upwind, (b) Lax-Wendroff, (c) CIP, (d) R-CIP, (e) R-CIP-CSL2 without anti-diffusion, and (f) R-CIP-CSL2 with anti-diffusion.

or overshoots ($f > 1$) are observed in the numerical result (panel c). In the R-CIP method, although the faint numerical diffusion has still remained, we obtain the excellent solution comparing with the above methods.

We also show the numerical results of the one-dimensional conservative equation. We use the same conditions with the one-dimensional advection equation. Note that Eq. (15) corresponds to Eq. (10) when the velocity u is constant. The panel (e) shows the result of the R-CIP-CSL2 method, which is similar to that of the R-CIP method. In the panel (f), we found that the combination of the R-CIP-CSL2 method and the anti-diffusion technique shows the excellent solution in which the numerical diffusion is prevented effectively.

3.2 Non-advection phase

3.2.1 C-CUP method

Using the finite difference method to Eq. (9), we obtain (Yabe & Wang, 1991)

$$\frac{\vec{u}^{**} - \vec{u}^*}{\Delta t} = -\frac{\vec{\nabla} p^{**}}{\rho^*} + \frac{\vec{Q}}{\rho^*}, \quad \frac{p^{**} - p^*}{\Delta t} = -\rho^* c_s^2 \vec{\nabla} \cdot \vec{u}^{**}, \quad (23)$$

where the superscripts * and ** indicate the times before and after calculating the non-advection phase, respectively. Since the sound speed is very large in the incompressible fluid, the term related to the pressure should be solved implicitly. In order to obtain the implicit equation for p^{**} , we take the divergence of the left equation and substitute \vec{u}^{**} into the right equation. Then we obtain an equation

$$\vec{\nabla} \cdot \left(\frac{\vec{\nabla} p^{**}}{\rho^*} \right) = \frac{p^{**} - p^*}{\rho^* c_s^2 \Delta t^2} + \frac{\vec{\nabla} \cdot \vec{u}^*}{\Delta t} + \vec{\nabla} \cdot \left(\frac{\vec{Q}}{\rho^*} \right). \quad (24)$$

The problem to solve Eq. (24) resolves itself into to solve a set of linear algebraic equations in which the coefficients becomes an asymmetric sparse matrix. After p^{**} is solved, we can calculate \vec{u}^{**} by solving the left equation in Eq. (23).

3.2.2 Ram pressure of free molecular flow

The ram pressure of the gas flow is acting on the droplet surface exposed to the high-velocity gas flow. It should be noted that the gas flow around a mm-sized droplet does not follow the hydrodynamical equations because the nebula gas is too rarefied. The mean free path of the nebula gas can be estimated by $l = 1/(ns)$, where s is the collisional cross section of gas molecules and n is the number density of the nebula gas. Typically, we adopt $n \approx 10^{14} \text{ cm}^{-3}$ based on the standard model of the early solar system at a distance from the sun of an astronomical unit (Hayashi et al., 1985). Substituting $s \approx 10^{-16} \text{ cm}^{-2}$ for the hydrogen molecule (Hollenbach & McKee, 1979), we obtain $l \approx 100 \text{ cm}$. On the other hand, the typical size of chondrules is about a few $100 \mu\text{m}$ (see Fig. 3). Since the object that disturbs the gas flow is much smaller than the mean free path of the gas, the free stream velocity field is not disturbed except of the direct collision with the droplet (free molecular flow).

Consider that the molecular gas flows for the positive direction of the x -axis. The x -component of the ram pressure $F_{g,x}$ is given by

$$F_{g,x} = p_{\text{fm}} \delta(x - x_i), \quad (25)$$

where x_i is the position of the droplet surface. This equation can be separated into two equations as

$$F_{g,x} = -\frac{\partial M}{\partial x}, \quad \frac{\partial M}{\partial x} = -p_{\text{fm}} \delta(x - x_i), \quad (26)$$

where M is the momentum flux of the molecular gas flow. The right equation in Eq. (26) means that the momentum flux terminates at the droplet surface. The left equation in Eq. (26) means that the decrease of the momentum flux per unit length corresponding to the ram pressure per unit area.

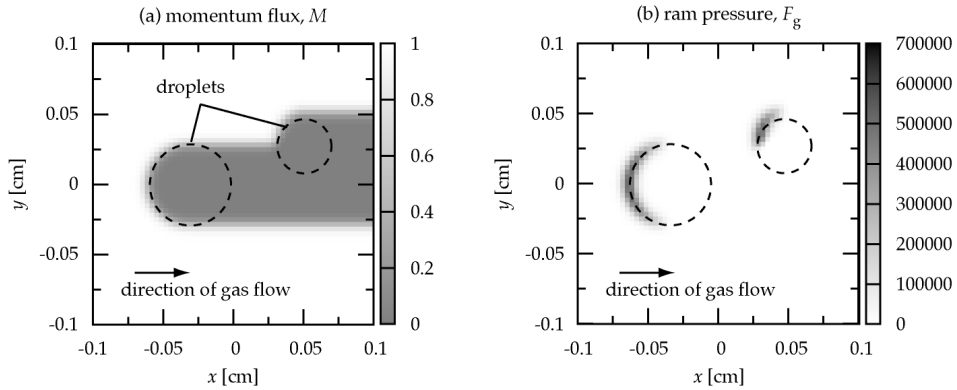


Fig. 7. Spatial distributions of the momentum flux M (a) and the ram pressure F_g (b) of the free molecular gas flow around a spherical droplet in xy -plane. The dashed circles are sections of the droplet surfaces in xy -plane. Units of the gray scales are p_{fm} for the panel (a) and dyn cm^{-3} for the panel (b), respectively. We adopt $p_{fm} = 5000 \text{ dyn cm}^{-2}$ in this figure.

Using the finite difference method to the right equation in Eq. (26), we obtain

$$M_{i+1} = M_i - p_{fm}(\bar{\phi}_{i+1} - \bar{\phi}_i) \quad \text{for } \bar{\phi}_{i+1} \geq \bar{\phi}_i, \tag{27}$$

where $\bar{\phi}$ is the smoothed profile of ϕ (see section 3.2.4), and $M_{i+1} = M_i$ for $\bar{\phi}_{i+1} < \bar{\phi}_i$ because the momentum flux does not increase when the molecular flow goes outward from inside of the droplet. Similarly, we obtain

$$F_{g,x_i} = -\frac{M_i - M_{i+1}}{\Delta x}, \tag{28}$$

from the left equation in Eq. (26). The momentum flux at upstream is $M_0 = p_{fm}$. First, we solve Eq. (27) and obtain the spatial distribution of the molecular gas flow in all computational domain. Then, we calculate the ram pressure by Eq. (28).

Fig. 7(a) shows the distribution of momentum flux M around two droplets in xy -plane. The dashed circles are the external shapes of large and small droplets. The gray scale is normalized by p_{fm} , so unity (white region) means undisturbed molecular flow and zero (dark region) means no flux because the free molecular flow is obstructed by the droplet. It is found that the gas flow is obstructed only behind the droplets. Fig. 7(b) shows the distribution of the ram pressure $F_{g,x}$ calculated from the momentum flux distribution. The ram pressure is acting at the droplet surface where M changes steeply. Note that no ram pressure acts at bottom half of the smaller droplet because the molecular flow is obstructed by the larger one. As shown in Fig. 7, the model of ram pressure shown here well reproduces the property of free molecular flow.

We calculate the momentum flux M and the ram pressure F_g at every time step in numerical simulations. Therefore, these spatial distributions are affected by droplet deformation.

3.2.3 Surface tension

The surface tension is the normal force per unit interfacial area. Brackbill et al. (Brackbill et al., 1992) introduced a method to treat the surface tension as a volume force by replacing the

discontinuous interface to the transition region which has some width. According to them, the surface tension is expressed as

$$\vec{F}_s = \gamma_s \kappa \vec{\nabla} \phi / [\phi], \quad (29)$$

where $[\phi]$ is the jump in color function at the interface between the droplet and the ambient gas. In our definition, we obtain $[\phi] = 1$. The curvature is given by

$$\kappa = -(\vec{\nabla} \cdot \vec{n}), \quad (30)$$

where

$$\vec{n} = \vec{\nabla} \phi / |\vec{\nabla} \phi|. \quad (31)$$

The finite difference method of Eq. (31) is shown in (Brackbill et al., 1992). When we calculate the surface tension, we use the smoothed profile of ϕ (see section 3.2.4).

3.2.4 Smoothing

We can obtain the numerical results keeping the sharp interface between the droplet and the ambient region. However, the smooth interface is suitable for calculating the smooth surface tension. We use the smoothed profile of ϕ only at the time to calculate the surface tension and the ram pressure acting on the droplet surface. In this study, the smoothed color function $\bar{\phi}$ is calculated by

$$\bar{\phi} = \frac{1}{2} \phi_{i,j,k} + \frac{1}{2} \frac{\phi_{i,j,k} + C_1 \sum_{L_1}^6 \phi_{L_1} + C_2 \sum_{L_2}^{12} \phi_{L_2} + C_3 \sum_{L_3}^8 \phi_{L_3}}{1 + 6C_1 + 12C_2 + 8C_3}, \quad (32)$$

where L_1 , L_2 , and L_3 indicate grid indexes of the nearest, second nearest, and third nearest from the grid point (i, j, k) , for example, $L_1 = (i + 1, j, k)$, $L_2 = (i + 1, j + 1, k)$, $L_3 = (i + 1, j + 1, k + 1)$, and so forth. It is easily found that in the three-dimensional Cartesian coordinate system, there are six for L_1 , twelve for L_2 , and eight for L_3 , respectively. The coefficients are set as

$$C_1 = 1/(6 + 12/\sqrt{2} + 8/\sqrt{3}), \quad C_2 = C_1/\sqrt{2}, \quad C_3 = C_1/\sqrt{3}. \quad (33)$$

We iterate the smoothing five times. Then, we obtain the smooth transition region of about twice grid interval width. We use the smooth profile of ϕ only when calculating the surface tension and the ram pressure. It should be noted that the original profile ϕ with the sharp interface is kept unchanged.

4. Deformation of droplet by gas flow

4.1 Vibrational motion

We assume that the gas flow suddenly affects the initially spherical droplet. Fig. 8 shows the time sequence of the droplet shape and the internal velocity. The horizontal and vertical axes are the x - and y -axes, respectively. The solid line is the section of the droplet surface in xy -plane. Arrows show the velocity field inside the droplet. The gas flow comes from the left side of the panel. The panel (a) shows the initial condition for the calculation. The panel (b) shows a snapshot at $t = 0.55$ msec. The droplet begins to be deformed due to the gas ram pressure. The fluid elements at the surface layer, which is directly facing the gas flow, are blown to the downstream. In contrast, the velocity at the center of the droplet turns to

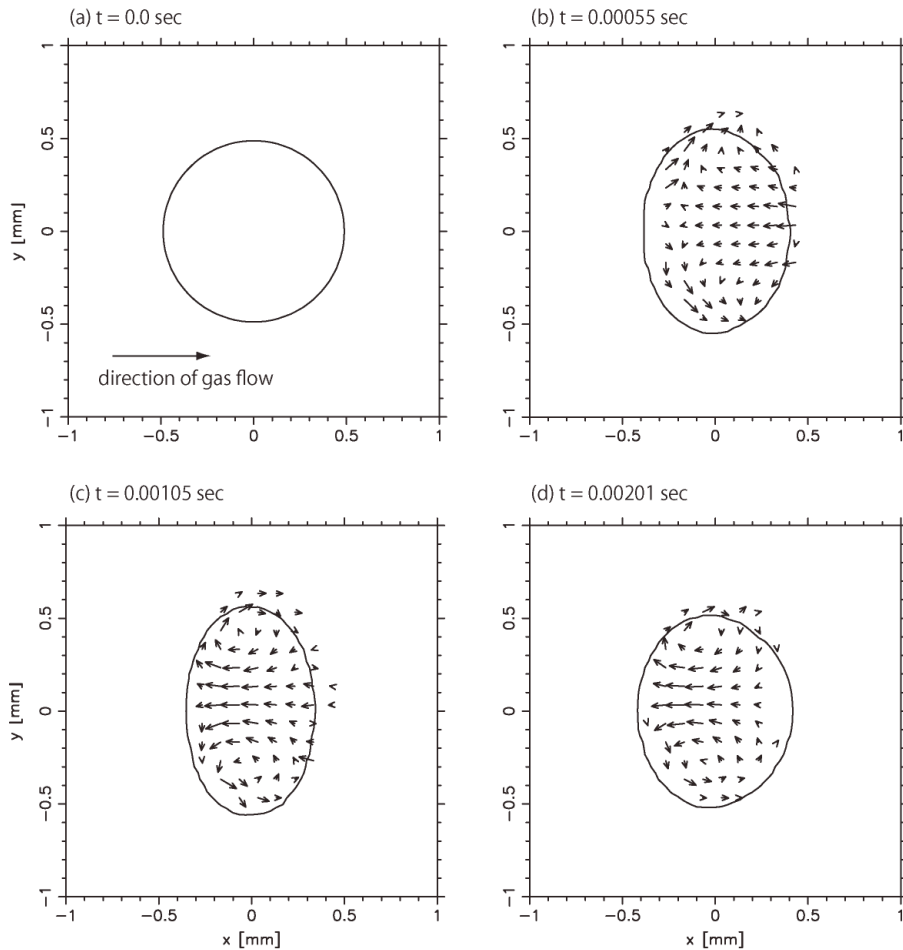


Fig. 8. Time evolution of molten droplet exposed to the gas flow. The gas flow comes from the left side of panels. We use $p_{fm} = 10^4 \text{ dyn cm}^{-2}$, $r_0 = 500 \text{ nm}$, and $\mu_d = 1.3 \text{ poise}$ for calculations.

upstream of the gas flow because the apparent gravitational acceleration takes place in our coordinate system. The droplet continues to be deformed further, and after $t = 1.0 \text{ msec}$, the degree of deformation becomes maximum (see panel (c)). After that, the droplet begins to recover its shape to the sphere due to the surface tension. The recovery motion is not all but almost over at the panel (d). The droplet repeats the deformation by the ram pressure and the recovery motion by the surface tension until the viscosity dissipates the internal motion of the droplet.

Fig. 9 shows the time variation of axial ratio c/b of the droplet. Each curve shows the calculation result for the different value of the ram pressure p_{fm} . The droplet is compressed unidirectionally by the gas flow, so the length of minor axis c corresponds to the half length of droplet axis in the direction of the gas flow. The axial ratio c/b is unity at the

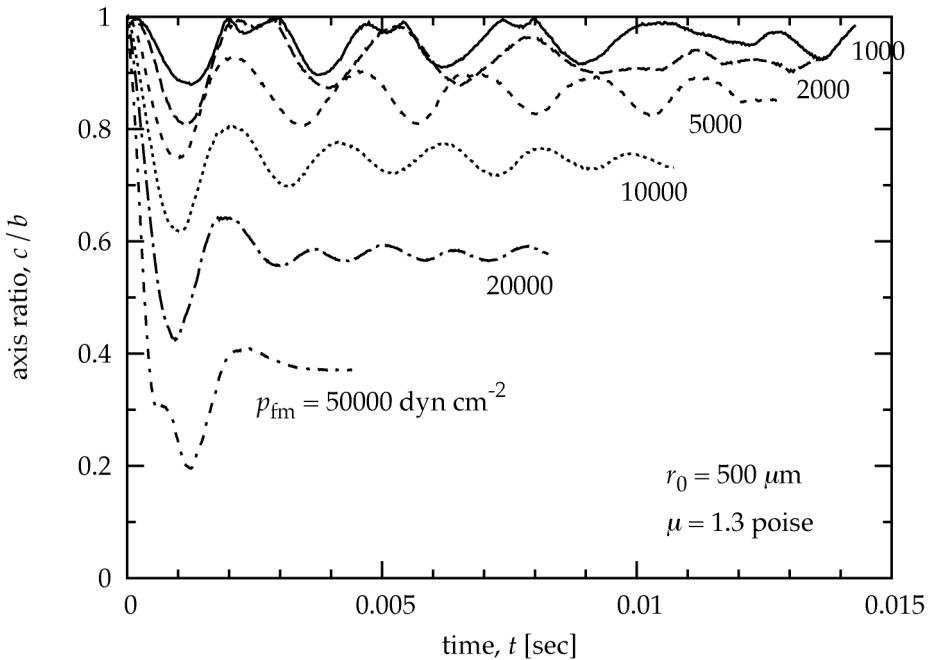


Fig. 9. Vibrational motions of molten droplet; the deformation by the ram pressure and the recovery motion by the surface tension. The horizontal axis is the time since the ram pressure begins to affect the droplet and the vertical axis is the axial ratio of the droplet c/b . Each curve shows the calculation result for the different value of the ram pressure p_{fm} . We use $r_0 = 500 \text{ }\mu\text{m}$ and $\mu_d = 1.3$ poise for calculations.

beginning because the initial droplet shape is a perfect sphere. The axial ratio decreases as time goes by because of the compression. After about 1 msec, c/b reaches minimum and then increases due to the surface tension. After this, the axial ratio vibrates with a constant frequency and finally the vibrational motion damps due to viscous dissipation. The calculated frequency of the vibrational motion is about 2 msec not depending on p_{fm} . The calculated frequency is consistent with that of a capillary oscillations of a spherical droplet given by $P_{vib} = 2\pi\sqrt{\rho_d r_0^3 / 8\gamma_s} \approx 2.15 \text{ msec}$ (Landau & Lifshitz, 1987).

4.2 Overdamping

Fig. 10 shows the time variation of the axial ratio c/b when the viscosity is 100 times larger than that in Fig. 9. It is found that the axial ratio converges on the value at steady state without any vibrational motion. This is an overdamping due to the strong viscous dissipation.

4.3 Effect of droplet rotation

We carried out the hydrodynamics simulations of non-rotating molten droplet in previous sections. However, the rotation of the droplet should be taken into consideration as the following reason. A chondrule before melting is an aggregate of numerous fine particles,

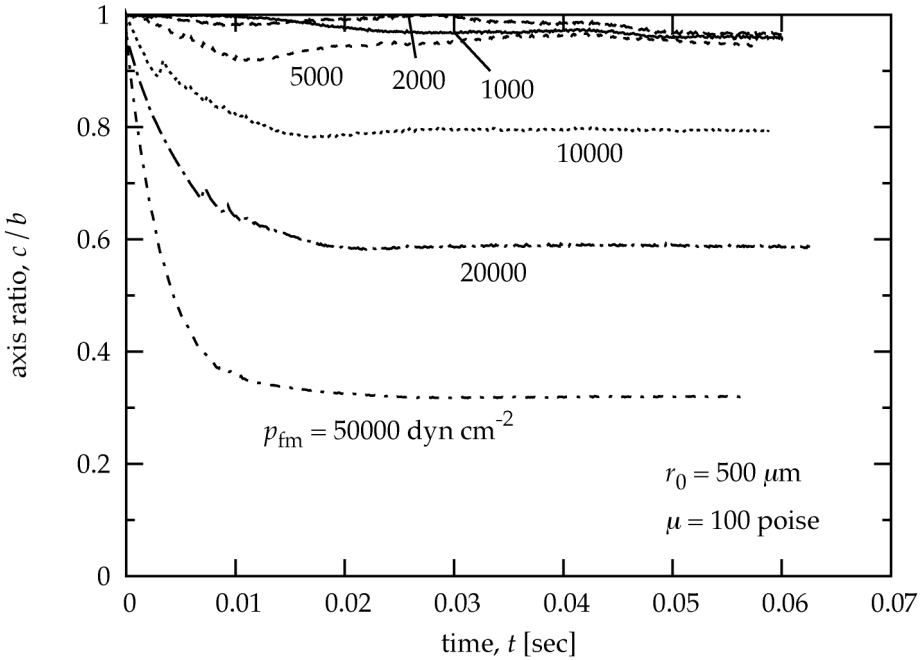


Fig. 10. Same as Fig. 9 except of $\mu_d = 100$ poise.

so the shape is irregular in general. The irregular shape causes a net torque in an uniform gas flow. Therefore, it is naturally expected that the molten chondrule also rotates at a certain angular velocity.

The angular velocity ω_f can be roughly estimated by $I\omega_f \approx N\Delta t$, where I is the moment of inertia of chondrule and Δt is the duration to receive the net torque N . Assuming that the small fraction f of the cross-section of the precursor contributes to produce the net torque N , we obtain $N \approx f\pi r_0^3 p_{fm}$. We can set $\Delta t \approx \pi/\omega_f$ (a half-rotation period) because the sign of N would change after half-rotation. Substituting $I = (8/15)\pi r_0^5 \rho_d$, which is the moment of inertia for a sphere with an uniform density ρ_d , we obtain the angular velocity (Miura, Nakamoto & Doi, 2008)

$$\begin{aligned} \omega_f &\approx \sqrt{15f\pi p_{fm}/8r_0^2\rho_d} \\ &= 140 \left(\frac{f}{0.01}\right)^{1/2} \left(\frac{p_{fm}}{10^4 \text{ dyn cm}^{-2}}\right)^{1/2} \left(\frac{r_0}{1 \text{ mm}}\right)^{-1} \text{ rad s}^{-1}. \end{aligned} \tag{34}$$

Therefore, in the shock-wave heating model, the droplet should be rotating rapidly if most of the angular momentum is maintained during melting.

In addition, it should be noted that the rotation axis is likely to be perpendicular to the direction of the gas flow unless the chondrule before melting has a peculiar shape as windmill.

Fig. 11 shows the deformation of a rotating droplet in gas flow in a three-dimensional view. The rotation axis is set to be perpendicular to the direction of the gas flow. We use $\mu_d =$

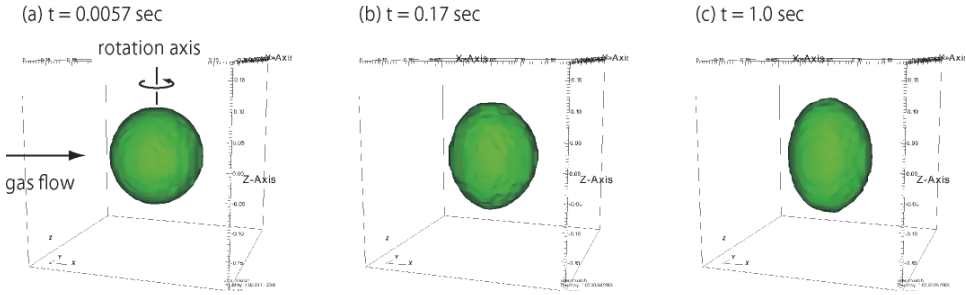


Fig. 11. Three-dimensional view of a rotating molten droplet exposed to a high-velocity gas flow. The object shows the external shape of the droplet (iso-surface of the color function of $\phi = 0.5$). The gas flow comes from the left side (arrow). The rotation axis of the droplet is perpendicular to the direction of the gas flow. After $t = 1.0$ sec, the droplet shape becomes a prolate. We use $\mu_d = 10^3$ poise, $p_{fm} = 10^4$ dyn cm^{-2} , $\omega = 100$ rad s^{-1} , and $r_0 = 1$ mm.

10^3 poise, $p_{fm} = 10^4$ dyn cm^{-2} , $\omega = 100$ rad s^{-1} , and $r_0 = 1$ mm. It is found that the droplet elongates in a direction of the rotation axis as the time goes by. Fig. 12 shows the time variation of the axial ratios b/a (solid) and c/b (dashed). The major axis a corresponds to the droplet elongation in a direction of the gas flow, so the decrease of b/a means the droplet elongation. The axial ratio b/a reaches a steady value of 0.76 after 1 sec. The axial ratio c/b is kept at a constant value of ≈ 0.95 during the calculation, which means that two droplet radius perpendicular to the rotation axis is almost uniform. The droplet shape at the steady state is prolate, in other words, a rugby-ball-like shape.

4.4 Origin of prolate chondrule

Why did the droplet shape become prolate? The reason, of course, is due to the droplet rotation. If there is no rotation on the droplet, its shape is only affected by the gas which comes from the fixed direction (see Fig. 13a). In this case, the droplet shape becomes disk-like (oblate) shape because only one axis, which corresponds to the direction of the gas flow, becomes shorter than the other two axes (Sekiya et al., 2003). In contrast, let us consider the case that the droplet is rotating. If the rotation period is much shorter than the viscous deformation timescale, the gas flow averaged during one rotation period can be considered to be axis-symmetrical about the rotation axis (see Fig. 13b). Therefore, the droplet shrinks due to the axis-symmetrical gas flow along directions perpendicular to the rotation axis and becomes prolate if the averaged gas ram pressure is strong enough to overcome the centrifugal force.

Doi (Doi, 2011) derived the analytic solution of deformation of a rotating droplet in gas flow in a case that the gas flow can be approximated as axis-symmetrical around the rotation axis as shown in Fig. 13(b). He considered that the droplet radius is given by $r(\theta) = r_0 + r_1(\theta)$, where r_0 is the unperturbed droplet radius and r_1 is the deviation from a perfect sphere. θ is the angle between the position (the origin is the center of the droplet) and the rotation axis. According to his solution, the droplet deformation is given by

$$\frac{r_1(\theta)}{r_0} = \frac{We}{12} \left(\frac{19}{20} - R \right) P_2(\cos \theta), \quad (35)$$

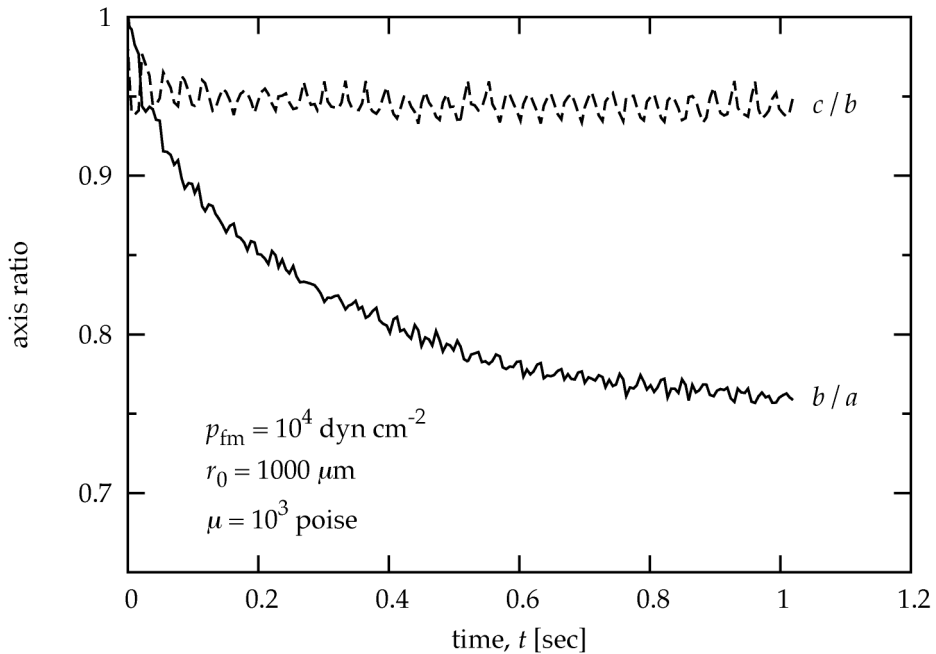


Fig. 12. Time evolutions of axial ratios b/a and c/b in the case of Fig. 11.

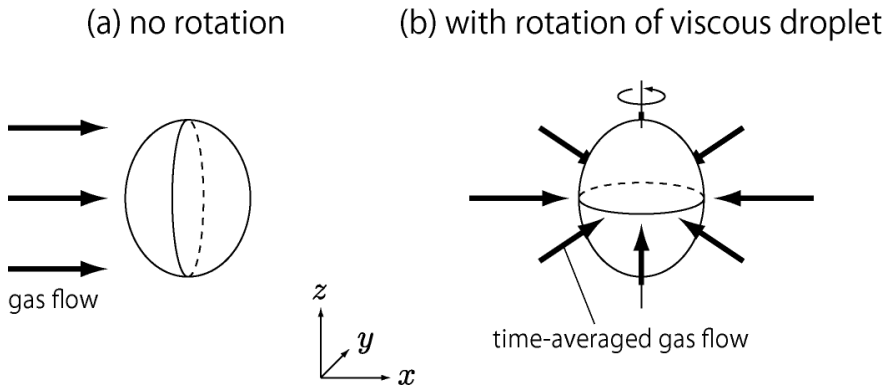


Fig. 13. The reason why the rotating droplet exposed to the gas flow is deformed to a prolate shape is illustrated. (a) If the droplet does not rotate, it is deformed only by the effect of the gas ram pressure. (b) If the droplet rotates much faster than the deformation due to the gas flow, the time-averaged gas flow can be approximated as axis-symmetrical around the rotation axis.

where W_e (Weber number) is the ratio of the ram pressure of the gas flow to the surface tension of the droplet defined as

$$W_e = \frac{p_{fm} r_0}{\gamma_s}, \quad (36)$$

R is the ratio of the centrifugal force to the ram pressure defined as

$$R = \frac{\rho_d r_0^2 \omega^2}{p_{fm}}, \quad (37)$$

ω is the angular velocity of the rotation, and $P_l(\cos \theta)$ is Legendre polynomials. This solution is applicable under the assumption of $r_1 \ll r_0$. Eq. (35) shows that the particle radius becomes the maximum at $\theta = 0$, and minimum at $\theta = \pi/2$. $R = 19/20$ is a critical value for the droplet shape to be prolate ($R < 19/20$) or oblate ($R > 19/20$). The droplet shape is sphere when $R = 19/20$ because the ram pressure balances with the centrifugal force.

Fig. 14 shows the droplet shape as functions of the Weber number W_e and the normalized centrifugal force R using Eq. (35). $R = 19/20$ (vertical dashed line) is a critical value for the droplet shape to be prolate ($R < 19/20$) or oblate ($R > 19/20$). In the prolate region, the axial ratio b/a is less than unity for $W_e > 0$ as shown by contours, but $c/b = 1$. On the other hand, in the oblate region, the axial ratio c/b is less than unity for $W_e > 0$, but $b/a = 1$. As W_e increases, the degree of deformation increases as shown in decrease of axial ratio b/a or c/b . The blue and red regions show ranges of axial ratios of group-A spherical chondrules and group-B prolate chondrules, respectively. We carried out the hydrodynamics simulations for a wide range of parameters and displayed on this diagram by symbols. It is found that the hydrodynamics simulation results show a good agreement with the analytic solution for a wide range of W_e and R .

Let us consider the shape of chondrule expected from the shock-wave heating model. Adopting ram pressure of the gas flow of $p_{fm} = 10^4$ dyn cm⁻² and the radius of chondrule of $r_0 = 1$ mm, we obtain $W_e = 2.5$ for $\gamma_s = 400$ erg cm⁻². According to Eq. (34), we evaluate $R = 0.06$ for $f = 0.01$. The evaluated value of R is smaller than the critical value of $19/20$, so the expected droplet shape is prolate. In addition, the axial ratio b/a comes into a range of group-B prolate chondrules (see Fig. 14). This suggests that the origin of group-B prolate chondrules can be explained by the shock-wave heating model. Of course, it should be noted that the shock-wave heating model does not reproduce the group-B prolate chondrules for arbitrary conditions because W_e and R depend on many factors, e.g., p_{fm} , r_0 , and f . Namely, it is possible that different shock conditions produce different chondrule shapes, even out of the range of group-A or -B. This fact, on the contrary, indicates that the chondrule shapes constrain shock conditions suitable for formation of these chondrules. The data of three-dimensional chondrule shapes measured by Tsuchiyama et al. (Tsuchiyama et al., 2003) is definitely valuable, however, the number of samples is twenty at most. We need more data to constrain the chondrule formation mechanism from their three-dimensional shapes.

5. Fragmentation

5.1 Direct fragmentation

When the droplet size is too large for the surface tension to keep the droplet shape against the gas ram pressure, the fragmentation will occur. Fig. 15 shows the three-dimensional views of

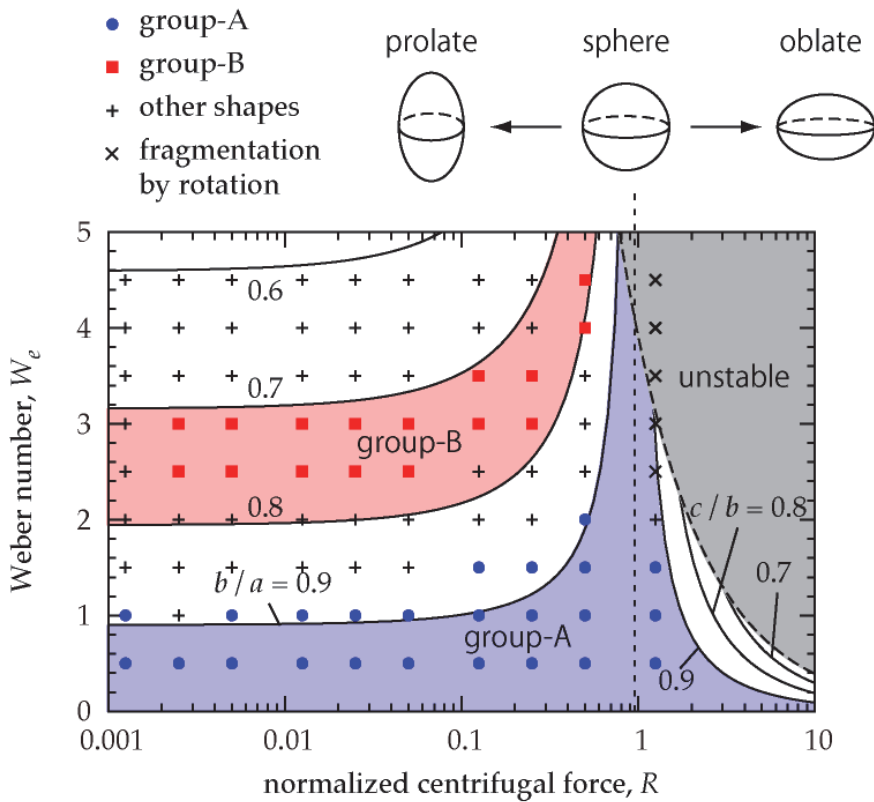


Fig. 14. Shapes of rotating droplets in gas flow. The horizontal axis is the centrifugal force normalized by ram pressure of the gas flow R . The vertical axis is the Weber number W_e . $R = 19/20$ (vertical dashed line) is a critical value for the droplet shape to be prolate ($R < 19/20$) or oblate ($R > 19/20$). Solid lines are contours of axial ratios of b/a ($R < 19/20$) or c/b ($R > 19/20$). A ranges of axial ratios of chondrules are shown by colored regions for group-A spherical chondrules (blue) and for group-B prolate chondrules (red), respectively. Symbols are results of hydrodynamics simulations (see legends in figure). Grayed region shows a condition in which the droplet will be fragmented by rapid rotation.

the break-up droplet. The droplet radius is $r_0 = 2$ cm, which corresponds to $W_e = 20$. The gas flow comes from the left side of the view along the x -axis. It is found that the droplet shape is deformed as the time goes by (panels (a) and (b)), and leads to fragmentation (panel (c)). The parent droplet breaks up to many smaller pieces.

Susa & Nakamoto (Susa & Nakamoto, 2002) suggested that the fragmentation of the droplets in high-velocity gas flow limits the sizes of chondrules (upper limit). They considered the balance between the surface tension and the inhomogeneity of the ram pressure acting on the droplet surface, and derived the maximum size of molten silicate dust particles above which the droplet would be destroyed by the ram pressure of the gas flow using an order of magnitude estimation. In their estimation, they adopted the experimental data in which

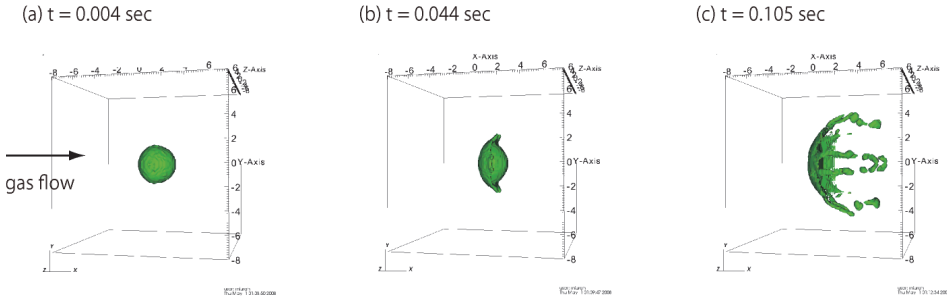


Fig. 15. Three-dimensional view of the fragmentation of molten droplet. We use $\mu_d = 1$ poise, $p_{fm} = 4000 \text{ dyn cm}^{-2}$, and $r_0 = 2 \text{ cm}$. The calculation was performed on a $100 \times 100 \times 100$ grid.

the droplets suddenly exposed to the gas flow fragment for $We_e > \sim 6$ (Bronshten, 1983, p.96). This results into the fragmentation of droplet for $r_0 > \sim 6 \text{ mm}$ if we adopt our calculation conditions: $p_{fm} = 4000 \text{ dyn cm}^{-2}$ and $\gamma_s = 400 \text{ dyn cm}^{-1}$. Our hydrodynamics simulations agree with the criterion for fragmentation.

5.2 Fragmentation via cavitation

Fig. 16 shows the internal pressure inside the droplet for various droplet sizes: $r_0 = 3, 4,$ and 5 mm from panels (a) to (c). We use $\mu_d = 1.3$ poise and $p_{fm} = 4000 \text{ dyn cm}^{-2}$. These droplets reach steady states, so their hydrodynamics do not change significantly after these panels. We found a high pressure region at the front of the droplet, and low pressure regions at centers of eddies in all cases. The high pressure is due to the ram pressure of the gas flow. The low pressure in eddy is clearly due to the non-linear effect caused by the advection term in Eq. (2). Surprisingly, the pressure in eddy decreases to almost zero in panels (b) and (c). In the “zero”-pressure region, the vaporization (or boiling) of the liquid would take place because the vapor pressure of the liquid exceeds the internal pressure. This phenomenon is well known as cavitation. We did not take into account the cavitation in our simulations, so no vaporization occurred in the calculation. If the cavitation was taken into consideration, the eddies are no longer maintained because of the cavitation, which would cause the fragmentation of the droplet.

Miura & Nakamoto (Miura & Nakamoto, 2007) proposed the condition for the “zero”-pressure region to appear by considering the balance between the centrifugal force and the pressure gradient force around eddies as $\rho_d v_{\text{circ}}^2 / r_{\text{eddy}} \approx p / r_{\text{eddy}}$, where v_{circ} is the fluid velocity around the eddy, r_{eddy} is the radius of the eddy, and p is the pressure inside the droplet. Substituting $p = 2\gamma_s / r_0$ from the Young-Laplace equation and $v_{\text{circ}} \approx v_{\text{max}} = 0.112 p_{fm} r_0 / \mu_d$ (Sekiya et al., 2003), we obtain

$$r_{0,\text{cav}} \approx \left(\frac{2\gamma_s \mu_d^2}{0.112^2 \rho_d p_{fm}^2} \right)^{1/3}. \quad (38)$$

This equation gives the critical radius of the droplet above which the cavitation takes place in the center of the eddy. We obtain $r_{0,\text{cav}} = 1.3 \text{ mm}$ for the calculation condition. In our hydrodynamic simulations, we observed the “zero”-pressure region for $r_0 = 4 \text{ mm}$ or larger.

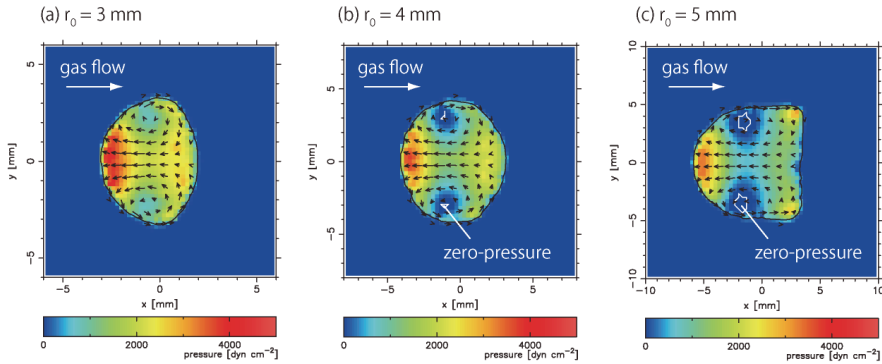


Fig. 16. Internal pressure inside droplet for different droplet radius r_0 : (a) 3 mm, (b) 4 mm, and (c) 5 mm. The pressure at a region surrounded by a white line decreases to almost zero by the eddy. We use $\mu_d = 1.3$ poise and $p_{fm} = 4000$ dyn cm⁻².

The inconsistency of cavitation criterion between hydrodynamics simulation and Eq. (38) might come from the fact that we substitute the linear solution into v_{circ} . The Sekiya's solution did not take into account the non-linear term in the Navier-Stokes equation. On the other hand, the cavitation would be caused by the non-linear effect. The substitution of the linear solution into the non-linear phenomenon might be a reason for the inconsistency. However, Eq. (38) provide us an insight of the cavitation criterion qualitatively.

5.3 Comparison with chondrule properties

It was found from the chondrule size distribution (see Fig. 3) that chondrules larger than a few mm in radius are very rare. The origin of the chondrule size distribution has been considered as some size-sorting process prior to chondrule formation in the early solar gas disk (Teitler et al., 2010, and references therein). On the other hand, in the framework of the shock-wave heating model, the upper limit of chondrule sizes can be explained by the fragmentation of a molten chondrule in high-velocity gas flow. The criterion of fragmentation is given by $W_e = p_{fm} r_0 / \gamma_s \approx 6$. Since the ram pressure of the gas flow is typically $p_{fm} \approx 10^3 - 10^5$ dyncm⁻², we obtain the upper limit of chondrule sizes as $r_{max} \approx 0.2 - 20$ mm. This is consistent with the fact that chondrules larger than a few mm in radius are very rare.

In addition, our hydrodynamics simulations show a new pathway to the fragmentation by cavitation. The cavitation takes place for $W_e < 6$ if viscosity of the molten chondrule is small. The viscosity decreases rapidly as temperature of the droplet increases. This suggests the following tendency: chondrules that experienced higher maximum temperature during melting have smaller sizes that that experienced lower maximum temperature. On the other hand, the data obtained by Nelson & Rubin (Nelson & Rubin, 2002) showed the tendency opposite from our prediction. They considered the reason of the difference in mean sizes among chondrule textural types being due mainly to parent-body chondrule-fragmentation events and not to chondrule-formation processes in the solar nebula. Therefore, to date, there is no evidence regarding the dependence of chondrule sizes on the maximum temperature. The relation between the chondrule sizes and the maximum temperature should be investigated in the future.

How about the distribution of sizes smaller than the maximum one? Kadono and his colleagues carried out aerodynamic liquid dispersion experiments using shock tube (Kadono & Arakawa, 2005; Kadono et al., 2008). They showed that the size distributions of dispersed droplets are represented by an exponential form and similar form to that of chondrules. In their experimental setup, the gas pressure is too high to approximate the gas flow around the droplet as free molecular flow. We carried out the hydrodynamics simulations of droplet dispersion and showed that the size distribution of dispersed droplets is similar to the Kadono's experiments (Yasuda et al., 2009). These results suggest that the shock-wave heating model accounts for not only the maximum size of chondrules but also their size distribution below the maximum size.

In addition, we recognized a new interesting phenomenon relating to the chondrule formation: the droplets dispersed from the parent droplet collide each other. A set of droplets after collision will fuse together into one droplet if the viscosities are low. In contrary, if the set of droplets solidifies before complete fusion, it will have a strange morphology that is composed of two or more chondrules adhered together. This is known as compound chondrules and has been observed in chondritic meteorites in actuality. The abundance of compound chondrules relative to single chondrules is about a few percents at most (Akaki & Nakamura, 2005; Gooding & Keil, 1981; Wasson et al., 1995). The abundance sounds rare, however, this is much higher comparing with the collision probability of chondrules in the early solar gas disk, where number density of chondrules is quite low (Gooding & Keil, 1981; Sekiya & Nakamura, 1996). In the case of collisions among dispersed droplets, a high collision probability is expected because the local number density is high enough behind the parent droplet (Miura, Yasuda & Nakamoto, 2008; Yasuda et al., 2009). The fragmentation of a droplet in the shock-wave heating model might account for the origin of compound chondrules.

6. Conclusion

To conclude, hydrodynamics behaviors of a droplet in space environment are key processes to understand the formation of primitive materials in meteorites. We modeled its three-dimensional hydrodynamics in a hypervelocity gas flow. Our numerical code based on the CIP method properly simulated the deformation, internal flow, and fragmentation of the droplet. We found that these hydrodynamics results accounted for many physical properties of chondrules.

7. References

- Akaki, T. & Nakamura, T. (2005). Formation processes of compound chondrules in cv3 carbonaceous chondrites: Constraints from oxygen isotope ratios and major element concentrations., *Geochim. Cosmochim. Acta* 69: 2907–2929.
- Amelin, T., Krot, A. N., Hutcheon, I. D. & Ulyanov, A. A. (2002). Lead isotopic ages of chondrules and calcium-aluminum-rich inclusions, *Science* 297: 1678–1683.
- Amelin, Y. & Krot, A. (2007). Pb isotopic age of the allende chondrules, *Meteorit. Planet. Sci.* 42: 1321–1335.
- Blander, M., Planner, H., Keil, K., Nelson, L. & Richardson, N. (1976). The origin of chondrules: experimental investigation of metastable liquids in the system $\text{mg}_2\text{SiO}_4\text{-SiO}_2$, *Geochimica et Cosmochimica Acta* 40(8): 889 – 892, IN1–IN2, 893–896.

- URL: <http://www.sciencedirect.com/science/article/B6V66-48C8H7W-BK/2/bdd79a0a3820afc4d06ac02bdc7cfaa7>
- Brackbill, J. U., Kothe, D. B. & Zemach, C. (1992). A continuum method for modeling surface tension, *Journal of Computational Physics* 100(2): 335 – 354.
- URL: <http://www.sciencedirect.com/science/article/pii/002199919290240Y>
- Bronshten, V. A. (1983). *Physics of Meteoric Phenomena*, Dordrecht: Reidel.
- Chandrasekhar, S. (1965). The stability of a rotating liquid drop, *Proceedings of the Royal Society of London. Ser. A, Mathematical and Physical Sciences* 286: 1–26.
- Ciesla, F. J. & Hood, L. L. (2002). The nebula shock wave model for chondrule formation: Shock processing in a particle-gas suspension, *Icarus* 158: 281–293.
- Ciesla, F. J., Hood, L. L. & Weidenschilling, S. J. (2004). Evaluating planetesimal bow shocks as sites for chondrule formation, *Meteorit. Planet. Sci.* 39: 1809–1821.
- Desch, S. J. & Jr., H. C. C. (2002). A model of the thermal processing of particles in solar nebula shocks: Application to the cooling rates of chondrules, *Meteorit. Planet. Sci.* 37: 183–207.
- Doi, M. (2011). *Formation of cosmic spherule: chemical analysis and theory for shapes, compositions, and textures*, PhD thesis, Tokyo Institute of Technology.
- Fredriksson, K. & Ringwood, A. (1963). Origin of meteoritic chondrules, *Geochimica et Cosmochimica Acta* 27(6): 639 – 641.
- URL: <http://www.sciencedirect.com/science/article/B6V66-48C8FST-5/2/baf33fee9f7f0a8d0a3ef0a92ac38cf7>
- Gooding, J. L. & Keil, K. (1981). Relative abundances of chondrule primary textural types in ordinary chondrites and their bearing on conditions of chondrule formation, *Meteoritics* 16: 17–43.
- Harold C. Connolly, J. & Hewins, R. H. (1995). Chondrules as products of dust collisions with totally molten droplets within a dust-rich nebular environment: An experimental investigation, *Geochimica et Cosmochimica Acta* 59: 3231–3246.
- Hayashi, C. K., Nakazawa, K. & Nakagawa, Y. (1985). *Formation of the solar system*, Protostars and Planets II, Univ. of Arizona Press, Tucson, pp. 1100–1153.
- Hewins, R. H. & Radomsky, P. M. (1990). Temperature conditions for chondrule formation, *Meteoritics* 25: 309–318.
- Hollenbach, D. & McKee, C. F. (1979). Molecular formation and infrared emission in fast interstellar shocks. i. physical processes, *Astrophys. J.* 41: 555–592.
- Hood, L. L. (1998). Thermal processing of chondrule precursors in planetesimal bow shocks, *Meteorit. Planet. Sci.* 33: 97–108.
- Hood, L. L. & Horanyi, M. (1991). Gas dynamic heating of chondrule precursor grains in the solar nebula, *Icarus* 93: 259–269.
- Hood, L. L. & Horanyi, M. (1993). The nebular shock wave model for chondrule formation - one-dimensional calculations, *Icarus* 106: 179–189.
- Hughes, D. W. (1978). A disaggregation and thin section analysis of the size and mass distribution of the chondrules in the bjurbíŠte and chainpur meteorites, *Earth and Planetary Science Letters* 38(2): 391 – 400.
- URL: <http://www.sciencedirect.com/science/article/pii/0012821X78901139>
- Iida, A., Nakamoto, T., Susa, H. & Nakagawa, Y. (2001). A shock heating model for chondrule formation in a protoplanetary disk, *Icarus* 153: 430–450.

- Jones, R. H., Lee, T., Jr., H. C. C., Love, S. G. & Shang, H. (2000). *Formation of chondrules and CAIs: Theory vs. observation*, Protostars and Planets IV, Univ. of Arizona Press, Tucson, pp. 927–962.
- Jones, R. H. & Lofgren, G. E. (1993). A comparison of feo-rich, porphyritic olivine chondrules in unequilibrated chondrites and experimental analogues, *Meteoritics* 28: 213–221.
- Kadono, T. & Arakawa, M. (2005). Breakup of liquids by high velocity flow and size distribution of chondrules, *Icarus* 173: 295–299.
- Kadono, T., Arakawa, M. & Kouchi, A. (2008). Size distributions of chondrules and dispersed droplets caused by liquid breakup: An application to shock wave conditions in the solar nebula, *Icarus* 197: 621–626.
- Kato, T., Nakamoto, T. & Miura, H. (2006). Maximal size of chondrules in shock wave heating model: Stripping of liquid surface in a hypersonic rarefied gas flow, *Meteorit. Planet. Sci.* 41: 49–65.
- Landau, L. D. & Lifshitz, E. M. (1987). *Fluid Mechanics, Course of Theoretical Physics*, Vol. 6, 2nd edn, Elsevier/Butterworth/Heinemann, Oxford, UK.
- Lofgren, G. & Russell, W. J. (1986). Dynamic crystallization of chondrule melts of porphyritic and radial pyroxene composition, *Geochim. Cosmochim. Acta* 50: 1715–1726.
- Miura, H. & Nakamoto, T. (2006). Shock-wave heating model for chondrule formation: Prevention of isotopic fractionation, *Astrophys. J.* 651: 1272–1295.
- Miura, H. & Nakamoto, T. (2007). Shock-wave heating model for chondrule formation: Hydrodynamic simulation of molten droplets exposed to gas flows, *Icarus* 188: 246–265.
- Miura, H., Nakamoto, T. & Doi, M. (2008). Origin of three-dimensional shapes of chondrules. i: Hydrodynamics simulations of rotating droplet exposed to high-velocity rarefied gas flow, *Icarus* 197: 269–281.
- Miura, H., Nakamoto, T. & Susa, H. (2002). A shock-wave heating model for chondrule formation: Effects of evaporation and gas flows on silicate particles, *Icarus* 160: 258–270.
- Miura, H., Yasuda, S. & Nakamoto, T. (2008). Fragment-collision model for compound chondrule formation: Estimation of collision probability, *Icarus* 194: 811–821.
- Morris, M. A. & Desch, S. J. (2010). Thermal histories of chondrules in solar nebula shocks, *Astrophys. J.* 722: 1474–1494.
- Morris, M. A., Desch, S. J. & Ciesla, F. J. (2009). Cooling of dense gas by H₂O line emission and an assessment of its effects in chondrule-forming shocks, *Astrophys. J.* 691: 320–331.
- Nagashima, K., Tsukamoto, K., Satoh, H., Kobatake, H. & Dold, P. (2006). Reproduction of chondrules from levitated, hypercooled melts, *J. Cryst. Growth* 293: 193–197.
- Nakagawa, Y., Sekiya, M. & Hayashi, C. (1986). Settling and growth of dust particles in a laminar phase of a low-mass solar nebula, *Icarus* 67: 375–390.
- Nakamura, T., Tanaka, R., Yabe, T. & Takizawa, K. (2001). Exactly conservative semi-lagrangian scheme for multi-dimensional hyperbolic equations with directional splitting technique, *Journal of Computational Physics* 174(1): 171 – 207.
URL: <http://www.sciencedirect.com/science/article/pii/S0021999101968883>
- Nelson, L. S., Blander, M., Skaggs, S. R. & Keil, K. (1972). Use of a CO₂ laser to prepare chondrule-like spherules from supercooled molten oxide and silicate droplets, *Earth Planet. Sci. Lett.* 14: 338–344.

- Nelson, V. E. & Rubin, A. E. (2002). Size-frequency distributions of chondrules and chondrule fragments in ll3 chondrites: Implications for parent-body fragmentation of chondrules, *Meteorit. Planet. Sci.* 37: 1361–1376.
- Radomsky, P. M. & Hewins, R. H. (1990). Formation conditions of pyroxene-olivine and magnesian olivine chondrules, *Geochim. Cosmochim. Acta* 54: 3475–3490.
- Rubin, A. E. (1989). Size-frequency distributions of chondrules in co3 chondrites, *Meteoritics* 24: 179–189.
- Rubin, A. E. & Grossman, J. N. (1987). Size-frequency-distributions of eh3 chondrules, *Meteoritics* 22: 237–251.
- Rubin, A. E. & Keil, K. (1984). Size-distributions of chondrule types in the inman and allan hills a77011 l3 chondrites, *Meteoritics* 19: 135–143.
- Ruzmaikina, T. V. & Ip, W. H. (1994). Chondrule formation in radiative shock, *Icarus* 112: 430–447.
- Sekiya, M. & Nakamura, T. (1996). Condition for the formation of the compound chondrules in the solar nebula, *Proc. NIPR Symp. Antarct. Meteorites* 9: 208–217.
- Sekiya, M., Uesugi, M. & Nakamoto, T. (2003). Flow in a liquid sphere moving with a hypersonic velocity in a rarefied gas—an analytic solution of linearized equations, *Prog. Theor. Phys.* 109: 717–728.
- Srivastava, A., Inatomi, Y., Tsukamoto, K., Maki, T. & Miura, H. (2010). In situ visualization of crystallization inside high temperature silicate melts, *J. Appl. Phys.* 107: 114907.
- Susa, H. & Nakamoto, T. (2002). On the maximal size of chondrules in shock wave heating model, *Astrophys. J.* 564: L57–L60.
- Teitler, S. A., Paque, J. M., Cuzzi, J. N. & Hogan, R. C. (2010). Statistical tests of chondrule sorting, *Meteorit. Planet. Sci.* .
- Tsuchiyama, A. & Nagahara, H. (1981-12). Effects of precooling thermal history and cooling rate on the texture of chondrules: A preliminary report, *Memoirs of National Institute of Polar Research. Special issue* 20: 175–192.
URL: <http://ci.nii.ac.jp/naid/110000009441/>
- Tsuchiyama, A., Nagahara, H. & Kushiro, I. (1980). Experimental reproduction of textures of chondrules, *Earth Planet. Sci. Lett.* 48: 155–165.
- Tsuchiyama, A., Osada, Y., Nakano, T. & Uesugi, K. (2004). Experimental reproduction of classic barred olivine chondrules: Open-system behavior of chondrule formation, *Geochim. Cosmochim. Acta* 68: 653–672.
- Tsuchiyama, A., Shigeyoshi, R., Kawabata, T., Nakano, T., Uesugi, K. & Shirono, S. (2003). Three-dimensional structures of chondrules and their high-speed rotation, *Lunar Planet. Sci.* 34: 1271–1272.
- Tsukamoto, K., Satoh, H., Takamura, Y. & Kuribayashi, K. (1999). A new approach for the formation of olivine-chondrules by aero-acoustic levitation, *Antarct. Meteorites* 24: 179–181.
- Uesugi, M., Akaki, T., Sekiya, M. & Nakamura, T. (2005). Motion of iron sulfide inclusions inside a shock-melted chondrule, *Meteorit. Planet. Sci.* 40: 1103–1114.
- Uesugi, M., Sekiya, M. & Nakamoto, T. (2003). Deformation and internal flow of a chondrule-precursor molten sphere in a shocked nebular gas, *Earth Planets Space* 55: 493–507.
- Wasson, J. T., Alexander, N. K., Lee, M. S. & Rubin, A. E. (1995). Compound chondrules, *Geochim. Cosmochim. Acta* 59: 1847–1869.

- Wood, J. A. (1984). On the formation of meteoritic chondrules by aerodynamic drag heating in the solar nebula, *Earth Planet. Sci. Lett.* 70: 11–26.
- Xiao, F., Yabe, T. & Ito, T. (1996). Constructing oscillation preventing scheme for advection equation by rational function, *Comp. Phys. Comm.* 93: 1–12.
- Yabe, T. & Aoki, T. (1991). A universal solver for hyperbolic equations by cubic-polynomial interpolation i. one-dimensional solver, *Comp. Phys. Comm.* 66: 219–232.
- Yabe, T. & Wang, P. Y. (1991). Unified numerical procedure for compressible and incompressible fluid, *J. Phys. Soc. Jpn.* 60: 2105–2108.
- Yabe, T., Xiao, F. & Utsumi, T. (2001). The constrained interpolation profile method for multiphase analysis., *J. Comp. Phys.* 169: 556–593.
- Yasuda, S., Miura, H. & Nakamoto, T. (2009). Compound chondrule formation in the shock-wave heating model: Three-dimensional hydrodynamics simulation of the disruption of a partially-molten dust particle, *Icarus* 204: 303–315.

Flow Evolution Mechanisms of Lid-Driven Cavities

José Rafael Toro and Sergio Pedraza R.
*Grupo de Mecánica Computacional, Universidad de Los Andes
Colombia*

1. Introduction

The flow in cavities studies the dynamics of motion of a viscous fluid confined within a cavity in which the lower wall has a horizontal motion at constant speed. There exist two important reasons which motivate the study of cavity flows. First is the use of this particular geometry as a benchmark to verify the formulation and implementation of numerical methods and second the study of the dynamics of the flow inside the cavity which become very particular as the Reynolds (Re) number is increased, i.e. decreasing the fluid viscosity.

Most of the studies, concerning flow dynamics inside the cavity, focus their efforts on the steady state, but very few study the mechanisms of evolution or transients until the steady state is achieved (Gustafson, 1991). Own to the latter approach it was considered interesting to understand the mechanisms associated with the flow evolution until the steady state is reached and the steady state per se, since for different Re numbers (1,000 and 10,000) steady states are "similar" but the transients to reach them are completely different.

In order to study the flow dynamics and the evolution mechanisms to steady state the Lattice Boltzmann Method (LBM) was chosen to solve the dynamic system. The LBM was created in the late 90's as a derivation of the Lattice Gas Automata (LGA). The idea that governs the method is to build simple mesoscale kinetic models that replicate macroscopic physics and after recovering the macro-level (continuum) it obeys the equations that governs it i.e. the Navier Stokes (NS) equations. The motivation for using LBM lies in a computational reason: Is easier to simulate fluid dynamics through a microscopic approach, more general than the continuum approach (Texeira, 1998) and the computational cost is lower than other NS equations solvers. Also is worth to mention that the prime characteristic of the present study and the method itself was that the primitive variables were the vorticity-stream function not as the usual pressure-velocity variables. It was intended, by choosing this approach, to understand in a better way the fluid dynamics because what characterizes the cavity flow is the lower wall movement which creates itself an impulse of vorticity which is transported within the cavity by diffusion and advection. This transport and the vorticity itself create the different vortex within the cavity and are responsible for its interaction.

In the next sections steady states, periodic flows and feeding mechanisms for different Re numbers are going to be studied within square and deep cavities.

2. Computational domains

The flow within a cavity of height h and wide w where the bottom wall is moving at constant velocity U_0 Fig.1 is going to be model. The cavity is completely filled by an incompressible fluid with constant density ρ and cinematic viscosity ν .

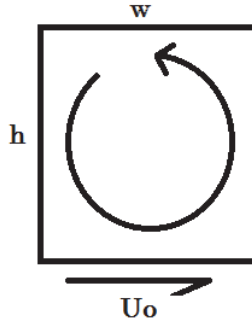


Fig. 1. Cavity

3. Flow modelling by LBM with vorticity stream-function variables

Is important to introduce the equations that govern the vorticity transport and a few definitions that will be used during the present study.

Definition 0.1. *A vortex is a set of fluid particles that moves around a common center*

The vorticity vector is defined as $\omega = \nabla \times v$ and its transport equation is given by

$$\frac{\partial \omega}{\partial t} + [\nabla \omega]v = [\nabla v]\omega + \nu \nabla^2 \omega. \quad (1)$$

which is obtained by calculating the *curl* of the NS equation. For a 2D flow Eq.(1) is simplified to obtain

$$\frac{\partial \omega}{\partial t} + [\nabla \omega]v = \nu \nabla^2 \omega. \quad (2)$$

In order to recover the velocity field from the vorticity field the Poisson equation for the stream function needs to be solved. The Poisson equation which involves the stream function is stated as

$$\nabla^2 \psi = -\omega \quad (3)$$

where ψ is the stream function who carries the velocity field information as

$$u = \frac{\partial \psi}{\partial y}, \quad v = -\frac{\partial \psi}{\partial x}. \quad (4)$$

and ensures the mass conservation. The motivation for adopting vorticity as the primitive variables lies in the fact that every potential, as the pressure, is eliminated which is physically desirable because being the vorticity an angular velocity, the pressure, which is always normal to the fluid can not affect the angular momentum of a fluid element.

3.1 Numerical method

Consider a set of particles that moves in a bidimensional lattice and each particle with a finite number of movements. Now a vorticity distribution function $g_i(x, t)$ will be assigned to each particle with unitary velocity e_i giving to it a dynamic consistent with two principles:

1. Vorticity transport
2. Vorticity variation in a node own to particle collision

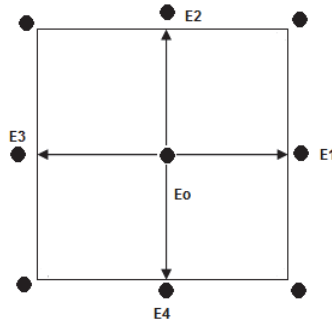


Fig. 2. D2Q5 Model.2 dimensions and 5 possible directions of moving

Observation 0.2. *The method only considers binary particle collisions.*

The evolution equation is described by

$$g_k(\vec{x} + c\vec{e}_k\Delta t, t + \Delta t) - g_k(\vec{x}, t) = -\frac{1}{\tau}[g_k(\vec{x}, t) - g_k^{eq}(\vec{x}, t)]^1 \tag{5}$$

where e_k are the possible directions where the vorticity can be transported as shown in Fig.2. $c = \Delta x/\Delta t$ is the fluid particle speed, Δx and Δt the lattice grid spacing and the time step respectively and τ the dimensionless relaxation time. Clearly Eq.(5) is divided in two parts, the first one emulates the advective term of (1) and the collision term, which is in square brackets, emulates the diffusive term of equation (1).

The equilibrium function is calculated by

$$g_k^{eq} = \frac{w}{5} [1 + 2.5 \frac{\vec{e}_k \cdot \vec{u}}{c}]. \tag{6}$$

The vorticity is calculated as

$$w = \sum_{k \geq 0} g_k \tag{7}$$

and τ , the dimensionless relaxation time, is determined by Re number

$$Re = \frac{5}{2c^2(\tau - 0.5)}. \tag{8}$$

¹ The evolution equations were taken from (Chen et al., 2008) and (Chen, 2009). Is strongly recommended to consult the latter references for a deeper understanding of the evolution equations and parameter calculations.

In order to calculate the velocity field Poisson equation must be solved (3). In order to do this (Chen et al., 2008) introduces another evolution equation.

$$f_k(\vec{x} + c\vec{e}_k\Delta t, t + \Delta t) - f_k(\vec{x}, t) = \Omega_k + \hat{\Omega}_k. \quad (9)$$

Where

$$\Omega_k = \frac{-1}{\tau_\psi} [f_k(\vec{x}, t) - f_k^e q(\vec{x}, t)], \quad \hat{\Omega}_k = \Delta t \zeta_k \theta D \quad (10)$$

and $D = \frac{c^2}{2}(0.5 - \tau_\psi)$. τ_ψ is the dimensionless relaxation time of the latter evolution equation which can be chosen arbitrarily. For the sake of understanding the evolution equations, the equation (9) consist on calculating $\frac{D\psi}{Dt} = \nabla^2\psi + \omega$ until $\frac{D\psi}{Dt} = 0$, having found a solution ψ for the Poisson equation.

By last, the equilibrium distribution function is defined as

$$f_k^{eq} = \begin{cases} \zeta_k \psi & k = 1, 2, 3, 4 \\ -\psi & k = 0 \end{cases} \quad (11)$$

where ζ_k and ζ_k are weight parameters of the equation.

3.2 Algorithm implementation

In order to implement the evolution equation Eq.(5) two main calculations are considered. First, the collision term is calculated as

$$g_k^{int} = -\frac{1}{\tau} [g_k(\vec{x}, t) - g_k^{eq}(\vec{x}, t)] \quad (12)$$

and next the vorticity distributions is transported as

$$g_k(\vec{x} + c\vec{e}_k\Delta t, t + \Delta t) = g_k^{int} + g_k(\vec{x}, t) \quad (13)$$

which is, as mentioned, the basic concept that governs the LBM, collisions and transportation of determined distribution in our case a vorticity distribution.

3.2.1 Algorithm and boundary conditions

1. Paramater Inicialization

- Moving wall velocity: $U_0 = 1$.
- $\psi|_{\partial\Omega} = 0$, own to the fact that no particle is crossing the walls.
- $u = v = 0$ in the whole cavity excepting the moving wall.
- Re number definition²

2. Wall vorticity calculation

$$\omega|_{\partial\Omega} = \frac{7\psi_w - 8\psi_{w-1} + \psi_{w-2}}{2\Delta n^2} \quad (14)$$

$$\omega|_{\partial\Omega} = \frac{7\psi_w - 8\psi_{w-1} + \psi_{w-2}}{2\Delta n^2} - \frac{3U_0}{\Delta n} \quad (15)$$

Both equations came from solving Poisson equation Eq.(3) on the walls by a second order Taylor approximation. Eq.(15) is used on the moving wall nodes.

² For the sake of clarity Re number is imposed in the method by the user which intrinsically is imposing different flow viscosities.

3. Velocity field calculation using Eq.(4)
4. Equilibrium probability calculation using Eq.(6)
5. Collision term calculation using Eq.(12)
6. Probability transport using Eq.(13)
7. Vorticity field calculation using Eq.(7)
8. Solution of Poisson equation: In order to solve Poisson equation the evolution equation Eq.(9) for the stream-function distribution was implemented within a loop wishing to compare f_k 's values (i.e. ψ) aiming to achieve that $\frac{D\psi}{Dt} = \nabla^2\psi + \omega = 0$. For the latter loop the process terminated when

$$\sum_{x,y} |f_k^+ - f_k| < 10^{-3}.$$

While the simulations were ran, it was found that the algorithm was demanding finer meshes for higher Re numbers, i.e. 700x700 nodes mesh for Re 6,000, increasing the computational cost and most of the times ending in overflows own to the fluid regime. To overcome this situations a turbulence model was introduced to the LBM proposed by (Chen, 2009).

4. Introduction of turbulence in LBM

The principal characteristic of a turbulent flow is that its velocity field is of random nature. Considering this, the velocity field can be split in a deterministic term and in a random term i.e. $U(x, t) = \bar{U}(x, t) + u(x, t)$, being the deterministic and random term respectively. In order to solve the velocity field, the NS equations are recalculated in deterministic variables adding to the set a closure equation own to the loss of information undertaken by solving only the deterministic term. At introducing a turbulent model there exist three different approaches: algebraic models, closure models and Large Eddy Simulations (LES) being the latter used in the present study. LES were introduced by James Deardorff on 1960 (Durbin & Petersson-Rief, 2010). Such simulations are based in the fact that the bulk of the system energy is contained in the large eddys of the flow making not necessary to calculate all the vortex dissipative range which would imply a high computational cost (Durbin & Petersson-Rief, 2010). If small scales are omitted, for example by increasing the spacing by a factor of 5, the number of grid points is substantially reduced by a factor of 125 (Durbin & Petersson-Rief, 2010). In LES context the elimination of these small scales is called filtering. But this filtering or omission of small scales is determined as follows: the dissipative phenomenon is replaced by an alternative that produces correct dissipation levels without requiring small scale simulations. The Smagorinsky model was introduced where another flow viscosity (usually known as subgrid viscosity) is considered which is calculated based on the fluid deformation stress. Specifically it is model as $\nu_t = (C\Delta)^2|S|$ Chen et al. (2008) where

$$S_{ij} = \frac{1}{2} \left(\frac{\partial \bar{U}_i}{\partial x_j} + \frac{\partial \bar{U}_j}{\partial x_i} \right),$$

Δ is the filter width and C the Smagorinsky constant. In the present study $C = 0.1$ and $\Delta = \Delta x$. Assuming this new **subgrid viscosity** ν_t the momentum equation is given by

$$\frac{\partial \omega}{\partial t} + [\nabla \omega]v = \frac{\partial}{\partial x} \left(\nu_e \frac{\partial \omega}{\partial x} \right) + \frac{\partial}{\partial y} \left(\nu_e \frac{\partial \omega}{\partial y} \right)$$

where

$$v_e = v_t + v.$$

As the transport equation has changed, the LBM evolution equation has also changed

$$g_k(\vec{x} + c\vec{e}_k\Delta t, t + \Delta t) - g_k(\vec{x}, t) = -\frac{1}{\tau_e}[g_k(\vec{x}, t) - g_k^{eq}(\vec{x}, t)] \tag{16}$$

where

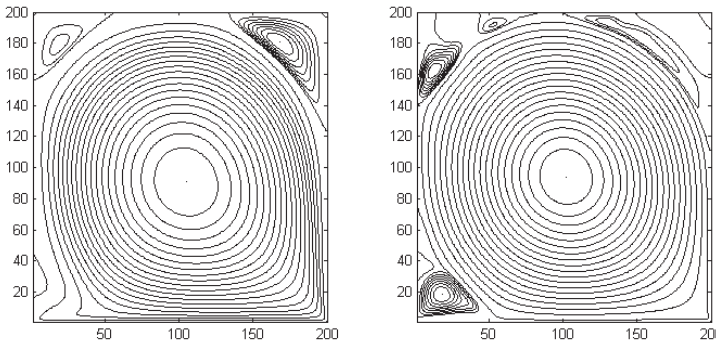
$$\tau_e = \tau + \frac{5(C\Delta)^2|S|}{2c^2\Delta t} \text{ and } |S| = |\omega|^3.$$

Having a new evolution equation Eq.(16) the algorithm has to be modified adding a new step where τ_e is calculated based on the vorticity field. After making this improvement to the method, the algorithm began to work efficiently allowing to achieve higher Re numbers without compromising the computer cost, justifying the use of a LBM.

5. Steady state study for different Re numbers

It is said that the flow has reached steady state when collisions and transport do not affect each node probability. Concerning the algorithm it was considered that the flow had reached the steady state when its energy had stabilized and when the maps of vorticity and stream function showed no changes through time.

Steady state vortex configuration for Re 1,000 and Re 10,000 is shown in Fig.3. It worth to notice that both are very similar, a positive vortex that fills the cavity and two negative vortices at the corners of the cavity. This configuration was observed from Re 1,000 to Re 10,000 being a prime characteristic of cavity flows. It is also important to clarify that for Re 10,000 the steady state presents a periodicity which is located in the upper left vortex that we shall see later, indeed Fig.3(b) is a "snapshot" of the flow.



(a) Stream-function map in steady state for Re 1,000. (b) Stream-function map in steady state for Re 10,000.

Fig. 3. Steady states. Maps were taken at 100,000 and 110,000 iterations respectively.

³ Is strongly recommended to consult (Chen, 2009) for a deeper understanding of the evolution equations and parameter calculations.

5.1 Deep cavities

Several studies have proposed to study the deep cavity geometry (Gustafson, 1991; Patil et al., 2006) but none has reached to simulate high Re numbers possibly because the mesh sizes. Due to the LBM low computational cost it was decided to present the study of a deep cavity with an aspect ratio (AR) of 1.5 for Re 8,000.

5.1.1 Vortex dynamics

A general description is presented emphasizing the most important configurations through evolution to steady state:

- **Step 1 Fig.4(a)** The positive vortex creates a negative vortex that arises from the right wall triggering an interaction since the beginning of the evolution.
- **Step 2 Fig.4 (b)** The negative vortex that arises from the right wall has taken the whole cavity confining the positive vortex to the bottom.
- **Step 3 Fig.4(c,d)** Positive vortices have joined in one by an interesting process described in Sec6. This union creates a "mirror" phenomenon inside the cavity.
- **Step 4 Fig.4(e)** The positive vortex expands into the cavity moving upward the negative vortex until the steady state is reached in which both vortices occupy the same space of the cavity. Is worth to notice that this vortex distribution is not achieved in the square cavity steady state.

5.1.2 Mirror phenomenon

During the evolution it was observed that after positive vortices joined (Fig.4(c, d)) the new big positive vortex acted as a moving wall for the negative vortex injecting vorticity to it. Reproducing the behavior seen in the square cavity, now by the negative vortex. Ergo a *quasi square cavity* was created in the top of the cavity but instead having a moving wall it had a vortex. The phenomenon is shown in Fig.5 where it is clear that the top of the deep cavity is a "reflection" of the square cavity with respect to an imaginary vertical axis drawn between these two.

6. Vortex binding

A particular process for Re 10,000 in square and deep cavities was found to take place through evolution. This process occurs several times throughout evolution, named Vortex Binding. In this process isolated vortices get connected forming a "massive" vortex which eventually will configure the steady state vortices distribution. A binding process that occurred through evolution is shown in Fig.6 binding a positive vortex that appeared in the upper right corner with the positive vortex that came from the movement of the bottom wall.

In order to explain the binding process, which is illustrated in Fig.6, recall the vorticity transport equation Eq.(1). The transport equation is divided in two terms that dictate the transport of vorticity, the diffusive term $\nu \nabla^2 \omega$ and the advective term $[\nabla \omega]v$. For a high Re number flow the diffusive term can be neglected, turning the attention in the advective term. As the flow evolved it was seen that the vorticity and stream-function contour lines tended to align as shown in Fig.7(a) making the vorticity gradient vector and velocity vector orthogonal at different places (Fig.7(a)) causing $[\nabla \omega]v = 0$, i.e. no vorticity transport.

As shown in Fig.7(b) vorticity contour lines started to curve, due to its own vorticity, crossing with the stream-function contour lines and making $[\nabla \omega]v \neq 0$. In Fig.7(b) can be seen that

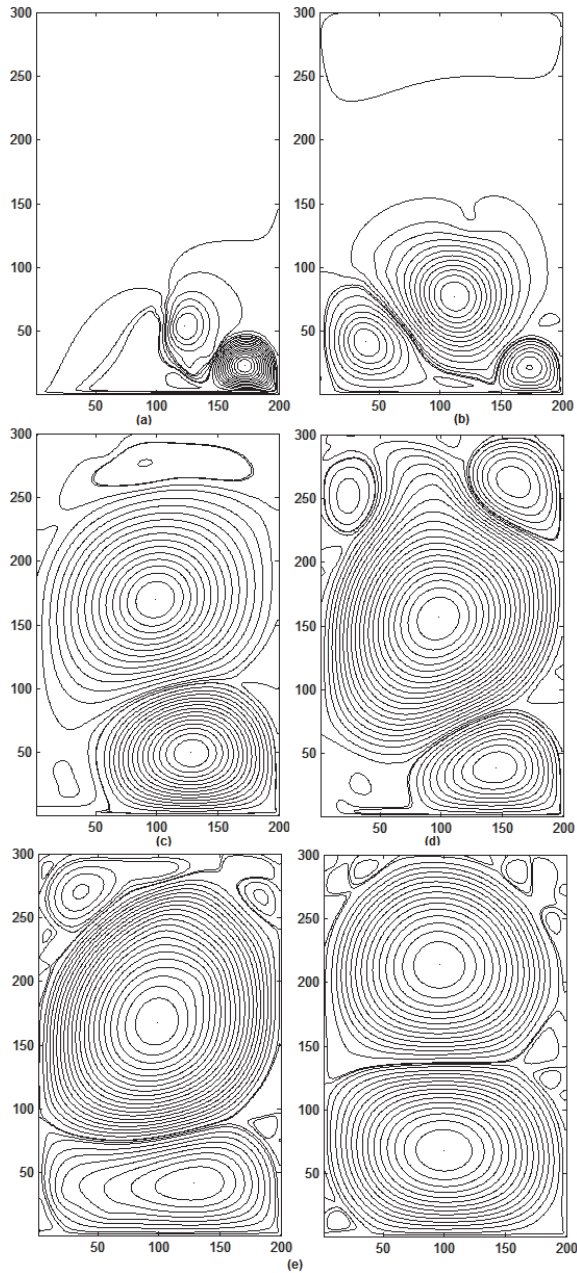


Fig. 4. Stream-function map for different times through evolution for a cavity with $AR=1.5$ and $Re\ 8,000$ in a 200×300 nodes mesh. *a, b, c, d* and *e* were taken at 20,000, 50,000, 150,000, 180,000 and 260,000-340,000 iterations.

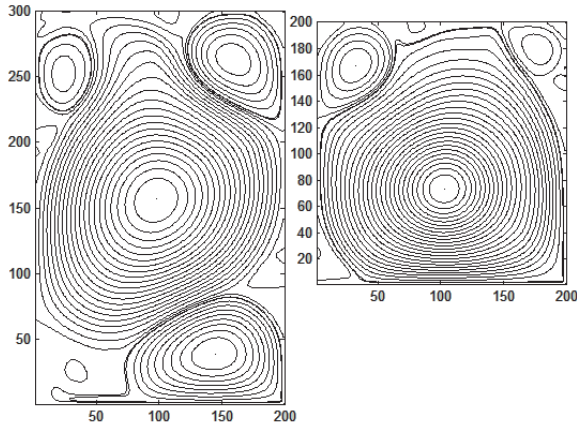


Fig. 5. *Left* Stream-function map for Re 8,000 in a cavity with AR=1.5 (200x300 nodes) *Right* Stream-function map in a square cavity for Re 8,000 (200x200 nodes).

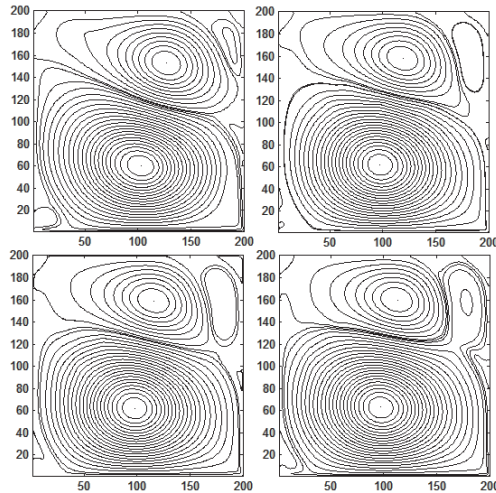


Fig. 6. Stream-function maps for Re 10,000 were Vortex binding process take place. Four maps were taken between 80,000 and 90,000 iterations

the vorticity gradient and the velocity vector are no longer orthogonal creating vorticity transport in different places which made possible the vortex binding to take place.

7. Periodicity in cavity flows

In the study of dynamic systems, being the case of the present study the NS equations, and their solutions there exist bifurcations leading to periodic solutions. Specifically in cavity flows, when the Re number is increased, such bifurcations take place known as **Hopf Bifurcations**. Willing to understand how this Bifurcation takes place the *Sommerfelds* infinitesimal perturbation model is introduced. This perturbation model considers a small

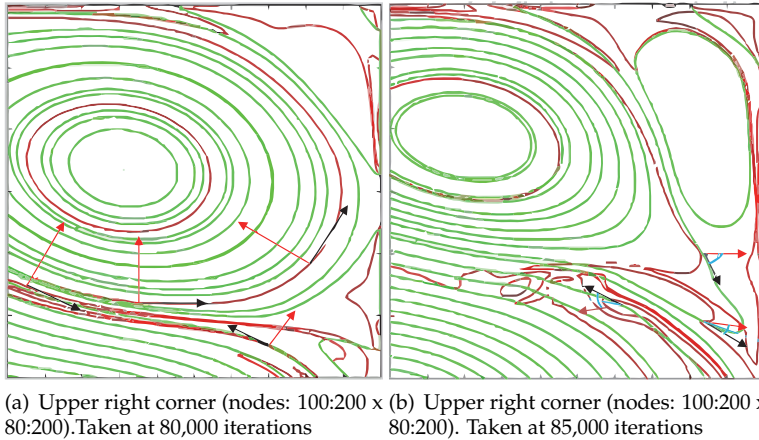


Fig. 7. *Left* Stream-function contour lines (**Green**), vorticity contour lines(**Red**), vorticity gradient(**Red**), velocity vector(**Black**).*Right* Stream-function contour lines (**Green**), vorticity contour lines(**Red**), vorticity gradient(**Red**), velocity vector(**Black**)and angle between $[\nabla\omega]$ and v (**Blue**)

perturbation of the dynamical system in order to study the equilibrium state or the lack of it. Let be considered the next dynamical system

$$\frac{d\dot{u}}{dt} = [M_v] \dot{u}. \quad (17)$$

The solution of Eq.(17) lies on finding the eigenvectors of the $[M_v]$ operator which is in function of the fluid viscosity. Depending on the Re number the eigenvalues (and eigenvector) can be complex i.e. $\lambda \in \mathbb{C}$, leading to periodic solutions(Toro, 2006) or Bifurcations. In (Auteri et al., 2002) the bifurcation for a cavity flow was located between 8017,6 and 8018,8 (Re numbers) but since 1995 (Goyon, 1995) reported the existence of particular periodic flow located in the upper left corner of a square cavity. In order to find the flow periodicity for Re 10,000 and determine if the system had reached its asymptotic state the system energy was used as a measure. A Periodic flow for a deep cavity is shown in Fig.8⁴

8. Flow transients

Studying vorticity and stream-function maps was found that the way to get to the *same* state in most of the flow (Fig.3(a) and Fig.3(b)), with the exception of the corners for Re 10,000 which oscillate, change significantly as the number of Re varies. In order to illustrate this "bifurcation" vorticity transients for Re 1,000 and Re 10,000 are shown in Figs.9, 10 and 11 until steady state configuration is reached.

8.1 Transient description

For Re 1,000 the positive vortex is created on the lower right corner by the bottom wall movement. Latter vortex is feeded and grows until the whole cavity is taken cornering

⁴ A well discribed periodic flow for square cavity can be found in (Goyon, 1995).

and breaking a negative vortex that has accompanied it since the beginning of evolution without qualitative form changes, only scaling the first configuration until the steady state configuration is achieved in Fig.3(a).

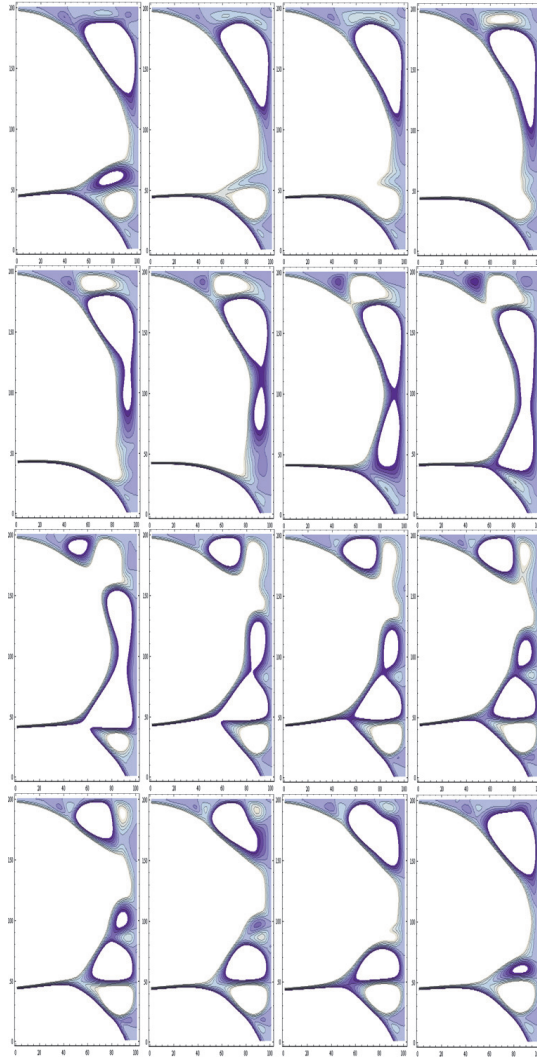


Fig. 8. Stream-function maps for a deep cavity with $AR=1.5$ and $Re\ 8,000$ where periodic flow take place. Maps were taken between 300,000 and 309,000 iterations. *White patches are vortices with high absolute vorticity.* Cavity upper right corner (100:200x100:300) nodes, see Fig.4(e-right)

For $Re\ 10,000$ the positive vortex is created due to the lower wall movement and immediately itself creates a negative vortex coming from the right wall. Unlike $Re\ 1,000$ these two

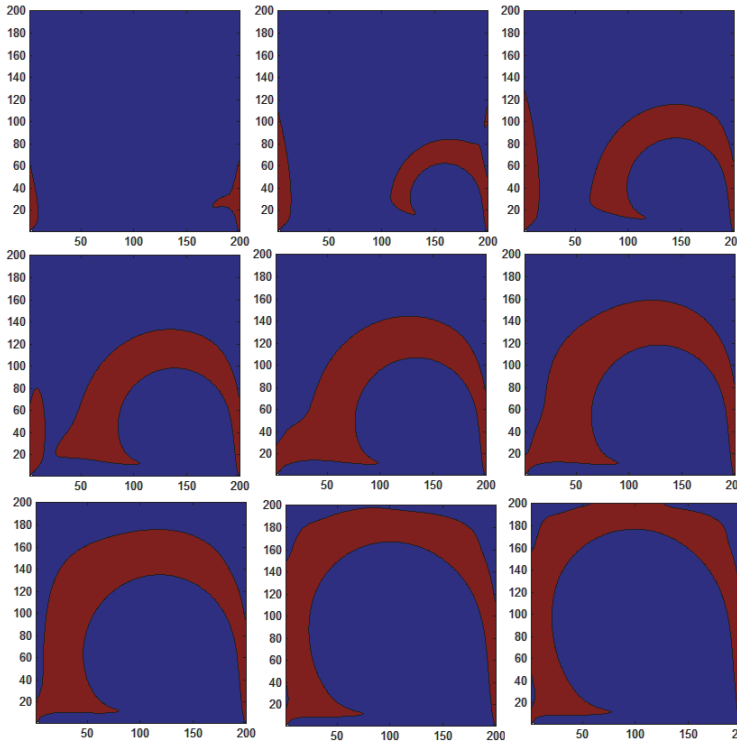


Fig. 9. Vorticity maps: Positive vorticity (Blue), Negative vorticity (Red) (200x200 nodes mesh). The nine maps were taken at 10,000, 20,000, 30,000, 40,000, 50,000, 60,000, 70,000, 80,000, 100,000 and 110,000 iterations respectively.

vortices qualitatively change during evolution, changing size and shape until the stable state configuration is reached shown in Fig.3(b).

It is worth to notice that vorticity maps for Re 1,000 and Re 10,000 are topologically very different. For Re 1,000 no interaction between positive and negative vorticity is presented but for Re 10,000 interaction is presented since the beginning of evolution until the steady state and in the steady state itself because what causes the flow periodicity is the interaction of positive and negative vortices on the corners of the cavity.

9. Vortex feeding mechanisms

Cavity flow is a phenomenon characterized by a continuous vorticity injection to the system induced by the moving wall. The vorticity arises because the no-slip condition (viscous fluid) creating an impulse of vorticity that is transported into the cavity by advection or diffusion Eq.(1). As seen since the beginning the vorticity transport equation is divided in a diffusive term $\nu \nabla^2 \omega \approx \frac{1}{Re} \nabla^2 \omega$ and in an advective term $[\nabla \omega] \cdot v$. At the beginning of the flow evolution the vorticity input is transported from the wall purely by diffusion but as the flow evolves both terms of the vorticity transport equation start to have different weights, being the diffusive term the most sensitive to Re number variations.

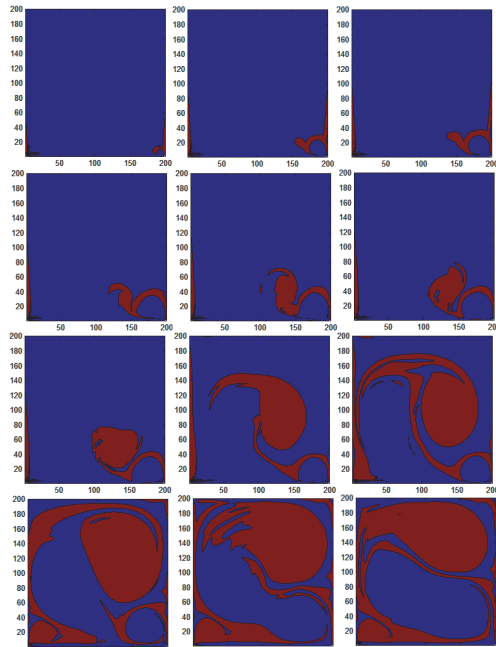


Fig. 10. Vorticity maps: Positive vorticity (**Blue**), Negative vorticity(**Red**) (200x200 nodes mesh). The twelve maps were taken from 10,000 to 60,000 iterations.

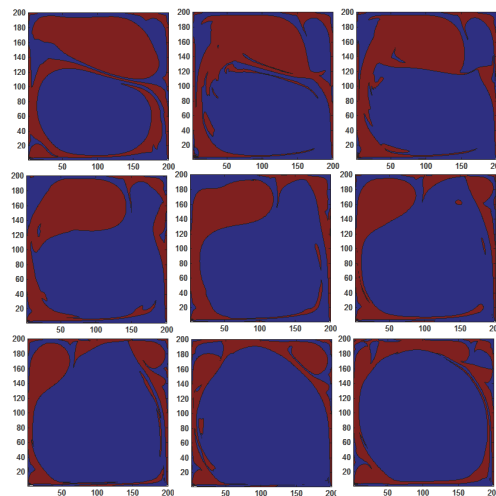


Fig. 11. Vorticity maps: Positive vorticity (**Blue**), Negative vorticity(**Red**) (200x200 nodes mesh). The nine maps were taken from 60,000 to 110,000 iterations.

Definition 0.3. A *vorticity channel* is a boundary layer, coming from a wall, that feeds and creates vortex.

9.1 Channel creation and some other characteristics

Channel creation is derived from two different phenomena: First is the energy transformation that occurs in the wall because the system continually transforms translational energy into rotational energy. Secondly a vortex whatever its sign is creates a channel of opposite sign. In order to understand the latter suppose a positive vortex near a wall. The vortex makes the particles that lie between it and the wall start spinning or *rotate*, due to viscosity, in the opposite direction causing a vorticity input - in this case negative - to the system.

There are three important features on the channels. The first and most important is that the channels transport vorticity from the walls inside the cavity and also diffuse vorticity along the route to nearby channels in proportion to the existing vorticity gradient. Secondly a positive channel always wraps a negative vortex and a negative channel always wraps a positive vortex. And finally channel thickness is function of the Re number.

9.2 Channel study for Re 1,000

- **Channel creation:** The transient is shown in Fig.9. Since the beginning there is a feeding channel from the right wall that grows merging in a left wall channel. It is worth noticing that the channel wraps the positive vortex during evolution (Fig.12(a)) but never interacts with it.
- **Channel characteristics:** In Fig.9 can be observed that the feeding channels are thick. This is due to the fact the diffusive term of the transport equation is big enough to let vorticity be spread within the fluid apart from being transported.

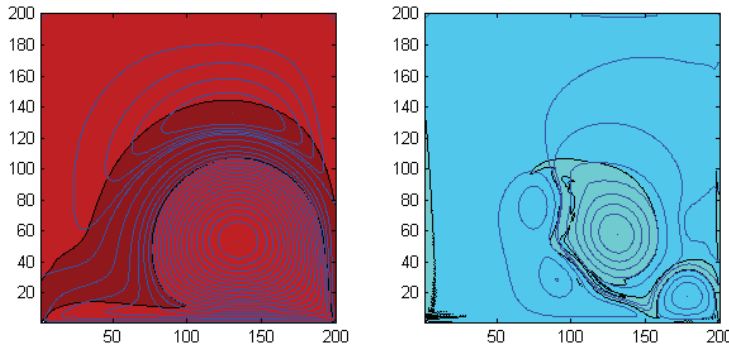
9.3 Channel study for Re 10,000

Before studying the channels it is worth to clarify that in Fig.10 and 11 channels are the thin red "tubes" and the color patches are formed vortices which are fed by channels.

- **Channel creation:** In the transient shown in Fig.10 can be seen since the beginning the appearance of a feeding channel coming from the right wall, but unlike the Re 1,000 transient, it begins to feed a vortex (sixth square of transient Fig.10) that grows inside the cavity. This vortex has the ability to interact in different ways (Fig.10 and 11) with the positive vortex that eventually will take the cavity. What is interesting about the vortex interaction, apart from the different forms that arise in the transient, is that the latter vortex has as many vorticity as the positive one, allowing them to interact in many ways. This interaction is able to produce a configuration seen in the deep cavity steady state where both vortices occupy the cavity without cornering each other but highly unstable (twelfth square Fig.10). This occurs because the diffusive term of the transport equation has less weight, allowing to concentrate vorticity without being spread across the cavity, which is the case for Re 1,000. It is also important to mention that for Re 10,000 negative channel wraps positive vortex and vice versa (Fig.12(b)) as happens for Re 1,000.
- **Channel characteristics:** Unlike Re 1,000 channels the thickness of Re 10,000 channels are smaller, due to the diffusive low weight term in the vorticity transport equation.

10. Circulation study for different Re numbers

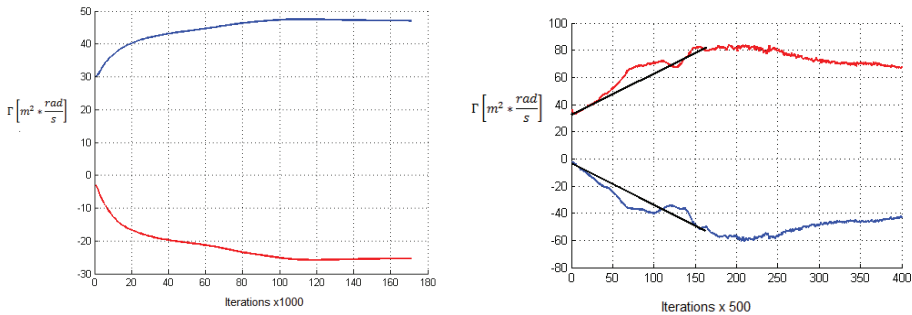
In order to understand more about what is happening with the vorticity of the system was decided to study the circulation behavior. The circulation is defined as $\Gamma = \int \omega dA$. An interesting aspect of the circulation is that, although it must be constant in the system over



(a) Superposition for Re 1,000 during evolution. (b) Superposition for Re 10,000 during evolution.

Fig. 12. Stream-function contour lines (blue) and vorticity maps superposition. *Left* Positive vorticity (Dark red) Negative vorticity (Light red), *right* Positive vorticity (Aqua) Negative vorticity (Aquamarine).

time according to Kelvins theorem, it can be split into positive and negative values. As seen, the prime characteristic of the flow is the positive vorticity input from the lower wall deriving in positive circulation diferential.



(a) Square cavity circulation evolution. Positive Γ (Red) and negative Γ (Blue) (b) Square cavity circulation evolution. Positive Γ (Red) and negative Γ (Blue)

Fig. 13. *Left* Square cavity circulation for Re 1,000. *Right* Square cavity circulation for Re 10,000.

In both figures can be seen that the flow reaches a maximum around the 100.000 iterations when the positive vortex has taken all the cavity (Fig.3.1 and 3.2). What is interesting are the values of circulation that are achieved for each value of Re (Table.1).

Several important things are shown in Table.1. First the circulation increase for Re 10,000 is three times bigger than Re 1,000 i.e. $\Delta\Gamma_{Re1,000} = 18.36$ compared with $\Delta\Gamma_{Re10,000} = 50.5$. Latter observation means that as the viscosity decreases the system is able to accumulate more circulation. Finally, system circulation is consistent whit Kelvin’s theorem even though

	Re 1,000		Re 10,000	
	max	min	max	min
Positive Γ	48.52	30.16	83.5	33
Negative Γ	23.8	3.09	60.67	2.55

Table 1. Circulation values comparison

positive circulation increases negative circulation increases too maintaining a circulation differential of about 30 throughout evolution (Fig.13 a and b).

10.1 Why does the circulation fall after rising for Re 10,000?

It can be seen in Fig.13 that for Re 1,000 positive (negative) circulation reaches its maximum (minimum) and stabilizes around latter value, which fails to happen for Re 10,000 where circulation peaks at a "constant" rate but after reaching maximum starts decreasing. The motivation of this subsection is to explain why this change of slope took place (Fig.13(b)) and try to predict it analytically because it was observed that for different Re numbers the same change in slope occurs reaching different values of maximum circulation.

In order to understand this phenomena recall that the cavity has vorticity channels that feed and remove vorticity into and out the system affecting the circulation values. Having mentioned this observation and due to the low weight diffusive term has in the transport equation, $\frac{d\Gamma}{dt}$ is calculated according to the gradient of vorticity on the walls (18), which is the same as quantifying how much vorticity is entering and leaving the system.

$$\frac{d\Gamma}{dt} = \int_{\partial\Omega} \nabla w \cdot n ds \quad (18)$$

After plotting Eq.(18) through time it was found that $\frac{d\Gamma}{dt}$ was constant until 100.000 iterations, which is when the positive vortex has taken the cavity, reflecting the "constant" increase of circulation Fig.13(b). More interesting and contradicting the assumption made was that $\frac{d\Gamma}{dt}$ does not fall after the 100,000 iterations, situation that was expected since a slope change was observed in the Fig.13(b) after 100,000 iterations. Willing to explain this behavior the following hypothesis was proposed:

Assume a unit of vorticity entering to the system Fig.14.

This unit feeds the positive vortex. The vortex is not able to accumulate more circulation, as it has reached the steady state configuration therefore this unit of vorticity has to be "passed" to each of the corner vortices, which also are not able to accumulate more circulation having to pass it to the upper wall and balancing the accounts of vorticity on the walls. Since the way of calculating the $\frac{d\Gamma}{dt}$ is based on counting how much vorticity is entering and leaving the system the circulation loss between vortice was not quantified, explaining why $\frac{d\Gamma}{dt}$ remains constant.

11. Discussion and open questions

Through the present study was seen that viscosity is who decides if vorticity can travel without diffusing itself, curl up, accumulate and form vortices. In a word is who decides how will the flow evolves. The interesting thing is that after being so influential in the flow pattern everything was in vain because the configuration of steady state regardless of the number Re (100-10,000) is very similar, a positive vortex has taken the cavity and two or three vortices were cornered. Latter observation trigger on of the most important remaining open

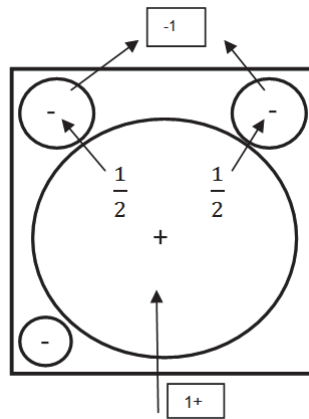


Fig. 14. Vortex diagram

question for future studies, why after so many turns, so many games, the flow reaches the same configuration?. It is believed that a study from game theory involving two players, "positive vorticity" and "negative vorticity" who fight a common good, the space of the cavity, can clarify why the positive vortex end taking the whole cavity behavior that is not achieved in the deep cavity scenario. Along with the latter question, other two remain open. First would be to answer, why the configuration of stable state coincide when the system can not store more vorticity and secondly why can not be achieved by the square cavity the configuration that occurs to happen in the deep cavity between the positive and negative knowing before that during the flow evolution this configuration is achieved but then lost.

12. Conclusions

Among all the results it was clearly seen the power and the preponderance of the viscosity in the evolution of cavity flows, how it affects the dynamics of vortices, transient or evolution of the flow and the accumulation or dissipation of energy. Was also observed the periodicity of steady-state flow for both cavities being the first to show a complete cycle of periodicity in the deep one. In conjunction with the above the feeding channels definition were proposed which were key to understanding the transient flow. It was also proposed a transient "Bifurcation" since they vary dramatically as the number of Re is increased. This "Bifurcation" is mainly due to viscosity.

As for deep cavities in addition to finding the periodicity of the flow for Re 8.000 it was presented an interesting phenomenon observed in Sec.5.1.2 where a *quasi cavity* is created that replicates cavity flow transients that occur before reaching steady state in a square cavity. Finally, the numerical method implemented, based on the equations presented in (Chen, 2009; Chen et al., 2008), was a great help for the simplicity of its programming and its primitive variable, vorticity, was central in the study.

13. Acknowledgments

The authors are very grateful to Dr.Omar López for helpful discussions and advice.

14. References

- Auteri, F., Parolini, N. & Quartapelle, L. (2002). Numerical investigation on the stability of singular driven cavity flow, *Journal of Computational Physics* 183: 1–25.
- Chen, S. (2009). A large-eddy-based lattice boltzmann model for turbulent flow simulation, *Applied mathematics and computation* .
- Chen, S. & Doolen, G. (1998). Lattice boltzmann method for fluid flows, *Annu. Rev. Fluid Mech.* pp. 329–364.
- Chen, S., Toelke, J. & Krafczyk, M. (2008). A new method for the numerical solution of vorticity- Ψ streamfunction formulations, *Computational methods Appl. Mech. Engrg.* (198): 367–376.
- Durbin, P. & Petersson-Rief, B. (2010). *Statistical theory and modeling for turbulent flow*, Wiley, UK.
- Goyon, O. (1995). High-reynolds number solutions of navier-stokes equations using incremental unknowns, *Computer Methods in Applied Mechanics and Engineering* 130: 319–335.
- Gustafson, K. E. (1991). Four principles of vortex motion, *Society for Industrial and Applied Mathematics* pp. 95–141.
- Hou, S., Q.Zou & S.Chen (1995). Simulation of cavity flow by the lattice boltzmann method, *Computational Physics* (118): 329–347.
- Patil, D., Lakshmisha, K. & Rogg, B. (2006). Lattice boltzmann simulation of lid-driven flow in deep cavities, *Computers and Fluids* 35: 1116–1125.
- Pope, S. (2000). *Turbulent Flows*, second edn, Cambridge University Press, Cambridge U.K.
- Texeira, C. (1998). Incorporation turbulence model into the lattice boltzmann method, *Internationa Journal of modern Physics* (8): 1159–1175.
- Toro, J. (2006). *Dinámica de fluidos con introducción a la teoría de turbulencia*, Publicaciones Uniandes, Bogotá.

Elasto-Hydrodynamics of Quasicrystals and Its Applications

Tian You Fan¹ and Zhi Yi Tang²

¹*Department of Physics, Beijing Institute of Technology, Beijing*

²*Southwest Jiaotong University Hope College, Nanchong, Sichuan
China*

1. Introduction

Quasicrystal as a new structure of solids as well as a new material, has been studied over twenty five years. The elasticity and defects play a central role in field of mechanical behaviour of the material, see e.g. Fan [1]. Different from crystals and conventional engineering materials, quasicrystals have two different displacement fields: phonon field $u(u_1, u_2, u_3)$ and phason field $w(w_1, w_2, w_3)$, which is a new degree of freedom to condensed matter physics as well as continuum mechanics, this leads to two strain tensors such as

$$\varepsilon_{ij} = \frac{1}{2} \left(\frac{\partial u_i}{\partial x_j} + \frac{\partial u_j}{\partial x_i} \right), w_{ij} = \frac{\partial w_i}{\partial x_j} \quad (1)$$

We call the first of equation (1) as phonon strain tensor, the second as phason strain tensor, respectively. The corresponding stress tensor is σ_{ij} and H_{ij} .

The constitutive law is the so-called generalized Hooke's law as follows

$$\begin{aligned} \sigma_{ij} &= C_{ijkl} \varepsilon_{kl} + R_{ijkl} w_{kl} \\ H_{ij} &= K_{ijkl} w_{kl} + R_{klij} \varepsilon_{kl} \end{aligned} \quad (2)$$

in which C_{ijkl} denotes the phonon elastic tensor, K_{ijkl} the phason one, and R_{ijkl} the phonon-phason coupling one, respectively. It is evident that the appearance of the new degree freedom yields a great challenge to the continuum mechanics.

In the dynamic process of quasicrystals problem presents further complexity. According to the point of view of Lubensky et al. [2,3], phonon represents wave propagation, while phason represents diffusion in the dynamic process. Following the argument of Lubensky et al., Rochal and Lorman [4] and Fan [1,5] put forward the equations of motion of quasicrystals as follows

$$\rho \frac{\partial^2 u_i}{\partial t^2} = \frac{\partial \sigma_{ij}}{\partial x_j} \quad (3)$$

$$\kappa \frac{\partial w_i}{\partial t} = \frac{\partial H_{ij}}{\partial x_j} \quad (4)$$

Equation (3) is the equation of motion of conventional elastodynamics, and equation (4) is the linearized equation of hydrodynamics of Lubensky et al., so equations (3), (4) are elasto-hydrodynamic equations of quasicrystals.

The equations (1)-(4) are the basis of dynamic analysis of quasicrystalline material.

2. The elasto-hydrodynamics of two-dimensional decagonal quasicrystals and application to dynamic fracture

2.1 Statement of formulation and sample problem

Among over 200 quasicrystals observed to date, there are over 70 two-dimensional decagonal quasicrystals, so this kind of solid phases play an important role in the material. For simplicity, here only point group 10mm two-dimensional decagonal quasicrystals will be considered. We denote the periodic direction as the z axis and the quasiperiodic plane as the $x-y$ plane. Assume that a Griffith crack in the solid along the periodic direction, i.e., the z axis. It is obvious that elastic field induced by a uniform tensile stress at upper and lower surfaces of the specimen is independent of z , so $\partial(\)/\partial z = 0$. In this case, the stress-strain relations are reduced to

$$\begin{aligned} \sigma_{xx} &= L(\varepsilon_{xx} + \varepsilon_{yy}) + 2M\varepsilon_{xx} + R(w_{xx} + w_{yy}) \\ \sigma_{yy} &= L(\varepsilon_{xx} + \varepsilon_{yy}) + 2M\varepsilon_{yy} - R(w_{xx} + w_{yy}) \\ \sigma_{xy} &= \sigma_{yx} = 2M\varepsilon_{xy} + R(w_{yx} - w_{xy}) \\ H_{xx} &= K_1 w_{xx} + K_2 w_{yy} + R(\varepsilon_{xx} - \varepsilon_{yy}) \\ H_{yy} &= K_1 w_{yy} + K_2 w_{xx} + R(\varepsilon_{xx} - \varepsilon_{yy}) \\ H_{xy} &= K_1 w_{xy} - K_2 w_{yx} - 2R\varepsilon_{xy} \\ H_{yx} &= K_1 w_{yx} - K_2 w_{xy} + 2R\varepsilon_{xy} \end{aligned} \quad (5)$$

where $L = C_{12}$, $M = (C_{11} - C_{12})/2$ are the phonon elastic constants, K_1 and K_2 are the phason elastic constants, R phason-phonon coupling elastic constant, respectively.

Substituting equations (5) into equations (3), (4) we obtain the equations of motion of decagonal quasicrystals as following:

$$\begin{aligned} \frac{\partial^2 u_x}{\partial t^2} &= c_1^2 \frac{\partial^2 u_x}{\partial x^2} + (c_1^2 - c_2^2) \frac{\partial^2 u_y}{\partial x \partial y} + c_2^2 \frac{\partial^2 u_x}{\partial y^2} + c_3^2 \left(\frac{\partial^2 w_x}{\partial x^2} + 2 \frac{\partial^2 w_y}{\partial x \partial y} - \frac{\partial^2 w_x}{\partial y^2} \right) \\ \frac{\partial^2 u_y}{\partial t^2} &= c_2^2 \frac{\partial^2 u_y}{\partial x^2} + (c_1^2 - c_2^2) \frac{\partial^2 u_x}{\partial x \partial y} + c_1^2 \frac{\partial^2 u_y}{\partial y^2} + c_3^2 \left(\frac{\partial^2 w_y}{\partial x^2} - 2 \frac{\partial^2 w_x}{\partial x \partial y} - \frac{\partial^2 w_y}{\partial y^2} \right) \\ \frac{\partial w_x}{\partial t} &= d_1^2 \left(\frac{\partial^2 w_x}{\partial x^2} + \frac{\partial^2 w_x}{\partial y^2} \right) + d_2^2 \left(\frac{\partial^2 u_x}{\partial x^2} - 2 \frac{\partial^2 u_y}{\partial x \partial y} - \frac{\partial^2 u_x}{\partial y^2} \right) \\ \frac{\partial w_y}{\partial t} &= d_1^2 \left(\frac{\partial^2 w_y}{\partial x^2} + \frac{\partial^2 w_y}{\partial y^2} \right) + d_2^2 \left(\frac{\partial^2 u_y}{\partial x^2} + 2 \frac{\partial^2 u_x}{\partial x \partial y} - \frac{\partial^2 u_y}{\partial y^2} \right) \end{aligned} \quad (6)$$

where

$$c_1 = \sqrt{\frac{L+2M}{\rho}}, c_2 = \sqrt{\frac{M}{\rho}}, c_3 = \sqrt{\frac{R}{\rho}}, d_1 = \sqrt{\frac{K_1}{\kappa}}, d_2 = \sqrt{\frac{R}{\kappa}}$$

Note that constants c_1, c_2 and c_3 have the meaning of elastic wave speeds, while d_1 and d_2 do not represent wave speed, and d_1^2 and d_2^2 are diffusive coefficients in physical meaning.

A decagonal quasicrystal with a crack is shown in Fig.1. It is a rectangular specimen with a central crack of length $2a(t)$ subjected to a dynamic or static tensile stress at its edges ED and FC, in which $a(t)$ represents the crack length being a function of time, and for dynamic initiation of crack growth, the crack is stable, so $a(t) = a_0 = \text{constant}$, for fast crack propagation, $a(t)$ varies with time. At first we consider dynamic initiation of crack growth, then study crack fast propagation. Due to the symmetry of the specimen only the upper right quarter is considered.

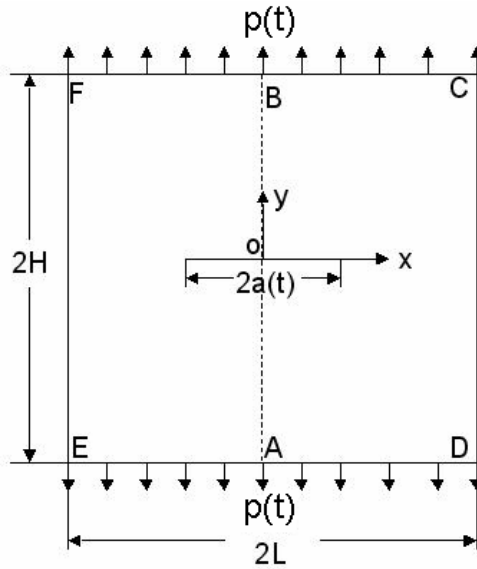


Fig. 1. The specimen with a central crack

Referring to the upper right part and considering a fix grips case, the following boundary conditions should be satisfied:

$$\begin{aligned}
 &u_x = 0, \sigma_{yx} = 0, w_x = 0, H_{yx} = 0 && \text{on } x = 0 \text{ for } 0 \leq y \leq H \\
 &\sigma_{xx} = 0, \sigma_{yx} = 0, H_{xx} = 0, H_{yx} = 0 && \text{on } x = L \text{ for } 0 \leq y \leq H \\
 &\sigma_{yy} = p(t), \sigma_{xy} = 0, H_{yy} = 0, H_{xy} = 0 && \text{on } y = H \text{ for } 0 \leq x \leq L \\
 &\sigma_{yy} = 0, \sigma_{xy} = 0, H_{yy} = 0, H_{xy} = 0 && \text{on } y = 0 \text{ for } 0 \leq x \leq a(t) \\
 &u_y = 0, \sigma_{xy} = 0, w_y = 0, H_{xy} = 0 && \text{on } y = 0 \text{ for } a(t) \leq x \leq L
 \end{aligned} \tag{7}$$

in which $p(t) = p_0 f(t)$ is a dynamic load if $f(t)$ varies with time, otherwise it is a static load (i.e., if $f(t) = \text{const}$), and $p_0 = \text{const}$ with the stress dimension. .

The initial conditions are

$$\begin{aligned} u_x(x, y, t)|_{t=0} &= 0 & u_y(x, y, t)|_{t=0} &= 0 \\ w_x(x, y, t)|_{t=0} &= 0 & w_y(x, y, t)|_{t=0} &= 0 \\ \frac{\partial u_x(x, y, t)}{\partial t}|_{t=0} &= 0 & \frac{\partial u_y(x, y, t)}{\partial t}|_{t=0} &= 0 \end{aligned} \quad (8)$$

For implementation of finite difference all field variables in governing equations (6) and boundary-initial conditions (7), (8) must be expressed by displacements and their derivatives. This can be done through the constitutive equations (2). The detail of the finite difference scheme is omitted here but can be referred to Fan [1].

For the related parameters in this section, the experimentally determined mass density for decagonal Al-Ni-Co quasicrystal $\rho = 4.186 \times 10^{-3} \text{ g} \cdot \text{mm}^{-3}$ is used and phonon elastic moduli are $C_{11} = 2.3433 \times 10^{12} \text{ dyn/cm}^2$, $C_{12} = 0.5741 \times 10^{12} \text{ dyn/cm}^2$ ($10^{10} \text{ dyn/cm}^2 = \text{GPa}$) which are obtained by resonant ultrasound spectroscopy, refer to Chernikov et al [6], we have also chosen phason elastic constants $K_1 = 1.22 \times 10^{12} \text{ dyn/cm}^2$ and $K_2 = 0.24 \times 10^{12} \text{ dyn/cm}^2$ ($10^{10} \text{ dyn/cm}^2 = \text{GPa}$) estimated by Monto-Carlo simulation given by Jeong and Steinhardt [7] and $\Gamma_w = 1/\kappa = 4.8 \times 10^{-19} \text{ m}^3 \cdot \text{s/kg} = 4.8 \times 10^{-10} \text{ cm}^3 \cdot \mu\text{s/g}$ which measured by de Boussieu and collected by Walz in his master thesis [8]. The coupling constant R has been measured for some special cases recently, see Chapter 6 and Chapter 9 of monograph written by Fan [1] respectively. In computation we take $R/M = 0.01$ for coupling case corresponding to quasicrystals, and $R/M = 0$ for decoupled case which corresponds to crystals.

2.2 Examination on the physical model

In order to verify the correctness of the suggested model and the numerical simulation, we first explore the specimen without a crack. We know that there are the fundamental solutions characterizing time variation natures based on wave propagation of phonon field and on motion of diffusion of phason, respectively according to mathematical physics

$$\begin{cases} u \sim e^{i\omega(t-x/c)} \\ w \sim \frac{1}{\sqrt{t-t_0}} e^{-(x-x_0)^2/\Gamma_w(t-t_0)} \end{cases} \quad (9)$$

where ω is a frequency and c a speed of the wave, t the time and t_0 a special value of t , x the distance, x_0 a special value of x , and Γ_w the kinetic coefficient of phason defined previously.

Comparison results are shown in Fig.2 (a-c), in which the solid line represents the numerical solution of quasicrystals and the dotted line represents fundamental solution given by formulas (9). From Fig. 2(a) and (b) we can see that both displacement components of phonon field are in excellent agreement to the fundament solutions of mathematical physics. However, there are some differences because the phonon field is influenced by phason field

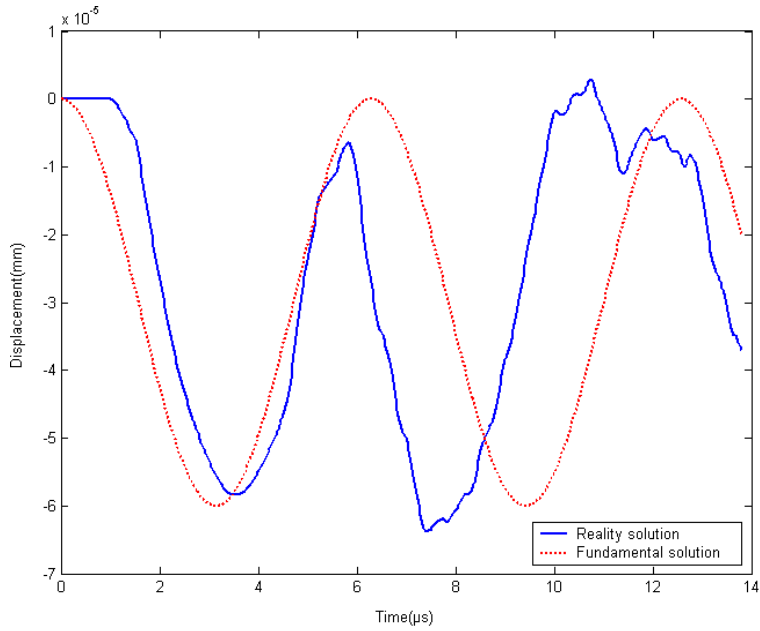


Fig. 2. (a) Displacement component of phonon field u_x versus time

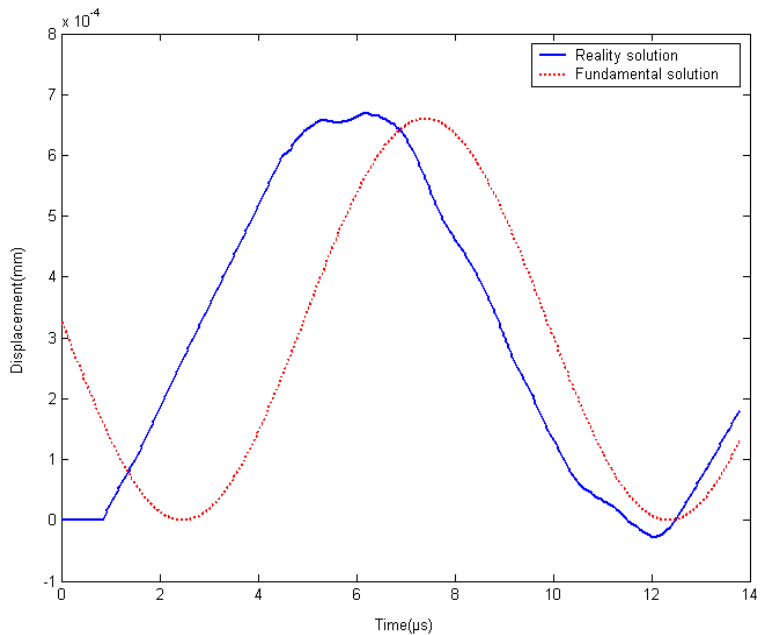


Fig. 2. (b) Displacement component of phonon field u_y versus time

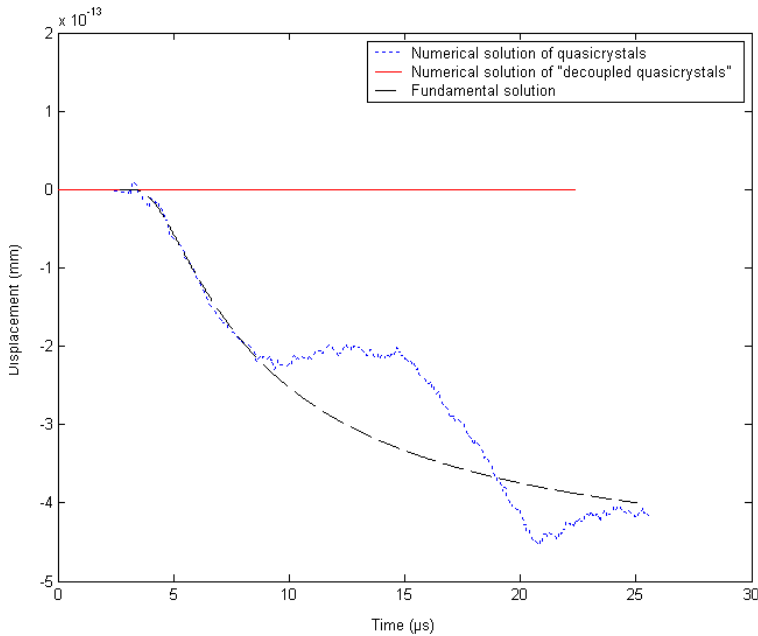


Fig. 2. (c) Displacement component of phason field w_x versus time

and the phonon-phason coupling effect. From Fig. 2(c), in the phason field we find that the phason mode presents diffusive nature in the overall tendency, but because of influence of the phonon and phonon-phason coupling, it can also have some characters of fluctuation. So the model describes the dynamic behaviour of phonon field and phason field in deed. This also shows the mathematical modeling of the present work is valid.

2.3 Testing the scheme and the computer program

2.3.1 Stability of the scheme

The stability of the scheme is the core problem of finite difference method which depends upon the choice of parameter $\alpha = c_1 \tau / h$, which is the ratio between time step and space step substantively. The choice is related to the ratio c_1 / c_2 , i.e., the ratio between speeds of elastic longitudinal and transverse waves of the phonon field. To determine the upper bound for the ration to guarantee the stability, according to our computational practice and considering the experiences of computations for conventional materials, we choose $\alpha = 0.8$ in all cases and results are stable.

2.3.2 Accuracy test

The stability is only a necessary condition for successful computation. We must check the accuracy of the numerical solution. This can be realized through some comparison with some well-known classical solutions (analytic as well as numerical solutions) of conventional fracture mechanics. For this purpose the material constants in the computation are chosen as $c_1 = 7.34 \text{ mm}/\mu\text{s}$, $c_2 = 3.92 \text{ mm}/\mu\text{s}$ and $\rho = 5 \times 10^3 \text{ kg}/\text{m}^3$, $p_0 = 1 \text{ MPa}$ which

are the same with those given in classical references for conventional fracture dynamics, discussed in Fan's monograph [1] in detail. At first the comparison to the classical exact analytic solution is carried out, in this case we put $w_x = w_y = 0$ (i.e., $K_1 = K_2 = R = 0$) for the numerical solution. The comparison has been done with the key physical quantity – dynamic stress intensity factor, which is defined by

$$K_I(t) = \lim_{x \rightarrow a_0} \sqrt{\pi(x - a_0)} \sigma_{yy}(x, 0, t) \quad (10)$$

The normalized dynamic stress intensity factor can be denoted as $K_I(t) / K_I^{static}$, in which K_I^{static} is the corresponding static stress intensity factor, whose value here is taken as $\sqrt{\pi a_0} p_0$. For the dynamic initiation of crack growth in classical fracture dynamics there is the only exact analytic solution – the Maue's solution (refer to Fan's monograph [1]), but the configuration of whose specimen is quite different from that of our specimen. Maue studied a semi-infinite crack in an infinite body, and subjected to a Heaviside impact loading at the crack surface. While our specimen is a finite size rectangular plate with a central crack, and the applied stress is at the external boundary of the specimen. Generally the Maue's model cannot describe the interaction between wave and external boundary. However, consider a very short time interval, i.e., during the period between the stress wave from the external boundary arriving at the crack tip (this time is denoted by t_1) and before the reflecting by external boundary stress wave emanating from the crack tip in the finite size specimen (the time is marked as t_2). During this special very short time interval our specimen can be seen as an "infinite specimen". The comparison given by Fig. 3 shows the numerical results are in excellent agreement with those of Maue's solution within the short interval in which the solution is valid.

Our solution corresponding to case of $w_x = w_y = 0$ is also compared with numerical solutions of conventional crystals, e.g. Murti's solution and Chen's solutions (refer to Fan [1] and Zhu and Fan [9] for the detail), which are also shown in Fig. 3, it is evident, our solution presents very high precise.

2.3.3 Influence of mesh size (space step)

The mesh size or the space step of the algorithm can influence the computational accuracy too. To check the accuracy of the algorithm we take different space steps shown in Table 1, which indicates if $h = a_0 / 40$ the accuracy is good enough. The check is carried out through static solution, because the static crack problem in infinite body of decagonal quasicrystals has exact solution given in Chapter 8 of monograph given by Fan [1], and the normalized static intensity factor is equal to unit. In the static case, there is no wave propagation effect, $L / a_0 \geq 3, H / a_0 \geq 3$ the effect of boundary to solution is very weak, and for our present specimen $L / a_0 \geq 4, H / a_0 \geq 8$, which may be seen as an infinite specimen, so the normalized static stress intensity factor is approximately but with highly precise equal to unit. The table shows that the algorithm is with a quite highly accuracy when $h = a_0 / 40$.

2.4 Results of dynamic initiation of crack growth

The dynamic crack problem presents two "phases" in the process: the dynamic initiation of crack growth and fast crack propagation. In the phase of dynamic initiation of crack growth, the length of the crack is constant, assuming $a(t) = a_0$. The specimen with stationary crack

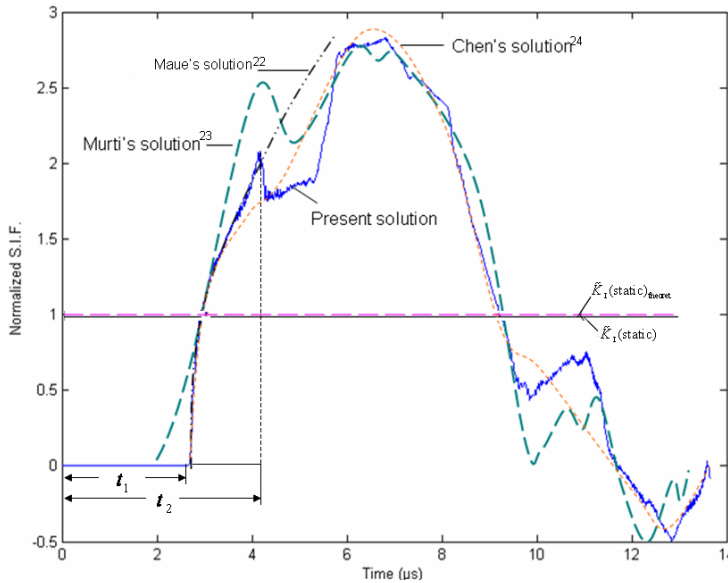


Fig. 3. Comparison of the present solution with analytic solution and other numerical solution for conventional structural materials given by other authors

H	$a_0/10$	$a_0/15$	$a_0/20$	$a_0/30$	$a_0/40$
K	0.9259	0.94829	0.9229	0.97723	0.99516
Errors	7.410%	5.171%	3.771%	2.277%	0.484%

Table 1. The normalized static S.I.F. of quasicrystals for different space steps

that are subjected to a rapidly varying applied load $p(t) = p_0 f(t)$, where p_0 is a constant with stress dimension and $f(t)$ is taken as the Heaviside function. It is well known the coupling effect between phonon and phason is very important, which reveals the distinctive physical properties including mechanical properties, and makes quasicrystals distinguish the periodic crystals. So studying the coupling effect is significant.

The dynamic stress intensity factor $K_1(t)$ for quasicrystals has the same definition given by equation (10), whose numerical results are plotted in Fig. 4, where the normalized dynamics stress intensity factor $K_1(t) / \sqrt{\pi a_0} p_0$ is used. There are two curves in the Fig. 4, one represents quasicrystal, i.e., $R/M = 0.01$, the other describes periodic crystals corresponding to $R/M = 0$, the two curves of the Fig. 4 are apparently different, though they are similar to some extends. Because of the phonon-phason coupling effect, the mechanical properties of the quasicrystals are obviously different from the classical crystals. Thus, the coupling effect plays an important role.

In Fig. 4, t_0 represents the time that the wave from the external boundary propagates to the crack surface, in which $t_0 = 2.6735 \mu s$. So the velocity of the wave propagation is $v_0 = H/t_0 = 7.4807 \text{ km/s}$, which is just equal to the longitudinal wave speed $c_1 = \sqrt{(L+2M)/\rho}$. This indicates that for the complex system of wave propagation-motion of diffusion coupling, the phonon wave propagation presents dominating role.

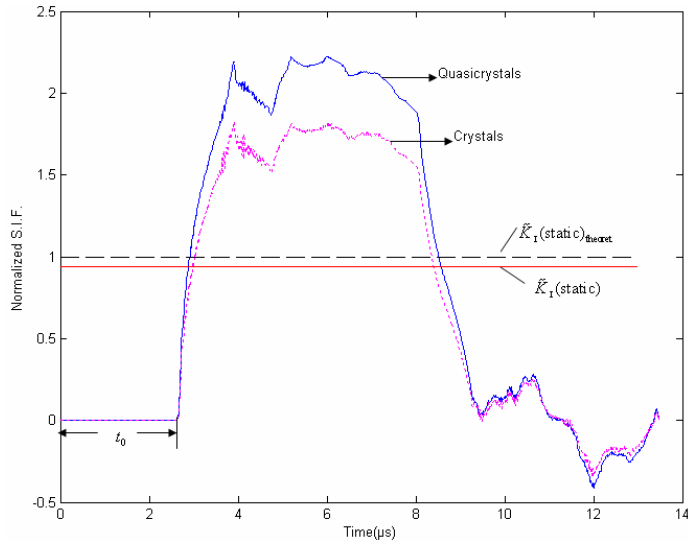


Fig. 4. Normalized dynamics stress intensity factor (DSIF) versus time

There are some oscillations of values of the stress intensity factor in the figure. These oscillations characterize the reflection and diffraction between waves coming from the crack surface and the specimen boundary surfaces. The oscillations are influenced by the material constants and specimen geometry including the shape and size very much.

3. Elasto-/hydro-dynamics and applications to fracture dynamics of three-dimensional icosahedral quasicrystals

3.1 Basic equations, boundary and initial conditions

There are over 50% icosahedral quasicrystals among observed the quasicrystals to date, this shows this kind of systems in the material presents the most importance. Within icosahedral quasicrystals, the icosahedral Al-Pd-Mn quasicrystals are concerned in particular by researchers, for which especially a rich set of experimental data for elastic constants accumulated so far, this is useful to the computational practice. So we focus on the elasto-hydrodynamics of icosahedral Al-Pd-Mn quasicrystals here. From the previous section we have known there are lack of measured data for phason elastic constants, the computation has to take some factors which are obtained by Monte Carlo simulation, this makes some undetermined factors for computational results for decagonal quasicrystals. This shows the discussion on icosahedral quasicrystals is more necessary, and the formalism and numerical results are presented in the following.

If considering only the plane problem, especially for the crack problems, there are much of similarities with those discussed in the previous section. We present herein only the part that are different.

For the plane problem, i.e.,

$$\frac{\partial(\)}{\partial z} = 0 \quad (11)$$

The linearized elasto-hydrodynamics of icosahedral quasicrystals have non-zero displacements u_z, w_z apart from u_x, u_y, w_x, w_y , so in the strain tensors

$$\varepsilon_{ij} = \frac{1}{2} \left(\frac{\partial u_i}{\partial x_j} + \frac{\partial u_j}{\partial x_i} \right) \quad w_{ij} = \frac{\partial w_i}{\partial x_j}$$

it increases some non-zero components compared with those in two-dimensional quasicrystals. In connecting with this, in the stress tensors, the non-zero components increase too relatively to two-dimensional ones. With these reasons, the stress-strain relation presents different nature with that of decagonal quasicrystals though the generalized Hooke's law has the same form with that in one- and two-dimensional quasicrystals, i.e.,

$$\sigma_{ij} = C_{ijkl} \varepsilon_{kl} + R_{ijkl} w_{kl} \quad H_{ij} = R_{kl ij} \varepsilon_{kl} + K_{ijkl} w_{kl}$$

In particular the elastic constants are quite different from those discussed in the previous sections, in which the phonon elastic constants can be expressed such as

$$C_{ijkl} = \lambda \delta_{ij} \delta_{kl} + \mu (\delta_{ik} \delta_{jl} + \delta_{il} \delta_{jk}) \quad (12)$$

and the phason elastic constant matrix [K] and phonon-phason coupling elastic one [R] are defined by the formulas of Fan's monograph [1], which are not listed here again.

Substituting these non-zero stress components into the equations of motion

$$\rho \frac{\partial^2 u_i}{\partial t^2} = \frac{\partial \sigma_{ij}}{\partial x_j}, \quad \kappa \frac{\partial w_i}{\partial t} = \frac{\partial H_{ij}}{\partial x_j} \quad (13)$$

and through the generalized Hooke's law and strain-displacement relation we obtain the final dynamic equations as follows

$$\begin{aligned} \frac{\partial^2 u_x}{\partial t^2} + \theta \frac{\partial u_x}{\partial t} &= c_1^2 \frac{\partial^2 u_x}{\partial x^2} + (c_1^2 - c_2^2) \frac{\partial^2 u_y}{\partial x \partial y} + c_2^2 \frac{\partial^2 u_x}{\partial y^2} + c_3^2 \left(\frac{\partial^2 w_x}{\partial x^2} + 2 \frac{\partial^2 w_y}{\partial x \partial y} - \frac{\partial^2 w_x}{\partial y^2} \right) \\ \frac{\partial^2 u_y}{\partial t^2} + \theta \frac{\partial u_y}{\partial t} &= c_2^2 \frac{\partial^2 u_y}{\partial x^2} + (c_1^2 - c_2^2) \frac{\partial^2 u_x}{\partial x \partial y} + c_1^2 \frac{\partial^2 u_y}{\partial y^2} + c_3^2 \left(\frac{\partial^2 w_y}{\partial x^2} - 2 \frac{\partial^2 w_x}{\partial x \partial y} - \frac{\partial^2 w_y}{\partial y^2} \right) \\ \frac{\partial^2 u_z}{\partial t^2} + \theta \frac{\partial u_z}{\partial t} &= c_2^2 \left(\frac{\partial^2}{\partial x^2} + \frac{\partial^2}{\partial y^2} \right) u_z + c_3^2 \left(\frac{\partial^2 w_x}{\partial x^2} - \frac{\partial^2 w_x}{\partial y^2} - 2 \frac{\partial^2 w_y}{\partial x \partial y} + \frac{\partial^2 w_z}{\partial x^2} + \frac{\partial^2 w_z}{\partial y^2} \right) \\ \frac{\partial w_x}{\partial t} + \theta w_x &= d_1 \left(\frac{\partial^2}{\partial x^2} + \frac{\partial^2}{\partial y^2} \right) w_x + d_2 \left(\frac{\partial^2}{\partial x^2} - \frac{\partial^2}{\partial y^2} \right) w_z + d_3 \left(\frac{\partial^2 u_x}{\partial x^2} - 2 \frac{\partial^2 u_y}{\partial x \partial y} - \frac{\partial^2 u_x}{\partial y^2} + \frac{\partial^2 u_z}{\partial x^2} - \frac{\partial^2 u_z}{\partial y^2} \right) \\ \frac{\partial w_y}{\partial t} + \theta w_y &= d_1 \left(\frac{\partial^2}{\partial x^2} + \frac{\partial^2}{\partial y^2} \right) w_y - d_2 \frac{\partial^2 w_z}{\partial x \partial y} + d_3 \left(\frac{\partial^2 u_y}{\partial x^2} + 2 \frac{\partial^2 u_x}{\partial x \partial y} - \frac{\partial^2 u_y}{\partial y^2} - 2 \frac{\partial^2 u_z}{\partial x \partial y} \right) \\ \frac{\partial w_z}{\partial t} + \theta w_z &= (d_1 - d_2) \left(\frac{\partial^2}{\partial x^2} + \frac{\partial^2}{\partial y^2} \right) w_z + d_2 \left(\frac{\partial^2 w_x}{\partial x^2} - \frac{\partial^2 w_x}{\partial y^2} - 2 \frac{\partial^2 w_y}{\partial x \partial y} \right) + d_3 \left(\frac{\partial^2}{\partial x^2} + \frac{\partial^2}{\partial y^2} \right) u_z \end{aligned} \quad (14)$$

in which

$$c_1 = \sqrt{\frac{\lambda + 2\mu}{\rho}}, c_2 = \sqrt{\frac{\mu}{\rho}}, c_3 = \sqrt{\frac{R}{\rho}}, d_1 = \frac{K_1}{\kappa}, d_2 = \frac{K_2}{\kappa}, d_3 = \frac{R}{\kappa} \tag{15}$$

note that constants c_1, c_2 and c_3 have the meaning of elastic wave speeds, while d_1, d_2 and d_3 do not represent wave speed, but are diffusive coefficients and parameter θ may be understood as a manmade damping coefficient as in the previous section.

Consider an icosahedral quasicrystal specimen with a Griffith crack shown in Fig. 1, all parameters of geometry and loading are the same with those given in the previous, but in the boundary conditions there are some different points, which are given as below

$$\begin{aligned} u_x = 0, \sigma_{yx} = 0, \sigma_{zx} = 0, w_x = 0, H_{yx} = 0, H_{zx} = 0 & \quad \text{on } x = 0 \text{ for } 0 \leq y \leq H \\ \sigma_{xx} = 0, \sigma_{yx} = 0, \sigma_{zx} = 0, H_{xx} = 0, H_{yx} = 0, H_{zx} = 0 & \quad \text{on } x = L \text{ for } 0 \leq y \leq H \\ \sigma_{yy} = p(t), \sigma_{xy} = 0, \sigma_{zy} = 0, H_{yy} = 0, H_{xy} = 0, H_{zy} = 0 & \quad \text{on } y = H \text{ for } 0 \leq x \leq L \\ \sigma_{yy} = 0, \sigma_{xy} = 0, \sigma_{zy} = 0, H_{yy} = 0, H_{xy} = 0, H_{zy} = 0 & \quad \text{on } y = 0 \text{ for } 0 \leq x \leq a(t) \\ u_y = 0, \sigma_{xy} = 0, \sigma_{zy} = 0, w_y = 0, H_{xy} = 0, H_{zy} = 0 & \quad \text{on } y = 0 \text{ for } a(t) < x \leq L \end{aligned} \tag{16}$$

The initial conditions are

$$\begin{aligned} u_x(x, y, t)|_{t=0} = 0 \quad u_y(x, y, t)|_{t=0} = 0 \quad u_z(x, y, t)|_{t=0} = 0 \\ w_x(x, y, t)|_{t=0} = 0 \quad w_y(x, y, t)|_{t=0} = 0 \quad w_z(x, y, t)|_{t=0} = 0 \\ \frac{\partial u_x(x, y, t)}{\partial t}|_{t=0} = 0 \quad \frac{\partial u_y(x, y, t)}{\partial t}|_{t=0} = 0 \quad \frac{\partial u_z(x, y, t)}{\partial t}|_{t=0} = 0 \end{aligned} \tag{17}$$

3.2 Some results

We now concentrate on investigating the phonon and phason fields in the icosahedral Al-Pd-Mn quasicrystal, in which we take $\rho = 5.1 \text{ g/cm}^3$ and $\lambda = 74.2 \text{ GPa}, \mu = 70.4 \text{ GPa}$ of the phonon elastic moduli, for phason ones $K_1 = 72 \text{ MPa}, K_2 = -37 \text{ MPa}$ and the constant relevant to diffusion coefficient of phason is $\Gamma_w = 1/\kappa = 4.8 \times 10^{-19} \text{ m}^3 \cdot \text{s/kg} = 4.8 \times 10^{-10} \text{ cm}^3 \cdot \mu\text{s/g}$. On the phonon-phason coupling constant, there is no measured result for icosahedral quasicrystals so far, we take $R/\mu = 0.01$ for quasicrystals, and $R/\mu = 0$ for "decoupled quasicrystals" or crystals.

The problem is solved by the finite difference method, the principle, scheme and algorithm are illustrated as those in the previous section, and shall not be repeated here. The testing for the physical model, scheme, algorithm and computer program are similar to those given in Section 2. The numerical results for dynamic initiation of crack growth problem, the phonon and phason displacements are shown in Fig. 5.

The dynamic stress intensity factor $K_I(t)$ is defined by

$$K_I(t) = \lim_{x \rightarrow a_0^+} \sqrt{\pi(x - a_0)} \sigma_{yy}(x, 0, t)$$

and the normalized dynamics stress intensity factor (D.S.I.F.) $\tilde{K}_I(t) = K_I(t) / \sqrt{\pi a_0 p_0}$ is used, the results are illustrated in Fig. 6, in which the comparison with those of crystals are shown, one can see the effects of phason and phonon-phason coupling are evident very much.

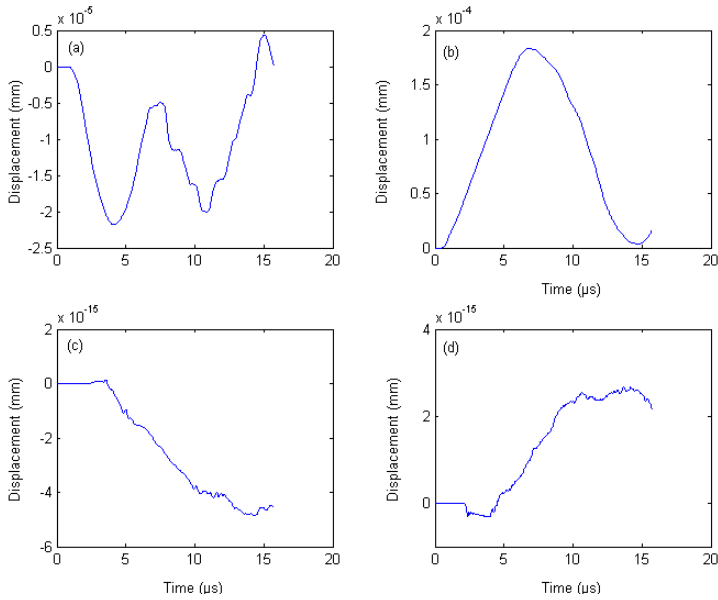


Fig. 5. Displacement components of quasicrystals versus time.

(a) displacement component u_x ; (b) displacement component u_y ;
 (c) displacement component w_x ; (d) displacement component w_y

For the fast crack propagation problem the primary results are listed only the dynamic stress intensity factor versus time as below

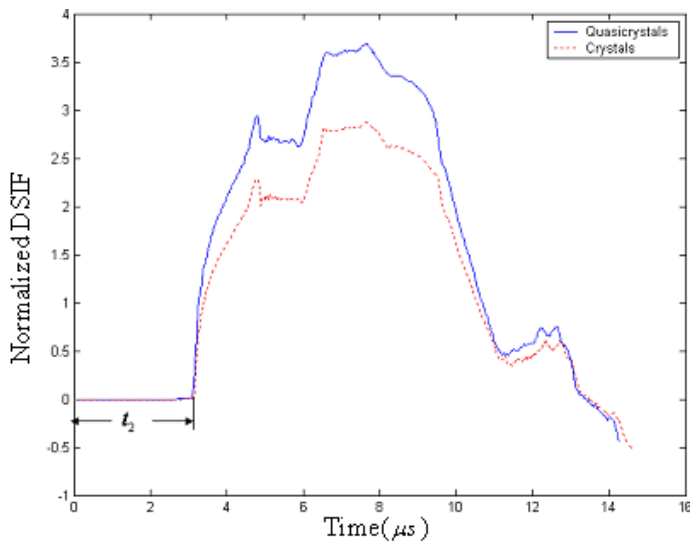


Fig. 6. Normalized dynamic stress intensity factor of central crack specimen under impact loading versus time

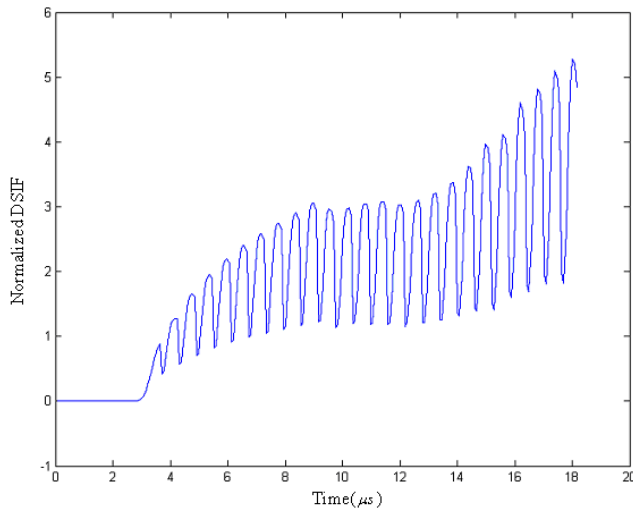


Fig. 7. Normalized stress intensity factor of propagating crack with constant crack speed versus time.

Details of this work can be given by Fan and co-workers [1], [10].

4. Conclusion and discussion

In Sections 1 through 3 a new model on dynamic response of quasicrystals based on argument of Lubensky et al is formulated. This model is regarded as an elasto-hydrodynamics model for the material, or as a collaborating model of wave propagation and diffusion. This model is more complex than pure wave propagation model for conventional crystals, the analytic solution is very difficult to obtain, except a few simple examples introduced in Fan's monograph [1]. Numerical procedure based on finite difference algorithm is developed. Computed results confirm the validity of wave propagation behaviour of phonon field, and behaviour of diffusion of phason field. The interaction between phonons and phasons are also recorded.

The finite difference formalism is applied to analyze dynamic initiation of crack growth and crack fast propagation for two-dimensional decagonal Al-Ni-Co and three-dimensional icosahedral Al-Pd-Mn quasicrystals, the displacement and stress fields around the tip of stationary and propagating cracks are revealed, the stress present singularity with order $r^{-1/2}$, in which r denotes the distance measured from the crack tip. For the fast crack propagation, which is a nonlinear problem—moving boundary problem, one must provide additional condition for determining solution. For this purpose we give a criterion for checking crack propagation/crack arrest based on the critical stress criterion. Application of this additional condition for determining solution has helped us to achieve the numerical simulation of the moving boundary value problem and revealed crack length-time evolution. However, more important and difficult problems are left open for further study. Up to now the arguments on the physical meaning of phason variables based on hydrodynamics within different research groups have not been ended yet, see e.g. Coddens [11], which may be solved by further experimental and theoretical investigations.

5. References

- [1] Fan T Y, 2010, *Mathematical Theory of Elasticity of Quasicrystals and Its Applications*, Beijing:Science Press/Heidelberg:Springer-Verlag.
- [2] Lubensky T C , Ramaswamy S and Joner J, 1985, Hydrodynamics of icosahedral quasicrystals, *Phys. Rev. B*, 32(11), 7444.
- [3] Socolar J E S, Lubensky T C and Steinhardt P J, 1986, Phonons, phasons and dislocations in quasicrystals, *Phys. Rev. B*, 34(5), 3345.
- [4] Rochal S B and Lorman V L, 2002 · Minimal model of the phonon-phason dynamics on icosahedral quasicrystals and its application for the problem of internal friction in the i-AlPdMn alloys, *Phys. Rev. B*, 66 (14), 144204.
- [5] Fan T Y , Wang X F, Li W et al., 2009, Elasto-hydrodynamics of quasicrystals, *Phil. Mag.*, 89(6),501.
- [6] Chernikov M A, Ott H R, Bianchi A et al., 1998, Elastic moduli of a single quasicrystal of decagonal Al-Ni-Co: evidence for transverse elastic isotropy, *Phys. Rev. Lett.* 80(2), 321-324.
- [7] H. C. Jeong and P. J. Steinhardt, 1993, Finite-temperature elasticity phase transition in decagonal quasicrystals , *Phys. Rev. B* 48(13), 9394.
- [8] Walz C, 2003, *Zur Hydrodynamik in Quasikristallen*, Diplomarbeit, Universitaet Stuttgart.
- [9] Zhu A Y and Fan T Y, 2008, Dynamic crack propagation in a decagonal Al-Ni-Co quasicrystal , *J. Phys.: Condens. Matter*, 20(29), 295217.
- [10] Wang X F, Fan T Y and Zhu A Y, 2009, Dynamic behaviour of the icosahedral Al-Pd-Mn quasicrystal with a Griffith crack, *Chin Phys B*, 18 (2), 709.(or referring to Zhu A Y: Study on analytic and numerical solutions in elasticity of three-dimensional quasicrystals and elastodynamics of two- and three-dimensional quasicrystals, Dissertation, Beijing Institute of Technology, 2009)
- [11] Coddens G, 2006, On the problem of the relation between phason elasticity and phason dynamics in quasicrystals, *Eur. Phys. J. B*, 54(1), 37.